Für Sandra

Neue Wege zu funktionalisierten Ferrocenylboranen und borhaltigen Oligoferrocenen

Dissertation

zur Erlangung des Doktorgrades

der Naturwissenschaften

vorgelegt beim Fachbereich Chemische und Pharmazeutische Wissenschaften

der Johann Wolfgang Goethe-Universität

in Frankfurt am Main

von

Matthias Scheibitz

aus Köln

Frankfurt am Main, 2004

vom Fachbereich Chemische und Pharmazeutische Wissenschaften der Johann Wolfgang Goethe-Universität als Dissertation angenommen.

Dekan: Prof. Dr. H. Schwalbe

Gutachter: (1) Prof. Dr. M. Wagner

           (2) Prof. Dr. N. Auner

Datum der Disputation: 21.01.2004

Die vorliegende Arbeit entstand in der Zeit von März 2002 bis August 2004 am Institut für Anorganische und Analytische Chemie der Johann Wolfgang Goethe-Universität Frankfurt am Main.

Mein herzlicher Dank gebührt meinem verehrten Lehrer

Herrn Prof. Dr. Matthias Wagner

für sein mir entgegengebrachtes Vertrauen, Wohlwollen und
für die stets gewährte größtmögliche Unterstützung.

Verwendete Abkürzungen:

Å	Angström
Bu	Butyl, $-(CH_2)_3CH_3$
bipy	2,2´-Bipyridin
br	breit (NMR)
bzw.	beziehungsweise
COG	Schwerpunkt eines Cp-Rings
Cp	Cyclopentadienyl, $-C_5H_5$
d	Dublett (NMR)
δ	chemische Verschiebung in der NMR-Spektroskopie [ppm]
Et	Ethyl, $-CH_2-CH_3$
DFT	Dichtefunktionaltheorie
DMAP	4-N,N-Dimethylaminopyridin
DMS	Dimethylsulfid
Et	Ethyl, $-CH_2CH_3$
exc.	Überschuss
Fc	Ferrocenyl, $-C_5H_4FeC_5H_5$
fc	1,1´-Ferrocendiyl, $(-C_5H_4)_2Fe$
h	Stunde(n)
$h_{1/2}$	Halbhöhenbreite
HOMO	highest occupied molecular orbital
Hz	Hertz
IR	Infrarot
$i_{p,f}$, $i_{p,r}$	Spitzenstrom des „forward-" bzw. „reverse-scans"
IS	Isomerieverschiebung
J	skalare Kopplungskonstante in der Kernresonanzspektroskopie [Hz]
K	Kelvin
12-Krone-4	1,4,7,10-Tetraoxacyclododecan
Lit.	Literaturstelle
LUMO	lowest unoccupied molecular orbital
M	Metallatom
Mc	Metallocenyl, $C_5H_4-M-C_5H_5$

Me	Methyl, -CH_3
MHz	Megahertz
min	Minute(n)
mm	Millimeter
mmol	Millimol
n.a.	Multiplett im NMR-Spektrum erwartet, aber nicht aufgelöst
n.b.	nicht beobachtet (NMR)
NMR	Kernresonanzspektroskopie
Ph	Phenyl, -C_6H_5
q	Quartett (NMR)
QS	Quadrupolaufspaltung
R	beliebiger Rest
RT	Raumtemperatur
s	Sekunde(n); Singulett (NMR)
s.o.	siehe oben
s.u.	siehe unten
sept	Septett (NMR)
THF	Tetrahydrofuran
tr	Triplett (NMR)
v	Vorschubgeschwindigkeit bei der Cyclovoltammetrie
V	Volt
vgl.	vergleiche
vs.	versus
vtr	virtuelles Triplett (NMR)
z.B.	zum Beispiel

Inhaltsverzeichnis

1 Übersicht über die experimentellen Ergebnisse

1.1 Einleitung und Aufgabenstellung

Makromoleküle auf Kohlenstoffbasis bilden die Grundlage des Lebens auf unserer Erde, und sowohl natürliche als auch synthetische Polymere aus Kohlenstoffketten sind in unserem Alltag allgegenwärtig. Sie werden unter anderem als Kunststoffe, Folien und Fasern zur Herstellung unterschiedlichster Produkte wie Autoreifen, Kleidung oder Verpackungen eingesetzt.[1] Vor allem ihre geringe Dichte und leichte Verarbeitbarkeit waren der Grund für den rasch wachsenden Einsatz von Materialien aus *organischen* Polymeren in der zweiten Hälfte des 20. Jahrhunderts. Wesentlichen Anteil am Erfolg dieser Substanzklasse hat die gute Verfügbarkeit preiswerter Monomere, aus denen sich Makromoleküle mit maßgeschneiderten Eigenschaften in hoher Ausbeute und mit geringem Syntheseaufwand darstellen lassen.[2] Deutlich weniger entwickelt sind die Polymerwissenschaften auf dem Gebiet der *anorganischen* und metallhaltigen Polymere.[3] Wirtschaftlich bedeutend sind heute vor allem die Anfang der 30er Jahre des vergangenen Jahrhunderts entwickelten Polysiloxane, die sich durch hohe Flexibilität bei niedrigen Temperaturen, thermische Stabilität und geringe Oxidationsempfindlichkeit auszeichnen,[4] sowie die zu den Polysiloxanen isoelektronischen Polyphosphazene, die unter anderem in der Raumfahrt und im Fahrzeugbau sowie – je nach Substitutionsmuster – als bioinerte oder auch bioaktive Materialien zum Einsatz kommen.[3]

Die anorganische Festkörperchemie stellt ein weiteres zentrales Gebiet der Materialwissenschaften dar, in dessen Rahmen vor allem die Möglichkeiten, die sich aus der chemischen Vielfalt des Periodensystems eröffnen, zur Entwicklung neuer Werkstoffe genutzt werden. Hieraus resultieren häufig Materialien mit vielen wünschenswerten Eigenschaften, die synthetischen Kunstoffen in der Regel fehlen. Dazu zählen die elektrische und thermische Leitfähigkeit, die Übernahme optischer und magnetischer Funktionen sowie die Eignung als Schaltungsträger. Nachteile bestehen

unter anderem darin, dass die Festkörperchemie noch stark empirisch orientiert ist, so dass neue Strukturmotive und physikalische Festkörpereigenschaften nur in eingeschränktem Maße gezielt vorhergesagt werden können. Darüber hinaus erfordern konventionelle Festkörperreaktionen in der Regel drastische Reaktionsbedingungen (hohe Temperaturen, hohe Drücke), und die resultierenden Werkstoffe sind meist schwer verarbeitbar.

Demgegenüber eröffnet das umfangreiche Repertoire der präparativen Komplex-Chemie nahezu unbegrenzte Möglichkeiten des kontrollierten Materialdesigns. Dem Konzept „vom Molekül zum Material" folgend, lassen sich zum Teil äußerst komplexe molekulare Bausteine in Lösung aufbauen, die sich in einem letzten Schritt aufgrund nicht-kovalenter Wechselwirkungen, wie zum Beispiel der Ausbildung von Metall-Ligand-Komplexen, unter Selbstassoziation zu makromolekularen Strukturen zusammenlagern (s.u.). Neben neuen Erkenntnissen für die Grundlagenforschung resultiert das große Interesse an metallhaltigen Polymeren vor allem aus der Kombination von Eigenschaften, die bislang für Festkörper charakteristisch sind, mit denen, die organische Polymere auszeichnen.

1.1.1   Eigenschaften metallhaltiger Polymere

a) Neue konformationelle und morphologische Eigenschaften

Die Koordinationszahl eines Kohlenstoffatoms ist in der Regel ≤ 4 und es werden nur drei unterschiedliche Geometrien eingenommen: linear, trigonal planar und tetraedrisch. Metallatome dagegen können Koordinationszahlen ≤ 12 aufweisen, wobei Komplexe mit vier oder sechs Liganden am häufigsten sind.[5] Überdies ist eine im Vergleich zum Kohlenstoff größere Anzahl unterschiedlicher Koordinationspolyeder bekannt. Komplexe mit vier Liganden können beispielsweise als Tetraeder oder auch quadratisch planar vorliegen. Die unterschiedlichen Bindungstypen, die Übergangsmetalle auszubilden vermögen, führen zu Strukturen, die in der Kohlenstoffchemie gänzlich

unbekannt sind. Zum Beispiel sind Vierfachbindungen zwischen Übergangsmetallatomen möglich, nicht jedoch zwischen Hauptgruppenelementen.

b) Magnetische, elektronische und optische Eigenschaften

Kohlenstoffatome bevorzugen spingepaarte Singulett-Grundzustände. Daher sind die meisten organischen Verbindungen diamagnetisch. Übergangsmetalle können in Abhängigkeit von der Elektronenkonfiguration und dem sie umgebenden Ligandenfeld stabile Ionen bilden, in denen ungepaarte Elektronen vorliegen. Ein besonderes Interesse besteht daher an metallhaltigen Polymeren, in denen geeignete Verknüpfungseinheiten eine Kopplung der magnetischen Momente der Metallatome zulassen, so dass das Gesamtensemble kooperative ferro-, antiferro- oder ferrimagnetische Eigenschaften aufweist.[6, 7]

Die Tatsache, dass viele Übergangsmetallatome in unterschiedlichen Oxidationsstufen vorliegen können, eröffnet den Zugang zu redoxaktiven Materialien, deren Eigenschaften auf elektrochemischem Wege beeinflussbar sind. Überdies wird durch den Einbau von Übergangsmetallen in polymere Strukturen die Erzeugung freier Ladungsträger erleichtert, was unter der Voraussetzung geeigneter Konjugationswege zu interessanten Ladungstransporteigenschaften entlang solcher Makromoleküle führen kann.

Oftmals werden durch die Gegenwart von Übergangsmetallzentren auch bemerkenswerte photophysikalische Eigenschaften in polymeren Strukturen hervorgerufen.[8-10] Beispielsweise führt in **O**rganic **L**ight **E**mitting **D**iodes der Einbau von phosphoreszierenden Platin- oder Iridiumkomplexen (mit relativ kurzen Phosphoreszenzlebensdauern < 100 µs) in die elektrolumineszierende Polymerschicht zu einer erhöhten Quantenausbeute, da angeregte Singulett- *und* Triplettzustände für die Lichterzeugung genutzt werden können.[11, 12] Dies lässt sich darauf zurückführen, dass die sehr starke Spin-Bahn-Kopplung der Schwermetallatome sowohl den *intersystem-crossing*-Prozess (Übergang vom angeregten Singulett- in den Triplettzustand) als auch

die für die Phosphoreszenz verantwortliche Interkombination vom Triplett- zum Grundzustand begünstigt.

c) Aggregationseigenschaften

Besonders interessante Perspektiven zur Herstellung neuer polymerer Materialien eröffnet der Einsatz von Metallionen in der supramolekularen Chemie. Neben den nicht-kovalenten Wechselwirkungen wie Wasserstoffbrücken, *van der Waals*-Kräften und *p*-Stapelung zwischen Aromaten („*p*-stacking"), die in den klassischen organischen Makromolekülen eine bedeutende Rolle spielen, stehen in der metallo-supramolekularen Chemie weitere solcher „schwacher" Wechselwirkungen zur Verfügung:

(1) Selbstorganisations- und Selbsterkennungsprozesse zwischen speziell für diesen Zweck gestalteten Liganden und koordinierenden Metallionen (Elektronenpaar-Donor-Akzeptor-Wechselwirkungen) können zu hochkomplexen, jedoch genau definierten Geometrien wie Helikaten, Fäden, Leitern, Rechen oder Gittern führen.[13-15] Helikale Strukturen beispielsweise werden in der Natur sowohl für die Kodierung von Information auf DNA- und RNA-Basis als auch im Makromolekül Collagen genutzt, das über ausgezeichnete mechanische Eigenschaften verfügt. Nachbilden lassen sich derartige Strukturen über Metallionen-induzierte Helixbildung, wie z. B. die Arbeiten von *Lehn* et. al zeigen (Bild 1.1.1).[16-18]

(2) „Hydrid-Proton"-Brücken ($H^{\delta-}\cdots H^{\delta+}$), an denen elektronenreiche Metallhydride und elektronenarme Wasserstoffsubstituenten beteiligt sind, lassen sich ebenfalls zum Aufbau neuer Materialien mit ausgedehnten Festkörperstrukturen nutzen.[19, 20]

(3) Auf relativistischen Effekten beruhende Anziehungskräfte zwischen Metallatomen (sogenannte d^{10}-d^{10}- Wechselwirkungen), die auf schwere Elemente beschränkt sind, haben ungefähr dieselbe Stärke wie Wasserstoffbrückenbindungen. Prominentestes Beispiel sind die sogenannten „aurophilen" Wechselwirkungen zwischen Gold(I)ionen [Au(I)$\cdots$Au(I)].[21-23]
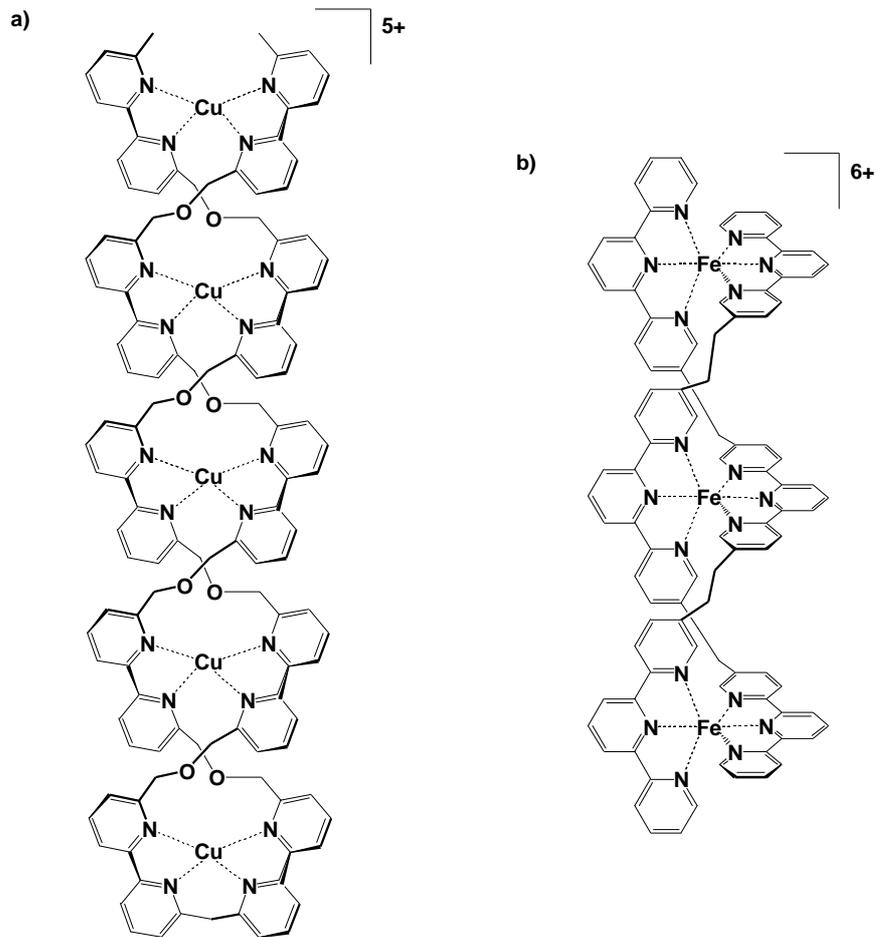
Bild 1.1.1   Helices auf der Grundlage von Bipyridin- und Terpyridinliganden: (a) Doppelhelix mit tetraedrischer Metallkoordination, (b) Doppelhelix mit oktaedrischer Metallkoordination.[18]

Aus diesem breiten Eigenschaftsspektrum metallorganischer Polymere eröffnen sich nicht nur Perspektiven für zahlreiche Anwendungen im Bereich der Materialwissenschaften (als neue leitfähige oder magnetische Werkstoffe sowie als gut verarbeitbare Vorstufen von Spezialkeramiken), sondern auch auf dem Gebiet der Katalyse: Es besteht großes Interesse daran, homogene Katalysatoren, die sich durch ihre hohe Reaktivität und Selektivität auszeichnen, durch Fixierung an polymere Strukturen zu heterogenisieren, wodurch die Rückgewinnung der Edelmetalle und die Abtrennung des Katalysators vom Produkt erleichtert werden.

1.1.2 Strukturelle Einteilung metallhaltiger Polymere

Metallhaltige Polymere lassen sich aufgrund ihrer Strukturmerkmale in unterschiedliche Gruppen einteilen. Eine gängige Einordnung erfolgt danach, ob sich die Metalle in den Seitengruppen (**A**) oder direkt im Polymerrückgrat (**B**) befinden (Bild 1.1.2). Es existieren allerdings auch Mischformen, die Metalle sowohl im Polymerrückgrat als auch in den Seitengruppen tragen. Dendrimere und hochverzweigte Polymere repräsentieren eine weitere Strukturklasse (**C**, Bild 1.1.2). Hier sind die Metallzentren in einigen Fällen über das ganze Molekül verteilt, in anderen hingegen auf den Kern beziehungsweise die Peripherie beschränkt.
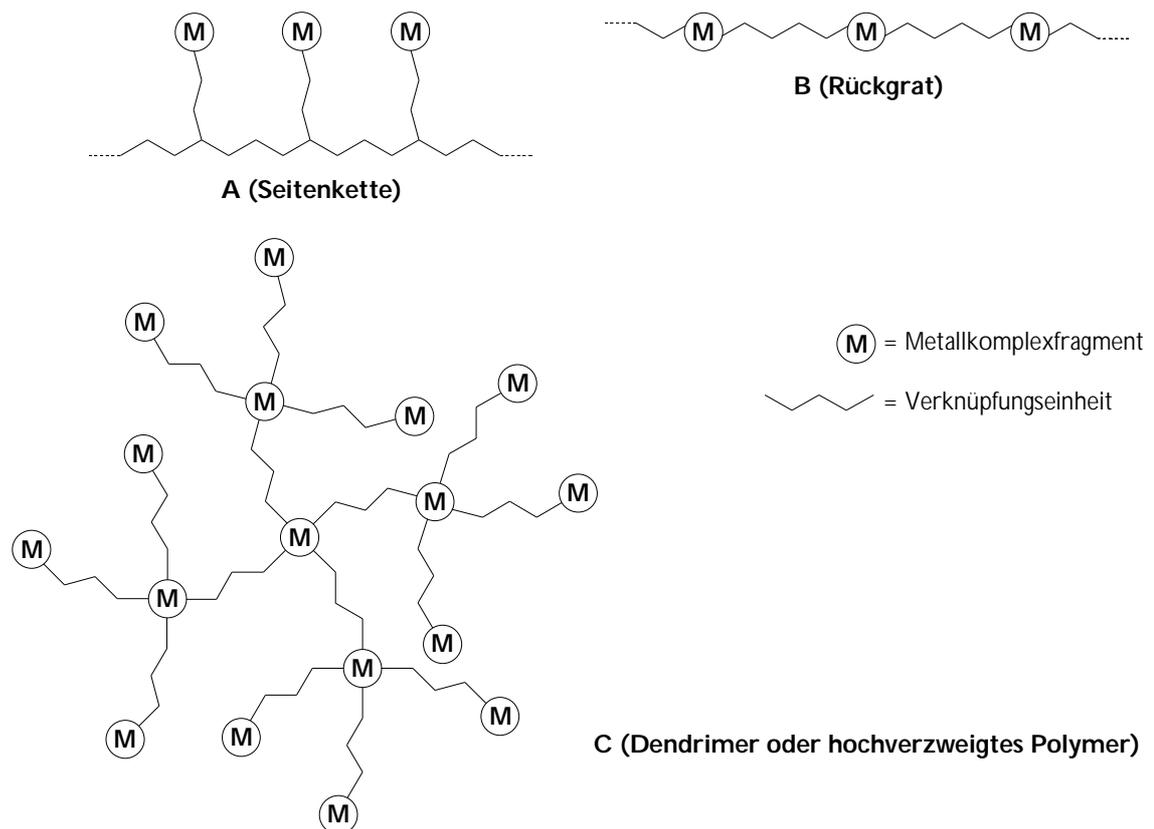
Bild 1.1.2 Strukturelle Einteilung metallhaltiger Polymere.[24]

Die Verknüpfungseinheiten zwischen den Metallzentren können sowohl delokalisierte als auch lokalisierte Elektronensysteme aufweisen, wobei hierdurch nur die beiden Extremzustände beschrieben werden. Untersuchungen, wie durch Variation der Verknüpfungseinheiten die Wechselwirkungen zwischen den Metallen und damit die physikalischen Eigenschaften (Leitfähigkeit, magnetisches Verhalten) der Makromoleküle beeinflusst werden können, sind Gegenstand intensiver Forschung.

1.1.3   Synthese metallhaltiger Polymere

Der Einbau von Metallatomen in die Seitengruppen von Polymeren ist weit entwickelt, da für die Synthese solcher Materialien Strategien modifiziert werden können, die sich bereits zur Darstellung der rein organischen Analoga bewährt haben. Als Beispiel sei hier das erste lösliche metallhaltige Polymer, Poly(vinylferrocen), genannt, das bereits im Jahr 1955 durch radikalische Polymerisation hergestellt wurde (**I**, Schema 1.1.1).[25] Ferner sind Polysilane und Polyphosphazene mit Metallocenseitengruppen, die durch Kondensation (**II**, Schema 1.1.1)[26] bzw. Ring öffnende Polymerisation (**III**, Schema 1.1.1)[27, 28] zugänglich sind, als Vertreter dieser Verbindungsklasse zu nennen.

Für viele Anwendungen sind Polymere **A** (Bild 1.1.2) ausreichend. Für andere Einsatzgebiete wären Makromoleküle des Typs **B** (Bild 1.1.2) besser geeignet, da für solche Materialien eine fundamentale Erweiterung des Eigenschaftsspektrums im Vergleich mit **A** zu erwarten ist:

(a) Interessante Ladungstransportphänomene, die auf Delokalisationseffekten beruhen, treten besonders dann auf, wenn das Metallion integraler Bestandteil eines konjugierten Polymerrückgrats ist.[29]

(b) Materialeigenschaften, die von der Wechselwirkung benachbarter Metallatome abhängen, werden durch konformationelle Änderungen des Polymers weniger beeinflusst, da die direkten Metall-Metall-Abstände weitgehend festgelegt sind.

(c) Der Einfluss der vielfältigen Koordinationsgeometrien von Übergangsmetallen auf die Struktur und die thermophysikalischen Eigenschaften des Polymers ist stärker ausgeprägt.

(1.1)

(1.2)

(1.3)
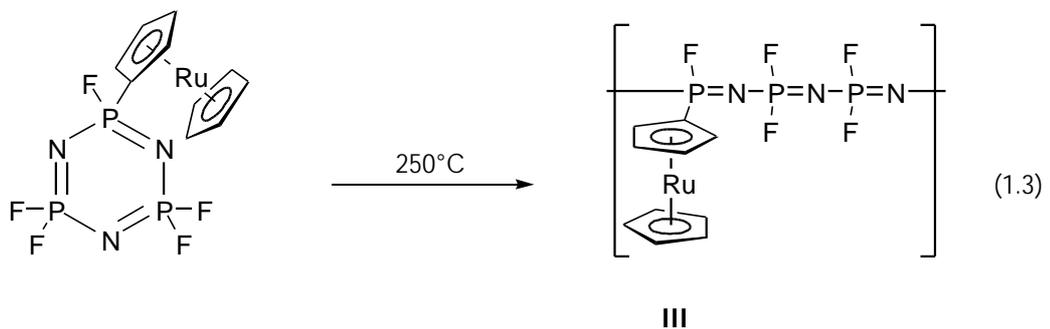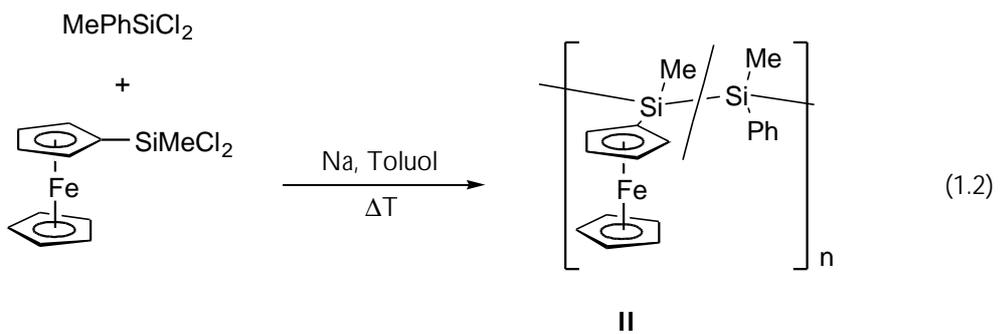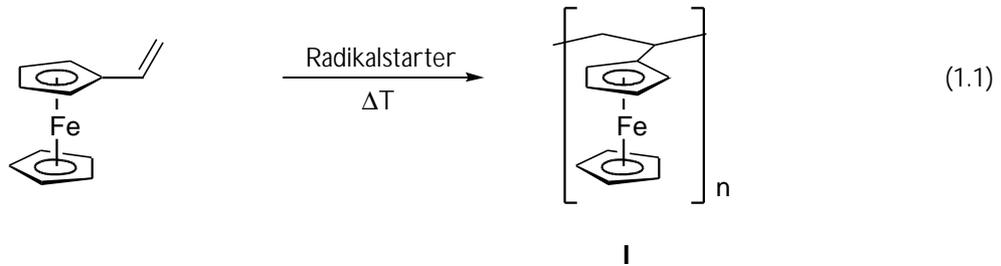
Schema 1.1.1 Synthese metallhaltiger Polymere mit Metallocenen als Seitenketten.

Im Vergleich mit Polymeren, die Metalle in den Seitengruppen tragen, ist die Synthese von Makromolekülen mit Metallzentren im Rückgrat weitaus weniger gut entwickelt. In den vergangenen 20 Jahren wurden drei vielversprechende Syntheserouten entwickelt:

(1) Die Koordinationspolymerisation von Metallkomplexfragmenten, welche durch difunktionelle Liganden miteinander verknüpft werden (**IV**, Schema 1.1.2).[30]

(2) Metallkatalysierte C-C-Kupplungsreaktionen (**V**, Schema 1.1.2).[31]

(3) Die thermisch induzierte[32-34] oder katalytisch geführte[35] Ringöffnungspolymerisation gespannter *ansa*-Ferrocene, die zu Poly(ferrocenylenen) mit unterschiedlichsten Brückenatomen führt (**VI**, Schema 1.1.2).

Ferrocen besitzt als Baustein für metallhaltige Polymere gegenüber anderen Komplexen eine Reihe von Vorzügen. Das Molekül ist sehr stabil, auch gegenüber thermischer Belastung, in großer Vielfalt derivatisierbar, und die meisten seiner Abkömmlinge zeigen einen reversiblen Fe(II)-Fe(III)-Redoxübergang.[36]

Trotz beträchtlicher Fortschritte auf dem Gebiet der Poly(ferrocenylene) (**VI**, Schema 1.1.2) blieben einige wichtige Probleme bislang ungelöst. Zum Beispiel bereitet die Synthese der stark gespannten *ansa*-Ferrocene oft erhebliche Schwierigkeiten, vor allem im Falle des Bors.[37] Aber gerade solche Polymere mit dreifach bzw. vierfach koordinierten Boratomen als Brücke zwischen den Ferroceneinheiten wären von großem Interesse, da aufgrund der Polarität von Bor-Element-Bindungen und – im Falle sp^2-hybridisierter Boratome – zusätzlich durch das leere p_z-Orbital interessante Eigenschaften für diese Materialen zu erwarten sind.

(2.1)

IV

$R = C_6H_{13}$, $Y = H$, Cl, OCH_3, $Ar = C_6H_4Y$

(2.2)

V

(2.3)

$E =$ u. a. Si, Ge, P, As **VI**
$R =$ u. a. Alkyl, Aryl, Halogen
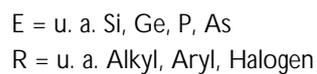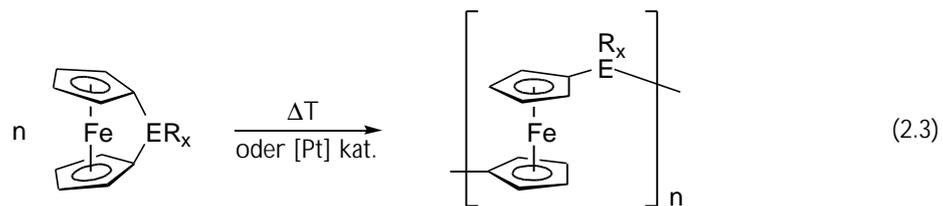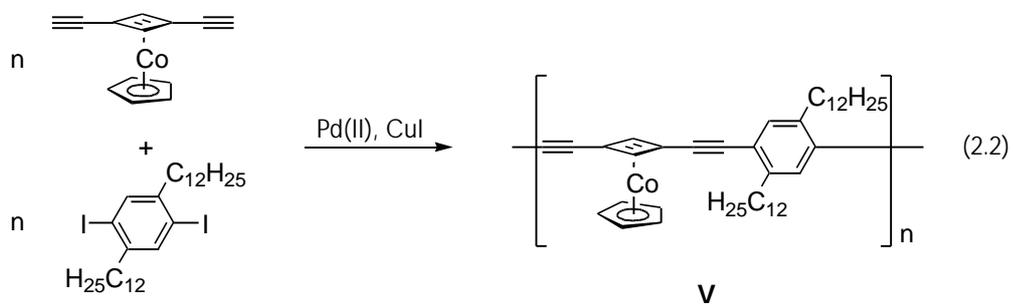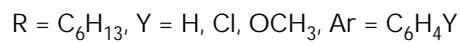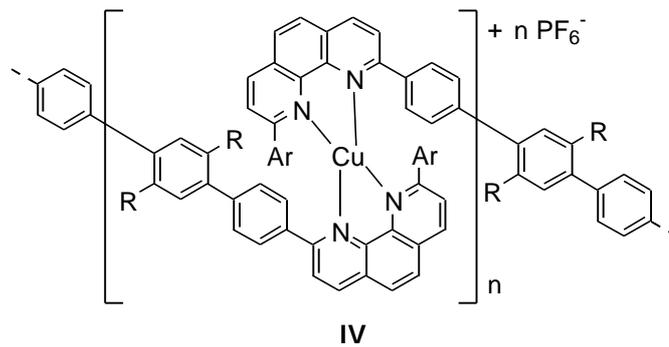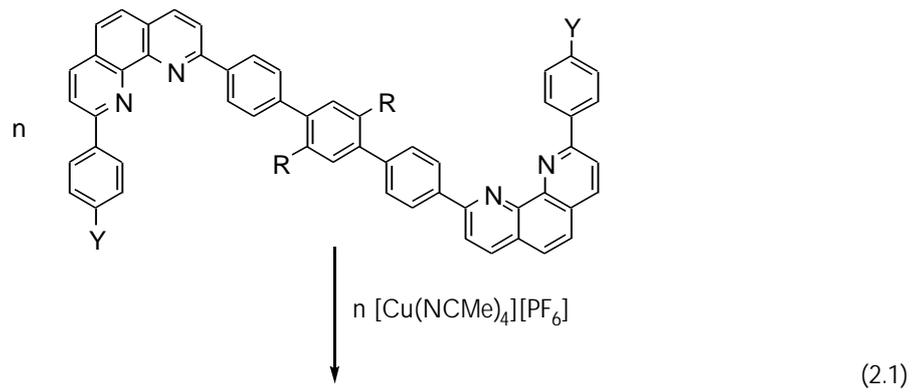
Schema 1.1.2 Ausgewählte Synthesen metallhaltiger Polymere mit Übergangsmetallen als Bestandteil des Polymerrückgrats.

Eine neuartige Syntheseroute für die wichtige Stoffklasse der ferrocenhaltigen Polymere wurde in der Arbeitsgruppe *Wagner* entwickelt.[38] Bei diesem Ansatz macht man sich zunutze, dass eine B-N-Donor-Akzeptor-Bindung isoelektronisch zu einer C-C-Einfachbindung ist (Bild 1.1.3).[39, 40]

M_1, M_2: Übergangsmetallkomplexe
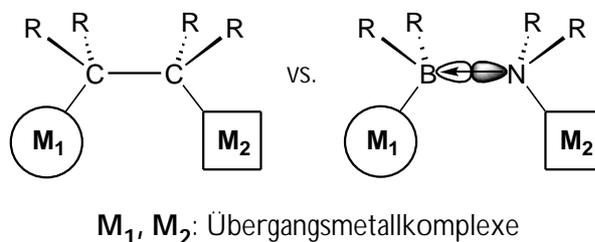
Bild 1.1.3 Verknüpfung von Übergangsmetallkomplexen durch eine dative B-N-Bindung anstelle einer C-C-Einfachbindung.

Enthält ein polymeres Zielmolekül also C-C-Bindungen, die sich nicht oder nur unter Schwierigkeiten aufbauen lassen, kann deren Ersatz durch isoelektronische B-N-Bindungen die Synthese bedeutend erleichtern, da man über die spontane Addukbildung zwischen einem Lewis-sauren Bor- und einem Lewis-basischen Stickstoffzentrum die Vorteile der Koordinationspolymerisation nutzt (siehe unten). Als Borkomponente bieten sich Ferrocenylborane des Typs $FcBR_2$ [$Fc = (C_5H_4)Fe(C_5H_5)$] und 1,1´-fc(BR_2)$_2$ [fc = $(C_5H_4)_2Fe$] mit einem oder zwei Borylsubstituenten an, da sie selektiv und in guten Ausbeuten zugänglich sind.[41, 42] Auf Grundlage des B-N-Verknüpfungskonzeptes wurden unter anderem die beiden Koordinationspolymere **VII** und **VIII** (Bild 1.1.4) hergestellt.

VII   **VIII**
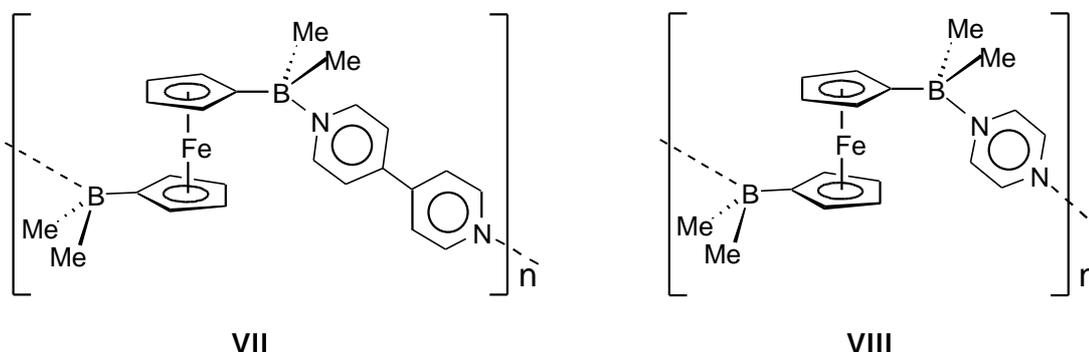
Bild 1.1.4 Ferrocen als Bestandteil von B-N-Koordinationspolymeren.

Die Vorteile der dativen B-N-Bindungen sollen hier noch einmal kurz zusammengefasst werden:

(a) Die Adduktbildung besitzt eine niedrige Aktivierungsbarriere, so dass die Verknüpfung der Monomeren bereits unter sehr milden Bedingungen in nahezu quantitativer Ausbeute erfolgt.

(b) Im Unterschied zu ionischen Kräften oder *van der Waals*-Wechselwirkungen sind B-N-Bindungen gerichtet. Daher ist die Gestalt eines makromolekularen B-N-Adduktes bei bekannter Geometrie der Bausteine in guter Näherung vorhersagbar.

(c) Die Bindungsstärke einer B-N-Brücke lässt sich durch Wahl der Substituenten an Bor und Stickstoff in weiten Grenzen einstellen und somit nach Bedarf maßschneidern. Dies ist ein großer Vorteil im Vergleich zu generell recht schwachen Wasserstoffbrückenbindungen. Darüber hinaus werden supramolekulare Aggregate, die durch Wasserstoffbrücken zusammengehalten werden, meist aus protischen Reaktionsmedien kristallisiert, in denen viele metallorganische Verbindungen nicht existenzfähig sind.

(d) B-N-Addukte lassen sich reversibel – zum Beispiel durch Erhöhung der Temperatur – heterolytisch brechen und eröffnen daher einen Weg zu Makromolekülen, die gezielt wieder depolymerisiert werden können.

(e) Über die starke Polarität von B-N-Bindungen kann die Ladungsdichteverteilung im Molekül, die maßgeblich für dessen physikalisch-chemische Eigenschaften verantwortlich ist, gezielt verändert werden.

Charakteristisch für das hier beschriebene Synthesekonzept ist, dass aus der Bildung dativer B-N-Addukte tetrakoordinierte Boratome als Verknüpfungseinheiten zwischen den Metallfragmenten resultieren (Bild 1.1.3).

Polymere Materialien, die im Gegensatz dazu dreifach koordiniertes Bor enthalten, haben in den vergangenen Jahren ebenfalls reges Interesse geweckt, da sie eine starke Photolumineszenz im blauen Wellenlängenbereich, eine große nichtlineare optische

Suszeptibilität dritter Ordnung sowie einen hohen Grad an Ladungsdelokalisation aufweisen.[43] Ersetzt man sp^2-hybridisierte Kohlenstoffatome innerhalb konjugierter *p*-Systeme durch dreifach koordinierte Boratome, gelangt man auf direktem Wege zu Materialien, die organischen Makromolekülen entsprechen, welche durch partielle Oxidation dotiert wurden.

Chujo et al. konnten durch Hydroborierungspolymerisation aromatischer und heteroaromatischer Diine Materialien mit den oben beschriebenen Eigenschaften herstellen (**IX**, Schema 1.1.3).[44] Mittlerweile sind auch Hybridpolymere bekannt, welche neben Bor die Übergangsmetalle Ruthenium, Palladium oder Platin in der Hauptkette tragen.[45] Die Fluoreszenzspektren dieser Substanzen deuten auf ausgeprägte *p*-Delokalisation hin, die sich sowohl über Bor als auch über das jeweilige Metallion erstreckt.

$$(3.1)$$

Ar = Aromat, Heteroaromat
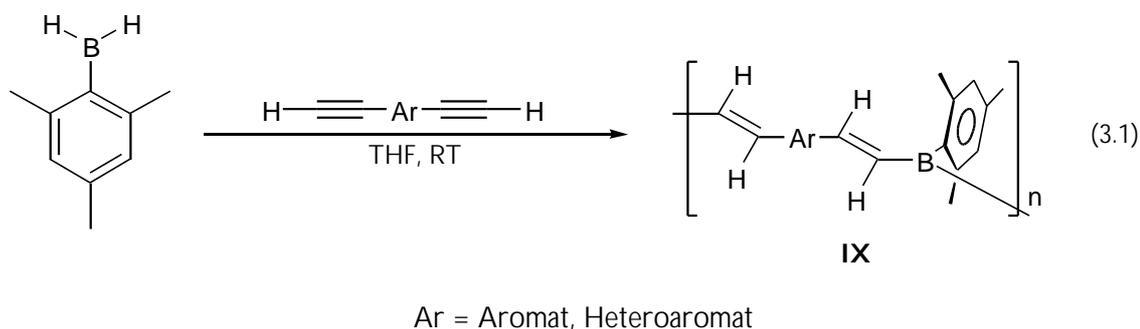
Schema 1.1.3 Hydroborierung von aromatischen Diinen mit Mesitylboran.[44]

1.1.4 Zielsetzung

Im Rahmen des in unserer Arbeitsgruppe entwickelten B-N-Verknüpfungskonzeptes (Bild 1.1.3) wurden bisher nur rein organische Lewis-Basen – in der Regel difunktionelle aromatische Amine wie 4,4´-Bipyridin oder Pyrazin – zur Verknüpfung borylierter Metallocene eingesetzt (Bild 1.1.4), was zwangsläufig zu relativ großen Abständen zwischen den Metallzentren führte.

Das Ziel der vorliegenden Arbeit bestand darin, die Synthesestrategie auf metallorganische Lewis-Basen zu übertragen, um auf diesem Wege mehrkernige Metallkomplexe herzustellen, die geringere Abstände zwischen den Übergangsmetallzentren aufweisen. Für diesen Zweck bieten sich Heterocyclenkomplexe des Eisens an, in denen ein Lewis-basisches Zentrum Bestandteil des fünfgliedrigen Ringes ist. Da 1,1´-Diazaferrocene bislang unbekannt sind, fiel die Wahl auf Phosphaferrocen-Derivate (**X**, **XI**; Bild 1.1.5), die verhältnismäßig gut zugänglich sind und in denen das zentrale Eisenatom ähnliche elektrochemische Eigenschaften wie in Ferrocen aufweist. Außerdem sollte untersucht werden, ob sich die deprotonierten Metallocenderivate Ferrocenyllithium (**XII,** Bild 1.1.5) und 1,1´-Dilithioferrocen (**XIII**, Bild 1.1.5), bei denen es sich um stark Lewis-basische Kohlenstoffanionen handelt, zum Aufbau oligonuclearer Metallkomplexe mit borverbrückten Ferroceneinheiten eignen.
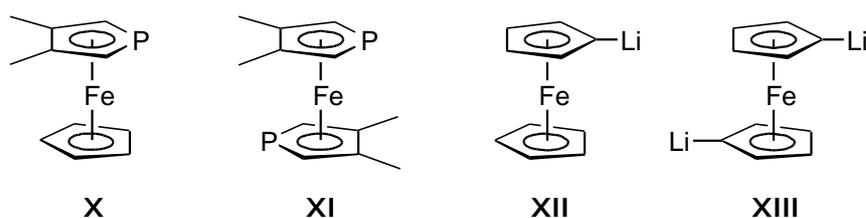
Bild 1.1.5 Von Ferrocen abgeleitete, metallorganische Lewis-Basen.

Da für Polymere mit dreifach koordinierten Boratomen in der Hauptkette interessante Eigenschaften beobachtet wurden (s.o.), bestand ein weiteres Ziel darin, durch die Synthese des Ferrocenylborans $FcBH_2$ einen Weg zu konjugierten Polymeren mit Bor im Rückgrat und Ferrocen in den Seitenketten zu eröffnen, bei dem die von *Chujo* et al. entwickelte Hydroborierungspolymerisation von aromatischen Diinen (Schema 1.1.3) ausgenutzt wird.

1.2 Monomere Ferrocenylborane

Seit mehr als 30 Jahren sind Sandwich- und Halbsandwichkomplexe mit dreifach oder vierfach koordinierten Boratomen als Substituenten an den Cyclopentadienylliganden Gegenstand der Forschung.[46] Einige Vertreter dieser Verbindungsklasse haben als Katalysatoren für die Olefinpolymerisation,[47-49] als Vorstufen oder Bausteine metallorganischer Polymere,[37, 50-52] als Sensoren für Anionen und neutrale Moleküle[53] oder in der Bor-Neutronen-Einfang-Therapie (BNCT) zur Behandlung von Krebs[54] Anwendungen gefunden. Die meisten dieser Komplexe enthalten Elemente der vierten oder achten Nebengruppe des Periodensystems. Für das in unserem Arbeitskreis entwickelte Synthesekonzept zum Aufbau funktioneller metallorganischer Makromoleküle mittels Lewis-Säure-Base-Adduktbildung (Bild 1.1.3) haben sich borylierte Cymantrene (Cyclopentadienylmangantricarbonyl-Komplexe), Ruthenocene und vor allem Ferrocene besonders bewährt. Als grundlegende Synthesebausteine wurden in der vorliegenden Arbeit die von *Siebert* et al. erstmals dargestellten Ferrocenylborane (Schema 1.2.1) gewählt,[41, 42] da

(a) Ferrocen in einem einzigen Schritt mit BBr_3 – in Abhängigkeit von der Stöchiometrie – selektiv ein- bis viermal boryliert werden kann (Schema 1.2.1).

(b) sich durch geeignete Substituenten am Bor die Lewis-Acidität der Borylgruppe leicht und über einen weiten Bereich einstellen lässt.

(c) die Oxidation am Eisenzentrum der meisten Ferrocenderivate reversibel verläuft.

(d) der Bindungszustand des Borzentrums (dreifach koordiniert – frei, vierfach koordiniert – Addukt) einen starken Einfluss auf das Redoxpotential des Eisens hat.[55]

Die primär erhaltenen Dibromoborylferrocene **1**, **2** und **3** lassen sich durch Substitutionsreaktionen an den Boratomen in Derivate unterschiedlicher Lewis-Acidität überführen (Schema 1.2.2).
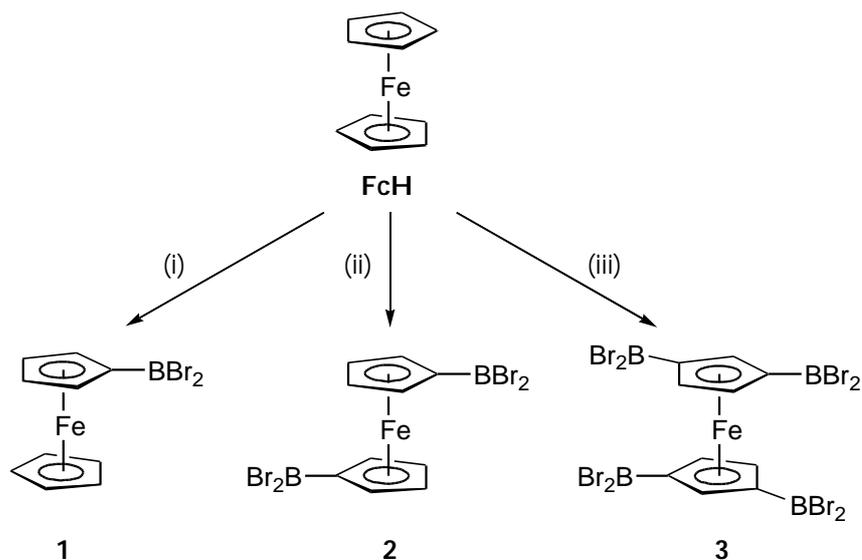
Schema 1.2.1 Darstellung der Ferrocenylborane FcBBr$_2$ (**1**), 1,1´-fc(BBr$_2$)$_2$ (**2**) und 1,1´,3,3´-Fe[C$_5$H$_3$(BBr$_2$)$_2$]$_2$ (**3**): (i) + BBr$_3$, Hexan, 68 °C, 5h; (ii) + 2.5 BBr$_3$, Hexan, 68 °C, 5h; (iii) 10 BBr$_3$, 91 °C, 48h.
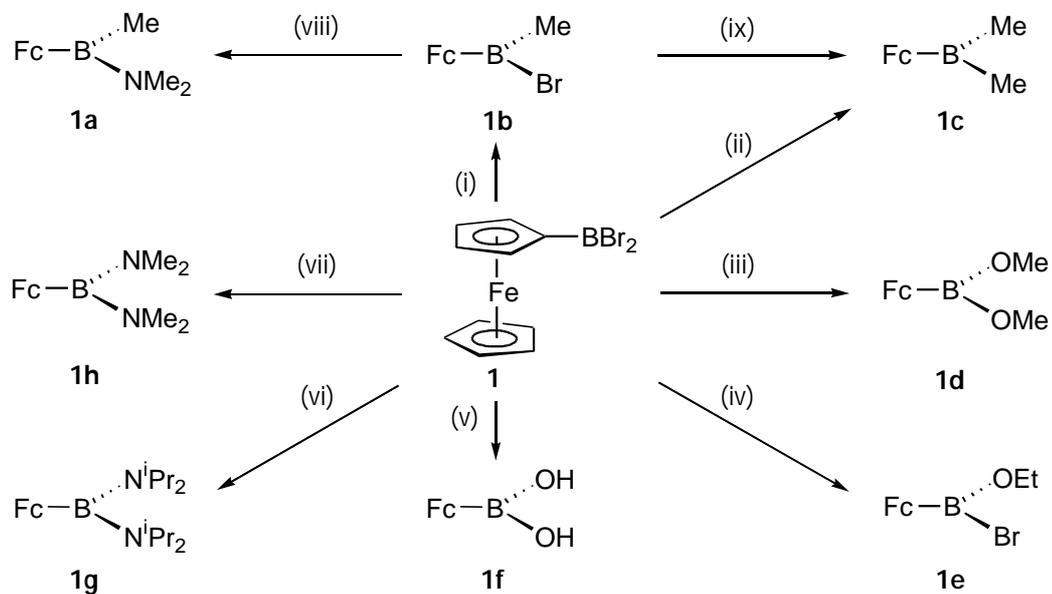
Schema 1.2.2 Ausgewählte Reaktionen von FcBBr$_2$ (**1**): (i) + 1 SnMe$_4$; (ii) + 2.5 SnMe$_4$; (iii) + 2 MeOSiMe$_3$, Toluol; (iv) Et$_2$O, Toluol; (v) + NaOH in H$_2$O; (vi) exc. HN^{i}Pr$_2$, Toluol; (vii) + 2 HNMe$_2$, Toluol; (viii) exc. HNMe$_2$, Toluol; (ix) exc. SnMe$_4$. Die Verbindungen **1b** bis **1e** wurden im Rahmen dieser Arbeit eingesetzt.

1.2.1 Ferrocenylborane FcBR$_2$ und 1,1´-fc(BR$_2$)$_2$ mit R = CR'$_3$, NR'$_2$, OR', Br

Als Fundament dieser Arbeit wurde zunächst eine detaillierte Untersuchung unterschiedlicher mono-, di- und tetraborylierter Ferrocenderivate hinsichtlich ihrer strukturellen und elektronischen Eigenschaften durchgeführt.[56]

Das auffälligste Strukturmerkmal ist die Abwinkelung des BR$_2$-Substitutenten zum Eisenatom hin, die in nahezu allen strukturell charakterisierten Ferrocenylboranen – mehr oder weniger stark ausgeprägt – beobachtet wird. Zur Quantifizierung dieses Effektes wurde der Abknickwinkel $\alpha^* = 180 - \alpha$ eingeführt (Bild 1.2.1).[57] Dabei ist α der Winkel, der vom Schwerpunkt des Cyclopentadienylrings, dem *ipso*-Kohlenstoff- und dem Boratom eingeschlossen wird.
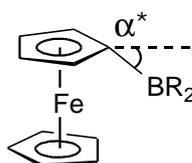
Bild 1.2.1 Definition des Winkel α^*.

Generell beobachtet man mit abnehmender Lewis-Acidität des Borylsubstituenten eine Abnahme von α^*. Ferner führt die successive Einführung mehrerer Borylgruppen am Ferrocen zu einer Verringerung der jeweiligen Abknickwinkel. Diese Ergebnisse werden durch quantenchemische Rechnungen bestätigt, mit Hilfe derer die den jeweiligen Gasphasenstrukturen entsprechenden Molekülgeometrien ermittelt wurden. Somit handelt es sich bei dem Abknickwinkel α^* nicht um einen reinen Kristallpackungseffekt. Da die berechneten Werte für α^* aber stets deutlich kleiner ausfallen als in den experimentell bestimmten Festkörperstrukturen, sind verstärkende Kristallpackungseffekte nicht auszuschließen.

Ursprünglich wurde als Ursache für die Abwinkelung des BR_2-Substituenten eine direkte Wechselwirkung zwischen gefüllten d-Orbitalen am Eisen und dem leeren p-Orbital am Bor postuliert.[57] Entgegen den Erwartungen zeigt eine topologische Analyse der Elektronendichteverteilung[58] für die hypothetische Modellverbindung $FcBH_2$, die in ihrer berechneten Struktur eine Abknickwinkel von $\alpha^* = 26.5°$ aufweist, dass kein bindungskritischer Punkt zwischen Eisen und Bor existiert. Eine detaillierte Untersuchung legt für die Abwinkelung zwei Ursachen nahe. Erstens konnten Molekülorbitale identifiziert werden, an denen das leere p-Orbital am Bor, das p-Orbital am *ipso*-Kohlenstoffatom, d-Orbitale am Eisen und p-Orbitale des zweiten Cyclopentadienylrings beteiligt sind. Überdies hat die Coulombattraktion zwischen dem Borylsubstituenten und dem gegenüberliegenden Cp-Ring wesentlichen Anteil an der Abwinkelung der BR_2-Gruppe.

Neben den strukturellen Besonderheiten der Ferrocenylborane sind vor allem ihre elektrochemischen Eigenschaften von Interesse. Daher wurden die Verbindungen $FcBMe_2$ (**1c**, $E°´ = +0.09V$ vs. FcH/FcH^+), $1,1´-fc(BMe_2)_2$ (**4**, $E°´ = +0.26V$) und $1,1´,3,3´-Fe[C_5H_3(BMe_2)_2]_2$ (**5**, $E°´ = +0.39V$) cyclovoltammetrisch untersucht. Das Halbstufenpotential $E°´$ des Fe(II)/Fe(III)-Übergangs erhöht sich mit steigender Anzahl der Borylsubstituenten kontinuierlich. Diese Verschiebung zu anodischeren Potentialen ist auf die π-Elektronen-ziehende Wirkung der dreifach koordinierten BMe_2-Gruppen zurückzuführen. Bemerkenswert ist die Beobachtung, dass durch Zugabe von 4-N,N-Dimethylaminopyridin [DMAP; ein Äquivalent für **1c** (Schema 1.2.2**), zwei Äquivalente für **4**] und der damit verbundenen Ausbildung der B-N-Addukte **6** und **7** (Bild 1.2.2**), dieser Effekt nicht nur aufgehoben wird, sondern zu einer kathodischen Verschiebung des Fe(II)/Fe(III)-Redoxübergangs deutlich über das Halbstufenpotential des reinen Ferrocens ($E°´ = ±0.00V$) hinaus führt [$E°´$(**6**) $= –0.40V$, $E°´$(**7**) $= –0.66V$; vs. FcH/FcH^+]. Das Diaddukt **7** ist demnach genauso leicht zu oxidieren, wie Decamethylferrocen, welches bereits in metallorganischen *charge-transfer*-Salzen als Elektronendonor eingesetzt wurde.[59] Um weitere Einzelheiten über den Einfluss von dreifach und vierfach koordinierten Borylsubstituenten auf die Elektronenverteilung im Ferrocenrückgrat zu erfahren, wurden die Verbindungen **1c**, **4**, **5**, **6** und **7** mittels Mößbauerspektroskopie untersucht.
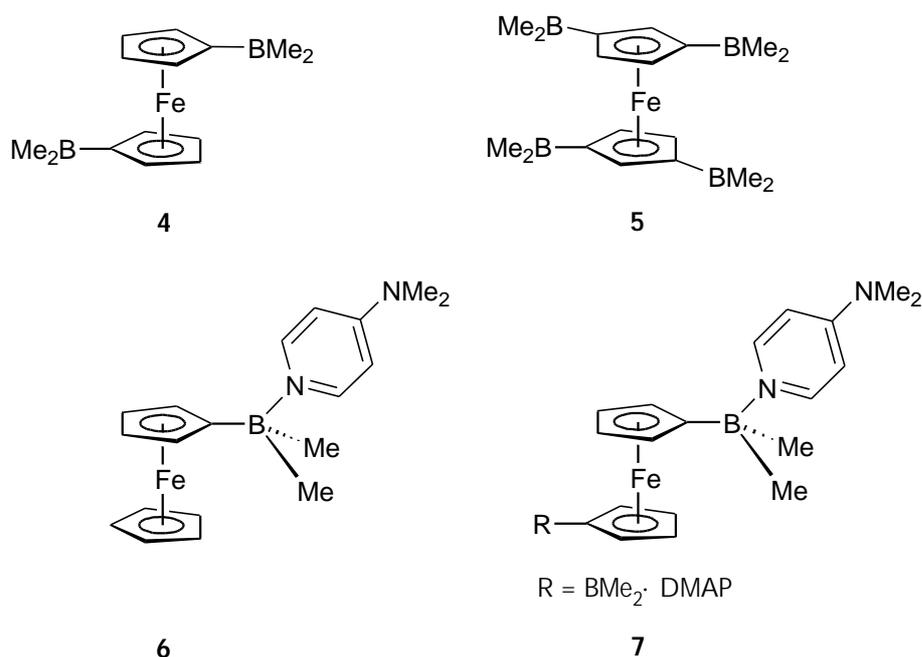
Bild 1.2.2   Die Ferrocenylborane 1,1´-fc(BMe$_2$)$_2$ (**4**) und 1,1´,3,3´-Fe[C$_5$H$_3$(BMe$_2$)$_2$]$_2$ (**5**) sowie die 4-N,N-Dimethylaminopyridin-Addukte von FcBMe$_2$ (**6**) und 1,1´-fc(BMe$_2$)$_2$ (**7**).

Wie erwartet beobachtet man für die Isomerieverschiebungen (IS) vernachlässigbare Unterschiede im Vergleich zu Ferrocen.[60-62] Die Werte für die Quadrupolaufspaltung (QS) dagegen werden mit zunehmender Anzahl an BMe$_2$-Gruppen deutlich kleiner [QS(**1c**) = 2.309(4) mm s^{-1}, QS(**4**) = 2.082(4) mm s^{-1}, und QS(**5**) = 1.891(4) mm s^{-1}]. Diese Ergebnisse zeigen in guter Übereinstimmung mit Untersuchungen anderer Ferrocenderivate,[63-65] dass elektronenziehende Substituenten am Ferrocen zu einer Abnahme von QS führen. Bemerkenswert ist, dass sich entgegen der Erwartung die Quadrupolaufspaltung für die 4-N,N-Dimethylaminopyridin-Addukte [QS(**6**) = 2.344(3) mm s^{-1}, QS(**7**) = 2.339(4) mm s^{-1}] nicht wesentlich von der des Ferrocens (QS = 2.37 mm s^{-1}) unterscheidet, obwohl für diese B-N-Addukte ein stark vermindertes Oxidationspotential beobachtet wird und Elektronen-schiebende Substituenten in der Regel zu einer Erhöhung der Quadrupolaufspaltung führen. Dieses Verhalten lässt sich, gestützt auf quantenchemische Rechnungen, dadurch erklären, dass für das Redoxpotential der Ferrocenylborane die Gesamtladungsdichte, für die

Quadrupolaufspaltung dagegen die relative Population der d-Orbitale nach der Formel $QS \sim 2p_2 - p_1$ verantwortlich ist (p_1: Gesamtpopulation des 3_{xz}- und des 3_{yz}-Orbitals, p_2: Gesamtpopulation des $3_{x^2-y^2}$- und 3_{xy}-Orbitals).[63, 64]

1.2.2   Ferrocenylborane FcBH$_2$ und 1,1´-fc(BH$_2$)$_2$

Die Hydroborierung ist eine äußerst nützliche Reaktion in der organischen Synthese und stellt einen einfachen Zugang zu einer Vielzahl von Organobor-Verbindungen dar.[66, 67] Sie ist auch, wie Arbeiten von *Chujo* et al. zeigen, zum Aufbau von Polymeren geeignet. Beispielsweise wurden durch die Hydroborierungspolymerisation aromatischer Diine mit Mesitylboran, MesBH$_2$ (Mes = 2,4,6-Trimethylphenyl), Makromoleküle mit einem konjugierten Rückgrat hergestellt (Schema 1.1.3), die sich durch eine starke Photolumineszenz im blauen Wellenlängenbereich und einen hohen Grad an Ladungsdelokalisation auszeichnen. Vor diesem Hintergrund bestand ein Ziel der vorliegenden Arbeit in der Synthese von Ferrocenylboranen mit ein oder zwei BH$_2$-Substituenten, um über die Hydroborierungsreaktion einen Weg zu konjugierten Polymeren mit Bor im Rückgrat und Ferrocen als Seitenkette zu eröffnen. Überdies wären BH$_2$-substituierte Ferrocenylborane aus folgenden Gründen von großem Interesse:

(a) Die Hydroborierung von ungesättigten Verbindungen ermöglicht auch in den Fällen die Einführung organischer Reste R am Borylsubstituenten des Metallocens, in denen die Verwendung von Organolithium- oder Grignardverbindungen nicht möglich ist.

(b) Es ist zu erwarten, dass es sich bei den sterisch wenig anspruchsvollen Metallocenylboranen (McBH$_2$) um relativ starke Lewis-Säuren handelt, so dass auch mit sperrigen Lewis-Basen – wie zum Beispiel Trialkylaminen – stabile Addukte möglich sind, die im Falle größerer Reste R am Bor nicht gebildet werden.

Vor diesem Hintergrund wurden bereits von zahlreichen Arbeitsgruppen vergebliche Versuche unternommen, Ferrocenylborane mit Wasserstoffsubstituenten am Bor herzustellen.[68] Im Rahmen dieser Arbeit konnte erstmals eine effiziente Syntheseroute zu den gewünschten Verbindungen erarbeitet werden.

1.2.2.1   Synthese, Struktur und Reaktivität von Ferrocenylboran FcBH$_2$

Die Synthese von Ferrocenylboran FcBH$_2$, das in Form seiner Lewis-Säure-Base-Addukte mit Dimethylethylamin (**9·NMe$_2$Et**) oder Dimethylsulfid (**9·DMS**) isoliert werden kann, geht von FcB(OEt)Br (**1e,** Schema 1.2.2)[69] oder – in einer verbesserten Variante – von FcB(OMe)$_2$ (**1d**, Schema 1.2.2) aus,[70] das im Rahmen dieser Arbeit erstmals dargestellt und strukturell charakterisiert wurde.[56] Durch Umsetzung mit Lithiumalanat in Diethylether erhält man in beiden Fällen das Lithiumsalz des Ferrocenylboranats FcBH$_3$Li (**8**) (Schema 1.2.3).
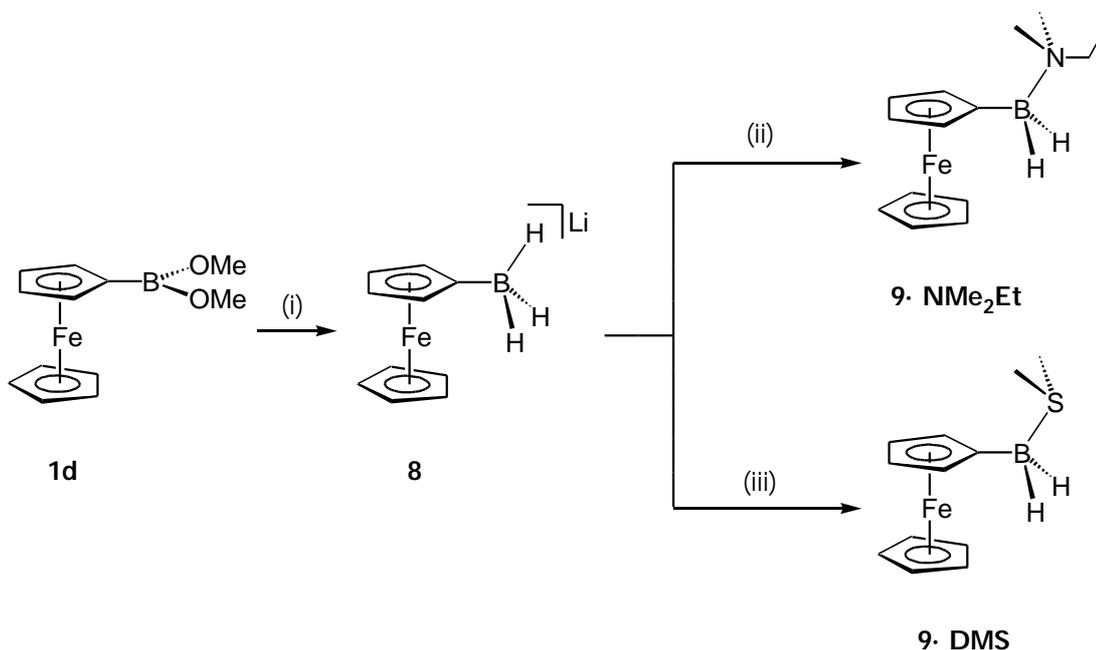
Schema 1.2.3 Synthese von FcBH$_2$•NMe$_2$Et (**9•NMe$_2$Et**) und FcBH$_2$•SMe$_2$ (**9•DMS**):
(i) + LiAlH$_4$, Et$_2$O, 0°C, 1h; (ii), + ClSiMe$_3$, NMe$_2$Et, Et$_2$O, –78 °C;
(iii) + ClSiMe$_3$, SMe$_2$, –78 °C.

Von Alkalimetall-Tetrahydroboraten sind zahlreiche Kristallstrukturen bekannt.[71] Die beobachtete strukturelle Vielfalt basiert auf den unterschiedlichen Koordinationsmöglichkeiten der BH_4^--Ionen an die Kationen. Der zweite wichtige die Struktur bestimmende Faktor sind die Lösungsmittel- bzw. Donormoleküle, die mit den Tetrahydroborat-Ionen um die Koordinationsstellen am Kation konkurrieren. Auch im Fall von **8** ist eine starke Abhängigkeit der Kristallstruktur von der Natur und der Anzahl der Solvatmoleküle zu beobachten. In Gegenwart von Kronenether, 12-Krone-4, wird $FcBH_3Li(12\text{-Krone-4})$ (**8a**) als monomerer Komplex erhalten, in dem die Koordinationssphäre des Lithiumions durch den Kronenether nahezu vollständig abgesättigt wird. In Abwesenheit von Kronenether kristallisiert $FcBH_3Li(Et_2O)_2$ (**8b**) aus Diethylether in Form eines Dimers, während bei der Umkristallisation von **8b** aus Pentan $FcBH_3Li(Et_2O)$ (**8c**) als Tetramer isoliert wird. Im Folgenden werden die Feskörperstrukturen von **8a**, **8b** und **8c** mit denen ausgewählter $LiBH_4$-Ethersolvate verglichen.[71]

Die BH₄-Einheit von $LiBH_4$ kann über ein, zwei oder drei Hydridliganden an ein Metallzentrum koordinieren oder aber isoliert vorliegen (Bild 1.2.3). Da das Tetrahydroborat-Ion auch mehrere Metallionen verbrücken kann, sind zweikernige oder polymere Strukturen keine Seltenheit.[71] Zur exakten Beschreibung der Koordination des Tetrahydroborat-Ions nutzt man das folgende allgemeine Symbol: am_c^b (Bild 1.2.3). Der Faktor a entspricht der Anzahl von Wasserstoffatomen im Komplex, welche dieselbe Koordination aufweisen, der Exponent b der Anzahl der Metallzentren, die an ein Wasserstoffatom koordinieren, und der Index c der Zahl der Wasserstoffatome, die mit demselben Metallzentrum in Wechselwirkung stehen. Mit Hilfe dieser Nomenklatur ist eine Beschreibung der Koordination der FcBH₃-Anionen an die Lithium-Kationen in den Festkörperstrukturen von **8a**, **8b** und **8c** möglich.

Nach Zugabe von 12-Krone-4 kristallisiert $FcBH_3Li$ (**8**) aus einer THF-Lösung zusammen mit einem Äquivalent Kronenether als einkerniger Komplex in der orthorhombischen Raumgruppe *Pnma*.[72]
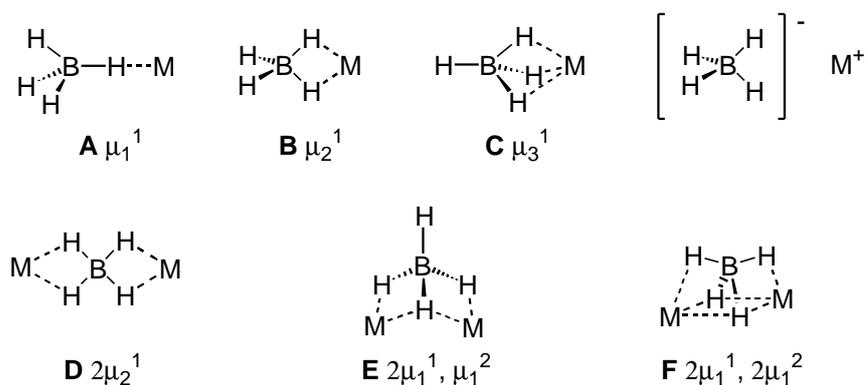
Bild 1.2.3 Koordinationsmöglichkeiten des Tetrahydroborats (Auswahl).

Jedes Li^+-Ion wird von vier Sauerstoffatomen eines Kronenether-Moleküls sowie zwei Wasserstoffatomen des BH_3-Fragmentes komplexiert. Aufgrund sterischer Abstoßung zwischen dem Kronenether und dem Ferrocenylrest nimmt die BH_3-Gruppe in $FcBH_3Li$(12-Krone-4) (**8a**) eine Position ein, die zwischen einer m_2^1- und einer m_3^1-Koordination liegt (Bild 1.2.3).

Aus einer gesättigten Etherlösung kristallisiert $FcBH_3Li(Et_2O)_2$ (**8b**) in der monoklinen Raumgruppe $P2_1/c$.[70] In der Elementarzelle befinden sich zwei Moleküle, welche über die Lithiumionen und BH_3-Substituenten am Ferrocen miteinander zu einem zentrosymmetrischen Dimer verknüpft sind (Bild 1.2.4). Jedes Li^+-Ion wird von zwei Ethermolekülen komplexiert. Aus einer $2m_1^1, m_1^2$-Koordination beider BH_3-Gruppen (zwei Wasserstoffatome koordinieren jeweils an ein Li-Atom und ein Wasserstoffatom verbrückt beide Li-Atome) resultiert ein nahezu quadratischer, planarer Li-B-Li-B-Vierring im Zentrum des Komplexes [B(1)···Li(1) = 2.510(6) Å, B(1)···Li(1A) = 2.455(6) Å, B(1)-Li(1)-B(1A) = 97.5(2)°, Li(1)-B(1)-Li(1A) = 82.4(2)°]. Aus der Anordnung der Ethermoleküle und der Ferrocenylreste resultiert eine organophile „Hülle" um den polaren Kern des Komplexes. Dies hat zur Folge, dass **8b** zu einem gewissen Maße auch in unpolaren Solventien löslich ist.[71]
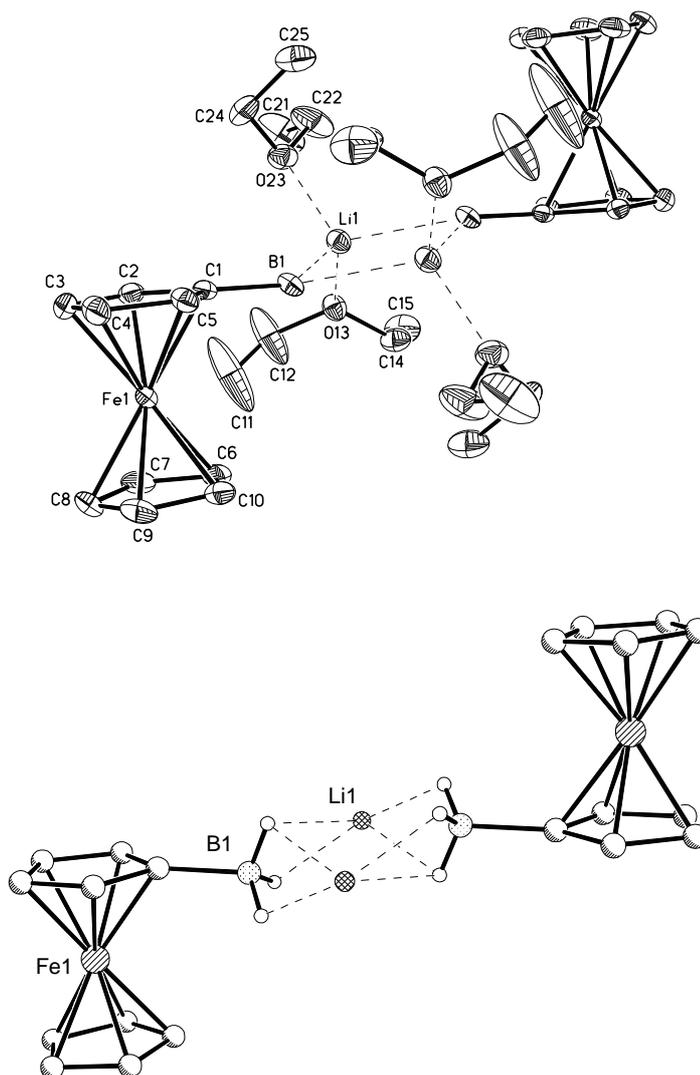
Bild 1.2.4   Struktur von **8b** im Kristall (oben; die anisotropen Auslenkungsparameter
                   entsprechen 50 % Aufenthaltswahrscheinlichkeit) und Koordination der
                   Boratgruppen an die Lithiumionen (unten; Lösungsmittelmoleküle wurden aus
                   Gründen der Übersichtlichkeit weggelassen).

Einkristalle von FcBH$_3$Li(Et$_2$O) (**8c**) konnten aus einer Pentanlösung von **8b** erhalten
werden. **8c** kristallisiert in der triklinen Raumgruppe $P\bar{1}$ mit vier Molekülen pro
Elementarzelle (Bild 1.2.5).[73] Die vier Moleküle sind über ihre BH$_3$-Fragmente und die
Lithiumionen zu einem Tetramer mit einem Inversionszentrum verknüpft.
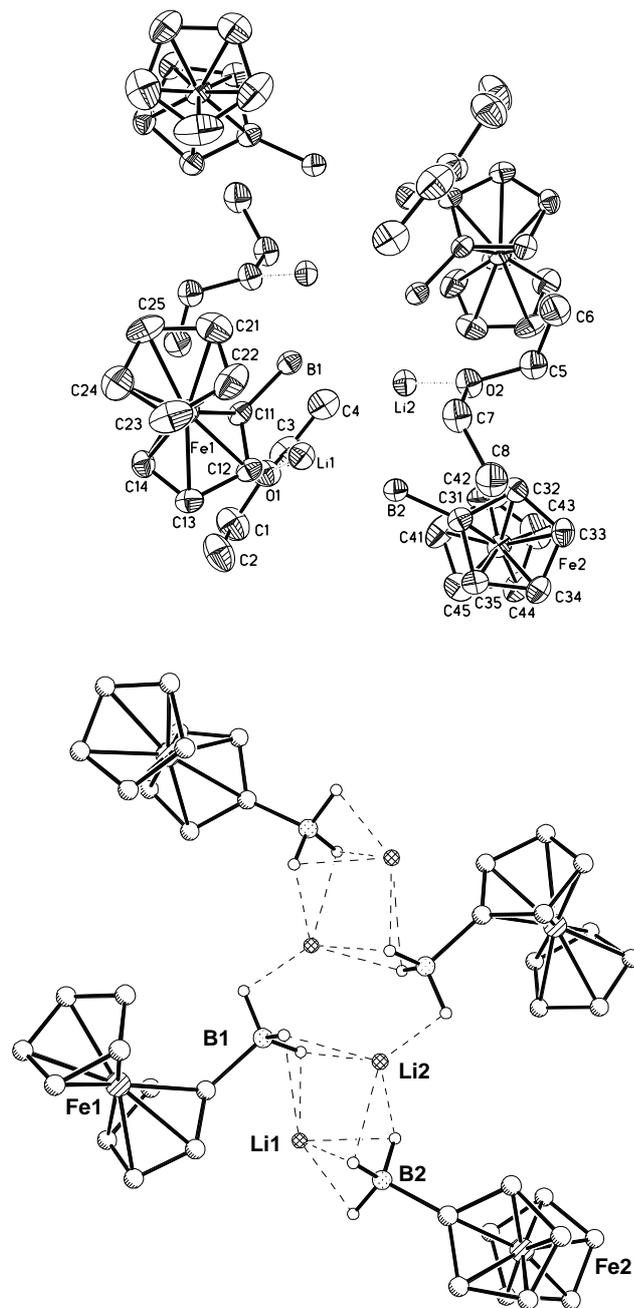
Bild 1.2.5 Einkristall-Röntgenstruktur von **8c** (oben; die anisotropen Auslenkungsparameter entsprechen 50 % Aufenthaltswahrscheinlichkeit) und Koordination der Boratgruppen an die Lithiumionen (unten; Lösungsmittelmoleküle wurden aus Gründen der Übersichtlichkeit weggelassen).

Wie in **8b** besteht das Zentrum des Oligomers in **8c** aus einem nahezu quadratischen Li-B-Li-B-Vierring, in dem die BH$_3$-Einheiten aber eine $2\eta_1^2, \eta_1^1$-Koordination einnehmen (zwei Wasserstoffatome verbrücken jeweils zwei Li-Atome und ein Wasserstoffatom koordinieren an nur ein Li-Atom). Die Kanten des Viereckes in **8c** sind etwas länger [B(1)···Li(2) = 2.579(6) Å, B(1)···Li(2A) = 2.553(6) Å, B(1)-Li(1)-B(1A) = 92.7(2)°, Li(2)-B(1)-Li(2A) = 87.3(2)°] als in **8b**. Die Strukturen von **8b** und **8c** unterscheiden sich vor allem durch die veränderte Koordinationssphäre an den Li$^+$-Ionen des Vierrings. Anstelle von zwei Ethermolekülen in **8b** (Bild 1.2.4) weist Li(2) in **8c** neben einem Ethermolekül zwei Wasserstoffatome einer weiteren Borateinheit als Liganden auf. Die BH$_3$-Gruppe an C(31) verknüpft die beiden Lithium-Atome Li(1) und Li(2) durch Einnahme einer $2\eta_1^2, \eta_1^1$-Koordination. Insgesamt ergibt sich für das Tetramer eine leiterartige Struktur aus sich abwechselnden Lithium-Kationen und BH$_3$-Fragmenten.

Um aus FcBH$_3$Li (**8**) das Lewis-Säure-Base-Addukt FcBH$_2$·NMe$_2$Et (**9·NMe$_2$Et**) zu erhalten, versetzt man eine Etherlösung von **8** in Gegenwart des Amins mit einem Überschuss an Trimethylchlorsilan (Schema 1.2.3).[69] Von FcBH$_2$·NMe$_2$Et (**9·NMe$_2$Et**) können zwei Polymorphe, **9·NMe$_2$Et^I** und **9·NMe$_2$Et^{II}**, isoliert werden, die sich strukturell nur im Torsionswinkel um die B-N-Bindung unterscheiden (Bild 1.2.6). In **9·NMe$_2$Et^I** (trikline Raumgruppe $P\bar{1}$; Kristallisation aus Pentan bei tiefen Temperaturen) beträgt der Torsionswinkel C(11)-B(1)-N(1)-C(3) = 178.5(5)°,[69] während in **9·NMe$_2$Et^{II}** (monokline Raumgruppe $P2_1$; Kristallisation durch langsames Entfernen des Lösungsmittels Pentan bei Raumtemperatur) ein Winkel C(11)-B(1)-N(1)-C(3) von −59.9(17)° beobachtet wird (Bild 1.2.6).[74]

Führt man die Reaktion von **8** mit Trimethylchlorsilan in Dimethylsulfid als Lösungsmittel durch (Schema 1.2.3), erhält man das Dimethylsulfid-Addukt von FcBH$_2$ (**9·DMS**).[75] Kristalle von **9·DMS** konnten aus Dimethylsulfid durch vorsichtiges Entfernen des Lösungsmittels erhalten werden [orthorhombische Raumgruppe $Pca2_1$, zwei kristallographisch unabhängige Moleküle in der asymmetrischen Einheit (**9·DMS^A**, **9·DMS^B**), Bild 1.2.7].
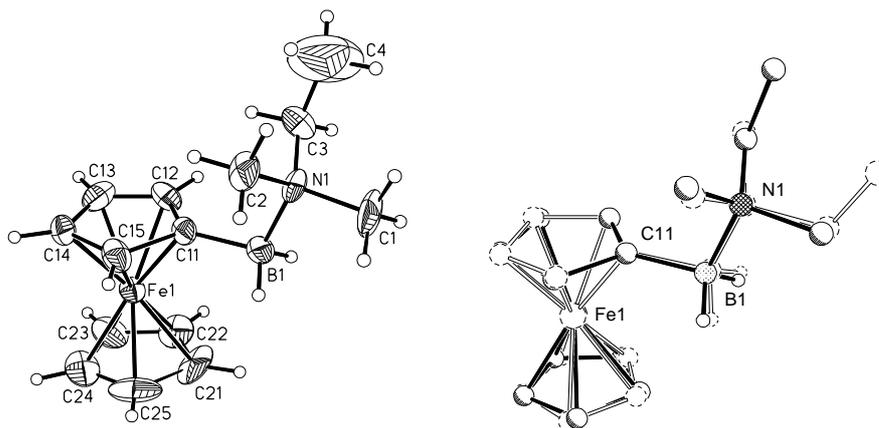
Bild 1.2.6   Struktur von **9·NMe₂Etᴵᴵ** im Kristall (links; die anisotropen Auslenkungsparameter entsprechen 50% Aufenthaltswahrscheinlichkeit) und Überlagerung der beiden Polymorphe **9·NMe₂Etᴵ** und **9·NMe₂Etᴵᴵ** (rechts).

Die beiden Moleküle **9·DMSᴬ** und **9·DMSᴮ** unterscheiden sich, ähnlich wie die beiden Polymorphe **9·NMe₂Etᴵ** und **9·NMe₂Etᴵᴵ**, vor allem in der Orientierung, die von der Lewis-Base relativ zum Ferrocenylboran eingenommen wird. In **9·DMSᴬ** beträgt der Torsionswinkel C(11)-B(1)-S(1)-C(1) um die B(1)-S(1)-Bindung 177.7(6)° in **9·DMSᴮ** hingegen –74.8(7)° (Bild 1.2.7).
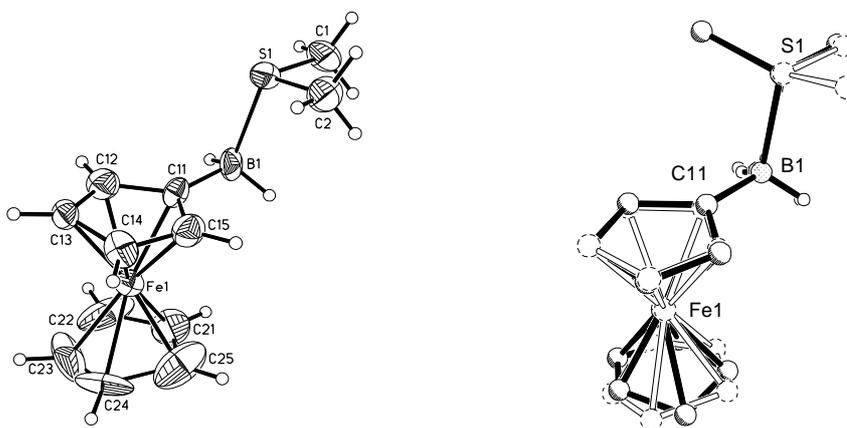

Bild 1.2.7   Einkristall-Röntgenstruktur von **9·DMSᴬ** (links; die anisotropen Auslenkungsparameter entsprechen 50% Aufenthaltswahrscheinlichkeit) und Überlagerung der beiden kristallographisch unabhängigen Moleküle **9·DMSᴬ** und **9·DMSᴮ** (rechts).

Die Koordination von FcBH$_2$ (**9**) an SMe$_2$ hat kaum einen Einfluss auf dessen Struktur. Der C$_2$S-Bindungswinkel von 100.0(5)° in **9·DMS^A** bzw. von 98.7(4)° in **9·DMS^B** und die SC-Abstände [**9·DMS^A**: S(1)-C(1) = 1.766(10) Å, S(1)-C(2) = 1.766(7) Å; **9·DMS^B**: S(1)-C(1) = 1.778(7) Å, S(1)-C(2) = 1.829(10) Å] lassen darauf schließen, dass den Schwefelatomen kein sehr ausgeprägter Sulfoniumcharakter zukommt. Im Trimethylsulfoniumiodid werden zum Beispiel deutlich längere SC-Abstände von 1.85(1) Å beobachtet.[76] Insgesamt gleichen die Strukturparameter von **9·DMS^A** und **9·DMS^B** weitgehend denen von (H$_3$C-S-CH2-BH$_2$)$_2$ [B-S = 1.951(2) Å; **9·DMS^A**: B(1)-S(1) = 1.991(11) Å; **9·DMS^B**: B(1)-S(1) = 1.953(11) Å].[77]

Das freie Ferrocenylboran FcBH$_2$ (**9**) kann nicht isoliert werden. Führt man die Hydridabspaltung mittels Trimethylchlorsilan (Schema 1.2.3) in Abwesenheit von Lewis-Basen durch, erhält man nicht das für eine RBH$_2$-Verbindung erwartete Dimer (FcBH$_2$)$_2$, welches durch B-H-B-Mehrzentrenbindungen stabilisiert würde, sondern Diferrocenylboran Fc$_2$BH (**10**) und Diboran (Schema 1.2.4).
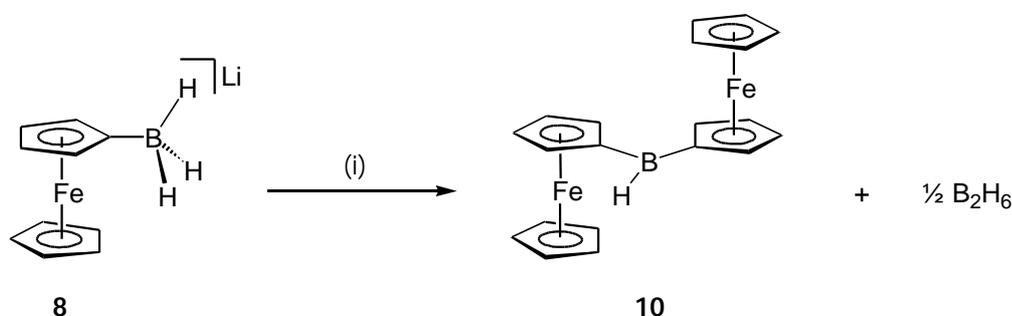
Schema 1.2.4 Synthese von Diferrocenylboran Fc$_2$BH (**10**): (i) + Me$_3$SiCl, Et$_2$O.

Bemerkenswert an Fc$_2$BH (**10**) ist, dass es sowohl in Lösung als auch im Festkörper monomer vorliegt. Im IR-Spektrum von **10** (Nujolverreibung) beobachtet man eine starke Absorption bei 2360 cm^{-1}, welche in dem für terminale B-H-Schwingungen typischen Bereich liegt (vgl. monomeres Dithexylboran:[78] 2470 cm^{-1}; Trip$_2$BH:[79] 2460 cm^{-1}, Trip = 2,4,6-Triisopropyphenyl). Diese Bande erscheint im Falle von Fc$_2$BD (**10a**)[80] zu deutlich geringeren Wellenzahlen verschoben (1830 cm^{-1}, Bild 1.2.8), wie

es für einen Austausch von Wasserstoff gegen Deuterium zu erwarten ist (vgl. Dithexylboran-d$_1$:[78] 1820 cm^{-1}).
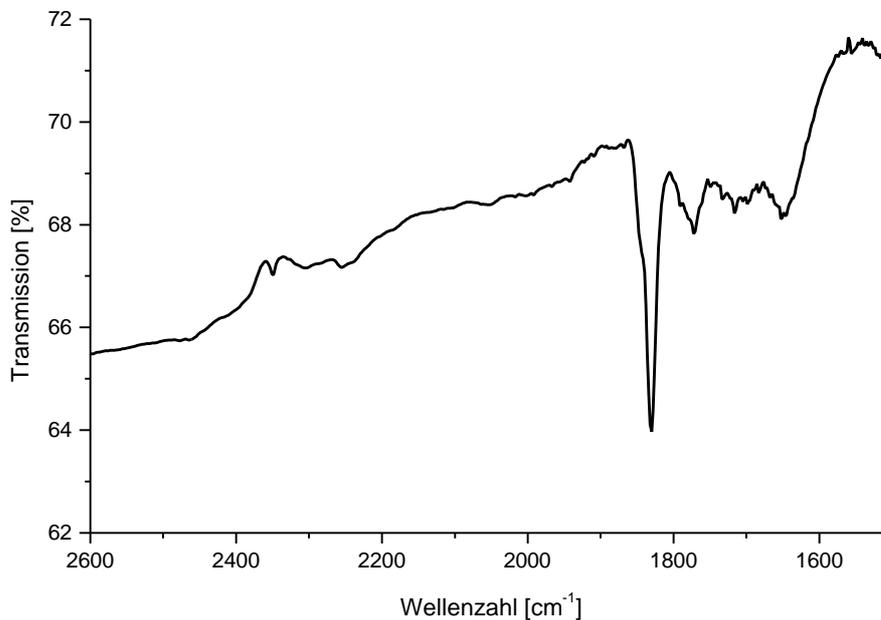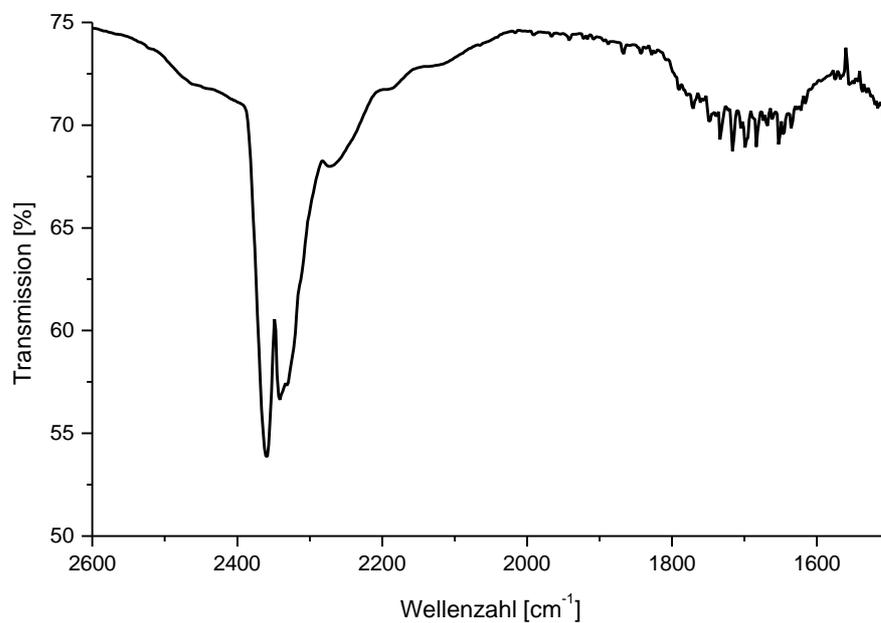
Bild 1.2.8 IR-Spektren von Fc$_2$BH (**10**, oben) und Fc$_2$BD (**10a**, unten) (Nujolverreibung).

Den endgültigen Strukturbeweis erbrachte schließlich die Einkristall-Röntgenstrukturanalyse von **10**.[69] Die Befunde der kristallographischen und NMR-spektroskopischen Untersuchungen weisen darauf hin, dass für die monomere Struktur von Fc_2BH (**10**) nicht nur sterische, sondern vor allem auch elektronische Faktoren verantwortlich sind: Die Ferrocenylgruppen können dem Boratom so effektiv Elektronendichte zur Verfügung stellen, dass eine Ausbildung von Mehrzentrenbindungen nicht notwendig ist.

Zusätzlich wurde Diferrocenylboran, Fc_2BH, mittels Cyclovoltammetrie untersucht, um herauszufinden, ob sich die beiden Ferroceneinheiten reversibel oxidieren lassen und ob die dreifach koordinierte Borbrücke eine elektronische Wechselwirkung zwischen den Metallzentren zulässt. Bei Raumtemperatur beobachtet man ein elektrochemisches Verhalten, das auf einen EC-Mechanismus schließen lässt, d. h. auf den Elektronentransfer folgt eine irreversible chemische Reaktion (EC_{irr}).[81] Dabei könnte es sich um die Zersetzung von **10** handeln, es wäre aber auch möglich, dass das Molekül nach der Oxidation durch Ausbildung von Mehrzentrenbindungen dimerisiert, da dem Boratom von den Ferroceneinheiten nur noch eine geringe Menge an Elektronendichte zur Verfügung gestellt werden kann. Um Folgereaktionen von monooxidiertem **10** zu unterdrücken, wurden Messungen auch bei tiefen Temperaturen durchgeführt. Senkt man die Temperatur der Messzelle auf –78°C, ändert sich das Cyclovoltammogramm signifikant. Bereits bei einer Vorschubgeschwindigkeit von 0.05 Vs^{-1} folgt auf den nun vollständig reversiblen ersten Oxidationsschritt bei –0.01 V ein weiterer bei 0.16 V, welcher der zweiten Ferrocenyleinheit zugeordnet werden kann (Bild 1.2.9).

Eine Analyse der Signale zeigt, dass die Kriterien für einen elektronisch reversiblen Einelektronenprozess bei beiden Redoxvorgängen nur bedingt erfüllt sind [$i_{p,f} \sim \sqrt{n}$; $\Delta E_{p1} = 0.19$ V und $\Delta E_{p2} = 0.21$ V sind etwas größer, als es für einen chemisch reversiblen Prozess unter diesen Bedingungen erwartet wird (FcH/FcH^+: $\Delta E_p = 0.11$ V); $i_{p,f}/i_{p,r}$ konnte aufgrund von zu kleinem $\Delta E^{\circ\prime}$ nicht bestimmt werden ($i_{p,f}$ und $i_{p,r}$ = Spitzenstrom des „forward-" bzw. „reverse-scans", n = Vorschubgeschwindigkeit)].[82] Die Tatsache, dass die Fe(II)/Fe(III)-Übergänge der beiden Ferrocenyleinheiten eine

Potentialaufspaltung von 170 mV aufweisen, spricht dafür, dass zwischen den Eisenzentren eine elektronische Wechselwirkung besteht.[83]
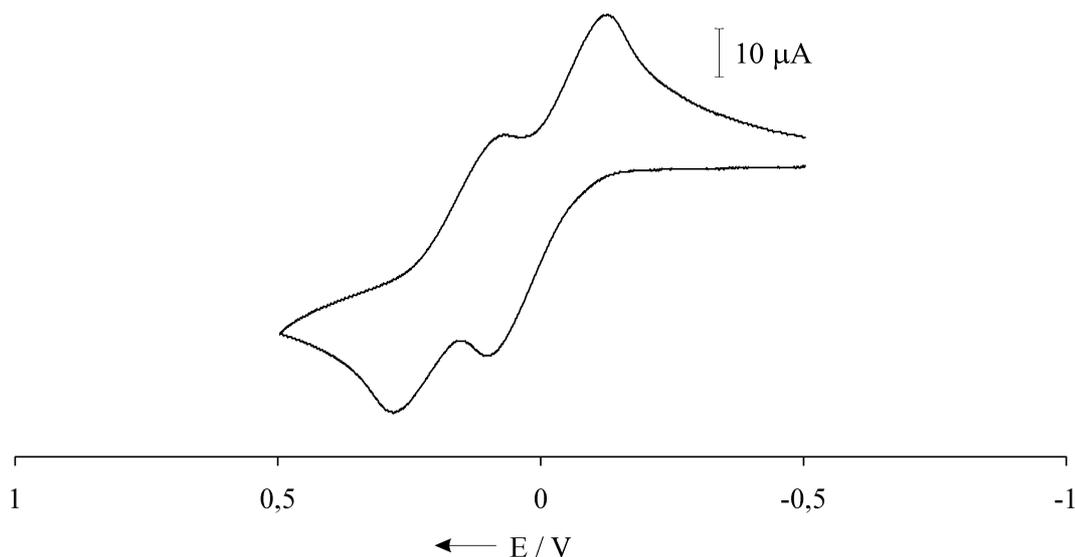
Bild 1.2.9   Cyclovoltammogramm einer CH_2Cl_2-Lösung von **10**, aufgenommen an einer Platinelektrode bei −78 °C unter Verwendung von $[^nBu_4N][PF_6]$ als Leitsalz und einem Silberdraht als Pseudoreferenzelektrode; Vorschubgeschwindigkeit $v = 0.10$ V s^{-1}.

Die Eigenschaften von **9** und **10** als Hydroborierungsreagenzien lassen sich wie folgt zusammenfassen: Erste Versuche zur Herstellung von $FcBR_2$ (R = Akyl, Alkenyl) durch Freisetzen von $FcBH_2$ (**9**) mittels Trimethylchlorsilan in Gegenwart eines Überschusses an Olefin bzw. Alkin waren nicht erfolgreich. Sowohl bei tiefen Temperaturen als auch bei Raumtemperatur ist die in Schema 1.2.4 beschriebene Dimerisierungsreaktion schneller. Dies wird dadurch deutlich, dass die Hydroborierungsprodukte Fc_2BR und BR_3 der *in situ* gebildeten Verbindungen **10** und B_2H_6 in Lösung NMR-spektroskopisch detektierbar sind. Im Falle der Hydroborierung von Cyclohexen (Schema 1.2.5) gelang die Kristallisation beider Reaktionsprodukte.[84]
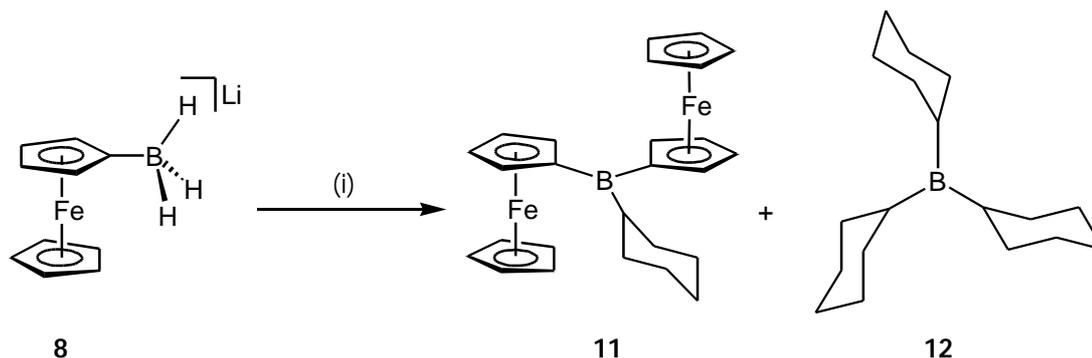
Schema 1.2.5 Hydroborierung von Cyclohexen mit intermediär gebildetem Fc$_2$BH (**10**): (i) + ClSiMe$_3$, exc. C$_6$H$_{10}$, Et$_2$O, −78 °C.

Fc$_2$BCy (**11**) kristallisiert in der monoklinen Raumgruppe *P*2$_1$/*n* (Bild 1.2.10). Ähnlich wie Fc$_2$BH (**10**) zeigt **11** eine *trans*-Anordnung der beiden Ferrocenylgruppen in Bezug auf die C(11)-B(1)-C(31)-Ebene. Sterische Abstoßung zwischen der Fe(2)-Ferrocenyleinheit und dem Cyclohexylsubstituenten führt zu eine Drehung dieses Ferrocenfragmentes aus der Ebene, die von C(11), C(31) und C(51) aufgespannt wird [Torsionswinkel C(11)-B(1)-C(31)-C(32) = -25(3)°].
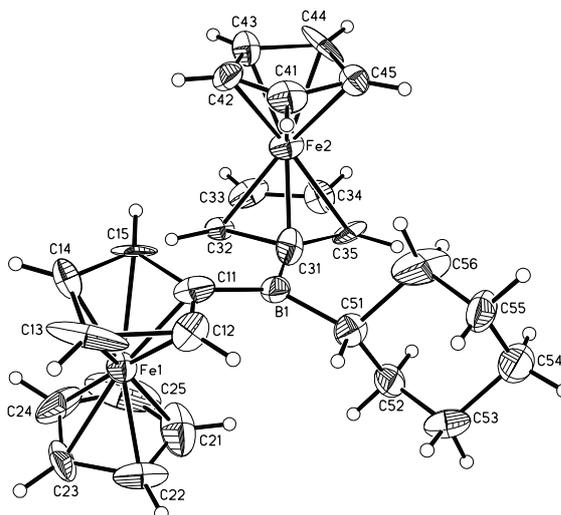
Bild 1.2.10   Struktur von Fc$_2$BCy (**11**; Cy = C$_6$H$_{11}$) im Kristall. Die anisotropen Auslenkungsparameter entsprechen 50 % Aufenthaltswahrscheinlichkeit.

Ein ähnliches Verhalten wird im Triferrocenylboran beobachtet, in dem sich die Ferrocenylsubstituenten propellerartig um das zentrale Boratom anordnen (Torsionswinkel zwischen 25.8° und 28.1°).[85]

Das Tricyclohexylboran (**12**), eines der wenigen strukturell charakterisierten Trialkylborane, kristallisiert in der hexagonalen Raumgruppe $P6_3/m$ (Bild 1.2.11).[86] Die Cyclohexylringe liegen in der Sesselkonformation vor und orientieren sich senkrecht zu der Ebene, die von Bor, welches auf einer dreizählige Achse liegt, und den drei C_{ipso}-Kohlenstoffatomen aufgespannt wird. Im Kristall bilden die einzelnen Moleküle von **12** Säulen aus, innerhalb derer die Boratome 6.697 Å voneinander entfernt sind.
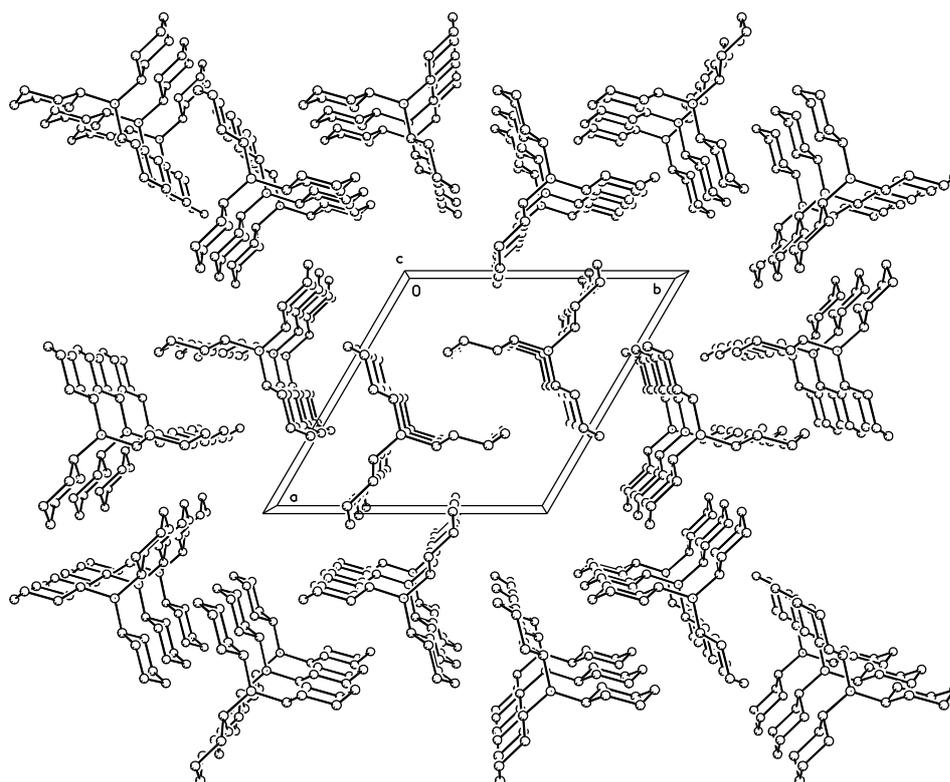
Bild 1.2.11 Packung von BCy_3 (**12**; $Cy = C_6H_{11}$) im Kristall.

Die Schwierigkeiten, die sich für die Synthese von FcBR$_2$ aus der in Schema 1.2.5 gezeigten Reaktionsführung ergeben, lassen sich umgehen, indem man die Lewis-Säure-Base-Addukte **9·NMe₂Et** und **9·DMS** als Hydroborierungsreagenzien einsetzt.[69] Es zeigt sich, dass bei Verwendung von **9·NMe₂Et** polare Lösungsmittel und erhöhte Temperaturen benötigt werden, da es sich um ein sehr stabiles Addukt handelt, die Hydroborierung aber über das unkomplexierte Ferrocenylboran **9** verläuft, welches durch Brechen der dativen B-N-Bindung erst freigesetzt werden muss. **9·DMS** zeichnet sich im direkten Vergleich mit **9·NMe₂Et** durch eine höhere Reaktivität aus. Aufgrund der schwächeren B-S-Bindung bilden sich die gewünschten Hydroborierungsprodukte FcBR$_2$ bereits bei Raumtemperatur innerhalb weniger Stunden. Dabei wird am besten in Dimethylsulfid als Lösungsmittel und mit einem Überschuss an Olefin bzw. Alkin gearbeitet, wodurch sich die Dimerisierungsreaktion zu Fc$_2$BH nahezu vollständig verhindern lässt.

1.2.2.2   Synthese, Struktur und Reaktivität von 1,1´-fc(BH$_2$)$_2$

Die Ergebnisse aus dem vorangegangenen Kapitel zeigen, dass es möglich ist, die Stammverbindung der Ferrocenylborane, FcBH$_2$ (**9**), darzustellen, vorausgesetzt, sie wird durch Adduktbildung mit Lewis-Basen stabilisiert. Es war daher zu untersuchen, ob auch das entsprechende Ferrocenylboran mit zwei BH$_2$-Gruppen auf ähnliche Weise hergestellt werden kann. In vielerlei Hinsicht wäre diese Verbindung von Interesse:

(a) Wie **9·NMe₂Et** zeigt (Schema 1.2.3), geht FcBH$_2$ (**9**) im Gegensatz zu FcBMe$_2$ (**1c**, Schema 1.2.2) auch mit Trialkylaminen sehr stabile Lewis-Säure-Base-Addukte ein. Ein Lewis-saures 1,1´-Bis(dihydridoboryl)ferrocen (**15**) könnte daher, mit einer Vielzahl unterschiedlicher difunktioneller Lewis-Basen zur Reaktion gebracht, zu einer Reihe neuer Koordinationspolymere oder Makrozyklen führen.

(b) In Abhängigkeit von der koordinierten Lewis-Base handelt es sich bei FcBH$_2$ (**9**) um ein aktives Hydroborierungsreagenz. Für das disubstituierte Derivat **15** ist eine ähnliche Reaktivität zu erwarten. So könnte die Umsetzung mit

zweifach ungesättigten Verbindungen einen Weg zu verzweigten Polymeren eröffnen.

(c) Schließlich stellt sich die Frage, ob freies 1,1´-Bis(dihydridoboryl)ferrocen sich durch inter- oder intramolekulare B-H-B-(2e3c)-Bindungen stabilisiert (Schema 1.2.6) oder ob eine Kondensationsreaktion unter Abspaltung von Diboran (Schema 1.2.4), wie im Falle von **9**, favorisiert ist. Der B···B-Abstand in B_2H_6 beträgt 1.770 Å und liegt damit im Bereich der B-B-Einfachbindung elektronenpräziser Diborane.[87] Ein Vergleich mit dem bekannten 1,2-Bis(dimethylamino)-1,2-dibora[2]ferrocenophan zeigt,[68] dass solche Brückenlängen grundsätzlich mit der Geometrie des Ferrocengerüstes vereinbar wären [B(1)-B(2) = 1.74(2) Å]. Die Bildung eines Ferrocenophans vom Typ *ansa*-**15** hängt jedoch vor allem davon ab, inwieweit die Stabilität der B-H-B-(2e3c)-Bindungen ausreicht, um die aus der Bildung einer *ansa*-Brücke resultierende Verzerrung des Ferrocens zu erzwingen.
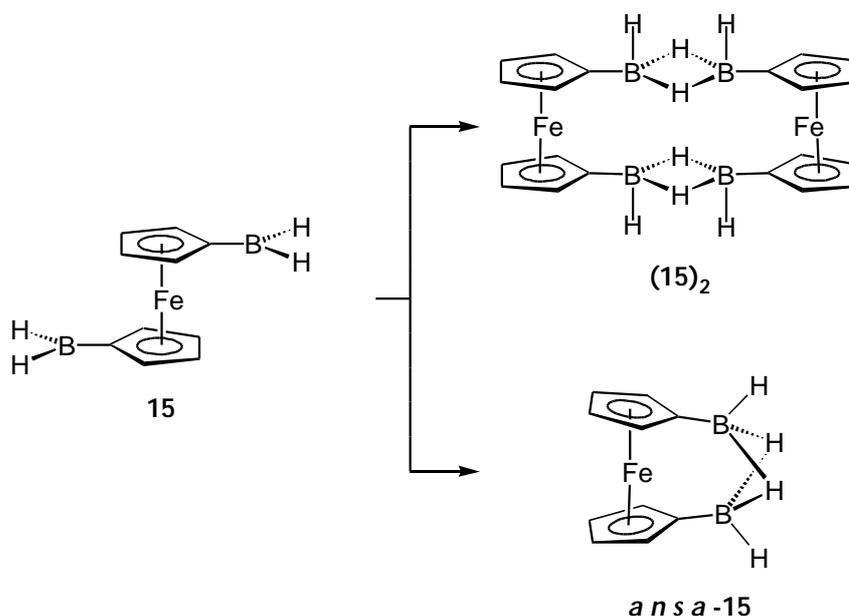
Schema 1.2.6 Intermolekulare (oben) bzw. intramolekulare (unten) Stabilisierung von 1,1´-Bis(dihydridoboryl)ferrocen (**15**).

Die Synthese von 1,1´-fc(BH$_2$)$_2$ (**15**) geht vom 1,1´-fc[B(OMe)$_2$]$_2$ (**13**) aus, welches seinerseits durch Umsetzung von 1,1´-Bis(dibromoboryl)ferrocen [1,1´-fc(BBr$_2$)$_2$, **2**]

mit einem Überschuss an Methoxytrimethylsilan (MeOSiMe$_3$)[56] erhalten wird (vgl. **1d**, Schema 1.2.2).[88] Die Reaktion von **13** mit Lithiumalanat in Diethylether führt zum Diboranat 1,1´-fc(BH$_3$)$_2$Li$_2$ (**14**). Nach Hydridabspaltung mittels Trimethylchlorsilan in Gegenwart eines Überschusses an Dimethylethylamin oder in reinem Dimethylsulfid erhält man schließlich 1,1´-fc(BH$_2$·NMe$_2$Et)$_2$ (**15·NMe$_2$Et**)[89] bzw. 1,1´-fc(BH$_2$·SMe$_2$)$_2$ (**15·DMS**)[90].
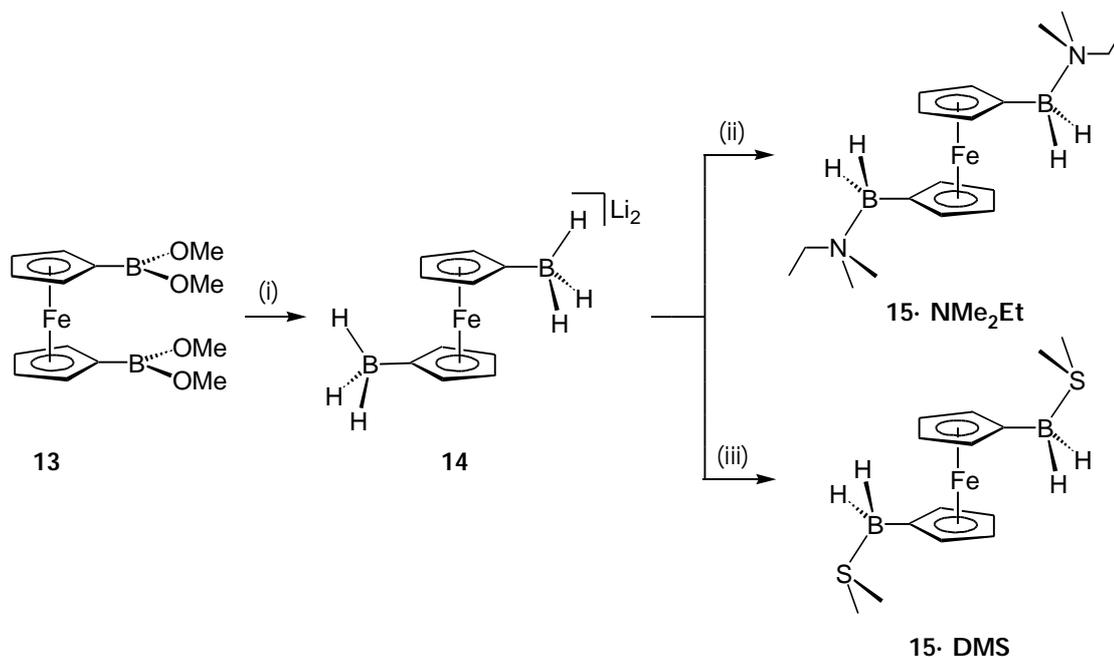
Schema 1.2.7 Synthese von 1,1´-fc(BH$_2$•NMe$_2$Et)$_2$ (**15•NMe$_2$Et**) und 1,1´-fc(BH$_2$•SMe$_2$)$_2$ (**15•DMS**): (i) + 2 LiAlH$_4$, Et$_2$O, 0 °C, 1h; (ii), + 2 ClSiMe$_3$, NMe$_2$Et, Et$_2$O, –78 °C; (iii) + 2 ClSiMe$_3$, SMe$_2$, –78 °C.

1,1´-fc(BH$_3$)$_2$Li$_2$ (**14**) kristallisiert in der triklinen Raumgruppe $P\bar{1}$ mit drei Molekülen in der asymmetrischen Einheit (Bild 1.2.12).[88] Über B-H-Li-Wechselwirkungen werden zwei unterschiedliche Dimere gebildet, von denen eines (**14^A**, Bild 1.2.12, oben) ein Inversionszentrum aufweist, das andere hingegen (**14^B**, Bild 1.2.12, unten) C$_1$-Symmetrie besitzt. Im Dimer **14^A** werden zwei Lithiumionen, Li(6) und Li(6A), von jeweils zwei Ethermolekülen und die anderen beiden, Li(5) und Li(5A), von jeweils einem Ethermolekül komplexiert. Die Koordinationssphäre der Lithiumatome wird durch kurze Kontakte zu Wasserstoffatomen der BH$_3$-Fragmente vervollständigt. Beide Ferroceneinheiten nehmen eine Konformation ein, in der ihre BH$_3$-Gruppen auf dieselbe

Seite und ins Zentrum des dimeren Aggregats weisen [Torsionswinkel: C(51)-COG$_{51}$-COG$_{61}$-C(61) = -15.7°, COG = Schwerpunkt des Cp-Rings]. Zwei der vier BH$_3$-Substituenten sind 2$\boldsymbol{m}_1^2, \boldsymbol{m}_1^1$- [B(6) und B(6A), zwei Wasserstoffatome verbrücken jeweils zwei Li-Atome, ein Wasserstoffatom bindet an nur ein Li-Atom] die anderen beiden 3$\boldsymbol{m}_1^2$-koordiniert [B(5) und B(5A), alle drei H-Atome verbrücken jeweils zwei Li-Atome]. Der Gesamtkomplex weist, ähnlich wie **8b** und **8c**, einen planaren Li-B-Li-B-Vierring in seinem Zentrum auf [Li(5)···B(5) = 2.516(10) Å , Li(5) ···B(5A) = 2.591(10) Å, Li(5)-B(5)-Li(5A) = 75.1(3)°, B(5)-Li(5)-B(5A) = 104.9(3)°]. Überdies bauen die vier Bor- und die vier Lithiumatome wiederum eine leiterartige Struktur auf (vgl. Struktur von **8c** im Kristall, Bild 1.2.5), die von einer unpolaren Hülle aus zwei Ferrocenresten und sechs Ethermolekülen umgeben ist.

Das Dimer **14^B** (Bild 1.2.12, unten) weist keine lokale Symmetrie auf. Auch hier zeigen die beiden Ferrocenfragmente eine Konformationen, die zu einer Ausrichtung beider BH$_3$-Substituenten zum Zentrum des Dimers hin führt [Torsionswinkel: C(11)-COG$_{11}$-COG$_{21}$-C(21) = -3.1°, C(31)-COG$_{31}$-COG$_{41}$-C(41) = -16.3°; COG = Schwerpunkt des Cp-Rings]. Daraus ergibt sich viermal eine 2$\boldsymbol{m}_1^1, \boldsymbol{m}_1^2$-Koordination zwischen den BH$_3$-Fragmenten und den Lithiumionen. Zwei Lithiumatome, Li(1) und Li(2), werden zusätzlich von je zwei Ethermolekülen komplexiert, während ein drittes Li$^+$-Ion, Li(4), ohne weitere Sauerstoffdonoren auskommt, also allein von Wasserstoffatomen der BH$_3$-Substituenten stabilisiert wird. Das letzte Lithiumion [Li(3)] weist neben einem Etherliganden und zwei Kontakten zu Wasserstoffatomen zweier unterschiedlicher BH$_3$-Gruppen zusätzlich einen kurzen Abstand zum Eisenatom Fe(1) auf [Fe(1)···Li(3) = 2.653(9) Å]. Dies legt die Vermutung nahe, dass in diesem Fall besetzte d-Orbitale am Eisen mit dem unbesetzten 2s-Orbital am Lithiumkation wechselwirken.
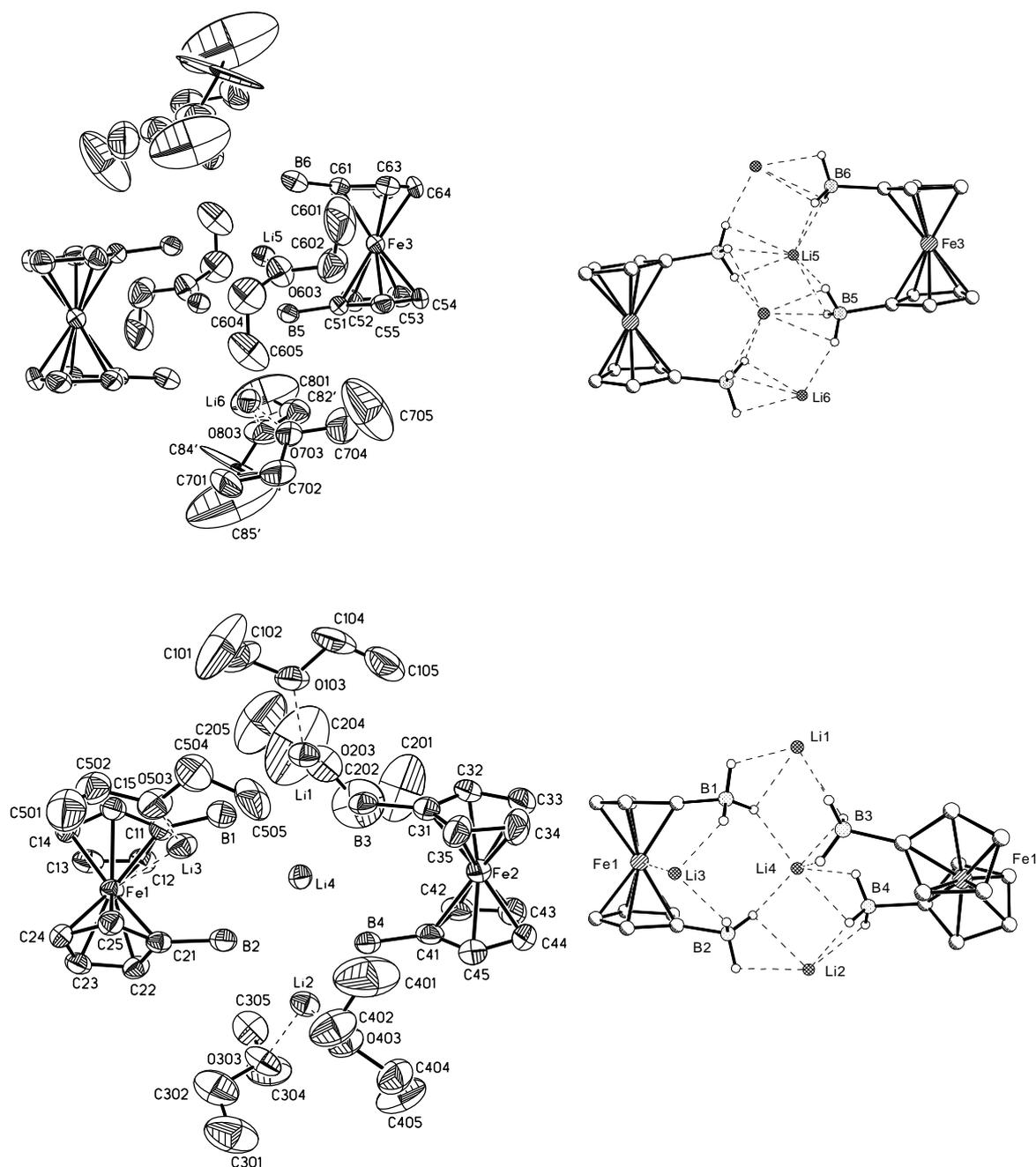
Bild 1.2.12 Festkörperstruktur der kristallographisch unabhängigen Dimere **14^A** (oben) und **14^B** (unten) von 1,1´-fc(BH$_3$)$_2$Li$_2$ (**14**) (die anisotropen Auslenkungsparameter entsprechen 50% Aufenthaltswahrscheinlichkeit); daneben jeweils die Koordination der Boratgruppen an die Lithiumionen (Lösungsmittelmoleküle wurden aus Gründen der Übersichtlichkeit weggelassen).

Die Metallbasizität des Eisenatoms wird schon seit langem im Zusammenhang mit der Protonierung bzw. mit elektrophilen Substitutionsreaktionen des Ferrocens diskutiert und ist in jüngster Zeit Gegenstand intensiver theoretischer Untersuchungen.[91] Seit den 60er Jahren des vergangenen Jahrhunderts weiß man, dass Ferrocen gegenüber starken Säuren als Base wirkt. Ein ungewöhnlich weit zu hohem Feld verschobenes Signal [$\delta(^1H)$ = -2.1] im ^{1}H-NMR-Spektrum einer Lösung von Ferrocen in Hydroxytrifluoroborsäure (BF$_3$·H$_2$O) wurde als Hinweis darauf gewertet, daß Ferrocen unter diesen Bedingungen am Eisenatom protoniert vorliegt.[92] Ferner ist bekannt, dass das Lithium-Kation in der Gasphase Addukte mit polaren Molekülen eingeht.[93] *Ugalde* et al. haben kürzlich die (in der Gasphase) stabilen Isomere des Ferrocen-Lithium-Kations (Cp$_2$Fe···Li$^+$) mittels Dichtefunktionalrechnungen vorhergesagt (Bild 1.2.13).[94] Für das stabilste Isomer **LM1** ergibt sich eine η^5-Koordination des Lithium-Ions an einen der Cp-Ringe des Ferrocens, während es im weniger stabilen Isomer **LM2** zu einer direkten Fe-Li-Wechselwirkung kommen sollte. Beide Isomere entsprechen Minima der Potentialhyperfläche; die Energiedifferenz zwischen ihnen (ΔE = 8.52 kcal/mol) ist gering. In **LM2** beträgt der Fe···Li-Abstand 2.4 Å. Der Übergangszustand **TS22**, der nur um einen Energiebetrag von 2.6 kcal/mol höher liegt als **LM2**, besitzt einen Fe···Li-Abstand von 2.53 Å.
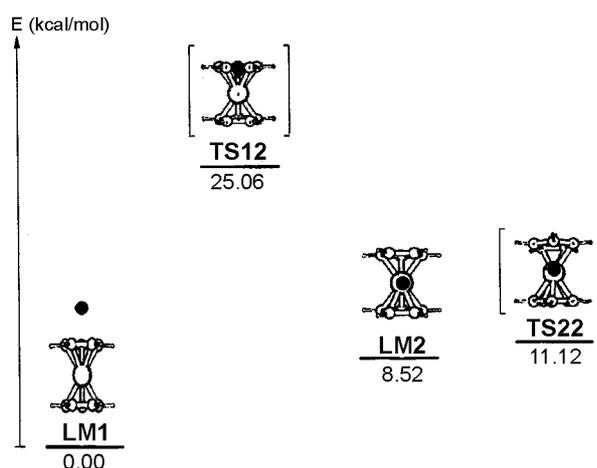
Bild 1.2.13   Energieminima und Übergangszustände von Cp$_2$Fe···Li$^+$ [B3LYP/TZVP+G(3df,p)-Niveau].[94]

Der berechnete Wert für die Fe-Li-Bindung stimmt gut mit der aus der Kristallstruktur von 1,1´-fc(BH$_3$)$_2$Li$_2$ (**14^B**, Bild 1.2.12) ermittelten Bindungslänge überein. Damit wurde das theoretische Ergebnis auch experimentell bestätigt. Vor kurzem konnten wir auch das zweite in Bild 1.2.13 gezeigte Strukturmotiv (**LM1**) mit einer η^5-Koordination des Lithium-Ions an einen der Cp-Ringe realisieren.[72] Allerdings erwies es sich als notwendig, das Li$^+$-Ion durch einen dirigierenden Lewis-basischen Seitenarm am Ferrocen in der gewünschten Position zu fixieren (**XIV**, Bild 1.2.14).
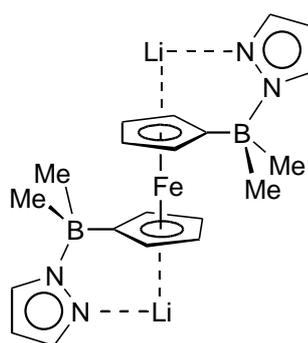
XIV

Bild 1.2.14   Li$_2$[1,1´-fc(BMe$_2$pz)$_2$] (**XIV**, pz = Pyrazolyl) als experimenteller Beweis für die Möglichkeit einer η^5-Koordination von Lithiumionen an die Cp-Ringe eines Ferrocenderivates.[72]

Auch   von   1,1´-fc(BH$_2$·NMe$_2$Et)$_2$ (**15·NMe$_2$Et**)   konnte   durch   eine Röntgenstrukturanalyse   die   Festkörperstruktur   ermittelt   werden.   **15·NMe$_2$Et** kristallisiert in der triklinen Raumgruppe $P\bar{1}$ (Bild 1.2.15).[89] Die Verbindung weist am zentralen Eisenatom ein Inversionszentrum auf. Ihre beiden Cp-Ringe liegen in einer perfekt gestaffelten Konformation vor, so dass die beiden B-NR$_3$-Gruppen auf gegenüberliegenden Seiten des Ferrocengerüstes liegen. Die Lewis-Basen sind wie in **9·NMe$_2$Et^I** so orientiert, dass die N-Ethyl-Bindung nahezu parallel zur C$_{ipso}$-B-Bindung verläuft [Torsionswinkel: C(1)-N(1)-B(1)-C(11) = 178.2(7)°].

Von **15·DMS** konnten keine Kristalle erhalten werden, die sich für eine Röntgenstrukturanalyse eignen. Die NMR-Spektren in S(CD$_3$)$_2$ zeigen aber in

eindeutiger Weise,[90] dass **15·DMS** in diesem Lösungsmittel für eine gewisse Zeit bei Raumtemperatur stabil ist.
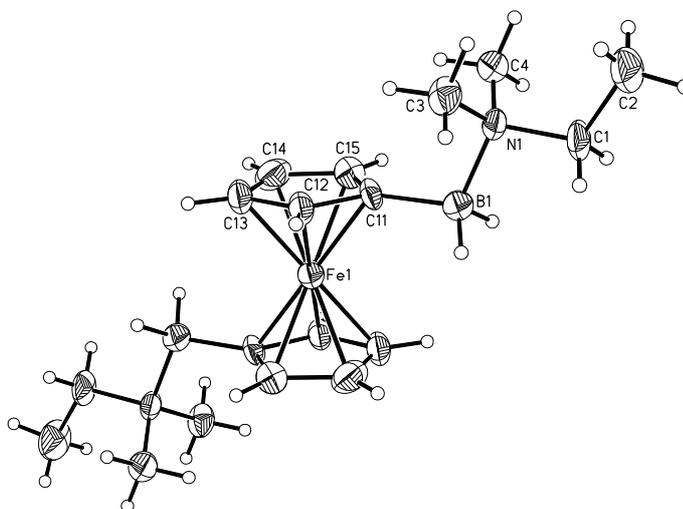
Bild 1.2.15   Struktur von 1,1´-fc(BH$_2$·NMe$_2$Et)$_2$ (**15•NMe₂Et**) im Kristall. Die anisotropen Auslenkungsparameter entsprechen 50 % Aufenthaltswahrscheinlichkeit.

Allerdings setzt auch hier nach einigen Tagen die in Schema 1.2.4 dargestellte Kondensationsreaktion unter Abspaltung von BH$_3$ ein, das im ^{11}B-NMR-Spektrum als BH$_3$·SMe$_2$-Addukt [δ([11]B) = -18.3, [1]$J_{B,H}$ = 106 Hz] nachgewiesen werden kann. Dies bedeutet, dass auch im Fall von 1,1´-fc(BH$_2$)$_2$ (**15**) das freie, nur durch intra- oder intermolekulare B-H-B-(2e3c)-Bindungen stabilisierte, Ferrocenylboran nicht existenzfähig ist. Die Ergebnisse weiterführender Versuche zur Kondensationsreaktion von **15** mit dem Ziel einer Polymersynthese sind in Kapitel **1.4.2** zusammengefasst.

1.3   Di- und trinucleare Modellverbindungen mit tetrakoordinierten Borbrücken

Die vielseitige Anwendbarkeit des beschriebenen B-N-Verknüpfungskonzeptes wurde bereits durch zahlreiche Beispiele auf unterschiedlichsten Gebieten wie der Synthese von *charge-transfer*-Polymeren,[95, 96] redoxaktiven Makrozyklen,[52, 97] schaltbaren *ansa*-Metallocenen[98-100] oder redoxaktiven Tris(1-pyrazolyl)boratliganden[50, 101-103] unter Beweis gestellt. Im Fall der Polymere und der Makrozyklen wurden fast ausschließlich difunktionelle, starre – meist aromatische – Stickstoffbasen wie 2,2´- und 4,4´-Bipyridin, Pyrazin oder Derivate dieser Heterozyklen zur Verknüpfung von Ferrocenylboranen eingesetzt. Dies führte ausnahmslos zu relativ großen Abständen zwischen den Ferroceneinheiten. Als Resultat wurden in der Regel keine Wechselwirkungen zwischen den Metallzentren beobachtet.

Es stellte sich daher die Frage, ob sich die erfolgreiche Verknüpfungsstrategie auf metallorganische Lewis-Basen ausdehnen lässt, um auf diesem Wege die Dichte der Metallatome im Polymer zu erhöhen. Für erste Versuche wurden Verbindungen auf Basis von Ferrocen ausgewählt, in denen das Lewis-basische Zentrum Bestandteil des Cp-Ringes ist, um Polymere des Typs **VI** [Schema 1.1.2; -(McBR$_2$)$_n$-, Mc = Metallocen, R = Alkyl oder Halogen) mit tetrakoordiniertem Bor als Brückenatom unter Umgehung der Ringöffnungspolymerisation (ROP) herzustellen. Da sich kleinere Oligomere wesentlich einfacher untersuchen und charakterisieren lassen als Polymere, wurden zunächst kurzkettige Modellverbindungen entwickelt. Die aus diesen Modellsystemen gewonnen Erkenntnisse gestatten bereits, in guter Näherung wesentliche Eigenschaften der entsprechenden Koordinationspolymere abzuschätzen.

1.3.1 Dinucleare Komplexe durch Bor-Phosphor-Adduktbildung

Lewis-Säure-Base-Addukte zwischen Bor und Phosphor wurden bisher nicht zur Verknüpfung von Ferrocenylboranen eingesetzt. Grundsätzlich sind dative B-P-Bindungen aber zu diesem Zweck geeignet. Wie die schaltbaren *ansa*-Metallocene **XV**[100] und **XVI**[98] (Bild 1.3.1) belegen, wird aber im Falle von Verbindungen, die sowohl Donor- als auch Akzeptoreigenschaften in einem Molekül vereinigen, eine Ausbildung von intramolekularen B-P-Addukten bevorzugt. Die im Vergleich zu einer B-N-Adduktbindung schwächere B-P-Bindung führt in **XV** und **XVI** zu einem dynamischen Gleichgewicht zwischen der offenkettigen Form, in der dreifach koordinierte Boratome vorliegen, und dem Ferrocenophan mit geschlossener *ansa*-Brücke (in Bild 1.3.1 exemplarisch für **XVI** dargestellt).
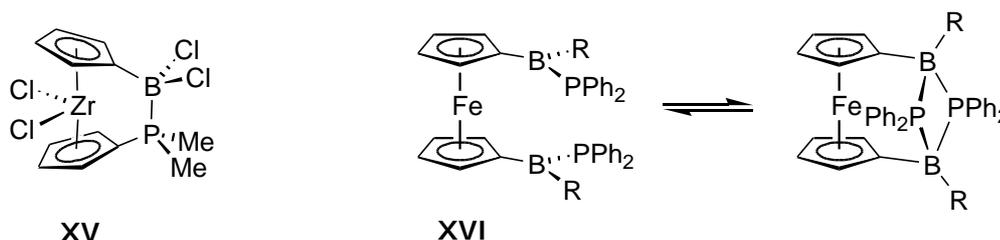
Bild 1.3.1   Zwei schaltbare *ansa*-Metallocene auf Basis von Zirkonocen (**XV**)[100] und von Ferrocen (**XVI**)[98].

Ein solches Gleichgewicht hätte auch bei einer intermolekularen Verknüpfung von Ferrocenylboranen Vorteile. Die weitaus weniger reversible B-N-Adduktbildung führt häufig dazu, dass die polymeren Produkte als unlösliche mikrokristalline Feststoffe aus der Lösung ausfallen. Ein Assoziations-Dissoziations-Gleichgewicht wie in **XVI** könnte hingegen die Kristallisation eines B-P-Polymers durch „Ausheilen" von Baudefekten erleichtern. Vor dem Hintergrund dieser Überlegungen wurden 3,4-Dimethyl-1-phosphaferrocen (**16**)[104] und 3,3´,4,4´-Tetramethyl-1,1´-diphosphaferrocen (**17**)[105] als metallorganische Lewis-Basen ausgewählt (Bild 1.3.2).
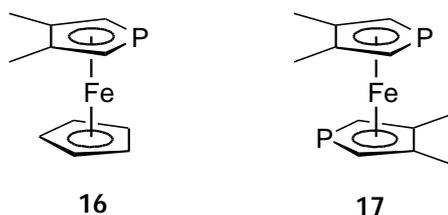
Bild 1.3.2   Die metallorganischen Lewis-Basen 3,4-Dimethyl-1-phosphaferrocen (**16**) und
3,3´,4,4´-Tetramethyl-1,1´-diphosphaferrocen (**17**).

Obwohl zahlreiche Übergangsmetallkomplexe von 1-Phosphaferrocenen und 1,1´-
Diphosphaferrocenen bekannt sind, wurde in der Literatur bisher kaum etwas über
Addukte von **16** und **17** mit Lewis-Säuren von Hautgruppenelementen berichtet. Das
freie Elektronenpaar an den P-Atomen der Phosphaferrocene **16** und **17** befindet sich
jeweils in einem energetisch niedrig liegenden Orbital mit starkem s-Charakter,
wodurch beide Verbindungen nur als schwache σ-Donoren wirken. Das LUMO
hingegen zeigt in **16** und **17** einen ausgeprägten p_z-Charakter an den Phosphoratomen
und ist daher besonders geeignet π-Elektronendichte aufzunehmen.[106, 107] Daher steigt
die Stabilität von Phosphaferrocen-κ-P-ML$_n$-Komplexen mit der Fähigkeit des ML$_n$-
Fragmentes zur Ausbildung einer π-Rückbindung an, was vor allem im Falle
elektronenreicher Metallkomplexe zu starken Bindungen führt. Die Tatsache, dass
Hauptgruppenelemente zu einer d_π-p_π-Rückbindung nicht fähig sind, erklärt die geringe
Anzahl bislang bekannter Addukte zwischen Dimethyl-1-phosphaferrocen (**16**) bzw.
3,3´,4,4´-Tetramethyl-1,1´-diphosphaferrocen (**17**) und Hauptgruppen-Lewis-Säuren.

Um zu testen, ob **16** stabile Addukte mit Lewis-aciden Borverbindungen eingeht und ob
diese in kristalliner Form erhalten werden können, wurde 3,4-Dimethyl-1-
phosphaferrocen (**16**) zunächst mit Bortribromid bzw. mit FcBBr$_2$ (**1**, Schema 1.2.1)
umgesetzt (Schema 1.3.1).[108] In beiden Fällen wird in Lösung bei Raumtemperatur ein
Assoziations-Dissoziations-Gleichgewicht   beobachtet   (NMR-spektroskopische
Kontrolle).
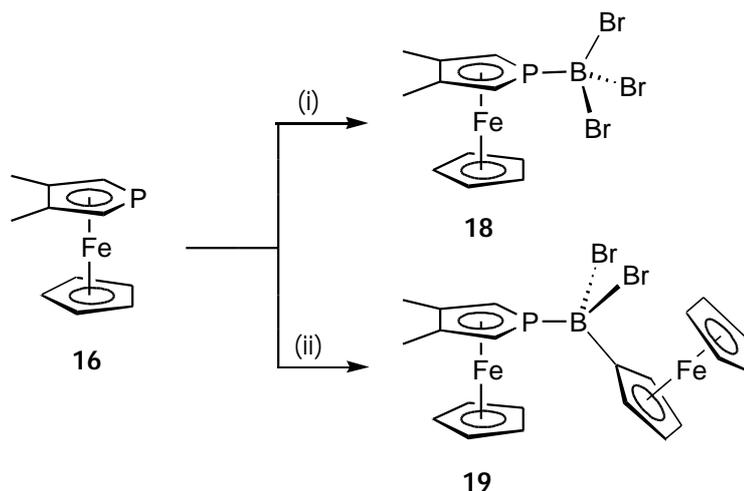
Schema 1.3.1 Synthese der Addukte von 3,4-Dimethyl-1-phosphaferrocen (**16**) mit BBr_3 und $FcBBr_2$: (i) + BBr_3, C_6H_6, Raumtemperatur; (ii) + $FcBBr_2$ (**1**), C_6H_6, Raumtemperatur.

Während **18** (Schema 1.3.1) jedoch bei –50 °C überwiegend als Addukt vorliegt, ist **19** auch noch bei dieser Temperaturen teilweise dissoziiert. Sowohl **18** als auch **19** (Bild 1.3.3) konnten im Festkörper mittels Röntgenstrukturanalyse strukturell charakterisiert werden.[108]
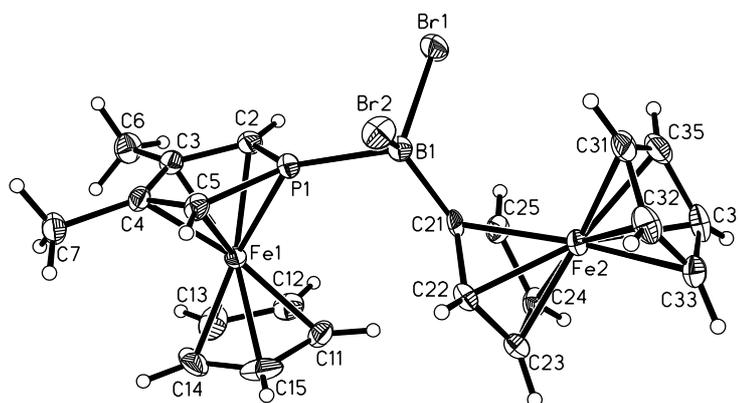

Bild 1.3.3 Struktur von **19** im Kristall. Die anisotropen Auslenkungsparameter entsprechen 50% Aufenthaltswahrscheinlichkeit.

Angesichts dieser Ergebnisse überrascht es nicht, dass bei der Reaktion des im Vergleich mit $FcBBr_2$ (**1**) weniger hydrolyseempfindlichen, aber auch deutlich weniger

Lewis-sauren Ferrocenylborans FcBMe$_2$ (**1c**, Schema 1.2.2) mit 3,4-Dimethyl-1-phosphaferrocen (**16**) weder in Lösung noch im Festkörper eine B-P-Adduktbildung zu beobachten ist. Mit FcBH$_2$ (**9**) als Lewis-Säure kann ebenfalls kein Addukt isoliert werden. FcBH$_2$ (**9**) dimerisiert stattdessen wieder zu Fc$_2$BH (**10**) unter Bildung von B$_2$H$_6$ (Schema 1.2.4).

Aufgrund dieser Resultate wurden 1,1´-fc(BBr$_2$)$_2$ (**2**) und 3,3´,4,4´-Tetramethyl-1,1´-diphosphaferrocen (**17**) als Edukte für Polymerisationsversuche ausgewählt. Als Ergebnis der Adduktbildung erwarteten wir entweder das Koordinationspolymer **XVII** oder den Makrozyklus **XVIII** (Bild 1.3.4).
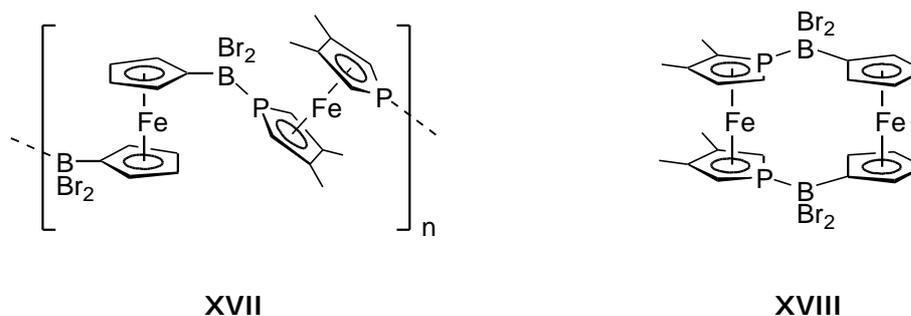
Bild 1.3.4   Koordinationspolymer **XVII** und Makrozyklus **XVIII** als Zielmoleküle der Umsetzung von 1,1´-fc(BBr$_2$)$_2$ (**2**) mit 3,3´,4,4´-Tetramethyl-1,1´-Diphosphaferrocen (**17**).

Überraschenderweise kann aber keines der beiden Zielmoleküle isoliert werden. Sowohl bei der Kristallisation unter kinetisch kontrollierten (–78°C/Methylenchlorid bzw. –30°C/Toluol) als auch unter thermodynamisch kontrollierten Bedingungen (langsames Entfernen des Lösungsmittels Benzol bei Raumtemperatur) bildete sich stets das offenkettige Addukt **20** (Schema 1.3.2), das nur eine dative Bindung zwischen **2** und **17** aufweist (Bild 1.3.5).[109] Wie bereits von *Roberts* und *Silver*, welche die Adduktbildung zwischen 3,3´,4,4´-Tetramethyl-1,1´-Diphosphaferrocen (**17**) und BF$_3$ mittels ^{31}P-NMR eingehend untersucht haben, vermutet wurde, scheint die Ausbildung eines P-B-

Adduktes am ersten P-Atom von **17** die Lewis-Basizität des zweiten Phosphordonors so stark herabzusetzen, dass dieser keine stabile dative Bindungen zu Lewis-aciden Verbindungen des Bors mehr ausbilden kann.[110]
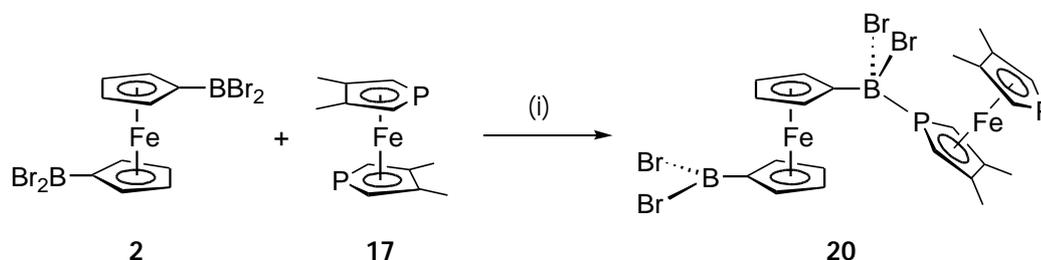
Schema 1.3.2 Synthese des Adduktes von 1,1´-fc(BBr$_2$)$_2$ (**2**) mit 3,3´,4,4´-Tetramethyl-1,1´-diphosphaferrocen (**17**): (i) −30 °C, Toluol.

Im Gegensatz dazu konnten *Mathey* et al. jedoch den ionischen Komplex [Octa-n-propyl-diphosphaferrocen/GaCl$_2$]$^+$[GaCl$_4$]$^-$ isolieren und strukturell charakterisieren, in dem ein 1,1´-Diphosphaferrocen als zweizähniger Ligand an ein Gallium(III)ion koordiniert.[111]
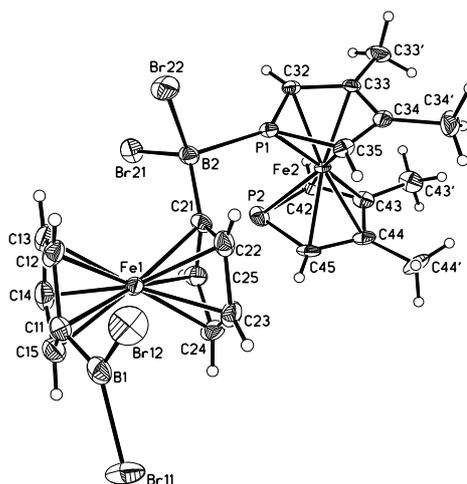
Bild 1.3.5 Struktur von **20** im Kristall. Die anisotropen Auslenkungsparameter entsprechen 50 % Aufenthaltswahrscheinlichkeit.

Im speziellen Fall des 1,1´-Bis(dibromoboryl)ferrocens (**2**) wird die Koordinationspolymerisation zusätzlich noch durch die Tatsache erschwert, dass die Tetrakoordination des ersten Borylsubstituenten die Lewis-Acidität der zweiten BBr_2-Gruppe deutlich senkt, da diese nun allein von der Elektronendichte profitiert, die vom Ferrocenrückgrat zur Verfügung gestellt wird. Diese Ergebnisse lassen den Schluss zu, dass 3,3´,4,4´-Tetramethyl-1,1´-diphosphaferrocen (**17**) zum Aufbau metallorganischer Polymere und Makrozyklen über die Verknüpfung mit Ferrocenylboranen nicht geeignet ist.

1.3.2   Di- und trinucleare Komplexe durch Bor-Kohlenstoff-Adduktbildung

Wie die Versuche zur Koordinationspolymerisation von diborylierten Ferrocenen mit 3,3´,4,4´-Tetramethyl-1,1´-diphosphaferrocen (**17**, Schema 1.3.2) zeigen, reicht die Lewis-Basizität von **17** nicht aus, um Makromoleküle des Typs **XVII** oder **XVIII** (Bild 1.3.4) zu erzeugen. Es war daher zu untersuchen, ob sich durch Umsetzung der starken Lewis-Basen Ferrocenyllithium (**21**) und 1,1´-Dilithioferrocen (**22**, Bild 1.3.6) mit einfach- bzw. zweifach substituierten Ferrocenylboranen oligonucleare Ferrocenkomplexe mit tetrakoordinierten Bor-Brücken darstellen lassen.

21   **22**
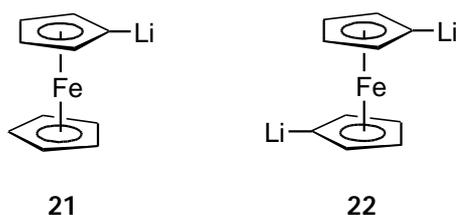
Bild 1.3.6   Die metallorganischen Lewis-Basen Ferrocenyllithium (**21**) und 1,1´-Dilithioferrocen (**22**).

Derartige Materialien sind attraktiv, da die Verknüpfung von Ferroceneinheiten durch tetrakoordiniertes Bor eine Wechselwirkung zwischen den Metallzentren zulässt, wie elektrochemische und spektroskopische Untersuchungen am gemischtvalenten

Ferricenyl(III)tris[ferrocenyl(II)]borat, [Fc(II)]₃BFc(III), belegen.[112] Überdies würde die vollständige Oxidation eines polyanionischen Makromoleküls, wie es beim Einsatz lithiierter Ferrocene als Lewis-Basen entstünde, zu einer neutralen Verbindung führen, in der die formal dreiwertigen Eisenatome durch die benachbarte negative Ladung einer verbrückenden Einheit stabilisiert werden.

Für die Synthese der kurzkettigen Modellverbindungen wurde diesmal als Metallocenylborankomponente das Ferrocenylboran FcBMe₂ (**1c**, Schema 1.2.2) ausgewählt, da es beim Einsatz von FcBBr₂ (**1**, Schema 1.2.1) aufgrund der nucleophilen Eigenschaften des Ferrocenylanions (Fc⁻) zu einem Brom-Ferrocen-Austausch kommen würde. Zur Darstellung der oligonuclearen Komplexe **Li[23]** und **Li₂[24]** wird FcBMe₂ (**1c**) mit einem Äquivalent Ferrocenyllithium (**21**) bzw. einem halben Äquivalent 1,1´-Dilithioferrocen (**22**) vereinigt (Schema 1.3.3).
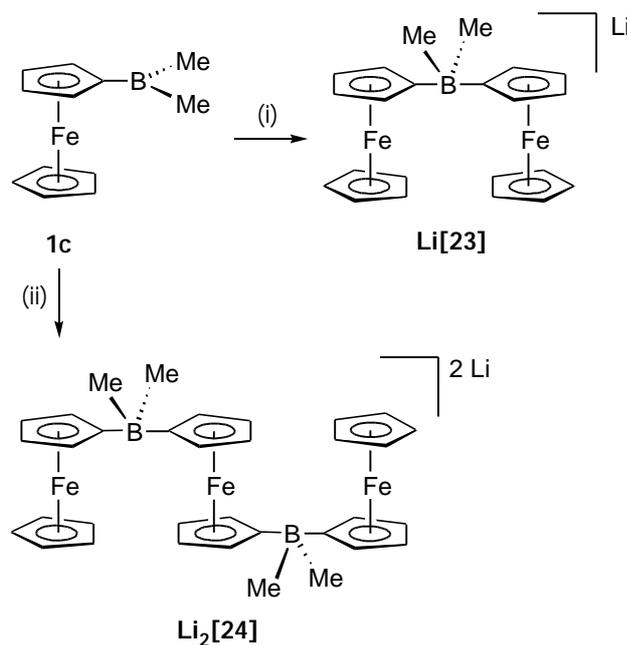
Schema 1.3.3 Synthese der dinuclearen und trinuclearen Modellverbindungen **Li[23]** und **Li₂[24]**: (i) + FcLi (**21**), THF, 0 °C, dann Raumtemperatur; (ii) + 1,1´-fcLi₂ (**22**), THF, –78 °C, dann Raumtemperatur.

Li[23] konnte sowohl in Lösung als auch im Festkörper vollständig charakterisiert werden: Das ^{11}B-NMR-Spektrum der Verbindung zeigt ein scharfes Signal im Bereich tetrakoordinierter Borverbindungen [δ([11]B) = –21.2 ppm, $h_{\frac{1}{2}}$ = 10 Hz].[113] Dies lässt darauf schließen, dass **Li[23]** auch in Lösung als dinuclearer Komplex vorliegt und dass kein Assoziations-Dissoziation-Gleichgewicht wie im Falle der Bor-Phosphor-Addukte **19** (Schema 1.3.1) und **20** (Schema 1.3.2) vorherrscht. Von **Li[23]** konnten zwei Pseudopolymorphe isoliert werden, die sich nur durch das im Kristall eingebaute Lösungsmittel unterscheiden. Im Fall von $Fc_2BMe_2Li(12$-Krone-$4)_2 \cdot CH_2Cl_2$, **Li[23]**[A] (Kristallisation aus Methylenchlorid/Hexan in Gegenwart von Kronenenether, monokline Raumgruppe $C2/c$), befindet sich eine Äquivalent CH_2Cl_2 im Kristallgitter,[114] während im Fall von $Fc_2BMe_2Li(12$-Krone-$4)_2 \cdot THF$, **Li[23]**[B] (Kristallisation aus THF/Heptan nach Zugabe von Kronenether, monokline Raumgruppe $P2_1/c$)**,** ein Molekül THF pro Formeleinheit mit auskristallisiert (Bild 1.3.7).[115]
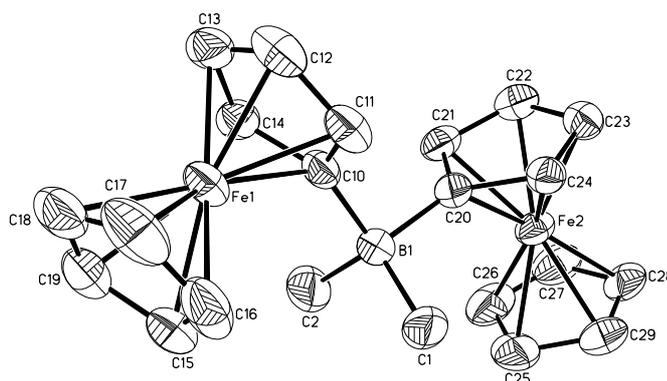
Bild 1.3.7   Struktur von $[Fc_2BMe_2]^-$, **[23]**[B][–], im Kristall. Die anisotropen Auslenkungsparameter entsprechen 50 % Aufenthaltswahrscheinlichkeit. Das $Li(12$-Krone-$4)_2^+$-Ion und das im Kristall eingebaute Lösungsmittel sind aus Gründen der Übersichtlichkeit weggelassen worden.

Wie **Li[23]**[A] zeigt auch **Li[23]**[B] im Festkörper annähernd $C_{2\boldsymbol{n}}$-Symmetrie. Das Boratom ist nahezu perfekt tetraedrisch von zwei Ferrocenylsubstituenten und zwei Methylgruppen umgeben. Der Winkel C(10)-B(1)-C(20) weicht mit 104.2(2)° am stärksten vom Idealwert (109.5°) ab. Grund dafür ist vermutlich sterische Hinderung

zwischen den Ferrocenyleinheiten und den beiden Methylgruppen. In Übereinstimmung mit **Li[23]**[A] werden für die beiden Fe-C_{ipso}-Bindungen von **Li[23]**[B] [Fe(1)-C(10) = 2.111(4) Å; Fe(2)-C(20) = 2.102(4) Å] größere Werte beobachtet als für alle anderen Eisen-Kohlenstoff-Abstände. Wäre dieser Effekt alleine auf sterische Hinderung zwischen der BMe$_2$-Brücke und dem C$_5$H$_5$-Ring zurückzuführen, würde man auch eine Verlängerung der Fe(1)-C(15)- und der Fe(2)-C(25)-Bindung erwarten. Da aber das Gegenteil der Fall ist – Fe(1)-C(15) und Fe(2)-C(25) sind die kürzesten Eisen-Kohlenstoffbindungen [Fe(1)-C(15) = 2.032(4) Å, Fe(2)-C(25) = 2.028(4) Å] – scheint auch der Elektronen schiebende Charakter der Boratgruppe Einfluss auf die Abweichung von der Idealgeometrie zu haben.

Um zu untersuchen, ob zwischen den Eisenzentren des Anions eine Wechselwirkung besteht, wurde **Li[23]** mittels Cyclovoltammetrie untersucht.[114] Bei Raumtemperatur ist ein elektochemisch irreversibler Prozess zu beobachten, der auf eine Zersetzung von **[23]**⁻ als Folge der Oxidation schließen lässt. Bei dieser Reaktion scheinen die Methylgruppen eine entscheidende Rolle zu spielen, da zwitterionische Ferricenyl(III)borate mit anderen Substituenten am Bor durchaus bekannt sind und auch schon isoliert werden konnten. Hierzu zählen so unterschiedliche Verbindungen wie das gemischtvalente Ferricenyl(III)[tris(ferrocenyl)]borat,[112] Fc(III)BPh$_3$[116, 117] sowie Fc(III)BF$_3$, das im Rahmen dieser Arbeit strukturell charakterisiert werden konnte.[118] Das Cyclovoltammogramm von **Li[23]** bei –78 °C hingegen zeigt zwei reversible Redoxwellen. Die Oxidation der ersten Ferroceneinheit erfolgt bei –0.64 V [vs. FcH(II)/FcH(III)], während das zweite Eisenzentrum erst bei –0.43 V oxidiert wird. Die Potentialdifferenz deutet darauf hin, dass, wie im Ferricenyl(III)[tris(ferrocenyl)]borat, eine Wechselwirkung zwischen den Eisenatomen besteht.

Weitere Erkenntnisse über die strukturellen und elektronischen Eigenschaften eines Polymers, in dem die Ferrocenfragmente über anionische BMe$_2$-Gruppen miteinander verknüpft sind, versprach die Untersuchung des trinuclearen Komplexes **Li$_2$[24]** (Schema 1.3.3).[114] Das Molekül (Kristallisation aus einem THF/Ether-Gemisch nach Zugabe von 12-Krone-4; trikline Raumgruppe $P\bar{1}$, Bild 1.3.8) bildet im Festkörper eine

treppenähnliche Struktur aus, wobei die zentrale Ferrocenyleneinheit perfekt gestaffelt vorliegt [Fe(2) liegt auf einem Inversionszentrum]. Damit zeigt **[24]⁻** im Gegensatz zu der analogen Kohlenstoffverbindung Fc-CMe$_2$-fc-CMe$_2$-Fc eine Konformation, wie sie von Pannell durch quantenchemische Rechnungen als ein Energieminimum für ER$_2$-verbrückte Trimetallocene (E = C, Si) ermittelt wurde.[119]
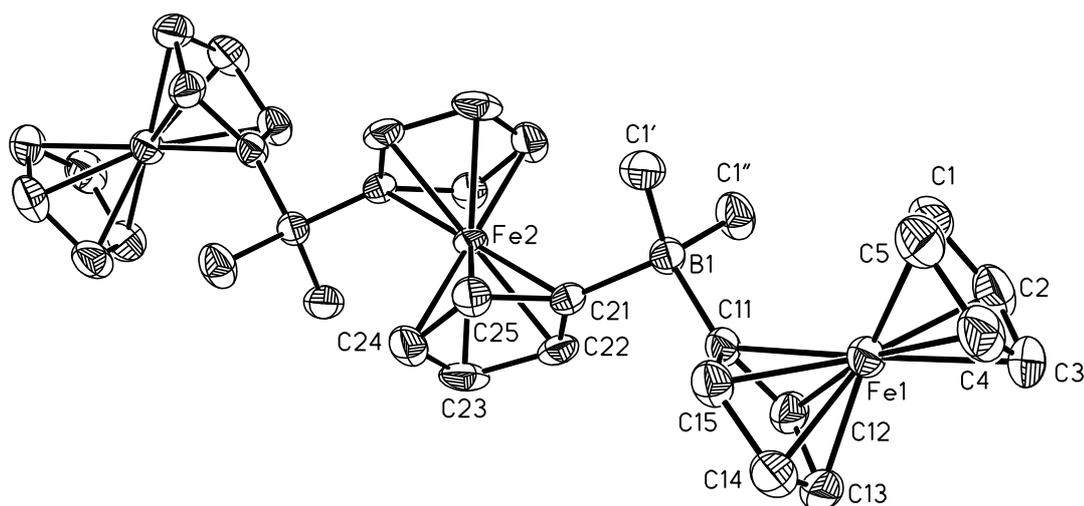
**Bild 1.3.8**   Struktur von **[24]²⁻** im Kristall. Die anisotropen Auslenkungsparameter entsprechen 50 % Aufenthaltswahrscheinlichkeit. Beide Li(12-Krone-4)$_2$⁺-Gegenionen sind aus Gründen der Übersichtlichkeit weggelassen worden.

Für das elektrochemische Verhalten von Verbindungen, die wie **[24]²⁻** drei in einer kettenförmigen Anordnung miteinander verknüpfte Redoxzentren aufweisen, sind zwei unterschiedliche Szenarien bekannt: (1) Im Falle voneinander isolierter Metallatome erhält man aufgrund der Molekülgeometrie im Cyclovoltammogramm zwei Signale im Integralverhältnis 1:2. Die größere Welle ist den beiden terminalen Redoxzentren zuzuordnen, da Elektronen aus zwei Metallzentren entfernt werden, welche dieselbe chemische Umgebung aufweisen. (2) Für lineare trinucleare Komplexe mit untereinander wechselwirkenden Metallzentren beobachtet man hingegen drei reversible Redoxwellen im Integralverhältnis 1:1:1. Eine plausible Reaktionssequenz, die im Einklang mit diesem Verhalten steht, lautet:

$$\text{Fc-fc-Fc} \;\xrightleftharpoons{\pm e^-}\; \text{Fc-fc}^+\text{-Fc} \;\xrightleftharpoons{\pm e^-}\; \text{Fc}^+\text{-fc-Fc}^+ \;\xrightleftharpoons{\pm e^-}\; \text{Fc}^+\text{-fc}^+\text{-Fc}^+$$
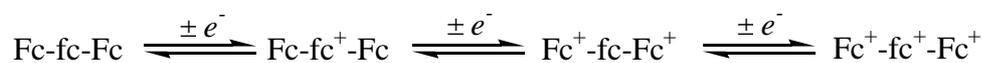
Das Cyclovoltammogramm von **Li₂[24]** wird durch zwei reversible Wellen im Integralverhältnis 2:1 charakterisiert.[114] Dies lässt darauf schließen, dass im Falle von **Li₂[24]** die folgende Oxidationssequenz durchlaufen wird:

$$\text{Fc-fc-Fc} \; \underset{}{\overset{\pm\,e^-}{\rightleftharpoons}} \; \text{Fc-fc}^+\text{-Fc} \; \underset{}{\overset{\pm\,2e^-}{\rightleftharpoons}} \; \text{Fc}^+\text{-fc}^+\text{-Fc}^+$$
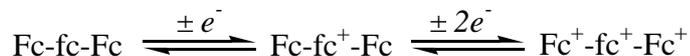
Die zentrale Ferrocenyleneinheit wird zuerst oxidiert ($E^{\circ\prime} = -1.21$ V), da durch die beiden Boratsubstituenten das Redoxpotential des zugehörigen Eisenatoms am stärksten herabgesetzt wird. Die Oxidation der beiden terminalen Ferrocene, die jeweils nur eine Boratgruppe aufweisen, erfolgt anschließend bei demselben Potential ($E^{\circ\prime} = -0.51$ V).

Aufgrund der Tatsache, dass sich 1,1′-Dilithioferrocen (**22**) durch Umsetzung mit Ferrocenylboranen zur Synthese stabiler oligonuclearer Metallkomplexe eignet (Schema 1.3.3), sollte versucht werden, auch Koordinationspolymere des Typs [-(C₅H₄)Fe(C₅H₄)-(BMe₂)-]ₙLiₙ (**25**) aufzubauen (Schema 1.3.4). Entgegen den Erwartungen wurde aber bei der Umsetzung von 1,1′-Dilithioferrocen **22** und 1,1′-fc(BMe₂)₂ (**4**) kein kettenförmiges Makromolekül, sondern das erste borverbrückte [1.1]Ferrocenophan (**Li₂[26]**, Schema 1.3.4) in guten Ausbeuten isoliert.[120]
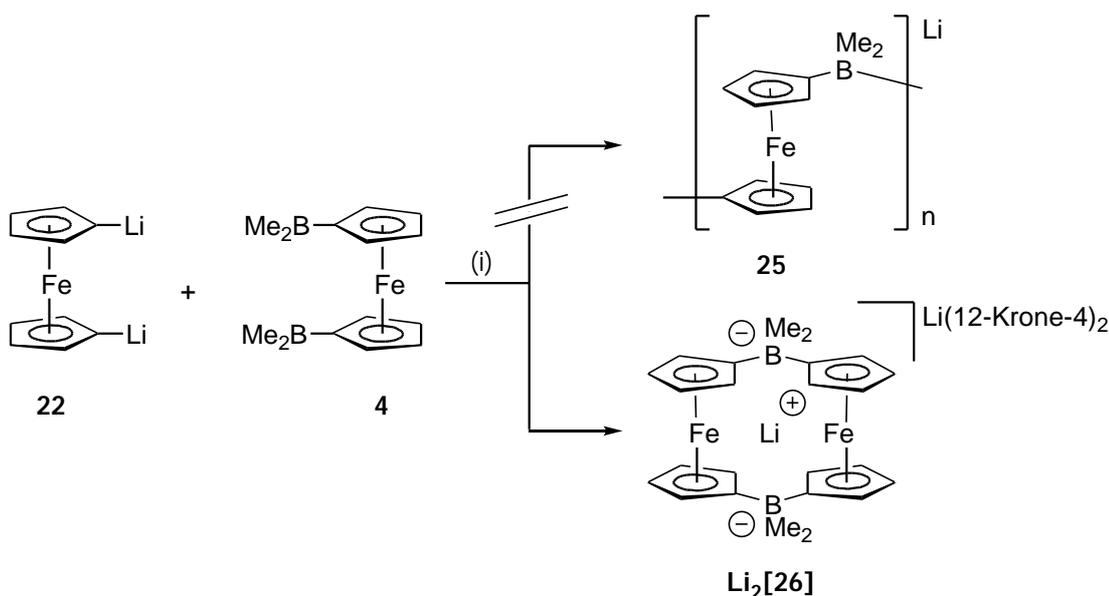
Schema 1.3.4 Synthese des [1.1]Ferrocenophans **Li₂[26]**: (i) THF/Hexan, Raumtemperatur.

Das auffallendste strukturelle Merkmal an **Li₂[26]** ist das nackte Lithium-Ion, das sich im Zentrum des Moleküls befindet (Bild 1.3.9). Von besonderem Interesse ist die Frage nach den Wechselwirkungen, die dieses Kation mit dem [1.1]Ferrocenophan eingeht. Aufgrund der Tatsache, dass es sich bei dem Makrozyklus um ein Dianion handelt, wird die anziehende Kraft vor allem elektrostatischer Natur sein. Aber auch kovalente Bindungsanteile sind nicht auszuschließen, wie die Diskussion der Struktur von 1,1´-fc(BH₃)Li₂ (**14**) zeigt, die ebenfalls einen sehr kurzen Fe-Li-Abstand aufweist (**14**: Fe(1)···Li(3) = 2.653(9) Å; **Li₂[26]**: Fe(1)···Li(1) = 2.720(6) Å, Fe(2)···Li(1) = 2.706(5) Å; **Bild 1.2.12**). Dies kann dahingehend interpretiert werden, dass in beiden Fällen Elektronendichte aus gefüllten d-Orbitalen des Eisens in das leere 2s-Orbital am Lithium übertragen wird.
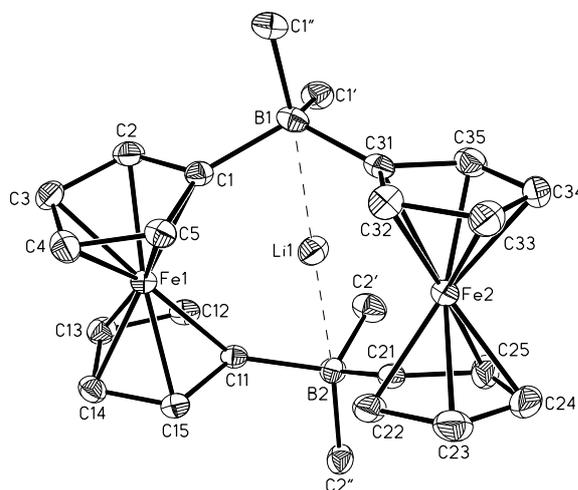
Bild 1.3.9   Struktur von **Li[26]⁻** im Kristall. Die anisotropen Auslenkungsparameter entsprechen 50 % Aufenthaltswahrscheinlichkeit. Das Li(12-Krone-4)₂⁺-Ion ist aus Gründen der Übersichtlichkeit weggelassen worden.

Das ⁷Li-NMR-Spektrum von **Li₂[26]** weist zwei Signale im Integralverhältnis von 1:1 auf [δ(⁷Li) = -0.19, 4.29; THF-d₈]. Ein Vergleich mit den ⁷Li-NMR-Spektren von Lithiumchlorid [δ(⁷Li) = 0.30] bzw. Li(12-Krone-4)₂Cl [δ(⁷Li) = -0.21] in THF-d₈ zeigt, dass das Signal bei hohem Feld dem Li(12-Krone-4)₂⁺-Kation zugeordnet werden kann, während die zweite Resonanz von einem Lithiumatom verursacht wird, das von einer deutlich anders gearteten Ligandensphäre umgeben ist. NMR-spektroskopisch ist kein

Austausch der Lithiumionen zwischen den beiden Koordinationszuständen zu beobachten. Überdies ändert sich bei Zugabe eines Überschusses an Kronenether das ^{7}Li-NMR-Spektrum nicht. Diese Ergebnisse zeigen, dass der Komplex **Li[26]**⁻ auch in Lösung stabil ist. Elektrochemische Untersuchungen zeigen, dass nach vollständiger Oxidation des [1.1]Ferrocenophans das Lithiumion an die Lösung abgegeben wird. Interessanterweise kehrt es nach der Reduktion beider Eisenzentren von **[26]** wieder in den Makrozyklus **[26]**²⁻ zurück.

1.3.3   Di- und trinucleare Komplexe durch Kondensationsreaktionen

Obwohl sich die spontane Bildung von Addukten zwischen Lewis-sauren Ferrocenylboranen und organischen Stickstoffbasen zum Aufbau metallhaltiger Koordinationspolymere als effizient und erfolgreich herausgestellt hat,[95, 96] belegen die vorangegangenen Kapitel, dass dieser Weg im Falle der metallorganischen Lewis-Basen 3,3´,4,4´-Tetramethyl-1,1-diphosphaferrocen (Bild 1.3.2) und 1,1´-Dilithioferrocen (Bild 1.3.6) bisher nicht zu den gewünschten kettenförmigen Makromolekülen führte. Daher stellte sich die Frage nach alternativen Verknüpfungskonzepten, die einen Zugang zu ferrocenhaltigen Polymeren mit tetrakoordinierten Boratomen im Rückgrat ermöglichen.

Einen aussichtsreichen Weg stellen Kondensationsreaktionen zwischen difunktionellen Monomeren X-M^{1}-X und Y-M^{2}-Y dar, bei denen unter Abspaltung kleiner Moleküle, XY, Polymere entstehen [M = Metallkomplexfragment, Schema 1.3.5, a)].[24] Eine vielversprechende Variante dieser Art Polykondensation nutzt Monomere des Typs X-M^{1}-Y, in denen der Metallkomplex beide an der Reaktion beteiligten funktionellen Gruppen trägt, wodurch, anders als im zuvor beschriebenen Fall, auf eine genaue Einhaltung der Stöchiometrie nicht mehr geachtet werden muss [Schema 1.3.5, b)]. Handelt es sich sowohl bei dem Metallkomplexfragment M^{1} als auch bei M^{2} um Ferrocenderivate, sollten auf diesen Wegen Poly(ferrocenylene) möglich sein. Ein gängiger Weg zum Aufbau von Bor-Kohlenstoff-Bindungen ist die Umsetzung von

Borhalogeniden $R_{(3-n)}BX_n$ (X = Cl, Br, I) mit zinnorganischen Verbindungen des Typs $Me_3SnR´$ (R´ = u. a. Alkyl-, Arylrest), die unter Abspaltung von Me_3SnX verläuft.[121]

a)
$$X—M^1—X$$
$$+$$
$$Y—M^2—Y$$
$$\xrightarrow{- XY} X\!\!-\!\!\left[M^1—M^2\right]\!\!-\!\!Y$$

b)
$$X—M^1—Y \xrightarrow{- XY} X\!\!-\!\!\left[M^1—M^1\right]\!\!-\!\!Y$$
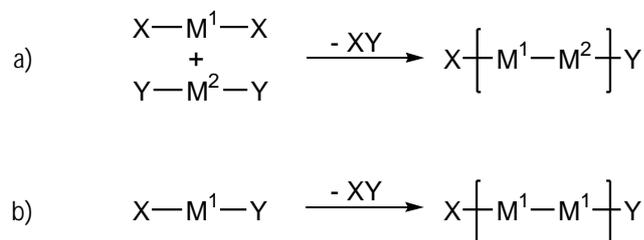
Schema 1.3.5 Verlauf von Kondensationspolymerisationen (M = Metallkomplexfragment).

Diese Reaktion wird beispielsweise auch zur Synthese von $FcBMe_2$ (**1c**, Schema 1.2.2) ausgenutzt, bei der man $FcBBr_2$ mit Tetramethylzinn ($SnMe_4$) methyliert. Zu Beginn unserer Untersuchungen wurden wiederum Synthesen für kurzkettige Modellverbindungen entworfen. Ausgehend von borylierten und stannylierten Ferrocenen erhielten wir di- und trinucleare Komplexe mit verbrückenden B(Br)-Einheiten (Schema 1.3.6).[114]
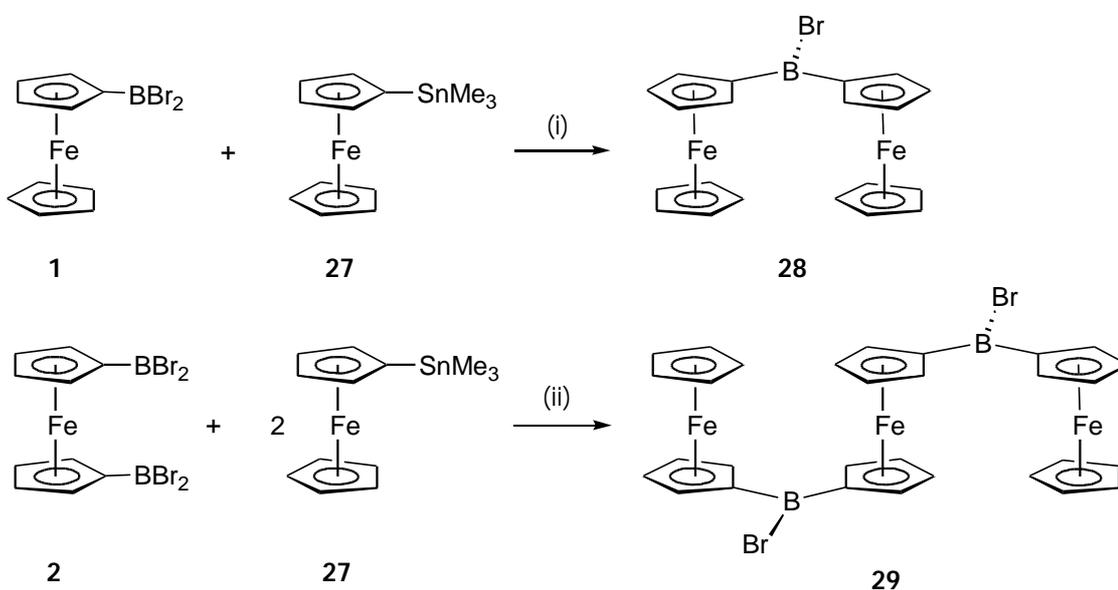
Schema 1.3.6 Synthese der di- und trinuclearen Komplexe **28** (oben) und **29** (unten): (i) C_6H_6, Raumtemperatur; (ii) + Toluol, −78 °C, dann Raumtemperatur.

FcBBr$_2$ (**1**) reagiert mit FcSnMe$_3$ (**27**) unter Bildung von Fc$_2$BBr (**28**) und Me$_3$SnBr. Auf entsprechende Weise wird 1,1´-fc(BBr$_2$)$_2$ (**2**) mit **27** zur Synthese des trinuclearen Komplexes **29** eingesetzt. Sowohl **28** als auch **29** können leicht in Derivate mit tetrakoordinierten Bor-Brücken überführt werden. In Abhängigkeit vom Substitutionsmuster am Boratom lassen sich auf diese Weise unterschiedlich geladene Verknüpfungseinheiten (anionisch, kationisch oder ungeladen) generieren. Beispielsweise wurde **28** durch Zugabe von 2,2´-Bipyridin (bipy) und anschließendes Umsalzen in den dinuclearen Komplex **[30]PF$_6$** mit einer kationischen B(bipy)-Brücke zwischen den Ferroceneinheiten umgewandelt (Schema 1.3.7).[114]
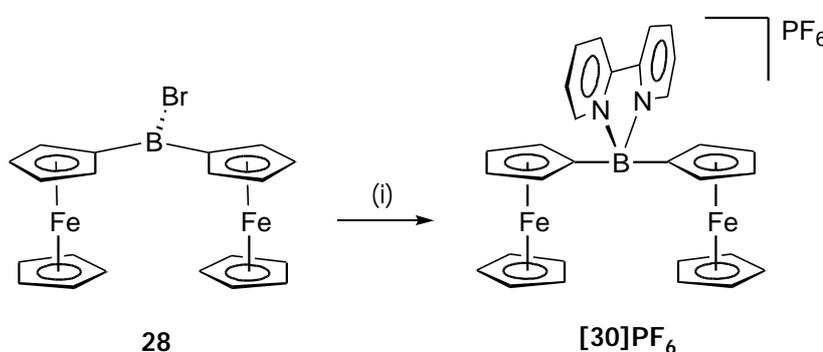
Schema 1.3.7 Darstellung des dinuclearen Komplexes **[30]PF$_6$**: (i) 1. + 2,2´-Bipyridin, Toluol, −78 °C, dann Raumtempertatur; 2. H$_2$O, exc. NH$_4$PF$_6$.

[30]PF$_6$ kristallisiert aus einem Acetonitril/Ether-Gemisch in der monoklinen Raumgruppe $P2_1/c$. Das Kation **[30]**$^+$ zeigt im Festkörper nahezu C_{2n}-Symmetrie (Bild 1.3.10). Die beiden Ferrocenyleinheiten weisen in die Richtung des 2,2´-Bipyridinsubstituenten. Daraus resultiert eine Struktur, die der von **[23]**$^−$ entspricht, wenn man sich die beiden Methylgruppen gegen den zweizähnigen Liganden 2,2´-Bipyridin ausgetauscht denkt. Aufgrund des fehlgeordneten PF$_6^−$-Gegenions und großer Mengen Lösungsmittel, die in das Kristallgitter eingebaut wurden, wird eine Verfeinerung der Daten erschwert, so dass die erhaltenen Werte für Bindungslängen und –winkel mit großen Fehlern behaftet sind.
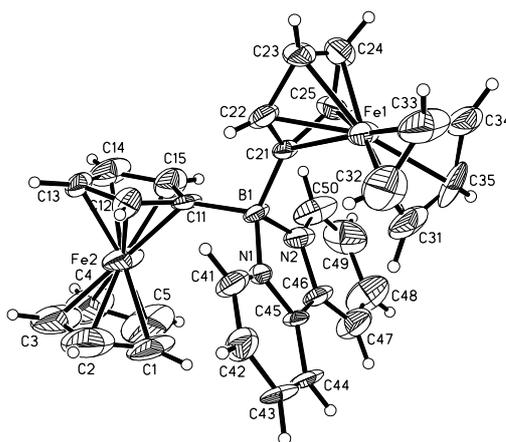
Bild 1.3.10   Festkörperstruktur von **[30]**⁺ (Die anisotropen Auslenkungsparameter entsprechen 50 % Aufenthaltswahrscheinlichkeit.). Das PF_6^--Ion wurde aus Gründen der Übersichtlichkeit weggelassen.

Bipyridylboronium-Kationen auf Ferrocenbasis, zu denen auch **[30]** zählt, zeichnen sich durch interessante *charge-transfer*-Eigenschaften aus.[122] Alle bisher untersuchten Verbindungen dieses Typs weisen in Lösung im UV-VIS-Spektrum eine breite Bande, die bei ca. 500 nm zentriert ist, auf. Für die verwandten Verbindungen **[31]PF₆** und **[32](PF₆)₂** (Bild 1.3.11) konnte mittels Femtosekunden-Laserspektroskopie nachgewiesen werden, dass diese Absorptionsbande durch Ladungsübertragung vom Ferrocen (Donor) auf das 2,2´-Bipyridin (Akzeptor) verursacht wird.[123]
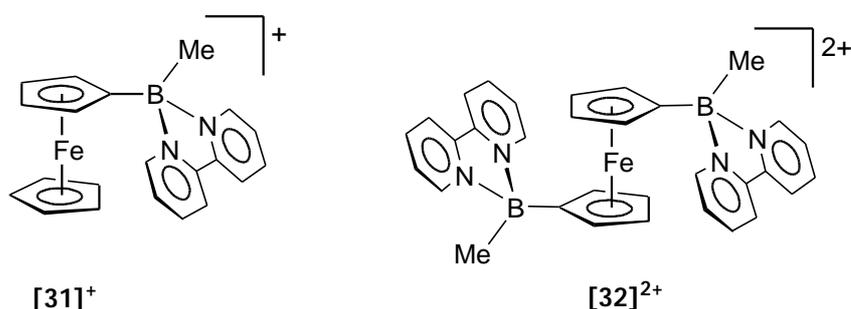
Bild 1.3.11 Die beiden Bipyridylboronium-Kationen **[31]**⁺ und **[32]**²⁺.

Diese Erkenntnis beruht unter anderem auf der Tatsache, dass das transiente Absorptionsspektrum von **[31]**[+] nach Einstrahlen von Laserlicht in die *charge-transfer-*Bande sehr gut mit der Überlagerung der Spektren übereinstimmt, die nach vollständiger Oxidation [Fe(III)/R_2B(bipy)]$^{2+}$ bzw. Reduktion [Fe(II)/R_2B(bipy$^{\bullet}$)]^0 von **[31]**[+] erhalten werden. Vor diesem Hintergrund wäre es wünschenswert, das Strukturmotiv eines Ferrocen-Donors in Nachbarschaft zu einem B-Bipyridin-Akzeptor in polymere Strukturen einzubauen. Am interessantesten erschiene ein Polymer, in dem die Ferroceneleneinheiten wie in **[30]**[+] direkt über den Akzeptor miteinander verknüpft sind. Dieses Makromolekül könnte durch Einstrahlen von Laserlicht der richtigen Wellenlänge von einem diamagnetischen Grundzustand [Fe(II)/R_2B(bipy)]$^+$ in einen paramagnetischen angeregten Zustand [Fe(III)/R_2B(bipy$^{\bullet}$)]$^+$ überführt werden, wodurch eine eindimensionale Spinkette entstünde.

Aufgrund des Halogensubstituenten am Boratom kann **28** in dinucleare Komplexe mit unterschiedlicher Ladung überführt werden. Neben 2,2´-Bipyridin wurde Bromdiferrocenylboran (**28**) daher auch mit einem anionischen 2-(2´-Pyridyl)indolyl-Liganden umgesetzt, woraus ein ungeladener dinuclearer Komplex mit einer Bor-Brücke resultiert (**33**, Schema 1.3.8).[114]
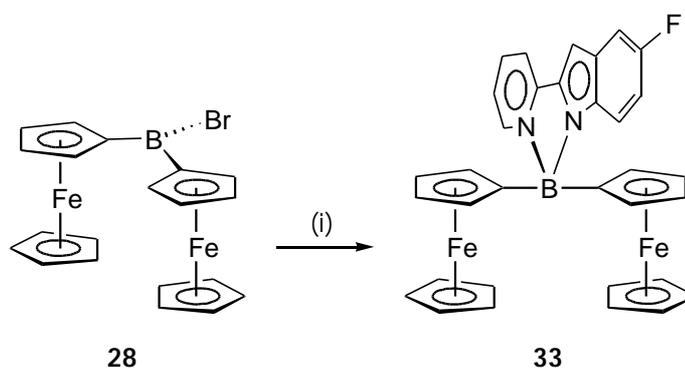
Schema 1.3.8 Synthese des ungeladenen dinuclearen Komplexes **33** mit tetrakoordiniertem Bor als Verknüpfungseinheit: (i) + Na[5-Fluoro-2-(2′-pyridyl)indolyl], Toluol, −78 °C, dann Raumtemperatur.

Auch der trinucleare Komplex **29** wurde mit zwei Äquivalenten 2,2´-Bipyridin umgesetzt und anschließend in das PF_6-Salz **[34](PF_6)_2** umgewandelt (Schema 1.3.9).
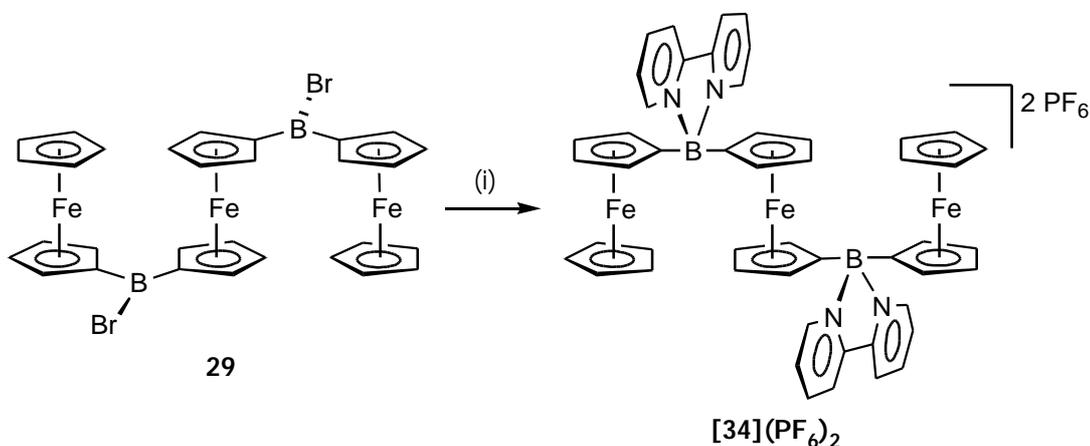
Schema 1.3.9 Synthese des trinuclearen Komplexes **[34](PF_6)_2**: (i) 1. + 2 2,2´-Bipyridin, Toluol, –78 °C, dann Raumtemperatur; 2. H_2O, exc. $[NH_4]PF_6$.

Ähnlich wie für das Trimer **[24]²⁻** mit anionischen BMe_2-Brücken (Schema 1.3.3) beobachtet man im Cyclovoltammogramm von **[34](PF_6)_2** zwei Oxidationswellen im Verhältnis 2:1. Diesmal werden jedoch die beiden terminalen Ferroceneinheiten zuerst oxidiert (E°´ = 0.03 V), da sie jeweils nur eine positive Ladung tragen. Die Oxidation des zentrale Eisenatoms, dem zwei positive Ladungen benachbart sind, erfolgt erst bei E°´ = 0.26 V.

Obwohl sich die in Schema 1.3.6 beschriebene Vorgehensweise hervorragend zur Darstellung di- und trinuclearer Komplexe eignet, kann sie nicht zur Synthese der entsprechenden Poly(ferrocenylene) erweitert werden. Der Grund dafür liegt in der Reaktivität des distannylierten Ferrocens 1,1´-fc(SnMe_3)_2 (**35**, Schema 1.3.10), welches bei der Polymerisation als Reaktionspartner von 1,1´-fc(BBr_2)_2 (**2**) eingesetzt werden müsste. Entgegen den Erwartungen reagiert 1,1´-fc(SnMe_3)_2 nicht in der gewünschten Weise mit Borhalogeniden. Wie von *Jäkle* et al. beschrieben, wird vielmehr eine

Umlagerungsreaktion beobachtet, die zu 1-Boryl-2-stannyl-substituierten Ferrocenen (**XIX**) führt.[124]
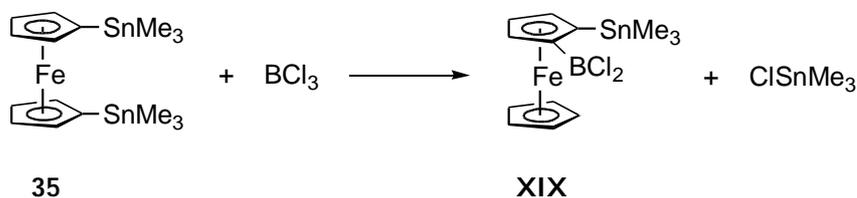
Schema 1.3.10 Reaktion von 1,1´-fc(SnMe₃)₂ (**35**) mit BCl₃ (nach *Jäkle*).[124]

Im Rahmen dieser Arbeit wurde aber eine neue Kondensationsreaktion entdeckt, die sich bei der Darstellung von Polymeren auf der Basis von Ferrocenylboranen als hilfreich herausstellen könnte. Nach Zugabe von HSiEt₃ zu einer Lösung von FcBBr₂ (**1**) in Toluol erhält man unter Abspaltung von „HBBr₂" das Bromdiferrocenylboran, **28**, in ausgezeichneten Ausbeuten (Schema 1.3.11, Bild 1.3.12).[114]
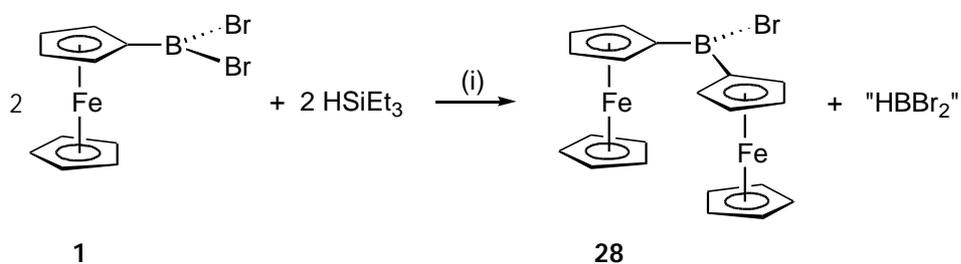
Schema 1.3.11 Alternative Synthese von Fc₂BBr (**28**): (i) Toluol, Raumtemperatur (vgl. Schema 1.3.6).

Diese Reaktion erinnert an die in Schema 1.2.4 beschriebene Dimerisierung von FcBH₂ (**9**) zu Fc₂BH (**10**). Aus dieser ungewöhnlichen Reaktivität der Ferrocenylborane mit B-H-Funktionalitäten ergäben sich neue Möglichkeiten für die Synthese von Poly(ferrocenylboranen), falls sich die beschriebenen Kondensationsreaktionen auf die analogen disubstituierten Ferrocenylborane übertragen ließen. Erste Polymerisationsversuche werden in Kapitel **1.4.2** beschrieben.
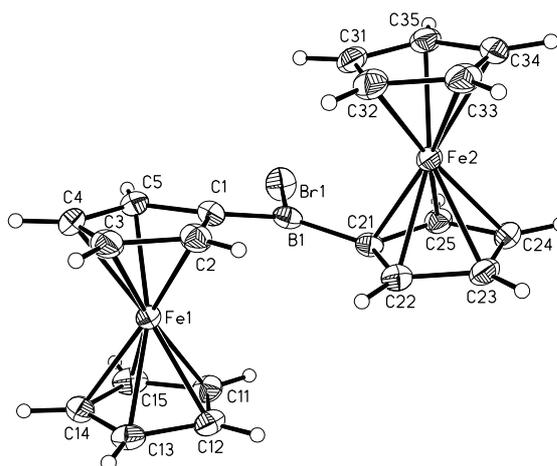
Bild 1.3.12   Struktur von Fc$_2$BBr (**28**) im Kristall. Die anisotropen Auslenkungsparameter entsprechen 50 % Aufenthaltswahrscheinlichkeit.

Zusammenfassend lassen die Ergebnisse zu di- und trinuclearen Ferrocenkomplexen mit tetrakoordinierten Boratomen als Verknüpfungseinheit folgende Schlüsse bezüglich der elektrochemischen Eigenschaften und vor allem der Wechselwirkung zwischen den Metallzentren zu: Wie zu erwarten beeinflussen vor allem Coulomb-Attraktion bzw. -Repulsion zwischen den Bor-Brücken und den oxidierten Ferroceneinheiten die Redoxpotentiale der Eisenzentren in **Li[23]**, **Li$_2$[24]**, **[30]PF$_6$** und **[34](PF$_6$)$_2$**. Während im Fall der anionischen BMe$_2$-verbrückten Komplexe eine Verschiebung zu kathodischeren Potentialen beobachtet wird, sind die Verbindungen mit kationischen B(bipy)-Brücken schwerer zu oxidieren als Ferrocen. Alle dinuclearen Verbindungen, die untersucht wurden, zeigen im Cyclovoltammogramm zwei gut aufgelöste Wellen, die jeweils der Oxidation einer Ferroceneinheit zugeordnet werden können (**Li[23]**: E$^{\circ\prime}$ = –0.43 V / –0.64V, **35**: E$^{\circ\prime}$ = –0.03 / –0.21 V; **[30]PF$_6$**: E$^{\circ\prime}$ = +0.23 / +0.07 V; in CH$_2$Cl$_2$ vs. FcH/FcH$^+$). Interessanterweise ist der Einfluss der Ladung auf das Redoxpotential des dinuclearen Komplexes mit anionischer BMe$_2$-Brücke (**[23]$^-$**) deutlich größer als im Fall der kationischen Verbindung **[30]$^+$**, obwohl der Betrag der Ladung zu Beginn in beiden Fällen gleich ist. Ferner nimmt die Differenz zwischen den Redoxpotentialen der beiden Fe(II)/Fe(III)-Oxidationen, ΔE$^{\circ\prime}$, von 0.21 V in **Li[23]** über 0.18 V (**35**) auf 0.16 V in **[30]PF$_6$** ab. Dies ist verwunderlich, da es eigentlich schwerer sein sollte, eine dritte positive Ladung in das Dikation **[30]$^{2+}$** einzuführen, als

eine erste positive Ladung in die neutrale Verbindung **23**. Daraus ergibt sich, dass nicht allein elektrostatische Effekte für die elektrochemischen Eigenschaften von **Li[23]**, **Li$_2$[24]**, **[30]PF$_6$** und **[34](PF$_6$)$_2$** verantwortlich sind. Vielmehr scheinen weitere Faktoren wie der positive induktive Effekt des B(R)Me$_2$-Substituenten (R = Fc, fc) oder positive Hyperkonjugation zwischen B-C-σ-Orbitalen und π*-Orbitalen der Cyclopentadienylringe eine wichtige Rolle zu spielen. Beide trinuclearen Komplexe, **Li$_2$[24]** und **[34](PF$_6$)$_2$**, zeigen im Cyclovoltammogramm einen Einelektronen- und einen Zweielektronenübergang für die Eisenzentren in den Ferroceneinheiten (**Li$_2$[24]**: E°´ = –0.51 V, E°´ = –1.21 V, Integralverhältnis 2:1; **[34](PF$_6$)$_2$:** E°´ = +0.03 V, E°´ = +0.26 V, Integralverhältnis 1:2). Wiederum ist der Einfluss der Ladung sowohl auf die Redoxpotentiale als auch auf die Potentialdifferenz, ΔE°´, im Falle des Dianions **[24]$^{2-}$** stärker ausgeprägt als im Dikation **[34]$^{2+}$**. Das beschriebene elektrochemische Verhalten unterscheidet sich signifikant von dem der literaturbekannten isoelektronischen Triferrocene Fc-EMe$_2$-fc-EMe$_2$-Fc (E = C, Si).[119, 125] In den Verbindungen mit CMe$_2$- und SiMe$_2$-Brücken werden im Cyclovoltammogramm drei gut aufgelöste Einelektronenübergänge beobachtet, die dafür sprechen, dass die elektronische Wechselwirkung zwischen den Metallzentren weit stärker ausgeprägt ist als in **Li$_2$[24]** und **[34](PF$_6$)$_2$**.

1.4 Borhaltige Oligoferrocene

Obwohl der Schwerpunkt dieser Arbeit auf der Synthese und Charakterisierung di- und trinuclearer Ferrocenkomplexe lag, welche als Modellsysteme für die entsprechenden Polymere anzusehen sind, wurden neben der Entwicklung neuer Bausteine und alternativer Verknüpfungsreaktionen auch erste Polymerisationsversuche unternommen. Das in Kapitel 1.1.3 beschriebene Synthesekonzept, das bereits erfolgreich zur Präparation metallhaltiger Koordinationspolymere auf der Basis von Ferrocenylboranen eingesetzt wurde (Bild 1.1.4), lässt sich nicht ohne weiteres auf die metallorganischen Lewis-Basen 3,3´,4,4´-Tetramethyl-1,1´-Diphosphaferrocen (**17**) und 1,1´-Dilithioferrocen (**22**) übertragen. Im ersten Fall zeigte sich (Schema 1.3.2), dass die Lewis-Basizität von **17** nicht ausreicht, um mit beiden Phosphoratomen gleichzeitig stabile Addukte zu Ferrocenylboranen aufzubauen. Dies verhindert die Bildung eines Koordinationspolymers. Im Fall des 1,1´-Dilithioferrocens (**22**) wird, vermutlich aufgrund seiner konformativen Flexibilität (Rotation der Cyclopentadienylringe) im Vergleich zu starren aromatischen Lewis-Basen wie Pyrazin oder 4,4´-Bipyridin, eine Cyclisierungsreaktion bevorzugt, so dass sich neben polymerem Material vornehmlich das [1.1]Ferrocenophan **[26]$^{2-}$** (Schema 1.3.4) bildet.

Charakteristisch für die im Folgenden beschriebenen Verbindungen ist, dass sie im Gegensatz zu den Polymeren, die über Lewis-Säure-Base-Adduktbildung hergestellt werden, dreifach koordiniertes Bor enthalten. An solchen Materialien besteht ein reges Interesse, da

(a) sie oftmals ungewöhnliche Eigenschaften aufweisen.[43]

(b) es sich bei derartigen Makromolekülen um polyfunktionelle Lewis-Säuren handelt, für welche Anwendungen als Kokatalysatoren oder in der supramolekularen Chemie (Ausbildung von Doppelsträngen mit polyfunktionellen Lewis-Basen) denkbar sind.

(c) sie an den dreifach koordinierten Boratomen vielfältig derivatisiert werden können, woraus sich – durch Umsetzung mit Nucleophilen – auch ein neuer Weg zu Polymeren mit tetrakoordinierten Boratomen im Rückgrat eröffnet. Als Beispiele seien hier die Reaktionen eines Polymers vom Typ B (Bild 1.4.1, R = Br) mit MeLi oder 2,2´-Bipyridin genannt, die zu Makromolekülen führen, welche mit Hilfe der bisher beschriebenen Syntheserouten (Kapitel 1.3) nicht darstellbar sind.

Im Rahmen dieser Arbeit wurden erste Experimente zur Hydroborierungspolymerisation von 1,4-Diethinylbenzol mittels FcBH$_2$ (**9**) durchgeführt, um Polymere des Typs **A** (Bild 1.4.1) herzustellen. Überdies wurde versucht, die in Schema 1.2.4 und Schema 1.3.11 skizzierten Kondensationsreaktionen zum Aufbau von Polymeren des Typs **B** (Bild 1.4.1) zu nutzen.

A
Ar = z. B. C$_6$H$_4$

B
R = H, Br
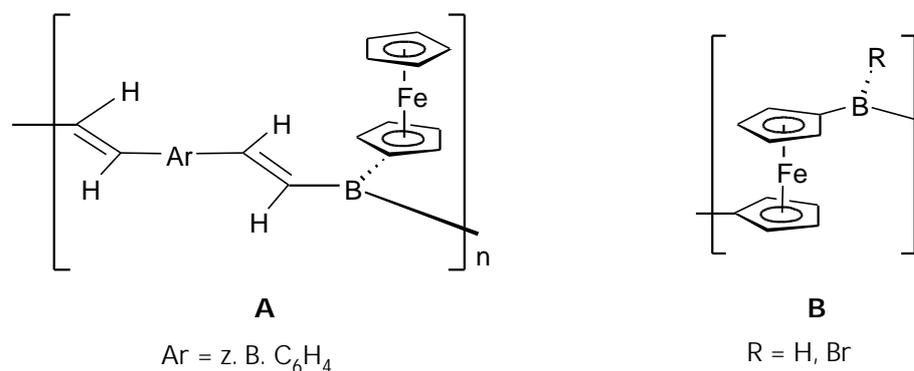
Bild 1.4.1 Ferrocenhaltige Polymere mit dreifach koordiniertem Bor im Rückgrat.

1.4.1   Hydroborierungspolymerisation

Chujo et al. konnten durch die Hydroborierungspolymerisation von Dialkinen mit Mesitylboran konjugierte Polymere darstellen, die mit Polyolefinen verwandt sind, in denen einzelne Kohlenstoffatome durch Boratome ersetzt sind (Schema 1.1.3).[44] Diese Materialien zeichnen sich durch eine ausgeprägt π-Delokalisation aus, die sich über die

Boratome hinweg erstreckt. Die analogen Ferrocenyl-substituierten Makromoleküle (**A**, Bild 1.4.1) würden durch Oxidation der Ferrocenyl-Seitenkette eine elektrochemische Modifizierung der Ladungsdichte an den Borzentren erlauben. Gleichzeitig ließen sich auf diese Weise paramagnetische Fe(III)-Ionen in unmittelbarer Nachbarschaft zu einem elektrisch leitfähigen Polymer generieren. Es wäre außerdem interessant zu untersuchen, ob durch elektronische Anregung von **A** mit Laserlicht freie Ladungsträger auf photochemischem Wege aus den Ferrocenylresten in das Polymerrückgrat injizierbar sind (vgl. den charge-transfer Komplex [**30**]$^+$, Bild 1.3.11). Aufgrund der Ergebnisse zum Hydroborierungsverhalten der Lewis-Säure-Base-Addukte von FcBH$_2$ (**9**) wurde **9·DMS** für die Polymerisationsversuche ausgewählt (Schema 1.4.1).[126]
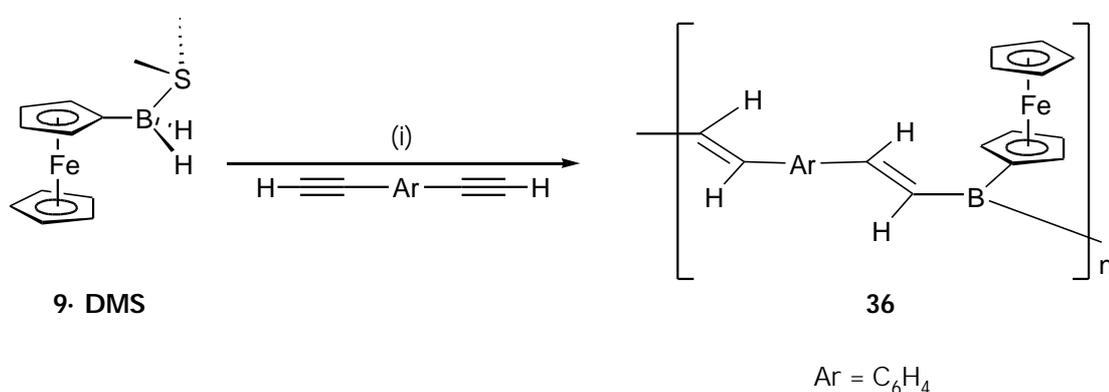
Schema 1.4.1 Hydroborierungpolymerisation von 1,4-Diethinylbenzol mit FcBH$_2$·SMe$_2$ (**9·DMS**): (i) SMe$_2$, Raumtemperatur, 12h.

Die Reaktion wurde in Dimethylsulfid als Lösungsmittel durchgeführt, um die Dimerisierung von FcBH$_2$ zu verhindern (Schema 1.2.4). IR- und NMR-spektroskopische Untersuchungen des Produktes **36** deuten darauf hin, dass die gewünschte Polymerisation in der Tat stattgefunden hat. Das ^{1}H-NMR-Spektrum zeigt drei sehr breite Signale [$\delta(^1$H) = 7.45, 4.59, 4.11] im Integralverhältnis von 8:4:5, die den acht Olefin- und Aromatenprotonen sowie den vier bzw. fünf Wasserstoffatomen am substituierten bzw. am unsubstituierten Cyclopentadienylring des Ferrocens zugeordnet werden können. Im für Alkylprotonen typischen Bereich des Spektrums

werden keine Signale beobachtet, so dass eine doppelte Hydroborierung der Dreifachbindungen am 1,4-Diethinylbenzol auszuschließen ist. Das ^{11}B-NMR-Spektrum zeigt ein sehr breites Signal [δ([11]B) = 31.2; $h_{1/2}$ = 1300 Hz] im Bereich dreifach koordinierter Boratome.[113] Das IR-Spektrum von **36** enthält Banden ($\tilde{n}$ = 1597 cm^{-1}, 1552 cm^{-1}, 1504 cm^{-1}), die in dem für C=C-Streckschwinungen charakteristischen Bereich liegen. Für die Anwesenheit eines ausgedehnten konjugierten Polymerrückgrats in **36** spricht ferner eine intensive Absorptionsbande im UV-VIS-Spektrum bei λ = 323 nm (ε = 7000), die in Übereinstimmung mit den in Schema 1.1.3 gezeigten Polymeren einem π–π*-Übergang zuzuordnen ist (Bild 1.4.2).[44] Eine weitere schwächere Absorption (ε =1000) ist bei 489 nm zu beobachten, die durch einen d-d-Übergang in den Ferrocenylseitenketten verursacht wird.[127]
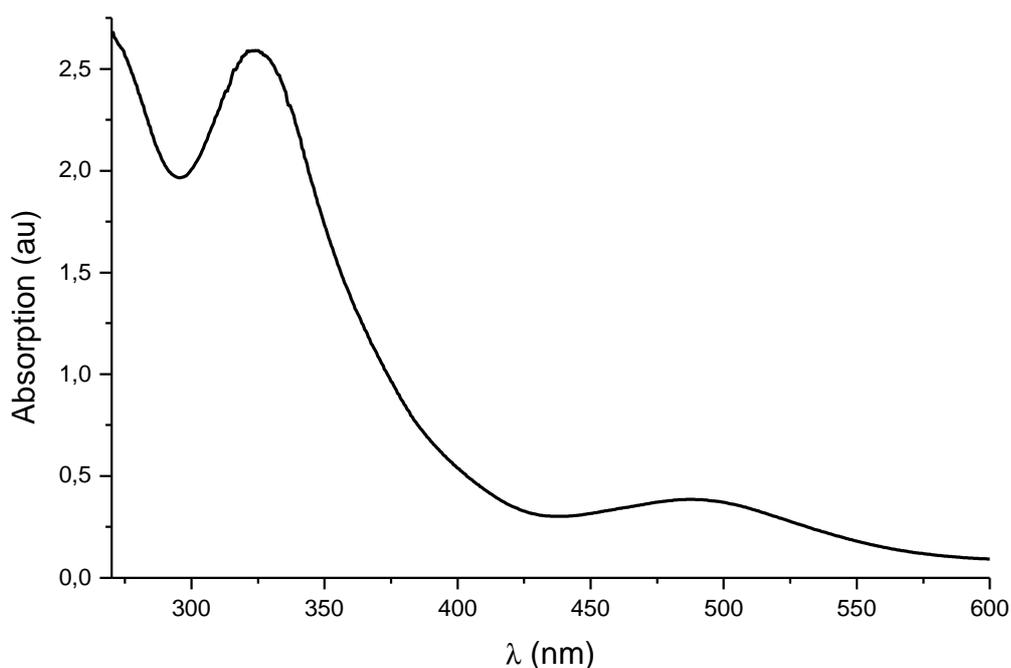
Bild 1.4.2 UV/Vis-Spektrum von **36** in CH$_2$Cl$_2$.

Aufgrund der hohen Luft- und Wasserempfindlichkeit von **36** (Rühren seiner Lösung in Methylenchlorid an Luft führt zu Zersetzung, die sich in einem Farbumschlag von tief rot nach orange äußert und durch veränderte NMR-Spektren bestätigt wird) gab die

Trennung des Reaktionsgemisches mittels Gelpermeationschromatographie bislang keine verlässliche Auskunft über die Molgewichtsverteilung des Polymers.

1.4.2 Polykondensationsreaktionen

Nach Entdeckung der in Schema 1.2.4 und Schema 1.3.11 gezeigten Kondensationsreaktionen war zu klären, ob sich durch den Einsatz difunktioneller Monomere mit zwei Borylsubstituenten Polymere darstellen lassen, die im Gegensatz zu **36** nicht nur dreifach koordinierte Boratome sondern auch Ferrocen als integralen Bestandteil der Hauptkette tragen (**B**, Bild 1.4.1). In einem solchen Polymer wäre ein geringer Abstand zwischen den Metallzentren gewährleistet und es könnte zusätzlich aufgrund seiner BH-Funktion durch Hydroborierungsreaktionen vielfältig derivatisiert werden.

Für die Polymerisation unter BH_3-Abspaltung (Schema 1.4.2) genügt es, eine Lösung des Dimethylsulfid-Adduktes $1,1´\text{-}fc(BH_2 \cdot SMe_2)_2$ (**15·DMS**) in Dimethylsulfid zu rühren. Bereits nach wenigen Stunden bei Raumtemperatur verfärbt sich das Reaktionsgemisch tief rot.[128] Gleichzeitig ist im ^{11}B-NMR-Spektrum die Bildung von $BH_3 \cdot SMe_2$ zu beobachten [$\delta(^{11}B) = -18.3$, $^1J_{B,H} = 106$ Hz].[113] Nach einigen Tagen ist die Reaktion abgeschlossen (die Reaktionsgeschwindigkeit lässt sich durch Verdünnen der Lösung mit CH_2Cl_2 steigern).
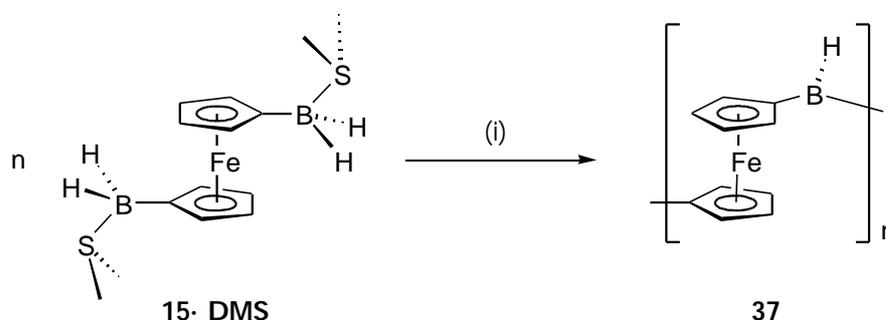
Schema 1.4.2 Polykondensation von $1,1´\text{-}fc(BH_2)_2$ (**15**). (i) SMe_2, 7 d, Raumtemperatur.

Bei der Interpretation der spektroskopischen Daten von **37** bietet sich ein Vergleich mit Fc$_2$BH (**10**) an. Die IR-Spektren von **10** und **37** stimmen nahezu überein [Bild 1.2.8; **10**: $\tilde{n}$ (BH) = 2360 cm^{-1}; **37**: $\tilde{n}$ (BH) = 2360 cm^{-1}], d. h. das Polymer bildet im Festkörper ebenfalls keine B-H-B-Mehrzentrenbindungen aus. Auch in Lösung wird keine Assoziation beobachtet. Das ^{11}B-NMR-Spektrum von **37** zeigt in guter Übereinstimmung mit **10** ein sehr breites Signal in dem für dreifach koordiniertes Bor typischen Bereich [δ(^{11}B) = 51.6 ppm, h$_{1/2}$ = 1200 Hz].[113] Wichtige Hinweise liefert auch das Protonenspektrum. Hier sind die Signale für das Wasserstoffatom am Bor [δ(^{1}H) = 5.68, sehr breit] und die Protonen an den substituierten Cyclopentadienylringen [δ(^{1}H) = 4.60, 4.40] zu beobachten. Außerdem ist ein vergleichsweise kleines Signal in dem Bereich des Spektrums sichtbar, in dem die Protonen der unsubstituierten Cp-Ringe von **10** absorbieren [δ(^{1}H) = 4.10]. Diese Resonanz ist vermutlich den Endgruppen des Polymers zuzuordnen. Aus dem Integralverhältnis der Signale für die Wasserstoffatome der substituierten und der unsubstituierten Ringe kann man die Länge des Polymers abschätzen. Danach bestünde ein Polymerstrang im Durchschnitt aus ca. 14 Ferroceneinheiten.

Ergebnisse, die für eine Polymerisationsreaktion sprechen, liefert auch die Umsetzung von 1,1´-fc(BBr$_2$)$_2$ (**2**) mit einem Überschuss an Triethylsilan (Schema 1.4.3).[129] Führt man die Reaktion in Toluol durch, fällt **38** als rotes hydrolyseempfindliches Pulver an, das in den meisten organischen Lösungsmittels nur schlecht löslich ist.
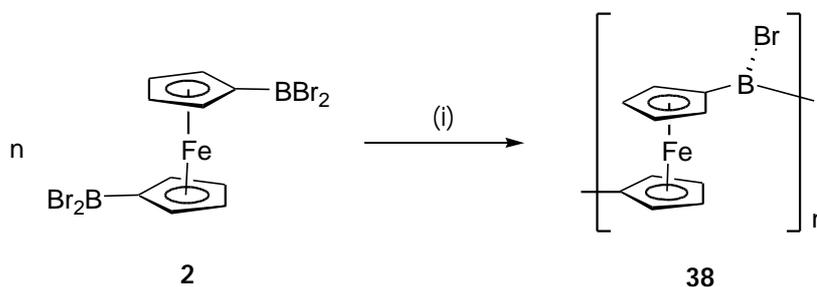
Schema 1.4.3 Kondensationspolymerisation von 1,1´-fc(BBr$_2$)$_2$ (**2**): (i) HSiEt$_3$, Toluol, −78 °C, dann Raumtemperatur, 12 h.

Die Löslichkeit verbessert sich deutlich, wenn der Bromosubstituent am Bor durch Umsetzung mit MeOSiMe$_3$ gegen eine Methoxy-Gruppe ausgetauscht wird. Die erhöhte Stabilität des Produktes erlaubte die Auftrennung des Reaktionsgemisches mittels Gelpermeationschromatographie. Die Ergebnisse lassen auf Kettenlängen zwischen 10 und 50 Ferroceneinheiten schließen.

Zusammenfassend kann gesagt werden, dass in allen drei Fällen eine Polymerisation beobachtet wird. Aufgrund der Empfindlichkeit des primär erhaltenen Materials gestaltet sich die Bestimmung der Molmassen bislang jedoch schwierig. Es ist aber davon auszugehen, dass die mittlere Kettenlänge zehn Ferroceneinheiten überschreitet und damit alle wesentlichen Polymereigenschaften beobachtbar sind.

1.5   Zusammenfassung

Der Einbau von Übergangsmetallionen in Polymerketten kann zu Materialien mit vielversprechenden optischen, elektronischen oder magnetischen Eigenschaften führen, wie sie auf der Basis konventioneller organischer Polymere nicht zu erzielen sind. Die für metallorganische Makromoleküle charakteristischen Eigenschaften resultieren vor allem aus der Vielfalt der Strukturtypen, die für Metallkomplexe auftreten, und in vielen Fällen aus kooperativen Effekten zwischen den Übergangsmetallzentren eines Polymerstranges. Gezieltes Materialdesign setzt daher neben einem grundlegenden Verständnis der Interaktion zwischen den Metallkomplexfragmenten die Fähigkeit voraus, diese durch geeignete Verknüpfungseinheiten so miteinander zu verbinden, dass Wechselwirkungen zwischen ihnen auftreten. Kooperative Phänomene lassen sich häufig bereits an kurzkettigen Oligomeren beobachten, die daher als Modellsysteme für die entsprechenden Polymere dienen. Vor diesem Hintergrund lag der Schwerpunkt der vorliegenden Arbeit auf der Synthese und Charakterisierung di- und trinuclearer Metallkomplexe. Darüber hinaus wurden aber auch entscheidende Fortschritte in Bezug auf die Synthese metallhaltiger Polymere auf der Basis ausgewählter Ferrocenderivate erzielt.

Zur Darstellung der Zielverbindungen wurden sowohl etablierte Verknüpfungs-Konzepte genutzt als auch neue Syntheserouten entwickelt. Als wichtige Startverbindungen wurden die Ferrocenylborane $FcBR_2$ (**1**) und $1,1´\text{-}fc(BR_2)_2$ (**2**) [Fc = $(C_5H_5)Fe(C_5H_4)$, fc = $Fe(C_5H_4)_2$, R = Br, H, $CR´_3$] eingesetzt, da sich deren Borylsubstituenten in vielfältiger Weise zur Verknüpfung der metallorganischen Bausteine nutzen lassen. Als Fundament dieser Arbeit galt es zunächst eine detaillierte Studie unterschiedlicher mono-, di- und tetraborylierter Ferrocenderivate hinsichtlich ihrer strukturellen und elektronischen Eigenschaften durchzuführen. Das auffälligste Merkmal der Festkörperstrukturen zahlreicher Ferrocenylboranderivate ist eine

Abwinkelung des BR_2-Substituenten aus der Ebene des Cyclopentadienylrings hin zum Eisenatom, die in Abhängigkeit von der Anzahl der Borylgruppen und elektronischen Eigenschaften der Reste R mehr oder weniger stark ausgeprägt ist (Bild 1.5.1). Je größer der Elektronenbedarf am Bor, desto größer ist der Abknickwinkel.

1c
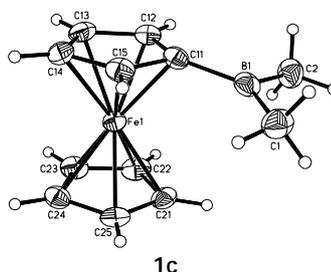
Bild 1.5.1

Als Ursache dieser Verzerrung wurde ursprünglich eine Wechselwirkung zwischen gefüllten d-Orbitalen am Eisen und dem leeren p-Orbital am Bor postuliert. Im Rahmen dieser Arbeit konnte durch ein umfangreiche Untersuchung (Kristallstrukturanalyse, Cyclovoltammetrie, Mößbauerspektroskopie, DFT-Rechnungen) ausgewählter Ferrocenylborane bewiesen werden, dass dieses einfache Modell den wirklichen Bindungsverhältnissen nicht vollständig gerecht wird. Eine Analyse der Elektronendichteverteilung in $FcBR_2$ legt für die beobachtete Abwinkelung zwei Ursachen nahe: Erstens konnten Molekülorbitale identifiziert werden, an denen das leere p-Orbital am Bor, das p-Orbital am *ipso*-Kohlenstoffatom, d-Orbitale am Eisen und p-Orbitale des zweiten Cyclopentadienylrings beteiligt sind. Überdies kommt der Coulomb-Attraktion zwischen dem Borylsubstituenten und dem gegenüberliegenden C_5H_5-Ring wesentlicher Anteil an der Abwinkelung der BR_2-Gruppe zu.

Aufgrund der Lewis-sauren Eigenschaften der Borylsubstituenten können Ferrocenylborane mit difunktionellen organischen Lewis-Basen wie 4,4´-Bipyridin oder Pyrazin zu Polymeren verknüpft werden. Um die Anzahl der Metallatome innerhalb derartiger Makromoleküle zu erhöhen, wurden im Rahmen dieser Arbeit erstmals metallorganische Lewis-Basen als Verknüpfungseinheiten eingesetzt. In dieser Hinsicht bieten sich 3,4-Dimethyl-1-phosphaferrocen (**16**) und 3,3´,4,4´-Tetramethyl-1,1´-diphosphaferrocen (**17**) sowie Ferrocenyllithium (**21**) und 1,1´-Dilithioferrocen (**22**) an,

da in diesen Verbindungen das Lewis-basische Zentrum Bestandteil des Cyclopentadienylrings ist. Die experimentellen Ergebnisse zeigen, dass Addukte der Phosphaferrocene selbst mit den starken Lewis-Säuren FcBBr$_2$ und 1,1´-fc(BBr$_2$)$_2$ nur im Festkörper stabil sind. Bei der Umsetzung von 3,3´,4,4´-Tetramethyl-1,1´-diphosphaferrocen mit 1,1´-fc(BBr$_2$)$_2$ wird auch im Kristall kein Polymer sondern lediglich ein dinuclearer Komplex isoliert (**20**, Bild 1.5.2). Dies lässt sich dadurch erklären, dass durch Komplexierung des einen Phosphoratoms die Lewis-Basizität des anderen so stark herabgesetzt wird, dass keine zweite stabile Adduktbindung mehr ausgebildet wird. Eine gegenseitige Beeinflussung der funktionellen Gruppen wird ebenfalls für 1,1´-fc(BBr$_2$)$_2$ beobachtet. Die erste Bindung an das Phosphaferrocen führt zu einer Verringerung der Lewis-Acidität des zweiten Borylsubstituenten.

20
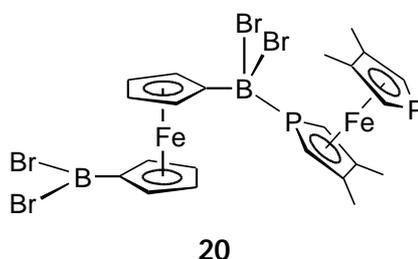
Bild 1.5.2

Im Gegensatz zu den Phosphaferrocenen bilden die starken Lewis-Basen Ferrocenyllithium (**21**) und 1,1´-Dilithioferrocen (**22**) mit dem Ferrocenylboran FcBMe$_2$ (**1c**, Bild 1.5.1) selbst in Lösung stabile Addukte (z. B. **[24]$^{2-}$**, Bild 1.5.3).

[24]$^{2-}$
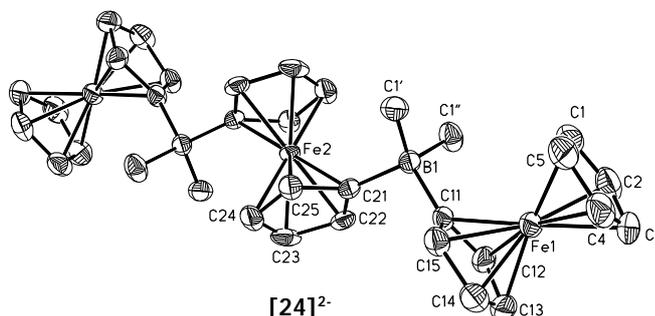
Bild 1.5.3

Polymerisationsversuche mit den Edukten 1,1´-(fcBMe$_2$)$_2$ (**4**) und 1,1´-Dilithioferrocen (**22**) führen entgegen den Erwartungen jedoch nicht zu polymerem Material, sondern

ergeben das borverbrückte [1.1]Ferrocenophan **[26]**$^{2-}$. Die Struktur von **[26]**$^{2-}$ im festen Zustand weist als hervorstechendstes Merkmal ein nacktes Lithium-Ion auf, das sich im Zentrum des Käfigs befindet (Bild 1.5.4). Dieses supramolekulare Aggregat ist auch in Lösung beständig. Werden jedoch beide Ferroceneinheiten oxidiert, verlässt das Li^{+}-Ion den Makrozyklus, um nach vollständiger Reduktion von **[26]** zu **[26]**$^{2-}$ wieder an seinen ursprünglichen Platz zurückzukehren.
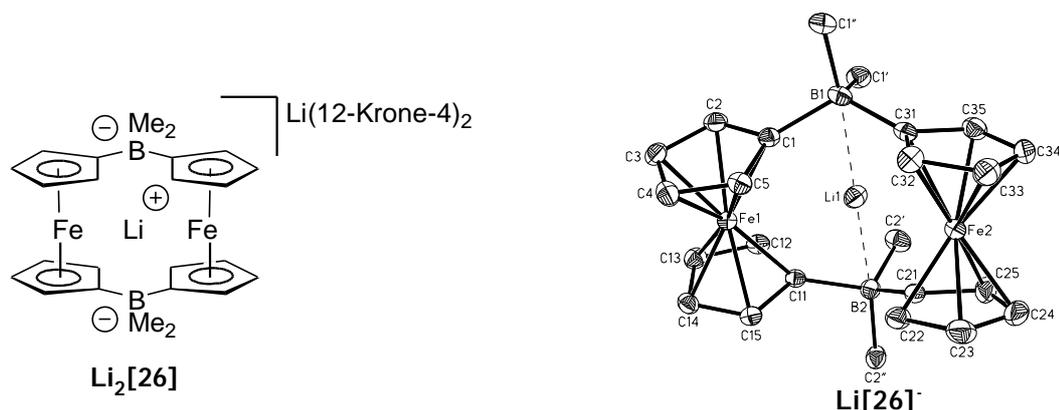
Bild 1.5.4

Komplementär zum Verknüpfungskonzept über dative Bor-Stickstoff-, Bor-Phosphor- und Bor-Kohlenstoff-Bindungen wurde im Rahmen dieser Arbeit eine Kondensationsreaktion erarbeitet, die auf einfachem Wege zu kovalent verknüpften di- und oligonuclearen Ferrocenkomplexen führt.
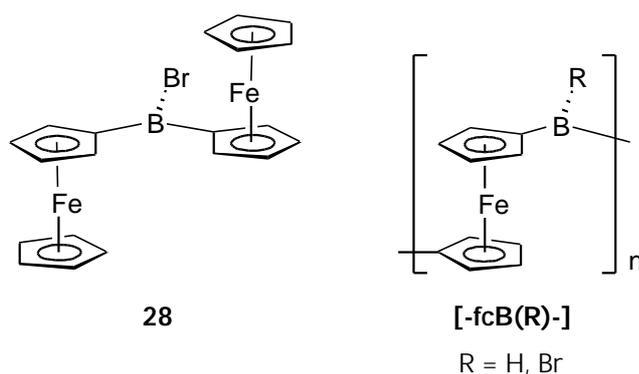
Bild 1.5.5

Bei der Umsetzung von FcBBr$_2$ (**1**) mit HSiEt$_3$ beobachtet man eine Dimerisierungsreaktion, die unter Bildung von Fc$_2$BBr (**28**, Bild 1.5.5, links) verläuft.

Einer entsprechenden Reaktion lässt sich auch 1,1´-fc(BBr$_2$)$_2$ (**2**) unterziehen, womit sich ein Weg zu Poly(ferrocenylenen) eröffnet, in denen die Ferroceneinheiten über dreifach koordiniertes Bor verknüpft sind (**[-fcB(R)-]**, R = Br, Bild 1.5.5, rechts).

Durch cyclovoltammetrische Messungen an ausgewählten di- und trinuclearen Komplexen wie zum Beispiel [Fc$_2$BMe$_2$]⁻ ([**23**]⁻), [Fc$_2$B(bipy)]⁺ ([**30**]⁺), [Fc-BMe$_2$-fc-BMe$_2$-Fc]$^{2-}$ ([**24**]$^{2-}$) oder [Fc-B(bipy)-fc-B(bipy)-Fc]$^{2+}$ ([**34**]$^{2+}$), welche tetrakoordinierte Borbrücken zwischen den Ferrocenen aufweisen, wurde der Einfluss der Brückenladung auf das Ausmaß der Wechselwirkung zwischen den Eisenatomen untersucht. Die erhaltenen Ergebnisse lassen folgende Schlussfolgerung zu: Sowohl die Halbstufenpotentiale der Ferroceneinheiten als auch die Potentialdifferenz zwischen den einzelnen Redoxprozessen innerhalb eines Moleküls werden wesentlich durch intramolekulare elektrostatische Effekte bestimmt. Der Einfluss einer positiven Brückenladung ([Fc$_2$B(bipy)]⁺, E°´ = +0.07 vs. FcH/FcH⁺) ist jedoch wesentlich geringer ausgeprägt als der einer negativen Brückenladung ([Fc$_2$BMe$_2$]⁻, E°´ = –0.64 V). Daraus lässt sich ableiten, dass noch weitere Faktoren berücksichtigt werden müssen. Beispielsweise scheinen im Falle der anionischen Verbindungen der positive induktive Effekt des B(R)Me$_2$-Substituenten (R = Fc, fc) oder positive Hyperkonjugation zwischen B-C-σ-Orbitalen und π*-Orbitalen der Cyclopentadienylringe eine wichtige Rolle zu spielen.

Weitere Wege zu ferrocenhaltigen Polymeren mit Bor im Polymerrückgrat wurden durch die erfolgreiche Synthese der Ferrocenylborane FcBH$_2$ (**9**) und 1,1´-fc(BH$_2$)$_2$ (**15**) eröffnet, die in Form ihrer Lewis-Säure-Base-Addukte mit Dimethylethylamin (**9·NMe$_2$Et**, **15·NMe$_2$Et**) oder Dimethylsulfid (**9·DMS**, **15·DMS**) isoliert werden konnten. **9·NMe$_2$Et** und **9·DMS** erwiesen sich als aktive und selektive Hydroborierungsreagenzien. Durch Umsetzung mit aromatischen Dialkinen werden dadurch konjugierte Polymere (Bild 1.5.6) zugänglich, welche mit Polyolefinen verwandt sind, in denen einige der Kohlenstoffatome durch Boratome ersetzt wurden. Diese Materialien zeichnen sich durch ausgeprägt π-Delokalisation aus, die sich über das Bor hinweg erstreckt, und weckten unser Interesse, da Oxidation der Ferrocenyl-

Seitenketten eine elektrochemische Modifizierung der Ladungsdichte an den Borzentren erlauben sollte. Gleichzeitig ließen sich auf diese Weise paramagnetische Fe(III)-Ionen in unmittelbarer Nachbarschaft zu einem elektrisch leitfähigen Polymer generieren.
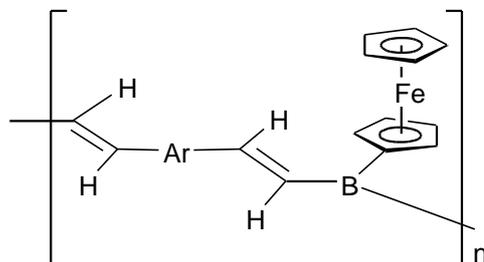
Bild 1.5.6

Überdies erhält man Polymere des Typs **[-fcB(R)-]** (Bild 1.5.5) nicht nur über die Reaktion von 1,1´-fc(BBr$_2$)$_2$ (**2**) mit HSiEt$_3$ (R = Br) sondern auch über die Kondensationsreaktion von 1,1´-fc(BH$_2$)$_2$ (**15**), die unter Abspaltung von BH$_3$ verläuft (R = H).

In der vorliegenden Arbeit konnte gezeigt werden, dass man über Donor-Akzeptor-Bindungen zwischen Ferrocenylboranen und metallorganischen Lewisbasen wie 3,3´,4,4´-Tetramethyl-1,1´-Diphosphaferrocen (**17**) oder 1,1´-Dilithioferrocen (**22**) oligomere metallhaltige Verbindungen aufbauen kann. Außerdem wurden Grundlagen für die weitergehende Entwicklung metallorganischer Polymere gelegt, welche sich durch elektronische Wechselwirkungen zwischen den Metallzentren auszeichnen.

1.6   Literaturverzeichnis

[1]   J. Alper, G. L. Nelson, *Polymeric Materials: Chemistry for the Future*, ACS, Washington DC, **1989**.

[2]   I. Manners, *Angew. Chem.* **1996**, *108*, 1712.

[3]   J. E. Mark, H. R. Allcock, R. West, *Inorganic Polymers*, Prentice-Hall Inc., Englewood Cliffs, NJ, **1992**.

[4]   E. G. Rochow, *Silicon and Silicones*, Springer Verlag, Heidelberg, **1987**.

[5]   F. A. Cotton, G. Wilkinson, C. A. Murillo, M. Bochman, *Advanced Inorganic Chemistry*, 6th ed., Wiley Interscience, Toronto, **1999**.

[6]   D. W. Bruce, D. O´Hare, *Inorganic Materials*, 2nd ed., John Wiley & Sons, Toronto, **1996**.

[7]   D. L. Leslie-Pelecky, R. D. Rieke, *Chem. Mater.* **1996**, *8*, 1770.

[8]   N. J. Long, *Angew. Chem. Int. Ed. Engl.* **1995**, *34*, 21.

[9]   I. R. Whitall, A. M. McDonagh, M. G. Humphrey, M. Samoc, *Adv. Organomet. Chem.* **1998**, *42*, 291.

[10]   I. R. Whitall, A. M. McDonagh, M. G. Humphrey, M. Samoc, *Adv. Organomet. Chem.* **1998**, *43*, 349.

[11]   M. A. Baldo, D. F. O´Brien, Y. You, A. Shoustikov, S. Sibley, M. E. Thompson, S. R. Forrest, *Nature* **1998**, *395*, 151.

[12]   M. A. Baldo, M. E. Thompson, S. R. Forrest, *Pure Appl. Chem.* **1999**, *71*, 2095.

[13]   J.-M. Lehn, *Supramolecular Chemistry, Concepts and Perspectives*, VCH, Weinheim, **1995**.

[14]   F. Vögtle, *Supramolekulare Chemie*, Teubner, Stuttgart, **1989**.

[15] J. W. Steed, J. L. Atwood, *Supramolecular Chemistry*, John Wiley & Sons, New York, **2000**.

[16] J.-M. Lehn, A. Rigault, J. Siegel, J. Harrowfield, B. Chevrier, D. Moras, *Proc. Natl. Acad. Sci. U.S.A* **1987**, *84*, 2565.

[17] W. Zarges, J. Hall, J.-M. Lehn , C. Bolm, *Helv. Chim. Acta.* **1991**, *74*, 1843.

[18] C. Piguet, G. Bernardinelli, G. Hopfgartner, *Chem. Rev.* **1997**, *97*, 2005.

[19] K. Abdur-Rashid, D. G. Gusev, S. E. Landau, A. J. Lough, R. H. Morris, *J. Am. Chem. Soc.* **1998**, *120*, 11826.

[20] R. H. Crabtree, P. E. M. Siegbahn, O. Eisenstein, A. L. Rheingold, T. F. Koetzle, *Acc. Chem. Res.* **1996**, *29*, 348.

[21] C. P. McArdle, J. J. Vittal, R. J. Puddephatt, *Angew. Chem. Int. Ed. Engl.* **2000**, *39*, 3819.

[22] R. E. Bachman, M. S. Fioritto, S. K. Fetics, T. M. Cocker, *J. Am. Chem. Soc.* **2001**, *123*, 5376.

[23] M. M. Olmstead, F. Jiang, S. Attar, A. L. Balch, *J. Am. Chem. Soc.* **2001**, *123*, 3260.

[24] I. Manners, *Synthetic Metal-Containing Polymers*, Wiley-VCH, Weinheim, **2003**.

[25] a) F. S. Arimoto, A. C. Haven, Jr., *J. Am. Chem. Soc.* **1955**, *77*, 6295; b) K. Schlogl, A. Mohar, *Monatsh. Chem.* **1961**, *92*, 219; c) J. C. Lai, T. Rounsefell, C. U. Pittman, Jr., *J. Polym. Sci. A-1*, **1971**, *9*, 651.

[26] K. H. Pannell, J. M. Rozell, J. M. Zeigler, *Macromolecules* **1988**, *21*, 276.

[27] H. R. Allcock, K. D. Lavin, G. H. Riding, *Macromolecules* **1985**, *18*, 1340.

[28] H. R. Allcock, G. H. Riding, K. D. Lavin, *Macromolecules* **1987**, *20*, 6.

[29] P. Nguyen, P. Gómez-Elipe, I. Manners, *Chem. Rev.* **1999**, *99*, 1515.

[30] M. Rehahn, *Acta Polymer.* **1998**, *49*, 201.

[31] M. Altmann, U. H. F. Bunz, *Angew. Chem. Int. Ed. Engl.* **1995**, *34*, 569.

[32]   D. A. Foucher, B. Z. Tang, I. Manners, *J. Am. Chem. Soc.* **1992**, *114*, 6246.

[33]   I. Manners, *Adv. Organomet. Chem.* **1995**, *37*, 131.

[34]   J. K. Pudelski, I. Manners, *J. Am. Chem. Soc.* **1995**, *117*, 7265.

[35]   J. B. Sheridan, K. Temple, A. J. Lough, I. Manners, *J. Chem. Soc., Dalton Trans.* **1997**, 711.

[36]   A. Togni, T. Hayashi, *Ferrocenes*, VCH Verlagsgesellschaft, Weinheim, **1995**.

[37]   H. Braunschweig, R. Dirk, M. Müller, P. Nguyen, R. Resendes, D. P. Gates, I. Manners, *Angew. Chem.* **1997**, *109*, 2433.

[38]   K. Ma, M. Scheibitz, S. Scholz, M. Wagner, *J. Organomet. Chem.* **2002**, *652*, 11.

[39]   E. Wiberg, *Naturwissenschaften* **1948**, *35*, 182.

[40]   E. Wiberg, *Naturwissenschaften* **1948**, *35*, 212.

[41]   W. Ruf, M. Fueller, W. Siebert, *J. Organomet. Chem.* **1976**, *64*, C45.

[42]   a) W. Ruf, T. Renk, W. Siebert, *Z. Naturforsch. B* **1976**, *31*, 1028; b) T. Renk, W. Ruf, W. Siebert, *J. Organomet. Chem.* **1976**, 1.

[43]   C. D. Entwistle, T. B. Marder, *Angew. Chem.* **2002**, *114*, 3051.

[44]   N. Matsumi, K. Naka, Y. Chujo, *J. Am. Chem. Soc.* **1998**, *120*, 5112.

[45]   N. Matsumi, Y. Chujo, O. Lavastre, P. H. Dixneuf, *Organometallics* **2001**, *20*, 2425.

[46]   S. Aldridge, C. Bresner, *Coord. Chem. Rev.* **2003**, *244*, 71.

[47]   M. T. Reetz, H. Brummer, M. Kessler, J. Kuhnigk, *Chimia* **1995**, *49*, 501.

[48]   M. Bochmann, S. J. Lancaster, O. B. Robinson, *Chem. Commun.* **1995**, 2081.

[49]   K. A. Rufanov, V. V. Kotov, N. B. Kazennova, D. A. Lemenovskii, E. V. Avtomonov, J. Lorberth, *J. Organomet. Chem.* **1996**, *525*, 287.

[50]   F. Jäkle, K. Polborn, M. Wagner, *Chem. Ber.* **1996**, *129*, 603

[51]   R. E. Dinnebier, M. Wagner, F. Peters, K. Shankland, W. I. F. David, *Z. Anorg. Allg. Chem.* **2000**, *626*, 1400.

[52]   L. Ding, K. Ma, M. Dürner, M. Bolte, F. F. de Biani, P. Zanello, M. Wagner, *Dalton Trans.* **2002**, 1566.

[53]   T. Yamamoto, A. Ori, K. Ueda, C. Dusemund, S. Shinkai, *Chem. Commun.* **1996**, 407.

[54]   L. Weissfloch, M. Wagner, T. Probst, R. Senekowitsch-Schmidtke, K. Tempel, M. Molls, *Biometals* **2001**, *14*, 43.

[55]   C. Dusemund, K. R. A. S. Sandanayake, S. Shinkai, *J. Chem. Soc., Chem. Commun.* **1995**, 333.

[56]   M. Scheibitz, M. Bolte, J. W. Bats, H.-W. Lerner, I. Nowik, R. H. Herber, A. Krapp, M. Lein, M. C. Holthausen, M. Wagner, *Chem. Eur. J.* **2004**, zur Veröffentlichung angenommen.

[57]   A. Appel, F. Jäkle, T. Priermeier, R. Schmid, M. Wagner, *Organometallics* **1996**, *15*, 1188.

[58]   R. F. W. Bader, F. W. Biegler-König, *J. Comput. Chem.* **1982**, *3*, 317.

[59]   J. S. Miller, *Inorg. Chem.* **2000**, *39*, 4392.

[60]   I. Nowik, M. Wagner, R. H. Herber, *J. Organomet. Chem.* **2003**, *688*, 11.

[61]   R. H. Herber, B. Bildstein, P. Denifl, H. Schottenberger, *Inorg. Chem.* **1997**, *36*, 3586.

[62]   H. Schottenberger, K. Wurst, R. H. Herber, *J. Organomet. Chem.* **2001**, *625*, 200.

[63]   J. Silver, D. A. Davies, R. M. G. Roberts, M. Herberhold, U. Dörfler, B. Wrackmeyer, *J. Organomet. Chem.* **1999**, *590*, 71.

[64]   A. Houlton, J. R. Miller, R. M. G. Roberts, J. Silver, *J. Chem. Soc., Dalton Trans.* **1990**, 2181.

[65]   J. Pebler, W. Ruf, W. Siebert, *Z. Anorg. Allg. Chem.* **1976**, *422*, 39.

[66]   H. C. Brown, *Boranes in Organic Chemistry*, Cornell University Press, Ithaca, **1972**.

[67]   H. C. Brown, *Organic Synthesis via Boranes*, Wiley, New York, **1975**.

[68]   A. Appel, *Dissertation*, Ludwig Maximilians Universität München, **1996**.

[69]   M. Scheibitz, J. W. Bats, M. Bolte, H.-W. Lerner, M. Wagner, *Organometallics* **2004**, *23*, 940.

[70]   Synthese von $FcBH_3Li(Et_2O)_2$ (**8b**): Zu einer Lösung von **1d** (2.72 g, 10.55 mmol) in Diethylether (20 ml) werden bei –78 °C 10.6 ml einer 1M $LiAlH_4$-Lösung in Et_2O (10.6 mmol) getropft. Nach 30 min lässt man die Mischung auf RT erwärmen und rührt 1h. Das Reaktionsgemisch wird über eine G4-Fritte filtriert und der Rückstand dreimal mit Diethylether (je 10 ml) extrahiert. Beim Abkondensieren des Lösungsmittels kristallisiert **8b** in Form großer gelber Kristalle, die sich für eine Röntgenstrukturanalyse eignen. Ausbeute: 2.83 g (76 %). ^1H NMR (400.1 MHz, d_8-THF, 300 K): d = 0.86 (q, $^1J_{BH}$ = 77.2 Hz, 3H, BH_3), 1.11 (tr, $^3J_{HH}$ = 6.9 Hz, 12H, CH_3), 3.38 (q, $^3J_{HH}$ = 6.9 Hz, 8H, CH_2), 3.75 (n.a., 2 × 2H, C_5H_4), 3.81 (s, 5H, C_5H_5). $^{13}C\{^1H\}$ NMR (62.9 MHz, d_8-THF, 300 K): d = 14.9 (CH_3), 66.3 (CH_2), 67.2 (q, $^3J_{CB}$ = 2.9 Hz, C_5H_4), 68.3 (C_5H_5), 75.1 (q, $^2J_{CB}$ = 3.4 Hz, C_5H_4), 92.4 (q, $^1J_{CB}$ = 59.4 Hz, CB). ^{11}B NMR (128.4 MHz, d_8-THF, 300K): d = -30.6 (q, $^1J_{BH}$ = 77.2 Hz). Kristallstrukturanalyse von **8b**: $C_{36}H_{64}B_2Fe_2Li_2O_4$, M_r = 708.07, monoklin, Raumgruppe $P2_1/c$, a = 10.5271(9), b = 13.3224(9), c = 15.1121(13) Å, b = 109.569(6)°, V = 1997.0(3) Å^3, Z = 2, $r_{ber.}$ = 1.178 Mg m^{-3}, m = 0.759 mm^{-1}, $F(000)$ = 760, $l(Mo_{K\alpha})$ = 0.71073 Å, T = 173(2) K, Kristallabmessungen 0.42 × 0.32 × 0.21 mm^3, $2Q_{max}$ = 51.6°, 29826 gemessene Reflexe, 3805 unabhängige Reflexe (R_{int} = 0.0608), 3805 berücksichtigte Reflexe, semiempirische Absorptionskorrektur, max./min. Transmission 0.8568/0.7410, 209 Parameter, $R1$ = 0.0574 (alle Daten), $wR2$ = 0.1262 (alle Daten), max./min. Restelektronendichte 0.559/-0.698 e Å^{-3}. Die Daten wurden auf einem STOE-IPDS-II Zweikreis-Diffraktometer an einem im Öltropfen gekühlten Kristall gesammelt. Zur Strukturlösung und -verfeinerung wurden die Programme SHELXS-97 und SHELXL-97 (G. M. Sheldrick, Universität Göttingen, **1997**) benutzt. Die Struktur wurde mit Direkten Methoden gelöst und mit anisotropen Auslenkungsparametern für Nicht-H-Atome gegen F^2 verfeinert. Die BH_3-Wasserstoffatome wurden in der

Differenzelektronendichtekarte gefunden und der Torsionswinkel um die CB-Bindung verfeinert. Alle H-Atome wurden mit dem Reiter-Modell verfeinert.

[71] H.-H. Giese, H. Nöth, H. Schwenk, S. Thomas, *Eur. J. Inorg. Chem.* **1998**, 941.

[72] A. Haghiri Ilkhechi, M. Scheibitz, M. Bolte, H.-W. Lerner, M. Wagner, *Polyhedron* **2004**, im Druck.

[73] Kristalle von **8c** werden aus einer gesättigten Lösung von **8b** in Pentan bei –30°C erhalten. Kristallstrukturanalyse von **8c**: $C_{56}H_{88}B_4Fe_4Li_4O_4$, $M_r = 1119.66$, triklin, Raumgruppe $P\bar{1}$, $a = 11.1642(13)$, $b = 11.4223(14)$, $c = 11.9409(15)$ Å, $\alpha = 73.147(10)$, $\beta = 81.396(10)$, $\gamma = 87.087(10)$ Å^3, $V = 1440.9(3)$ Å^3, $Z = 1$, $\rho_{ber.} = 1.290$ Mg m^{-3}, $\mu = 1.029$ mm^{-1}, $F(000) = 592$, $\lambda(Mo_{K\alpha}) = 0.71073$ Å, $T = 100(2)$ K, Kristallabmessungen $0.24 \times 0.13 \times 0.12$ mm^3, $2\Theta_{max} = 53.2°$, 15275 gemessene Reflexe, 5578 unabhängige Reflexe ($R_{int} = 0.0596$), 5578 berücksichtigte Reflexe, semiempirische Absorptionskorrektur, max./min. Transmission 0.8865/0.7903, 327 Parameter, $R1 = 0.0650$ (alle Daten), $wR2 = 0.0722$ (alle Daten), max./min. Restelektronendichte 0.524/-0.377 e Å^{-3}. Die Daten wurden auf einem STOE-IPDS-II Zweikreis-Diffraktometer an einem im Öltropfen gekühlten Kristall gesammelt. Zur Strukturlösung und -verfeinerung wurden die Programme SHELXS-97 und SHELXL-97 (G. M. Sheldrick, Universität Göttingen, **1997**) benutzt. Die Struktur wurde mit Direkten Methoden gelöst und mit anisotropen Auslenkungsparametern für Nicht-H-Atome gegen F^2 verfeinert. Die BH$_3$-Wasserstoffatome wurden in der Differenzelektronendichtekarte gefunden und der Torsionswinkel um die CB-Bindung verfeinert. Alle H-Atome wurden mit dem Reiter-Modell verfeinert.

[74] Kristalle von **9·NMe₂Et**^{II}, die sich für eine Röntgenstrukturanalyse eignen, werden durch langsames Abkondensieren des Lösungsmittels Pentan im Vakuum erhalten. Kristallstrukturanalyse von **9·NMe₂Et**^{II}: $C_{14}H_{22}BFeN$, $M_r = 270.99$, monoklin, Raumgruppe $P2_1$, $a = 5.9189(15)$, $b = 10.096(2)$, $c = 11.576(3)$ Å, $\beta = 96.170(19)°$, $V = 687.7(3)$ Å^3, $Z = 2$, $\rho_{ber.} = 1.309$ Mg m^{-3}, $\mu = 1.073$ mm^{-1}, $F(000) = 288$, $\lambda(Mo_{K\alpha}) = 0.71073$ Å, $T = 173(2)$ K, Kristallabmessungen $0.21 \times 0.18 \times 0.06$ mm^3, $2\Theta_{max} = 51.1°$, 3337 gemessene Reflexe, 2219 unabhängige Reflexe ($R_{int} = 0.0976$), 2219 berücksichtigte

Reflexe, semiempirische Absorptionskorrektur, max./min. Transmission 0.9384/0.8060, 154 Parameter, $R1$= 0.1242 (alle Daten), $wR2$ = 0.2128 (alle Daten), max./min. Restelektronendichte 1.645/-0.610 e Å^{-3}. Die Daten wurden auf einem STOE-IPDS-II Zweikreis-Diffraktometer an einem im Öltropfen gekühlten Kristall gesammelt. Zur Strukturlösung und -verfeinerung wurden die Programme SHELXS-97 und SHELXL-97 (G. M. Sheldrick, Universität Göttingen, **1997**) benutzt. Die Struktur wurde mit Direkten Methoden gelöst und mit anisotropen Auslenkungsparametern für Nicht-H-Atome gegen F^2 verfeinert. Alle H-Atome wurden mit dem Reiter-Modell verfeinert.

[75] Synthese von FcBH$_2$·SMe$_2$ (**9·DMS**): Zu einer Lösung von **8c** (190 mg, 0.68 mmol) in Dimethylsulfid (5 ml) wird bei –78 °C Trimethylchlorsilan (0.5 ml, 3.9 mmol) in 5 ml SMe$_2$ getropft. Nach 30 min lässt man die Mischung auf 0 °C erwärmen und rührt 1h. Das Reaktionsgemisch wird über eine G4-Fritte filtriert. Das Filtrat wird auf ca. 2 ml eingeengt und drei Tage bei –30°C gehalten, wobei **9·DMS** in Form langer gelber Nadeln, die sich für eine Röntgenstrukturanalyse eignen, auskristallisiert. Ausbeute: 148 mg (0.57 mmol, 84 %). ^{1}H NMR (250.1 MHz, S(CD$_3$)$_2$, 297 K): d = 2.05 (s, 6H, CH$_3$), 2.60 (br, 2H, BH$_2$), 3.93 (n.a., 2H, C$_5$H$_4$), 3.99 (s, 5H, C$_5$H$_5$), 4.07 (n.a., 2H, C$_5$H$_4$). ^{13}C{^{1}H} NMR (62.9 MHz, S(CD$_3$)$_2$, 297 K): d = 18.0 (CH$_3$), 68.2 (C$_5$H$_5$), 69.7, 75.4 (C$_5$H$_4$), n.b. (CB). ^{11}B NMR (128.4 MHz, S(CD$_3$)$_2$, 297 K): d = -10.1 (tr, $^1J_{BH}$ = 101.5 Hz). Kristallstrukturanalyse von **9·DMS**: C$_{12}$H$_{17}$BFeS, M_r = 259.98, orthorhombisch, Raumgruppe $Pca2_1$, a = 16.2127(18), b = 5.8859(9), c = 25.442(3) Å, V = 2427.8 Å^3, Z = 8, $r_{ber.}$ = 1.423 Mg m^{-3}, m= 1.376 mm^{-1}, $F(000)$ = 1088, l(Mo$_{K\alpha}$) = 0.71073 Å, T = 173(2) K, Kristallabmessungen 0.38 × 0.12 × 0.08 mm^3, $2Q_{max}$ = 51.68°, 15448 gemessene Reflexe, 4506 unabhängige Reflexe (R_{int} = 0.0693), 4506 berücksichtigte Reflexe, semiempirische Absorptionskorrektur, max./min. Transmission 0.8979/0.6228, 272 Parameter, $R1$= 0.0840 (alle Daten), $wR2$ = 0.1010 (alle Daten), max./min. Restelektronendichte 0.406/-0.264 e Å^{-3}. Die Daten wurden auf einem STOE-IPDS-II Zweikreis-Diffraktometer an einem im Öltropfen gekühlten Kristall gesammelt. Zur Strukturlösung und -verfeinerung wurden die Programme SHELXS-97 und SHELXL-97 (G. M. Sheldrick, Universität Göttingen, **1997**) benutzt. Die Struktur wurde mit Direkten

Methoden gelöst und mit anisotropen Auslenkungsparametern für Nicht-H-Atome gegen F^2 verfeinert. Alle H-Atome wurden mit dem Reiter-Modell verfeinert.

[76]   D. E. Zuccaro, J. D. McCullough, *Z. Krist.* **1959**, *112*, 401.

[77]   H. Nöth, D. Sedlak, *Chem. Ber.* **1983**, *116*, 1479.

[78]   E. Negishi, J.-J. Katz, H. C. Brown, *J. Am. Chem. Soc.* **1972**, *94*, 4025.

[79]   A. Pelter, K. Smith, D. Buss, A. Norbury, *Tetrahedron Lett.* **1991**, *32*, 6239.

[80] $FcBD_3Li(Et_2O)_2$ (**8d**) und Fc_2BD (**10a**) werden in Abwandlung der Literaturvorschrift [70] ausgehend von **1d** und $LiAlD_4$ erhalten. Spektroskopische Daten für **8d**: ^1H NMR (400.1 MHz, d_8-THF, 300 K): 1.11 (tr, $^3J_{HH}$ = 6.9 Hz, 12H, CH_3), 3.38 (q, $^3J_{HH}$ = 6.9 Hz, 8H, CH_2), 3.75 (n.a., $2 \times 2H$, C_5H_4), 3.81 (s, 5H, C_5H_5). $^{13}C\{^1H\}$ NMR (62.9 MHz, d_8-THF, 300 K): d = 14.9 (CH_3), 66.3 (CH_2), 67.2 (q, $^3J_{CB}$ = 2.9 Hz, C_5H_4), 68.3 (C_5H_5), 75.1 (q, $^2J_{CB}$ = 3.4 Hz, C_5H_4), 92.4 (q, $^1J_{CB}$ = 59.4 Hz, CB). ^{11}B NMR (128.4 MHz, d_8-THF, 298K): d = -31.1 (sept, $^1J_{BD}$ = 11.9 Hz). Spektroskopische Daten für **10a**: ^1H NMR (250.1 MHz, C_6D_6, 303 K): d = 4.03 (s, 10H, C_5H_5), 4.48 (mult, 8H, C_5H_4). $^{13}C\{^1H\}$ NMR (62.9 MHz, C_6D_6, 303 K): d = 68.8 (C_5H_5), 75.0, 77.8 (C_5H_4), n.o. (CB). ^{11}B NMR (128.4 MHz, C_6D_6, 303K): d = 54.7 (n.a., $h_{1/2}$ = 270 Hz). IR: 1830 cm^{-1} (B-D).

[81]   J. Heinze, *Angew. Chem.* **1984**, *96*, 823.

[82]   E. R. Brown, J. Sandifer, in *Physical Methods in Chemistry, Vol. 2, Kap. 4* (Eds.: B. W. Rossiter, J. F. Hamilton), John Wiley & Sons, New York, London, Sydney, **1986**.

[83]   S. Barlow, D. O´Hare, *Chem. Rev.* **1997**, *97*, 637.

[84]   Synthese von Fc_2BCy (**11**): Zu einer Lösung von **8c** (130 mg, 0.46 mmol) und Cyclohexen (320 mg, 3.90 mmol) in Diethylether (5 ml) wird bei –75 °C Trimethylchlorsilan (0.5 ml, 3.9 mmol) in 5 ml Et_2O langsam zugetropft. Man lässt die Mischung auf Raumtemperatur kommen und rührt für eine Stunde. Das Reaktionsgemisch wird über eine G4-Fritte filtriert und der Rückstand zweimal

mit Diethylether (je 5 ml) extrahiert. Das Lösungsmittel wird im Vakuum abkondensiert und der Rückstand in wenig warmem Heptan aufgenommen. Nach 12 h bei –30 °C erhält man dunkelorangefarbene Kristalle von **11**, die durch Filtration von der Mutterlauge abgetrennt werden. Ausbeute: 68 mg (64 %). ^{1}H NMR (250.1 MHz, C_6D_6, 300 K): $\textbf{\textit{d}}$ = 1.22 - 2.11 (m, 11H, C_6H_{11}), 4.01 (s, 10H, C_5H_5), 4.43, 4.64 (2 × n.a., 2 × 4H, C_5H_4). ^{13}C{^{1}H} NMR (62.9 MHz, C_6D_6, 300 K): $\textbf{\textit{d}}$ = n.b. (BCH), 27.8, 29.0, 31.1 (C_6H_{11}), 69.0 (C_5H_5), 73.5, 76.8 (C_5H_4), n.b. (CB). ^{11}B NMR (128.4 MHz, C_6D_6, 300 K): $\textbf{\textit{d}}$ = 66.2 ($h_{½}$ = 390 Hz). Kristallstrukturanalyse von **11**: $C_{26}H_{29}BF_2$, M_r = 464.00, monoklin, Raumgruppe $P2_1/n$, a = 7.4731(11), b = 29.742(5), c = 9.3452(18) Å, $\textbf{\textit{b}}$ = 90.120(14)°, V = 2077.1(6) Å^3, Z = 4, $\textbf{\textit{r}}_{ber.}$ = 1.484 Mg m^{-3}, $\textbf{\textit{m}}$ = 1.407 mm^{-1}, F(000) = 968, $\textbf{\textit{l}}$($Mo_{Kα}$) = 0.71073 Å, T = 173(2) K, Kristallabmessungen 0.27 × 0.25 × 0.22 mm^3, $2\textbf{\textit{Q}}_{max}$ = 50.8°, 15557 gemessene Reflexe, 3661 unabhängige Reflexe (R_{int} = 0.0999), 3661 berücksichtigte Reflexe, semiempirische Absorptionskorrektur, max./min. Transmission 0.7472/0.7026, 263 Parameter, R1 = 0.1359 (alle Daten), wR2 = 0.1544 (alle Daten), max./min. Restelektronendichte 0.975/-0.373 e Å^{-3}. Die Daten wurden auf einem STOE-IPDS-II Zweikreis-Diffraktometer an einem im Öltropfen gekühlten Kristall gesammelt. Zur Strukturlösung und -verfeinerung wurden die Programme SHELXS-97 und SHELXL-97 (G. M. Sheldrick, Universität Göttingen, **1997**) benutzt. Die Struktur wurde mit Direkten Methoden gelöst und mit anisotropen Auslenkungsparametern für Nicht-H-Atome gegen F^2 verfeinert. Alle H-Atome wurden mit dem Reiter-Modell verfeinert.

[85]   B. Wrackmeyer, U. Dörfler, W. Milius, M. Herberhold, *Z. Naturforsch.* **1995**, *50b*, 201.

[86]   Die Mutterlauge (siehe Lit. [84]) wird mehrere Tage bei –30°C gehalten, wobei BCy_3 (**12**) in Form farbloser Nadeln, die sich für eine Röntgenstrukturanalyse eignen, auskristallisiert. ^{1}H NMR (250.1 MHz, C_6D_6, 300 K): $\textbf{\textit{d}}$ = 1.00 - 2.07 (m, 33H, 3 × C_6H_{11}). ^{13}C{^{1}H} NMR (62.9 MHz, C_6D_6, 300 K): $\textbf{\textit{d}}$ = n.b. (BCH), 26.9, 27.4, 27.7 (C_6H_{11}). ^{11}B NMR (128.4 MHz, C_6D_6, 300 K): $\textbf{\textit{d}}$ = 81.8 ($h_{½}$ = 530 Hz). Kristallstrukturanalyse von **12**: $C_{18}H_{33}B$, M_r = 260.25, hexagonal,

Raumgruppe $P6_3/m$, $a = 12.778(3)$, $b = 12.778(3)$, $c = 6.6970(14)$ Å, $g = 120°$, V = 947.0(4) Å^3, $Z = 2$, $r_{ber.} = 0.913$ Mg m^{-3}, $m = 0.049$ mm^{-1}, $F(000) = 292$, $l(Mo_{K\alpha}) = 0.71073$ Å, $T = 173(2)$ K, Kristallabmessungen $0.24 \times 0.11 \times 0.08$ mm^3, $2Q_{max} = 50.62°$, 5835 gemessene Reflexe, 623 unabhängige Reflexe (R_{int} = 0.0787), 623 berücksichtigte Reflexe, keine Absorptionskorrektur, max./min. Transmission 0.9961/0.9882, 33 Parameter, $R1 = 0.1477$ (alle Daten), $wR2 = 0.3449$ (alle Daten), max./min. Restelektronendichte 1.866/-0.202 e Å^{-3}. Die Daten wurden auf einem STOE-IPDS-II Zweikreis-Diffraktometer an einem im Öltropfen gekühlten Kristall gesammelt. Zur Strukturlösung und -verfeinerung wurden die Programme SHELXS-97 und SHELXL-97 (G. M. Sheldrick, Universität Göttingen, **1997**) benutzt. Die Struktur wurde mit Direkten Methoden gelöst und mit anisotropen Auslenkungsparametern für Nicht-H-Atome gegen F^2 verfeinert. Alle H-Atome wurden mit dem Reiter-Modell verfeinert.

[87] A. F. Hollemann, E. Wiberg, *Lehrbuch der Anorganischen Chemie*, 101. ed., Walter de Gruyter, Berlin, **1995**.

[88] Synthese von 1,1´-fc(BH$_3$)$_2$Li$_2$ (**14**): Zu einer Lösung von **13** (1.81 g, 5.49 mmol) in Diethylether (20 ml) werden bei –78 °C 11.0 ml einer 1M LiAlH$_4$-Lösung in Et$_2$O (11.0 mmol) getropft. Nach 30 min lässt man die Mischung auf RT erwärmen und rührt 1h. Das Reaktionsgemisch wird über eine G4-Fritte filtriert und der Rückstand viermal mit Diethylether (je 15 ml) extrahiert. Beim Abkondensieren des Lösungsmittels kristallisiert **14** in Form großer gelber Kristalle, die sich für eine Röntgenstrukturanalyse eignen. Ausbeute: 1.70 g (73 %). ^{1}H NMR (400.1 MHz, d$_8$-THF, 300 K): $d = 0.75$ (q, $^1J_{BH} = 79.2$ Hz, 6H, BH$_3$), 1.10 (tr, $^3J_{HH} = 7.0$ Hz, 6H, CH$_3$), 3.38 (q, $^3J_{HH} = 7.0$ Hz, 4H, CH$_2$), 3.51, 3.75 (2 × n.a., 2 × 4H, C$_5$H$_4$). ^{13}C{^{1}H} NMR (62.9 MHz, d$_8$-THF, 303 K): $d =$ 15.2 (CH$_3$), 66.4 (CH$_2$), 68.0, 74.4 (C$_5$H$_4$), 87.8 (q, $^1J_{CB} = 54.3$ Hz, CB). ^{11}B NMR (128.4 MHz, d$_8$-THF, 300K): $d = -33.7$ (q, $^1J_{BH} = 79.2$ Hz). Kristallstrukturanalyse von **14**: C$_{41.33}$H$_{81.33}$B$_4$Fe$_2$Li$_4$O$_{5.33}$, $M_r = 846.43$, triklin, Raumgruppe $P\bar{1}$, $a = 14.798(3)$, $b = 15.367(3)$, $c = 17.476(4)$ Å, $a =$ 103.324(16), $b = 92.741(16)$, $g = 99.274(16)$, $V = 3801.6(14)$ Å^3, $Z = 3$, $r_{ber.} =$

1.109 Mg m^{-3}, $\boldsymbol{m}$ = 0.609 mm^{-1}, $F(000)$ = 1368, $\boldsymbol{l}$(Mo$_{K\alpha}$) = 0.71073 Å, T = 173(2) K, Kristallabmessungen 0.48 × 0.45 × 0.38 mm^3, 2$\boldsymbol{Q}_{max}$ = 51.9°, 26134 gemessene Reflexe, 13536 unabhängige Reflexe (R_{int} = 0.1060), 13536 berücksichtigte Reflexe, semiempirische Absorptionskorrektur, max./min. Transmission 0.8016/0.7587, 800 Parameter, $R1$= 0.1554 (alle Daten), $wR2$ = 0.1018 (alle Daten), max./min. Restelektronendichte 0.318/-0.346 e Å^{-3}. Die Daten wurden auf einem STOE-IPDS-II Zweikreis-Diffraktometer an einem im Öltropfen gekühlten Kristall gesammelt. Zur Strukturlösung und -verfeinerung wurden die Programme SHELXS-97 und SHELXL-97 (G. M. Sheldrick, Universität Göttingen, **1997**) benutzt. Die Struktur wurde mit Direkten Methoden gelöst und mit anisotropen Auslenkungsparametern für Nicht-H-Atome gegen F^2 verfeinert. Die BH$_3$-Wasserstoffatome wurden in der Differenzelektronendichtekarte gefunden und der Torsionswinkel um die CB-Bindung verfeinert. Alle H-Atome wurden mit dem Reiter-Modell verfeinert.

[89] Synthese von 1,1´-fc(BH$_2$·NMe$_2$Et)$_2$ (**15·NMe$_2$Et**): Zu einer Lösung von **14** (412 mg, 0.97 mmol) und NMe$_2$Et (1 ml, 9.2 mmol) in Diethylether (20 ml) wird bei –78 °C Trimethylchlorsilan (1.5 ml, 11.7 mmol) in 5 ml Diethylether getropft. Nach 30 min lässt man die Mischung auf 0 °C erwärmen und rührt 1h. Das Reaktionsgemisch wird über eine G4-Fritte filtriert. Das Filtrat wird auf ca. 5 ml eingeengt und 24 h bei –30°C gehalten, wobei **15·NMe$_2$Et** als hellgelber mikrokristalliner Feststoff ausfällt. Ausbeute: 318 mg (92 %). ^{1}H NMR (250.1 MHz, C$_6$D$_6$, 300 K): $\boldsymbol{d}$ = 0.58 (tr, $^3J_{HH}$ = 7.3 Hz, 6H, CH$_2$CH_3), 1.86 (s, 12H, NCH$_3$), 2.31 (q, $^3J_{HH}$ = 7.3 Hz, 4H, CH_2CH$_3$), 2.88 (br, 4H, BH$_2$), 4.41, 4.62 (2 × vtr, 2 × 4H, $^3J_{HH}$ = $^4J_{HH}$ = 1.6 Hz, C$_5$H$_4$). ^{13}C{^{1}H} NMR (62.9 MHz, C$_6$D$_6$, 300 K): $\boldsymbol{d}$ = 8.2 (CH$_2$CH$_3$), 47.2 (NCH$_3$), 55.7 (CH$_2$CH$_3$), 70.5, 76.8 (C$_5$H$_4$), n.o. (CB). ^{11}B NMR (128.4 MHz, C$_6$D$_6$, 303): $\boldsymbol{d}$ = -2.8 (n.a., h$_{\frac{1}{2}}$ = 290 Hz). Kristalle, die sich für eine Röntgenstrukturanalyse eignen, werden durch Kristallisation bei –30 °C aus einer gesättigten Lösung (Heptan/Toluol, 1:1) erhalten. Kristallstrukturanalyse von **15·NMe$_2$Et**: C$_{18}$H$_{34}$B$_2$FeN$_2$, M$_r$ = 355.94, triklin, Raumgruppe $P\bar{1}$, a = 5.944(2), b = 9.561(3), c = 9.609(3) Å, $\boldsymbol{a}$ = 113.82(2), $\boldsymbol{b}$ = 97.85(3), $\boldsymbol{g}$ = 92.99 (3), V = 491.4(3) Å^3, Z = 1, $\boldsymbol{r}_{ber.}$ = 1.203 Mg m^{-3}, $\boldsymbol{m}$= 0.767

mm^{-1}, $F(000)$ = 192, $l(Mo_{K\alpha})$ = 0.71073 Å, T = 173(2) K, Kristallabmessungen 0.53 × 0.08 × 0.06 mm^3, $2Q_{max}$ = 52.06°, 3568 gemessene Reflexe, 1806 unabhängige Reflexe (R_{int} = 0.1287), 1806 berücksichtigte Reflexe, semiempirische Absorptionskorrektur, max./min. Transmission 0.9554/0.6865, 106 Parameter, R1= 0.1506 (alle Daten), $wR2$ = 0.3527 (alle Daten), max./min. Restelektronendichte 3.014/-0.839 e Å^{-3}. Die Daten wurden auf einem STOE-IPDS-II Zweikreis-Diffraktometer an einem im Öltropfen gekühlten Kristall gesammelt. Zur Strukturlösung und -verfeinerung wurden die Programme SHELXS-97 und SHELXL-97 (G. M. Sheldrick, Universität Göttingen, **1997**) benutzt. Die Struktur wurde mit Direkten Methoden gelöst und mit anisotropen Auslenkungsparametern für Nicht-H-Atome gegen F^2 verfeinert. Alle H-Atome wurden mit dem Reiter-Modell verfeinert.

[90]   Synthese von 1,1´-fc(BH$_2$·SMe$_2$)$_2$ (**15·DMS**): Zu einer Lösung von **14** (265 mg, 0.63 mmol) in Dimethylsulfid (10 ml) wird bei –78 °C Trimethylchlorsilan (0.5 ml, 3.9 mmol) in 5 ml SMe$_2$ getropft. Nach 30 min lässt man die Mischung auf 0 °C erwärmen und rührt 1h. Das Reaktionsgemisch wird über eine G4-Fritte filtriert. Das Filtrat wird auf ca. 3 ml eingeengt und drei Tage bei –30°C gehalten, wobei **15·DMS** als gelber mikrokristalliner Feststoff ausfällt. Ausbeute: 167 mg (91 %). ^{1}H NMR (250.1 MHz, S(CD$_3$)$_2$, 297 K): d = 2.05 (s, 12H, CH$_3$), 2.54 (br, 4H, BH$_2$), 3.80, 3.96 (2 × n.a., 2 × 4H, C$_5$H$_4$). ^{13}C{^{1}H} NMR (62.9 MHz, S(CD$_3$)$_2$, 297 K): d = 18.0 (CH$_3$), 70.2, 75.4 (C$_5$H$_4$), n.b. (CB). ^{11}B NMR (128.4 MHz, S(CD$_3$)$_2$, 297 K): d = -7.8 (n.a., h½ = 300).

[91]   M. Mayor-López, J. Weber, B. Mannfors, A. F. Cunningham, *Organometallics* **1998**, *17*, 4983.

[92]   T. J. Curphey, J. O. Santer, M. Rosenblum, J. H. Richards, *J. Am. Chem. Soc.* **1960**, *82*, 5249.

[93]   A. M. Sapse, P. v. R. Schleyer, *Lithium Chemistry: A Theoretical and Experimental Overview*, John Wiley, New York, **1995**.

[94]   A. Irigoras, J. M. Mercero, I. Silanes, J. M. Ugalde, *J. Am. Chem. Soc.* **2001**, *123*, 5040.

[95]   M. Fontani, F. Peters, W. Scherer, W. Wachter, M. Wagner, P. Zanello, *Eur. J. Inorg. Chem.* **1998**, 1453.

[96]   M. Grosche, E. Herdtweck, F. Peters, M. Wagner, *Organometallics* **1999**, *18*, 4669.

[97]   R. E. Dinnebier, L. Ding, K. Ma, M. A. Neumann, N. Tanpipat, F. J. J. Leusen, P. W. Stephens, M. Wagner, *Organometallics* **2001**, *20*, 5642.

[98]   F. Jäkle, M. Mattner, T. Priermeier, M. Wagner, *J. Organomet. Chem.* **1995**, *502*, 123.

[99]   E. Herdtweck, F. Jäkle, M. Wagner, *Organometallics* **1997**, *16*, 4737.

[100] K. A. Ostoja Starzewski, W. M. Kelly, A. Stumpf, D. Freitag, *Angew. Chem.* **1999**, *111*, 2588.

[101] S. Guo, J. W. Bats, M. Bolte, M. Wagner, *J. Chem. Soc., Dalton Trans.* **2001**, 3572.

[102] F. F. d. Biani, F. Jäkle, M. Spiegler, M. Wagner, P. Zanello, *Inorg. Chem.* **1997**, *36*, 2103.

[103] S. Guo, F. Peters, F. F. d. Biani, J. W. Bats, E. Herdtweck, P. Zanello, M. Wagner, *Inorg. Chem.* **2001**, *40*, 4928.

[104] F. Mathey, A. Mitschler, R. Weiss, *J. Am. Chem. Soc.* **1977**, *99*, 3537.

[105] G. de Lauzon, B. Deschamps, J. Fischer, F. Mathey, A. Mitschler, *J. Am. Chem. Soc.* **1980**, *102*, 994.

[106] F. Mathey, *Coord. Chem. Rev.* **1994**, *137*, 1.

[107] C. Ganter, *J. Chem. Soc., Dalton Trans.* **2001**, 3541.

[108] M. Scheibitz, J. W. Bats, M. Bolte, M. Wagner, *Eur. J. Inorg. Chem.* **2003**, 2049.

[109] M. Scheibitz, M. Bolte, H.-W. Lerner, M. Wagner, *Organometallics* **2004**, *23*, 3556.

[110] R. M. G. Roberts, J. Silver, A. S. Wells, *Inorg. Chim. Acta.* **1986**, *119*, 165.

[111] X. Sava, M. Melaimi, N. Mézailles, L. Ricard, F. Mathey, P. Le Floch, *New J. Chem.* **2002**, *26*, 1378.

[112] D. O. Cowan, P. Shu, F. L. Hedberg, M. Rossi, T. J. Kistenmacher, *J. Am. Chem. Soc.* **1979**, *105*, 1304.

[113] H. Nöth, B. Wrackmeyer, in *NMR Basic Principles and Progress.* (Eds.: P. Diehl, E. Fluck, R. Kosfeld), Springer, Berlin, **1978**.

[114] M. Scheibitz, J. B. Heilmann, R. F. Winter, M. Bolte, J. W. Bats, M. Wagner, *Dalton Trans.* **2004**, zur Veröffentlichung eingereicht.

[115] Kristallstrukturanalyse von **[23]$^{B-}$**: $C_{42}H_{64}BFe_2LiO_9$, M_r = 842.38, monoklin, Raumgruppe $P2_1/c$, a = 8.5571(10), b = 25.329(2), c = 19.782(2) Å, $\boldsymbol{b}$ = 104.020(9)°, V = 4159.9(7) Å^3, Z = 4, $\boldsymbol{r}_{\text{ber.}}$ = 1.345 Mg m^{-3}, $\boldsymbol{m}$ = 0.750 mm^{-1}, $F(000)$ = 1792, $\boldsymbol{l}(Mo_{K\alpha})$ = 0.71073 Å, T = 173(2) K, Kristallabmessungen 0.28 × 0.21 × 0.18 mm^3, $2\boldsymbol{Q}_{\text{max}}$ = 51.14°, 20080 gemessene Reflexe, 7616 unabhängige Reflexe (R_{int} = 0.0825), 7616 berücksichtigte Reflexe, semiempirische Absorptionskorrektur, max./min. Transmission 0.8768/0.8174, 496 Parameter, R1= 0.1059 (alle Daten), wR2 = 0.1389 (alle Daten), max./min. Restelektronendichte 0.522/-0.659 e Å^{-3}. Die Daten wurden auf einem STOE-IPDS-II Zweikreis-Diffraktometer an einem im Öltropfen gekühlten Kristall gesammelt. Zur Strukturlösung und -verfeinerung wurden die Programme SHELXS-97 und SHELXL-97 (G. M. Sheldrick, Universität Göttingen, **1997**) benutzt. Die Struktur wurde mit Direkten Methoden gelöst und mit anisotropen Auslenkungsparametern für Nicht-H-Atome gegen F^2 verfeinert. Alle H-Atome wurden mit dem Reiter-Modell verfeinert.

[116] A. N. Nesmeyanov, V. A. Sazoniva, V. A. Blinova, *Dokl. Akad. Nauk SSSR* **1971**, *198*, 848.

[117] A. N. Nesmeyanov, V. A. Sazonova, V. A. Blinova, S. G. Dychenko, *Dokl. Akad. Nauk SSSR* **1971**, *200*, 1365.

[118] J. W. Bats, M. Scheibitz, M. Wagner, *Acta Cryst.* **2003**, *C59*, m355.

[119] K. H. Pannell, V. V. Dementiev, H. Li, F. Cervantes-Lee, M. T. Nguyen, A. F. Diaz, *Organometallics* **1994**, *13*, 3644.

[120] M. Scheibitz, R. F. Winter, M. Bolte, H.-W. Lerner, M. Wagner, *Angew. Chem.* **2003**, *115*, 954.

[121] Houben-Weyl, *Methoden der organischen Chemie, Organobor-Verbindungen, Bd. I - III*, Köster, R. (Hrsg.), Stuttgart, New York, **1982**.

[122] F. F. d. Biani, T. Gmeinwieser, E. Herdtweck, F. Jäkle, F. Laschi, M. Wagner, P. Zanello, *Organometallics* **1997**, *16*, 4776.

[123] M. D. Thomson, M. Novosel, H. G. Roskos, T. Müller, M. Scheibitz, M. Wagner, F. F. de Biani, P. Zanello, *J. Phys. Chem. A* **2004**, *108*, 3281.

[124] J. A. Gamboa, A. Sundararaman, L. Kakalis, A. J. Lough, F. Jäkle, *Organometallics* **2002**, *21*, 4169.

[125] S. Barlow, V. J. Murphy, J. S. O. Evans, D. O´Hare, *Organometallics* **1995**, *14*, 3461.

[126] Synthese von **36**: Zu einer Lösung von **8c** (180 mg, 0.64 mmol) in Dimethylsulfid (10 ml) wird bei –78 °C Trimethylchlorsilan (0.5 ml, 3.9 mmol) in 5 ml SMe$_2$ getropft. Nach 30 min lässt man die Mischung auf 0 °C erwärmen und rührt 1h. Das Reaktionsgemisch wird über eine G4-Fritte filtriert. Zu dem Filtrat wird bei Raumtemperatur 1,4-Diethinylbenzol (90 mg, 0.71 mmol) in 5 ml Et$_2$O getropft. Anschließend wird für 15 h bei Raumtemperatur gerührt. Es wird von Unlöslichem abfiltriert. Nach Entfernen des Lösungsmittels vom Filtrat im Vakuum wird der Rückstand in 3 ml CH$_2$Cl$_2$ aufgenommen und in Hexan (10 ml) getropft, wobei **36** als blassroter Feststoff ausfällt, der mit Hexan gewaschen wird (3 × 5 ml). Der Feststoff wird über Nacht im Vakuum getrocknet. Ausbeute: 127 mg (61 %). ^{1}H NMR (250.1 MHz, CDCl$_3$, 297 K): **d** = 3.60 – 4.19 (5H, C$_5$H$_5$), 4.48 – 4.81 (4H, C$_5$H$_4$), 6.75 – 7.89 (8H, C$_6$H$_4$, B-CH=CH). ^{13}C{^{1}H} NMR (100.6 MHz, C$_6$D$_6$, 303 K): **d** = 67.4 – 70.2 (C$_5$H$_5$), 72.8 – 73.9 (C$_5$H$_4$), n.o. (C$_{ipso}$B), 126.3 – 129.5 (C$_6$H$_4$), 131.6 – 133.2 (B-CH=*C*H), n.o. (B-*C*H=CH). ^{11}B NMR (128.4 MHz, C$_6$D$_6$, 303K): **d** = 31.2 (h$_{1/2}$ = 1300 Hz). IR: 1597, 1552, 1504 cm^{-1} (C=C).

[127] Y. S. Sohn, D. N. Hendrickson, H. B. Gray, *J. Am. Chem. Soc.* **1971**, *93*, 3603.

[128] Synthese von **37**: Zu einer Lösung von **14** (239 mg, 0.56 mmol) in Dimethylsulfid (10 ml) wird bei –78 °C Trimethylchlorsilan (0.5 ml, 3.9 mmol) in 5 ml SMe$_2$ getropft. Nach 30 min lässt man die Mischung auf 0 °C erwärmen und rührt 1h. Das Reaktionsgemisch wird über eine G4-Fritte filtriert. Es wird für 7 d bei Raumtemperatur gerührt. Nach Abkondensieren des Lösungsmittels im Vakuum wird der Rückstand in 5 ml CH$_2$Cl$_2$ aufgenommen. Es wird von Unlöslichem abfiltriert und das Filtrat in Hexan (10 ml) getropft, wobei **37** als blassroter Feststoff ausfällt, der mit Hexan gewaschen wird (3 × 5 ml). Der Feststoff wird über Nacht im Vakuum getrocknet. Ausbeute: 70 mg (64 %). ^{1}H NMR (250.1 MHz, CDCl$_3$, 297 K): ***d*** = 4.05 – 4.18 (~ 0.7H, C$_5$H$_5$), 4.21 – 4.52, 4.53 – 4.72 (8H, C$_5$H$_4$), 5.68 (br, BH). ^{13}C{^{1}H} NMR (100.6 MHz, CDCl$_3$, 303 K): ***d*** = 67.0 – 70.5 (C$_5$H$_5$), 71.4 – 79.1 (C$_5$H$_4$), n.o. (C$_{ipso}$B). ^{11}B NMR (128.4 MHz, CDCl$_3$, 301K): ***d*** = 51.6 (h$_{1/2}$ = 1200 Hz). IR: 2360, 2341 cm^{-1} (B-H).

[129] J. B. Heilmann, M. Wagner, *Manuskript in Vorbereitung*.

2 Vollständige Publikationsliste

2.1   Veröffentlichungen in wissenschaftlichen Journalen

1.   K. Ma, M. Scheibitz, S. Scholz, M. Wagner, *J. Organomet. Chem.* **2002**, *652,* 11 – 19.

        „Applications of boron-nitrogen- and boron-phosphorus adducts in organometallic chemistry"

        Faksimile in Kapitel 3.10, Seite 286

2.   M. Scheibitz, H.-W. Lerner, M. Bolte, *Acta Cryst.* **2003**, *E59*, o253 – o254.

        „Dimethylethylammonium bromide"

3.   M. Scheibitz, R. F. Winter, M. Bolte, H.-W. Lerner, M. Wagner, *Angew. Chem.* **2003**, *115*, 954 – 957.

        „[1.1]Diborataferrocenophane: A highly efficient Li$^+$ scavenger"

        Faksimile in Kapitel 3.1, Seite 99

4.   M. Scheibitz, J. W. Bats, M. Bolte, M. Wagner, *Eur. J. Inorg. Chem.* **2003**, 2049 – 2053.

        „P-B Adducts of 3,4-dimethyl-1-phosphaferrocene with bromoboranes"

        Faksimile in Kapitel 3.2, Seite 104

5.   J. W. Bats, M. Scheibitz, M. Wagner, *Acta Cryst.* **2003**, *C59*, m355 – m357.

        „The twinned structure of ferricenyltrifluoroborate"

        Faksimile in Kapitel 3.3, Seite 110

6.   M. Scheibitz, M. Bolte, H.-W. Lerner, M. Wagner, *Organometallics* **2004**, *23(14)*, 3556 – 3559.

        „Ferrocenylborane - amine and monomeric diferrocenylborane: Novel organometallic hydroborating reagents"

        Faksimile in Kapitel 3.4, Seite 114

7. M. D. Thomson, M. Novosel, H. G. Roskos, T. Müller, M. Scheibitz, M. Wagner, F. Fabrizi de Biani, P. Zanello, *J. Phys. Chem. A* **2004**, *108(16)*, 3281 – 3291.

   „Electronic structure, photophysics and relexation dynamics of charge transfer excited states in boron-nitrogen-bridged ferrocene-donor compounds"

   Faksimile in Kapitel 3.5, Seite 118

8. M. Scheibitz, M. Bolte, H.-W. Lerner, M. Wagner, *Organometallics* **2004**, *23(14),* 3556 – 3559.

   „The 1:1 adduct of 1,1'-bis(dibromoboryl)ferrocene and 3,3´,4,4´-tetramethyl-1,1´-diphosphaferrocene"

   Faksimile in Kapitel 3.6, Seite 130

9. A. Haghiri, M. Scheibitz, H.-W. Lerner, M. Bolte, M. Wagner, *Polyhedron* **2004**, *im Druck.*

   „On the way to ferrocene-based multipledecker sandwich complexes"

   Faksimile in Kapitel 3.7, Seite 135

10. M. Scheibitz, M. Bolte, J. W. Bats, H.-W. Lerner, I. Nowik, R. H. Herber, A. Krapp, M. Lein, M. C. Holthausen, M. Wagner, *Chem. Eur. J*, **2004**, *zur Veröffentlichung angenommen.*

    „C_5H_4-BR_2 Bending in ferrocenylboranes: A delocalized through-space interaction between iron and boron"

    Faksimile in Kapitel 3.8, Seite 144

11. M. Scheibitz, J. Heilmann, M. Bolte, R. F. Winter, M. Wagner, *Dalton Trans.* **2004**, *zur Veröffentlichung eingereicht.*

    „Electronic interactions in oligoferrocenes with cationic, neutral and anionic tetracoordinated boron bridges"

    Faksimile in Kapitel 3.9, Seite 230

2.2   Vorträge und Posterpräsentationen

1.   <u>M. Scheibitz</u>, S. Scholz, H.-W. Lerner, R. Winter, M. Wagner

   5th International Symposium on Functional p-Electron Systems, 30. Mai – 4. Juni 2002, Ulm:

   Poster: „*Ferrocene as a functional p-electron system*"

2.   <u>M. Scheibitz</u>, M. Wagner

   Deutsche Borchemikertagung, 11. – 13. Oktober 2002, Rothenfels:

   Vortrag: „*Eigenschaften borverbrückter Oligoferrocenylene*"

3.   <u>M. Scheibitz</u>, S. Scholz, H.-W. Lerner, M. Wagner

   225th ACS National Meeting, 23. – 27. März 2003, New Orleans:

   Vortrag: „*Interaction between ferrocene and main group metals*"

4.   <u>M. Scheibitz</u>, M. Wagner

   Stipendiatentreffen des Fonds der chemischen Industrie, 10. Oktober 2003, Universität Frankfurt:

   Vortrag: „*Neue Wege zu metallhaltigen Polymeren und Makrozyklen*"

5.   <u>M. Scheibitz</u>, H.-W. Lerner, M. Wagner

   227th ACS National Meeting, 28. März – 1. April 2004, Anaheim:

   Vortrag: „*Novel ferrocene-based macrocycles and polymers*"

3 Ausgewählte Veröffentlichungen

3.1 „[1.1]Diborataferrocenophane: A highly efficient Li⁺ scavenger"

M. Scheibitz, R. F. Winter, M. Bolte, H.-W. Lerner, M. Wagner,

Angew. Chem. **2003**, *115*, 954 – 957.

Zuschriften

Dapprich, J. M. Millam, A. D. Daniels, K. N. Kudin, M. C. Strain, O. Farkas, J. Tomasi, V. Barone, M. Cossi, R. Cammi, B. Mennucci, C. Pomelli, C. Adamo, S. Clifford, J. Ochterski, G. A. Petersson, P. Y. Ayala, Q. Cui, K. Morokuma, D. K. Malick, A. D. Rabuck, K. Raghavachari, J. B. Foresman, J. Cioslowski, J. V. Ortiz, B. B. Stefanov, G. Liu, A. Liashenko, P. Piskorz, I. Komaromi, R. Gomperts, R. L. Martin, D. J. Fox, T. Keith, M. A. Al-Laham, C. Y. Peng, A. Nanayakkara, C. Gonzalez, M. Challacombe, P. M. W. Gill, B. G. Johnson, W. Chen, M. W. Wong, J. L. Andres, M. Head-Gordon, E. S. Replogle, J. A. Pople, Gaussian, Inc., Pittsburgh, PA, **1998**.

[10] D. Wittenberg, H. A. McNince, H. Gilman, *J. Am. Chem. Soc.* **1958**, *80*, 5418–5422.

[11] For examples, see M. S. Newman, *Effects in Organic Chemistry*, Wiley, New York, **1956**; L. N. Ferguson, *The Modern Structural Theory of Organic Chemistry*, Prentice-Hall, Englewood Cliffs, NJ, **1963**.

[12] a) M. Beller, *Angew. Chem.* **1995**, *107*, 1436–1437; *Angew. Chem. Int. Ed. Engl.* **1995**, *34*, 1316; b) J. F. Hartwig, *Synlett* **1997**, 329; c) J. F. Hartwig, *Angew. Chem.* **1998**, *110*, 2154–2177; *Angew. Chem. Int. Ed.* **1998**, *37*, 2046–2067; d) J. P. Wolfe, S. Wagaw, J.-F. Marcoux, S. L. Buchwald, *Acc. Chem. Res.* **1998**, *31*, 805; e) J. F. Hartwig, *Acc. Chem. Res.* **1998**, *31*, 852.

[13] Physical data for **1**: White solid; ^{1}H NMR (400 MHz, CDCl$_3$): $\delta = 7.30$ (d, 4H), 7.17 (d, 4H), 6.90 (d, 4H), 6.75 (dd, 4H), 6.47 (d, 4H), 3.94 (s, 6H), 3.64 ppm (s, 12H); ^{13}C NMR (75 MHz, CDCl$_3$): $\delta = 158.9$, 152.5, 145.2, 136.83, 132.30, 119.5, 118.0, 117.3, 116.8, 116.1, 55.5 ppm; ^{13}C NMR (75 MHz, C$_6$D$_6$): $\delta = 159.4$, 153.7, 146.0, 137.5, 132.8, 119.3, 119.0, 118.7, 117.6, 116.4, 55.0, 54.9 ppm; elemental analysis (%): calcd for C$_{42}$H$_{38}$N$_2$O$_6$Si: C 72.60, H 5.51, N 4.03; found: C 72.41, H 5.44, N 3.97.

[14] The oxidation potential of trianisylamine was 0.16 V vs Fc/Fc$^+$ under the same conditions. This discrepancy of the first oxidation potential between **1** and trianisylamine probably results from a difference in conformation of the trianisylamine moieties. In **1**, the propellerlike conformation can be hardly adopted because of its spiro structure.

[15] Compound **1** (69 mg, 0.1 mmol) was dissolved in dry dichloromethane and stirred at −78 °C under argon. SbCl$_5$ (0.5 ml, 1M in CH$_2$Cl$_2$) was added to the solution. After 10 min, the resulting blue solution was poured into dry diethyl ether. The precipitate was washed with dry diethyl ether to provide **1**(SbCl$_6$)$_2$ (110 mg, 81 %) as a greenish blue solid. **1**(SbCl$_6$)$_2$: elemental analysis (%): calcd for C$_{42}$H$_{38}$Cl$_{12}$N$_2$O$_6$Sb$_2$Si: C 36.99, H 2.81, N 2.05, Cl 31.19; found: C 36.99, H 2.71, N 2.05, Cl 29.61.

[16] The isolated solid sample was dissolved in CH$_2$Cl$_2$, and the ESR signal intensity was compared to that of a sample oxidized in situ at the same concentration. The two signals gave the same fine structure with almost the same intensity.

[17] Example of oxidation with SbCl$_5$ in CH$_2$Cl$_2$: H. Bock, A. Rauschenbach, K. Ruppert, Z. Havlas, *Angew. Chem.* **1991**, *103*, 706–708; *Angew. Chem. Int. Ed.* **1998**, *37*, 714–716.

[18] N. Hirota, *J. Am. Chem. Soc.* **1967**, *89*, 32–41.

[19] K. Mukai, A. Sogabe, *J. Chem. Phys.* **1980**, *72*, 598–601.

[20] B. Bleaney, K. D. Bowers, *Proc. R. Soc. London Ser. A* **1952**, *214*, 451–456.

[1.1]Diborataferrocenophane: A Highly Efficient Li$^+$ Scavenger**

Matthias Scheibitz, Rainer F. Winter, Michael Bolte, Hans-Wolfram Lerner, and Matthias Wagner

In various cases, electrophilic substitution reactions of ferrocene are known to proceed via precomplexation of the iron atom by the electrophile.[1] Moreover, direct iron-to-metal bonding appears to influence the complexation behavior of certain ferrocene-based redox-switchable cryptands,[2] as well as the properties of catalytically active 2-metalla[3]-ferrocenophanes (metal = Ti^{IV}, Pd^{II}, Pt^{II}).[3] The interaction of ferrocene with Li$^+$ was studied theoretically by Ugalde et al.,[4] who located two minima on the energy surface. In the lower energy structure, the lithium cation is η^5-coordinated on top of one of the cyclopentadienyl rings (**I**; Scheme 1). The second minimum structure **II** is 8 kcal mol^{-1} higher in energy and has the Li$^+$ ion bonded laterally to the iron atom. We recently reported the synthesis and structural characterization of a ferrocene/gallium(I) cation complex with essentially the same structural motif as **I**.[5] Here we report on the isolation of a ferrocene/lithium complex that provides experimental evidence for the existence of structure **II**.

When a slurry of 1,1'-dilithioferrocene (**1**)[6] in hexane is treated with a solution of 1,1'-bis(dimethylboryl)ferrocene (**2**) in THF,[7] the cyclic dinuclear aggregate **3**$^{2-}$ is formed in good yield (Scheme 1). X-ray quality crystals of [**3**-Li]Li([12]crown-4)$_2$ were grown by gas-phase diffusion of diethyl ether into a solution of the crude material in THF after addition of [12]crown-4.

The ^{11}B NMR spectrum of [**3**-Li]Li([12]crown-4)$_2$ reveals one signal at $\delta(^{11}$B, [D$_8$]THF) = −21.8 ppm, which testifies to

[*] Prof. Dr. M. Wagner, Dipl.-Chem. M. Scheibitz, Dr. H.-W. Lerner
Institut für Anorganische Chemie
Johann Wolfgang Goethe-Universität Frankfurt
Marie-Curie-Strasse 11, 60439 Frankfurt/Main (Germany)
Fax: (+49) 69-798-29260
E-mail: matthias.wagner@chemie.uni-frankfurt.de

Dr. R. F. Winter
Institut für Anorganische Chemie
Universität Stuttgart
Pfaffenwaldring 55, 70569 Stuttgart (Germany)

Dr. M. Bolte$^+$
Institut für Organische Chemie
Johann Wolfgang Goethe-Universität Frankfurt
Marie-Curie-Strasse 11, 60439 Frankfurt/Main (Germany)

[+] X-ray crystallography
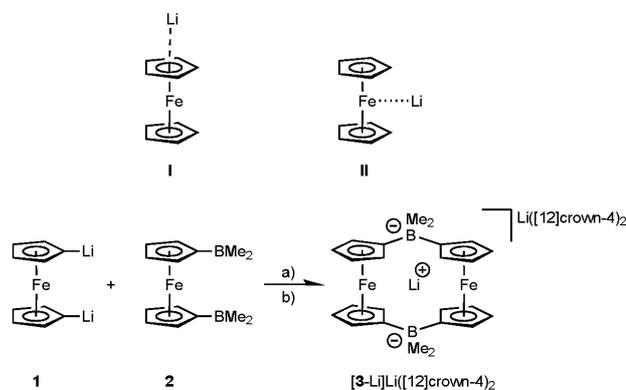
Scheme 1. a) THF/hexane, RT; b) excess [12]crown-4, RT.

the presence of tetracoordinate boron atoms.[8] In the ^{1}H NMR spectrum, only one signal is observed for all four methyl groups ($\delta(^1$H, [D$_8$]THF) = −0.25 ppm). The signal is broad and has a doublet line shape due to partially resolved ^2J(B,H) coupling. The cyclopentadienyl rings give rise to two well-resolved pseudotriplets at $\delta(^1$H, [D$_8$]THF) = 3.86 and 3.99 ppm; the corresponding carbon resonances appear at $\delta(^{13}$C, [D$_8$]THF) = 69.8 and 74.0 ppm. Both the ^{1}H and the ^{13}C NMR patterns indicate a high average symmetry of the molecule in solution. This observation can be explained by a degenerate *syn–syn* isomerization of the [1.1]ferrocenophane framework, which leads to fast exchange of the methyl groups in the *exo* and *endo* positions of the BMe$_2$ bridges (the *anti* conformation of [1.1]ferrocenophanes with small bridging atoms is disfavored for steric reasons).[9]

Most interestingly, the ^{7}Li NMR spectrum displays two signals at $\delta(^7$Li, [D$_8$]THF) = −0.19 and 4.29 ppm with an integral ratio of 1:1. Comparison with the spectra of LiCl ($\delta(^7$Li, [D$_8$]THF) = 0.30 ppm) and Li([12]crown-4)$_2$Cl ($\delta(^7$Li, [D$_8$]THF) = −0.21 ppm) clearly shows that the signal at higher field must be assigned to a [Li([12]crown-4)$_2$]$^+$ cation. The signal at 4.29 ppm obviously corresponds to the second lithium cation, which appears to be surrounded by a distinctly different ligand sphere. At ambient temperature, any exchange of Li$^+$ between the two coordination sites is clearly slow on the NMR timescale. The ^{7}Li NMR spectrum does not change when more [12]crown-4 is added to the NMR tube.

The structure of [3-Li]Li([12]crown-4)$_2$ in the solid state was finally established by X-ray crystallography (Figure 1).[10] The molecule contains a [1.1]ferrocenophane ring in a twisted *syn* conformation (dihedral angles: C1–C5//C31–C35 21.3°; C11–C15//C21–C25 23.1°).[11] In agreement with the NMR data, one of the lithium cations is coordinated by two crown ether molecules and forms the well-known complex [Li([12]-crown-4)$_2$]$^+$. The second lithium cation is located inside the ferrocenophane cavity, most likely trapped by the electrostatic field originating from the two anionic dimethylborate bridges (Li1···B1 2.314(6), Li1···B2 2.309(6) Å; B1···Li1···B2 179.2(3)°; Li1 is not located on a special position). The

distances between the Li$^+$ ion and the iron centers are somewhat larger than the value calculated for structure **II** (**II**: Li···Fe 2.4 Å; [3-Li]$^-$: Li1···Fe1 2.720(6), Li1···Fe2 2.706(5) Å; Fe1···Li1···Fe2 128.2(2)°). As was predicted by Ugalde et al.,[4] the close vicinity of the Li$^+$ ion does not lead to a major distortion of the ferrocene structure (COG-Fe1-COG′ 175.6°, COG-Fe2-COG′ 174.9°; COG: center of gravity of a C$_5$H$_4$ ring). We observe only little bending of the boron centers out of the planes of the attached Cp rings (av COG-C(*ipso*)-B 167.3(3)°), and the distances between the carbon atoms C1, C11, C21, C31 and the Li$^+$ ion are rather large (av C(*ipso*)···Li1 2.361(5) Å). These findings suggest that there is no substantial degree of charge transfer from the Cp rings to the lithium cation. The question thus arises whether the function of the diborylated ferrocenophane is adequately described as merely providing an anionic macrocycle in which Li$^+$ is trapped. [3-Li]$^-$ containing a naked lithium cation in close proximity to a ferrocene moiety represents a reasonable approximation of **II**, as it was predicted to exist under gas-phase conditions. Ugalde et al. calculated the lithium cation basicity (LCB) of ferrocene at T = 298 K for structure **II** and obtained a value of 29.4 kcal mol^{-1},[4] which, in comparison with other LCB data determined both theoretically and experimentally by Burk et al.,[12] leads to the conclusion that ferrocene behaves as a moderately strong base toward the lithium cation. Since [3-Li]$^-$ has two ferrocene moieties which, in addition, are much more electron-rich than ferrocene itself (see below and also ref. [13]), a contribution from bonding Fe···Li interactions to the stability of the aggregate should be considered.
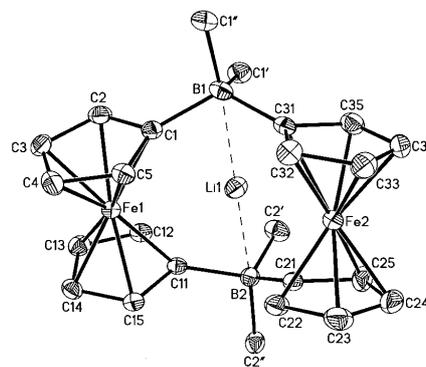
Figure 1. Molecular structure and numbering scheme of [3-Li]Li([12]-crown-4)$_2$ (thermal ellipsoids shown at the 50% probability level, Li([12]crown-4)$_2$$^+$ fragment and hydrogen atoms omitted for clarity). Selected atom–atom distances [Å], bond lengths [Å], angles [°], and torsion angles [°]: B1-C1 1.651(5), B1-C31 1.651(5), B2-C11 1.646(5), B2-C21 1.659(5), Li1···B1 2.314(6), Li1···B2 2.309(6), Li1···Fe1 2.720(6), Li1···Fe2 2.706(5); C1-B1-C31 115.7(3), C11-B2-C21 114.8(3), B1···Li1···B2 179.2(3), Fe1···Li1···Fe2 128.2(2); C2-C1-B1-C1′ −38.9(4), C2-C1-B1-C1″ 78.1(3), C25-C21-B2-C2′ −38.7(4), C25-C21-B2-C2″ 78.5(4).

Zuschriften

In cyclic voltammetry experiments (CH_2Cl_2, 0.2 M NBu_4PF_6) [3-Li]Li([12]crown-4)$_2$ was irreversibly oxidized at a peak potential of -0.58 V (vs FcH/FcH$^+$, $\upsilon = 0.1$ V s^{-1}; Figure 2a).[14] This sizable cathodic shift with respect to ferrocene reflects the high electron density in the anionic [1.1]ferrocenophane.[15] When, after oxidation, the sweep is continued into the cathodic regime, two partially reversible waves emerge at even more negative half-wave potentials
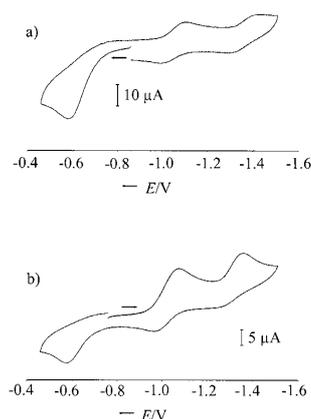
Figure 2. a) Cyclic voltammogram of [3-Li]Li([12]crown-4)$_2$ (CH_2Cl_2, 0.2 M NBu_4PF_6, $\upsilon = 0.1$ V s^{-1}, vs FcH/FcH$^+$); b) Cyclic voltammogram of [3-Li]Li([12]crown-4)$_2$ after exhaustive oxidation (CH_2Cl_2, 0.2 M NBu_4PF_6, $\upsilon = 0.1$ V s^{-1}, vs FcH/FcH$^+$).

($E_{1/2} = -1.02$, -1.33 V; $\Delta E_p = 84$ and 111 mV, respectively).[16] These waves are not observed if the cathodic scan is performed first and are thus assigned to electroactive product(s) arising from a chemical step following oxidation. On bulk electrolysis at -0.38 V the electroactive product(s) mentioned above were cleanly produced. Voltammetric scans after electrolysis reveal both cathodic waves to be only partially reversible, and this again indicates a chemical process following electron transfer. If after the cathodic scan the sweep is taken back into the more anodic regime, the oxidation wave of the parent [3-Li]Li([12]crown-4)$_2$ reappears (Figure 2b). In accordance with the voltammetric data, bulk reduction at -1.20 V gives back the starting material as the principal product. We conclude that the oxidation/reduction sequence constitutes an overall chemically reversible cycle connected by irreversible individual steps. Considering the pronounced cathodic shift of both reduction potentials relative to the oxidation potential of parent [3-Li]$^-$, a plausible scenario is that upon oxidation of [3-Li]$^-$ the encapsulated Li$^+$ ion is expelled from the macrocycle.

[3]$^{2-}$ is a novel type of redox-switchable lithium scavenger. Contrary to other functionally related complexes,[17] the lithium ion in [3-Li]$^-$ is not coordinated by main-group Lewis bases. We therefore suggest that [3-Li]Li([12]crown-4)$_2$ could be used as an easily accessible model system to study the interaction of ferrocene with the unperturbed naked lithium cation.

Experimental Section

[3-Li]Li([12]crown-4)$_2$: A solution of **2** (0.29 g, 1.09 mmol) in THF (5 mL) was added to a slurry of **1**·2 tmeda (0.47 g, 1.09 mmol; tmeda = N,N,N',N'-tetramethylethylenediamine) in hexane (20 mL) with stirring at ambient temperature. The reaction mixture was stirred for 2 h. After filtration, the remaining solid was triturated in hexane (2 × 10 mL) and dried in vacuo. A solution of the crude product in THF was treated with [12]crown-4 (0.37 g, 2.20 mmol) and then slowly layered with diethyl ether by gas-phase diffusion to yield X-ray quality crystals of [3-Li]Li([12]crown-4)$_2$. Yield: 0.39 g (44 %).

^{11}B NMR (128.4 MHz, [D$_8$]THF): $\delta = -21.8$ ppm ($h_{1/2} = 20$ Hz); ^{7}Li NMR (155.5 MHz, [D$_8$]THF): $\delta = -0.19$ ([Li([12]crown-4)$_2$]$^+$), 4.29 ppm ([3-Li]$^-$); ^{1}H NMR (250.1 MHz, [D$_8$]THF): $\delta = -0.25$ (br, 12H; CH$_3$), 3.61 (s, 32H; CH$_2$), 3.86, 3.99 ppm (2 × t, 2 × 8H, ^3J(H,H) = ^4J(H,H) = 1.7 Hz; C$_5$H$_4$); ^{13}C NMR (62.9 MHz, [D$_8$]THF): $\delta =$ not observed (CH$_3$), 69.8 (C$_5$H$_4$), 72.0 (CH$_2$), 74.0 ppm (C$_5$H$_4$), not observed (C$_5$H$_4$-$ipso$). ^{11}B and ^{7}Li NMR spectra are reported relative to external BF$_3$·Et$_2$O and LiCl/D$_2$O, respectively. Elemental analysis (%) calcd for C$_{40}$H$_{60}$B$_2$Fe$_2$Li$_2$O$_8$ (816.08): C 58.87, H 7.41; found: C 58.55, H 7.51.

[1] M. J. Mayor-López, J. Weber, B. Mannfors, A. F. Cunningham, Jr., *Organometallics* **1998**, *17*, 4983–4991.
[2] J. C. Medina, T. T. Goodnow, M. T. Rojas, J. L. Atwood, B. C. Lynn, A. E. Kaifer, G. W. Gokel, *J. Am. Chem. Soc.* **1992**, *114*, 10583–10595.
[3] M. Herberhold, *Angew. Chem.* **2002**, *114*, 998–1000; *Angew. Chem. Int. Ed.* **2002**, *41*, 956–958.
[4] A. Irigoras, J. M. Mercero, I. Silanes, J. M. Ugalde, *J. Am. Chem. Soc.* **2001**, *123*, 5040–5043.
[5] S. Scholz, J. C. Green, H.-W. Lerner, M. Bolte, M. Wagner, *Chem. Commun.* **2002**, 36–37.
[6] M. D. Rausch, D. J. Ciappenelli, *J. Organomet. Chem.* **1967**, *10*, 127–136.
[7] W. Ruf, T. Renk, W. Siebert, *Z. Naturforsch. B* **1976**, *31*, 1028–1034.
[8] "Nuclear Magnetic Resonance Spectroscopy of Boron Compounds": H. Nöth, B. Wrackmeyer in *NMR Basic Principles and Progress, Vol. 14* (Eds.: P. Diehl, E. Fluck, R. Kosfeld), Springer, Berlin, **1978**.
[9] U. T. Mueller-Westerhoff, *Angew. Chem.* **1986**, *98*, 700–716; *Angew. Chem. Int. Ed. Engl.* **1986**, *25*, 702–717.
[10] X-ray crystal structure analysis of [3-Li]Li([12]crown-4)$_2$: STOE-IPDS-II two-circle diffractometer, Mo$_{K\alpha}$ radiation ($\lambda =$ 0.71073 Å), ω scans, empirical absorption correction, the structure was solved by direct methods using SHELXS-97 and refined with SHELXL-97 (G. M. Sheldrick, Universität Göttingen, Germany, **1997**) by full-matrix least-squares methods against F^2. Hydrogen atoms were placed on ideal positions and refined with fixed isotropic displacement parameters using a riding model. In addition, the torsion angles about the B–CH$_3$ bonds were refined. [C$_{24}$H$_{28}$B$_2$Fe$_2$Li]·[(C$_8$O$_4$H$_{16}$)$_2$Li]$^+$, $M_r =$ 816.08 g mol^{-1}, crystal dimensions 0.62 × 0.16 × 0.14 mm, pale yellow needle, triclinic, space group $P\bar{1}$; $a = 10.519(1)$, $b = 13.643(1)$, $c = 14.986(2)$ Å, $\alpha = 69.208(8)$, $\beta = 88.794(8)$, $\gamma = 81.104(8)°$, $V = 1985.1(4)$ Å^3, $Z = 2$; $\rho_{calcd} = 1.365$ g cm^{-3}; $\mu = 0.781$ mm^{-1}, min./max. transmission 0.643/0.8985; $2\theta_{max} = 50.7°$; $T = 100(2)$ K; of 25706 measured reflections, 6953 were independent ($R_{int} = 0.0826$); 489 parameters refined; $R1 = 0.070$ (all data), $wR2 = 0.1048$ (all data); $S = 1.019$, min./max. residual electron density $-0.597/0.337$ e Å^{-3}. CCDC-189707 contains the supplementary crystallographic data for this paper. These data can be obtained free of charge via www.ccdc.cam.ac.uk/conts/

retrieving.html (or from the Cambridge Crystallographic Data Centre, 12, Union Road, Cambridge CB21EZ, UK; fax: (+44) 1223-336-033; or deposit@ccdc.cam.ac.uk).

[11] For crystal structures of a) [1.1]disila-, b) [1.1]distanna-, c) [1.1]diplumba-, and d) [1.1]digallaferrocenophanes, see a) D. L. Zechel, D. A. Foucher, J. K. Pudelski, G. P. A. Yap, A. L. Rheingold, I. Manners, *J. Chem. Soc. Dalton Trans.* **1995**, 1893–1899; b) A. Clearfield, C. J. Simmons, H. P. Withers, Jr., D. Seyferth, *Inorg. Chim. Acta* **1983**, *75*, 139–144; c) G. Utri, K. E. Schwarzhans, G. M. Allmaier, *Z. Naturforsch. B* **1990**, *45*, 755–762; d) W. Uhl, I. Hahn, A. Jantschak, T. Spies, *J. Organomet. Chem.* **2001**, *637–639*, 300–303; P. Jutzi, N. Lenze, B. Neumann, H.-G. Stammler, *Angew. Chem.* **2001**, *113*, 1470–1473; *Angew. Chem. Int. Ed.* **2001**, *40*, 1424–1427.

[12] P. Burk, I. A. Koppel, I. Koppel, R. Kurg, J.-F. Gal, P.-C. Maria, M. Herreros, R. Notario, J.-L. M. Abboud, F. Anvia, R. W. Taft, *J. Phys. Chem. A* **2000**, *104*, 2824–2833.

[13] M. Fontani, F. Peters, W. Scherer, W. Wachter, M. Wagner, P. Zanello, *Eur. J. Inorg. Chem.* **1998**, 1453–1465; M. Fontani, F. Peters, W. Scherer, W. Wachter, M. Wagner, P. Zanello, *Eur. J. Inorg. Chem.* **1998**, 2087.

[14] a) The cell for voltammetric studies was designed as detailed in ref. [14b]. Voltammetric scans were referenced by addition of a small amount of ferrocene as internal standard at an appropriate time of the experiment. For referencing of the oxidized solution a small sample (ca. 3 mL) was transferred from the electrolysis cell to the voltammetric cell, the required amount of ferrocene added, and voltammetric traces were recorded. Higher electric currents could not be obtained in the CVs due to solubility and adsorption problems; b) R. F. Winter, F. M. Hornung, *Organometallics* **1999**, *18*, 4005–4014.

[15] For general information on the electrochemistry of ferrocenes, see a) P. Zanello in *Ferrocenes* (Eds.: A. Togni, T. Hayashi), VCH, Weinheim, **1995**; b) D. Astruc, *Electron Transfer and Radical Processes in Transition Metal Chemistry*, Wiley-VCH, Weinheim, **1995**.

[16] Values at $v = 0.2 \, \mathrm{Vs^{-1}}$. For the internal ferrocene standard, a peak potential difference ΔE_p of 82 mV was obtained under these conditions.

[17] P. D. Beer, P. A. Gale, G. Z. Chen, *J. Chem. Soc. Dalton Trans.* **1999**, 1897–1909.

<div style="text-align:right">*Angewandte*
Chemie</div>

Li-Intercalated Oxometallocubanes

Intercalation of Alkali Metal Cations into Layered Organotitanium Oxides**

José Gracia, Avelino Martín, Miguel Mena,*
María del Carmen Morales-Varela, Josep-M. Poblet,
and Cristina Santamaría

Dedicated to Professor Pascual Royo
on the occasion of his 65th birthday

Species with a metallocubane structure constitute an interesting building block in inorganic solids, and considerable effort has been invested in selecting the composition and geometry of the precursor complexes to obtain specific characteristics and properties.[1] Some examples of the wide variety of inorganic materials whose structures are based on molecular cubane-like motifs are the molybdenum[2] and aluminum phosphates,[3] $M_vMo_xP_yO_z$ (M = metal cation), or various hydroxometalates $[M_xO_y(OH)_z]L$ (M = Ge, Ln,...).[4]

We have reported the formation and structure of the oxoheterometallocubanes $[\{(CO)_3Mo\}(\mu_3\text{-O})_3\{Ti_3\text{-}(\eta^5\text{-}C_5Me_5)_3(\mu_3\text{-CR})\}]$ (R = H, Me)[5], which were obtained from the preorganized organometallic oxides $[\{Ti(\eta^5\text{-}C_5Me_5)\text{-}(\mu\text{-O})\}_3(\mu_3\text{-CR})]$ (R = H (**1**), Me (**2**)).[6] Once we observed that the latter might be involved directly as macrocyclic tridentate ligands in encapsulation processes of different metals, we became interested in incorporating diverse metal complex fragments at the free vertex of the μ_3-alkylidyne oxo derivatives to build up the corresponding oxoheterometallocubanes.

As part of these ongoing studies, here we present the intercalation of alkali metal ions into layered organometallic titanium oxides by treatment of the alkylidyne complex **1** with different alkali metal alkyl and amide reagents.

The one-pot reaction of the tripodal starting material **1** with MR (M = Li, R = CH$_2$SiMe$_3$, CH$_2$CMe$_3$, nBu; M = Na, R = nBu; M = K, R = nBu, CH$_2$Ph) in toluene/hexane at room temperature leads to the oxoheterometallodicubanes **3**–**5** in good yields. These compounds can be also obtained by

---

[*] Dr. M. Mena, Dr. A. Martín, M. d. C. Morales-Varela,
Dr. C. Santamaría
Departamento de Química Inorgánica
Universidad de Alcalá, Campus Universitario
28871 Alcalá de Henares-Madrid (Spain)
Fax: (+34) 91-885-4683
E-mail: miguel.mena@uah.es

J. Gracia, Prof. Dr. J.-M. Poblet
Departament de Química Física i Inorgánica
Universitat Rovira i Virgili
Imperial Tarraco 1, 43005 Tarragona (Spain)

3.2 „P-B Adducts of 3,4-dimethyl-1-phosphaferrocene with bromoboranes"

M. Scheibitz, J. W. Bats, M. Bolte, M. Wagner

Eur. J. Inorg. Chem. **2003**, 2049 – 2053.

SHORT COMMUNICATION

P−B Adducts of 3,4-Dimethyl-1-phosphaferrocene with Bromoboranes

Matthias Scheibitz,[a] Jan W. Bats,[b][‡] Michael Bolte,[b][‡] and Matthias Wagner*[a]

Dedicated to Prof. Dr. Herbert Wagner on the occasion of his retirement

The crystalline adducts FcP–BBr₃ (**2**) and FcP–BBr₂Fc (**3**), which are very rare examples of *P*-bonded complexes between phosphaferrocene and a main-group metal atom, were obtained by the reaction of 3,4-dimethyl-1-phosphaferrocene (FcP) with BBr₃ and FcBBr₂ (Fc: ferrocenyl). According to X-ray crystallography, the Fe–P bond length in **2** is 0.085 Å shorter than in the parent phosphaferrocene. All structural changes resulting from P–B acid–base pairing follow the

same qualitative trend, but are significantly larger than those occurring from the formation of transition metal complexes of phosphaferrocene. In contrast to **2**, NMR spectroscopy reveals **3** to be almost completely dissociated in CDCl₃ solution at room temperature.

(© Wiley-VCH Verlag GmbH & Co. KGaA, 69451 Weinheim, Germany, 2003)

Introduction

Oligonuclear transition metal complexes are receiving great attention because of their numerous applications both in homogeneous catalysis[1] and in materials science.[2] The sandwich complex ferrocene has proven to be a particularly important building block in this context. 1,2-Disubstituted ferrocene derivatives give access to chelate ligands possessing planar chirality that have been employed successfully in asymmetric catalysis.[3−5] In the field of materials science, Manners et al. took advantage of the ring-opening polymerisation of strained *ansa*-ferrocenes for the generation of poly(ferrocenylene)s that exhibit interesting optical and electronical properties.[6] Phosphaferrocenes **A**[7] and 1,1′-diphosphaferrocenes **B**[8] (Figure 1), which became available from the work of Mathey et al., were soon recognized to form stable κ-*P* complexes with various transition metals.[9] Ganter et al. developed appropriately substituted derivatives of **A** as a new class of chiral chelate ligands,[10,11] while **B** was used as bridging unit in the formation of heterotrimetallic aggregates.[12]

Our group recently reported a convenient approach to ferrocene-containing macromolecules that benefits from the facile formation of Lewis acid−base adducts. For example, the reaction of the diborylated ferrocene 1,1′-fc(BMe₂)₂

[a] Institut für Anorganische Chemie, J. W. Goethe-Universität Frankfurt,
Marie-Curie-Strasse 11, 60439 Frankfurt (Main), Germany
Fax: (internat.) + 49-69/79829260
E-mail: Matthias.Wagner@chemie.uni-frankfurt.de
[b] Institut für Organische Chemie, J. W. Goethe-Universität Frankfurt,
Marie-Curie-Strasse 11, 60439 Frankfurt (Main), Germany
[‡] X-ray crystallography
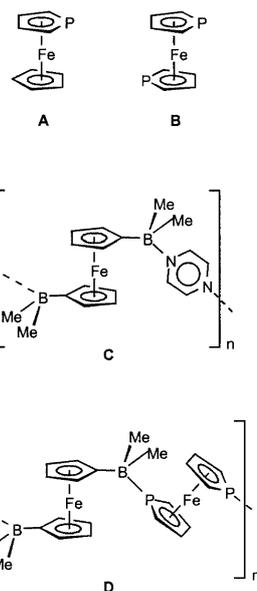
Figure 1. Phosphaferrocene **A**, 1,1′-diphosphaferrocene **B** (only the parent molecules are shown as representatives of the whole class of derivatives), a B−N-bonded charge-transfer coordination polymer **C**, and the final target molecule **D**

[fc = (C₅H₄)₂Fe] with selected difunctional Lewis bases (e.g., pyrazine) gives access to polymeric materials in high yield and under very mild conditions (e.g., **C**, Figure 1).[13−15] We decided to investigate whether the or-

SHORT COMMUNICATION

M. Scheibitz, J. W. Bats, M. Bolte, M. Wagner

ganic linker in **C** can be replaced by the redox-active organometallic template ligand **B** to generate target molecules like **D** (Figure 1).

A particular challenge is offered by the fact that despite the plethora of well-characterized complexes of phosphaferrocene and transition metals, no adducts of **A** and only one adduct of **B**[16] with main-group Lewis acids has been isolated so far. In contrast to the related azaferrocene, which is readily quaternized by methyl iodide,[17] diphosphaferrocene **B** was found to react only at elevated temperature, even in neat benzyl bromide. The reaction leads to the decomposition of the phosphaferrocene moiety with liberation of *P,P*-dibenzylphospholium bromide.[18] Acetylations, formylations and carboxylations of phosphaferrocenes occur selectively at the α-carbon atoms of the coordinated phospholyl ring.[8,18,19] Moreover, treatment of **A** or **B** with trifluoromethanesulfonic acid leads to protonation on the iron atom, rather than on the phosphorus atom.[20] In summary, the P atom of phosphaferrocenes possesses an energetically low-lying lone pair of electrons and consequently acts as a rather poor σ donor. The LUMO, on the other hand, has pronounced p_z character on the phosphorus atom and is well suited to accept π-electron density.[9,11] The stability of phosphaferrocene-κ-*P*–ML$_n$ complexes is, therefore, expected to grow with an increasing degree of back bonding from electron-rich ML$_n$ fragments. Thus, the fact that main-group elements are not able to have $d_π$–$p_π$ interactions with **A** or **B** might explain why corresponding κ-*P* η^1-adducts are virtually unknown up to now. One report on the reaction of phosphaferrocene with BF$_3$·OEt$_2$ has been published that provides evidence for the existence of a phosphorus-bonded adduct in solution (^{31}P NMR spectroscopic control).[20] Moreover, the hypothetical P–B complex **A·BH$_3$** has been studied theoretically using DFT methods.[21] Mathey et al. recently reported the reaction of octa-*n*-propyldiphosphaferrocene with GaCl$_3$, which leads to the formation of a tetrahedral gallium(III) complex featuring a chelating diphosphaferrocene ligand.[16] Here, we describe the synthesis, isolation and structural characterization of two P–B adducts of 3,4-dimethyl-1-phosphaferrocene (**1**, Scheme 1).

Results and Discussion

Synthesis and Spectroscopic Characterization

The phosphaferrocene derivative **1** (Scheme 1) was chosen for our investigation because it is accessible in high yield by an established procedure.[7,22] When **1** is treated with the strong Lewis acid BBr$_3$ in CDCl$_3$ (stoichiometric ratio: 1:1), no obvious reaction takes place since the resulting clear mixture still possesses the orange colour of the initial phosphaferrocene solution. NMR spectroscopy at ambient temperature, however, reveals significant shifts of some characteristic resonances. The phosphorus nucleus in **2** [δ(^{31}P) = −13.2 ppm, $h_{1/2}$ = 30.1 Hz] is deshielded by 69.3 ppm compared to that of the free ligand **1** [δ(^{31}P) = −82.5 ppm, $h_{1/2}$= 6.5 Hz]. A strong downfield shift of the
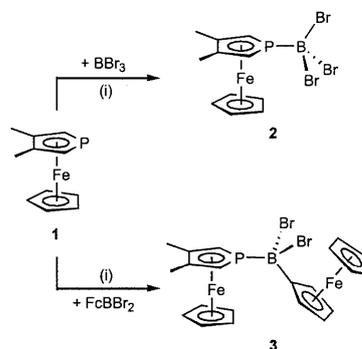
Scheme 1. Synthesis of the P−B-bonded phosphaferrocene adducts **2** and **3**; (i) ambient temperature, C$_6$H$_6$

^{31}P NMR signal is also generally observed upon complexation of phosphaferrocenes with transition metal ions.[9] No signal is detectable in the ^{11}B NMR spectrum, which is most likely due to severe line broadening resulting from a dynamic adduct equilibrium. In the ^{1}H NMR spectrum of **2**, and with respect to parent 3,4-dimethyl-1-phosphaferrocene [**1**: δ(^{1}H) = 3.74 ($^2J_{P,H}$ = 36.3 Hz, phospholyl α-C*H*), 4.15 (C$_5$H$_5$) ppm], the resonances of the phospholyl α-protons [**2**: δ(^{1}H) = 4.18 ($^2J_{P,H}$ = 29.1 Hz) ppm] and the cyclopentadienyl ring [**2**: δ(^{1}H) = 4.55 ppm] are shifted to lower field by 0.44 ppm and 0.40 ppm, respectively. Moreover, the $^2J_{P,H}$ coupling constant decreases by 7.2 Hz. Both the ^{31}P and ^{11}B NMR spectra were recorded also at −50 °C (CDCl$_3$). Under these conditions, the ^{31}P NMR resonance appears at δ = −12.9 ppm as a well-resolved quadruplet with intensity ratios of 1:1:1:1 and a coupling constant of $^1J_{P,B}$ = 138.5 Hz ($^1J_{P,B}$ values have been reported within a range of 10−180 Hz[23]). The ^{11}B NMR signal possesses a chemical shift value of δ = −20.9 ppm (d, $^1J_{P,B}$ = 138.5 Hz). Consequently, at −50 °C the solution contains mainly the adduct **2**, rather than free **1** and BBr$_3$.

The ^{11}B and ^{1}H NMR spectra of an equimolar mixture of **1** with FcBBr$_2$ in CDCl$_3$ at ambient temperature show only negligible differences to the NMR spectra of the individual components. In the ^{13}C NMR spectrum of **1**/FcBBr$_2$, the doublet of the phospholyl α-carbon atoms is broad, while the other signals remain unchanged. The chemical shift of the ^{31}P NMR resonance is the same in **1**/FcBBr$_2$ as in the case of **1**, but the width at half height increases from $h_{1/2}$ = 6.5 Hz (**1**) to $h_{1/2}$ = 165.6 Hz (**1**/FcBBr$_2$). Thus, NMR spectroscopy reveals the Lewis acid−base pair **1**/FcBBr$_2$ to be almost completely dissociated at room temperature in CDCl$_3$ solution. Slow evaporation of an equimolar mixture of **1** and FcBBr$_2$ in benzene, however, yielded X-ray-quality crystals of the desired P−B-bonded dinuclear species **3**.

X-ray Crystal Structure Determination

The phosphaferrocene−borane adducts **2** and **3** crystallize from benzene in the space groups *Pna*2$_1$

P−B Adducts of 3,4-Dimethyl-1-phosphaferrocene with Bromoboranes _____ **SHORT COMMUNICATION**

(orthorhombic) and $P2_1/c$ (monoclinic), respectively (Table 1). A comparison of the molecular geometries of **1**, **2** (Figure 2) and **3** (Figure 3) reveals remarkable structural changes as a result of P−B bond formation (Table 2). The Fe(1)−P(1) bond length in the BBr$_3$ adduct **2** possesses a value of 2.199(2) Å, which is 0.085 Å shorter than the iron−phosphorus bond in the parent 3,4-dimethyl-1-phosphaferrocene (**1**) [2.284(1) Å].[24] FcBBr$_2$ is known to be a weaker Lewis acid than BBr$_3$ because the ferrocenyl substituent acts as an electron donor towards the formally empty p orbital of the boron atom.[25] Consequently, the length of the Fe(1)−P(1) bond in **3** [2.216(1) Å] is intermediate between the values determined for **1** and **2**. These findings are consistent with the general trend observed for transition metal complexes of phosphaferrocenes. A search of the Cambridge Structural Database (CSD, Version 5.24, November 2002)[26] reveals the average Fe−P bond length in monophosphaferrocene derivatives to be 2.285(13) Å (10 structures). This value is reduced to 2.238(16) Å in the corresponding phosphorus-bonded transition metal complexes (22 structures). Interestingly, the effect of Fe−P bond contraction is larger in the borane adducts **2** and **3** than in the corresponding transition metal complexes. P−B acid−base pairing also has a pronounced influence on the C(2)−P(1)−C(5) angle, which is stretched from 88.9(2)° in **1** to 94.7(4)° in **2**, and to 92.7(2)° in **3**. Again, these findings are in good qualitative agreement with the structural features obtained for phosphaferrocene−transition metal aggregates [C−P−C angle in free phosphaferrocene (mean value of 10 derivatives): 89(1)°; C−P−C angle in phosphaferrocene−transition metal complexes (mean value of 22 structures): 92(1)°]. Thus, in all phosphaferrocene de-

rivatives investigated so far (including **2** and **3**), a long Fe−P bond appears to be associated with a small C−P−C angle. It has to be noted that the degree of phospholyl ring puckering is largely unaffected by P−B bond formation. In the case of **1**, the P atom is located at a position 0.048(1) Å above the C(2)C(3)C(4)C(5) plane, while in **2** this displacement is only slightly reduced to a value of 0.043(1) Å. Thus, the phosphorus atom is not just pulled toward the iron centre upon coordination of BBr$_3$, which would result in a flattening of the phospholyl ligand, but rather it moves toward the C(3)−C(4) bond along a line almost parallel to the C(2)C(3)C(4)C(5) plane {**1**: d[P(1)· MP] = 2.589 Å; **2**: d[P(1)· MP] = 2.504 Å; MP: midpoint of the C(3)−C(4) bond}. As a result, the P−Fe bond, as well as the P−C bonds, become shorter [cf. **1**: P(1)−C(2) = P(1)−C(5) = 1.774(3) Å; **2**: P(1)−C(2) = P(1)−C(5) = 1.745(8) Å], the C−P−C angle increases, and the adjacent P−C−C angles decrease [cf. **1**: P(1)−C(2)−C(3) = 113.9(2)°, P(1)−C(5)−C(4) = 114.0(2)°; **2**: P(1)−C(2)−C(3) = 109.0(5)°, P(1)−C(5)−C(4) = 110.0(5)°]. The differences observed between the geometrical parameters of **1** and **3** are rather similar to those described above for **1** and **2** and, thus, do not merit further discussion. The P(1)−B(1) bond in **2** [1.972(9) Å] is 0.051 Å shorter than in **3** [2.023(4) Å]. The bond angles around the boron atoms cover a range between P(1)−B(1)−Br(3) = 104.9(4)° and Br(1)−B(1)−Br(3) = 112.2(4)° in the case of **2**, and P(1)−B(1)−Br(1) = 102.9(2)° and C(21)−B(1)−Br(1) = 114.2(2)° in the case of **3**. The relevant Br−B−Br angles of 110.9(4)°, 111.9(4)°, and 112.2(4)° in **2** are slightly larger than the value expected for an sp^3-hybridized boron atom with ideal tetrahedral geometry (109.5°). In **3**, the boron centre is somewhat less pyramidalized, which, together with the longer P(1)−B(1) bond, again indicates a weaker acid−base interaction as is the case in **2**. This interpretation is in agreement with the conclusions drawn from our NMR spectroscopic studies (see above). The BBr$_3$ adduct **2** features a torsion angle C(2)−P(1)−B(1)−Br(2) of 85.4(5)°. A similar conformation is observed in **3** for the BBr$_2$P fragment with respect to the ferrocenyl substituent [C(22)−C(21)−B(1)−P(1) = −87.9(3)°], whereas, com-

Table 1. Selected crystallographic data for **2** and **3**

Compound	2	3
Formula	C$_{11}$H$_{13}$BBr$_3$FeP	C$_{21}$H$_{22}$BBr$_2$Fe$_2$P
M	482.57	587.69
Crystal system	orthorhombic	monoclinic
Space group	$Pna2_1$	$P2_1/c$
a [Å]	14.1040(10)	10.561(3)
b [Å]	15.5060(10)	22.221(5)
c [Å]	6.9450(9)	8.8365(17)
β [°]	90	97.366(14)
V [Å^3]	1518.8(2)	2056.5(8)
Z	4	4
D_c [g cm^{-3}]	2.110	1.898
T [K]	173(2)	144(2)
μ(Mo-K_α) [mm^{-1}]	8.965	5.378
$2\theta_{max.}$ [°]	56.56	65.42
Measured reflections	25504	36221
Unique reflections (R_{int})	3772 (0.083)	7009 (0.072)
Observed reflections [$I > 2\sigma(I)$]	3174	4777
Parameters refined	157	246
R1 [$I > 2\sigma(I)$]	0.051	0.051
wR2 [$I > 2\sigma(I)$]	0.121	0.080
GOOF on F^2	1.031	1.074
Largest diff. peak/hole [e·Å^{-3}]	0.74/−0.83	1.13/−0.65
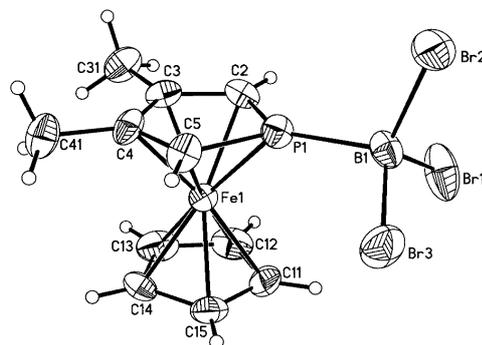
Figure 2. Molecular structure and numbering scheme of compound **2**; thermal ellipsoids shown at the 50% probability level

SHORT COMMUNICATION

M. Scheibitz, J. W. Bats, M. Bolte, M. Wagner

pared to compound **2**, the phosphaferrocene moiety is rotated by almost 180° about the P(1)−B(1) bond [C(2)−P(1)−B(1)−C(21) = −90.8(3)°]. This conformation results in a short intramolecular C−H· π interaction between the C(11)−H(11) bond and the cyclopentadienyl ring C(21)C(22)C(23)C(24)C(25) [H(11)· Cg = 2.68 Å, C(11)−H(11)· Cg = 152°; Cg: centroid of the cyclopentadienyl ligand]. Both the ferrocene and phosphaferrocene groups have approximately eclipsed conformations. In **3**, the angle between the planes of the five-membered rings is 1.7° for the ferrocenyl group and 4.2° for the phosphaferrocene moiety.
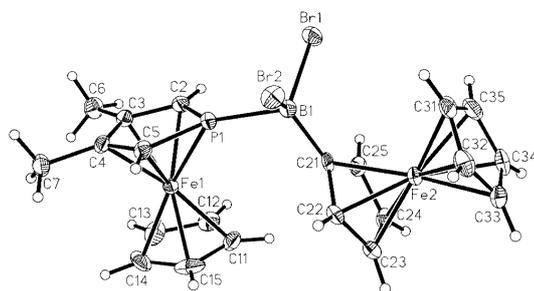
Figure 3. Molecular structure and numbering scheme of compound **3**; thermal ellipsoids shown at the 50% probability level

Table 2. Selected bond lengths [Å], angles [°] and torsion angles [°] of **1**,[24] **2** and **3**; Note: The atom labels of compound **1** have been adapted to the numbering scheme of **2** and **3**

Compound	1 (T = 74 K)	2 (T = 173 K)	3 (T = 144 K)
Fe(1)−P(1)	2.284(1)	2.199(2)	2.216(1)
Fe(1)−C(2)	2.072(2)	2.075(7)	2.076(3)
Fe(1)−C(3)	2.057(2)	2.070(7)	2.066(3)
Fe(1)−C(4)	2.054(2)	2.073(7)	2.062(3)
Fe(1)−C(5)	2.060(2)	2.095(7)	2.075(3)
P(1)−C(2)	1.774(3)	1.745(8)	1.744(3)
P(1)−C(5)	1.774(3)	1.745(8)	1.741(3)
C(2)−C(3)	1.424(4)	1.441(11)	1.420(4)
C(3)−C(4)	1.436(3)	1.438(10)	1.427(4)
C(4)−C(5)	1.422(4)	1.431(10)	1.419(4)
P(1)−B(1)	–	1.972(9)	2.023(4)
C(2)−P(1)−C(5)	88.9(2)	94.7(4)	92.7(2)
P(1)−C(2)−C(3)	113.9(2)	109.0(5)	110.9(2)
P(1)−C(5)−C(4)	114.0(2)	110.0(5)	111.1(2)
C(2)−C(3)−C(4)	111.6(2)	113.7(6)	112.7(3)
C(5)−C(4)−C(3)	111.6(2)	112.6(6)	112.7(3)
C(2)−P(1)−B(1)−Br(2)	–	85.4(5)	–
C(2)−P(1)−B(1)−C(21)	–	–	−90.8(3)

Conclusion

In contrast to the rich chemistry that has been developed for complexes between phosphaferrocene and transition metals, examples of *P*-bonded adducts between phosphaferrocene and main-group Lewis acids remained unknown un-

til recently.[16] We have shown that adducts FcP−BBr$_3$ (**2**) and FcP−BBr$_2$Fc (**3**) are readily obtained from the reaction of 3,4-dimethyl-1-phosphaferrocene (FcP) with BBr$_3$ and FcBBr$_2$, respectively (Fc: ferrocenyl). NMR spectroscopy using CDCl$_3$ solutions reveals a considerable amount of adduct **2** to be present in the equilibrium at ambient temperature while **3** is largely dissociated even at −50 °C (cf. theory predicts a small P−B bond-dissociation energy in A·BH$_3$ of D_e = 17.4 kcal·mol^{-1}; B3LYP/6−31G* level).[21] In the solid state, however, **1** binds not only to BBr$_3$, but also to FcBBr$_2$. All structural changes resulting from P−B acid−base pairing follow the same qualitative trend as those that occur in the formation of complexes of phosphaferrocene with transition metals. The experimental results obtained for **1** and **2** are also in good agreement with the theoretical calculations on **A** and **A·BH$_3$**. For example, the Fe−P bond is contracted by 0.085 Å upon going from **1** to **2** and by 0.050 Å upon going from **A** to **A·BH$_3$**. Moreover, the P(1)−B(1) bond length in **2** possesses a value of 1.972(9) Å, which is in good agreement with the theoretically predicted bond length of 1.987 Å in **A·BH$_3$**.[21]

The dinuclear ferrocenyl aggregate **3** contains all the key structural motifs underlying the target compound **D** (Figure 1). Work is currently in progress to synthesise corresponding coordination polymers from 1,1′-diphosphaferrocene derivatives and 1,1′-diborylferrocenes.

Experimental Section

General Remarks: All reactions and manipulations of air-sensitive compounds were carried out in dry, oxygen-free argon using standard Schlenk glassware. Solvents were freshly distilled under argon from Na/benzophenone (C$_6$H$_6$) or passed through a 4-Å molecular sieve column (CDCl$_3$) prior to use. NMR: Bruker AMX 250, AMX 400, DPX 250; abbreviations: s = singlet, d = doublet, vtr = virtual triplet, q = quadruplet, n.r. = multiplet expected in the NMR spectrum, but not resolved; n.o. = signal not observed. ^{11}B [^{31}P] NMR spectra are reported relative to external BF$_3$·Et$_2$O [H$_3$PO$_4$, 85% in water]. 3,4-Dimethylphosphaferrocene (**1**)[7,22] and dibromoborylferrocene[27] were synthesized according to literature procedures.

Syntheses

2: A solution of BBr$_3$ (14 mg, 0.056 mmol) in CDCl$_3$ (0.25 mL) was added in an NMR tube to a frozen solution of **1** (13 mg, 0.056 mmol) in CDCl$_3$ (0.25 mL). The reaction mixture was warmed to ambient temperature within 30 min and investigated by NMR spectroscopy. When the same quantities of BBr$_3$ and **1** were mixed together in toluene at −78 °C, **2** was obtained as a microcrystalline solid. Yield: 21 mg (78%). X-ray-quality crystals of **2** were grown from a highly dilute benzene solution by slow evaporation of the solvent. ^{1}H NMR (250.1 MHz, CDCl$_3$, 303 K): δ = 2.23 (s, 6 H, CH$_3$), 4.18 (d, $^2J_{P,H}$ = 29.1 Hz, 2 H, α-CH), 4.55 (s, 5 H, C$_5$H$_5$) ppm. ^{13}C NMR (62.9 MHz, CDCl$_3$, 303 K): δ = 15.9 (CH$_3$), 75.2 (C$_5$H$_5$), n.o. (C-α), n.o. (CCH$_3$) ppm. ^{11}B NMR (80.3 MHz, CDCl$_3$, 303 K): n.o. (BBr$_3$). ^{11}B NMR (80.3 MHz, CDCl$_3$, 223 K): δ = −20.9 (d, $^1J_{P,B}$ = 138.5 Hz, BBr$_3$) ppm. ^{31}P NMR (101.3 MHz, CDCl$_3$, 303 K): δ = −13.2 (n.r., $h_{1/2}$ = 30.1 Hz, phospholyl-P) ppm. ^{31}P NMR (101.3 MHz, CDCl$_3$, 223 K): δ = −12.9 (q, $^1J_{P,B}$ = 138.5 Hz, phospholyl-P) ppm.

P—B Adducts of 3,4-Dimethyl-1-phosphaferrocene with Bromoboranes

SHORT COMMUNICATION

3: 1 (13 mg, 0.056 mmol) and FcBBr$_2$ (20 mg, 0.056 mmol) were dissolved in CDCl$_3$ (0.50 mL) at ambient temperature and the resulting mixture was sealed in an NMR tube. X-ray-quality crystals of **3** were grown from a benzene solution by slow evaporation of the solvent. Yield: 31 mg (94%). ^{1}H NMR (250.1 MHz, CDCl$_3$, 303 K): δ = 2.18 (s, 6 H, CH$_3$), 3.78 (d, $^2J_{P,H}$ = 35.5 Hz, 2 H, α-CH), 4.19, 4.23 (2 × s, 2 × 5 H, 2 × C$_5$H$_5$), 4.52, 4.91 (2 × vtr, 2 × 2 H, $^3J_{H,H}$ = $^4J_{H,H}$ = 1.8 Hz, C$_5$H$_4$) ppm. ^{13}C NMR (100.6 MHz, CDCl$_3$, 303 K): δ = 16.4 (CH$_3$), 71.5 (2 × C$_5$H$_5$), 78.1 (br. d, $^1J_{P,C}$ = 57.3 Hz, C-α), n.o. (CCH$_3$), 77.1, 78.2 (C$_5$H$_4$) ppm. ^{11}B NMR (80.3 MHz, CDCl$_3$, 303 K): δ = 46.1 (s, $h_{1/2}$ = 119.0 Hz, BBr$_2$) ppm. ^{11}B NMR (80.3 MHz, CDCl$_3$, 223 K): δ = 45.1 (s, $h_{1/2}$ = 466.2 Hz, BBr$_2$) ppm. ^{31}P NMR (101.3 MHz, CDCl$_3$, 303 K): δ = −81.9 (s, $h_{1/2}$ = 165.6 Hz, phospholyl-P) ppm. ^{31}P NMR (101.3 MHz, CDCl$_3$, 223 K): δ = −80.4 (s, $h_{1/2}$ = 252.8 Hz, phospholyl-P) ppm.

X-ray Crystallographic Studies

2: A single crystal (red needle; 0.06 × 0.07 × 0.31 mm) was analysed with a STOE IPDS II two-circle diffractometer with graphite-monochromated Mo-K_α radiation. An empirical absorption correction was performed using the MULABS option[28] in PLATON;[29] the minimum and maximum transmissions were 0.1676 and 0.6153, respectively. The structure was determined by direct methods using the program SHELXS[30] and refined against F^2 with full-matrix least-squares techniques using the program SHELXL-97.[31] The data/parameter ratio was 24.0. All non-hydrogen atoms were refined with anisotropic displacement parameters. Hydrogen atoms were located by difference Fourier synthesis and refined using a riding model.

3: A single crystal (orange block; 0.19 × 0.24 × 0.45 mm) was analysed with a SIEMENS SMART CCD diffractometer; repeatedly measured reflections remained stable. An empirical absorption correction using the program SADABS[32] gave a correction factor between 0.674 and 1.000. Equivalent reflections were averaged (R_{int} = 0.072). The structure was determined by direct methods using the program SHELXS.[30] Hydrogen atoms were geometrically positioned and treated as riding atoms. All non-hydrogen atoms were refined with anisotropic thermal parameters. The structure was refined on F^2 values using the program SHELXL-97.[31]

CCDC-203030 and -203031 contain the supplementary crystallographic data for this paper. These data can be obtained free of charge at www.ccdc.cam.ac.uk/conts/retrieving.html [or from the Cambridge Crystallographic Data Centre, 12 Union Road, Cambridge CB2 1EZ, UK; Fax: (internat.) + 44-1223/336-033; E-mail: deposit@ccdc.cam.ac.uk].

[1] B. Cornils, W. A. Herrmann, *Applied Homogeneous Catalysis with Organometallic Compounds — A Comprehensive Handbook*, 2nd ed., Wiley-VCH, Weinheim, Germany, **2002**.
[2] D. W. Bruce, D. O'Hare, *Inorganic Materials*, 2nd ed., John Wiley & Sons, Chichester, UK, **1996**.
[3] A. Togni, T. Hayashi, *Ferrocenes*, Wiley-VCH, Weinheim, Germany, **1995**.
[4] I. Ojima, *Catalytic Asymmetric Synthesis*, Wiley-VCH, Weinheim, Germany **2000**.
[5] E. N. Jacobsen, A. Pfaltz, H. Yamamoto, *Comprehensive Asymmetric Catalysis*, vol. I−III, Springer, New York, USA, **1999**.
[6] P. Nguyen, P. Gómez-Elipe, I. Manners, *Chem. Rev.* **1999**, *99*, 1515−1548.
[7] F. Mathey, A. Mitschler, R. Weiss, *J. Am. Chem. Soc.* **1977**, *99*, 3537−3538.
[8] G. de Lauzon, B. Deschamps, J. Fischer, F. Mathey, A. Mitschler, *J. Am. Chem. Soc.* **1980**, *102*, 994−1000.
[9] F. Mathey, *Coord. Chem. Rev.* **1994**, *137*, 1−52.
[10] C. Ganter, L. Brassat, C. Glinsböckel, B. Ganter, *Organometallics* **1997**, *16*, 2862−2867.
[11] C. Ganter, *J. Chem. Soc., Dalton Trans.* **2001**, 3541−3548.
[12] B. Deschamps, F. Mathey, J. Fischer, J. H. Nelson, *Inorg. Chem.* **1984**, *23*, 3455−3462.
[13] M. Fontani, F. Peters, W. Scherer, W. Wachter, M. Wagner, P. Zanello, *Eur. J. Inorg. Chem.* **1998**, 1453−1465; M. Fontani, F. Peters, W. Scherer, W. Wachter, M. Wagner, P. Zanello, *Eur. J. Inorg. Chem.* **1998**, 2087.
[14] M. Grosche, E. Herdtweck, F. Peters, M. Wagner, *Organometallics* **1999**, *18*, 4669−4672.
[15] R. E. Dinnebier, M. Wagner, F. Peters, K. Shankland, W. I. F. David, *Z. Anorg. Allg. Chem.* **2000**, *626*, 1400−1405.
[16] X. Sava, M. Melaimi, N. Mézailles, L. Ricard, F. Mathey, P. Le Floch, *New. J. Chem.* **2002**, *26*, 1378−1383.
[17] K. K. Joshi, P. L. Pauson, A. R. Quazi, W. H. Stubbs, *J. Organomet. Chem.* **1964**, *1*, 471−475.
[18] G. de Lauzon, B. Deschamps, F. Mathey, *Nouv. J. Chim.* **1980**, *4*, 683−685.
[19] F. Mathey, *J. Organomet. Chem.* **1977**, *139*, 77−87.
[20] R. M. G. Roberts, J. Silver, A. S. Wells, *Inorg. Chim. Acta* **1986**, *119*, 165−169.
[21] G. Frison, F. Mathey, A. Sevin, *J. Phys. Chem. A* **2002**, *106*, 5653−5659.
[22] A. Breque, F. Mathey, P. Savignac, *Synthesis* **1981**, 983−985.
[23] S. Berger, S. Braun, H.-O. Kalinowski, *NMR-Spektroskopie von Nichtmetallen*, vol. 3 ("^{31}P- NMR-Spektroskopie"), Thieme Verlag, Stuttgart, Germany, **1993**.
[24] R. Wiest, B. Rees, A. Mitschler, F. Mathey, *Inorg. Chem.* **1981**, *20*, 2966−2970.
[25] A. Appel, F. Jäkle, T. Priermeier, R. Schmid, M. Wagner, *Organometallics* **1996**, *15*, 1188−1194.
[26] F. H. Allen, *Acta Crystallogr., Sect. B* **2002**, *58*, 380−388.
[27] T. Renk, W. Ruf, W. Siebert, *J. Organomet. Chem.* **1976**, *120*, 1−25.
[28] R. H. Blessing, *Acta Crystallogr., Sect. A* **1995**, *51*, 33−38.
[29] A. L. Spek, *Acta Crystallogr., Sect. A* **1990**, *46*, C34.
[30] G. M. Sheldrick, *Acta Crystallogr., Sect. A* **1990**, *46*, 467−473.
[31] G. M. Sheldrick, *SHELXL-97 — A Program for the Refinement of Crystal Structures*, Universität Göttingen, Göttingen, Germany, **1997**.
[32] G. M. Sheldrick, *SADABS*, Universität Göttingen, Göttingen, Germany, **2000**.

Received February 14, 2003

3.3 „The twinned structure of ferricenyltrifluoroborate"

J. W. Bats, M. Scheibitz, M. Wagner

Acta Cryst. **2003**, *C59*, m355 – m357.

metal-organic compounds

The twinned structure of ferricenyltrifluoroborate

Jan W. Bats,[a]* Matthias Scheibitz[b] and Matthias Wagner[b]

[a]Institut für Organische Chemie, Universität Frankfurt, Marie-Curie-Straße 11,
D-60439 Frankfurt am Main, Germany, and [b]Institut für Anorganische Chemie,
Universität Frankfurt, Marie-Curie-Straße 11, D-60439 Frankfurt am Main, Germany
Correspondence e-mail: bats@chemie.uni-frankfurt.de

Crystals of the title compound, [Fe(C_5H_5)($C_5H_4BF_3$)], are monoclinic and twinned. The twinning initially resulted in a misleading unit-cell assignment. The formal oxidation state of Fe is 3+, and the crystal packing consists of intermolecular C—H···F and π–π interactions.

Comment

Oligonuclear aggregates of organometallic compounds are receiving increased attention because of their potential applications as magnetic, electronic and liquid-crystalline materials. We have recently synthesized the trinuclear ferrocene complex 1,3,5-tris(4-methoxyphenyl)-2,4,6-triferrocenylborazine in order to investigate the efficiency of a borazine bridging unit as a transmitter of electronic interactions (Ma *et al.*, 2002). Partial oxidation of that compound was expected to lead to a mixed-valence state with interesting electronic and spectroscopic properties. For this reason, the compound was treated with the oxidizing agent $AgBF_4$ in various stoichiometric ratios. In most cases, a small number of dark-colored crystals of (I) were obtained from the reaction mixture. Thus 1,3,5-tris(4-methoxyphenyl)-2,4,6-triferrocenylborazine is not stable in the presence of $AgBF_4$, but decomposes to give ferricenyltrifluoroborate, (I).

(I)
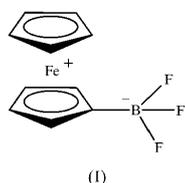
Crystals of (I) were found to be twinned, and the twinned cell can be obtained by the unit-cell transformation $a_{twin} = -a$, $b_{twin} = -b$ and $c_{twin} = c + 2a/3$ (see Fig. 1). Initially, the unit-

cell assignment resulted in an orthogonal cell with a volume three times that of the correct monoclinic unit cell and a β_{ortho} angle of 90.001 (13)° at 146 K. The assignment of the correct crystal system was only possible after the structure had been determined and refined. This ambiguity could have been avoided if the structure determination had been performed at a higher temperature. Cell measurements at different temperatures gave β_{ortho} angles of 90.241 (13), 90.111 (11) and 90.047 (12)° at 294, 224 and 174 K, respectively. At room temperature, several reflection profiles were split and the twinning of the crystal was quite obvious.

The ferrocene group has an eclipsed conformation (Fig. 2). The C—$Cg1$—$Cg2$—C torsion angles range from 3.6 to 4.1° for the five eclipsed atom pairs ($Cg1$ and $Cg2$ are the centroids of the two five-membered rings), and the angle between the two cyclopentadiene planes is 1.64 (8)°. The B atom deviates by 0.027 (5) Å from the C11–C15 plane and is slightly tilted toward the center of the molecule. The Fe—C11 bond length (involving the BF_3-substituted C atom) is about 0.02 Å longer than the other nine Fe—C bond lengths. The ring bond angle at atom C11 [105.8 (2)°] is ~2° smaller than the value in unsubstituted ferrocene (108.0°; Seiler & Dunitz, 1979, 1982). The average Fe—C bond length in (I) [2.084 (3) Å] is comparable to Fe—C bond lengths in ferrocenium cations but is about 0.04–0.05 Å longer than Fe—C bond lengths in neutral ferrocene groups. As Fe—C bonds in several ferrocenyl and ferrocene groups are considerably affected by libration, however, it appears more realistic to consider the distances from the Fe atom to the centers of the cyclopentadiene rings as a measure of the formal oxidation state of the Fe atom. Values of 1.697 (2) and 1.703 (2) Å are observed in (I), which are in very good agreement with the range 1.686–1.702 Å (mean 1.696 Å) found for a number of ferrocenium cations (Sullivan & Foxman, 1983; Rheingold *et al.*, 1983; Bullen *et al.*, 1986; Cotton *et al.*, 1998), thus confirming the formal oxidation state of Fe in (I) as 3+. The distances of the Fe^{2+} ions from the centers of the cyclopentadiene rings in the crystal structure of ferrocene are between 1.646 and 1.661 Å, with a mean value of 1.653 Å (Seiler & Dunitz, 1979, 1982). A mean value of 1.646 Å was found in a recent determination of a ferrocenyltrifluoroborate anion (Quach *et al.*, 2001a), in which Fe has a formal oxidation state of 2+. Otherwise, the dimensions of the neutral molecule and the anion are similar. The B—C bond distance is little affected by the charge of the ferrocene group. The value of 1.616 (4) Å in (I) agrees within experimental uncertainty with the values of 1.605 (4) and 1.608 (3) Å found for the anion and is also similar to the values of 1.600 (3) and 1.610 (10) Å found in phenyltrifluoroborate anions (Conole *et al.*, 1995; Quach *et al.*, 2001b). Longer B—C distances of 1.63, 1.64, 1.65 and 1.66 Å have, however, been observed in ferricenyltriferrocenylborate (Cowan *et al.*, 1979). Thus, the difference in electronegativity between fluorine and ferrocene has a measurable influence on the B—C bond length.

There are no short intramolecular contacts, but the crystal packing exhibits four intermolecular C—H···F interactions, with H···F distances of less than 2.6 Å (Fig. 3 and Table 1). One C—H···F interaction (C13—H13···F2) is very short and

metal-organic compounds

has an H$\cdots$F distance of only 2.24 Å. The other three C—H$\cdots$F interactions have H$\cdots$F distances of 2.43, 2.53 and 2.58 Å. Neighboring ferrocenyl groups translated in the a

Figure 1
A projection of the structure of (I) along b. The monoclinic lattice defined by a and c is represented by solid lines, the twin lattice defined by a' and c' is represented by broken lines, and the pseudo-orthogonal lattice defined by a and c'' is indicated by bold lines.
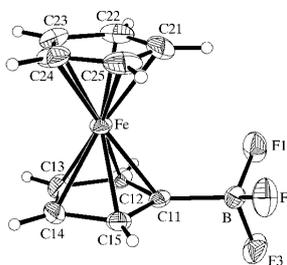
Figure 2
The molecular structure of (I), with displacement ellipsoids shown at the 50% probability level.
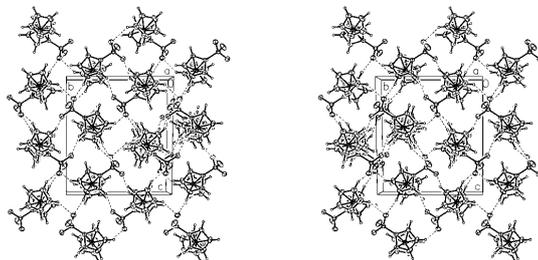
Figure 3
The crystal packing of (I), viewed along a.

direction are connected by π–π interactions between the cyclopentadiene rings. The shortest contact is 3.251 (4) Å, between atom C13 and atom C24 at ($x - 1, y, z$).

Experimental

A dry solution of AgBF$_4$ (25 mg, 0.139 mmol) in tetrahydrofuran (THF, 2.0 ml) was added dropwise at room temperature, with stirring, to a solution of 1,3,5-tris(4-methoxyphenyl)-2,4,6-triferrocenylborazine (40 mg, 0.042 mmol) in THF ($\sim$3.0 ml). The color of the solution changed gradually from yellow to blue and the resulting mixture was stirred at room temperature for $\sim$2 h. After all insolubles had been removed by filtration, the filtrate was evaporated *in vacuo* to yield a deep-blue solid and the crude product was dissolved in dry acetonitrile ($\sim$10 ml). Deep-blue, almost black, crystals of (I) were obtained by gas-phase diffusion (at room temperature) of dry diethyl ether into the acetonitrile solution of (I) over a period of one month.

Crystal data

[Fe(C$_5$H$_5$)(C$_5$H$_4$BF$_3$)]	$D_x = 1.728$ Mg m^{-3}
$M_r = 252.83$	Mo $K\alpha$ radiation
Monoclinic, $P2_1/n$	Cell parameters from 118
$a = 6.8603$ (10) Å	reflections
$b = 11.248$ (2) Å	$\theta = 3$–$23°$
$c = 12.804$ (3) Å	$\mu = 1.55$ mm^{-1}
$\beta = 100.290$ (13)°	$T = 146$ (2) K
$V = 972.1$ (3) Å^3	Rod, deep blue
$Z = 4$	$0.45 \times 0.12 \times 0.08$ mm

Data collection

Siemens SMART 1K CCD diffractometer	$R_{int} = 0.046$
	$\theta_{max} = 32.0°$
ω scans	$h = -9 \rightarrow 10$
Absorption correction: numerical (*SHELXTL*; Sheldrick, 1996)	$k = -16 \rightarrow 16$
	$l = -18 \rightarrow 18$
$T_{min} = 0.596$, $T_{max} = 0.886$	385 standard reflections
20 212 measured reflections	frequency: 600 min
5254 independent reflections	intensity decay: none
4283 reflections with $I > 2\sigma(I)$	

Refinement

Refinement on F^2	H-atom parameters constrained
$R[F^2 > 2\sigma(F^2)] = 0.066$	$w = 1/[\sigma^2(F_o^2) + (0.03P)^2 + P]$
$wR(F^2) = 0.127$	where $P = (F_o^2 + 2F_c^2)/3$
$S = 1.30$	$(\Delta/\sigma)_{max} = 0.002$
5254 reflections	$\Delta\rho_{max} = 0.50$ e Å^{-3}
137 parameters	$\Delta\rho_{min} = -0.58$ e Å^{-3}

Table 1
Hydrogen-bonding geometry (Å, °).

D—H$\cdots A$	D—H	H$\cdots A$	$D\cdots A$	D—H$\cdots A$
C12—H12$\cdots$F1^{i}	0.95	2.43	3.168 (3)	135
C13—H13$\cdots$F2^{ii}	0.95	2.24	3.138 (3)	158
C23—H23$\cdots$F3^{iii}	0.95	2.58	3.455 (4)	154
C24—H24$\cdots$F2^{iv}	0.95	2.53	3.232 (4)	130

Symmetry codes: (i) $-x, -y, 1 - z$; (ii) $x - \frac{1}{2}, \frac{1}{2} - y, z - \frac{1}{2}$; (iii) $\frac{1}{2} + x, \frac{1}{2} - y, z - \frac{1}{2}$; (iv) $\frac{1}{2} - x, \frac{1}{2} + y, \frac{3}{2} - z$.

The initial unit-cell determination of (I) revealed an orthogonal cell [$a = 6.8615$ (7) Å, $b = 11.2481$ (16) Å, $c = 37.781$ (6) Å, $\alpha = \beta = \gamma = 90°$ and $V = 2915.9$ (9) Å^3]. Merging of the equivalent reflections showed the crystal system to be monoclinic ($R_{int} = 0.054$) rather than

metal-organic compounds

orthorhombic (R_{int} = 0.211), and the systematic absences indicated the monoclinic space group $P2_1/c$. No acceptable orthorhombic space group could be found. Initially, the structure was determined and refined assuming the space group to be $P2_1/c$. Each reflection, hkl, coincided with a twin reflection, $h\bar{k}\bar{l}$, and the twin fraction refined to 0.369 (1). Refinement in $P2_1/c$ converged at $wR2 = 0.167$ and $R1 = 0.099$, and the resulting structure contained three independent molecules that were found to be related by translation vectors of $\frac{2}{3}0\frac{1}{3}$ and $\frac{1}{3}0\frac{2}{3}$. Thus, the pseudo-orthogonal cell is an artifact of the twinning and the correct unit cell has a volume of one-third of the observed cell. The new monoclinic unit cell can be obtained from the pseudo-orthogonal cell by the transformation $a_{new} = a_{ortho}$, $b_{new} = b_{ortho}$ and $c_{new} = -a_{ortho}/3 + c_{ortho}/3$, while the unit cell of the twin domain is obtained by the transformation $a_{twin} = -a_{ortho}$, $b_{twin} = -b_{ortho}$ and $c_{twin} = a_{ortho}/3 + c_{ortho}/3$. Reflections hkl of the main domain coincide with reflections $\bar{h},\bar{k},l + 2h/3$ of the twin domain for $h = 3n$, while no overlap occurs for reflections with $h = 3n + 1$ or $3n + 2$. Reflections with $h = 3n$ were omitted from the final cell refinement so that lattice constants unbiased by twinning could be obtained. The space group of the new cell is $P2_1/n$. H atoms were positioned geometrically and were refined using a riding model, with fixed individual displacement parameters [U_{iso}(H) = 1.2U_{eq}(C)] and a fixed H—C distance of 0.95 Å. Reflections of both the major domain and the twin domain were used for the structure refinement. The final value of the twin fraction refined to 0.371 (1).

Data collection: *SMART* (Siemens, 1995); cell refinement: *SMART*; data reduction: *SAINT* (Siemens, 1995); program(s) used to solve structure: *SHELXS*97 (Sheldrick, 1997); program(s) used to refine structure: *SHELXL*97 (Sheldrick, 1997); molecular graphics: *XP* in *SHELXTL* (Sheldrick, 1996); software used to prepare material for publication: *SHELXL*97.

References

Bullen, G. J., Howlin, B. J., Silver, J., Fitzsimmons, B. W., Sayer, I. & Larkworthy, L. F. (1986). *J. Chem. Soc. Dalton Trans.* pp. 1937–1940.
Conole, G., Clough, A. & Whiting, A. (1995). *Acta Cryst.* C**51**, 1056–1059.
Cotton, F. A., Daniels, L. M. & Pascual, I. (1998). *Acta Cryst.* C**54**, 1575–1578.
Cowan, D. O., Shu, P., Hedberg, F. L., Rossi, M. & Kistenmacher, T. J. (1979). *J. Am. Chem. Soc.* **101**, 1304–1306.
Ma, K., Lerner, H.-W., Scholz, S., Bats, J. W., Bolte, M. & Wagner, M. (2002). *J. Organomet. Chem.* **664**, 94–105.
Quach, T. D., Batey, R. A. & Lough, A. J. (2001*a*). *Acta Cryst.* E**57**, m320–m321.
Quach, T. D., Batey, R. A. & Lough, A. J. (2001*b*). *Acta Cryst.* E**57**, o688–o689.
Rheingold, A. L., Uhler, A. D. & Landers, A. G. (1983). *Inorg. Chem.* **22**, 3255–3258.
Seiler, P. & Dunitz, J. D. (1979). *Acta Cryst.* B**35**, 2020–2032.
Seiler, P. & Dunitz, J. D. (1982). *Acta Cryst.* B**38**, 1741–1745.
Sheldrick, G. M. (1996). *SHELXTL.* Siemens Analytical X-ray Instruments Inc., Madison, Wisconsin, USA.
Sheldrick, G. M. (1997). *SHELXS*97 (Version 4.05) and *SHELXL*97 (Version 4.05). University of Göttingen, Germany.
Siemens (1995). *SMART* and *SAINT.* Siemens Analytical X-ray Instruments Inc., Madison, Wisconsin, USA.
Sullivan, B. W. & Foxman, B. M. (1983). *Organometallics,* **2**, 187–189.

3.4 „Ferrocenylborane - amine and monomeric diferrocenyl-borane: Novel organometallic hydroborating reagents"

M. Scheibitz, J. W. Bats, M. Bolte, H.-W. Lerner, M. Wagner

Ferrocenylborane–Amine and Monomeric Diferrocenylborane: Novel Organometallic Hydroborating Reagents

Matthias Scheibitz,[†] Jan W. Bats,[‡] Michael Bolte,[‡] Hans-Wolfram Lerner,[†] and Matthias Wagner*,[†]

*Institut für Anorganische Chemie and Institut für Organische Chemie,
J. W. Goethe-Universität Frankfurt, Marie-Curie-Strasse 11,
D-60439 Frankfurt (Main), Germany*

Summary: The ferrocenylboranes $FcBH_2 \cdot NMe_2Et$ and Fc_2BH have been synthesized and characterized by X-ray crystallography, which revealed Fc_2BH to be monomeric in the solid state. Both compounds undergo hydroboration reactions upon addition of alkynes.

Boryl- and borate-substituted metallocenes are of great current interest. Applications ranging from homogeneous catalysis to anion sensing and organometallic polymer chemistry have been the topic of two recent reviews.[1] At present, most syntheses of borylated metallocenes simply rely on nucleophilic substitution reactions at the boryl group(s). To get access to ever more sophisticated derivatives, novel reactive building blocks are thus required. Since the hydroboration of alkenes and alkynes offers a convenient route to organoboron compounds,[2] the parent metallocenylboranes $McBH_2$ (Mc = metallocenyl substituent) appear to be attractive starting materials for further reactions. As an example, Chujo et al. pioneered the hydroboration polymerization of diynes[3] for the preparation of π-conjugated macromolecules containing boron in their main chain. The compounds obtained are related to all-carbon systems, from which electrons have been removed by oxidation. Many of these materials possess large third-order nonlinear susceptibilities and show photo- as well as electroluminescent behavior.[3] It is therefore interesting to investigate how the physical properties will change when the polymers' backbones are (partially) reduced. One of our future aims is to create photochemically dopable macromolecules by using metallocenylboranes as the hydroborating reagents. Irradiation of the resulting polymers with laser light can be expected to induce $d\pi$–$p\pi^*$ transitions and thus inject mobile charge carriers into the polymer chain. Moreover, due to the low steric bulk of the BH_2 substituent, it should be possible to obtain adducts with those Lewis bases that do not form stable acid–base pairs in the case

of $McBR_2$ derivatives bearing substituents R larger than H. Novel and interesting reaction pathways may also open up when $McBH_2$ interacts with other boranes (including other $McBH_2$ molecules) via BHB two-electron–three-center bonds.

The purpose of this paper is to present the first two examples of metallocenylborane species $McBH_2$ and Mc_2BH, where Mc equals a ferrocenyl (Fc) substituent. The synthesis of $FcBH_2$, which is isolated as its amine adduct, starts from the well-known derivative $FcB(OEt)$-Br (**1**)[4] (Scheme 1). **1** and 1 equiv of $Li[AlH_4]$ in ether/pentane give lithium ferrocenylborohydride (**2**) in excellent yield.[5] Subsequent addition of excess NMe_2Et results in the precipitation of ethoxyalane–dimethylethylamine complexes, while **2** remains in solution. After filtration, the filtrate is treated with excess Me_3SiCl, whereupon $FcBH_2 \cdot NMe_2Et$ (**3**) is formed.[6] Addition of Me_3SiCl to **2** in the absence of amine does not lead to the expected dimeric $[FcBH_2]_2$ but generates diferrocenylborane (**4**) and B_2H_6 (Scheme 1).[7] Jutzi et al. reported $1,1'\text{-}Fe(C_5H_4GaMe_2)_2$ to undergo a similar reaction, yielding the digalla[1.1]ferrocenophane [{Fe-$(C_5H_4)_2$}$_2${GaMe}$_2$] and $GaMe_3$.[8]

(4) Renk, T.; Ruf, W.; Siebert, W. *J. Organomet. Chem.* **1976**, *120*, 1–25.

(5) Synthesis of **2**: a solution of $LiAlH_4$ (0.15 g, 3.95 mmol) in Et_2O (20 mL) was added dropwise at 0 °C to a slurry of **1** (1.12 g, 3.49 mmol) in pentane. The resulting clear solution was stirred at 0 °C for 1 h. The solvent was removed and the solid residue dissolved in 15 mL of Et_2O. After addition of NMe_2Et (2.19 g, 30.0 mmol) in Et_2O (10 mL), a colorless precipitate formed. The suspension was filtered and the precipitate extracted with ether (2 × 10 mL). The ether phases were combined and evaporated to dryness to give **2**·4NMe_2Et as a yellow microcrystalline solid. Yield: 1.45 g (83%). ^{1}H NMR (250.1 MHz, d_8-THF, 303 K): δ 0.87 (q, $^1J_{BH}$ = 77.1 Hz, 3H, BH_3), 1.15 (tr, $^3J_{HH}$ = 7.4 Hz, 12H, CH_2CH_3), 2.36 (s, 24H, NCH_3), 2.73 (q, $^3J_{HH}$ = 7.4 Hz, 8H, CH_2CH_3), 3.93, 4.01 (2 × virtual tr, 2 × 2H, $^3J_{HH}$ = $^4J_{HH}$ = 1.6 Hz, C_5H_4), 3.93 (s, 5H, C_5H_5). ^{13}C{^{1}H} NMR (62.9 MHz, d_8-THF, 303 K): δ 8.8 (CH_2CH_3), 48.0 (NCH_3), 56.8 (CH_2CH_3), 68.4 (C_5H_5), 69.5, 76.8 (C_5H_4), n.o. (CB). ^{11}B NMR (80.3 MHz, d_8-THF, 303 K): δ −30.7 (q, $^1J_{BH}$ = 77.1 Hz). Anal. Calcd for $C_{26}H_{56}BFeLiN_4$ (498.35): C, 62.66; H, 11.33; N, 11.24. Found: C, 62.69; H, 11.47; N, 11.61.

(6) Synthesis of **3**: Me_3SiCl (1.00 g, 9.20 mmol) was condensed on the suspension of **2**·4NMe_2Et (0.25 g, 0.49 mmol) in Et_2O (20 mL) under reduced pressure at liquid nitrogen temperature. The reaction mixture was warmed to room temperature, stirred for 2 h, and filtered and the filtrate evaporated to dryness in vacuo. Single crystals of **3** were obtained from pentane. Yield: 0.12 g (90%). ^{1}H NMR (250.1 MHz, C_6D_6, 303 K): δ 0.54 (tr, $^3J_{HH}$ = 7.3 Hz, 3H, CH_2CH_3), 1.79 (s, 6H, NCH_3), 2.24 (q, $^3J_{HH}$ = 7.3 Hz, 2H, CH_2CH_3), 2.67 (very broad, 2H, BH_2), 4.26 (virtual tr, 2H, $^3J_{HH}$ = $^4J_{HH}$ = 1.8 Hz, C_5H_4), 4.33 (mult, 7H, C_5H_4/C_5H_5). ^{13}C{^{1}H} NMR (100.6 MHz, C_6D_6, 303 K): δ 8.2 (CH_2CH_3), 47.1 (NCH_3), 55.7 (CH_2CH_3), 68.6 (C_5H_5), 69.6, 76.6 (C_5H_4), n.o. (CB). ^{11}B NMR (128.4 MHz, C_6D_6, 303 K): δ −3.4 (tr, $^1J_{BH}$ = 92.3 Hz). Anal. Calcd for $C_{14}H_{22}BFeN$ (270.99): C, 62.05; H, 8.18; N, 5.17. Found: C, 62.28; H, 8.38; N, 5.44.

* To whom correspondence should be addressed. Fax: +49 69 798 29260. E-mail: Matthias.Wagner@chemie.uni-frankfurt.de.
† Institut für Anorganische Chemie.
‡ Institut für Organische Chemie.

(1) (a) Aldridge, S.; Bresner, C. *Coord. Chem. Rev.* **2003**, *244*, 71–92. (b) Ma, K.; Scheibitz, M.; Scholz, S.; Wagner, M. *J. Organomet. Chem.* **2002**, *652*, 11–19.
(2) Pelter, A.; Smith, K.; Brown, H. C. *Borane Reagents*; Academic Press: London, 1988.
(3) (a) Matsumi, N.; Naka, K.; Chujo, Y. *J. Am. Chem. Soc.* **1998**, *120*, 5112–5113. (b) Yuan, Z.; Collings, J. C.; Taylor, N. J.; Marder, T. B.; Jardin, C.; Halet, J.-F. *J. Solid State Chem.* **2000**, *154*, 5–12.

Scheme 1. Synthesis of 2−4[a]
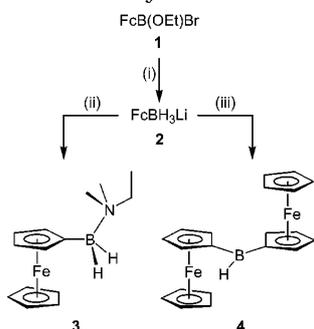
[a] Legend: (i) Li[AlH$_4$] in Et$_2$O/C$_5$H$_{12}$; (ii) excess Me$_3$SiCl/ NMe$_2$Et in Et$_2$O; (iii) excess Me$_3$SiCl in Et$_2$O.

The ^{11}B NMR spectrum of **2** shows a quartet at −30.7 ppm ($^1J_{BH}$ = 77.1 Hz)[5] characteristic for a tetracoordinated boron atom[9] bearing three hydrogen substituents. In the ^{1}H NMR spectrum of **2**, a well-resolved quadruplet is visible at δ 0.87 ($^1J_{BH}$ = 77.1 Hz),[5] which has to be assigned to three magnetically equivalent hydrogen atoms coupling with an ^{11}B nucleus. In comparison to **2**, the ^{11}B NMR resonance of **3** is observed at significantly lower field strength (δ −3.4, triplet, $^1J_{BH}$ = 92.3 Hz).[6] Both the chemical shift value and the multiplicity of the signal indicate the presence of a BH$_2$−amine adduct group in the molecule.[9] The BH_2 protons of **3** appear at δ 2.67. The ^{11}B NMR spectrum of **4**[7] shows a signal at 54.7 ppm, testifying to the presence of three-coordinate boron nuclei.[9] The BH hydrogen atom gives rise to a broad hump at δ(^{1}H) 6.23 with an integral value corresponding to one proton. In the infrared spectrum, **4** shows a strong absorption at 2302 cm^{-1} (shoulder at 2400 cm^{-1}), which lies in a region typical of terminal B−H stretching modes.[10]

The adduct FcBH$_2$·NMe$_2$Et (**3**) crystallizes from pentane in the triclinic space group $P\bar{1}$ (Figure 1).[11] The B−N bond of **3** is rotated into a position almost perpendicular to the borylated cyclopentadienyl ring

Figure 1. Crystal structure of compound **3**. Thermal ellipsoids are shown at the 50% probability level. Selected bond lengths (Å), bond angles (deg), and torsion angles (deg): B(1)−C(11) = 1.621(9), B(1)−N(1) = 1.655(7); C(11)−B(1)−N(1) = 111.1(4); N(1)−B(1)−C(11)−C(12) = 94.0(6), N(1)−B(1)−C(11)−C(15) = −92.0(6), C(11)−B(1)−N(1)−C(3) = 178.5(5), B(1)−N(1)−C(3)−C(4) = −176.3(5).
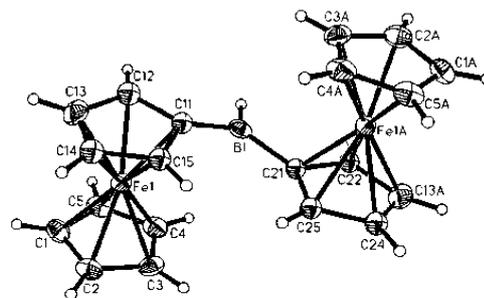
Figure 2. Crystal structure of compound **4**. Thermal ellipsoids are shown at the 50% probability level. Selected bond lengths (Å), bond angles (deg), torsion angles (deg), and angles between planes (deg): B(1)−C(11) = 1.530(6), B(1)−C(21) = 1.545(6), B(1)−H = 1.12(4); C(11)−B(1)−C(21) = 126.5(3), COG(1)−C(11)−B(1) = 165.6, COG(2)−C(21)−B(1) = 167.4; C(15)−C(11)−B(1)−C(21) = −8.9(6), C(25)−C(21)−B(1)−C(11) = −4.7(6); C(11)C(12)C(13)C-(14)C(15)//C(11)B(1)C(21) = 14.4, C(21)C(22)C(13A)C(24)C-(25)//C(11)B(1)C(21) = 13.6, C(11)C(12)C(13)C(14)C(15)// C(21)C(22)C(13A)C(24)C(25) = 4.8. COG(1) (COG(2)) is the center of gravity of the plane C(11)C(12)C(13)C(14)C(15) (C(21)C(22)C(13A)C(24)C(25)).

(N(1)−B(1)−C(11)−C(12) = 94.0(6)°), with the bulky ethyl group pointing away from the ferrocenyl substituent (C(11)−B(1)−N(1)−C(3) = 178.5(5)°). Single crystals of diferrocenylborane (**4**; monoclinic, $P2_1/c$) were obtained from the reaction mixture (Et$_2$O/pentane) at room temperature (Figure 2).[12] Most interestingly, the molecule is monomeric in the solid state, featuring a planar three-coordinate boron atom and a trans config-

(7) Synthesis of **4**: a solution of LiAlH$_4$ (0.19 g, 5.01 mmol) in Et$_2$O (20 mL) was added dropwise at 0 °C to a slurry of **1** (1.50 g, 4.68 mmol) in pentane. The resulting clear solution was warmed to room temperature and stirred for 1 h. Neat Me$_3$SiCl (1.72 g, 15.83 mmol) was added to the solution via syringe. Stirring was stopped and the clear solution kept at room temperature for 1 h, whereupon X-ray-quality crystals of **4** formed. Yield: 1.38 g (77%). ^{1}H NMR (250.1 MHz, C$_6$D$_6$, 303 K): δ 4.03 (s, 10H, C$_5$H$_5$), 4.48 (mult, 8H, C$_5$H$_4$), 6.23 (very broad, 1H, BH). ^{13}C{^{1}H} NMR (62.9 MHz, C$_6$D$_6$, 303 K): δ 68.8 (C$_5$H$_5$), 75.0, 77.8 (C$_5$H$_4$), n.o. (CB). ^{11}B NMR (128.4 MHz, C$_6$D$_6$, 303 K): δ 54.7 (n.r.). IR: ν (cm^{-1}) 2302 (shoulder at 2400), BH. Anal. Calcd for C$_{20}$H$_{19}$BFe$_2$ (381.86): C, 62.91; H, 5.02. Found: C, 62.51; H, 4.83.

(8) Althoff, A.; Jutzi, P.; Neumann, B.; Stammler, A.; Stammler, H.-G. *Organometallics* **2003**, *22*, 2766−2774.

(9) Nöth, H.; Wrackmeyer, B. Nuclear Magnetic Resonance Spectroscopy of Boron Compounds. In *NMR Basic Principles and Progress*; Diehl, P., Fluck, E., Kosfeld, R., Eds.; Springer: Berlin, Heidelberg, New York, 1978.

(10) Negishi, E.; Katz, J.-J.; Brown, H. C. *J. Am. Chem. Soc.* **1972**, *94*, 4025−4027. Note that monomeric HBTrip$_2$ (Trip = 2,4,6-i-Pr$_3$C$_6$H$_2$) shows a corresponding B−H stretch at ν 2460 cm^{-1}: Pelter, A.; Smith, K.; Buss, D.; Norbury, A. *Tetrahedron Lett.* **1991**, *32*, 6239−6242.

(11) Crystal data of **3**: C$_{14}$H$_{22}$BFeN, M_r = 270.99, triclinic, $P\bar{1}$, a = 5.9524(18) Å, b = 9.868(3) Å, c = 11.948(3) Å, α = 92.48(2)°, β = 94.08-(2)°, γ = 100.60(3)°, V = 686.9(3) Å^3, Z = 2, T = 100 K, μ(Mo Kα) = 1.075 mm^{-1}, 4733 reflections measured, 2425 unique (R_{int} = 0.1140), which were used in all calculations. The final R_w(F^2) value was 0.1415 (all data), and the minimum/maximum residual electron density was −0.73/0.61 e Å^{-3}. The H atom positions were taken from a difference Fourier synthesis and refined using a riding model. The CCDC reference number is 224814.

(12) Crystal data of **4**: C$_{20}$H$_{19}$BFe$_2$, M_r = 381.86, monoclinic, $P2_1/c$, a = 7.5664(9) Å, b = 10.3258(12) Å, c = 10.4377(15) Å, β = 105.299-(5)°, V = 786.59(17) Å^3, Z = 2, T = 149 K, μ(Mo Kα) = 1.838 mm^{-1}, 13 317 reflections measured, 2534 unique (R_{int} = 0.0348), which were used in all calculations. The final R_w(F^2) value was 0.0807 (all data), and the minimum/maximum residual electron density was−0.50/0.55 e Å^{-3}. The C$_5$H$_4$−B(H)−C$_5$H$_4$ fragment was disordered about a crystallographic inversion center. Both disordered groups coincide at the positions of atoms C(13) and C(13A) ($-x$, $-y$, $-z$), with an occupancy factor of 0.5. The position of the H atom at B(1) was taken from a difference Fourier synthesis and refined isotropically. The CCDC reference number is 224815.

uration of its ferrocenyl substituents with respect to the C(11)B(1)C(21) plane. There is only one other example of a structurally characterized monomeric organylborane, HBTrip$_2$ (Trip = 2,4,6-i-Pr$_3$C$_6$H$_2$), known in the literature.[13] The B$-$C bond lengths of this compound (average value 1.567(6) Å) are significantly longer than those of **4** (average value 1.538(6) Å), whereas the C$-$B$-$C angles of both molecules are rather similar (HBTrip$_2$, 128.0(4)°; **4**, C(11)$-$B(1)$-$C(21) = 126.5(3)°). In the case of HBTrip$_2$, dimerization is clearly prevented by the extremely bulky Trip substituents. Considering the fact that tetraferrocenylethene exists, which shows a central C=C bond length of only 1.381 Å,[14] while the boron atoms of dimeric [HBMes$_2$]$_2$ (Mes = 2,4,6-Me$_3$C$_6$H$_2$) are as far as 1.851(3) Å apart from each other,[13] steric congestion of the boron atom in **4** is probably not the sole reason for the monomeric nature of this compound. Torsion angles C(15)$-$C(11)$-$B(1)$-$C(21) and C(25)$-$C(21)$-$B(1)$-$C(11) of $-$8.9(6) and $-$4.7-(6)°, respectively, indicate that the ferrocenyl substituents can act as strong π-donors toward the boron bridge. This conclusion is also supported by the fact that the ^{11}B NMR resonance of **4** (δ 54.7) is shifted by 18.8 ppm to higher field compared to the boron resonance of HBTrip$_2$ (δ 73.5),[13] which reflects a significant accumulation of π-charge density at boron in **4**.[9] Moreover, the boron atom is bent out of the planes of the C$_5$H$_4$ rings toward the iron atoms with dip angles α of 14.4 and 12.6°, thereby suggesting[15] some charge transfer from filled d-type orbitals of iron into the vacant p orbital at boron (α = 180° $-$ α^*, α^* = COG$-$C(ipso)$-$B; COG = center of gravity of the C$_5$H$_4$ ring). In addition to steric shielding, electronic factors are thus likely to play an important role in the stabilization of monomeric **4**.

Hydroboration of *tert*-butylacetylene using **3** (stoichiometric ratio 2:1, CD$_2$Cl$_2$, 50 °C, sealed NMR tube) is complete after a few hours and selectively stops at the olefin stage.[16] Two doublets for the olefinic protons are observed (δ 6.25, 6.59) with a coupling constant $^3J_{HH}$ of 17.9 Hz, which points toward a vicinal rather than to a geminal position of the two H atoms.[17] The ^{13}C DEPT-135 NMR spectrum of the product shows one resonance for an olefinic CH group (δ 162.1). The signal of the second CH group (δ 127.6) is extremely broadened, which has to be attributed to the quadrupolar relaxation of the adjacent boron nucleus. No resonances assignable to olefinic CH_2 groups could be detected. It has to be concluded, therefore, that borylation has occurred at the terminal position of *tert*-butylacetylene. Hydroboration of *tert*-butylacetylene with **4** (stoichiometric ratio 1:1, C$_6$D$_6$, room temperature, 30 min) gives a similar result and leads to the corresponding 1,2-disubstituted olefin in quantitative yield.[18]

Work is in progress to synthesize organic$-$inorganic hybrid materials by using the ferrocenylborane adduct FcBH$_2$·NMe$_2$Et in the hydroboration polymerization of aromatic diynes. Moreover, the B$-$C coupling reaction underlying the formation of **4** may provide facile access to oligomers [$-$(H$_4$C$_5$)Fe(C$_5$H$_4$)B(H)$-$]$_n$, starting from [1,1'-Fe(C$_5$H$_4$BH$_3$)$_2$]Li$_2$ and 2 equiv of Me$_3$SiCl.

Supporting Information Available: Tables giving crystallographic data for **3** and **4**; these data are also available as CIF files. This material is available free of charge via the Internet at http://pubs.acs.org.

OM034353T

(13) Bartlett, R. A.; Dias, H. V. R.; Olmstead, M. M.; Power, P. P.; Weese, K. J. *Organometallics* **1990**, *9*, 146$-$150.

(14) Bildstein, B.; Denifl, P.; Wurst, K.; André, M.; Baumgarten, M.; Friedrich, J.; Ellmerer-Müller, E. *Organometallics* **1995**, *14*, 4334$-$4342.

(15) Appel, A.; Jäkle, F.; Priermeier, T.; Schmid, R.; Wagner, M. *Organometallics* **1996**, *15*, 1188$-$1194. For an X-ray crystal structure analysis of the related triferrocenylborane, see: Wrackmeyer, B.; Dörfler, U.; Milius, W.; Herberhold, M. *Z. Naturforsch.* **1995**, *50b*, 201$-$204.

(16) Hydroboration product of *tert*-butylacetylene with **3**: ^{1}H NMR (400.1 MHz, CD$_2$Cl$_2$, 303 K) δ 1.12 (s, 18H, CH$_3$), 4.02 (s, 5H, C$_5$H$_5$) 4.45, 4.62 (2 × virtual tr, 2 × 2H, $^3J_{HH}$ = $^4J_{HH}$ = 1.8 Hz, C$_5$H$_4$), 6.25 (d, 2H, $^3J_{HH}$ = 17.9 Hz, B$-$CH), 6.59 (d, 2H, $^3J_{HH}$ = 17.9 Hz, *t*Bu$-$CH); ^{13}C{^{1}H} NMR (62.9 MHz, CD$_2$Cl$_2$, 303 K) δ 29.5 (CH$_3$), 35.4 (*C*CH$_3$), 69.5 (C$_5$H$_5$), 74.7, 76.0 (C$_5$H$_4$), 127.6 (B$-$*C*H), 162.1 (*t*Bu$-$*C*H); ^{11}B NMR (128.4 MHz, CD$_2$Cl$_2$, 303 K) δ 54.2.

(17) Günther, H. *NMR-Spektroskopie*; Thieme: Stuttgart, New York, 1983.

(18) Hydroboration product of *tert*-butylacetylene with **4**: ^{1}H NMR (250.1 MHz, C$_6$D$_6$, 303 K) δ 1.11 (s, 9H, CH$_3$), 4.00 (s, 10H, C$_5$H$_5$) 4.47, 4.65 (2 × virtual tr, 2 × 4H, $^3J_{HH}$ = $^4J_{HH}$ = 1.7 Hz, C$_5$H$_4$), 6.52 (d, 1H, $^3J_{HH}$ = 18.1 Hz, B$-$CH), 6.84 (d, 1H, $^3J_{HH}$ = 18.1 Hz, *t*Bu$-$CH); ^{13}C{^{1}H} NMR (62.9 MHz, C$_6$D$_6$, 303 K) δ 29.6 (CH$_3$), 35.1 (*C*CH$_3$), 69.4 (C$_5$H$_5$), 73.9, 76.7 (C$_5$H$_4$), 128.8 (B$-$CH), 159.7 (*t*Bu$-$*C*H); ^{11}B NMR (128.4 MHz, C$_6$D$_6$, 303 K) δ 56.9.

3.5 „Electronic structure, photophysics and relexation dynamics of charge transfer excited states in boron-nitrogen-bridged ferrocene-donor compounds"

M. D. Thomson, M. Novosel, H. G. Roskos, T. Müller, M. Scheibitz, M. Wagner, F. Fabrizi de Biani, P. Zanello

Electronic Structure, Photophysics, and Relaxation Dynamics of Charge Transfer Excited States in Boron−Nitrogen-Bridged Ferrocene-Donor Organic-Acceptor Compounds

M. D. Thomson, M. Novosel, and H. G. Roskos*

Physikalisches Institut, Robert-Mayer-Strasse 2-4, Johann Wolfgang Goethe-Universität, D-60054 Frankfurt am Main, Germany

T. Müller, M. Scheibitz, and M. Wagner

Institut für Anorganische Chemie, Marie-Curie-Strasse 11, Johann Wolfgang Goethe-Universität, D-60439 Frankfurt am Main, Germany

F. Fabrizi de Biani and P. Zanello

Dipartimento di Chimica dell'Università, Via Aldo Moro, I-53100 Siena, Italy

We present a study of the electronic, photophysical, and picosecond excited-state relaxation characteristics of a class of derivatives comprised of multiple bipyridylboronium acceptors covalently linked to a ferrocene donor. These compounds exhibit a broad visible absorption band, which we attribute to a metal-to-ligand charge transfer transition between the donor and the acceptor. A comparison of optical absorption, spectroelectrochemical, and theoretical results confirms the assignment of the band and provides information on the degree of electron delocalization between the donor and the acceptor. Picosecond transient absorption measurements reveal that the back-electron transfer relaxation is critically dependent on the structural flexibility of the bridging bonds between the donor and the acceptor. In the case where the acceptor substituents are free to rotate about the bridging bonds between the boron and the cyclopentadienyl rings of the ferrocene, a significant portion of the excited state decays directly back to the ground state on a time scale of ∼18 ps, whereas in the case where an additional *ansa*-bridge that connects acceptor substituents enforces a more rigid conformation, the ground-state recovery proceeds only on a ∼800-ps time scale. This demonstrates the importance of conformational degrees of freedom for the internal conversion and back-electron transfer in these systems.

Introduction

Optically induced charge transfer (CT) has a central role in many fundamental processes, such as those in biological systems,[1−3] as well as being a functional mechanism in various areas of optoelectronics, such as solar cells,[4,5] photoconductors[6,7] and nonlinear optical devices.[8] Of particular interest are materials that contain organometallic moieties, e.g., ferrocene (Fc), which possess desirable qualities because of their ability to exist in different stable oxidation and spin states,[9] and the ability to tune their properties by a suitable choice of substituents.[9−11] Several detailed studies exist on Fc-donor organic-acceptor metal-to-ligand charge transfer (MLCT) compounds in the context of nonlinear materials, where the donor and the acceptor are connected via conjugated bridges[8,12,13] and both the highest occupied molecular orbital (HOMO) and the lowest unoccupied molecular orbital (LUMO) are delocalized over the entire structure. Although these studies have covered a large number of various organic acceptors, as well as the use of other bridging units (e.g., −C=N−[14,15]), there is still much scope for the development of new materials. Moreover, only very few studies exist on the excited-state photophysics and relaxation of the MLCT states in Fc-donor organic-acceptor compounds,[16,17]

despite the fact that many interesting excited-state phenomena have been observed in other organometallic CT compounds.[18−22]

In this paper, we present a study of novel organometallic CT compounds that are composed of a Fc donor and multiple organic (bipyridylboronium, B-bipy) acceptors, connected by bridging bonds between C atoms on the cyclopentadienyl (Cp) rings and the 4-coordinated B atom (see structures **1-X, 2-X,** and **3**−**7** in Figure 1), which have previously been characterized by NMR, electrochemical, and crystal structure analysis.[23−25] The spontaneous formation of B−N bonds allows one to achieve sophisticated target structures less readily accessible using conventional organic methodologies. This approach has been successfully applied in the synthesis of *ansa*-metallocenes[26,27] and oligometallic complexes,[28,29] which are related to the prototype monomers presented here. Because these compounds can undergo reversible oxidation and multiple reduction steps, they potentially allow electronic switching of their (nonlinear) optical properties. We are interested in electronic interaction and optical excitation across the B−N bonds, especially in terms of their use as versatile linkers between electron donors and polymers that exhibit strong electronic and magnetic correlation phenomena.[30] The properties of B−N bonds when incorporated into molecular assemblies still are not fully understood, although the basic properties of B−N bonds have attracted several recent theoretical studies.[31−35]

* Author to whom correspondence should be addressed. E-mail address: roskos@physik.uni-frankfurt.de.
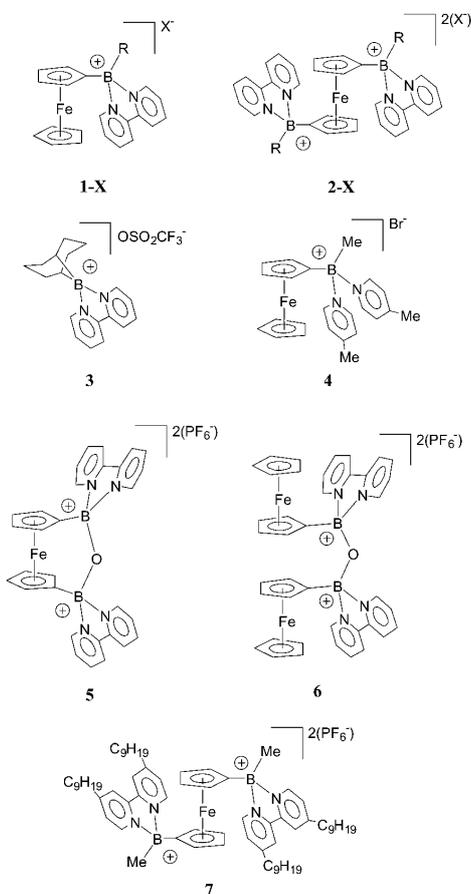
Figure 1. Ferrocene-donor bipyridylboronium-acceptor and control compounds under study here. (For compounds **1-X** and **2-X** the counteranion is $X^- = PF_6^-$, or Br^-. Note that, unless otherwise specified, $R = CH_3$ in the text.)

Figure 2. (a) UV−Vis absorption spectra of (—) **1-Br** and isolated fragment compounds, (- - -) ferrocene, (— — —) 2,2′-bipyridine, and (— · —) **3** (in CH_3CN). (b) Comparison of *n*-X versus the number of acceptor substituents (*n* = 1.2 as indicated) and counteranions $X = Br$ (solid) and $X = PF_6^-$ (dashed).

Here, we combine UV−Vis, spectroelectrochemical, and picosecond transient absorption measurements with theoretical calculations, which confirm that the observed visible optical transition corresponds to a through-bond MLCT transition between the Fc and B-bipy units. Comparison of the derivatives **2-PF₆**, **5**, and **6** allows us to determine how the MLCT transition and excited-state evolution are affected by certain structural and electronic factors. For the compounds **1-PF₆** and **2-PF₆**, NMR measurements[23] indicate that the uncoupled acceptor groups are free to rotate about the B−C(Cp) bridging bonds. In the case of compounds **5** and **6**, the CH_3 groups at the B-sites have been replaced by an O atom that forms a bridge between the B atoms of each B-bipy acceptor group, such that the electronic environment is relatively similar between the two compounds, as evidenced by cyclovoltammetry measurements.[25] However, NMR measurements[24,25] reveal that the rotational freedom of the B−C(Cp) bonds in the *ansa*-form (**5**) is suppressed, whereas for the diferrocene compound (**6**), this degree of freedom is still retained. Electrochemical measurements for both derivatives **5** and **6**[24,25] suggest a moderate amount of electronic communication between the B-bipy groups across this bridge, so that these compounds allow the study of the effect of electronic coupling between acceptors on the CT states. A comparison of the two

compounds allows us to isolate the effect of structural rigidity of the bridging bonds between the donor and acceptor groups.

From the picosecond transient absorption measurements of the back-electron transfer (bET) dynamics for the derivatives **2-PF₆**, **5**, and **6**, we find that the structural flexibility of the bridging bonds between the donor and the acceptor strongly affects the rate and mechanism for the bET. Specifically, in the case of compound **2-PF₆**, a significant fraction (∼45%) of the excited ensemble relaxes directly back to the ground state with a time constant of 18 ps, whereas for compound **5**, the ground-state recovery occurs only on a much slower time scale (∼800 ps).

UV−Vis Absorption Spectra

Figure 2a shows the UV−Vis absorption spectra of **1-Br** and of ferrocene, 2,2′-bipyridine, and compound **3** (all in CH_3CN), for comparison. For **1-Br**, two dominant absorption bands can be resolved: one is centered at 310 nm, and a broad visible absorption band with a peak near 500 nm is observed. Comparison with the spectra of 2,2′-bipyridine and **3** shows that this UV band at 310 nm corresponds to a modified $\pi-\pi^*$ transition between states localized on the B-bipy substituent, with the absorption peak of **1-Br** and **3** red-shifted some 35 nm (2900 cm^{-1}), relative to 2,2′-bipyridine, because of the modification of the π and π^* energy levels resulting from the increased electronegativity of the boron-coordinated N atoms.

The origin of the broad visible band is attributed to an intramolecular MLCT transition from orbitals concentrated on the Fc donor into those of the B-bipy acceptor, based on the following observations. As shown in Figure 2b, the character of the visible band is almost independent of the counteranion, and the absorption strength increases in proportion with the number of acceptor substituents (also confirmed for the case of four acceptor substituents, $\lambda_{max} = 540$ nm, $\epsilon_{max} = 1700$ M^{-1} cm^{-1}; see ref 23). Although this would be consistent with a transition localized on isolated B-bipy chromophores, this is ruled out by the absence of any absorptive feature in the Vis region in the spectra of compound **3**. Moreover, previous synthetic studies[23] have shown that the visible transition is absent in compound **4**, where the C−C bond between the two pyridine

B—N-Bridged Charge Transfer Compounds
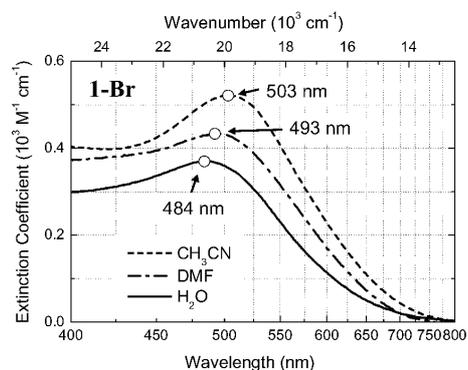
Figure 3. MLCT absorption band for **1-Br** in various polar solvents ((- - -) CH$_3$CN, (− • −) dimethylformamide (DMF), (—) H$_2$O) demonstrating negative solvatochromism and decreasing absorption strength with solvent polarizability.

Figure 4. (- - -) Gaussian fit to MLCT band for (—) **1-Br** (in CH$_3$CN) and (− • −) residual absorption. Inset uses a logarithmic vertical scale.

Figure 5. MLCT absorption spectra (solid lines) of (a) **2-PF$_6$**, and the B—O—B bridged-acceptor compounds (b) **5** and (c) **6** (all in CH$_3$CN) relevant to the electrochemistry and transient absorption measurements. Also shown are the single Gaussian curves fitted to (- - -) the low-energy side of the absorption band and (− • −) the residual absorption.

rings has been removed (which has the effect of strongly degrading the electron-accepting quality of the substituent without posing any significant changes in the structural or electronic environment seen by electronic states localized on the Fc unit). This rules out the possibility that the transition only involves orbitals that are localized on the Fc unit.

Figure 3 shows the effect of solvent interaction on the absorption spectra for **1-Br**, which shows a marked negative solvatochromism in going from CH$_3$CN to H$_2$O ($\Delta\nu = 780$ cm^{-1} for **1-Br** and $\Delta\nu = 710$ cm^{-1} for **2-Br**). This behavior has been observed for CT transitions in similar cationic species,[8,13] contrary to the typical positive solvatochromism of CT transitions in neutral species, and is to be expected, based on the fact that the ground state in these cationic species is actually more polar (and, hence, more strongly stabilized by polar solvents) than the CT excited state. Moreover, the strength of the transition decreases as the solvent polarizability increases, which suggests that the solvent interaction causes a Stokes shift between the ground state and the excited state, which affects the Franck—Condon factor for the transition. Given these observations, we also attribute the small red-shift of the absorption band of compound **2-X**, relative to compound **1-X** ($\Delta\nu = -349$ cm^{-1} for **X** = PF$_6^-$), in Figure 2 to a reduced stabilization of the ground state in compound **2-X**, because of the reduction in polarity, which results from the symmetric positions of the two acceptor groups.

To better resolve the MLCT band from the absorptive shoulder on the blue side, we fit the low-energy portion of the band with a single Gaussian function, $\epsilon(\nu)$,[36] which, as shown in Figure 4, reproduces the resolvable portion of the band exceptionally well, yielding a full width (at half-maximum) of $\Delta\nu_{fwhm} = 6330$ cm^{-1}, and an estimate for the oscillator strength of $f \approx 0.014$.[37] Subtracting this fitted Gaussian from the total absorption spectrum yields a physically acceptable residual absorption profile (see Figure 4), which shows evidence for another absorption band with an absorption maximum near 380 nm that is partially resolvable from the onset of the 310-nm B-bipy UV absorption band. The fact that the low-energy portion of the MLCT band fits very closely to a single Gaussian function suggests that only a single electronic transition is involved, although the question arises as to the origin of the strong line broadening (see below).

Figure 5 displays the absorption spectra for compounds **2-PF$_6$**, **5**, and **6** (in CH$_3$CN), which all exhibit a similar MLCT band. As can be seen, the visible absorption band peaks of both

compound **5** ($\lambda_{max} = 532$ nm) and compound **6** ($\lambda_{max} = 554$ nm) are red-shifted, relative to compound **2-PF$_6$** ($\Delta\nu = -785$ cm^{-1} and $\Delta\nu = -990$ cm^{-1}, respectively), which is indicative of an increasing stabilization of the acceptor LUMO in these compounds, because of the aforementioned electronic communication between acceptors across the —O— bridge. We note that the absorption band of a derivative of **1-PF$_6$** with R = −OH is significantly less red-shifted ($\lambda_{max} = 523$ nm), which rules out the possibility that the effect is purely due to the electron-withdrawing effects of the O atom. For compounds **2-PF$_6$** and **6**, the lower-energy side of the MLCT band is still very closely Gaussian, with fitted fwhm widths very similar to that of **1-Br** ($\Delta\nu_{fwhm} = 6260$ and 6240 cm^{-1} for compounds **2-PF$_6$** and **6**, respectively), whereas for the case of compound **5**, the fwhm is reduced by ~10%−15% ($\Delta\nu_{fwhm} = 5500$ cm^{-1}) and slight deviations from a Gaussian form are evident.

Three main mechanisms could be responsible for the broad, featureless MLCT band, which we discuss, in turn, in the following.

(1) Given the significant rearrangement of the electronic charge distribution upon excitation, a strong interaction between

Thomson et al.
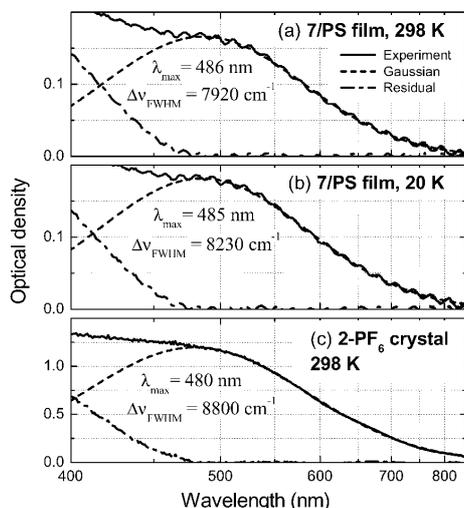
Figure 6. MLCT absorption band and Gaussian fits for compound **7** in a drop-cast polystyrene film ($\sim$10 μm thick) at (a) 298 K and (b) 20 K (note that the modulation of the curves is due to multiple pass interference). (c) Corresponding absorption for the compound **2-PF$_6$** crystal sample.

the solute and the distribution of local polar solvent molecules can lead to considerable line width broadening. To remove the role of polar solvation on the MLCT transition, we have also performed measurements on thin polystyrene films that have been doped with compound **7** (a close derivative of compound **2-PF$_6$**, only with additional nonyl chains attached to the pyridine rings for improved solubility), which were drop-cast from a tetrahydrofuran (THF) solution. The measured MLCT absorption spectra are shown in Figure 6, both at room temperature (see Figure 6a) and at 20 K (see Figure 6b). The MLCT absorption band at 298 K is similar to that in solution, although somewhat blue-shifted (λ_{max} = 486 nm) and additionally broadened ($\Delta\nu_{fwhm}$ = 7920 cm^{-1}). Considering such modest changes upon switching to the relatively nonpolar polymer environment, one can rule out solvation as the key source of broadening. We also note that cooling the film to 20 K leads to only very small changes in the absorption spectrum (with the width of the spectrum actually increasing $\sim$4%) and does not reveal any resolvable structure. This suggests that the width of the spectrum is not associated with a thermal distribution of ground-state vibrational levels (at least for vibrational quanta >14 cm^{-1}).

(2) In analogy to *intermolecular* CT between separate donor and acceptor molecules, a distribution of relative distances and/or orientations between the donor and the acceptor can result in appreciable broadening in the transition energy.[38,39] This could be applicable for compounds **1-X**, **2-X**, and **6**, where the unhindered rotation about the B—C(Cp) bonds yields such a conformational distribution. However, this degree of freedom is strongly hindered for compound **5** and, hence, is unlikely to account for the majority of broadening observed. To examine this further, we have also performed absorption measurements on a thin crystalline sample of **2-PF$_6$** (Figure 6c), where all molecules share the same fixed conformation. As can be seen, the MLCT band is even further blue-shifted and broadened (λ_{max} = 480 nm, $\Delta\nu_{fwhm}$ = 8800 cm^{-1}), ruling out the role of a conformational distribution. Hence, we attribute the majority of the line width to the final mechanism.

(3) A large displacement in the equilibria of certain modes between the ground and excited states results in a broad manifold
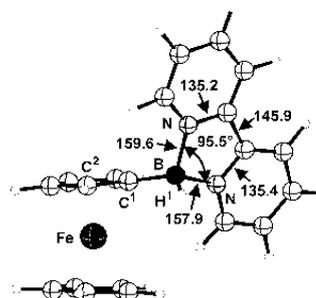
of closely spaced vibrational transitions with a Gaussian envelope. Presumably, any residual structure is washed out by additional broadening, because of rapid dephasing of the initial excited state.[40]

Returning to Figure 5, we also note that, for compounds **2-X**, **5**, and **6**, the relative orientation (or distribution thereof) and, hence, through-space separation of the acceptor groups, relative to the Fe core, vary significantly, whereas the through-bond distances are relatively constant.[23–25] The absorption character and strength are comparable for these compounds, which leads us to conclude that the MLCT is due to through-bond coupling between the donor and acceptor orbitals across the (Cp)C—B—N network, as opposed to through-space.

In terms of the relaxation of the MLCT excited states, we note that no measurable luminescence in the range of 500—900 nm (i.e., a quantum efficiency of <0.05%) or photochemistry was observed upon excitation of the MLCT band for all the derivatives tested, which suggests that the relaxation occurs through nonradiative photophysical pathways, which are addressed in the section that presents the picosecond transient absorption results.

Quantum Chemistry Calculations and Electronic Structure

Gas-phase calculations were performed on the monocation **1** (with R = H), to substantiate and better understand the origin of the MLCT transition between the donor and the acceptor. Geometry optimizations were performed at the hybrid density functional level of theory, using Becke's three-parameter functional with the nonlocal correlation provided by the Perdew-86 equation (B3P86) in connection with the 6-31G(d) basis set for carbon, boron, nitrogen, and hydrogen.[41] For iron, the SDD pseudopotential was used, in combination with a DZP valence basis set.[42–44] This model has provided theoretical structures for ferrocene that are very close to those experimentally determined from gas-phase measurements.[45] The UV—Vis transition energies were calculated with the time-dependent (TD) method,[46] using a 6-31+G(d) basis set.

These density functional calculations predict a theoretical structure (see Figure 7) that is very close to the experimentally determined crystal structure for compound **1-PF$_6$**.[23] Even very weak modes (for example, the conformation of the B—R bond, relative to the plane of the C$_5$H$_5$ ring of the ferrocenyl group) are reproduced by our computational model (i.e., $\Theta(H^1BC^1C^2)$ = 35° (theory), compared to $\Theta(MeBC^1C^2)$ = 39.7° (experiment)[23]). This correspondence implies that certain distortions of the structure of **1-PF$_6$** reported in ref 23 result because of internal molecular forces, as opposed to crystal packing forces.

Figure 7. Calculated gas-phase structure of compound **1** (with R = H) (using B3P86/6-31G(d) for C, B, N, H and SDD for Fe). All bond lengths reported in picometers.
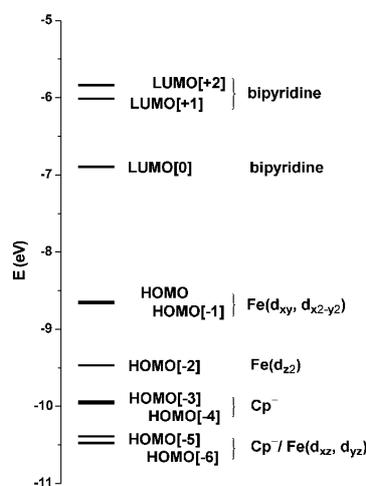
Figure 8. Calculated energy diagram for the frontier orbitals of compound **1** (R = H).
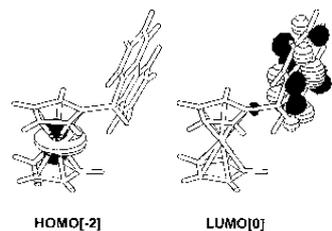
Figure 9. Qualitative molecular orbital diagram for selected frontier orbitals consistent with MLCT transitions.

TABLE 1: Low-Energy Optical Transitions for 1 (R=H) and Corresponding Dominant Molecular Orbitals Predicted by the Time-Dependent Density Functional Theory (TD−DFT) Calculations

HOMO[m]	LUMO[n]	E_{max} (eV)	λ_{max} (nm)	oscillator strength, f
0	0	1.17	1058	0.0006
−1	0	1.21	1029	0.0028
−2	0	2.01	618	0.0084
0	+1	2.08	598	0.0004
−1	+1	2.11	589	0.0030
0	+2	2.26	548	0.0013
−1	+2	2.28	544	0.0004
−3/−4	0	2.49	499	0.0013
−3/−4	0	2.52	492	0.0003

An energy diagram of the calculated frontier orbitals (calculated at the B3P86/6-31+G(d) level) are shown in Figure 8, with selected orbitals being shown in Figure 9. The frontier orbitals can be divided into three groups: (i) relatively low-lying molecular orbitals with main contributions from the cyclopentadienyl substituent (HOMO[−3] and HOMO[−4]); (ii) metal-centered orbitals, essentially of nonbonding character, which are the highest occupied orbitals (HOMO[−2]−HOMO[0]); and (iii) vacant orbitals of low energy (LUMO[0]−LUMO[+2]) that are centered on the bipyridine unit.

Transition energies and oscillator strengths from the TD calculation are presented in Table 1. These results provide evidence that the lowest-energy optical transitions result from excitations from Fc-based occupied orbitals into unoccupied orbitals located on the bipyridine unit. The predicted oscillator strengths are relatively small, most probably because of a small

spatial overlap between the donor and acceptor orbitals. The most intense absorption, according to the calculations, results from excitations from the HOMO[−2], predominantly of Fe(d_{z^2}) character, into the LUMO[0]. This transition has a predicted oscillator strength of $f = 0.0084$ (which is of the same order of magnitude as the estimate of 0.014 that is extracted from the experimental absorption spectra). Moreover, the fact that the transition energy predicted from the gas-phase calculation ($\lambda_{max} = 618$ nm) is lower than the measured value in solution is consistent with the negative solvatochromism reported in the last section.

In addition to the model calculations for the monocation **1** (R = H) discussed here, we also performed the corresponding ground-state calculation for the dication (i.e., the same single-acceptor compound with one electron removed), to gain a better understanding of the electronic changes to be expected upon electrochemical oxidation of an electron from the Fc-centered HOMO (discussed in the following sections). These results confirm that electron removal strongly increases the binding energy of all molecular orbitals, with the frontier (Fc-centered) occupied molecular orbitals being more strongly stabilized than the B-Bipy-centered unoccupied MOs. This leads to an increase in the energy between the HOMO[−2] and LUMO[0] from 2.6 eV for the monocation to 4.9 eV for the dication. Assuming that the error due to approximating the optical transition energies by HOMO/LUMO energy spacings is the same for the two redox states, this increase in energy suggests that the MLCT band would be blue-shifted some 2.3 eV, which corresponds to a peak wavelength of <300 nm (based on the experimental peak value for **1-Br** in solution of ~500 nm).

Electrochemistry

Electrochemical measurements allow one to extract useful correlations between the oxidized-donor and reduced-acceptor species (D$^+$A and DA$^-$) and those of a weakly coupled CT excited state, which can often be well-represented as an excited redox pair, (D$^+$A$^-$)*.[47,48] By examining trends in the redox potentials versus the energy of the CT transitions for a set of related compounds, one can estimate the degree of interaction between the relevant donor and acceptor molecular orbitals and reorganization energy upon CT,[49] whereas UV−Vis spectroelectrochemistry data can provide details on the effect of CT on the frontier orbitals and suggest expected spectroscopic properties of the excited MLCT state for comparison, e.g., with transient excited-state absorption measurements.[20] Generally, the range of compounds under study here readily undergo reversible oxidation and reduction steps, allowing a relatively straightforward interpretation of the redox measurements. From these measurements, one can also gain insight into how the linear and nonlinear optical properties of the system (governed by the MLCT) may be reversibly switched by external electronic means.[50,51]

Figure 10a and b present typical cyclovoltammetry traces of compounds **2-PF$_6$** and **5**, respectively (reported previously[23,24] but reprinted here for comparison). In both compounds, a single one-electron (1-e$^-$) oxidation peak is present, at $E^{o'}_{ox} = +0.43$ V (**2-PF$_6$**) and +0.57 V (**5**) (denoted by "ox" in both graphs), which is derived from the removal of an electron centered on the Fc unit (note that $E^{o'}_{ox} = +0.49$ V for ferrocene under the same conditions), and testifies that the presence of the acceptor groups attached to the Cp rings leads to only a small perturbation of the donor orbitals relevant to oxidation. At a negative cell potential, compound **2-PF$_6$** exhibits two reduction waves (denoted "red,1" and "red,2"), each of which has been shown

Thomson et al.
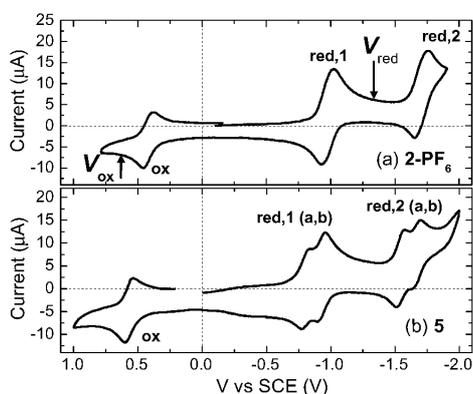
Figure 10. Cyclic voltammograms of (a) compound **2-PF$_6$** and (b) compound **5** indicating the 1-e$^-$ oxidation (ox) and first (red,1) and second (red,2) 2-e$^-$ reduction waves (both with 0.6 × 10^{-3} mol dm^{-3} in DMF containing 0.2 mol dm^{-3} [NEt$_4$][PF$_6$], platinum electrode, scan rate of 0.2 mol dm^{-3}). "V_{ox}" and "V_{red}" denote the static potentials used for the UV–Vis spectroelectrochemical measurements.
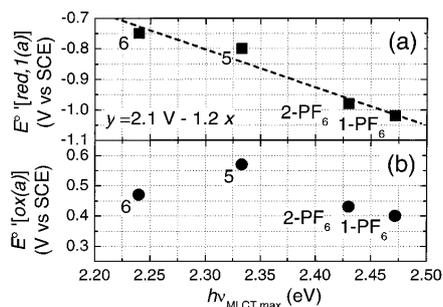
Figure 11. Graph of (a) first reduction-wave potential $E^{o\prime}_{red,1(a)}$ and (b) oxidation-wave potential $E^{o\prime}_{ox(a)}$ for compounds **1-PF$_6$**, **2-PF$_6$**, **5**, and **6** versus MLCT absorption peak energy (in CH$_3$CN). (A linear fit to the reduction wave potentials is included in Figure 11a, as indicated.)

to involve the addition of two electrons (one electron per acceptor unit).[23] In comparison with the cyclovoltammetry trace of compound **1-PF$_6$** (which features two 1-e$^-$ reduction waves),[23] both reduction peaks are only slightly shifted and broadened, because of the presence of the second acceptor unit (i.e., $E^{o\prime}_{red,1}$ = -1.02 V for **1-PF$_6$** and $E^{o\prime}_{red,1}$ = -0.98 V for **2-PF$_6$**), which implies only a weak interaction between the acceptor groups in compound **2-PF$_6$**. In contrast, it is evident in Figure 10b that, for compound **5**, the degeneracy between the two electrons in each reduction step is lifted (e.g., for the first 2-e$^-$ reduction, $E^{o\prime}_{red,1a}$ = -0.80 V, $E^{o\prime}_{red,1b}$ = -0.93 V),[24] which indicates significant interaction between the acceptor units. As mentioned previously, this interaction is most likely due to a degree of through-bond communication across the $-$O$-$ bridge, and the additional shift to less-negative potentials is consistent with the red-shift seen in the UV absorption band for this compound.

To test the correspondence between the energy levels of the redox pairs and the observed CT bands, we plot the relevant redox potential data against the corresponding UV–Vis absorption maxima of the MLCT bands in Figure 11 for compounds **1-PF$_6$**, **2-PF$_6$**, **5**, and **6**. Figure 11a shows that the reduction potential fits a linear trend fairly well (as shown); in this figure, the potential progresses to less-negative values (and, hence, the LUMO is increasingly stabilized) as the MLCT band transition
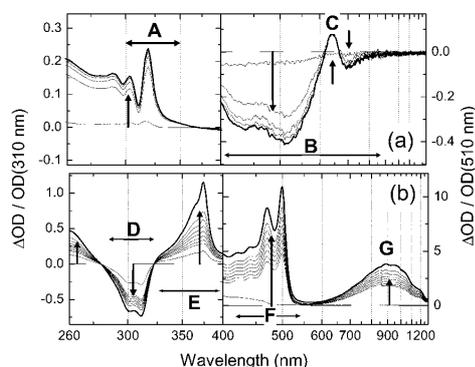
Figure 12. Time-series differential absorption spectra of compound **2-PF$_6$** (DMF) upon (a) 1-e$^-$ oxidation and (b) first 2-e$^-$ reduction (experimental conditions and static redox potentials (V_{ox}, V_{red}) as indicated in Figure 10). UV (left) and Vis (right) data are normalized to the initial absorption band peaks as indicated. (Note that all qualitative features were also reproduced in the corresponding measurements on **1-PF$_6$**.)

energy decreases, which is consistent with the hypothesis that both the first reduction and the MLCT transition involve LUMO[0]. In contrast, the oxidation potential (Figure 11b) shows only a weak correspondence with the MLCT transition energy. One possible explanation for this phenomenon refers to the predictions of the orbital calculations of the previous section, where the results suggest that the observed MLCT band results not from the HOMO[0] located on the ferrocene, but rather between the HOMO[−2] and the LUMO[0] on the acceptor. Assuming that the observed oxidation (reduction) processes involve the removal (addition) of an electron from (into) the primary frontier orbitals (HOMO[0] and LUMO[0]), one should only expect a direct correlation of the CT transition energy with the observed reduction potentials.

Figure 12 shows the change in UV–Vis absorption spectra for compound **2-PF$_6$** during exhaustive oxidation (Figure 12a) and 2-e$^-$ reduction (Figure 12b) (at the static potentials indicated in Figure 10). In Figure 12a (oxidation), the increase in absorption in the region of 300−350 nm (labeled band "A") corresponds to an increase in the strength and reshaping of the modified $\pi-\pi^*$ transition, which is associated with the B-bipy unit (see Figure 2), because of the increased electronegativity of the oxidized Fc unit. The broad feature in the range of 370− 900 nm that exhibits a negative differential absorption is due to the suppression of the MLCT band, which reflects the strong energetic changes between the associated molecular orbitals upon oxidation, as mentioned at the end of the theoretical results section. However, several new absorptive features are manifested in this range (which is evident from the oscillatory structure in the region labeled "B"), including a band which results in a net absorption increase, which is observed from the small positive region of the curve (λ_{max} = 637 nm, labeled "C"). This spectral feature is in almost quantitative agreement with previous reports of the absorption changes upon oxidation of ferrocene to form the ferrocenium cation.[52] We assign this band to a transition from some low-energy Fc-centered occupied molecular orbital into the HOMO[0] orbital, which can accommodate one electron after oxidation.

The corresponding absorption changes upon reduction of compound **2-PF$_6$** (Figure 12b) are markedly larger in magnitude. In the UV range, one observes an almost-complete depletion of the original B-bipy absorption band (labeled "D"). Two new bands (labeled "E" and "F"), in the range of 320−500 nm,

B—N-Bridged Charge Transfer Compounds

appear: band E exhibits one clear maximum at 374 nm, whereas band F possesses a resolvable vibrational structure, with the first two lowest-energy peaks at 470 and 500 nm ($\Delta\nu = 1260$ cm^{-1}). These absorption bands have been reported[53] for reduced [bipy-BR$_2$]$^+$ compounds (with aromatic or alicyclic substituents attached to the 4-coordinated B atom); e.g., for compound **3-PF$_6$**, the corresponding peak positions are $\lambda_{max} = 378$ nm (band E) and 463/494 nm (band F). However, ref 53 reported that, in the case where electron-attracting O or F ligands are attached to the B atom, band F is significantly blue-shifted ($\lambda_{max} = 422/$ 460 nm), whereas band E is relatively unaffected by the nature of the ligands. We will return briefly to this point in the following section when interpreting the excited-state transient spectra. In the case of CT excitation (as opposed to sole reduction of the acceptor), one would expect the Fc to become more electron-withdrawing and, hence, produce such a blue-shift of band F. The last feature is a broad Vis—NIR absorption band (band "G"). This absorption band is unlikely to result from CT transitions from Fc onto the acceptor, which should generally be blue-shifted upon reduction of the acceptor. Hence, we attribute this new band to a transition localized on the reduced B-bipy units.

Several key results emerge from the electrochemistry data presented here. The linear relationship between the peak absorption energies and reduction potentials supports a MLCT transition between the weakly coupled donor and acceptor, whereas the poor correlation with the oxidation potentials is consistent with the theoretical prediction that the CT transition originates from lower-lying occupied molecular orbitals. Moreover, as will be shown in the next section, the UV—Vis absorption changes upon oxidation/reduction are in qualitative agreement with the transient spectra and aid in the interpretation of the excited-state dynamics.

Transient Absorption Measurements

To understand the nonradiative relaxation dynamics of the MLCT state, we performed transient absorption measurements, using the femtosecond (fs) pump—probe technique. For the excitation (pump) pulses, we used 30-fs pulses that were tuned to a center wavelength of 500 nm from a commercially obtained noncollinear OPA (NOPA),[54] which is pumped by a 1-kHz Ti: sapphire amplifier laser that produces 150-fs pulses with a center wavelength of 775 nm (Clark-MXR CPA-2001). For the broadband probe source, we used white-light continuum pulses[55-57] that were generated by focusing a small fraction of the 775-nm light into a 3-mm-thick sapphire disk, producing a usable white-light spectrum from 450 nm to 770 nm. To minimize temporal dispersion, an off-axis paraboloidal mirror with an effective focal length of $f = 50$ mm was used to collimate the white-light probe beam. A second paraboloid ($f = 100$ mm) was used to focus the noncollinear pump and probe beams into the sample (a static 1-mm-thick cuvette, ~3.5 mM in CH$_3$CN). This yielded an instrument response of ~100 fs (as determined from control measurements with a rhodamine 6G sample, which was also used for determination of the zero-delay position versus probe wavelength). In all the kinetic data presented, the temporal region about a zero delay, which exhibits a relatively strong coherent artifact (due to nonlinear refraction that occurs in the cuvette and solvent[58]), has been removed. The pump—pulse energy used in these experiments was ~70 nJ. After the sample, the white-light probe was dispersed by a computer-controlled monochromator with a bandpass ~5 nm wide and was detected by a silicon photodetector. A custom-built mechanical chopper was used
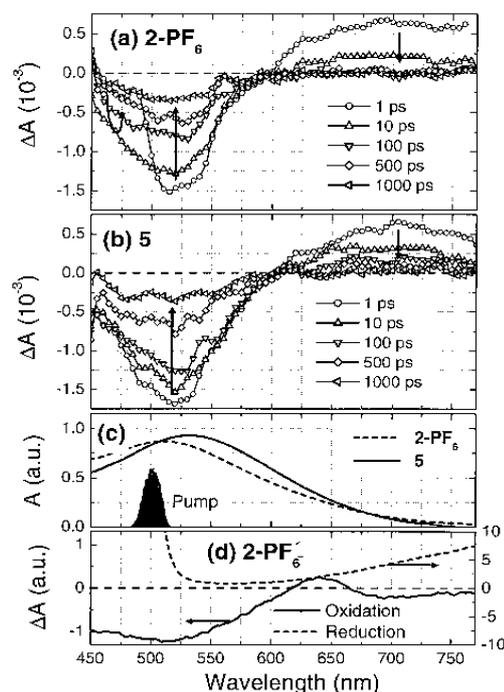
Figure 13. Picosecond transient absorption spectra of (a) compound **2-PF$_6$** and (b) compound **5** ($\lambda_{pump} = 500$ nm, ~3.5 mM in CH$_3$CN in both cases) at selected pump—probe delays. (c) Ground-state absorption and excitation spectra. (d) Differential spectra of compound **2-PF$_6$** upon electrochemical oxidation and reduction.

ahead of the sample to downsample the pump and probe pulse trains to 333 and 500 Hz, respectively, which allows the differential transient absorption signal to be detected by a lock-in amplifier at the 166-Hz difference frequency (which also rejected any uncontrolled stray pump light). Care was taken to ensure that the shape of the measured signals was not dependent on the pump and probe fluences, and that the white-light probe was focused more tightly in the sample than the pump beam, to avoid measurement errors that are due to the radial spatial chirp of the white light.

Figure 13 shows the transient absorption spectra for compounds **2-PF$_6$** (Figure 13a) and **5** (Figure 13b) (both in CH$_3$CN), following excitation at 500 nm, for a set of selected delays in the range of 1—1000 ps over the wavelength range of 450—770 nm, along with the relevant ground-state absorption and pump—pulse spectra in Figure 13c and the differential spectra that results from electrochemical oxidation and reduction (Figure 13d). Evident for both compounds is a negative-differential absorption band that extends from ~460 nm to 600 nm, where the saturation (bleach) of the MLCT absorption band dominates, whereas at wavelengths above a quasi-isosbestic point near 600 nm, a region of dominant excited-state absorption (ESA) is present, which extends at least to the red edge of the measurement window at 770 nm. Comparison with Figure 13c indicates that, although the bleach band is no longer dominant at wavelengths of >600 nm, the strength of the ground-state absorption band at this wavelength is still ~50% of that of the absorption maximum. Moreover, although the regions of bleach and ESA signals decay at clearly different rates for compound **2-PF$_6$** (discussed further below), the position of the zero-crossing of the transient spectra does not red-shift significantly with time.

Thomson et al.
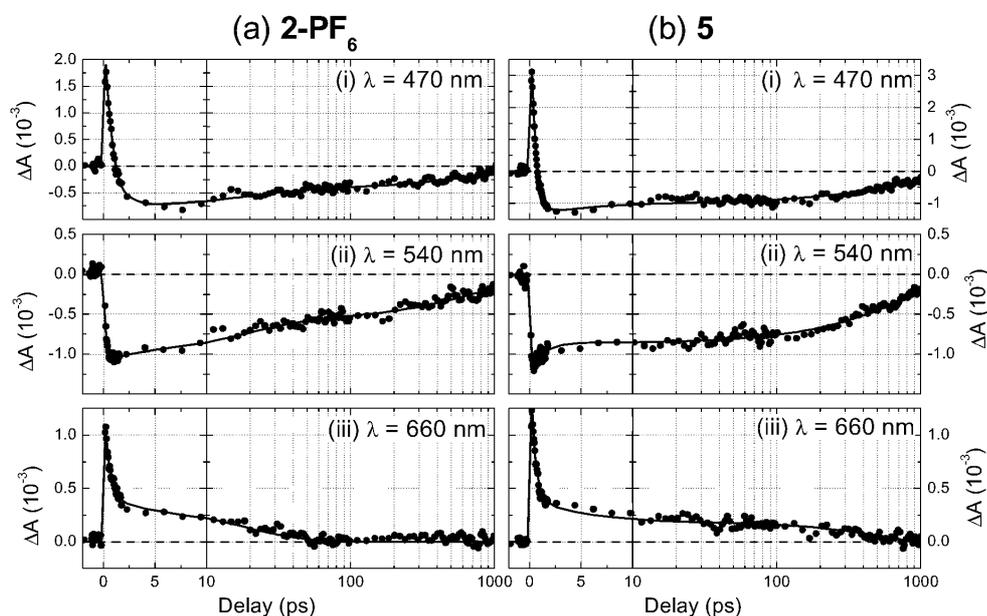
Figure 14. Experimental pump—probe kinetics (points) and multiexponential fits (solid line) for (a) compound **2-PF₆** and (b) compound **5** upon 500-nm excitation at selected probe wavelengths: (i) 470 nm, (ii) 540 nm, and (iii) 660 nm.

One possible explanation is that the excitation at 500 nm affects only a spectroscopically distinct portion of the ground-state molecules; i.e., hole burning of the ground-state absorption because of an inhomogeneous broadening of the ensemble.[59] However, given that no red-shifting of the bleach band is observed over the full delay range, this would imply a characteristic time scale for the broadening mechanism of $\tau \gg$ 1 ns. Although one could consider this for the case of compound **2-PF₆**, where rotation about the B—C bonds between the donor and the acceptor might occur on such a time scale, this is unlikely to be the case for compound **5**, where the —O— bridge should enforce a much more rapid fluctuation in the relative conformation of donor and acceptor.

Thus, to explain the reduced width of the bleach band, we are led to conclude that there are actually two distinct ESA bands in the transient spectra of Figure 13: one band (ESA-I) that is dominant in the wavelength range of ∼550—650 nm and suppresses the bleach band in this region, and a second band (ESA-II) that dominates the signal in the wavelength range of >650 nm.

Concerning the origin of these ESA bands, it is interesting to consider certain features of the differential absorption spectra of compound **2-PF₆** upon oxidation and reduction (Figure 13d; refer to Figure 12 for the full spectral range). We note that, upon electrochemical oxidation of compound **2-PF₆**, one also does not observe a negative differential absorption of the same shape as the ground-state absorption, mostly due to the fact that a new absorptive feature (labeled band C in Figure 12a) appears, which has a differential peak at 637 nm. Thus, we propose that the same transition is present in the transient spectra of Figure 13, which we identify as the ESA-I band. Based on the assumption that a predominantly HOMO[−2] orbital is involved in the CT transition, this implies that one electron in the higher HOMO[0] orbital relaxes rapidly into the HOMO[−2] vacancy, allowing the transition that corresponds to band C (which corresponds to a vacancy in the HOMO[0] orbital) to be active. The fact that the combined signal of the bleach and ESA-I band

does not change shape over the excited-state lifetime implies that the ESA-I band decays with the same kinetics as the recovery of the ground state. This is consistent with the assertion that the transition is between electrons localized on the Fc unit.

Moreover, for the origin of the ESA-II band, we note that, upon reduction of the B-Bipy acceptors, a new absorption band appears in the Vis—NIR region. Hence, we assign the presence of the ESA-II band to the occupation of an initial excited state of similar electronic character to that of the reduced species, which is consistent with the assertion that the orbitals occupied by the excited electron are mostly localized on the B-bipy unit, as suggested by the calculated molecular orbitals. In reference to the comment near the end of the last section, the absence of the absorptive feature in the range of ∼450—500 nm that is observed upon reduction (band F in Figure 12b) is not surprising, given that, in the excited state, the Fc unit is formally oxidized and, hence, becomes more electron-withdrawing, such that this band would be blue-shifted to the short-wavelength edge of the measurement window. Interestingly, one observes some evidence for the onset of another ESA band at this edge in the transient spectra.

To better quantify the relaxation dynamics, in Figure 14, we present the transient absorption kinetics for compounds **2-PF₆** (Figure 14a) and **5** (Figure 14b) at three characteristic probe wavelengths: (i) $\lambda_{probe} = 470$ nm (at the high-energy tail of the bleach band), (ii) $\lambda_{probe} = 540$ nm (on the low-energy side of the bleach band), and (iii) $\lambda_{probe} = 660$ nm (ESA-II band). For both compounds, the kinetics exhibit three distinct time scales (<1 ps, ∼5—20 ps, and ∼800 ps), although the relative weights of these components are dependent on the probe wavelength. We fit the positive delay data using a multiexponential fitting function,

$$\Delta A(t) = \sum_{j=1}^{3} A_j \exp\left(-\frac{t}{\tau_j}\right)$$

with global values for the two longer time constants τ_2 and τ_3,

B—N-Bridged Charge Transfer Compounds

TABLE 2: Parameters from the Multiexponential Fits of the Transient Absorption Kinetics of Compounds 2-PF$_6$ and 5 (Shown in Figure 14) and Compound 6 (Shown in Figure 15)^a

compound	τ_1 (ps)	$A_1{}^b$	τ_2 (ps)	A_2	τ_3 (ps)	A_3
		$\lambda_{\text{probe}} = 470$ nm				
2-PF$_6$	0.80 (0.03)	+4.4	17.8 (1.3)	−0.46	810 (33)	−0.54
5	0.46 (0.02)	+5.1	4.6 (1.3)	−0.31	774 (19)	−0.69
		$\lambda_{\text{probe}} = 540$ nm				
2-PF$_6$			17.8 (1.3)	−0.45	810 (33)	−0.55
5	1.13 (0.25)	−0.47			774 (19)	−1
		$\lambda_{\text{probe}} = 660$ nm				
2-PF$_6$	0.56 (0.07)	+2.5	17.8 (1.3)	+1		
5	0.41 (0.06)	+2.9	4.6 (1.3)	+0.45	774 (19)	+0.55
6	0.61 (0.04)	+3.3	31.2 (2.4)	+1		

^{a} Standard errors given in parentheses. Subscripts denote the time scale in increasing order. Missing values indicate that the additional component did not assist significantly in the fitting of the data. ^{b} All amplitudes are normalized by $|A_2| + |A_3|$.

the results of which are listed in Table 2. To assess the relative weight of each signal component, the amplitudes in Table 2 are normalized by the combined amplitude of the two slower components, i.e., $A_j \rightarrow A_j/(|A_2| + |A_3|)$.

The kinetics for $\lambda_{\text{probe}} = 540$ nm represent the ground-state recovery of the excited ensemble, which, in both compounds, is essentially complete after 1 ns. For compound 2-PF$_6$, the fit required an almost 1:1 (0.45:0.55) combination of both a relatively fast picosecond component and a nanosecond component ($\tau_2 = 17.8$ ps, $\tau_3 = 810$ ps), whereas for compound 5, the ground-state recovery is essentially monoexponential ($\tau_3 = 774$ ps), with the inclusion of a small additional femtosecond decay component ($\tau_1 = 1.3$ ps).

In contrast to the 540-nm data, this femtosecond component is present as a relatively larger and positive absorption signal for both compounds and both $\lambda_{\text{probe}} = 470$ nm and $\lambda_{\text{probe}} = 660$ nm, with time constants in the range of 0.4−1.1 ps. From control measurements of pure solvents, it is unlikely that these femtosecond transients occur because of pure solvent artifacts, especially given the fact that they are of almost-negligible amplitude specifically in the region of the bleach band ($\lambda_{\text{probe}} = 540$ nm). Instead, we attribute these transients to ultrafast intramolecular rearrangement and solvation of the initial excited state, which are typically observed on this time scale.[60,61]

For $\lambda_{\text{probe}} = 470$ nm, after the initial femtosecond-induced absorption, the kinetics for compound 2-PF$_6$ are similar to that of the 540-nm curve, with very similar relative weights for the τ_2 and τ_3 components (0.46:0.54) as for the 540-nm kinetics. The data for compound 5 at 470 nm are also similar to those obtained at 540 nm, except that an additional picosecond transient ($\tau_2 = 4.6$ ps) is present, which indicates the onset of other spectral features at the blue edge of the bleach band. Most striking of all is the comparison of the ESA-II signals ($\lambda_{\text{probe}} = 660$ nm) between the two compounds. In the case of compound 2-PF$_6$, no signal component on the 810-ps ground-state recovery time scale is observed, and the signal decays completely with the 17.8-ps time constant. In contrast, a majority (0.55) of the ESA-II signal for compound 5 persists on the longer 774-ps time scale. These differences in the decay of the ESA-II signal and the ground-state recovery for both compounds implies the involvement of at least one intermediate electronic state in the relaxation pathway of both compounds (which is essentially "dark" in the probe wavelength range used here), or at least a shift of the reaction coordinates of the excited state away from the Franck−Condon region, where the ESA-II transition is allowed.
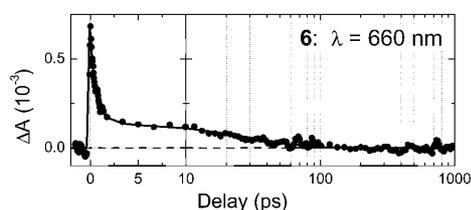
Figure 15. Transient absorption kinetics for $\lambda = 660$ nm (ESA) for compound **6**, with multiexponential fit (solid line).
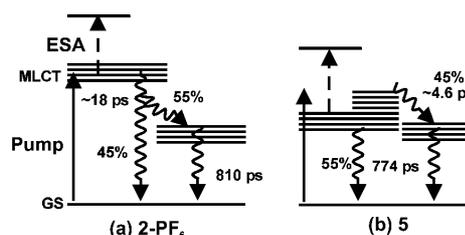
Figure 16. Simplified Jablonksi diagrams for the relaxation of the MLCT states for (a) compound 2-PF$_6$ and (b) compound 5.

To understand the factors leading to these differences, we also measured the kinetics for compound **6** for $\lambda_{\text{probe}} = 660$ nm, which is displayed in Figure 15 (with the multiexponential fit data included in Table 2). As is evident, the decay of the ESA-II signal for compound **6** is very similar to that of compound 2-PF$_6$ (and not **5**), in that after an initial femtosecond relaxation, the ESA-II signal decays completely with a time constant of $\tau_2 = 31.2$ ps, albeit some ~10 ps slower than that observed for compound 2-PF$_6$. As mentioned previously, the inclusion of compound **6** in the comparison allows one to distinguish characteristic effects that result from the −O− bridge at boron from the structural rigidity of the compounds. Given that the initial excited state is vacated on the same time scale in compounds 2-PF$_6$ and **6**, this leads us to conclude that this relaxation mechanism relies more on the structural flexibility of the bridging bonds between the donor and the acceptor, which permits the excited state to reach a conformation where either an internal conversion is allowed (possibly involving a through-space bET) or where the Franck−Condon factor for the ESA-II transition becomes negligible. The fact that there is a significant component (0.45) in the ground-state recovery for compound 2-PF$_6$ on the same 17.8-ps time scale as the decay of the ESA-II signal implies that this portion of the excited molecules decays directly back to the ground state. The remaining fraction of the ensemble branches into an intermediate state with the far-slower (810-ps) ground-state recovery, presumably because of the involvement of additional active modes. These conclusions are summarized in the simplified energy diagram in Figure 16a.

For the case of compound 5, the appreciable component of decay in the 470-nm and 660-nm kinetics at 4.6 ps, which is absent in the 540-nm data (which has a monoexponential decay of 774 ps), implies that the ground-state recovery of compound 5 from the initial excited and intermediate states proceeds via a similar pathway. However, if this 4.6-ps relaxation mechanism was available to the entire excited ensemble, one would observe a complete decay of the ESA-II signal on the same time scale. We rationalize this by proposing that this fast relaxation pathway is only energetically available to a fraction of the compounds that have sufficient net excess energy to overcome a barrier between the initial excited and intermediate state (Figure 16b),

possibly because of the relatively large bandwidth of the excitation pulse.

Conclusion

We have provided an experimental basis to confirm and better understand the origin of metal-to-ligand charge transfer (MLCT) transitions between donor and acceptor groups that incorporate B−N architecture. A comparison of the UV−Vis spectra for various derivatives and theoretical calculation provides strong evidence that the visible absorption band of the ferrocene−bipyridylboronium (Fc−B-Bipy) compounds studied here result from a direct MLCT transition from Fc-centered orbitals into those of the B-Bipy unit. The electrochemistry data show that the redox properties of the donor and the acceptor are only moderately perturbed from those of the isolated compounds, which is consistent with the localized nature of the theoretically calculated molecular orbitals, while the reduction potential of the acceptor has been shown to correlate with the MLCT transition energy. The correspondence between the UV−Vis spectra upon oxidation/reduction with the excited-state transient absorption spectra also reflect that the initial excited state is qualitatively similar to a superposition of an oxidized-donor and a reduced-acceptor. Of key interest is the effect of structural rigidity in the bridging bonds between the donor and the acceptor, which has been demonstrated to effect the rate and mechanism of the back-electron transfer (bET) strongly. In the case where the acceptor group is free to rotate, relative to the donor (e.g., compound **2**), the initially excited state decays on an ∼18-ps time scale, with a significant portion of the ensemble returning directly to the ground state. In the case where this degree of freedom is hindered (compound **5**), the entire ground-state recovery occurs on an ∼800 ps time scale.

These results will greatly facilitate the rational design of macromolecular assemblies that use these building blocks to achieve efficient charge transfer for applications such as charge injectors for molecular electronics and nonlinear optics. The potential for reversible switching between multiple stable redox states, where the MLCT transition can be present or suppressed, allows the possibility for external electronic control of the linear and nonlinear optical properties of these compounds. The important role of structural factors that affect the bET mechanisms motivates the design of more-rigid systems, to enhance the excited-state lifetime and allow for improved performance in applications based on optically induced charge injection and molecular-based memory storage.

References and Notes

(1) Huppman, P.; Arlt, T.; Penzkofer, H.; Schmidt, S.; Bibikova, M.; Dohse, B.; Oesterhelt, D.; Wachtveitl, J.; Zinth, Z. *Biophys. J.* **2002**, *82*, 3186.

(2) Book, L.; Ostafin, A.; Ponomarenko, N.; Norris, J.; Sherer, N. *J. Phys. Chem. A* **2000**, *104*, 8295.

(3) Walker, G.; Maiti, S.; Cowen, B.; Moser, C.; Dutton, P.; Hoch-strasser, R. *J. Phys. Chem.* **1994**, *98*, 5778.

(4) Shaheen, S.; Brabec, C.; Sariciftci, N.; Padinger, F.; Fromherz, T.; Hummelen, J. *Appl. Phys. Lett.* **2001**, *78*, 841.

(5) Parisi, J.; Dyakonov, V.; Pientka, M.; Riedel, I.; Deibel, C.; Brabec, C.; Sariciftci, N.; Hummelen, J. *Z. Naturforsch. A: Phys. Sci.* **2002**, *57a*, 995.

(6) Tan, L.; Curtis, M.; Francis, A. *Macromolecules* **2002**, *35*, 4628.

(7) Samok, M.; Williams, D. *J. Chem. Phys.* **1983**, *78*, 1924.

(8) Barlow, S.; Bunting, H.; Ringham, C.; Green, J.; Bublitz, G.; Boxer, S.; Perry, J.; Marder, S. *J. Am. Chem. Soc.* **1999**, *121*, 3715.

(9) Togni, A., Hayashi, T., Eds. *Ferrocenes*; VCH Verlagsgesell-schaft: Weinheim, Germany, 1995.

(10) Yang, E.; Chan, M.; Wahl, A. *J. Phys. Chem.* **1980**, *84*, 3094.

(11) Thiel, W.; Priermeier, T.; Fiedler, D.; Bond, A.; Mattner, M. *J. Organomet. Chem.* **1996**, *514*, 137.

(12) Calabrese, J.; Cheng, L.; Green, J.; Marder, S.; Tam, W. *J. Am. Chem. Soc.* **1991**, *113*, 7227.

(13) Alain, V.; Fort, A.; Barzoukas, M.; Chen, C.; Blanchard-Desce, M.; Marder, S.; Perry, J. *Inorg. Chim. Acta* **1996**, *242*, 43.

(14) Pal, S.; Krishnan, A.; Das, P.; Samuelson, A. *J. Organomet. Chem.* **2000**, *604*, 248.

(15) Krishnan, A.; Pal, S.; Nandakumar, P.; Samuelson, A.; Das, P. *Chem. Phys.* **2001**, *265*, 313.

(16) Gilch, P.; Pöllinger-Dammer, F.; Musewald, C.; Michel-Beyerle, M.; Steiner, U. *Science* **1998**, *281*, 982.

(17) Baigar, E.; Gilch, P.; Zinth, W.; Stöckl, M.; Härter, P.; von Feilitzsch, T.; Michel-Beyerle, M. *Chem. Phys. Lett.* **2002**, *352*, 176.

(18) Ruthkosky, M.; Kelly, C.; Zaros, M.; Meyer, G. *J. Am. Chem. Soc.* **1997**, *119*, 12004.

(19) Abbott, L.; Arnold, C.; Ye, T.; Gordon, K.; Perutz, R.; Hester, R.; Moore, J. *J. Phys. Chem. A* **1998**, *102*, 1252.

(20) Damrauer, N.; McCusker, J. *J. Phys. Chem. A* **1999**, *103*, 8440.

(21) Yeh, A.; Shank, C.; McCusker, J. *Science* **2000**, *289*, 935.

(22) Tyson, D.; Luman, C.; Zhou, X.; Castellano, F. *Inorg. Chem.* **2001**, *40*, 4063.

(23) Fabrizi de Biani, F.; Gmeinwieser, T.; Herdtweck, E.; Jäkle, F.; Laschi, F.; Wagner, M. *Organometallics* **1997**, *16*, 4776.

(24) Ding, L.; Ma, K.; Fabrizi de Biani, F.; Bolte, M.; Zanello, P.; Wagner, M. *Organometallics* **2001**, *20*, 1041.

(25) Ma, K.; Fabrizi de Biani, F.; Bolte, M.; Zanello, P.; Wagner, M. *Organometallics* **2002**, *21*, 3979.

(26) Jäkle, F.; Mattner, M.; Preiermeier, T.; Wagner, M. *J. Organomet. Chem.* **1995**, *502*, 123.

(27) Herdtwerk, E.; Jäkle, F.; Opromolla, G.; Spiegler, M.; Wagner, M.; Zanello, P. *Organometallics* **1996**, *15*, 5524.

(28) Jäkle, F.; Priermeier, T.; Wagner, M. *Chem. Ber.* **1995**, *128*, 1163.

(29) Fabrizi de Biani, F.; Jäkle, F.; Spiegler, M.; Wagner, M.; Zanello, P. *Inorg. Chem.* **1997**, *36*, 2103.

(30) Thomson, M.; Roskos, H.; Wagner, M. *Appl. Phys. A* **2004**, *78*, 477.

(31) Hirao, H.; Fujimoto, H. *J. Phys. Chem. A* **2000**, *104*, 6649.

(32) Fiacco, D.; Leopold, K. *J. Phys. Chem. A* **2003**, *107*, 2808.

(33) Anane, H.; Boutalib, A.; Tomás, F. *J. Phys. Chem. A* **1997**, *101*, 7879.

(34) Anane, H.; Boutalib, A.; Nebot-Gil, I.; Tomás, F. *J. Phys. Chem. A* **1998**, *102*, 7070.

(35) Anane, H.; Boutalib, A.; Nebot-Gil, I.; Tomás, F. *Chem. Phys. Lett.* **1998**, *287*, 575.

(36) $\epsilon(\nu) = \epsilon_{max} \exp[-4 \ln 2(\nu - \nu_0)^2 / \Delta \nu_{fwhm}^2$.

(37) Using $f \approx 4.32 \times 10^{-9} \int \epsilon(\nu) \, d\nu$, e.g., the relationship from Klessinger, M.; Michl, J. *Excited States and Photochemistry of Organic Molecules*; VCH Publishers: New York, 1995.

(38) Turro, N. *Modern Molecular Photochemistry*; University Science Books: Mill Valley, CA, 1991.

(39) Birks, J. *Photophysics of Aromatic Molecules*; Wiley: New York, 1970.

(40) Nagasawa, Y.; Passino, S.; Joo, T.; Fleming, G. *J. Chem. Phys.* **1997**, *106*, 4840.

(41) All calculations were performed with Gaussian 98, Revisions A3−A9, Gaussian, Inc., Pittsburgh, PA, 1999.

(42) Becke, A. *J. Chem. Phys.* **1993**, *98*, 5648.

(43) Perdew, J. *Phys. Rev. B* **1986**, *33*, 8822.

(44) Fuentealba, P.; von Szentpaly, L.; Preuss, H.; Stoll, H. *J. Phys. B* **1985**, *18*, 1287.

(45) Using the method described for the isolated ferrocene molecule, we obtained $r(CC) = 142.2$ pm and $r(Fe−C) = 204.9$ pm), as compared to the experimentally determined gas-phase values of $r(CC) = 143.1$ pm and $r(Fe−C) = 205.8$ pm (from Bohn, R.; Haaland, A. *J. Organomet. Chem.* **1966**, *5*, 470).

(46) Burke. K., Gross, E., Joubert, D., Eds. *Lecture Notes in Physics*; Springer: Heidelberg, 1998; Vol. 500.

(47) Seneviratne, D.; Uddin, J.; Swayambunathan, V.; Schlegel, H.; Endicott, J. *Inorg. Chem.* **2002**, *41*, 1502.

(48) Gilch, P.; Pöllinger-Dammer, F.; Steiner, U.; Michel-Beyerle, M. *Chem. Phys. Lett.* **1997**, *275*, 339.

(49) Daub, J.; Engl, R.; Kurzawa, J.; Miller, S.; Schneider, S.; Stock-mann, A.; Wasielewski, M. *J. Phys. Chem. A* **2001**, *105*, 5655.

(50) Zhu, Y.; Wolf, M. *J. Am. Chem. Soc.* **2000**, *122*, 10121.

(51) Malaun, M.; Reeves, Z.; Paul, R.; Jeffery, J.; McCleverty, J.; Ward, M.; Asselberghs, I.; Clays, K.; Persoons, A. *Chem. Commun.* **2001**, 49.

B−N-Bridged Charge Transfer Compounds

(52) Thander, A.; Mallik, B. *Proc. Indian Acad. Sci. (Chem. Sci.)* **2000**, *112*, 475.

(53) Hünig, S.; Wehner, I. *Heterocycles* **1989**, *28*, 359.

(54) Riedle, E.; Beutter, M.; Lochbrunner, S.; Piel, J.; Schenkl, S.; Spörlein, S.; Zinth, W. *Appl. Phys. B* **2000**, *71*, 457.

(55) Fork, R.; Shank, C.; Hirlimann, C.; Yen, R.; Tomlinson, W. *Opt. Lett.* **1983**, *8*, 1.

(56) Reed, M.; Steiner-Shepard, M.; Armas, M.; Negus, D. *J. Opt. Soc. Am. B* **1995**, *12*, 2229.

(57) Huber, R.; Satzger, H.; Zinth, W.; Wachtveitl, J. *Opt. Commun.* **2001**, *194*, 443.

(58) Ekvall, K.; van der Meulen, P.; Dhollande, C.; Berg, L.; Pommeret, S.; Naskrecki, R.; Mialocq, J. *J. Appl. Phys.* **2000**, *87*, 2340.

(59) Brito Cruz, C.; Fork, R.; Knox, W.; Shank, C. *Chem. Phys. Lett.* **1986**, *132*, 341.

(60) Fleming, G.; Cho, M. *Annu. Rev. Chem.* **1996**, *47*, 109.

(61) Kahlow, M.; Jarzeba, W.; Kang, T.; Barbara, P. *J. Chem. Phys.* **1989**, *90*, 151.

3.6 „The 1:1 adduct of 1,1′-bis(dibromoboryl)ferrocene and 3,3´,4,4´-tetramethyl-1,1´-diphosphaferrocene"

M. Scheibitz, M. Bolte, H.-W. Lerner, M. Wagner

Organometallics **2004**, *23(14)*, 3556 – 3559.

1:1 Adduct of 1,1′-Bis(dibromoboryl)ferrocene and 3,3′,4,4′-Tetramethyl-1,1′-diphosphaferrocene

Matthias Scheibitz, Michael Bolte, Hans-Wolfram Lerner, and Matthias Wagner*

Institut für Anorganische Chemie, J.W. Goethe-Universität Frankfurt, Marie-Curie-Strasse 11, D-60439 Frankfurt (Main), Germany

Summary: The Lewis acid−base adduct between 1,1′-bis(dibromoboryl)ferrocene and 3,3′,4,4′-tetramethyl-1,1′-diphosphaferrocene has been characterized by multinuclear variable-temperature NMR spectroscopy and single-crystal X-ray diffraction analysis. Irrespective of the crystallization conditions applied, the molecular structure of the adduct is that of an open-chain dinuclear complex featuring only one P−B bond.

Introduction

Metal-containing polymers are receiving increasing attention due to their useful properties, such as electrical conductivity and cooperative magnetic behavior.[1] Two classes of compounds have attracted particular interest during the last 20 years: (a) polyferrocenylenes, mainly derived from strained, ring-tilted *ansa*-ferrocenes by thermal or catalytic ring-opening polymerization,[2] and (b) low-dimensional solids comprised of coordinatively unsaturated metal complex fragments and ditopic bridging ligands.[3]

Our group is currently developing an alternative synthesis strategy to ferrocene-containing macromolecules which takes advantage of coordination polymer synthesis. Starting from 1,1′-diborylated ferrocene derivatives and aromatic diamines (e.g. 4,4′-bipyridine, pyrazine), we have already succeeded in the preparation of various boron−nitrogen bridged polymeric species (e.g. **A** in Figure 1).[4−6] In this specific example, the facile formation of boron−nitrogen adduct bonds provided a convenient way of connecting the mononuclear building blocks. The solid materials not only are reasonably stable toward air and moisture but also possess intense colors resulting from charge-transfer interactions between the ferrocene donors and the organic acceptor bridges.[4,7] To test the scope of our approach and to increase the number of metal atoms in the polymer chain, we decided to replace the diamine linkers by
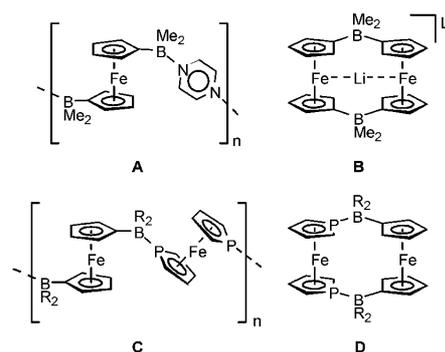
Figure 1. The B−N-bonded charge-transfer coordination polymer **A**, the B−C-bonded macrocyclic lithium scavenger **B**, and the structurally related hypothetical 1,1′-diphosphaferrocene adducts **C** and **D** (any substituents on 1,1′-diphosphaferrocene are omitted for clarity).

Lewis basic ferrocene derivatives. 1,1′-Dilithioferrocene appeared to be a well-suited building block, since this compound is readily available and provides two anionic sp^2-hybridized electron-pair donor sites as part of its cyclopentadienyl ligands. However, treatment of 1,1′-dilithioferrocene with 1,1′-bis(dimethylboryl)ferrocene did not lead to linear polymers but rather gave the cyclic dimer **B** (Figure 1), which is stable in solution and behaves as a highly efficient lithium scavenger.[8]

Given this background, it appeared to be worthwhile to explore the suitability of 3,3′,4,4′-tetramethyl-1,1′-diphosphaferrocene[9] as a difunctional organometallic Lewis base for the preparation of polymers **C** or macrocycles **D** (Figure 1). Even though numerous transition-metal complexes of monophosphaferrocenes and 1,1′-diphosphaferrocenes have been published up to now,[10,11] not much is known about the reactivity of these ligands toward main-group Lewis acids. Theoretical investigations indicate phosphaferrocene derivatives to be weakly σ-donating and strongly π-accepting ligands.[12] This is due to the fact that their electron lone pair(s) is (are) energetically low-lying and their LUMO possesses largely p_z character at the phosphorus atom(s). Since $d_\pi−p_\pi$

* To whom correspondence should be addressed. Fax: +49 69 798 29260. E-mail: Matthias.Wagner@chemie.uni-frankfurt.de.

(1) Pittman, C. U.; Carraher, C. E.; Zeldin, M.; Sheats, J. E.; Culbertson, B. M., Eds. *Metal-Containing Polymeric Materials*; Plenum Press: New York, 1996.

(2) Nguyen, P.; Gómez-Elipe, P.; Manners, I. *Chem. Rev.* **1999**, *99*, 1515−1548.

(3) Archer, R. D. *Inorganic and Organometallic Polymers*; Wiley-VCH: Weinheim, Germany, 2001.

(4) Fontani, M.; Peters, F.; Scherer, W.; Wachter, W.; Wagner, M.; Zanello, P. *Eur. J. Inorg. Chem.* **1998**, 1453−1465, 2087.

(5) Grosche, M.; Herdtweck, E.; Peters, F.; Wagner, M. *Organometallics* **1999**, *18*, 4669−4672.

(6) Dinnebier, R. E.; Wagner, M.; Peters, F.; Shankland, K.; David, W. I. F. *Z. Anorg. Allg. Chem.* **2000**, *626*, 1400−1405.

(7) Ding, L.; Fabrizi de Biani, F.; Bolte, M.; Zanello, P.; Wagner, M. *Organometallics* **2000**, *19*, 5763−5768.

(8) Scheibitz, M.; Winter, R. F.; Bolte, M.; Lerner, H.-W.; Wagner, M. *Angew. Chem.* **2003**, *115*, 954−957; *Angew. Chem., Int. Ed.* **2003**, *42*, 924−927.

(9) de Lauzon, G.; Deschamps, B.; Fischer, J.; Mathey, F.; Mitschler, A. *J. Am. Chem. Soc.* **1980**, *102*, 994−1000.

(10) Mathey, F. *Coord. Chem. Rev.* **1994**, *137*, 1−52.

(11) Ganter, C. *J. Chem. Soc., Dalton Trans.* **2001**, 3541−3548.

(12) Frison, G.; Mathey, F.; Sevin, A. *J. Phys. Chem. A* **2002**, *106*, 5653−5659.

Notes

Scheme 1. Synthesis of the P–B Adduct 1/2[a]
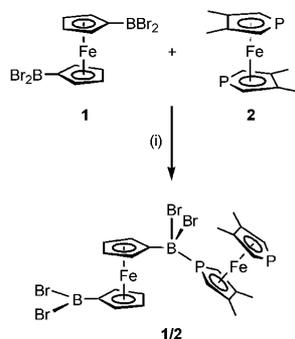
[a] Legend: (i) −30 °C, toluene.

back-bonding is not possible for s- and p-block elements, adduct bonds between main-group compounds and phosphaferrocenes are expected to be weak. Nevertheless, Mathey[13] recently succeeded in the structural characterization of the ionic complex [octa-*n*-propyl-diphosphaferrocene/GaCl$_2$]$^+$[GaCl$_4$]$^-$, while Roberts and Silver[14] have gained NMR spectroscopic evidence for the existence of a 3,3′,4,4′-tetramethyl-1,1′-diphosphaferrocene/BF$_3$ adduct in CDCl$_3$ solution. In the course of our own studies, we synthesized and structurally characterized adducts of 3,4-dimethyl-1-phosphaferrocene with boron tribromide on one hand and dibromoborylferrocene on the other.[15] The latter P–B complex can already be regarded as an important substructure of our target compounds **C** and **D**. With these encouraging results in hand, we focused on the reaction of 1,1′-bis(dibromoboryl)ferrocene (**1**) with 3,3′,4,4′-tetramethyl-1,1′-diphosphaferrocene (**2**; Scheme 1). The purpose of this paper is to report on the structural characterization of the unexpected open-chain dinuclear complex **1/2**, which turned out to be the sole reaction product.

Results and Discussion

Synthesis and NMR Spectroscopic Characterization. For all NMR spectroscopic investigations, solutions of **1** and **2** in toluene-d_8 were mixed in equimolar proportions and sealed in an NMR tube. Similar to the 3,4-dimethyl-1-phosphaferrocene/dibromoborylferrocene system,[15] the ^{11}B, ^{13}C, and ^{1}H NMR spectra of **1/2** at 30 °C show only negligible differences from the NMR spectra of the individual components (Table 1). This is no longer true for the ^{31}P NMR spectrum (30 °C, toluene-d_8) of **2** compared to that of **1/2**. Even though the phosphorus chemical shifts of both species differ by as little as 2.7 ppm (**2**, $\delta(^{31}$P) −68.1; **1/2**, $\delta(^{31}$P) −65.4), the width at half-height increases considerably from $h_{1/2} = 14$ Hz (**2**) to $h_{1/2} = 100$ Hz (**1/2**), thereby indicating a dynamic association/dissociation equilibrium in the latter case. This result is in striking contrast to the work of Roberts and Silver,[14] who observed two ^{31}P NMR resonances for the complex **2**/BF$_3$

(13) Sava, X.; Melaimi, M.; Mézailles, N.; Ricard, L.; Mathey, F.; Le Floch, P. *New J. Chem.* **2002**, *26*, 1378−1383.
(14) Roberts, R. M. G.; Silver, J.; Wells, A. S. *Inorg. Chim. Acta* **1986**, *119*, 165−169.
(15) Scheibitz, M.; Bats, J. W.; Bolte, M.; Wagner, M. *Eur. J. Inorg. Chem.* **2003**, 2049−2053.

Table 1. ^{11}B and ^{31}P Chemical Shift Values of an Equimolar Mixture of 1 and 2 in Toluene-d_8 at Various Temperatures

	T (°C)			
	30	0	−30	−60
$\delta(^{11}$B)	52.5[a] (210)[c]	49.8 (360)	38.1 (890)	n.o.[d]
$\delta(^{31}$P)	−65.4[b] (100)	−63.0 (90)	−48.5 (140)	−37.2 (950)

[a] Cf. **1**: $\delta(^{11}$B) 53.3 (190). [b] Cf. **2**: $\delta(^{31}$P) −68.1 (14). [c] $h_{1/2}$ values (Hz) given in parentheses. [d] n.o. = not observed.

($\delta(^{31}$P) 31.0 and −62.2; room temperature, CDCl$_3$), one of them deshielded by 103 ppm with respect to the ^{31}P NMR signal of **2** ($\delta(^{31}$P) −72.0; room temperature, CDCl$_3$). This leads to the conclusion that **2** forms a much weaker Lewis acid−base adduct with **1** than with BF$_3$. It is, however, important to note that even in the presence of excess BF$_3$·OEt$_2$ only the monoadduct **2**/BF$_3$ is formed,[14] which suggests that complexation of one phosphorus site deactivates the other. To gain further insight into the temperature dependence of the adduct equilibrium, variable-temperature ^{11}B and ^{31}P NMR spectra have been recorded. The results are summarized in Table 1. At 30 °C, the ^{11}B NMR signal appears at 52.5 ppm ($h_{1/2} = 210$ Hz). Lowering the sample temperature leads to an upfield shift of this resonance together with an increase of its width at half-height (e.g. $T = -30$ °C: $\delta(^{11}$B) 38.1, $h_{1/2} = 890$ Hz). No signal is detectable in the ^{11}B NMR spectrum at −60 °C, which is most likely due to severe line broadening caused by decelerated exchange processes. The ^{31}P NMR resonance is shifted to lower field upon cooling, again accompanied by broadening of the signal. The ^{11}B and ^{31}P NMR data obtained at a given temperature represent average values of all components present in the reaction mixture. Our data therefore testify to an increase in the concentration of the adduct **1/2** at low temperatures. However, even at −30 °C, the absolute concentration of **1/2** is apparently not very high, since ^{11}B NMR shift values of stable boron−phosphorus adducts are typically observed in a range upfield of 10 ppm.[16]

X-ray Crystal Structure Determination. X-ray-quality crystals of **1/2** were grown (Scheme 1) at three different temperatures to maximize the chance of getting both the product of a *thermodynamically* controlled crystallization process and the product of a *kinetically* controlled process ($T_1 = 20$ °C, benzene, slow evaporation of the solvent; $T_2 = -30$ °C, toluene; $T_3 = -78$ °C, methylene chloride). In all three cases, crystals possessing identical cell parameters were obtained. Thus, only the result of the structure analysis of a crystal grown from toluene at −30 °C (triclinic space group $P\bar{1}$) is discussed here (Tables 2 and 3). Compound **1/2** establishes neither a polymeric nor a cyclic structure but, rather, forms an open-chain dinuclear complex in the solid state (Figure 2). Each of these complexes consists of a 3,3′,4,4′-tetramethyl-1,1′-diphosphaferrocene together with a 1,1′-bis(dibromoboryl)ferrocene unit linked by one phosphorus−boron bond. The second BBr$_2$ substituent, which features a trigonal-planar boron center (sum of angles around boron 360°), and the second phosphorus atom are not engaged in intra- or

(16) Nöth, H.; Wrackmeyer, B. Nuclear Magnetic Resonance Spectroscopy of Boron Compounds. In *NMR Basic Principles and Progress*; Diehl, P., Fluck, E., Kosfeld, R., Eds.; Springer: Berlin, Heidelberg, New York, 1978.

Table 2. Selected Crystallographic Data for 1/2

formula	$C_{22}H_{24}B_2Br_4Fe_2P_2$
fw	803.31
color, shape	red, block
cryst size (mm)	0.55 × 0.45 × 0.36
temp (K)	173(2)
radiation	Mo Kα, 0.710 73 Å
cryst syst	triclinic
space group	$P\bar{1}$
a (Å)	7.0864(7)
b (Å)	11.0523(11)
c (Å)	17.5153(18)
α (deg)	85.952(8)
β (deg)	83.493(8)
γ (deg)	73.518(8)
V (Å^3)	1305.9(2)
Z	2
D_{calcd} (g cm^{-3})	2.043
$F(000)$	776
μ (mm^{-1})	7.364
$2\theta_{max}$ (deg)	53.08
no. of rflns collected	19 390
no. of indep rflns (R_{int})	5363 (0.0726)
no. of rflns obsd ($I > 2\sigma(I)$)	4548
no. of data/restraints/params	5363/0/294
GOF on F^2	1.023
R1, wR2 ($I > 2\sigma(I)$)	0.0373, 0.0899
R1, wR2 (all data)	0.0458, 0.0934
largest diff peak and hole (e Å^{-3})	0.905/−0.737

Table 3. Selected Bond Lengths (Å), Angles (deg), and Torsion Angles (deg) of 1/2

P(1)−B(2)	2.001(4)	B(1)−C(11)	1.493(7)
P(1)−Fe(2)	2.194(1)	B(2)−C(21)	1.572(5)
P(2)−Fe(2)	2.279(1)		

C(11)−B(1)−Br(11)	121.3(3)	C(32)−P(1)−C(35)	92.9(2)
C(11)−B(1)−Br(12)	122.7(3)	C(42)−P(2)−C(45)	88.1(2)
Br(11)−B(1)−Br(12)	116.1(3)	Br(21)−B(2)−Br(22)	110.7(2)
P(1)−B(2)−C(21)	104.5(3)	C(21)−B(2)−Br(21)	115.2(3)
P(1)−B(2)−Br(21)	105.5(2)	C(21)−B(2)−Br(22)	114.2(3)
P(1)−B(2)−Br(22)	105.6 (2)	COG−C(11)−B(1)^a	161.9

C(12)−C(11)−B(1)−Br(12)	14.6(5)
C(32)−P(1)−B(2)−C(21)	150.8(3)
C(32)−P(1)−B(2)−Br(21)	29.0(3)
C(32)−P(1)−B(2)−Br(22)	−88.3(3)

^{a} COG = centroid of the cyclopentadienyl ligand.

intermolecular bonding interactions (shortest intermolecular P···B distance 6.813 Å). The P−B bond of 1/2 (P(1)−B(2) = 2.001(4) Å) is slightly shorter than that of the related compound 3,4-dimethyl-1-phosphaferrocene/dibromoborylferrocene (P−B = 2.023(4) Å[15]) but somewhat longer than the P−B bond of the corresponding BBr$_3$ adduct (P−B = 1.972(9) Å[15]). The degree of pyramidalization of the tetracoordinate boron substituent is lower (C(21)−B(2)−Br(21) = 115.2(3)°, C(21)−B(2)−Br(22) = 114.2(3)°, Br(21)−B(2)−Br(22) = 110.7-(2)°) than expected for a fully sp^3-hybridized boron atom with ideal tetrahedral geometry (R−B−R = 109.5°). This feature, together with the rather long P−B bond, points toward a weak acid−base interaction in 1/2, as has already been concluded from our NMR spectroscopic studies (see above). P−B adduct formation nevertheless leads to remarkable structural changes at the boron-bound phospholyl ligand compared to the second phospholyl ring. Major differences lie in the lengths of the P−Fe bonds (P(1)−Fe(2) = 2.194(1) Å, P(2)−Fe(2) = 2.279(1) Å, Δ = 0.085 Å) as well as in the C−P−C angles (C(32)−P(1)−C(35) = 92.9(2)°, C(42)−P(2)−C(45) = 88.1(2)°, Δ = 4.8°). Qualitatively similar—but less pronounced—effects can be observed when the molecular
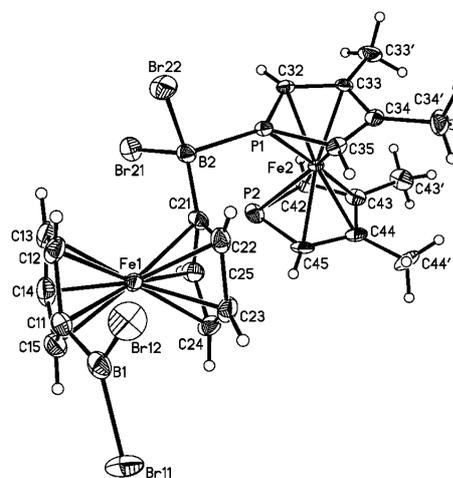
Figure 2. Molecular structure and numbering scheme of compound 1/2. Thermal ellipsoids are shown at the 50% probability level.

structures of phosphaferrocene−transition-metal complexes are compared with those of the corresponding free phosphaferrocene ligands.[15] B−P acid−base pairing also has an impact on the second—uncomplexed—BBr$_2$ substituent of the dibromoborylferrocene fragment in 1/2. It is known that three-coordinate boron groups attached to a ferrocene backbone tend to be bent out of the plane of the C$_5$H$_4$ ring toward the iron atom.[17] The dip angle $\alpha^* = 180° − \beta^*$ ($\beta^* = $ B−C$_{ipso}$−COG; COG = centroid of the C$_5$H$_4$ ring) has been introduced as a measure of the degree of this distortion.[17] Large values of α^* are usually observed with strongly Lewis acidic boryl substituents (cf. FcBBr$_2$ with $\alpha^* = 17.7°/18.9°$ (two crystallographically independent molecules in the asymmetric unit)[17] and 1,1'-fc(B(N^{i}Pr$_2$)$_2$)$_2$ with $\alpha^* = 0°$;[18] Fc = (C$_5$H$_5$)Fe-(C$_5$H$_4$)). Moreover, α^* tends to become smaller when additional boryl substituents are introduced into the ferrocene core (cf. FcBBr$_2$ with $\alpha^* = 17.7°/18.9°$[17] and 1,1'-fc(BBr$_2$)$_2$ with $\alpha^* = 9.1°$;[18] fc = (C$_5$H$_4$)Fe(C$_5$H$_4$)). Bending of the exocyclic BR$_2$ substituent(s) is likely due to electronic interactions between filled d-type orbitals at iron and the empty p orbital at boron.[17] In the case of 1/2, a negligible dip angle α^* of 1.3° is found for the tetracoordinate B(2)Br(21)Br(22) group, since the p orbital at B(2) is filled by the P(1) lone pair. The C$_5$H$_4$−B(1)Br(11)Br(12) moiety, however, is bent by $\alpha^* = 18.1°$, which is double the value observed for the free Lewis acid 1,1'-fc(BBr$_2$)$_2$ and equal to the dip angle exhibited by the monoborylated FcBBr$_2$. We may therefore assume that a delicate interplay exists between the individual BR$_2$ substituents in diborylated ferrocenes: satisfying the electron demand of one of the competing boryl groups by adduct formation with an external Lewis base promotes the electronic interaction between the remaining (and still three-coordinate) boryl substituent and the iron atom.

(17) Appel, A.; Jäkle, F.; Priermeier, T.; Schmid, R.; Wagner, M. *Organometallics* **1996**, *15*, 1188−1194.

(18) Wrackmeyer, B.; Dörfler, U.; Milius, W.; Herberhold, M. *Polyhedron* **1995**, *14*, 1425−1431.

When the two phospholyl rings of free 3,3',4,4'-tetramethyl-1,1'-diphosphaferrocene (**2**) are projected on each other, the P atom of one ring superposes with a β-C atom of the other.[9] In contrast, the diphosphaferrocene unit of **1/2** adopts a staggered conformation in which P(1) and P(2) are more closely approaching each other (cf. P(1)−COG(1)−COG(2)−P(2) = 29.8°; COG(1), COG(2) = centroids of the two phospholyl rings). As a result, steric strain between the methyl groups of the P(2)-phospholyl ring and the ferrocene molecule is avoided. The relative position of the ferrocene and the diphosphaferrocene in **1/2** is characterized by the torsion angle C(32)−P(1)−B(2)−C(21) = 150.8(3)° and a dihedral angle of 99.3° between the C(21)C(22)C(23)C(24)C-(25) ring and the P(1)-phospholyl ligand. The tilt angles between the two C_5H_4 rings are 2.9 and 2.3° between the two phospholyl ligands.

Conclusion

Even though P-bonded complexes between phosphaferrocenes and main-group Lewis acids were generally believed to be rather unstable, our group recently succeeded in the synthesis and structural characterization of P−B adducts between 3,4-dimethyl-1-phosphaferrocene and boron tribromide as well as dibromoborylferrocene. The existence of the latter aggregate in particular prompted us to investigate the suitability of 1,1'-diphosphaferrocenes and 1,1'-diborylferrocenes as building blocks for the synthesis of polymers or macrocycles via Lewis acid−base pairing. For practical reasons we chose 3,3',4,4'-tetramethyl-1,1'-diphosphaferrocene (**2**) as the base and treated it with 1,1'-bis-(dibromoboryl)ferrocene (**1**), which is one of the most strongly Lewis acidic derivatives available. In contrast to a priori expectations, neither polymeric material nor a macrocycle was formed from **1** and **2** in solution or in the solid state. Rather, the compound obtained by crystallization consisted of the open-chain dinuclear complex **1/2**, featuring only one P−B adduct bond. This result was reproduced both at higher ($T = 20$ °C, benzene, slow evaporation of the solvent) and at lower crystallization temperatures ($T = -78$ °C, methylene chloride). As has already been mentioned by Roberts and Silver, who investigated the 3,3',4,4'-tetramethyl-1,1'-diphosphaferrocene/BF_3 couple in various stoichiometric ratios using ^{31}P NMR spectroscopy, P−B adduct formation at the first phosphorus atom apparently reduces the Lewis basicity of the second phosphorus donor to such an extent that it no longer forms stable dative bonds to boron Lewis acids. In our special case, the problem is aggravated by the fact that tetracoordination of the first boryl substituent in **1** likely leads to a decrease in the Lewis acidity of the second boryl group, which profits from the full electron density provided by the ferrocene backbone. Our results lead to the conclusion that 1,1'-diphosphaferrocenes are not suitable as organometallic bridging elements for the coordination polymerization of 1,1'-diborylferrocenes. In the future, we will therefore focus primarily on 1,1'-diazaferrocenes and 1,1'-dilithioferrocenes as alternative difunctional Lewis bases.

Experimental Section

General Remarks. All reactions were carried out under a nitrogen atmosphere using Schlenk tube techniques. Toluene-d_8 was freshly distilled under argon from Na/benzophenone. The starting materials **1**[19] and **2**[9] were prepared according to published procedures. NMR: Bruker DPX 250. Chemical shifts are referenced to residual solvent peaks (^{1}H, [13]C{[1]H}), external H_3PO_3 ([31]P{[1]H}), or external $BF_3·Et_2O$ ([11]B {[1]H}). Abbreviations: s = singlet; d = doublet; vtr = virtual triplet; n.o. = signal not observed.

Preparation of 1/2. 1,1'-fc(BBr_2)$_2$ (**1**; 56 mg, 0.11 mmol) and 3,3',4,4'-tetramethyl-1,1'-diphosphaferrocene (**2**; 30 mg, 0.11 mmol) were dissolved in 0.8 mL of toluene-d_8, the resulting mixture was sealed in an NMR tube and investigated by NMR spectroscopy.

^{1}H NMR (250.1 MHz, toluene-d_8, 303 K): δ 1.84 (s, 12H, CH_3), 3.59 (d, 4H, $^2J_{P,H}$ = 36.1 Hz, CH), 4.32, 4.38 (2 × vtr, 2 × 4H, $^3J_{H,H}$ = $^4J_{H,H}$ = 1.7 Hz, C_5H_4). ^{13}C NMR (62.9 MHz, toluene-d_8, 303 K): δ 15.5 (CH_3), 79.0, 80.3 (C_5H_4), 81.6 (d, $^1J_{P,C}$ = 56.9 Hz, CH), 97.1 (d, $^2J_{P,C}$ = 6.4 Hz, CCH$_3$), n.o. (CB). ^{11}B NMR (80.3 MHz, toluene-d_8, 303 K): δ 52.5 ($h_{1/2}$ = 210 Hz). ^{31}P NMR (101.3 MHz, toluene-d_8, 303 K): δ −65.4 ($h_{1/2}$ = 100 Hz).

X-ray-quality crystals of **1/2** were grown (i) from a highly diluted benzene solution upon slow evaporation of the solvent at 20 °C, (ii) from toluene at −30 °C, and (iii) from methylene chloride at −78 °C (typical amounts of starting material used in the crystallization reactions are 68 mg, 0.13 mmol (**1**) and 36 mg, 0.13 mmol (**2**); yield of **1/2** 68 mg (65%)).

X-ray Crystal Structure Analysis of 1/2. A single crystal (red block; 0.55 × 0.45 × 0.36 mm) was analyzed with a STOE IPDS II two-circle diffractometer with graphite-monochromated Mo Kα radiation. An empirical absorption correction was performed using the MULABS[20] option in PLATON;[21] the minimum and maximum transmissions were 0.1067 and 0.1769, respectively. The structure was solved by direct methods using the program SHELXS[22] and refined against F^2 with full-matrix least-squares techniques using the program SHELXL-97.[23] All non-hydrogen atoms were refined with anisotropic displacement parameters. Hydrogen atoms were located by difference Fourier synthesis and refined using a riding model. CCDC reference number: 236748.

Supporting Information Available: Crystallographic data of **1/2** in the Crystallographic Information File (CIF) format. This material is available free of charge via the Internet at http://pubs.acs.org.

OM049707A

(19) Ruf, W.; Renk, T.; Siebert, W. *Z. Naturforsch.* **1976**, *31b*, 1028−1034.
(20) Blessing, R. H. *Acta Crystallogr., Sect. A* **1995**, *51*, 33−38.
(21) Spek, A. L. *Acta Crystallogr., Sect. A* **1990**, *46*, C34.
(22) Sheldrick, G. M. *Acta Crystallogr., Sect. A* **1990**, *46*, 467−473.
(23) Sheldrick, G. M. SHELXL-97: A Program for the Refinement of Crystal Structures, Universität Göttingen, Göttingen, Germany, 1997.

3.7 „On the way to ferrocene-based multipledecker sandwich complexes"

A. Haghiri, M. Scheibitz, H.-W. Lerner, M. Bolte, M. Wagner

2 # On the way to ferrocene-based multiple-decker sandwich complexes ✩

3 ## Alireza Haghiri Ilkhechi, Matthias Scheibitz, Michael Bolte, Hans-Wolfram Lerner, 4 ## Matthias Wagner *

5 *Institut für Anorganische Chemie, J.W. Goethe-Universität Frankfurt, Marie-Curie-Strasse 11, D-60439 Frankfurt (Main), Germany*

8 Dedicated to Professor Malcolm L.H. Green on the occasion of his retirement.

9 **Abstract**

10   Three ferrocene derivatives, Li[FcBH$_3$], Li$_2$[1,1'-fc(BMe$_3$)$_2$] and Li$_2$[1,1'-fc(BMe$_2$pz)$_2$] [Fc = (C$_5$H$_5$)Fe(C$_5$H$_4$), fc = (C$_5$H$_4$)$_2$Fe, 11 pz = pyrazolyl], have been synthesized and structurally characterized to investigate the interaction of the negatively charged 12 sandwich complex with its Li$^+$ counterion(s) in the solid state. Single crystals of Li[FcBH$_3$] · (12-crown-4), obtained from a THF 13 solution after addition of 12-crown-4, contain hexacoordinated Li$^+$ ions, which are bonded to one molecule of crown ether and to 14 two hydrogen atoms of the BH$_3$ fragment. The compound Li$_2$[1,1'-fc(BMe$_3$)$_2$] crystallized from THF as solvent-separated ion pairs 15 with each Li$^+$ being encapsulated by four THF molecules. Single crystals of Li$_2$[1,1'-fc(BMe$_2$pz)$_2$] were grown from diethyl ether. In 16 this compound, the lithium ions are coordinated by two solvent molecules, the pyrazolyl side-arm and the cyclopentadienyl ring. 17 Thus, Li$_2$[1,1'-fc(BMe$_2$pz)$_2$] can be regarded as a trinuclear segment of the polymeric structure [–(C$_5$H$_4$R)Li(C$_5$H$_4$R)Fe–]$_\infty$ with 18 R = BMe$_2$pz. 19 © 2004 Elsevier Ltd. All rights reserved.

20 *Keywords:* Multiple-decker sandwich complex; Ferrocene; Boron; Lithium; Crystal structure

21 ## 1. Introduction

22   For more than 30 years, multiple-decker sandwich 23 complexes have been in the focus of attention due to 24 their promising potential as building blocks for nano- 25 scale applications (e.g., one-dimensional wires and spin- 26 chains) [1]. A most remarkable representative of this 27 class of compounds was reported in 1985 by Siebert 28 [2,3], who succeeded in the synthesis of extended co- 29 lumnar structures from Ni ions and η^5,μ-2,3-dihydro- 30 1,3-diborolyl ligands. Later, this one-dimensional sys- 31 tem was shown to possess semiconducting properties in 32 the solid state [4–6]. For practical reasons, it would,

however, be desirable to substitute simple cyclopenta- 33 dienyl ligands for the sophisticated boron heterocycle. 34 Numerous triple-decker sandwich complexes of the 35 permethylated cyclopentadienyl derivative [C$_5$Me$_5$]$^-$ 36 have already been isolated and structurally character- 37 ized [1]. In contrast, the number of known examples 38 featuring exclusively the unsubstituted [C$_5$H$_5$]$^-$ ligand is 39 still rather small (e.g., [Ni$_2$(C$_5$H$_5$)$_3$]$^+$ [7,8], [Tl$_2$(C$_5$H$_5$)$_3$]$^-$ 40 [9]). Even though Schildcrout [10] reported as early as 41 1973 the detection of [Fe$_2$(C$_5$H$_5$)$_3$]$^+$ in the high-pressure 42 electron-impact mass spectrum of ferrocene, this com- 43 pound has not been isolated yet. However, clusters of 44 the general formula V$_n$[Fe(C$_5$H$_5$)$_2$]$_{n+1}$ (n = 1–3) have 45 recently been generated by two-laser vaporization of 46 vanadium and ferrocene targets. Time-of-flight mass 47 spectra measured with and without the addition of NH$_3$ 48 gas indicate that these species possess multiple-decker 49 sandwich structures rather than consisting of a central 50 core of vanadium atoms capped by ferrocene molecules 51 [11]. 52

---

* Corresponding author. Tel.: +49-69-798-29156; fax: +49-69-798-29260.
E-mail address: Matthias.Wagner@chemie.uni-frankfurt.de (M. Wagner).
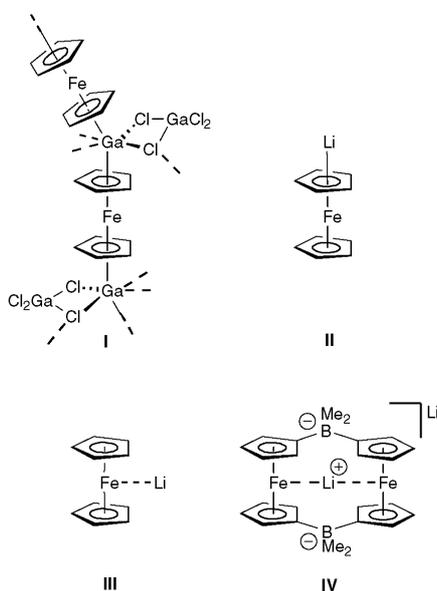
Fig. 1. The Ga^+–ferrocene multiple-decker sandwich complex **I**, the two calculated minimum structures **II** and **III** of the $Li^+ \cdots$ferrocene complex in the gas phase, and the lithium [1.1]diborataferrocenophane **IV**.

The purpose of this paper is to describe the synthesis and structural characterization of type-**II** ferrocene–Li^+ adducts, which appears to be a realistic goal given the fact that the ferrocene–Ga^+ fragments in **I** already resemble the geometry of our target structure. It has, however, to be borne in mind that the synthesis protocol leading to **I** is quite unique in that we are starting from the covalent molecule $GaCl_3$ which is readily soluble in non-coordinating solvents. Consequently, there is no competition between the ferrocene donor and Lewis basic solvent molecules for the Ga(I) ion formed in situ in the course of the reaction. Moreover, in the calculated gas phase structure **II** any possible perturbations of the molecular geometry caused by the presence of solvent molecules are necessarily neglected. For a more general approach to ferrocene–metal multiple-decker sandwich complexes, however, we will have to use transition metal salts as starting materials which usually require strongly coordinating solvents as the reaction media. It therefore seemed reasonable to employ ferrocene derivatives equipped with suitable functional groups able to assist the cyclopentadienyl ring in metal ion binding. Such auxiliary substituents will greatly enhance the stability of the ferrocene–metal aggregate but still allow for those metal$\cdots$Cp interactions that have been theoretically predicted and experimentally proven to exist in the solid state (cf. the unsupported multiple-decker complex **I**).

Our group has published the synthesis and X-ray crystal structure analysis of compound **I** (Fig. 1), in which an array of alternating Ga(I) and Fe(II) ions is connected by η^5,μ-$[C_5H_5]^-$ moieties [12]. According to density functional (DFT) calculations, the binding energy of two ferrocenes to Ga^+ is about 80 $kJ\,mol^{-1}$ higher than that for the formation of $[Ga(C_6H_6)_2]^+$ from Ga^+ and two benzene molecules. Fragment analysis of $\{[Fe(C_5H_5)_2]_2Ga\}^+$ indicated a transfer of 0.4 electrons into the gallium 4p orbitals compared with a zero occupancy for the isolated ion. More detailed insight into the gas phase basicity of ferrocene toward metal cations is provided by a recent DFT study on the ferrocene–Li^+ complex [13]. Two minima have been located on the energy surface: in the lower energy structure, the lithium cation is coordinated on top of one of the cyclopentadienyl rings (cf. **II**; Fig. 1), whereas the second minimum structure **III**, being 33 $kJ\,mol^{-1}$ higher in energy, has the Li^+ ion bonded laterally to the iron atom. We found a similar structural motif as predicted for the hypothetical aggregate **III** in the [1.1]diborataferrocenophane **IV**, which crystallizes with one lithium cation inside its molecular cavity [d(Fe$\cdots$Li): 2.4 Å (**III**); 2.706(5), 2.720(6) Å (**IV**)] [14,15]. ^7Li NMR spectroscopy shows this ferrocenophane–Li^+ complex to be stable in THF solution even in the presence of excess 12-crown-4.

2. Results and discussion

To bring about close contacts between a lithium cation and the ferrocene cyclopentadienyl ring, we decided to introduce substituents into the ferrocene core that (i) increase the electron density on the organometallic moiety and (ii) bear a negative charge able to attract Li^+ electrostatically. It is important to know in this context, that the Fe(II)/Fe(III) redox potentials of ferrocenylborane-amine adducts have a pronounced shift to cathodic values with respect to the parent ferrocene [cf. $FcBMe_2$–picoline: $E^{0\prime} = -0.33$ V, 1,1'-$fc(BMe_2$–picoline$)_2$: $E^{0\prime} = -0.56$ V; in CH_2Cl_2 vs. FcH/FcH^+, Fc = $(C_5H_5)Fe(C_5H_4)$, fc = $(C_5H_4)_2Fe$] [16,17]. This effect becomes even stronger when the amine base is replaced by a negatively charged organyl group [14,15]. Thus, tetra-coordinated boryl substituents appear to be particularly well-suited to meet the two requirements outlined above. Starting from the well-known ferrocenylboranes $FcB(Br)OEt$ (**1**) [18] and 1,1'-$fc(BMe_2)_2$ (**2**) [19], three derivatives of ferrocenylborates were chosen for our further investigations (Scheme 1): $Li[FcBH_3]$ (**3**), $Li_2[1,1'$-$fc(BMe_3)_2]$ (**4**) and $Li_2[1,1'$-$fc(BMe_2pz)_2]$ (**5**; pz = pyrazolyl), in which the aimed-for $Li\cdots$Cp coordination may be stabilized by a chelating pyrazolyl side-arm.
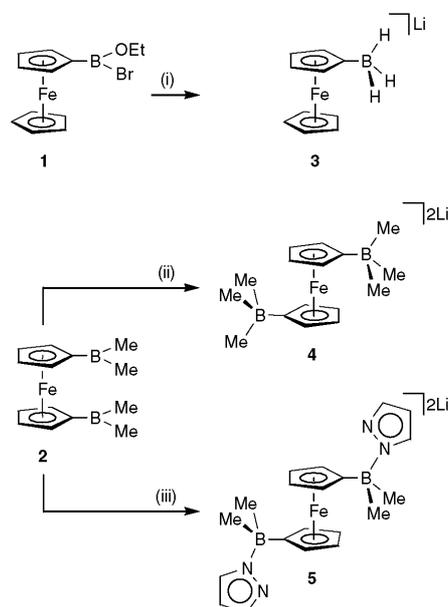
Scheme 1. Syntheses of the lithium ferrocenylborates **3**, **4** and **5**: (i) +Li[AlH$_4$], Et$_2$O/C$_5$H$_{12}$, 0 °C; (ii) +2LiMe, Et$_2$O, −78 °C; (ii) +2Lipz, Et$_2$O, −78 °C.

2.1. Syntheses and NMR spectroscopic characterization   133

FcB(OEt)Br (**1**) and 1 equiv. of Li[AlH$_4$] in ether/ pentane gave lithium ferrocenylborohydride **3** in excellent yield (Scheme 1). Details of the synthesis procedure and NMR data of **3** have been published elsewhere [20]. Single crystals of Li[FcBH$_3$]·(12-crown-4) were grown by gas phase diffusion of diethylether onto a THF solution of **3**, to which a small amount of 12-crown-4 had been added. In the absence of the crown ether, no single crystalline material could be obtained. Reaction of 1,1'-fc(BMe$_2$)$_2$ (**2**) with either 2 equiv. of LiMe or 2 equiv. of Lipz in diethyl ether at −78 °C gave Li$_2$[1,1'-fc(BMe$_3$)$_2$] (**4**) and Li$_2$[1,1'-fc(BMe$_2$pz)$_2$] (**5**). The ^{11}B NMR spectra of **4** and **5** show resonances at $\delta = -21.8$ and −9.0, respectively, which agree nicely with those of Li[BMe$_4$] [$\delta(^{11}$B$) = -20.2$] [21] on one hand and Na[B(NH$_2$)Et$_3$] [$\delta(^{11}$B$) = -9.8$] [22] on the other. The ^{11}B NMR signal of **4** possesses a narrow linewidth ($h_{1/2} = 25$ Hz) testifying to a high local symmetry at the boron atom. In contrast, the less symmetrical boron coordination sphere in **5** results in a significantly broader ^{11}B NMR resonance ($h_{1/2} = 300$ Hz). In the ^{1}H NMR spectrum of **4**, three signals appear at −0.47, 3.55 and 3.75 ppm (integral ratio = 9:2:2), which are assigned to the methyl protons and the two types of magnetically non-equivalent ferrocene hydrogen atoms. In the ^{1}H NMR spectrum of **5**, the corresponding signals are visible at 0.11, 4.05 and 4.19 ppm. This time, an integral ratio of 6:2:2 reveals the

<div style="text-align:right">

134
135
136
137
138
139
140
141
142
143
144
145
146
147
148
149
150
151
152
153
154
155
156
157
158
159
160

</div>

Table 1
Selected crystallographic data for **3**·(12-crown-4), **4**·(THF)$_8$ and **5**·(Et$_2$O)$_4$

Compound	**3**·(12-crown-4)	**4**·(THF)$_8$	**5**·(Et$_2$O)$_4$
Formula	C$_{18}$H$_{28}$BFeLiO$_4$	C$_{48}$H$_{90}$B$_2$FeLi$_2$O$_8$	C$_{36}$H$_{66}$B$_2$FeLi$_2$N$_4$O$_4$
Molecular weight	382.00	886.55	710.28
Crystal size (mm)	0.46 × 0.35 × 0.19	0.42 × 0.33 × 0.28	0.41 × 0.36 × 0.33
Crystal system	orthorhombic	orthorhombic	triclinic
Space group	*Pnma*	*Pca*2$_1$	*P*$\bar{1}$
Unit cell dimensions			
a (Å)	20.629(5)	17.4302(16)	10.6219(8)
b (Å)	10.3594(15)	17.5219(13)	13.1216(11)
c (Å)	8.6903(11)	17.2759(14)	15.2509(13)
α (°)	90	90	98.722(7)
β (°)	90	90	97.012(7)
γ (°)	90	90	93.914(6)
V (Å^3)	1857.2(6)	5276.2(8)	2077.1(3)
Z	4	4	2
D_c (g cm^{-3})	1.366	1.116	1.136
T (K)	100(2)	173(2)	173(2)
μ(Mo Kα) (mm^{-1})	0.830	0.332	0.402
$2\theta_{max}$ (°)	54.56	51.80	53.08
Measured reflections	6792	22966	33516
Unique reflections (R_{int})	2095 (0.0534)	8934 (0.0638)	8567 (0.0476)
Observed reflections [$I > 2\sigma(I)$]	1252	5285	6765
Parameters refined	167	551	442
R_1 [$I > 2\sigma(I)$; all data]	0.0259; 0.0584	0.1337; 0.1690	0.0577; 0.0709
wR_2 [$I > 2\sigma(I)$; all data]	0.0438; 0.0481	0.3402; 0.3603	0.1645; 0.1718
Goodness-of-fit on F^2	0.568	1.198	1.073
Largest difference peak and hole (e Å^{-3})	0.21 and −0.31	0.52 and −1.01	1.075 and −1.131

161 presence of only two methyl substituents at each boron
162 atom. Moreover, the electronegative pyrazolyl groups
163 lead to a downfield shift of the methyl and ferrocenyl
164 resonances of **5** compared to **4** and to a pattern of three
165 signals in the aromatic region of the proton spectrum
166 [$\delta(^1H) = 5.95, 7.01, 7.48$]. In the ^{13}C NMR spectrum of
167 **4**, a 1:1:1:1 quadruplet for the methyl groups is observed
168 [$\delta(^{13}C) = 16.4$, $^1J_{BC} = 40$ Hz] as a result of ^{11}B ($I = 3/2$)
169 coupling. The methyl resonance of the less symmetri-
170 cally substituted derivative **5** [$\delta(^{13}C) = 12.8$] is severely
171 broadened and its multiplet structure was not resolved,
172 which was attributed to the quadrupolar relaxation of
173 the adjacent boron nucleus [22].

174 *2.2. X-ray crystal structure determinations*

175   Selected crystallographic data are summarized in Ta-
176 ble 1. Lithium ferrocenylborohydride **3** crystallizes to-
177 gether with 1 equiv. of 12-crown-4 in the orthorhombic
178 space group *Pnma* (Fig. 2). Each Li$^+$ ion is complexed by
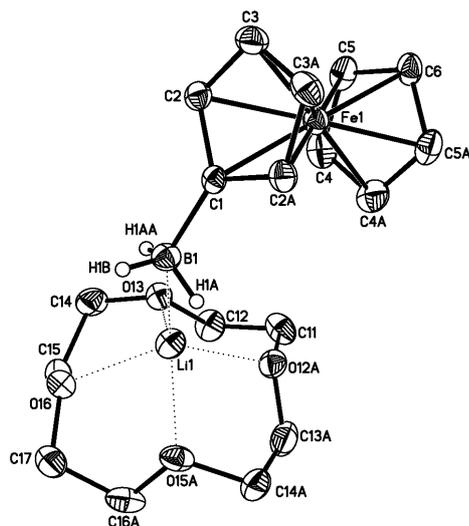
Fig. 2. Molecular structure of compound **3** · (12-crown-4); thermal el-
lipsoids are shown at the 50% probability level. Selected bond lengths
(Å), atom· · ·atom distances (Å), angles (°), torsion angles (°) and di-
hedral angles (°): B(1)–C(1) = 1.600(4), B(1)· · ·Li(1) = 2.382(4), B(1)–
H(1A) = 1.14(2),   B(1)–H(1B) = 1.15(3),   Li(1)–H(1A) = 1.97(2),
Li(1)· · ·H(1B) = 2.94(2);   C(2)–C(1)–C(2A) = 104.2(2),   C(2)–C(1)–
B(1) = 127.8(1),   C(1)–B(1)· · ·Li(1) = 141.3(2),   C(1)–B(1)–
H(1A) = 112.6(10),   C(1)–B(1)–H(1B) = 111.6(14),   H(1A)–B(1)–
H(1B) = 105.1(12),   Li(1)–H(1A)–B(1) = 96.4(12);   COG–C(1)–
B(1) = 176.5;   C(2)–C(1)–B(1)· · ·Li(1) = 92.4(2),   C(2)–C(1)–B(1)–
H(1B) = −87.6(2),   C(1)–COG–COG′–C(4A) = −36.1;
C(1)C(2)C(3)C(3A)C(2A)//C(4)C(5)C(6)C(5A)C(4A) = 0.2.   COG:
centre of gravity of a C$_5$H$_4$ ring. Symmetry transformation used to
generate equivalent atoms: $x, −y + 3/2, z$.

179 four oxygen atoms of a crown ether molecule and es-
180 tablishes close contacts to two hydrogen atoms of the
181 BH$_3$ fragment [Li(1)–H(1A) = 1.97(2) Å]. The Li· · ·H
182 distance to the third hydrogen atom is almost 1 Å longer
183 [Li(1)· · ·H(1B) = 2.94(2) Å]. Thus, [FcBH$_3$]$^-$ acts as a
184 bidentate ligand toward the lithium cation. In metal
185 borohydrides, this is the most common binding mode
186 [23]. The coordination geometry of Li$^+$ in **3** · (12-crown-
187 4) is reminiscent of the structure determined for
188 Li[BH$_4$] · 2DME in the solid state (DME = dimethoxye-
189 thane) [23]. Here, the hexacoordinated Li ion is sur-
190 rounded by four oxygen atoms of two DME molecules
191 and two hydrogen atoms from a μ$_2$-[BH$_4$]$^-$ group.
192 Consequently, the Li–H bond lengths {**3** · (12-crown-4):
193 1.97(2) Å; Li[BH$_4$] · 2DME: 2.02(2) Å}, as well as the Li–
194 H–B   bond   angles   {**3** · (12-crown-4):   96.4(12)°;
195 Li[BH$_4$] · 2DME: 98.1(9)°} are rather similar in both
196 compounds. A significantly shorter B· · ·Li distance is
197 found in **3** · (12-crown-4) [2.382(4) Å] compared to
198 Li[BH$_4$] · 2DME [2.470(4) Å]. Using Edelstein's correla-
199 tion of metal–boron distances as a measure of the den-
200 ticity of borohydride groups [24], values of 1.6 ± 0.1 and
201 1.36 ± 0.06 Å are estimated for the ionic radii of biden-
202 tate and tridentate borohydride ligands, respectively.
203 Thus, B· · ·Li distances of about 2.50 and 2.26 Å are to be
204 expected for Li-μ$_2$-BH$_3$R and Li-μ$_3$-BH$_3$R coordination
205 modes [ionic radius of hexacoordinated Li$^+$ = 0.90 Å
206 [25]]. It may therefore be concluded, that the [BH$_4$]$^-$ ion
207 in Li[BH$_4$] · 2DME represents the ideal Li-μ$_2$-BH$_3$R ar-
208 rangement, whereas the BH$_3$ fragment in **3** · (12-crown-4)
209 is slightly tilted in the direction of a Li-μ$_3$-BH$_3$ R coor-
210 dination {cf. the distance between Li$^+$ and the non-co-
211 ordinating H atom(s) is shorter in **3** · (12-crown-4) than
212 in Li[BH$_4$] · 2DME with values of 2.94(2) and 3.27(2) Å,
213 respectively}. This effect is most likely caused by steric
214 repulsion between the crown ether ligand and the bulky
215 ferrocenyl substituent in **3** · (12-crown-4).

216   The molecular structure of **3** · (12-crown-4) indicates
217 coordination of Li$^+$ to the BH$_3$ group via two hydride
218 bridges to be preferred over Li$^+$· · ·η^5-ferrocene bond-
219 ing. The system was therefore developed further by re-
220 placing the hydrogen substituents with methyl groups,
221 which can be expected to interact less strongly with
222 lithium cations. Moreover, two borate substituents were
223 introduced into the ferrocene core in order to increase
224 the electrostatic attraction of Li$^+$ ions. Single crystals of
225 the resulting compound **4** were obtained from THF
226 [**4** · (THF)$_8$: orthorhombic, *Pca2$_1$*; Fig. 3]; addition of 12-
227 crown-4 was not required. The crystal lattice of
228 **4** · (THF)$_8$ consists of solvent-separated ions with each
229 Li$^+$ being coordinated to four THF molecules in a tet-
230 rahedral fashion. The [1,1′-fc(BMe$_3$)$_2$]$^{2-}$ ion adopts a
231 conformation in which the BMe$_3$ substituents are
232 pointing away from each other [C(11)–COG–COG′–
233 C(21) = 154.1°; COG: centre of gravity of a cyclopen-
234 tadienyl ring].
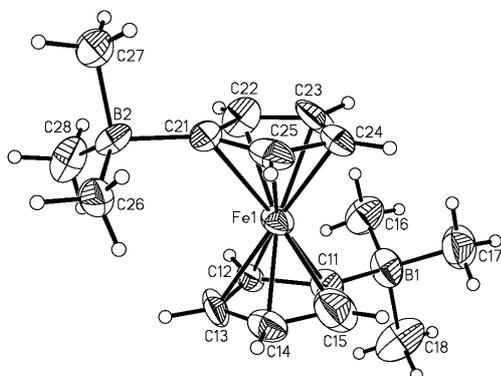
Fig. 3. Molecular structure of the anionic part of compound **4**·(THF)$_8$; thermal ellipsoids are shown at the 30% probability level. Selected bond lengths (Å), angles (°), torsion angles (°) and dihedral angles (°): B(1)–C(11) = 1.734(16), B(2)–C(21) = 1.634(16); C(12)–C(11)–C(15) = 102.7(11), C(12)–C(11)–B(1) = 127.6(10), C(15)–C(11)–B(1) = 129.7(13), C(22)–C(21)–C(25) = 101.7(10), C(22)–C(21)–B(2) = 126.4(11), C(25)–C(21)–B(2) = 131.9(11), COG–C(11)–B(1) = 174.9, COG–C(21)–B(2) = 177.7; C(12)–C(11)–B(1)–C(18) = −94.3(14), C(22)–C(21)–B(2)–C(27) = −88.5(13), C(11)–COG–COG′–C(21) = 154.1; C(11)C(12)C(13)C(14)C(15)// C(21)C(22)C(23)C(24)C(25) = 2.2.

235   Since the desired Li–ferrocene interaction could not
236 be achieved just by increasing the number of negatively
237 charged side-chains, each of the borate groups was
238 equipped with a Lewis-basic pyrazolyl sustituent in or-
239 der to anchor the Li$^+$ ion via a Li–N adduct bond. The
240 lithium pyrazolylborate **5** crystallizes from diethyl ether
241 together with four solvent molecules in the triclinic
242 space group $P\bar{1}$ [**5**·(Et$_2$O)$_4$; Fig. 4]. This time, each Li$^+$
243 ion is bonded to two ether molecules and to the nitrogen
244 lone-pair of the pyrazolyl side-arm [Li(1)–N(32) =
245 1.998(5), Li(2)–N(42) = 1.999(6) Å], which places it on
246 top of the cyclopentadienyl ring [C(12)–C(11)–B(1)–
247 N(31) = 97.7(3)°, C(22)–C(21)–B(2)–N(41) = −81.3(3)°].
248 As a consequence, three lithium–carbon contacts [Li(1)–
249 C(11) = 2.646(5), Li(1)–C(12) = 2.395 (5), Li(1)–C(13) =
250 2.910(6), Li(2)–C(21) = 2.475(5), Li(2)–C(22) = 2.496(5),
251 Li(2)–C(25) = 2.730(6) Å] are established by Li(1) as well
252 as Li(2). As the internal angles of the C(Cp)–B–N–N–Li
253 chains do not depart appreciably from the ideal values
254 of 109° [C(11)–B(1)–N(31) = 105.3(2)°, C(21)–B(2)–
255 N(41) = 106.6(2)°] and 120° [B(1)–N(31)–N(32) =
256 121.9(2)°, N(31)–N(32)–Li(1) = 124.0(2)°, B(2)–N(41)–
257 N(42) = 124.2(2)°, N(41)–N(42)–Li(2) = 122.3(2)°], the
258 molecular framework of the heterotrimetallic aggregate
259 is apparently free of ring strain. Compound **5** is related
260 to the ferrocene-based tris(1-pyrazolyl)borates **V** [26]
261 (Fig. 5), of which several metal complexes [27,28] (in-
262 cluding one Li$^+$ salt) [29] have been synthesized and
263 structurally characterized. In all these cases, the tris(1-
264 pyrazolyl)borate units act as di- or trihapto ligand to-

ward the metal centre, which in turn was never found to interact with the ferrocene backbone. Thus, as is to be expected, Li$^+$–ferrocene bonding appears to be less favourable than lithium-pyrazolyl adduct formation. Some key structural features of **5**·(Et$_2$O)$_4$ resemble Laguna's coordination polymer **VI** [30] (Fig. 5), consisting of 1,1′-ferrocenediyl bis(dialkyldithiocarbamate) ligands [31] and Ag(I) ions. Here, each silver ion is not only bonded to two sulfur atoms of different ferrocene moieties but also to two cyclopentadienyl rings in an η^2 fashion. In 1998, **VI** represented the first example where an η^5-cyclopentadienyl ring of ferrocene was shared with another metal atom via the π-system.
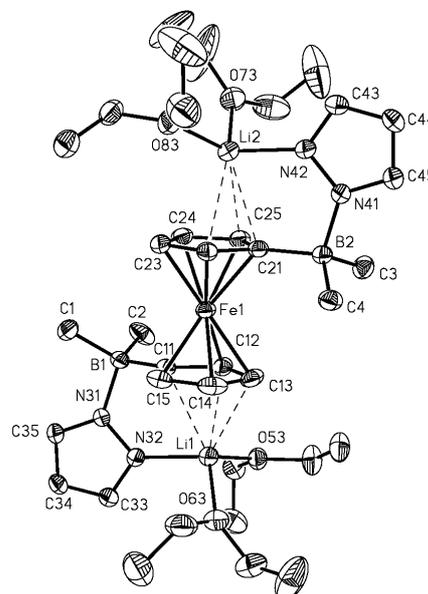

Fig. 4. Molecular structure of compound **5**·(Et$_2$O)$_4$; thermal ellipsoids are shown at the 30% probability level. Selected bond lengths (Å), angles (°) and dihedral angles (°): B(1)–C(11) = 1.617(4), B(1)–N(31) = 1.611(3), B(2)–C(21) = 1.621(4), B(2)–N(41) = 1.610(3), Li(1)–N(32) = 1.998(5), Li(1)–C(11) = 2.646(5), Li(1)–C(12) = 2.395(5), Li(1)–C(13) = 2.910(6), Li(2)–N(42) = 1.999(6), Li(2)–C(21) = 2.475(5), Li(2)–C(22) = 2.496(5), Li(2)–C(25) = 2.730(6); C(12)–C(11)–C(15) = 104.5(2), C(12)–C(11)–B(1) = 128.8(2), C(15)–C(11)–B(1) = 126.7(2), C(22)–C(21)–C(25) = 104.9(2), C(22)–C(21)–B(2) = 127.0(2), C(25)–C(21)–B(2) = 128.1(2), C(11)–B(1)–N(31) = 105.3(2), B(1)–N(31)–N(32) = 121.9(2), N(31)–N(32)–Li(1) = 124.0(2), C(21)–B(2)–N(41) = 106.6(2), B(2)–N(41)–N(42) = 124.2(2), N(41)–N(42)–Li(2) = 122.3(2), N(32)–Li(1)–O(53) = 109.0(3), N(32)–Li(1)–O(63) = 106.3(3), O(53)–Li(1)–O(63) = 111.2(2), N(42)–Li(2)–O(73) = 105.4(3), N(42)–Li(2)–O(83) = 109.4(3), O(73)–Li(2)–O(83) = 107.1(2), COG–C(11)–B(1) = 177.5, COG–C(21)–B(2) = 179.3; C(12)–C(11)–B(1)–N(31) = 97.7(3), C(11)–B(1)–N(31)–N(32) = −35.4(3), B(1)–N(31)–N(32)–Li(1) = 14.2(4), C(22)–C(21)–B(2)–N(41) = −81.3(3), C(21)–B(2)–N(41)–N(42) = 4.0(3), B(2)–N(41)–N(42)–Li(2) = −9.2(4), C(11)–COG–COG′–C(21) = −157.9; C(11)C(12)C(13)C(14)C(15)//C(21)C(22)C(23)C(24)C(25) = 1.0.
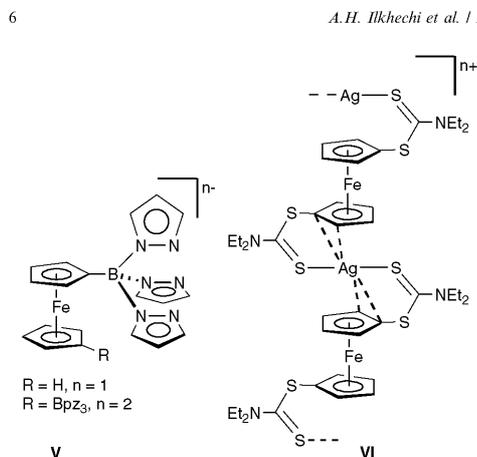
Fig. 5. Ferrocene-based tris(1-pyrazolyl)borate derivatives **V** and a double sandwich silver(I)–ferrocene polymer **VI**.

278   3. Conclusions

279   Inspired by a DFT study on the ferrocene–Li$^+$ com-
280 plex in the gas phase [13], we synthesized three ferrocene
281 derivatives, Li[FcBH$_3$], Li$_2$[1,1'-fc(BMe$_3$)$_2$] and Li$_2$[1,1'-
282 fc(BMe$_2$pz)$_2$] [Fc = (C$_5$H$_5$)Fe(C$_5$H$_4$), fc = (C$_5$H$_4$)$_2$Fe,
283 pz = pyrazolyl], in order to establish the structural motif
284 of a Li$^+$ cation located on top of a ferrocene–Cp ring.
285 Our rationale was to stabilize a potential interaction
286 between both components by introducing negatively
287 charged substituents into the ferrocene core. Initially, it
288 appeared to be of prime importance to use anionic side-
289 chains that do *not* possess electron lone pairs able to
290 compete with the cyclopentadienyl π-system for Li$^+$
291 coordination. Thus, borate substituents were chosen for
292 all further investigations. A crystal structure analysis of
293 Li[FcBH$_3$] · (12-crown-4), obtained from a THF solu-
294 tion after addition of 12-crown-4, revealed hexacoordi-
295 nated Li$^+$ ions bonded to one molecule of crown ether
296 and two hydrogen atoms of the BH$_3$ fragment. Even a
297 hydridoborate fragment is thus preferred over the Cp π-
298 system for Li$^+$ coordination. Attempts to block this
299 coordination site by substitution of methyl groups for
300 the hydrogen atoms failed, since the related methylb-
301 orate crystallized from THF as solvent-separated ion
302 pairs {[Li(THF)$_4$]$^+$}$_2$[1,1'-fc(BMe$_3$)$_2$]$^{2-}$. Single crystals
303 of this compound from less strongly coordinating sol-
304 vents (e.g., diethyl ether) could not be obtained up to
305 now. Contrary to our a priori assumptions, we thus
306 came to the conclusion that a Lewis-basic functionality
307 might be required to stabilize the aimed-for Li$^+$–ferro-
308 cene complex, provided the electron lone pair is part of a
309 side-arm designed to put the Li$^+$ ion on the cyclopen-
310 tadienyl ring. From molecular modelling studies, the

311 rigid pyrazolyl ring appeared to be well-suited for this
312 purpose. Single crystals of Li$_2$[1,1'-fc(BMe$_2$pz)$_2$] were
313 grown from diethyl ether. In this compound, the lithium
314 ions are coordinated by two solvent molecules, the
315 pyrazolyl side-arm and the cyclopentadienyl ring. Thus,
316 Li$_2$[1,1'-fc(BMe$_2$pz)$_2$] can be regarded as a trinuclear
317 segment   of   the   polymeric   structure   [–
318 (C$_5$H$_4$R)Li(C$_5$H$_4$R)Fe–]$_\infty$ with R = BMe$_2$pz. In the fu-
319 ture, we are planning to employ the [1,1'-fc(BMe$_2$pz)$_2$]$^{2-}$
320 ligand in combination with metals other than Li$^+$ for the
321 synthesis of multiple-decker ferrocene-based complexes.

4. Experimental section   322

4.1. General remarks   323

324   All reactions and manipulations of air-sensitive
325 compounds were carried out in dry, oxygen-free argon
326 using standard Schlenk ware. Solvents were freshly
327 distilled under N$_2$ from Na–benzophenone (diethyl
328 ether, THF) prior to use. NMR: Bruker DPX 400,
329 Bruker DPX 250. ^{11}B NMR spectra are reported relative
330 to external BF$_3$·Et$_2$O. Unless stated otherwise, all NMR
331 spectra were run at ambient temperature; abbreviations:
332 s, singlet, d, doublet, vtr, virtual triplet, q, quadruplet,
333 n.r., multiplet expected in the ^{1}H NMR spectrum but
334 not resolved, n.o., signal not observed. Compounds **1**
335 [18] and **2** [19] were synthesized according to the litera-
336 ture procedures.

4.2. Preparation of 3   337

338   For the synthesis of compound **3** see [20]. Single
339 crystals of **3** · (12-crown-4) were grown by gas phase
340 diffusion of diethylether onto a THF solution of **3** to
341 which a small amount of 12-crown-4 had been added.
342 Compound **3** is sensitive to air and moisture. *Anal.* Calc.
343 for C$_{18}$H$_{28}$BFeLiO$_4$ [382.00]: C, 56.60; H, 7.39. Found:
344 C, 56.33; H, 7.12%.

4.3. Preparation of 4   345

346   LiMe (1.6 M, 4.42 mL, 7.07 mmol) in Et$_2$O was ad-
347 ded dropwise with stirring at −78 °C to **2** (0.94 g, 3.54
348 mmol) in Et$_2$O (20 mL). The mixture was slowly
349 warmed to room temperature and the solvent removed
350 under reduced pressure. The remaining highly viscous
351 oily residue was dissolved in THF (20 ml) and the so-
352 lution stored at 5 °C overnight, whereupon dark red
353 X-ray quality crystals of **4** · (THF)$_8$ formed. Yield: 2.79 g
354 (89%). ^{11}B NMR (128.4 MHz, d$_8$-THF): δ −21.8
355 ($h_{1/2}$ = 25 Hz). ^{1}H NMR (400.1 MHz, d$_8$-THF): δ −0.47
356 (s, 18H, CH$_3$), 3.55, 3.75 (2 × n.r., 2 × 4H, C$_5$H$_4$). ^{13}C
357 NMR (100.6 MHz, d$_8$-THF): δ 16.4 (q, $^1J_{BC}$ = 40 Hz,
358 CH$_3$), 67.8, 70.7 (C$_5$H$_4$). The compound is extremely

359 sensitive to air and the crystals lose THF rapidly when
360 isolated at ambient temperature; a decent elemental
361 analysis was therefore not obtained.

362 *4.4. Preparation of 5*

363   Lipz (0.34 g, 4.60 mmol) in Et_2O (15 mL) was added
364 dropwise with stirring at $-78\ ^\circ C$ to **2** (0.61 g, 2.30 mmol)
365 in Et_2O (15 mL). The mixture was slowly warmed to
366 room temperature, filtered and the clear yellow filtrate
367 stored at 5 °C overnight, whereupon yellow–orange
368 X-ray quality crystals of **5** $\cdot (Et_2O)_4$ formed. Yield: 1.52 g
369 (93%). ^{11}B NMR (128.4 MHz, d_8-THF): δ −9.0
370 ($h_{1/2} = 300$ Hz). ^1H NMR (400.1 MHz, d_8-THF): δ 0.11
371 (s, 12H, CH_3), 4.05, 4.19 (2 × vtr, 2 × 4H,
372 $^3J_{HH} = {}^4J_{HH} = 1.6$ Hz, C_5H_4), 5.95 (vtr, 2H, $^3J_{HH} = 1.9$
373 Hz, pz–H4), 7.01, 7.48 (2 × d, 2 × 2H, $^3J_{HH} = 1.7$, 2.0
374 Hz, pz–H3,5). ^{13}C NMR (100.6 MHz, d_8-THF): δ 12.8
375 (n.r., CH_3), 71.0, 72.2 (C_5H_4), 102.8 (pz–C4), 131.9,
376 135.4 (pz–C3,5). The compound is sensitive to air and
377 the crystals lose diethylether rapidly when isolated at
378 ambient temperature; a decent elemental analysis was
379 therefore not obtained.

380 *4.5. X-ray crystal structure analyses*

381   The crystals of **3** $\cdot$ (12-crown-4), **4** $\cdot (THF)_8$ and
382 **5** $\cdot (Et_2O)_4$ were measured on a STOE IPDS II two-circle
383 diffractometer with graphite-monochromated Mo Kα
384 radiation. An empirical absorption correction was per-
385 formed using the MULABS [32] option in the program
386 PLATON [33]. The structures were solved by direct
387 methods using the program SHELXS [34] and refined
388 against F^2 with full-matrix least-squares techniques us-
389 ing the program SHELXL [35]. The crown ether ring in
390 **3** $\cdot$ (12-crown-4) is located on a crystallographic mirror
391 plane and therefore disordered over two equally occu-
392 pied sites. **4** $\cdot (THF)_8$ is a racemic twin composed of two
393 domains with an occupancy ratio of 0.70(6)/0.30(6). All
394 non-H atoms of **3** $\cdot$ (12-crown-4), **4** $\cdot (THF)_8$ and
395 **5** $\cdot (Et_2O)_4$ were refined with anisotropic displacement
396 parameters. The BH_3 hydrogen atoms of **3** $\cdot$ (12-crown-
397 4) could be located in the difference Fourier map and
398 were freely refined. All other H atoms were refined using
399 a riding model.
400   CCDC reference numbers: 230425 [**3** $\cdot$ (12-crown-4)],
401 230426 [**4** $\cdot (THF)_8$], 230427 [**5** $\cdot (Et_2O)_4$].

402 **5. Supplementary material**

403   Crystallographic data for the structural analyses have
404 been deposited with the Cambridge Crystallographic
405 Data Centre, CCDC reference numbers: 230425 [**3** $\cdot$ (12-
406 crown-4)], 230426 [**4** $\cdot (THF)_8$], 230427 [**5** $\cdot (Et_2O)_4$].
407 Copies of this information may be obtained free of

charge from The Director, CCDC, 12 Union Road, 408
Cambridge, CB2 1EZ, UK (fax: +44-1223-336033; 409
email: deposit@ccdc.cam.ac.uk or www: http:// 410
www.ccdc.cam.ac.uk). 411

References 419

[1] N.J. Long, Metallocenes, Blackwell Science, London, 1998. 420
[2] W. Siebert, Angew. Chem. 97 (1985) 924. 421
[3] W. Siebert, Angew. Chem., Int. Ed. Engl. 24 (1985) 943. 422
[4] T. Kuhlmann, S. Roth, J. Rozière, W. Siebert, Angew. Chem. 98 423
    (1986) 87. 424
[5] T. Kuhlmann, S. Roth, J. Rozière, W. Siebert, Angew. Chem., Int. 425
    Ed. Engl. 25 (1986) 105. 426
[6] M.Y. Lavrentiev, H. Köppel, M.C. Böhm, Chem. Phys. 169 427
    (1993) 85. 428
[7] A. Salzer, H. Werner, Angew. Chem. 84 (1972) 949. 429
[8] A. Salzer, H. Werner, Angew. Chem., Int. Ed. Engl. 11 (1972) 930. 430
[9] D.R. Armstrong, A.J. Edwards, D. Moncrieff, M.A. Paver, P.R. 431
    Raithby, M.-A. Rennie, C.A. Russell, D.S. Wright, J. Chem. Soc., 432
    Chem. Commun. (1995) 927. 433
[10] S.M. Schildcrout, J. Am. Chem. Soc. 95 (1973) 3846. 434
[11] S. Nagao, A. Kato, A. Nakajima, K. Kaya, J. Am. Chem. Soc. 435
    122 (2000) 4221. 436
[12] S. Scholz, J.C. Green, H.-W. Lerner, M. Bolte, M. Wagner, Chem. 437
    Commun. (2002) 36. 438
[13] A. Irigoras, J.M. Mercero, I. Silanes, J.M. Ugalde, J. Am. Chem. 439
    Soc. 123 (2001) 5040. 440
[14] M. Scheibitz, R.F. Winter, M. Bolte, H.-W. Lerner, M. Wagner, 441
    Angew. Chem. 115 (2003) 954. 442
[15] M. Scheibitz, R.F. Winter, M. Bolte, H.-W. Lerner, M. Wagner, 443
    Angew. Chem., Int. Ed. Engl. 42 (2003) 924. 444
[16] M. Fontani, F. Peters, W. Scherer, W. Wachter, M. Wagner, P. 445
    Zanello, Eur. J. Inorg. Chem. (1998) 1453. 446
[17] M. Fontani, F. Peters, W. Scherer, W. Wachter, M. Wagner, P. 447
    Zanello, Eur. J. Inorg. Chem. (1998) 2087. 448
[18] T. Renk, W. Ruf, W. Siebert, J. Organomet. Chem. 120 (1976) 1. 449
[19] W. Ruf, T. Renk, W. Siebert, Z. Naturforsch. B 31 (1976) 1028. 450
[20] M. Scheibitz, J.W. Bats, M. Bolte, H.-W. Lerner, M. Wagner, 451
    Organometallics 23 (2004) 940. 452
[21] R.J. Thompson, J.C. Davis Jr., Inorg. Chem. 4 (1965) 1464. 453
[22] H. Nöth, B. Wrackmeyer, in: P. Diehl, E. Fluck, R. Kosfeld 454
    (Eds.), NMR Basic Principles and Progress, vol. 14, Springer, 455
    Berlin, 1978. 456
[23] H.-H. Giese, H. Nöth, H. Schwenk, S. Thomas, Eur. J. Inorg. 457
    Chem. (1998) 941. 458
[24] N. Edelstein, Inorg. Chem. 20 (1981) 297. 459
[25] R.D. Shannon, Acta Crystallogr. Sect. A 32 (1976) 751. 460
[26] F. Jäkle, K. Polborn, M. Wagner, Chem. Ber. 129 (1996) 603. 461
[27] F. Fabrizi de Biani, F. Jäkle, M. Spiegler, M. Wagner, P. Zanello, 462
    Inorg. Chem. 36 (1997) 2103. 463
[28] E. Herdtweck, F. Peters, W. Scherer, M. Wagner, Polyhedron 17 464
    (1998) 1149. 465

8   *A.H. Ilkhechi et al. / Polyhedron xxx (2004) xxx–xxx*

466   [29] S.L. Guo, F. Peters, F. Fabrizi de Biani, J.W. Bats, E. Herdtweck,
467   P. Zanello, M. Wagner, Inorg. Chem. 40 (2001) 4928.
468   [30] O. Crespo, M.C. Gimeno, P.G. Jones, A. Laguna, C. Sarroca,
469   Chem. Commun. (1998) 1481.
470   [31] B. McCulloch, C.H. Brubaker Jr., Organometallics 3 (1984) 1707.
471   [32] R.H. Blessing, Acta Crystallogr. Sect. A 51 (1995) 33.

[33] A.L. Spek, Acta Crystallogr. Sect. A 46 (1990) C34.   472
[34] G.M. Sheldrick, Acta Crystallogr. Sect. A 46 (1990) 467.   473
[35] G.M. Sheldrick, SHELXL-97. A Program for the Refinement of   474
     Crystal Structures, Unversität Göttingen, Göttingen, Germany,   475
     1997.   476

3.8   „C$_5$H$_4$-BR$_2$ Bending in ferrocenylboranes: A delocalized through-space interaction between iron and boron"

M. Scheibitz, M. Bolte, J. W. Bats, H.-W. Lerner, I. Nowik, R. H. Herber, A. Krapp, M. Lein, M. C. Holthausen, M. Wagner

C_5H_4–BR_2 Bending in Ferrocenylboranes:
A Delocalized Through-Space Interaction Between Iron and Boron

Matthias Scheibitz,[a] Michael Bolte,[a] Jan W. Bats,[b] H.-Wolfram Lerner,[a]

Israel Nowik,[c] Rolfe H. Herber,[c] Andreas Krapp,[d] Matthias Lein,[d]

Max C. Holthausen,*[d] and Matthias Wagner*[a]

[a]*Institut für Anorganische Chemie, J.W. Goethe-Universität Frankfurt, Marie-Curie-Strasse*
11, D-60439 Frankfurt (Main), Germany.
Fax: +49 69 798 29260, E-mail: Matthias.Wagner@chemie.uni-frankfurt.de

[b] *Institut für Organische Chemie, J.W. Goethe-Universität Frankfurt, Marie-Curie-Strasse 11,*
D-60439 Frankfurt (Main), Germany.

[c] *Racah Institute of Physics, The Hebrew University of Jerusalem, 91904 Jerusalem, Israel.*
E-mail: Herber@VMS.HUJI.AC.IL

[d] *Fachbereich Chemie, Philipps-Universität Marburg, Hans-Meerwein-Strasse,*
D-35043 Marburg, Germany.
Fax: +49 6421 28 25566, E-mail: Max.Holthausen@chemie.uni-marburg.de

Abstract:

A comparison of the molecular structures of mono-, di- and tetraborylated ferrocenes $FcBR^1R^2$ (R^1/R^2 = Br/Br, Br/Fc, Br/Me, Me/Me, Me/OH, OMe/OMe), $1,1'$-fc(BR^1R^2)$_2$ (R^1/R^2 = Br/Br, Br/Me, OMe/OMe) and $1,1',3,3'$-Fe[$C_5H_3(BMe_2)_2$]$_2$ revealed the boryl substituent(s) to be bent out of the Cp ring plane towards the iron center. The corresponding dip angle α^* decreases with decreasing Lewis acidity of the boron atom, as well as with an increasing degree of borylation at the ferrocene core. This trend is well reproduced by DFT calculations (including the derivative $FcBH_2$ not yet accessible experimentally). A Bader analysis of the electron density topology of $FcBH_2$ (α^* = 26.5°; BP86/TZVP) clearly showed that there is no direct iron-boron bonding in this compound. Instead, strongly delocalized orbital interactions have been identified which involve the boron p-orbital, C$ipso$ of the adjacent Cp ring, d-orbitals at iron and a through-space interaction with the second Cp ring. A second important factor comes from attractive electrostatic interactions which are enhanced upon ligand bending. Cyclic voltammetric measurements on the series $FcBMe_2$, $1,1'$-fc(BMe_2)$_2$, and $1,1',3,3'$-Fe[$C_5H_3(BMe_2)_2$]$_2$ indicate a substantial anodic shift in the oxidation potential of the central iron atom upon introduction of BMe_2 substituents. Addition of 4-dimethylaminopyridine (DMAP) does not just counterbalance this effect but leads to a cathodic shift of the Fe(II)/Fe(III) redox transition far beyond the halfwave potential of parent ferrocene. In the Mössbauer spectra, a continuous decrease of the quadrupole splitting (QS) is observed upon going from parent ferrocene to $FcBMe_2$, to $1,1'$-fc(BMe_2)$_2$, and to $1,1',3,3'$-Fe[$C_5H_3(BMe_2)_2$]$_2$. In contrast, no significant differences are found between the QS values of ferrocene, $FcBMe_2$•DMAP and $1,1'$-fc(BMe_2•DMAP)$_2$.

Keywords

Boron • Ferrocenoid complexes • Density functional calculations • Mössbauer spectroscopy • Cyclic voltametry

Introduction

Mono- [FcBR^{1}R^2; Fc: (C$_5$H$_5$)Fe(C$_5$H$_4$)][1] and 1,1'-diborylated ferrocenes [1,1'-fc(BR^{1}R^2)$_2$; fc: (C$_5$H$_4$)$_2$Fe][2] are highly interesting redox-active Lewis acids, which have already found applications in various areas of research, e.g. oligonuclear metallocene aggregates,[3, 4] charge-transfer polymers,[5-7] difunctional chelators of Lewis bases,[8-10] ferrocene-based tris(1-pyrazolyl)borate ligands,[11-14] B–N- or B–P-bridged *ansa*-ferrocenes,[15-18] and 1,3-dibora-[3]ferrocenophanes[19]. This area of research has been reviewed recently.[20, 21] In all these cases, the question whether a pronounced electronic interaction between the ferrocenyl moiety and the boryl substituent(s) exists is of prime importance. Evidence has been gathered that indicates tetracoordination of boron in FcBR$_2$ to greatly facilitate iron oxidation.[5] Moreover, a crystal structure analysis of FcBBr$_2$ (two crystallographically independent molecules in the asymmetric unit) showed the BBr$_2$ group to be bent towards the iron atom by a dip angle α* of 17.7° (molecule I) and 18.9° (molecule II; α* = 180° – α, α: angle between the geometric center of the carbon atoms constituting the substituted cyclopentadienyl ring, the *ipso* carbon atom C*ipso* and the boron atom).[22] These findings suggest a general opportunity (i) to monitor the coordination state of boron in ferrocenylboranes *via* the Fe(II)/Fe(III) redox potential and (ii) to influence the Lewis acidity of the boron atom by changing the oxidation state of iron.

Here we present a detailed study of selected ferrocenylborane derivatives, which differ greatly in the Lewis acidity of their boryl substituents. Special emphasis is put on the understanding of the question whether there is a direct iron-boron interaction in ferrocenylboranes. To this end we report results from X-ray crystal structure analyses, cyclic voltammetric measurements, Mössbauer spectroscopy, and DFT calculations.

Results and Discussion

Syntheses and NMR-spectroscopic Characterization

All compounds under investigation in the context of this paper are compiled in Figure 1. The prototype computational model FcBH$_2$ (1) was included in the list although it is not

experimentally accessible[23] and the discussion of its structural features has to be restricted to theoretically obtained data (note that the corresponding amine adduct $FcBH_2 \cdot NMe_2Et$ has recently been synthesized and structurally characterized by X-ray crystallography[23]). **1** serves as an important benchmark system since hydrogen atoms can be expected to have only very little steric or electronic impact on the degree of iron-to-boron bonding. Syntheses and X-ray crystal structure analyses of $FcBBr_2$ **(2)**[1, 22] and $1,1'$-$fc(BBr_2)_2$ **(8)**[2, 24] have already been published; selected structural parameters will be quoted below for comparison. The mono- and diborylated ferrocenes **3**[1] and **9**[2] are accessible by methylation of **2** and **8** with neat $SnMe_4$. Sublimation techniques (40 °C, 10^{-3} torr) yielded single crystals of **3** and **9**. The dimethyl derivative **4** was synthesized according to a literature procedure.[1] Amber-colored single crystals of the compound, which is normally obtained from the reaction mixture as a dark red oil, were grown by sublimation (40 °C, 10^{-3} torr). The boron-nitrogen adduct **4•DMAP**[5] crystallized from toluene when the solution was gradually concentrated *in vacuo* (DMAP: 4-(dimethylamino)pyridine). Careful hydrolysis of a benzene solution of $FcB(Me)Br$ **(3)** in the presence of NEt_3 led to the (hydroxy)boryl ferrocene $FcB(Me)OH$, **5**, which bears a π-donating substituent at boron that can be expected to greatly affect any electronic interaction between iron and boron. Single crystals of **5** formed serendipitously from the crude oily compound **4** upon prolonged exposure to air. Both dimethoxyboryl ferrocenes **6** and **11** are readily accessible upon treatment of **2** and **8** with excess $MeOSiMe_3$ in pentane and toluene, respectively. X-ray quality crystals of **6** were grown by vacuum sublimation, whereas **11** was recrystallized from hexane. The diferrocenylborane **7** can be synthesized in high yield from **2** and 1 equiv. of $FcSnMe_3$[25] in benzene at ambient temperature. Crystals were obtained from a saturated toluene solution of **7**. So far, single crystals of the diborylated species **10**[2] and **10•DMAP**[5] are not available for X-ray crystallography. Nevertheless, cyclic voltammetric measurements and Mössbauer spectroscopy provided important information about the electronic structure of these compounds. The tetraborylated ferrocene **12** was synthesized from a mixture of neat $1,1',3,3'$-$Fe[C_5H_3(BBr_2)_2]_2$[26] and neat $SnMe_4$ (8 equiv.) at elevated temperature. Crystalline material was obtained by vacuum sublimation.

NMR spectra of **2**,[1] **3**,[1] **4**,[1] **4•DMAP**,[5] **8**,[2] **9**,[2] **10**[2] and **10•DMAP**[5] have been published previously. When a hydroxy group is substituted for one of the methyl groups in **4** [$\delta(^{11}B) =$

70.5] the ^{11}B NMR resonance is shifted to higher field strengths by 20.9 ppm [**5**: $\delta(^{11}$B) = 49.6].

Replacement also of the second methyl group leads to additional magnetic shielding [**6**: $\delta(^{11}$B)

= 30.0; $\Delta\delta(\mathbf{5}$–**6**) = 19.6 ppm]. There is no difference between the ^{11}B NMR shift of **6** and **11**

[$\delta(^{11}$B) = 30.0]. The ^{11}B NMR resonances of the diferrocenylborane **7** and the tetraborylated

ferrocene **12** appear at 55.3 ppm and 74.8 ppm, respectively. The ^{1}H- and ^{13}C-NMR spectra of

5, **6**, **7**, **11** and **12** exhibit the expected signal patterns and chemical shift values and therefore

do not merit further discussions (see Experimental Section).

X-ray Crystal Structure Determinations

Selected crystallographic data of **3**, **4**, **4•DMAP**, **5**, **6**, **7**, **9**, **11** and **12** are compiled in Table 1.

In compound **3** (monoclinic, $P2_1/n$; Figure 2), the B(Me)Br substituent is disordered over two

positions (occupancies: 68:32), which results in large error margins of bond lengths and angles

involving the methyl carbon atom C(6). Despite of this deficiency, the crystal structure analysis

of **3** was included in this paper, since the most important structural parameter, the dip angle

$\alpha^* = 13.7°$, is not affected. Compound **4** (orthorhombic, $Pbca$; Figure 3) was chosen for a

comparison of the structural characteristics of a ferrocenylborane possessing a three-coordinate

boron center and its respective Lewis base adduct with a four-coordinate boryl group

(**4•DMAP**; monoclinic, $P2_1/c$; Figure 4). Bromoboranes R_2BBr such as **2** and **3** are not suitable

for this kind of investigation, because they tend to form boronium salts $[R_2B(LB)_2]^+Br^-$ upon

reaction with strong Lewis bases LB.[27] The free Lewis acid **4** exhibits a dip angle α^* of 13.0°,

which is reduced to a value of $\alpha^* = 1.1°$ in the B–N adduct **4•DMAP**. At the same time, the

bond between boron and the cyclopentadienyl ring is elongated by 0.080 Å [**4**: B(1)–C(11) =

1.545(4) Å, **4•DMAP**: B(1)–C(11) = 1.625(3) Å]. This effect is less pronounced for the boron-

methyl bonds, which are only 0.047 Å (average value) longer in **4•DMAP** than in **4** [**4**:

B(1)–C(1) = 1.570(4) Å, B(1)–C(2) = 1.578(4) Å; **4•DMAP**: B(1)–C(7) = 1.622(3) Å,

B(1)–C(8) = 1.619(3) Å]. It may therefore be concluded that the increased B(1)–C(11) bond

length in **4•DMAP** is not just caused by a rehybridization of boron (**4**: sp^2-B; **4•DMAP**: sp^3-B),

because this should have similar consequences for all three boron-carbon bond lengths. Even

though the BMe_2 substituent is bent out of the plane of the cyclopentadienyl ring there appears

to be a considerable degree of Cp–B π-bonding in **4**, which no longer exists in the B–N adduct

4•DMAP. The DMAP ligand adopts a position almost orthogonal to the substituted

5

cyclopentadienyl ring [N(1)–B(1)–C(11) = 102.7(2)°, C(12)–C(11)–B(1)–N(1) = –90.5(2)°].

The torsion angle C(11)–B(1)–N(1)–C(2), which characterizes the conformation of the DMAP

plane relative to the $FcBMe_2$ fragment, possesses a value of –85.6(2)°. As expected, a torsion

angle C(3)–C(4)–N(4)–C(41) of only –1.6(3)° is found between the NMe_2 group and the

aromatic ring of the DMAP ligand, indicating N(4) to act as an efficient π-electron donor

towards the pyridine ring, which guarantees a high Lewis basicity of the nitrogen atom N(1).

Despite the fact that even in solution the Lewis acid-base association/dissociation equilibrium

lies quantitatively on the side of the adduct [4•DMAP: $\delta(^{11}B) = –3.0$], a rather long B–N bond

is observed [B(1)–N(1) = 1.670(3) Å]. Currently, 94 adducts between sp^2 nitrogen donors and

three-coordinate boron atoms are included in the Cambridge Crystal Structure File (Release

5.24 of April 2003)[28] with 84 of them possessing shorter B–N bonds than 4•DMAP [cf.

$(C_6F_5)_3$B•DMAP: B–N = 1.602(6) Å[29]]. This does, however, not necessarily indicate $FcBMe_2$

(4) to be a weak Lewis acid since it is known that the correlation between the strength of a

coordinative B–N bond and the length of this bond must not be overemphasized. For example,

the B–N bonds in $FcBMe_2$–pyz–Me_2BFc [B–N = 1.683(5) Å; pyz: pyrazine][6] are not much

longer than those of 4•DMAP despite the fact that the former compound completely dissociates

in solution already at ambient temperature. Another example refers to the triferrocenylborane

adduct Fc_3B•pyridine, which is sterically more congested than 4•DMAP and contains a weaker

Lewis acid but nevertheless possesses a shorter B–N bond of 1.658(4) Å.[30] The hydroxy

derivative 5 (triclinic, P–1, three crystallographically independent molecules 5, 5^A, 5^B; Figure

5) exhibits a dip angle of $\alpha^* = 10.8°$ [5^A: 12.9°, 5^B:10.3°] and a boron-oxygen bond length of

B(1)–O(1) = 1.370(4) Å [5^A, 5^B: 1.378(4) Å]. While the dip angles are significantly larger in 5,

5^A and 5^B than those found for triferrocenylboroxine [$\alpha^* = 8.0°$ (average value at 154 K)], the

B–O bond lengths of both compounds lie in the same range [triferrocenylboroxine: 1.383 Å

(average value at 154 K)]. 5 and 5^B, featuring very similar α^* values, adopt the same

conformation   with   torsion   angles   H(1)–O(1)–B(1)–C(11)   =   176°   and

H(1B)–O(1B)–B(1B)–C(11B) = –180°. The main difference in molecule 5^A ($\alpha^* = 12.9°$) lies

in the fact, that the OH group is rotated by almost 180° about the B–O bond

[H(1A)–O(1A)–B(1A)–C(11A) = –6°]. Each molecule of 5 establishes hydrogen bonds to two

neighbouring molecules with the hydroxy group acting both as hydrogen bond donor and

acceptor, which may in turn have an impact on the degree of O–B π bonding and consequently

influence the dip angle α^*. Compared to **5**, the dip angle of the di(methoxy)boryl ferrocene derivative **6** (triclinic, $P-1$, two crystallographically independent molecules **6** and **6^A**; Figure 6) is further reduced to a value of 6.6° [**6^A**: 5.6°], most likely due to the presence of two π-donating substituents at boron that are, moreover, not involved in any additional hydrogen bonding. In the dinuclear species **7** (monoclinic, $P2_1/c$; Figure 7), the ferrocenyl substituents adopt a *trans* position with regard to the trigonal planar boron atom [dihedral angle between C(1)C(2)C(3)C(4)C(5) and C(21)C(22)C(23)C(24)C(25): 9.2°]. The coplanarity of the two cyclopentadienyl rings appears to be sterically less favorable than the propeller-like arrangement observed for Fc$_3$B [*cis* configuration of the three Fc substituents with regard to the trigonal planar boron atom; dihedral angles between the borylated cyclopentadienyl rings: 39.8°, 42.3°, 43.7°].[31] One problem arises from the fact that the hydrogen atoms attached to C(2) and C(22) of **7** closely approach each other. This becomes evident from an inspection of the angle C(1)–B(1)–C(21), which is stretched to 128.8(2)°. Steric strain is, on the other hand, alleviated as a result of Cp–B–Cp bending [α^* = 11.0° at C(1) and 15.3° at C(21); distance between H(2) and H(22) = 2.154 Å]. The molecular structure of **7** is very similar to that of the related monomeric diferrocenylborane Fc$_2$BH[23], which also shows a bent C$_5$H$_4$–B–C$_5$H$_4$ backbone with α^* values of 12.6° and 14.4° (in contrast to **7**, however, the C$_5$H$_4$–B(H)–C$_5$H$_4$ fragment is disordered about a crystallographic inversion center). Delocalization of cyclopentadienyl π electrons into the empty boron p orbital is more favourable in **7** and Fc$_2$BH than in the twisted compound Fc$_3$B. The molecular structures of the diborylated ferrocenes **9** (triclinic, $P-1$; Figure 8) and **11** (monoclinic, $P2_1/n$; Figure 9) have been determined for comparison with the related monoborylated species **3** and **6**. Most relevant structural features are similar in **3**/**9** on one hand and **6**/**11** on the other [**9**, however, does not suffer from similar B(Me)Br–disorder problems as **3**], apart from the fact that introduction of a second boryl substituent into the ferrocene core leads to reduced C$_5$H$_4$–BR$_2$ bending [**3**/**9**: α^* = 13.7°/9.4°; **6**/**11**: α^* = 6.1°/5.2° (average values)] as has already been observed for **2** [α^* = 18.3° (average value)][22] and **8** (α^* = 9.1°)[24]. In contrast to **8** and **9**, which are centrosymmetric with perfectly staggered Cp ligands, both crystallographically independent molecules of **11** have their B(OMe)$_2$ substituents pointing into the same direction [**11**: C(1)–COG–COG*–C(11) = 1.4°; **11^A**: C(1A)–COG–COG*–C(11A) = 4.6°]. The molecular structure of tetraborylated **12** (orthorhombic, $P2_12_12$; Figure 10) possesses C_2-symmetry in the crystal lattice and closely

resembles the structure of $1,1',3,3'$-$Fe[C_5H_3(BBr_2)_2]_2$[26]. The dip angles in **12** ($\alpha^* = 6.1°, 9.3°$) are considerably smaller than in monoborylated **4** ($\alpha^* = 13.0°$) as has already been observed in the case of $2/8/1,1',3,3'$-$Fe[C_5H_3(BBr_2)_2]_2$ [$\alpha^* = 18.3° / 9.1° / 4.2°$ (average values)] and **6/11** [$\alpha^* = 6.1° / 5.2°$ (average values)].

The conformation adopted by the BR^1R^2 substituent(s) in **2–9**, **11**, **12** with respect to the ferrocenyl fragment brings the formally empty boron-centered p-orbital(s) into a position parallel to the filled p-orbital(s) of the ipso carbon atom(s). However, any Cp-B π interaction is likely to be disfavoured by bending of the boryl substituent out of the plane of the cyclopentadienyl ring towards the iron atom, as it is observed for **2–9**, **11**, and **12**. The question thus arises, whether this structural feature is caused by a direct iron-boron interaction, which could also lead to a transfer of electron density into the boron p-orbital and thus outweigh the reduction of Cp–B π bonding. As far as the monoboryl ferrocenes are concerned, a gradual decrease of α^* values is observed (Figure 11) upon going from **2** [$\alpha^* = 18.3°$ (average value)] to **3** ($\alpha^* = 13.7°$), **4** ($\alpha^* = 13.0°$), **5** [$\alpha^* = 11.3°$ (average value)] and **6** [$\alpha^* = 6.1°$ (average value)]. The Fe$\cdots$B distances are found to increase in the same order [**2**: 2.840 Å / 2.856 Å, **3**: 2.971(8) Å, **4**: 3.008(3) Å, **5**: 3.014(4) Å / 3.056(3) Å / 3.057(3) Å, **6**: 3.179(3) / 3.197(3) Å]. In the diferrocenyl borane **7**, α^* values of 15.3° and 11.0° are observed corresponding to Fe$\cdots$B bond lengths of 2.950(2) Å and 3.022(2) Å, respectively. Here, two Fc–B fragments of identical chemical composition differ in their dip angles by as much as 4.3°, which indicates a rather shallow potential energy surface related to the Cp–BR^1R^2 bending mode. This conclusion is further supported by the significantly different α^* values of the three crystallographically independent molecules of compound **5** ($\Delta\alpha^* = 2.6°$). Smaller dip angles as in the monoborylated molecules **2-7** are found in the corresponding $1,1'$-diborylated species **8** ($\alpha^* = 9.1°$), **9** ($\alpha^* = 9.4°$), and **11** (**11**: $\alpha^* = 4.2°, 5.0°$; **11**[A]: 5.4°, 6.0°). It has to be mentioned that compound **2**, possessing the largest dip angle α^*, shows the shortest B–Cp bond [17.7° / 1.474(9) Å and 18.9° / 1.482(8) Å for the two crystallographically independent molecules], while **4**, possessing a smaller dip angle ($\alpha^* = 13.0°$), shows a much longer B–Cp bond of $B(1)$–$C(11) = 1.545(4)$ Å. This correlation, which can be seen in most other ferrocenylborane derivatives, is inverse to the trend expected using the simple picture of competing Fe–B σ- and

Cp=B π interactions. We will investigate the electronic basis of these observations by quantum chemical means further below.

To get a more complete overview, two other series of closely related ferrocenylborane derivatives have also to be considered: (i) Crystal structure analyses of triferrocenyltriselenatriborinane [(FcB)$_3$Se$_3$],[32] triferrocenylboroxine [(FcB)$_3$O$_3$][33] and triferrocenylborazine [(FcB)$_3$(NH)$_3$][33] revealed dip angles α^* of 10.5°, 7.9° and 5.1°, respectively. (ii) Apart from **7** [α^* = 13.2° (average value)] and Fc$_2$BH [α^* = 13.5° (average value)], two other diferrocenylboranes have been structurally characterized. These are the chloro compound ClB(FcSiMe$_2$Cl)$_2$ [α^* = 11.9° (average value), the borylated cyclopentadienyl rings and the BCl bridge are disordered over two positions with occupancies of 50:50][34] and the oxo-bridged tetraferrocene aggregate (ClMe$_2$SiFc)$_2$B–O–B(FcSiMe$_2$Cl)$_2$ [α^* = 4.5° (average value)][34]. In both series, the dip angles decrease as the degree of B–X π bonding increases (X = Se, O, N; Br, Cl, O). It is worth mentioning in this context, that the smallest dip angles of all three-coordinate ferrocenylboranes investigated so far have been found for 1,1'-fc[B(N^{i}Pr$_2$)$_2$]$_2$ which bears two strongly π-donating diisopropylamino groups at each of its boryl substituents (α^* = −1.8°, 2.8°).[24] In this special case, however, the steric bulk of the N^{i}Pr$_2$ groups might have a strong influence on the size of α^* as well.

The data collected in this paragraph clearly reveal a causal relationship between the Lewis acidity of the boryl group in ferrocenylboranes and the dip angle α^*: The more Lewis acidic the BR^{1}R^2 substituent is, the more it is bent towards the iron atom. This effect is less pronounced in 1,1'-diborylated and 1,1',3,3'-tetraborylated ferrocenes than in the monoborylated species.

Electrochemical measurements

All potential values are referenced against the FcH/FcH$^+$ redox couple; where necessary, literature data used for comparison have been recalculated for FcH/FcH$^+$ as the reference. The cyclic voltammograms of **4**, **10** and **12** (CH$_2$Cl$_2$, 0.1 M [NBu$_4$][PF$_6$]) exhibit redox transitions with half-wave potentials of $E^{\circ\prime}$ = +0.09 V, $E^{\circ\prime}$ = +0.26 V and $E^{\circ\prime}$ = +0.39 V, respectively. When the scan rates are varied from 0.02 Vs^{-1} to 1.00 Vs^{-1}, the current ratio i_{pc}/i_{pa} is constantly equal to 1, the current function $i_{pa}/v^{1/2}$ remains constant and the peak-to-peak separation does not

depart appreciably from the value of 59 mV theoretically expected for an electrochemically reversible one-electron process. Thus, any possible structural reorganizations accompanying iron oxidation in **4**, **10** and **12** must be fast and reversible. Introduction of BMe_2 substituents into the ferrocene core increases the oxidation potential of the central iron atom. This anodic shift, which is apparently additive, may be attributed to the π electron-withdrawing nature of three-coordinate boryl groups. It is important to note that addition of DMAP (1 equiv. for **4**, 2 equivs. for **10**) with subsequent B–N adduct formation does not just neutralize this effect but leads to a cathodic shift of the Fe(II)/Fe(III) redox transition far beyond the halfwave potential of parent ferrocene [$E°'$(**4**•DMAP) = −0.40 V (CH_2Cl_2), $E°'$(**10**•DMAP) = −0.66 V (CH_2Cl_2)].[5]

^{57}Fe-Mössbauer Spectroscopy (MS)

As is true for all neutral ferrocene-related compounds, the Mössbauer spectra of **4**, **4**•DMAP, **10**, **10**•DMAP, and **12** consist of simple well-resolved doublets which can be characterized in terms of their isomeric shift (IS), quadrupole splitting (QS), and area under the resonance curve (A). As typical example the spectrum of **4** at 90 K is shown in Figure 12; MS parameters of all compounds investigated are summarized in Table 2.

Compounds 4 and 4•DMAP: Similar to all other derivatives examined in this study, the IS of **4** (0.524 ± 0.004 mm s^{-1} at 90 K) is very similar to that of parent ferrocene (0.537 ± 0.001 mm s^{-1} at 90 K). In consonance with previous observations[35-37] ring substitution of a $B(CH_3)_2$ group for a hydrogen atom has only a small effect on the s-electron density at the metal center. The effective vibrating mass[38] of the metal atom (M_{eff}) calculated from the temperature dependence of the IS, is 107 Daltons. The difference between this value and the "bare" iron atom mass of 57 Daltons is a measure for the covalency of the iron-ligand interaction in these ferrocenoids. The temperature dependence of lnA, which can be related to the mean-square-amplitude-of-vibration $<x^2>$ of the iron atom, is a linear function over the temperature range of 86-273 K. From the temperature dependence of the IS and lnA we calculate a Mössbauer lattice temperature[38] Θ_M of 87 K. It is also worth mentioning that the iron atom in **4** evidences only a small vibrational anisotropy in the crystalline phase, in consonance with the ORTEP representation in Figure 3. The QS of **4**, (2.309 ± 0.004 mm s^{-1} at 90 K), is significantly smaller than that of ferrocene (2.418 mm s^{-1} at 90 K). The relationship between the QS of ferrocene

derivatives and the electron withdrawing properties of the ring substituents has been discussed in detail previously.[39-41] We note an interesting observation connected to the QS parameter. When the sample, which had originally been cooled rapidly from room temperature to 87 K, is examined in a warming mode, the QS has a value of ~2.21 mm s^{-1} and is essentially temperature independent up to 200 K. Above this temperature, QS rapidly rises to 2.27-2.31 mm s^{-1} and remains at this higher value even if the sample is subsequently cooled back to 90 K. This sequence is summarized graphically in Figure 13. When this sample is warmed to about 310 K for periods of up to 60 minutes, cooled, and then re-examined, the higher QS value of ~2.31 mm s^{-1} is observed, essentially independent of temperature. To explain these findings we note that for the glove-box transfer (*vide infra*) the sample had been warmed above its melting point. Upon rapid cooling it first sets to a supercooled liquid at 77 K, which is then annealed to the crystalline state upon slow warming to 210 K. Somewhat counter-intuitively the QS parameter observed for **4•DMAP** (2.344 ± 0.003 mm s^{-1}) is rather similar to the value measured for **4** even though a pronounced difference of 0.49 V is observed in the redox potentials of both compounds (**4**: $E^{\circ\prime}$ = +0.09 V, **4•DMAP** $E^{\circ\prime}$ = −0.40 V). In the case of solid **4•DMAP**, MS spectra were acquired up to 340 K. Such measurement were not possible for the free **4** due to its lower melting point. The high temperature spectra of **4•DMAP** revealed a marked deviation from linearity in the ln f plot, especially for temperatures above 250 K, as is also observed in the corresponding data for **4** (cf. Figure 14). This non-linearity presumably arises from the onset (upon warming) of additional vibrational modes of the iron atom, associated with the onset of ring rotation in the monoborylated species.

Compounds 10 and 10•DMAP. The MS parameters of **10** and 10•DMAP are summarized in Table 2. M_{eff} of iron is about 22 % larger in **10** than the M_{eff} calculated for monoborylated **4**. However, Θ_M is 23 % lower in **10** as compared to **4**, consistent with the observation that **10** is a liquid at room temperature, while **4** is a semi-solid. The QS parameter is significantly smaller for **10** compared to **4**, presumably due to the presence of two rather than one electron withdrawing boryl substituents. The vibrational anisotropy observed for the iron atom in **10** is illustrated in Figure 14. Especially at higher temperatures, the Mössbauer spectra show a temperature-dependent intensity ratio, R, which is related to the change in the motional anisotropy $[k^2<x^2_{para}> - k^2<x^2_{perp}>]$ of the iron atom.[42] On the other hand, the recoil-free

11

fraction, f, is related to the average square of the motional amplitude by the relation $f = -\exp(k^2<x^2>)$, where k is the wave vector of the 14.4 keV radiation. Thus, from R and f it is possible to calculate mean square amplitude of vibration parallel and perpendicular to the molecular symmetry axis, assuming that $k^2<x^2_{ave}> = 1/3 \ k^2<x^2_{para}> + 2/3 \ k^2<x^2_{perp}>$], cf. Figure 14. At temperatures below 170 K the difference between $[<x^2_{perp}>]^{1/2}$ and $[<x^2_{para}>]^{1/2}$ is small but becomes appreciable at higher temperatures (e.g., 0.12 Å at 190 K and 0.16 Å at 210 K). Moreover, as illustrated in Figure 14 this anisotropy is a reflection of the greater $[<x^2_{perp}>]^{1/2}$ compared to the $[<x^2_{para}>]^{1/2}$ at the higher temperatures. In contrast to the 4/4•DMAP couple with rather similar QS values, 10•DMAP has a QS value 0.257 mm s^{-1} larger than the free Lewis acid 10. As was true for 10 and 4, the iron atom vibrational anisotropy is somewhat larger in 10•DMAP than in 4•DMAP. As for 4 it was not possible to obtain MS spectra at temperatures higher than 230 K due to the liquid nature of 10 at room temperature.

Compound 12: Because this compound melts to a red liquid just above room temperature, MS data were acquired only in the range 86 < T < 273 K (Table 2). Yet, adequate temperature-dependent parameters could readily be extracted from this measurements. The IS(T) plot is well fitted by a linear regression [slope = $-(4.02 \pm 0.11) \times 10^{-4}$ mm sec^{-1} K^{-1}] with a correlation coefficient of 0.997 for 13 data points. The corresponding M_{eff} is 104 $\pm$ 1 Daltons. Likewise, the temperature dependence of the recoil-free fraction is linear over the whole temperature range. From these two slopes an effective lattice temperature as "seen" by the iron atom of $\Theta_M = 97$ K can be extracted. Moreover, data acquired in a warming/cooling cycle (between 90 K and 273 K) show the MS hyperfine parameters to be completely reversible. A moderate vibrational anisotropy is evident in the MS data; however, because of the limitations in the accessible temperature range we refrain from translating this to a quantitative measure[43] of the vibrational amplitudes parallel and perpendicular to the major symmetry axis passing through the metal atom. The magnitude of the QS parameter of 12 (1.891 $\pm$ 0.004 mm sec^{-1} at 90 K) is the smallest observed for the dimethylboryl complexes examined in this study. An investigation of the hypothetical tetraadduct 12•DMAP would be desirable. Unfortunately we found this compound experimentally inaccessible, because the ferrocene backbone of 12 decomposed upon addition of 4 equiv. of DMAP as indicated by NMR spectroscopy control .

Quantum Chemical Calculations

We commence this theoretical section with a calibration of methods for the description of molecular geometries and binding energies (cf. Experimental and Computational Details section below). The reliability of a variety of density functional approaches to correctly describe donor-acceptor bonding situations involving boron Lewis acids and nitrogen Lewis bases has been questioned recently.[44] As the DMAP complexes investigated in this study involve this bonding motif we deemed a careful calibration for the present class of systems particularly important. As a first benchmark, calculated structures at selected levels of theory are compared with X-ray crystallographic results. Due to the lack of experimental calorimetric data for the present class of compounds, we take for four representative boron-nitrogen donor/acceptor complexes accurate binding energies computed at post-HF levels of theory as an exacting testing ground to benchmark the density functional approaches in the description of binding energies.

Calibration for Molecular Structures and Binding Energies: We tested several functionals in combination with two different basis sets with respect to the quality of structure predictions by comparison with X-ray crystal structure analyses. Apart from our general interest to learn about advantages and shortcomings of contemporary implementations of Kohn-Sham methods,[45] this comparison aims at an identification of a reliable, yet computationally efficient approach to describe structures of borylated ferrocenes. Figure 15 illustrates the key geometric parameters discussed in the following.

Several systematic trends become obvious from the data compiled in Tables 3-9. Most notably, for **2** and **3** use of the very small DGA1 fit basis in RI calculations results in optimized structures exhibiting a strong pyramidalization of the BR_2 groups (cf. Tables 4 and 5, torsion angles γ^*, δ, and δ'). Independent of the GGA employed, use of the DGA1 fit basis results in deviations of these angles by about 20° with respect to the experimental structure, which exhibits an essentially planar BBr_2 group. Also the calculated B−Br bond lengths are significantly elongated exceeding the averaged experimental value by 0.099 Å to 0.122 Å. All other computations employing either the pure (non-RI) GGAs or both hybrid functionals, result in only minor deviations from experiment (cf. Table 4). Remarkably, BP86/TZVP(RI)

13

geometry optimizations on **2** and **3** using the TZVP-J Coulomb fit basis of Ahlrichs and coworkers[46] for all atoms within the Turbomole program yields geometries identical to the non-RI BP86/TZVP results. Thus, the pronounced deviations found in Gaussian RI calculations on **2** and **3** can clearly be identified as a problem in the atomic DGA1 fit basis for Br. In the following we nevertheless report Gaussian RI results obtained with the DGA1 fit basis to document the performance of this approach.

A statistical analysis of the data compiled in Tables 3-9 reveals additional, although less spectacular effects on optimized geometries introduced by the DGA1 fit basis. For example the Fe–X and the Fe–C*ipso* distances become significantly shorter on average by 0.027 and 0.023 Å, respectively. Hence, it appears as if in addition to interactions with the bromine atoms, also the rather remote interaction between the iron atom and the Cp rings are error-prone due to use of the DGA1 fit basis. The B–C bond as well as the angles α^*, β^*, and γ^* in turn are hardly affected at all by the RI procedure.

When going from the SVP to the TZVP basis, the Fe–X and Fe–C*ipso* bond lengths are elongated on average by 0.011 or 0.006 Å, respectively, whereas the B–C*ipso* bond length becomes shorter on average by −0.008 Å. By the same token, α^* becomes smaller on average by merely −1.4°. Other geometry parameters are hardly affected at all. These trends are nearly independent of the method used and also the choice of the DGA1 fit basis in RI computations has no appreciable influence. Hence, general effects of the one-particle basis are somewhat less pronounced.

From a comparison of computed and experimental data for key geometry parameters (Fe–C*ipso*, B–C*ipso*, and α^*, cf. Table 10) we can draw the following conclusions: a) Judged from the mean absolute deviations, an excellent description of the Fe–C*ipso* bond length is found for the BP86 and the HCTH functional in combination with both, the SVP and the TZVP basis sets. Use of the DGA1 fit basis increases the mean deviations significantly and is therefore discouraged. The hybrid functionals B98 and B3LYP tend to overestimate the Fe–C*ipso* bond length. b) All methods show particularly large deviations for the B–C*ipso* bond length in **2**. The experimentally determined B–C*ipso* bond length of **2** (average value 1.479 Å)

14

is significantly shorter than the corresponding length in all other derivatives investigated here (average value 1.544 ± 0.02 Å). In contrast, all theoretically obtained B–C*ipso* bond lengths for **1-4**, fall within the range of 1.517 Å and 1.563 Å. Therefore we tend to attribute the poor agreement between experiment and theory for **2** to artifacts of the crystal structure analysis. Excluding this species from the comparison results in a significantly improved overall agreement between experiment and theory and we find an excellent performance for all functionals in combination with the TZVP basis set. c) For the present study the accurate description of the dip angle α^* is crucial. From the data compiled in Table 10 we note that this parameter is generally underestimated. Again errors are most pronounced for **2**. As the bending potential for changes of α^* by 5° to 10° about the minimum structure is evidently very shallow (less than 1 kcal mol^{-1}, see below), crystal packing effects might account for the observed deviations in the comparison between experiment and theoretical data.

Finally we note inconsistencies for some method/basis set combinations between the optimized geometries of the **4•DMAP** donor/acceptor complex and the experimentally determined structure. Although the experimental geometry, which shows a perpendicular orientation ($\varepsilon =$ 87°, cf. Table 9) of the DMAP ring with respect to the B–C*ipso* bond, was used as a starting point for all calculations, geometry optimizations at the BP86/TZVP, HCTH/SVP, B3LYP/SVP, and B3LYP/TZVP levels of theory led to a rotation of the DMAP subunit about the B–N bond (by $\varepsilon =$ 180°, 136°, 178°, and 180°, respectively). At all other levels both, the perpendicular and the collinear conformer were found. However, the collinear conformer was determined to be more stable than the perpendicular conformer (between 0.1 and 1.3 kcal mol^{-1}). Other geometry parameters, such as the bond angle ζ or the B–N bond length, are almost independent of the orientation of the DMAP ring. We compare in Table 9 the geometries of the perpendicular conformer with experiment where possible. Given the negligible energy difference between the two conformers identified, it appears justified to use the collinear conformer for comparison for those method/basis set combinations not suitable to locate the perpendicular conformer identified experimentally.

Compared to the experimental structure all optimized geometries of **4•DMAP** show too long B–N bonds (+0.031 Å on average). This trend is significantly more pronounced if the DGA1 fit

15

basis is used but quite independent of the one-particle basis set quality. In line with the findings of Gilbert,[44] we find a superior performance of the pure BP86 and the B98 hybrid compared to the B3LYP functional, irrespective of the basis set quality employed. The HCTH GGA suffers from errors even larger than those observed in the B3LYP structures.

Table 11 shows the computed binding energies (total energy differences) and optimized B−N bond lengths for the donor-acceptor complexes $BH_3 \bullet NH_3$, $BH_3 \bullet$pyridine, $BMe_3 \bullet NH_3$, and $BMe_3 \bullet$pyridine. For $BH_3 \bullet NH_3$ we performed CCSD(T) geometry optimizations employing Dunning's correlation consistent cc-pVDZ, cc-pVTZ, and cc-pVQZ basis sets. At the extrapolated basis set limit (cf. Experimental Section and Computational Details below) we obtain a binding energy of 31.7 kcal mol^{-1}, which serves as the highest level benchmark for this complex. These calculations were feasible only for the $BH_3 \bullet NH_3$ complex due to the extraordinary computational scaling of CCSD(T) calculations with system and basis set size. We also performed geometry optimizations at the RIMP2 level in combination with the same set of Dunning bases, and at the extrapolated basis set limit we obtain a binding energy of 32.3 kcal mol^{-1}, which is in pleasing agreement with the CCSD(T) value. This computationally efficient approach could be used to investigate also the larger complexes $BH_3 \bullet$pyridine, $BMe_3 \bullet NH_3$, and $BMe_3 \bullet$pyridine. As a third post-HF approach we employed the CBS-QB3 extrapolation scheme, which yields a binding energy of 31.8 kcal mol^{-1} for the $BH_3 \bullet NH_3$ complex in almost perfect agreement with the CCSD(T) extrapolated basis set limit. The binding energies of $BH_3 \bullet NH_3$, $BH_3 \bullet$pyridine, $BMe_3 \bullet NH_3$, and $BMe_3 \bullet$pyridine obtained at the RIMP2 basis set limit and by CBS-QB3 calculations agree within 2 kcal mol^{-1} (Table 11). Although the CBS-QB3 scheme relies on the use of B3LYP geometries, which are evidently of inferior quality at least for the larger complexes (compared to RIMP2/cc-pVQZ geometries, differences in the B−N bond length amount to up to 0.043 Å for $BMe_3 \bullet$pyridine), we note a fair overall agreement between both methods in the evaluation of binding energies (within 2 kcal mol^{-1}). Apparently, the B−N stretching potential is so weak that too long B−N distances lead to only minor consequences for computed binding energies within the CBS-QB3 scheme. In any case, in the present context we tend to consider the RIMP2 data generally more reliable to describe bonding in this class of donor-acceptor complexes, and in the following we use the

RIMP2 extrapolated basis set limit data to assess the performance of the various density functionals employed.

The benchmark computations reveal that pyridine forms stronger bonds to monoboranes than NH_3 (to BH_3 by 4.2 kcal mol^{-1} and to BMe_3 by 3.1 kcal mol^{-1}). Thus, in agreement with chemical intuition (e.g., $pK_B(NH_3)$ = 9.25; pK_B(Pyridine) = 5.21), we find that pyridine is a stronger Lewis base than NH_3. When going from BH_3 to BMe_3, in turn, the computed binding energies drop significantly (NH_3: -13.2 kcal mol^{-1} and pyridine: -14.3 kcal mol^{-1} at the RIMP2 basis set limit), illustrating the weaker Lewis acidity of BMe_3 as compared to BH_3.

For the BH_3•NH_3 adduct, all density functionals investigated yield binding energies in fair agreement with the post-HF benchmarks if used in combination with the TZVP basis set: the largest differences occur for the HCTH and the B3LYP functional, which both underestimate the binding energy by about 2 kcal mol^{-1}. Use of the smaller SVP basis constantly increases the computed binding energies by about 5 kcal/mol, which can probably be attributed to significant basis set superposition errors. Use of the DGA1 Coulomb fit basis has a negligible influence on computed binding energies. The stronger binding of pyridine to BH_3 is reproduced at all density functional levels with the TZVP basis, but compared to the benchmark data, the increase in bond strength is substantially underestimated. With the SVP basis all functionals yield essentially identical binding energies for both complexes. B–N bond strengths in BMe_3 complexes are severely underestimated at all density functional levels and, even worse, the stronger binding of pyridine as compared to NH_3 documented in all benchmark calculations is not reproduced. This is a verification of the findings of Gilbert, who identified severe shortcomings of various flavours of DFT in the description of binding energies in this class of donor-acceptor complexes, with more pronounced problems the larger the degree of alkyl substitution.[44] We therefore attribute the discrepancies in the optimized geometries of the 4•DMAP complexes noted above to a pronounced tendency of all functionals investigated to underestimate B–N bond strengths. It is interesting to note that in particular the highly parameterized HCTH functional suffers most from these problems, but also the otherwise highly successful B3LYP hybrid functional fails dramatically. While the origins of these problems evade an unequivocal interpretation and deserve an in-depth investigation of its own

right, we conclude for the present study that we should moderate our expectations with respect to the accuracy of the current functionals to describe B–N bonding situations.

In summary, notwithstanding the problems documented above in the description of B–N bond strengths, which strike all functionals more or less equally and for which no cure is obvious at present, we have identified the BP86/TZVP level in combination with the Ahlrichs TZVP-J Coulomb fit basis as a computationally efficient level of theory, which performs very well in the structure prediction of borylated ferrocenes. All results reported in the following have been obtained at this level of density functional theory using its highly efficient implementation in the TURBOMOLE program.

Computed redox potentials - correlation with cyclic voltammetric and ^{57}Fe-Mössbauer data: As a qualitative approximation to assess the results from the cyclic voltammetric experiments by quantum chemical means we computed the adiabatic ionization potentials (IEs) at the BP86/TZVP/RI(TZVP-J) level employing the COSMO continuum model (solvent dichloromethane, dielectric constant at room temperature ε = 8.93). For parent ferrocene we compute an adiabatic ionization energy (IE) of 5.14 eV, which is used as reference in the following discussion. Introduction of BMe_2 substituents into the ferrocene core leads to an increase in the corresponding computed ΔIEs (data relative to FcH = 0.00 eV: **4** = 0.16 eV, **10** = 0.25 eV, **12** = 0.40 eV, cf. Table 12). We assign this effect, which is also reproducible with other substituents BRR' (R,R' = Me, F, Cl, Br, I, OH, see Table 12), to the π-electron withdrawing nature of the three coordinate boron atom. The only exception is the $FcB(NH_2)_2$ derivative, for which we find an IE of −0.08 eV relative to FcH. Here, the electron deficiency of the boron atom is obviously fully compensated already by the two π-electron donating NH_2 groups. This interpretation is in line with the fact that we find in the neutral $FcB(NH_2)_2$ only a minute dip angle α^* = 0.4° and an almost planar $B(NH_2)_2$ moiety, which is tilted by 24° out of the plane of the adjacent Cp-ring. Hence it appears that the above-mentioned corresponding properties of the 1,1'-fc[B(N^{i}Pr$_2$)$_2$]$_2$ derivative are not only caused by steric bulk, but rather are a consequence of efficient N→B π-donation. The increased IE of **4** agrees nicely with the experimental observation of an anodic shift of its redox potential ($E^{0'}$ = +0.09 V) relative to the FcH reference. As stated above the QS of ferrocenes in Mössbauer spectroscopy becomes

smaller upon substitution by electron withdrawing groups. The QS value of **4** (-0.109 mm s^{-1} at 90 K vs. FcH) thus correlates both with the calculated ΔIE and the anodically shifted redox potential. Considering also the di- and tetraborylated derivatives, common trends become apparent (a) for redox potentials, which are shifted monotonously to more positive values along the series FcH ($E^{0'} = 0.00$ V), **4** ($E^{0'} = +0.09$ V), **10** ($E^{0'} = +0.26$ V), and **12** ($E^{0'} = +0.39$ V) and (b) for the quadrupole splittings, which show a corresponding decrease (Figure 16) from FcH (QS $= 2.418$ mm s^{-1}) to **4** (QS $= 2.309$ mm s^{-1}) to **10** (QS $= 2.082$ mm s^{-1}), and finally to **12** (QS $= 1.891$ mm s^{-1}). Adduct formation of **4** and **10** with DMAP leads to a cathodic shift of the redox potentials of **4•DMAP** ($E^{0'} = -0.40$ V vs. FcH/FcH$^+$ or $E^{0'} = -0.49$ V vs. **4/4$^+$**) and **10•DMAP** ($E^{0'} = -0.66$ V vs. FcH/FcH$^+$ or $E^{0'} = -0.92$ V vs. **10/10$^+$**). This trend is well reproduced by the calculated ΔIEs (**4•DMAP**: -0.43 eV vs. FcH/FcH$^+$ or -0.59 eV vs. **4/4$^+$**; **10•DMAP**: -0.60 vs. FcH/FcH$^+$ or -0.85 eV vs **10/10$^+$**). Even though it has experimentally been established that electron donating substituents at FcH cause an increase in the QS relative to ferrocene,[40] the Mössbauer data obtained here for **4•DMAP** (QS $= 2.344$ mm s^{-1}) and **10•DMAP** (QS $= 2.339$ mm s^{-1}) do not show any significant differences to FcH (QS $= 2.418$ mm s^{-1}).

As a means to understand the trends observed in the present Mössbauer measurements we used the qualitative relation (1) established by Silver and coworkers,[39, 40] which relates the quadrupole splitting of iron sandwich compounds to the iron $3d$ orbital population.

$$QS \sim 2p_2 - p_1 \tag{1}$$

Given an orientation of the Fe–COG bond in (substituted) ferrocenes along the z-axis, p_1 represents the collective electron population of the $3d_{xz}$ and $3d_{yz}$ orbitals, and p_2 that of the $3d_{x^2-y^2}$ and $3d_{xy}$ orbitals. Essentially, an increase in p_1 corresponds to a stronger π donation from the Cp ligands to the metal giving rise to negative contributions to the QS, whereas a larger p_2 value indicates weaker δ back-bonding from the metal to the ligand (i.e. more density remains at the iron), leading to positive QS contributions with twice the effect compared to p_1.[47] Both, p_1 and p_2 are sensitive to substitution at the Cp-rings, whereas other iron valence orbitals ($3d_{z^2}$, $4s$, and $4p$) are considered to provide only negligible contributions to the QS.[39, 40] Comparison

of p_1^{FcH} and p_2^{FcH} obtained for FcH with the p_1 and p_2 populations in substituted ferrocenes leads to an expression for the corresponding changes in the QS according to (2).

$$\Delta QS \sim \Delta p = [2(p_2 - p_2^{FcH}) - (p_1 - p_1^{FcH})] \tag{2}$$

To allow for a consistent comparison of iron d-orbital occupations we oriented all optimized structures from the TURBOMOLE BP86/TZVP/RI(TZVP-J)+COSMO calculations of the neutral species considered in the following by coordinate transformation in the same way (iron at the origin, Fe–COG along the z-axis, C$ipso$ in the yz plane) and performed BP86/TZVP single point calculations to obtain the orbital populations by means of the natural population analysis (NPA) as implemented in the Gaussian program.[48, 49] We note in passing that populations obtained from a Mulliken analysis gave nearly identical results for Δp. The results obtained for Δp according to eq. (2) are shown in Table 13. Although it is evident that no unique proportionality factor connects the computed Δp values with the experimental QS data, the theoretical results qualitatively reproduce all experimentally observed trends when scaled uniformly by a factor of 2.052 obtained as the Δp/QS quotient for parent ferrocene. In line with the trend observed for measured QS values, successively smaller Δp_{scaled} values are found when going from FcH, **4**, **10** to **12**. Also the counter-intuitive finding mentioned above that the QS parameters for **4** and **4•DMAP** are rather similar ($\Delta QS = 0.035$ mm s^{-1}), while the redox potentials differ by 0.49 V, is well reproduced by theory ($\Delta\Delta p_{scaled} = 0.037$ and $\Delta\Delta IE = 0.58$ eV). Further, for the **4•DMAP/10•DMAP** couple we find an identical Δp_{scaled} of 2.408 and a difference in ΔIE of 0.17 eV, which nicely fits the experimental findings ($\Delta QS = 0.005$ mm s^{-1} and a difference in redox potentials of 0.26 V).

The opposite trends visible in the computed populations p_1 and p_2 (cf. Table 13) allow for a qualitative interpretation of the binding situations in borylated ferrocenes: With an increasing number of electron withdrawing boryl substituents in the row FcH, **4**, **10**, **12**, the electron acceptor capability of the Cp rings is gradually increased. Accordingly, in this row the degree of iron → Cp δ back-boding becomes stronger, as clearly indicated by the decreasing p_2 population. By the same token, the degree of Cp → iron π donation increases, which is reflected in the gradually increasing p_1 populations. The increase in p_1, however, amounts to

merely one third of the decrease in p_2. Thus, the changes in the electronic environment about iron visible in the QS values in this row are a consequence of a gradual improvement in δ back-donation. The improvements of π donation, which exert an opposite effect on the QS, are significantly less pronounced.

Selected charges obtained from a natural population analysis (NPA) on the neutral and ionized FcH, **1**, and the complex **1•pyridine** are shown in Table 14. For parent ferrocene, the removal of one electron leads to an increase of positive charge at the iron atom by about half an electron (0.45 e) and the group charges on both Cp rings increase uniformly by 0.28 e. Upon ionization of **1** the charge at iron increases by 0.43 electrons and that of the unsubstituted Cp_U ring by 0.22 electrons. The substituted Cp_S ring contributes only 0.14 electrons, and, significantly, 0.19 electrons are removed from the boron atom. This picture changes in the presence of a coordinating pyridine group (**1•pyridine**): While the charge on iron is again increased by 0.44 e, both Cp rings now contribute uniformly 0.23 electrons to the ionization, whereas only negligible changes occur for the charge at the boron atom. The pyridine group apparently compensates the higher charge deficiency at boron in the ion as documented by its increased charge after ionization (by 0.09 e). Apparently, it is possible to decouple the boron atom quite efficiently from the ionization process by coordination with an N-donor base. The fact that the ionization potential of $FcB(NH_2)_2$ is very similar to that of parent ferrocene indicates that the same effect can also be accomplished by appropriate choice of the σ substituents at boron to efficiently compensate the electron deficiency at boron. The similarities in the computed charge distribution in the neutral and cationic **1•pyridine** and FcH indicate that such a decoupling essentially leads to species with electronic (and electrochemical) properties very similar to parent ferrocene. This view is supported by the observed similarities in the QS for the neutral FcH, **4•DMAP**, and **10•DMAP**. In this context, we attribute the finding of much lower ionization potentials compared to ferrocene or $FcB(NH_2)_2$ for the N-donor substituted species **1•pyridine**, **4•DMAP**, and **10•DMAP** to the better distribution of charge over the entire, larger molecule. For all three species investigated, ionization leads to the removal of about half an electron from the iron atom, which is the largest observed change in the charge distributions and quite independent of the presence of substituents or N-donor groups. We consider the substantial decrease in bending upon ionization observed for all relevant species (cf. Table 12)

a consequence of the constantly increased electron deficiency of the iron center in all ionized species, such that the electron deficiency at boron cannot be satisfied anymore by orbital or electrostatic interactions, which lead to bending in the neutral compounds (see below). All in all we conclude from this section, that in the presence of a coordinating N-donor group the boron atom does not contribute to the redistribution of charge in ionization processes, while its electron deficiency controls the ionization potential of substituted ferrocenes.

Analysis of the nature of bending in borylated ferrocenes: As a tentative explanation for the out-of-plane bending observed in borylated ferrocenes $FcBX_2$, direct iron-boron interactions have been proposed, but previous experimental and theoretical work has been inconclusive in this respect.[50] In order to gain deeper insight into the nature of these hypothetical interactions, we performed a Bader analysis of the electron density topology for the model complex $FcBH_2$ (**1**). Figure 17 shows the Laplacian of the electron density distribution in the Fe–C*ipso*–B plane. Despite of careful searching, no bond critical point between iron and boron was identified. In fact, the analysis unambiguously reveals that there is no common zero flux surface joining the iron and boron atomic basins. In other words, according to the quantum theory of atoms in molecules, there is no sign of covalent iron-boron bonding in **1**.

In order to identify potential alternatives to understand the nature of the experimental findings one has first to assess the scale of the energetic consequences of the out-of-plane bending. To this end we performed relaxed potential energy scans for the bending in $FcBH_2$ (**1**), and in the two fragments $[Fe(CpBH_2)]^+$ and $[CpBH_2]^-$. In these calculations we incrementally varied the bending angle Fe–C*ipso*–B, which corresponds to a systematic variation of the dip angle α^*. The potential energy curves obtained are shown in Figure 18. Commencing with the bending potential of the $[CpBH_2]^-$ fragment, we first note a rather shallow potential for the variation of α^*. In line with a low Cp–BH_2 out-of-plane bending frequency ($\tilde{\nu} = 239$ cm^{-1}), a deviation of 30° from the planar equilibrium geometry raises the energy by mere 4.5 kcal mol^{-1}. An even shallower potential results for the bending motion in $[Fe(CpBH_2)]^+$ (Figure 18). Its minimum structure exhibits a significant dip angle α^* of 7.5°, but is stabilized by only 0.2 kcal mol^{-1} with respect to the planar geometry. Correspondingly, an α^* of +30° leads to a very small energy increase of 2.0 kcal mol^{-1} and the associated out-of-plane bending frequency is significantly

lowered ($\tilde{\nu}$ = 130 cm^{-1}). Also for **1** an equally weak bending potential results (Figure 18). In the optimized minimum structure, the boryl group is now bent substantially towards the iron center by about 25°. The energy difference to the planar structure, however, is again only 2.0 kcal mol^{-1}. Frequency analysis on minimum **1** reveals $\tilde{\nu}$ = 106 cm^{-1} for the out-of-plane bending vibration. Starting from the minimum, a further increase of α^* leads to a somewhat steeper repulsive potential than in [Fe(CpBH$_2$)]$^+$ due to the presence of the second Cp$^-$ ring. However, even the heavily distorted structure at the end of the scan (α^* = 50°, Fe–B distance: 2.240 Å) is just 8 kcal mol^{-1} higher in energy. Taken together, from this subsection it becomes immediately clear that the energetic effects underlying the experimentally observed deviations from planarity for the borylated ferrocenes under study are of rather small magnitude.

To further understand the changes in electronic structure accompanying the bending we performed natural population analyses for several points along the scan of **1** (cf. Table 15). According to the NPA a small amount of charge is transferred onto the BH$_2$ group as it is bent towards the iron atom, e.g., 0.09 e$^-$ in the minimum structure (α^* = 26°) and 0.22 e$^-$ in the limit of the scan (α^* = 45°). This charge stems mainly from the C*ipso* atom and the unsubstituted Cp ring, which donates up to 0.1 electrons to the boron group. The iron atom is hardly involved at all in the overall charge redistribution, which is in line with the finding of rather constant IS values in the Mössbauer spectra of FcH and **4** presented above. Thus, bending results essentially in a polarization of charge within the Cp–BH$_2$ moiety.

Some degree of iron-boron interaction can in fact be identified in a Wiberg bond order analysis:[51] The Fe–B bond order increases from 0.12 (planar structure) to 0.18 in the minimum structure to 0.22 in the limit of α^* = 45°. To put this result into perspective we note that the Fe–C*ipso* bond order is somewhat larger (0.28), but remains constant upon bending. According to these results, the iron-boron interaction in the minimum structure amounts to about two thirds of the iron-carbon interaction. Similar findings in the context of Mayer bond orders in fact led Appel et al. to propose a direct iron-boron bonding interaction.[22] In the analysis of natural bond orbitals (NBOs), however, we do not find any particular orbital corresponding to a direct Fe–B bond. Instead, after involving an orbital localization procedure based on NBOs, the only significant interaction of these two atoms is found in a three-center natural localized

molecular orbital (NLMO) distributed over Fe, C*ipso*, and B (Figure 19). Note, however, that we found in additional calculations that the use of different methods or basis sets results in somewhat different orbital compositions, which clearly indicates some ambiguity in the concept of orbital localizations within the NBO framework. Hence, notwithstanding the intuitively appealing outcome, this result cannot be seen as a rigorous basis for interpretations of the binding situation. All in all, also in view of our findings arising from the Bader analysis, we refrain from correlating the NBO results with direct covalent iron-boron bonding at this point. The bonding situation appears to be better described as a strongly delocalized, multi-center bonding interaction involving Fe, C*ipso*, and B of the Cp–BH_2 moiety.

A comparison of canonical Kohn-Sham molecular orbitals of the parent ferrocene with those of its borylated derivative **1** reveals some interesting trends in the energetic ordering. Figure 20 shows a qualitative correlation of valence orbitals in the D_{5h} symmetric minimum structure of ferrocene with those of the species **1**, for which C_s symmetry has been enforced to facilitate the analysis. Apart from a general energetic lowering of the orbitals in **1** introduced by the presence of the boryl group we note an additional stabilization of all a' relative to a'' valence orbitals. In **1**, the formally unoccupied p_x orbital at boron (i.e., the p-orbital perpendicular to the plane of the adjacent Cp ring) and the C*ipso*–B bond orbital are symmetric with respect to the molecular mirror plane and thus of a' symmetry. In particular the HOMO–2 a' orbital experiences a strong stabilization, which can be attributed to a constructive interaction of the d_{xy} orbital at iron with the p_x-orbitals composing the local π bond between C*ipso* and B. Similar interactions can be identified for the a' symmetric orbitals HOMO–1 and HOMO–6. Notably, the unsubstituted Cp ring participates significantly in the Aufbau of the HOMO–4 orbital (Figure 21), such that in principle a direct constructive interaction between the formally empty p_x orbital at boron with the C'*ipso* center of the unsubstituted Cp ring is involved. Here, the iron contributes only a small amount of antibonding $4p$ character. From Figure 20 it becomes obvious that this through-space type of interaction in **1** arises as a mere consequence of the orbital structure of parent ferrocene, where a similar type of delocalized interaction is present in the corresponding a'-symmetric orbitals. In HOMO–4 and HOMO–6 of **1** this delocalization is visibly extended to involve the boryl π-system. This picture lends weight to the interpretation of strongly delocalized orbital interactions being responsible for the bending in borylated ferrocenes. The

24

only localized direct iron-boron interaction is visible in HOMO−2, with obviously minor contributions of the boron p_x orbital only.

A Walsh diagram illustrating the changes in MO energies upon systematic variations of α* in **1** is shown in Figure 22. Consistent with the discussion above, we note a much stronger dependence from α* for the symmetric a' orbitals than for a'' orbitals. These effects are particularly prominent for the HOMO−2 orbital, which is strongly stabilized upon bending. The HOMO−8 orbital, on the other hand, experiences a similarly strong destabilization with increasing α*. While these two orbitals dominate the picture for the α* = 50° limit of the scan, the stabilization of the HOMO−6 orbital is equally strong as that of HOMO−2 in the minimum structure (α* = 26°). In summary, the qualitative picture arising from this analysis intuitively renders these two orbitals the root of attractive interactions responsible for the observed bending. This stabilization is obviously counterbalanced by the destabilization of the C*ipso*−B σ-bonding orbital (HOMO−8) upon bending.

As an extension of these qualitative arguments, which are essentially based on an orbital overlap picture, we performed an energy partitioning analysis (EPA) as implemented in the ADF program. For this analysis we divided **1** into the fragments [FeCp]$^+$ and [CpBH$_2$]$^−$. Both are treated as singlet states and the analysis has been performed under C_s symmetry constraints. The changes in the relative energy contributions upon systematic variations of α* shown in Figure 23a clearly reveal that stabilizing orbital contributions to the bending arise from the a' set of orbitals, while a'' contributions remain essentially constant and thus cannot be responsible as a driving force for bending. This is in agreement with the qualitative conclusions drawn above from the Walsh diagram. A similarly strong contribution originates in the electrostatic term (E$_{ELSTAT}$). Destabilizing contributions stem from the Pauli energy term (E$_{PAULI}$) and from the preparation energy. The latter term arises almost completely from distortion of the [CpBH$_2$]$^−$ fragment in the complex. From this analysis we conclude that the driving force for bending is rooted in the stabilization of a' orbitals as well as in significantly enhanced electrostatic interactions.

In order to assess the energetic contributions of the second Cp ring to the bending potential, we performed a corresponding energy partitioning analysis also for the $[FeCpBH_2]^+$ subunit, which has been divided into $CpBH_2^-$ and Fe^{2+}. For the latter fragment, the closed shell $(d_{z^2})^2$, $(d_{x^2-y^2})^2$, and $(d_{xz})^2$ reference electron configuration has been employed, which constitutes a highly excited state for the bare Fe^{2+} ion, but serves here as a reasonable valence state of Fe^{2+} in the $[FeCpBH_2]^+$ complex to obtain relative EPA energy contributions during a scan of α^*. For the evaluation of the preparation energy term E_{PREP}, however, the correct $3d^6$ (^5D) configuration has been employed.[52] The results are shown in Figure 23b. Interestingly, we find entirely different trends for the respective energy components compared to **1**. Most strikingly, the differential E_{ELSTAT} contributions here do not add to the stabilizing factors of the bending. In fact, in sharp contrast to our findings for **1**, up to $\alpha^* = 30°$ the differential Pauli contributions constitute the only stabilizing factor. From $\alpha^* = 35°$ on the $\Delta E_{ORB}(a')$ term acts strongly stabilizing, the E_{PAULI} term becomes destabilizing, whereas $\Delta E_{ORB}(a'')$ and E_{ELSTAT} show only negligible contributions. The E_{PREP} term is destabilizing along the entire scan. While the reasons for the pronounced qualitative differences in the EPA results for **1** and its $[FeCpBH_2]^+$ subunit are hard to rationalize (this is particularly true for the peculiar shape of the E_{PAULI} curve), we note that the overall differential contributions of all constituent energy terms are below 5 kcal mol^{-1} for the range of $\alpha^* = 0 - 30°$ and are thus of limited importance. On the basis of these analyses, however, we feel safe to state that the second Cp ring in **1** contributes significant electrostatic factors favoring a bending of the boryl substituent.

In the overall picture arising from our analysis, the bending cannot be understood in terms of direct bonding interactions involving the boryl group and the iron center – on the basis of a Bader electron topology analysis we can safely exclude such a direct bond. Based on in-depth investigations on our computational model for borylated ferrocenes, **1**, our analysis rather indicates that the bending is rooted in several contributions. We identified two apparently cooperative factors giving rise to the bending in this class of organometallic compounds: Two MOs of a' symmetry (HOMO–2 and HOMO–6) experience a substantial energy lowering upon bending. These orbitals represent covalent contributions to bending involving (a) a strongly delocalized interaction of both Cp rings, which is effectively mediated by the d_{xy} orbital at iron (HOMO–6) and (b) a rather localized interaction of the $d_{x^2-y^2}$ orbital at iron and the C*ipso*–B π-

system (HOMO−2). Both orbitals, however, are present already in parent ferrocene and contain only limited contributions from the formally empty p_x orbital of the boron substituent. The most significant interaction involving the boron p_x orbital as part of the C*ipso*−B π-system is present in HOMO−4, which represents a delocalized through-space interaction with the second Cp ring without involving iron orbitals − a minor contribution of the iron $4p_y$ orbital to this MO is antibonding in nature. HOMO−4, however, does not experience any significant energy lowering with increasing dip angle α^* and is therefore unlikely to be the origin of the observed bending. As a second and according to the EPA equally important factor we identified electrostatic interactions, which are enhanced substantially upon bending. These interactions depend essentially on the presence of a second Cp ring. Contrary to chemical intuition NPA analyses indicate that bending is not accompanied (or caused) by any significant charge-transfer from the metal to the electron-deficient boron center. Instead, a reorganization of charge within the $CpBH_2^−$ moiety is observed leading to a flow of charge from the C*ipso* center to the BH_2 group. The NPA results indicate a constant electron density about the iron center which is unaffected by the electronic situation of the boryl substituent. This picture is in line with the IS values measured in our Mössbauer study on the present set of systems bearing one, two, or four BMe_2 groups.

Conclusions

This paper presents a joint crystallographic, electrochemical and Mössbauer spectroscopy study on selected derivatives of mono-, di- and tetraborylated ferrocenes $FcBR^1R^2$, $1,1'$-$fc(BR^1R^2)_2$ (R^1, R^2 = Br, Me, OH, OMe) and $1,1',3,3'$-$Fe[C_5H_3(BMe_2)_2]_2$. The results obtained are put face to face with detailed DFT calculations which include the hypothetical parent compound $FcBH_2$ even though this molecule is not experimentally accessible. As a common feature of all molecular structures investigated, the three coordinate boryl substituents are bent out of the plane of the adjacent cyclopentadienyl ring towards the iron atom. For a quantitative assessment of ligand bending we used the dip angle $\alpha^* = 180° − \alpha$ with α defined as the angle COG−C*ipso*−B (COG: geometric center of the Cp-constituting carbon atoms). As a general rule, α^* tends to decrease with decreasing Lewis acidity of the boron atom, as well as with an increasing degree of borylation at the ferrocene core. A similar structural motif is also clearly

visible in all structures obtained from quantum chemical calculations, even though we do not always find a full quantitative agreement between theory and experiment. Nevertheless, the systematic trend in α^* values as a function of the Lewis acidity of the boryl groups is well reproduced by density functional calculations. This leads to the conclusion that ligand bending is not merely an artifact of crystal packing but rooted in the electronic structure of the individual molecules. However, since the potential energy surface associated with changes in the dip angle is apparently very shallow, solid state effects may well have some non-negligible influence on α^*, which in turn may account for the deviations between theory and experiment visible in the quantitative description of the phenomenon.

At first, we hypothesized about $Cp–BR^1R^2$ bending as originating from a direct interaction between filled d-type orbitals at iron and the empty p-orbital at boron. However, a Bader analysis of the electron density topology for the model complex $FcBH_2$ (**1**), which exhibits a pronounced bending of $\alpha^* = 26.5°$ at the BP86/TZVP level, clearly shows that there is no direct iron-boron bonding in **1**. Further detailed analysis rather reveals that two cooperative factors exist, which are responsible for ligand bending. We identified several orbital interactions of delocalized nature, which involve the formally empty p-orbital at the boryl substituent, C*ipso* of the adjacent Cp ring, d-orbitals at iron and also a significant through-space interaction with the second Cp ring. As a second, and according to our analysis equally important factor we identified electrostatic interactions, which are enhanced substantially upon bending, and which depend critically on the presence of the second Cp ring.

Apart from the structural features of ferrocenylboranes, we are particularly interested in their electrochemical behavior and potential use for the development of novel electron-transfer regents. Thus, the series $FcBMe_2$ (**4**, $E^{\circ\prime} = +0.09$ V *vs.* FcH/FcH^+), $1,1\prime\text{-fc}(BMe_2)_2$ (**10**, $E^{\circ\prime} = +0.26$ V) and $1,1\prime,3,3\prime\text{-Fe}[C_5H_3(BMe_2)_2]_2$ (**12**, $E^{\circ\prime} = +0.39$ V) was investigated by cyclic voltammetry. Our study reveals the introduction of BMe_2 substituents into the ferrocene core to increase the oxidation potential of the central iron atom. This anodic shift, which is apparently additive, may be attributed to the π electron-withdrawing nature of three coordinate boryl groups. Most importantly, the addition of 4-dimethylaminopyridine (DMAP; 1 equiv. for **4**, 2 equivs. for **10**) with subsequent B–N adduct formation does not just neutralize this effect but

leads to a cathodic shift of the Fe(II)/Fe(III) redox transition far beyond the halfwave potential of parent ferrocene [$E^{\circ\prime}$(**4•DMAP**) = −0.40 V, $E^{\circ\prime}$(**10•DMAP**) = −0.66 V; vs. FcH/FcH$^+$]. It is noteworthy that the diadduct **10•DMAP** is as easy to oxidize as decamethylferrocene, which represents one of the most prominent electron donors for the generation of organometallic charge transfer salts. Cyclic voltammetry was augmented by DFT calculations, including solvent simulations, on the adiabatic ionization energies (IEs) of **4**, **10**, **12**, **4•DMAP**, and **10•DMAP**. In all these cases we find an excellent correlation between the experimentally obtained $E^{\circ\prime}$ values and the calculated IE data.

To get further insight into the charge-density flow within the ferrocene backbone upon introduction of BMe$_2$− or BMe$_2$•DMAP substituents, the series **4**, **10**, **12**, **4•DMAP**, and **10•DMAP** was also investigated by Mössbauer spectroscopy. As to be expected, only negligible differences in the isomer shift (IS) of the borylated species and parent ferrocene are observed. The quadrupole splitting (QS) values, however, become significantly smaller upon going from **4** (2.309(4) mm s^{-1}) to **10** (2.082(4) mm s^{-1}) and **12** (1.891(4) mm s^{-1}). These results are in agreement with previous findings which indicated electron-withdrawing substituents at ferrocene to cause a decrease in QS. Electron-donating substituents, on the other hand, tend to cause an increase in the quadrupole splitting relative to ferrocene (QS = 2.37 mm s^{-1}). In contrast to *a priori* expectations, the QS values of **4•DMAP** (2.344(3) mm s^1) and **10•DMAP** (2.339(4) mm s^{-1}) do not differ significantly from that of ferrocene despite of the low oxidation potentials and ionization energies found for these B−N adducts. Based on an empirical correlation between the d-orbital populations and the QS we have rationalized the experimentally observed trends in the QS data for these species in terms of changes in the Cp-Fe bonding features of ferrocene resulting from different degrees of borylation. Furthermore, by comparison with parent ferrocene, we found for the model compounds **1** and **1•pyridine** that the ionization process removes about half an electron from the iron atom, which is the largest charge difference uniformly for all three species. Notably, the charge of the boron atom in three coordinate **1** is increased by 0.2 e upon ionization, whereas no change is seen at boron after the ionization of **1•pyridine**. With this result, we interpret the experimentally observed trends in the redox potentials as follows: for borylated ferrocenes such as **4**, **10**, and **12** the electron deficiency at the three coordinate boron center(s), which can be modulated by choice of

appropriate substituents at boron, leads to an increase in the ionization potential of the complexes with respect to ferrocene. This is a result of the π-electron withdrawing nature of the boryl substitutents. In the presence of coordinating Lewis bases or strong π-donors at boron (cf. $FcB(NH_2)_2$), however, the boron is effectively decoupled from the ionization process and the redox potentials of the resulting complexes are equal or even lower than the redox potential of ferrocene itself. Hence, cyclic voltammetry can be seen as an analytical tool for the identification of base adducts in such complexes. Furthermore, given the constantly good agreement (within 0.1 V) between theory and experiment observed for all species under investigation, it appears possible to predict the redox properties of related complexes *a priori*, which opens the way to a rational design of taylor-made redox active ferrocenoid complexes with fine-tuned redox potentials. It is important to state, however, that careful benchmarking is always required to obtain reliable results. In the present study we have documented by comparison with high level post-HF results that the DFT approximations presently in use can fail miserably in the description of N-donor B-acceptor bond strengths. Notwithstanding these problems, which need to be identified for every new class of molecules by adequate scrutiny prior to any predictive application, we clearly demonstrated that DFT calculations constitute a reliable tool with predictive capabilities for the description of demanding electronic situations as present in borylated ferrocenes with their very subtle electronic and/or structural properties.

Experimental Section and Computational Details

General Remarks: All reactions and manipulations of air-sensitive compounds were carried out in dry, oxygen-free argon using standard Schlenk ware. Solvents were freshly distilled under N_2 from Na-benzophenone (benzene, toluene) or Na/Pb alloy (hexane) prior to use. NMR: Bruker DPX 400, Bruker DPX 250. ^{11}B NMR spectra are reported relative to external $BF_3 \cdot Et_2O$. Unless stated otherwise, all NMR spectra were run at ambient temperature; abbreviations: s = singlet, d = doublet, tr = triplet; vtr = virtual triplet; n.o. = signal not observed; n.r. = multiplet expected but not resolved. $FcSnMe_3$[25] and the compounds **2**,[1] **3**,[1] **4**,[1] **4•DMAP**,[5] **8**,[2] **10**,[2] and **10•DMAP**[5] were synthesized according to literature procedures.

Preparation of 5: Triethylamine (0.19 g, 1.88 mmol) and water (0.10 g, 5.55 mmol) were added dropwise with stirring at ambient temperature to a solution of **3** (0.54 g, 1.86 mmol) in 6 ml of benzene. The solution was stirred for 1 h. After the benzene had been removed *in vacuo*, 15 ml of hexane was added to the residue and the resulting slurry cooled to $-40°C$ for 6 h. After filtration from triethylammonium bromide, all volatiles were driven off from the filtrate under reduced pressure to leave behind a pale yellow microcrystalline solid. Yield: 0.19 g (45 %). Single crystals of **5** formed serendipitously from the crude oily compound $FcBMe_2$, **4**, upon prolonged exposure to air. ^{11}B-NMR (128.4 MHz, $CDCl_3$): δ 49.6 ($h_{½}$ = 250 Hz). ^{1}H-NMR (250.1 MHz, $CDCl_3$): δ 0.62 (s, 3H, CH_3), 4.10 (s, 5H, C_5H_5), 4.33, 4.45 (2 × vtr, 2 × 2H, $^{3}J(H,H) = {}^{4}J(H,H)$ = 1.8 Hz, C_5H_4), 4.92 (s, 1H, OH). ^{13}C-NMR (62.9 MHz, $CDCl_3$): δ n.o. (CH_3), 68.5 (C_5H_5), 72.9, 73.3 (C_5H_4), n.o. (C_5H_4-*ipso*). Anal. Calcd. for $C_{11}H_{13}BFeO$ [227.87]: C, 57.98; H, 5.75. Found: C, 57.51; H, 5.49 %.

Preparation of 6: $MeOSiMe_3$ (1.56 g, 14.97 mmol) was added via syringe to a suspension of **2** (2.13 g, 5.99 mmol) in pentane (20 ml) at $-78°C$. The mixture was allowed to warm to room temperature and stirred for 30 min. All volatiles were removed *in vacuo*. Distillation of the crude product gave **6** as an orange solid. Yield: 1.45 g (94 %). X-ray quality crystals were obtained by sublimation under reduced pressure. ^{11}B-NMR (128.4 MHz, $CDCl_3$): δ 30.0 ($h_{½}$ = 160 Hz). ^{1}H-NMR (250.1 MHz, $CDCl_3$): δ 3.75 (s, 6H, CH_3), 4.15 (s, 5H, C_5H_5), 4.38, 4.44 (2 × n.r., 2 × 2H, C_5H_4). ^{13}C-NMR (100.6 MHz, $CDCl_3$): δ 52.0 (CH_3), 68.5 (C_5H_5), 71.8, 74.4 (C_5H_4), n.o. (C_5H_4-*ipso*). Anal. Calcd. for $C_{12}H_{15}BFeO_2$ [257.90]: C, 55.88; H, 5.86. Found: C, 55.51; H, 5.58 %.

Preparation of 7: A solid mixture of **2** (0.07 g, 0.20 mmol) and $FcSnMe_3$ (0.07 g, 0.20 mmol) was dissolved in 1 ml of C_6D_6 in an NMR tube. Subsequently, the NMR tube was cooled to liquid nitrogen temperature, evacuated and sealed. The reaction mixture was allowed to warm to ambient temperature, whereupon a colorless precipitate formed (Me_3SnBr). The NMR tube was turned bottom up and the solid separated from the mother liquid by centrifugation. After NMR-investigation, the NMR tube was opened under inert gas and all volatiles removed *in vacuo* to yield a red microcrystalline solid. Yield: 0.06 g (65 %). X-ray quality crystals were obtained from toluene upon slow evaporation of the solvent *in vacuo*. ^{11}B-NMR (128.4 MHz,

C_6D_6): δ 55.3 ($h_{1/2}$ = 450 Hz). ^{1}H-NMR (250.1 MHz, C_6D_6): δ 4.00 (s, 10H, C_5H_5), 4.43, 4.71 (2

× vtr, 2 × 4H, ^3J(H,H) = ^4J(H,H) = 1.8 Hz, C_5H_4). ^{13}C-NMR (62.9 MHz, C_6D_6): δ 70.2 (C_5H_5),

75.4, 77.0 (C_5H_4), n.o. (C_5H_4-*ipso*). **7** is very sensitive to air and moisture; a decent elemental

analysis was therefore not obtained.

Preparation of 11: MeOSiMe$_3$ (3.78 g, 36.27 mmol) was added via syringe to a solution of **8**

(3.86 g, 7.35 mmol) in toluene (30 ml) at −78°C. The mixture was allowed to warm to room

temperature and stirred for 30 min. All volatiles were removed *in vacuo*. X-ray quality crystals

were obtained be recrystallisation of the crude product from hexane. Yield: 1.79 g (74 %). ^{11}B-

NMR (128.4 MHz, $CDCl_3$): δ 30.0 ($h_{1/2}$ = 210 Hz). ^{1}H-NMR (250.1 MHz, $CDCl_3$): δ 3.74 (s,

12H, CH$_3$), 4.35, 4.42 (2 × vtr, 2 × 4H, ^3J(H,H) = ^4J(H,H) = 1.5 Hz, C_5H_4). ^{13}C-NMR (100.6

MHz, $CDCl_3$): δ 51.9 (CH$_3$), 72.1, 74.7 (C_5H_4), n.o. (C_5H_4-*ipso*). Anal. Calcd. for $C_{14}H_{20}B_2FeO_4$

[329.77]: C, 50.99; H, 6.11. Found: C, 50.73; H, 5.92 %.

Preparation of 12: Neat 1,1',3,3'-Fe[C_5H_3(BBr$_2$)$_2$]$_2$[26] (0.70 g, 0.81 mmol) was cooled to −30

°C. Neat SnMe$_4$ (1.30 g, 7.27 mmol) was added with gentle stirring via syringe. The mixture

was allowed to warm to room temperature and heated to 80 °C for 2h. All volatiles were

removed *in vacuo* while the mixture was still hot. Sublimation of the residue at 60 °C / 10^{-3} torr

gave dark red X-ray quality crystals. Yield: 0.25 g (89 %). ^{11}B-NMR (128.4 MHz, C_6D_6): δ

74.8 ($h_{1/2}$ = 310 Hz). ^{1}H-NMR (400.0 MHz, C_6D_6): δ 0.88 (s, 24H, CH$_3$), 4.48 (d, 4H, ^4J(H,H) =

1.2 Hz, C_5H_3), 4.56 (tr, 2H, ^4J(H,H) = 1.2 Hz, C_5H_3). ^{13}C-NMR (100.6 MHz, $CDCl_3$): δ 11.5

(CH$_3$), 81.1, 82.4 (C_5H_3), n.o. (C_5H_3-*ipso*). Anal. Calcd. For $C_{18}H_{30}B_4Fe$ [345.51]: C, 62.57; H,

8.75. Found: C, 62.05; H, 8.51 %.

X-ray Crystal Structure Analyses: The crystals of **3**, **4**, **4•DMAP**, **5**, **6**, **7**, **9**, and **11** were

measured on a STOE IPDS II two-circle diffractometer with graphite-monochromated MoK_α

radiation. An empirical absorption correction was performed using the MULABS[53] option in

the program PLATON[54]. **12** was measured on a Siemens SMART CCD diffractometer with

graphite-monochromated MoK_α radiation. A numerical absorption correction was performed

using the program SHELXTL.[55] All structures were solved by direct methods using the

program SHELXS[56] and refined against F^2 with full-matrix least-squares techniques using the

program SHELXL[57]. All non-hydrogen atoms were refined with anisotropic displacement parameters. Hydrogen atoms, except those of the disordered methyl group in **3**, were located by difference Fourier synthesis and refined using a riding model. The methyl and OH groups were allowed to rotate but not to tip. The methyl group and the Br atom of **3** are disordered. The Br/CH$_3$ ratio is 0.681(3)/0.319(3) on one position and 0.319(3)/ 0.681(3) on the other. Similarity restraints were used for the displacement parameters of these atoms. CCDC 242167 (**3**), 242165 (**4**), 242168 (**4•DMAP**), 242164 (**5**), 242170 (**6**), 242169 (**7**), 242166 (**9**), 242171 (**11**), and 242172 (**12**) contain the supplementary crystallographic data for this paper. These data can be obtained free of charge at www.ccdc.cam.ac.uk/conts/retrieving.html (or from the Cambridge Crystallographic Data Centre, 12, Union Road, Cambridge CB2 1EZ, UK; fax: (internat.) +44-1223/336-033; E-mail: deposit@ccdc.cam.ac.uk).

Electrochemical Measurements: Cyclic voltametry was performed in CH$_2$Cl$_2$ solutions containing [Nbu$_4$][PF$_6$] (0.1 mol·dm^{-3}) as supporting electrolyte. All potential values are referred to the FcH/FcH$^+$ redox couple. Voltammetric scans were referenced by addition of a small amount of ferrocene as internal standard at an appropriate time of the experiment. The cell for electrochemistry measurements was designed as detailed in ref. [[58]].

Mössbauer Spectroscopy: The details of ^{57}Fe temperature-dependent Mössbauer spectroscopy have been described earlier.[59-61] In the present study, due to the air and moisture sensitivity of the compounds, sample transfer to high temperature silicone grease lubricated, O-ring sealed, perspex sample holders was effected in an inert atmosphere glove box (VAC model DLX-001-S-P) having a partial oxygen pressure of less than 0.5 ppm and of H$_2$O less than 1 ppm. Since **4** is a low-melting semi-solid at room temperature, and **10** is a liquid, both compounds were transferred *via* capillary pipette. **4•DMAP** and **10•DMAP** were transferred as neat microcrystalline solid. The filled and sealed sample holders were removed from the glove box, immediately cooled to liquid nitrogen temperature, and then placed into the Mössbauer spectrometer pre-cooled to 90 K. Data accumulation (in the first instance) was effected in a warming mode as discussed above. All isomer shifts are reported with respect to the centroid of a room temperature α-Fe absorber spectrum which was also used for spectrometer calibration.

Quantum Chemical Calculations: Quantum chemical calculations were carried out at various levels by means of the programs Gaussian03,[62] Turbomole, [63-67] Molpro,[68] and ADF.[69, 70] At the density functional level we employed the standard BP86[71, 72] functional as well as the HCTH407[73-75] functional of Boese et al., which was newly implemented in the Gaussian03 program (HCTH for short). Both of these functionals are based on the generalized gradient approximations (GGA) and can make use of the resolution of identity (RI) approximation,[46, 76-79] which usually improves the computational efficiency and scalability with system size substantially. At the hybrid DFT level we employed the B3LYP functional[80, 81] and the B98 functional of Schmider and Becke[82, 83]. All Gaussian and Turbomole calculations have been done in combination with the SVP and TZVP basis sets of Ahlrichs and coworkers[84, 85]. In RI computations with the Gaussian program we used the small DGA1 Coulomb density fitting basis available in the basis set library.[86] Calculations on redox potentials were performed at the BP86(RI) level with the Turbomole program, employing its very efficient implementation of the COSMO continuum model[87] to account for effects (solvent dichloromethane, dielectric constant at room temperature $\varepsilon = 8.93$). The TZVP basis set was used for B, C, N, O, F, and H atoms. For Cl, Br, and I atoms the relativistic effective core potentials of Dolg and coworkers[88, 89] were used. The respective TZV-type standard basis sets for the latter atoms were each augmented by one *d*-polarization function available in the Turbomole basis set libraries. For all atoms, the TZVP Coulomb fitting basis was used. Please note that we report in the tables ionization energies obtained from total energy differences because we cannot account for thermochemical corrections to obtain ΔG values due to the lack of analytic second derivatives in the COSMO calculations. We therefore provide only a qualitative assessment of the electrochemical conditions and accordingly, we report computed ionization energies in eV, whereas the differences in redox potentials obtained in electrochemical measurements are given in V and relate to free energy differences. A gas phase calculation on **4** at the BP86/TZVP/RI(DGA1) level, i.e. without solvent simulation, however, yields zero point vibrational energy and thermal contribution effects (ΔG at 298K) on the adiabatic ionization potential of the order or 2 kcal mol^{-1} or 0.1 eV, respectively. Better agreement with experimental measurements can probably be obtained if these contributions are included in the computations.[90]

34

All calculations with Gaussian and Turbomole were performed in C_I symmetry. The minimum character of the resulting stationary points has been confirmed by the absence of negative eigenvalues in analytically computed Hessian matrices. In a number of cases, which are documented in the Table below, we observed the occurrence of a single low imaginary mode ($i5$-$i70$ cm^{-1}) in the harmonic frequency analyses. In all cases these imaginary modes correspond to a rotation of one Cp ring out of an almost eclipsed (D_{5h}-like) arrangement. However, geometry optimizations starting from a staggered (D_{5d}-like) arrangement of rings all lead back to the nearly eclipsed conformations. In order to exclude technical artifacts we checked the influence of the integration grid size (ultrafine) and of the geometry convergence criteria (verytight) settings. But in all cases we were unable to obtain structures without these peculiar imaginary modes. Because these spurious modes spoil the quality of computed zero point vibrational energies in systematic comparisons, we report here only total energy differences.

For the calibration of computed binding energies we performed coupled cluster calculations in combination with the correlation consistent basis set series cc-pVXZ (X=D,T, and Q) of Dunning and coworkers including an extrapolation to the basis set limit.[91, 92] The extrapolation was performed employing the mixed exponential/Gaussian function $E(x) = E_\infty + b\cdot e^{-(x-1)} + c\cdot e^{-(x-1)**2}$, with x being the cardinal number (DZ=2, TZ=3, QZ=4) and E_∞ the asymptotic value to approximate the basis set limit.[93, 94] The underlying molecular structures of the complex and its fragments were optimized at each respective level based on numerically evaluated gradients. These calculations were performed with the program Molpro.[68] As an alternative, computationally much more efficient procedure to extrapolate the CCSD(T) level to the limit of infinite basis-set size we employed the CBS-QB3 scheme of Peterson and coworkers[95] as implemented in the Gaussian program. Additional Turbomole calibration calculations were done employing second order Møller-Plesset perturbation theory in combination with the cc-pVXZ (X=D,T, and Q) series of Dunning. For energies and analytic gradients the RI technique was used in combination with the optimized MP2 auxiliary basis provided in the Turbomole libraries.[96, 97]

The AIMPAC program has been used for the Bader analysis of the electron density distribution.
[98, 99] Additional analyses on relevant model complexes were performed with the ADF program
package[100-102] at the BP86 level employing an uncontracted Slater-type orbital (STO) basis of
polarized triple-ζ quality augmented by two sets of polarization functions.[103] The (1s)2 core
electrons on the carbon and the boron atoms and the (1s2s2p)10 core electrons on the iron atom
were treated by the frozen-core approximation.[104] Scalar relativistic effects have been
considered by the zero order regular approximation (ZORA).[105-110] Based on the work of
Morokuma[111] and Ziegler and Rauk,[112] the EPA analysis as implemented in the ADF
program[113, 114, 70] partitions the bond dissociation energy D_e for the process A•B → A + B into
several contributions. First, D_e is formally separated into the two components ΔE_{INT} and ΔE_{PREP}
according to (3)

$$-D_e = \Delta E_{INT} + \Delta E_{PREP} \tag{3}$$

ΔE_{INT} is the interaction energy defined as the energy of the complex A•B minus the energies of
its constituting fragments A* and B*, which are kept frozen in the geometry and electronic state
they adopt in the complex. ΔE_{PREP} then is the energy difference to promote A and B from their
equilibrium geometry and electronic state to the geometry and electronic state in A* and B*.
ΔE_{INT} can further be divided into three components,

$$\Delta E_{INT} = \Delta E_{ELSTAT} + \Delta E_{PAULI} + \Delta E_{ORB} \tag{4}$$

Herein ΔE_{ELSTAT} is the quasi-classical Coulomb interaction energy computed from the frozen
electron densities of the fragments A* and B* superimposed at the geometry of the complex.
The corresponding electron density, however, violates the Pauli exclusion principle because it
leads to regions of space, which are occupied by two electrons of like spin. The Pauli exclusion
principle is enforced in the next step by antisymmetrization and renormalization of the Kohn-
Sham determinant, which is constructed from the superposition of the formerly non-interacting
orbitals of A* and B*. The corresponding change in energy is denoted ΔE_{PAULI}, the Pauli
repulsion term. As last step of the EPA analysis the stabilizing orbital interaction term ΔE_{ORB} is
calculated by relaxing the orthonormalized Kohn-Sham orbitals to the optimized Kohn-Sham

determinant of the complex. ΔE_{ORB} can be further decomposed into orbital contributions arising from the respective sets of irreducible representations defined by the molecular symmetry. The EPA has found widespread application (see, e.g., [115] and refs. 24-26 cited therein). For further details and physical interpretations of the various terms comprising ΔE_{INT} the interested reader is referred to a comprehensive exposition by Bickelhaupt and Baerends.[70]

Acknowledgements

References

[1]   T. Renk, W. Ruf, W. Siebert, *J. Organomet. Chem.* **1976**, *120*, 1-25.
[2]   W. Ruf, T. Renk, W. Siebert, *Z. Naturforsch.* **1976**, *31b*, 1028-1034.
[3]   M. Scheibitz, R. F. Winter, M. Bolte, H.-W. Lerner, M. Wagner, *Angew. Chem.* **2003**, *115*, 954-957.
[4]   M. Scheibitz, J. W. Bats, M. Bolte, M. Wagner, *Eur. J. Inorg. Chem.* **2003**, 2049-2053.
[5]   M. Fontani, F. Peters, W. Scherer, W. Wachter, M. Wagner, P. Zanello, *Eur. J. Inorg. Chem.* **1998**, 1453-1465.
[6]   M. Grosche, E. Herdtweck, F. Peters, M. Wagner, *Organometallics* **1999**, *18*, 4669-4672.
[7]   R. E. Dinnebier, M. Wagner, F. Peters, K. Shankland, W. I. F. David, *Z. Anorg. Allg. Chem.* **2000**, *626*, 1400-1405.
[8]   W. E. Piers, G. J. Irvine, V. C. Williams, *Eur. J. Inorg. Chem.* **2000**, 2131-2142.
[9]   B. E. Carpenter, W. E. Piers, M. Parvez, G. P. A. Yap, S. J. Rettig, *Can. J. Chem.* **2001**, *79*, 857-867.
[10]   B. E. Carpenter, W. E. Piers, R. McDonald, *Can. J. Chem.* **2001**, *78*, 291-295.
[11]   F. Jäkle, K. Polborn, M. Wagner, *Chem. Ber.* **1996**, *129*, 603 - 606.
[12]   F. F. d. Biani, F. Jäkle, M. Spiegler, M. Wagner, P. Zanello, *Inorg. Chem.* **1997**, *36*, 2103-2111.
[13]   E. Herdtweck, F. Peters, W. Scherer, M. Wagner, *Polyhedron* **1998**, *17*, 1149 - 1157.

[14]   S. L. Guo, F. Peters, F. F. d. Biani, J. W. Bats, E. Herdtweck, P. Zanello, M. Wagner, *Inorg. Chem.* **2001**, *40*, 4928-4936.
[15]   F. Jäkle, T. Priermeier, M. Wagner, *J. Chem. Soc., Chem. Commun.* **1995**, 1765-1766.
[16]   F. Jäkle, T. Priermeier, M. Wagner, *Organometallics* **1996**, *15*, 2033-2040.
[17]   E. Herdtweck, F. Jäkle, G. Opromolla, M. Spiegler, M. Wagner, P. Zanello, *Organometallics* **1996**, *15*, 5524-5535.
[18]   F. Jäkle, M. Mattner, T. Priermeier, M. Wagner, *J. Organomet. Chem.* **1995**, *502*, 123-130.
[19]   M. Herberhold, U. Dörfler, W. Milius, B. Wrackmeyer, *J. Organomet. Chem.* **1995**, *492*, 59-63.
[20]   S. Aldridge, C. Bresner, *Coord. Chem. Rev.* **2003**, *244*, 71-92.
[21]   K. Ma, M. Scheibitz, S. Scholz, M. Wagner, *J. Organomet. Chem.* **2002**, *652*, 11-19.
[22]   A. Appel, F. Jäkle, T. Priermeier, R. Schmid, M. Wagner, *Organometallics* **1996**, *15*, 1188-1194.
[23]   M. Scheibitz, J. W. Bats, M. Bolte, H.-W. Lerner, M. Wagner, *Organometallics* **2004**, *23*, 940-942.
[24]   B. Wrackmeyer, U. Dörfler, W. Milius, M. Herberhold, *Polyhedron* **1995**, *14*, 1425-1431.
[25]   N. Lenze, B. Neumann, A. Salmon, A. Stammler, H.-G. Stammler, P. Jutzi, *J. Organomet. Chem.* **2001**, *619*, 74-87.
[26]   A. Appel, H. Nöth, M. Schmidt, *Chem. Ber.* **1995**, *128*, 621-626.
[27]   F. F. d. Biani, T. Gmeinwieser, E. Herdtweck, F. Jäkle, F. Laschi, M. Wagner, P. Zanello, *Organometallics* **1997**, *16*, 4776-4787.
[28]   F. H. Allen, *Acta Cryst.* **2002**, *B58*, 380-388.
[29]   M. J. G. Lesley, A. Woodward, N. J. Taylor, T. B. Marder, I. Cazenobe, I. Ledoux, J. Zyss, A. Thornton, D. W. Bruce, A. K. Kakkar, *Chem. Mater* **1998**, *10*, 1355-1365.
[30]   M. Soriano-Garcia, R. A. Toscano, T. Lopez, A. Campero-Celis, *J. Crystallogr. Spectrosc. Res.* **1987**, *17*, 719-728.
[31]   B. Wrackmeyer, U. Dörfler, W. Milius, M. Herberhold, *Z. Naturforsch.* **1995**, *50b*, 201-204.
[32]   H. Horn, F. Rudolph, R. Ahlrichs, K. Merzweiler, *Z. Naturforsch.* **1992**, *B47*, 1-4.
[33]   J. W. Bats, K. Ma, M. Wagner, *Acta Cryst.* **2002**, *C58*, m129-m132.
[34]   F. Jäkle, A. Berenbaum, A. J. Lough, I. Manners, *Chem. Eur. J.* **2000**, *6*, 2762-2771.
[35]   I. Nowik, M. Wagner, R. H. Herber, *J. Organomet. Chem.* **2003**, *688*, 11-14.
[36]   R. H. Herber, B. Bildstein, P. Denifl, H. Schottenberger, *Inorg. Chem.* **1997**, *36*, 3586-3592.
[37]   H. Schottenberger, K. Wurst, R. H. Herber, *J. Organomet. Chem.* **2001**, *625*, 200-207.
[38]   R. H. Herber, in *Chemical Mössbauer Spectroscopy* (Ed.: R. H. Herber), Plenum Press, New York, **1984**, pp. 199-216.
[39]   J. Silver, D. A. Davies, R. M. G. Roberts, M. Herberhold, U. Dörfler, B. Wrackmeyer, *J. Organomet. Chem.* **1999**, *590*, 71-76.
[40]   A. Houlton, J. R. Miller, R. M. G. Roberts, J. Silver, *J. Chem. Soc., Dalton Trans.* **1990**, 2181-2184.
[41]   J. Pebler, W. Ruf, W. Siebert, *Z. Anorg. Allg. Chem.* **1976**, *422*, 39-42.
[42]   V. I. Gol'danskii, E. F. Makarov, in *Chemical Applications of Mössbauer Spectroscopy* (Eds.: V. I. Gol'danskii, R. H. Herber), Academic Press, New York, **1968**, pp. 102-107.
[43]   I. Nowik, R. H. Herber, *Journal of Physics and Chemistry of Solids* **2003**, *64*, 313-317; 1225.
[44]   T. M. Gilbert, *J. Phys. Chem. A* **2004**, *108*, 2550-2554.
[45]   W. Koch, M. C. Holthausen, *A Chemist's Guide to Density Functional Theory*, 2nd ed., Wiley-VCH, Weinheim, **2001**.
[46]   K. Eichkorn, O. Treutler, H. Öhm, M. Häser, R. Ahlrichs, *Chem. Phys. Lett* **1995**, *240*, 283-289.

[47]   T. C. Gibb, in *Principles of Mössbauer Spectroscopy*, Chapman and Hall, London, **1976**, pp. 97-100.

[48]   A. E. Reed, F. Weinhold, *J. Chem. Phys.* **1983**, *78*, 4066-4073.

[49]   A. E. Reed, R. B. Weinstock, F. Weinhold, *J. Chem. Phys* **1985**, *83*, 735-746.

[50]   A. Appel, F. Jäkle, T. Priermeier, R. Schmid, M. Wagner, *Organometallics* **1996**, *15*, 1188-1194.

[51]   K. B. Wiberg, *Tetrahedron* **1968**, *24*, 1083-1096.

[52]   C. E. Moore, *Atomic Energy Levels, Vol. 467*, Natl. Bur. Stand. (US), **1949**.

[53]   R. H. Blessing, *Acta Crystallogr. Sect. A.* **1995**, *51*, 33-38.

[54]   A. L. Spek, *Acta Crystallogr. Sect. A.* **1990**, *46*, C34.

[55]   G. M. Sheldrick, *Siemens Analytical X-ray Instruments Inc., Madison, Wisconsin, USA*, **1996**.

[56]   G. M. Sheldrick, *Acta Crystallogr. Sect. A.* **1990**, *46*, 467-473.

[57]   SHELXL-97. A Program for the Refinement of Crystal Structures., G. M. Sheldrick, Unversität Göttingen, 1997.

[58]   R. F. Winter, F. M. Hornung, *Organometallics* **1999**, *18*, 4005-4014.

[59]   R. H. Herber, I. Nowik, *Hyperfine Interactions* **2001**, *136*, 699-703.

[60]   I. Nowik, R. H. Herber, *Inorg. Chem. Acta* **2000**, *310*, 191-195.

[61]   R. H. Herber, I. Nowik, *Hyperfine Interactions* **2000**, *126*, 127-130.

[62]   *Gaussian 03*, Revision B.3, M. J. Frisch, G. W. Trucks, H. B. Schlegel, G. E. Scuseria, M. A. Robb, J. R. Cheeseman, J. J. A. Montgomery, T. Vreven, K. N. Kudin, J. C. Burant, J. M. Millam, S. S. Iyengar, J. Tomasi, V. Barone, B. Mennucci, M. Cossi, G. Scalmani, N. Rega, G. A. Petersson, H. Nakatsuji, M. Hada, M. Ehara, K. Toyota, R. Fukuda, J. Hasegawa, M. Ishida, T. Nakajima, Y. Honda, O. Kitao, H. Nakai, M. Klene, X. Li, J. E. Knox, H. P. Hratchian, J. B. Cross, C. Adamo, J. Jaramillo, R. Gomperts, R. E. Stratmann, O. Yazyev, A. J. Austin, R. Cammi, C. Pomelli, J. W. Ochterski, P. Y. Ayala, K. Morokuma, G. A. Voth, P. Salvador, J. J. Dannenberg, V. G. Zakrzewski, S. Dapprich, A. D. Daniels, M. C. Strain, O. Farkas, D. K. Malick, A. D. Rabuck, K. Raghavachari, J. B. Foresman, J. V. Ortiz, Q. Cui, A. G. Baboul, S. Clifford, J. Cioslowski, B. B. Stefanov, G. Liu, A. Liashenko, P. Piskorz, I. Komaromi, R. L. Martin, D. J. Fox, T. Keith, M. A. Al-Laham, C. Y. Peng, A. Nanayakkara, M. Challacombe, P. M. W. Gill, B. Johnson, W. Chen, M. W. Wong, C. Gonzalez, J. A. Pople, Gaussian, Inc, Pittsburgh, PA, 2003.

[63]   *TurboMole - Program System for ab initio Electronic Structure Calculations* Version 5.6., R. Ahlrichs, M. Bär, H. P. Baron, R. Bauernschmitt, S. Böcker, M. Ehrig, K. Eichkorn, S. Elliott, F. Furche, F. Haase, M. Häser, C. Hättig, H. Horn, C. Huber, U. Huniar, M. Kattanek, A. Köhn, C. Kölmel, M. Kollwitz, K. May, C. Ochsenfeld, H. Öhm, A. Schäfer, U. Schneider, O. Treutler, K. Tsereteli, B. Unterreiner, M. v. Arnim, F. Weigend, P. Weis, H. Weiss, Universität Karlsruhe, Germany, 2002.

[64]   R. Ahlrichs, in *Encyclopedia Computational Chemistry* (Ed.: P. v. R. Schleyer), Wiley, Chichester, **1998**, pp. 3123-3129.

[65]   M. v. Arnim, R. Ahlrichs, *J. Comput. Chem.* **1998**, *19*, 1746-1757.

[66]   O. Treutler, R. Ahlrichs, *J. Chem. Phys.* **1995**, *102*, 346-354.

[67]   R. Ahlrichs, M. Bär, M. Häser, H. Horn, C. Kölmel, *Chem. Phys. Lett.* **1989**, *162*, 165-169.

[68]   MOLPRO Version 2002.6, R. D. Amos, A. Bernhardsson, A. Berning, P. Celani, D. L. Cooper, M. J. O. Deegan, A. J. Dobbyn, F. Eckert, C. Hampel, G. Hetzer, P. J. Knowles, T. Korona, R. Lindh, A. W. Lloyd, S. J. McNicholas, F. R. Manby, W. Meyer, M. E. Mura, A. Nicklass, P. Palmieri, R. Pitzer, G. Rauhut, M. Schütz, U. Schumann, H. Stoll, A. J. Stone, R. Tarroni, T. Thorsteinsson, H.-J. Werner.,

[69]   G. te Velde, F. M. Bickelhaupt, E. J. Baerends, S. J. A. van Gisbergen, C. Fonseca Guerra, J. G. Snijders, T. Ziegler, *J. Comput. Chem.* **2001**, *22*, 931.

[70]   F. M. Bickelhaupt, E. J. Baerends, in *Reviews in Computational Chemistry, Vol. 15* (Eds.: K. B. Lipkowitz, D. B. Boyd), Wiley-VCH, New York, **2000**, pp. 1-86.

[71]   A. D. Becke, *Phys. Rev. A* **1988**, *38*, 3098-3100.
[72]   J. B. Perdew, *Phys. Rev. B* **1986**, *33*, 8822-8824.
[73]   F. A. Hamprecht, A. J. Cohen, D. J. Tozer, N. C. Handy, *J. Chem. Phys.* **1998**, *109*, 6264-6271.
[74]   A. D. Boese, N. L. Doltsinis, N. C. Handy, M. Sprik, *J. Chem. Phys* **2000**, *112*, 1670-1678.
[75]   A. D. Boese, N. C. Handy, *J. Chem. Phys* **2001**, *114*, 5497-5503.
[76]   R. A. Kendall, H. A. Früchtl, *Theor. Chem. Acc.* **1997**, *97*, 158-163.
[77]   B. I. Dunlap, *J. Mol. Struct. (Theochem)* **2000**, *529*, 37.
[78]   B. I. Dunlap, *J. Chem. Phys* **1983**, *78*, 3140-3142.
[79]   K. Eichkorn, F. Weigend, O. Treutler, R. Ahlrichs, *Theor. Chem. Acc* **1997**, *97*, 119-124.
[80]   A. D. Becke, *J. Chem. Phys.* **1993**, *98*, 5648-5652.
[81]   P. J. Stephens, F. J. Devlin, C. F. Chabalowski, M. J. Frisch, *J. Phys. Chem.* **1994**, *98*, 11623-11627.
[82]   A. D. Becke, *J. Chem. Phys* **1997**, *107*, 8554-8560.
[83]   H. L. Schmider, A. D. Becke, *J. Chem. Phys.* **1998**, *108*, 9624-9631.
[84]   A. Schäfer, H. Horn, R. Ahlrichs, *J. Chem. Phys* **1992**, *97*, 2571-2577.
[85]   A. Schäfer, C. Huber, R. Ahlrichs, *J. Chem. Phys* **1994**, *100*, 5829-5835.
[86]   N. Godbout, D. R. Salahub, J. Andzelm, E. Wimmer, *Can. J. Chem.* **1992**, *70*, 560.
[87]   A. Klamt, G. Schüürmann, *J. Chem. Soc. Perkin Trans.* **1993**, *2*, 799.
[88]   P. Schwerdtfeger, M. Dolg, W. H. E. Schwarz, G. A. Bowmaker, P. D. W. Boyd, *J. Chem. Phys* **1989**, *91*, 1762.
[89]   A. Bergner, M. Dolg, W. Kuechle, H. Stoll, H. Preuss, *Mol. Phys.* **1993**, *80*, 1431.
[90]   P. Winget, E. J. Weber, C. J. Cramer, D. G. Truhlar, *Phys. Chem. Chem. Phys.* **2000**, *2*, 1231-1239.
[91]   T. H. Dunning Jr., *J. Chem. Phys* **1989**, *90*, 1007-1023.
[92]   T. H. Dunning Jr., *J. Phys. Chem. A* **2000**, *104*, 9062-9080.
[93]   K. A. Peterson, D. E. Woon, T. H. Dunning Jr., *J. Chem. Phys* **1994**, *100*, 7410-7415.
[94]   D. E. Woon, T. H. Dunning Jr., *J. Chem. Phys* **1994**, *101*, 8877-8893.
[95]   J. J. A. Montgomery, M. J. Frisch, J. W. Ochterski, G. A. Petersson, *J. Chem. Phys.* **1999**, *110*, 2822-2827.
[96]   F. Weigend, M. Häser, *Theor. Chem. Acc* **1997**, *97*, 331-340.
[97]   F. Weigend, M. Häser, H. Patzelt, R. Ahlrichs, *Chem. Phys. Lett* **1998**, *294*, 143-152.
[98]   AIMPAC95 program package, R. F. W. Bader, McMaster University, Hamilton, ON, Canada, 1995.
[99]   F. W. Biegler-König, R. F. W. Bader, *J. Comput. Chem.* **1982**, *3*, 317-328.
[100]   ADF2003.1, SCM, Theoretical Chemistry, Vrije Universiteit, Amsterdam, The Netherlands, 2003, http://www.scm.com.
[101]   C. Fonseca Guerra, J. G. Snijders, G. te Velde, E. J. Baerends, *Theor. Chem. Acc.* **1998**, *99*, 391-403.
[102]   G. te Velde, F. M. Bickelhaupt, E. J. Baerends, S. J. A. van Gisbergen, C. Fonseca Guerra, J. G. Snijders, T. Ziegler, *J. Comput. Chem.* **2001**, *22*, 931-967.
[103]   J. G. Snijders, E. J. Baerends, P. Vernooijs, *At. Nucl. Data Tables* **1982**, *26*, 483.
[104]   E. J. Baerends, D. E. Ellis, P. Ros, *Chem. Phys.* **1973**, *2*, 41-51.
[105]   E. van Lenthe, E. J. Baerends, J. G. Snijders, *J. Chem. Phys.* **1993**, *99*, 4597-4610.
[106]   E. van Lenthe, E. J. Baerends, J. G. Snijders, *J. Chem. Phys.* **1994**, *101*, 9783-9792.
[107]   E. van Lenthe, A. E. Ehlers, E. J. Baerends, *J. Chem. Phys.* **1999**, *110*, 8943-8953.
[108]   C. Chang, M. Pelissier, P. Durand, *Phys. Scr.* **1986**, *34*, 394-404.
[109]   J.-L. Heully, I. Lindgren, E. Lindroth, S. Lundquist, A.-M. Martensson-Pendrill, *J. Phys. B* **1986**, *18*, 2799-2815.
[110]   J. G. Snijders, A. H. Sadlej, *Chem. Phys. Lett.* **1996**, *252*, 51-61.
[111]   K. Morokuma, *J. Chem. Phys.* **1971**, *55*, 1236-1244.
[112]   T. Ziegler, A. Rauk, *Theor. Chim. Acta* **1977**, *46*, 1-10.

[113]   T. Ziegler, A. Rauk, *Inorg. Chem.* **1979**, *18*, 1558-1565.

[114]   T. Ziegler, A. Rauk, *Inorg. Chem.* **1979**, *18*, 1755-1759.

[115]   F. Bessac, G. Frenking, *Inorg. Chem.* **2003**, *42*, 7990-7994.

[116]   G. Schaftenaar, J. H. Noordik, *J. Comput.-Aided Mol. Design* **2000**, *14*, 123-134.

[117]   Z.-F. Xu, Y. Xie, W.-L. Feng, H. F. Schaefer III, *J. Phys. Chem. A* **2003**, *107*, 2716-2729.

Figure captions

Figure 2: Molecular structure of compound **3**; thermal ellipsoids shown at the 50% probability level. Selected bond lengths [Å], angles [°] and torsion angles [°]: B(1)–C(1) = 1.529(10), B(1)–C(6) = 1.67(3), B(1)–Br(1) = 1.868(8); C(1)–B(1)–C(6) = 126.6(15), C(1)–B(1)–Br(1) = 121.3(5), C(6)–B(1)–Br(1) = 112.0(14); C(2)–C(1)–B(1)–Br(1) = −168.3(4), C(5)–C(1)–B(1)–Br(1) = −8.7(8); Fe(1)⋯B(1) = 2.971(8); COG–Fe(1)–COG* = 178.2; α* = 13.7.

Figure 3: Molecular structure of compound **4**; thermal ellipsoids shown at the 50% probability level. Selected bond lengths [Å], angles [°] and torsion angles [°]: B(1)–C(11) = 1.545(4), B(1)–C(1) = 1.570(4), B(1)–C(2) = 1.578(4); C(11)–B(1)–C(1) = 121.1(2), C(11)–B(1)–C(2) = 119.6(2), C(1)–B(1)–C(2) = 119.2(2); C(12)–C(11)–B(1)–C(1) = −170.6(2), C(15)–C(11)–B(1)–C(1) = −9.5(4), C(12)–C(11)–B(1)–C(2) = 11.3(4), C(15)–C(11)–B(1)–C(2) = 172.4(2); Fe(1)⋯B(1) = 3.008(3); COG–Fe(1)–COG* = 178.2; α* = 13.0.

Figure 4: Molecular structure of compound **4●DMAP**; thermal ellipsoids shown at the 50% probability level. Selected bond lengths [Å], angles [°] and torsion angles [°]: B(1)–C(11) = 1.625(3), B(1)–C(7) = 1.622(3), B(1)–C(8) = 1.619(3), B(1)–N(1) = 1.670(3), C(4)–N(4) = 1.352(3); C(11)–B(1)–C(7) = 113.5(2), C(11)–B(1)–C(8) = 112.1(2), C(7)–B(1)–C(8) = 112.0(2), N(1)–B(1)–C(11) = 102.7(2), N(1)–B(1)–C(7) = 107.7(2), N(1)–B(1)–C(8) = 108.2(2); C(12)–C(11)–B(1)–N(1) = −90.5(2), C(15)–C(11)–B(1)–N(1) = 88.4(2), C(11)–B(1)–N(1)–C(2) = −85.6(2), C(11)–B(1)–N(1)–C(6) = 87.4(2), C(3)–C(4)–N(4)–C(41) = −1.6(3), C(5)–C(4)–N(4)–C(42) = −0.4(3); Fe(1)⋯B(1) = 3.347(2); COG–Fe(1)–COG* = 178.9; α* = 1.1.

Figure 5: Molecular structure of compound **5** [**5^A**, **5^B**] thermal ellipsoids shown at the 50% probability level. Selected bond lengths [Å], angles [°] and torsion angles [°]: B(1)–C(11) = 1.548(4) [1.545(4), 1.547(5)], B(1)–C(1) = 1.569(4) [1.576(4), 1.566(4)], B(1)–O(1) = 1.370(4) [1.378(4), 1.378(4)]; C(11)–B(1)–C(1) = 123.0(3) [123.3(3), 122.9(3)], C(11)–B(1)–O(1) = 117.9(3) [120.3(3), 117.5(3)], C(1)–B(1)–O(1) = 119.1(3) [116.4(3), 119.6(3)];

C(12)–C(11)–B(1)–C(1) = −6.0(4) [9.4(5), 8.7(4)], C(15)–C(11)–B(1)–C(1) = 158.1(3) [171.0(3), 173.5(3)], C(12)–C(11)–B(1)–O(1) = 174.7(3) [-170.5(3), −171.6(3)], C(15)–C(11)–B(1)–O(1) = −21.2(4) [−8.9(5), −6.7(4)], H(1)–O(1)–B(1)–C(11) = 176.0 [−5.6, −179.8]; Fe(1)···B(1) = 3.056(3) [3.014(4), 3.057(3)]; COG–Fe(1)–COG* = 178.2[176.9, 179.9]; α^* = 10.8 [12.9, 10.3]. Hydrogen bonds: O(1)–H(1) = O(1A)–H(1A) = O(1B)–H(1B) = 0.84, H(1)···O(1A)#1 = 1.91, H(1A)···O(1B)#2 = 1.97, H(1B)···O(1)#1 = 1.86; O(1)–H(1)···O(1A)#1 = 175.7, O(1A)–H(1A)···O(1B)#2 = 148.4, O(1B)–H(1B)···O(1)#1 = 173.6. Symmetry transformations to generate equivalent atoms: #1: −x+2, −y+1, −z+1; #2: −x+2, −y+2, −z+1.

Figure 6: Molecular structure of compound **6 [6^A]**; thermal ellipsoids shown at the 50% probability level. Selected bond lengths [Å], angles [°] and torsion angles [°]: B(1)–C(11) = 1.562(4) [1.556(3)], B(1)–O(1) = 1.370(3) [1.368(3)], B(1)–O(2) = 1.360(3) [1.360(3)]; C(11)–B(1)–O(1) = 114.9(2) [115.2(2)], C(11)–B(1)–O(2) = 127.7(2) [127.5(2)], O(1)–B(1)–O(2) = 117.5(2) [117.3(2)]; C(12)–C(11)–B(1)–O(1) = 173.6(2) [178.0(2)], C(15)–C(11)–B(1)–O(1) = −13.0(3) [−6.2(3)], C(12)–C(11)–B(1)–O(2) = −5.9(4) [−0.4(4)], C(15)–C(11)–B(1)–O(2) = 167.5(2) [175.4(2)], C(1)–O(1)–B(1)–O(2) = 1.5(3) [0.2(3)], C(2)–O(2)–B(1)–(O1) = 178.2(2) [174.5(2)]; Fe(1)···B(1) = 3.179(3) [3.197(3)]; COG–Fe(1)–COG* = 178.9 [177.9]; α^* = 6.6 [5.6].

Figure 7: Molecular structure of compound **7**; thermal ellipsoids shown at the 50% probability level. Selected bond lengths [Å], angles [°] and torsion angles [°]: B(1)–C(1) = 1.524(3), B(1)–C(21) = 1.538(3), B(1)–Br(1) = 1.969(2); C(1)–B(1)–C(21) = 128.8(2), C(1)–B(1)–Br(1) = 116.3(2), C(21)–B(1)–Br(1) = 114.9(2); C(2)–C(1)–B(1)–C(21) = -1.5(3), C(5)–C(1)–B(1)–C(21) = −165.5(2), C(2)–C(1)–B(1)–Br(1) = 179.5(2), C(5)–C(1)–B(1)–Br(1) = 15.6(2), C(22)–C(21)–B(1)–C(1) = 1.8(3), C(25)–C(21)–B(1)–C(1) = -156.0(2), C(22)–C(21)–B(1)–Br(1) = −179.2(2), C(25)–C(21)–B(1)–Br(1) = 23.0(2); Fe(1)···B(1) = 3.022(2), Fe(2)···B(1) = 2.950(2); COG–Fe(1)–COG* = 179.0, COG–Fe(2)–COG* = 179.1; α^* = 11.0 [at C(1)], 15.3 [at C(21)].

Figure 8: Molecular structure of compound **9**; thermal ellipsoids shown at the 50% probability level. Selected bond lengths [Å], angles [°] and torsion angles [°]: B(1)–C(1) = 1.523(8), B(1)–C(6) = 1.606(7), B(1)–Br(1) = 1.941(6); C(1)–B(1)–C(6) = 126.0(5), C(1)–B(1)–Br(1) = 118.3(4), C(6)–B(1)–Br(1) = 115.7(4); C(2)–C(1)–B(1)–C(6) = -178.4(5), C(5)–C(1)–B(1)–C(6) = −11.6(8), C(2)–C(1)–B(1)–Br(1) = 1.6(7), C(5)–C(1)–B(1)–Br(1) = 168.4(4); Fe(1)···B(1) = 3.056(6); COG–Fe(1)–COG* = 180.0; α* = 9.4.

Figure 9: Molecular structure of compound **11** [**11**^{A}]; thermal ellipsoids shown at the 50% probability level. Selected bond lengths [Å], angles [°] and torsion angles [°]: B(1)–C(1) = 1.554(2) [1.554(2)], B(2)–C(11) = 1.556(2) [1.561(2)], B(1)–O(1) = 1.359(2) [1.357(2)], B(1)–O(2) = 1.361(2) [1.365(2)], B(2)–O(11) = 1.365(2) [1.366(2)], B(2)–O(12) =1.354(2) [1.352(2)]; C(1)–B(1)–O(1) = 128.0(1) [127.7(1)], C(1)–B(1)–O(2) = 114.6(1) [114.8(1)], O(1)–B(1)–O(2) = 117.3(1) [117.5(1)], C(11)–B(2)–O(11) = 115.9(1) [114.6(2)], C(11)–B(2)–O(12) = 127.3(1) [128.4(2)], O(11)–B(2)–O(12) = 116.8(1) [117.1(1)]; C(2)–C(1)–B(1)–O(1) = −5.5(3) [-4.5(3)], C(5)–C(1)–B(1)–O(1) = 172.8(1) [172.7(1)], C(2)–C(1)–B(1)–O(2) = 173.1(1) [174.7(2)], C(5)–C(1)–B(1)–O(2) = −8.7(2) [−8.2(2)], C(12)–C(11)–B(2)–O(11) = −7.3(2) [−5.0(2)], C(15)–C(11)–B(2)–O(11) = 174.7(1) [178.8(2)], C(12)–C(11)–B(2)–O(12) = 174.2(1) [175.5(2)], C(15)–C(11)–B(2)–O(12) = −3.8(3) [−0.8(3)], C(6)–O(1)–B(1)–O(2) = 179.3(2) [177.3(1)], C(7)–O(2)–B(1)–O(1) = −3.3(2) [−5.9(2)], C(16)–O(11)–B(2)–O(12) = −4.6(2) [−5.0(2)], C(17)–O(12)–B(2)–O(11) = −178.8(1) [−179.1(2)]; Fe(1)···B(1) = 3.226(2) [3.216(2)], Fe(1)···B(2) = 3.225(2) [3.212(2)]; COG–Fe(1)–COG* = 177.6 [177.6]; α* = 5.0 [at C(1)], 4.2 [at C(11)], 6.0 [at C(1A)], 5.4 [at C(11A)].

Figure 10: Molecular structure of compound **12**; thermal ellipsoids shown at the 50% probability level. Selected bond lengths [Å], angles [°] and torsion angles [°]: B(1)–C(11) = 1.546(3), B(2)–C(13) = 1.548(3), B(1)–C(16) = 1.566(4), B(1)–C(17) = 1.573(4), B(2)–C(18) = 1.571(3), B(2)–C(19) = 1.571(4); C(11)–B(1)–C(16) = 120.2(2), C(11)–B(1)–C(17) = 120.7(2), C(16)–B(1)–C(17) = 119.1(2), C(13)–B(2)–C(18) = 121.1(2), C(13)–B(2)–C(19) = 119.9(2), C(18)–B(2)–C(19) = 119.0(2); C(12)–C(11)–B(1)–C(16) = 15.3(3), C(15)–C(11)–B(1)–C(16) = −173.8(2), C(12)–C(11)–B(1)–C(17) = −166.4(2),

44

C(15)–C(11)–B(1)–C(17)   =   4.5(3),   C(12)–C(13)–B(2)–C(18)   =   −3.1(3),

C(14)–C(13)–B(2)–C(18)   =   −170.0(2),   C(12)–C(13)–B(2)–C(19)   =   176.3(2),

C(14)–C(13)–B(2)–C(19)   =   9.5(3);   Fe(1)···B(1)   =   3.164(3),   Fe(1)···B(2)   =   3.096(3);

COG–Fe(1)–COG* = 177.3; α* = 6.1 [at C(11)], 9.3 [at C(13)]. Symmetry transformations to generate equivalent atoms: A: −x+1, −y+1, z.

Figure 11: Correlation between the dip angle α* and the boryl substituents of selected derivatives $FcBR^1R^2$.

Figure 12: ^{57}Fe Mössbauer spectrum of **4** at 90 K. The velocity scale is with respect to the centroid of a room temperature α-Fe spectrum.

Figure 13: The temperature dependence of the QS parameter of **4**. The original sample was rapidly quenched from room temperature to 78 K. The initial warming regime data are indicated by the open circles and the sequence by the arrows. A second warming data set is represented by the filled and half filled circles. The low QS values are ascribed to a supercooled liquid phase which converts to the stable crystallographic phase at ∼ 200 K (see text).

Figure 14: The $k^2<x^2>$ parameter as a function of temperature for **10** as discussed in the text. The filled circles are the average values determined from the recoil-free fraction data. The triangles reflect the motion perpendicular to the local symmetry axis, the starred points those parallel to this axis.

Figure 15: Illustration of geometry parameters referred to in tables 3-10 given for the example of **1**.

Figure 16: Variation of the quadrupole splitting (in mm sec^{-1}) at 90 K with the number of trimethylboron groups attached to the ferrocene backbones in compounds **4**, **10**, and **12**. The data point for n = 0 pertains to the parent ferrocene.

Figure 17: Laplacian of the electron density, zero-flux surface sections, and bond paths in the Fe-C*ipso*-B plane of the model complex Fc-BH$_2$ (**1**) obtained from BP86/TZVP calculations.

Figure 18: BP86/TZ2P (ADF) relaxed potential energy scan of the bending angle α^* in (a) [Cp-BH$_2$]$^-$, (b) [Fe(Cp-BH$_2$)]$^+$, and (c) Fc-BH$_2$.

Figure 19: Three center bonding NLMO involving Fe, C*ipso*, and B obtained from an NBO analysis for the model complex Fc-BH$_2$ (**1**).

Figure 20: Correlation diagram for selected MOs in ferrocene (C_s representation of the D_{5h}-symmetric MOs of ferrocene, left) and FcBH$_2$ **1** (right).

Figure 21: Molden[116] plots of selected valence MOs for **1**.

Figure 22: Walsh diagram illustrating the changes in MO energies upon systematic variation of α^* in **1** (obtained at the BP86/TZ2P level). See Figures 6 and 7 for the numbering scheme of orbitals.

Figure 23: Differential changes of energy contributions from the energy partitioning analysis (EPA) upon variation of α^* in **1** (a, left) and [FeCpBH$_2$]$^+$ (b, right) based on BP86/TZ2P results.

Table 1. Selected Crystallographic Data for **3**, **4**, **4•DMAP**, **5**, **6**, **7**, **9**, **11**, and **12**.

Compound	3	4	4•DMAP	5	6	7	9	11	12
Formula	$C_{11}H_{12}BBrFe$	$C_{12}H_{15}BFe$	$C_{19}H_{25}BFeN_2$	$C_{11}H_{13}BFeO$	$C_{12}H_{15}BFeO_2$	$C_{20}H_{18}BBrFe_2$	$C_{12}H_{14}B_2Br_2Fe$	$C_{14}H_{20}B_2FeO_4$	$C_{18}H_{30}B_4Fe$
M	290.78	225.90	348.07	227.87	257.90	460.76	395.52	329.77	345.51
Crystal size [mm]	0.14×0.12×0.08	0.34×0.31×0.08	0.38×0.13×0.12	0.23×0.14×0.05	0.43×0.38×0.35	0.42×0.27×0.22	0.27×0.14×0.08	0.48×0.33×0.23	0.40×0.22×0.09
Crystal system	monoclinic	orthorhombic	monoclinic	triclinic	triclinic	monoclinic	triclinic	monoclinic	orthorhombic
Space group	$P2_1/n$	$Pbca$	$P2_1/c$	$P\text{-}1$	$P\text{-}1$	$P2_1/c$	$P\text{-}1$	$P2_1/n$	$P2_12_12$
a (Å)	10.4548(18)	9.5961(8)	9.2709(15)	11.6677(11)	10.3886(12)	10.4521(8)	6.3985(12)	16.2224(9)	15.068(3)
b (Å)	7.6663(10)	8.7619(7)	19.940(2)	12.5059(13)	10.4644(12)	12.2603(6)	6.8862(12)	9.2084(5)	7.2030(14)
c (Å)	14.331(3)	25.580(2)	10.1081(14)	12.9675(12)	11.4338(13)	13.8391(11)	8.4905(15)	20.2143(9)	9.1660(14)
α (°)	90	90	90	97.385(8)	83.432(9)	90	83.226(14)	90	90
β (°)	102.770(14)	90	113.191(11)	111.553(7)	73.997(9)	106.529(6)	81.124(14)	96.803(4)	90
γ (°)	90	90	90	110.408(7)	76.077(9)	90	67.651(13)	90	90
U (Å³)	1120.2(3)	2150.8(3)	1717.6(4)	1576.3(3)	1158.2(2)	1700.1(2)	341.14(11)	2998.4(3)	994.8(3)
Z	4	8	4	6	4	4	1	8	2
D_c (g cm^{-3})	1.724	1.395	1.346	1.440	1.479	1.800	1.925	1.461	1.153
T (K)	173(2)	100(2)	173(2)	100(2)	173(2)	100(2)	173(2)	173(2)	155(2)
μ(Mo-Kα) (mm^{-1})	4.867	1.355	0.878	1.395	1.281	4.053	6.933	1.016	0.752
$2\theta_{max}$ (°)	50.44	57.74	50.42	54.12	59.56	55.38	50.20	51.66	63.18
Measured reflections	13666	13708	5768	23506	23192	30306	4658	56512	13193
Unique reflections (R_{int})	1972 (0.103)	2800 (0.066)	2955 (0.031)	6877 (0.064)	6493(0.086)	3942(0.052)	1217 (0.062)	5727(0.051)	3070 (0.058)
Obsd. reflections [$I>2\sigma(I)$]	1359	1876	2034	4486	5022	2981	998	4764	2686
Parameters refined	146	129	210	385	293	217	80	387	109
$R1$ [$I>2\sigma(I)$]	0.045	0.035	0.028	0.037	0.054	0.021	0.044	0.023	0.044
$wR2$ [$I>2\sigma(I)$]	0.098	0.065	0.046	0.072	0.133	0.030	0.115	0.057	0.083
GOOF on F^2	0.747	0.902	0.828	0.869	0.961	0.999	1.036	0.943	1.156
Largest diff. peak and hole (eÅ^{-3})	0.33, -0.45	0.29, -0.46	0.22, -0.23	0.35, -0.47	0.99, -1.23	0.32, -0.41	1.20, -0.76	0.28, -0.27	+0.38, -0.23

Table 2. Mössbauer parameters for **4**, **4•DMAP**, **10**, **10•DMAP**, and **12.** Values in parentheses are estimated errors in the last significant figure(s).

	4	**4•DMAP**	**10**	**10•DMAP**	**12**	units
IS(90)	0.524(4)	0.515(3)	0.528(4)	0.520(4)	0.546(4)	mm s^{-1}
QS(90)	2.309(4)	2.344(3)	2.082(4)	2.339(4)	1.891(4)	mm s^{-1}
-d IS/dT	3.91(15)	4.75(37)	3.17(41)	3.17(6)	4.02(11)	mm s^{-1} K^{-1} x 10^{-4}
-d ln$A$/dT	9.57(5)	5.42(14)	12.9(3)	11.1(1)	7.94(17)	K^{-1} x 10^{-3}
M_{eff}	107(10)	130(12)	131(13)	131(13)	104(1)	Daltons
Θ_M	87	105	68	73	97	K
vibrational anisotropy	small	small	above ~180 K	small	moderate	

48

Table 3: Comparison of selected geometry parameters for computed and experimental structures of ferrocene (distances in Å).

	BP86				HCTH				B98		B3LYP		Exp[a]
	SVP/DGA1	SVP	TZVP/DGA1	TZVP	SVP/DGA1	SVP	TZVP/DGA1	TZVP	SVP	TZVP	SVP	TZVP	
Fe-X1[b]	1.668	1.641	1.679	1.655	1.651	1.620	1.659	1.632	1.674	1.687	1.681	1.694	1.660
Fe-C	2.071	2.048	2.077	2.057	2.051	2.026	2.055	2.033	2.070	2.079	2.074	2.083	2.064
Imag. Freq.	i34	i20	i19	–	i48	i54	i43	i39	–	–	i34	i19	

[a] Experimental data taken from Xu et al.[117] [b] Distance between the iron atoms and the geometric center of the Cp carbon skeleton

Table 4: Comparison of selected geometry parameters for computed structures of FcBH$_2$ (**1**) (distances in Å, angles and torsion angles in °).

	BP86				HCTH				B98		B3LYP	
	SVP/DGA1	SVP	TZVP/DGA1	TZVP	SVP/DGA1	SVP	TZVP/DGA1	TZVP	SVP	TZVP	SVP	TZVP
α*[a]	25.0	27.3	23.7	26.5	20.1	22.0	18.0	20.1	20.4	18.9	16.8	15.7
β*[b]	3.4	4.0	3.2	3.7	3.6	4.0	3.4	3.7	2.5	2.4	2.5	2.5
Fe-X1	1.667	1.644	1.678	1.657	1.651	1.627	1.659	1.638	1.679	1.691	1.683	1.697
Fe-X2	1.683	1.656	1.693	1.669	1.666	1.636	1.674	1.647	1.680	1.694	1.687	1.701
Fe-Cipso[c]	2.047	2.030	2.054	2.038	2.040	2.022	2.047	2.032	2.057	2.066	2.064	2.074
Fe-C'ipso[c]	2.095	2.078	2.099	2.085	2.077	2.056	2.081	2.062	2.084	2.093	2.089	2.097
B-Cipso	1.532	1.531	1.524	1.524	1.530	1.528	1.523	1.522	1.526	1.520	1.523	1.517
B-H	1.225	1.220	1.211	1.206	1.222	1.217	1.208	1.203	1.210	1.197	1.209	1.195
γ*[d]	1.1	2.0	0.7	1.8	-0.3	0.1	0.0	0.1	-0.8	-0.3	-0.4	-0.4
Imag. Freq.	–	–	–	–	–	–	–	–	i6	–	–	–

[a] Bending angle defined as 180°-α(X1-Cipso-B) [b] Bending angle defined as 180° - β(X1-Fe-X2) [c] Cipso is the borylated carbon atom in the substituted Cp ring, C'ipso is the corresponding carbon atom of the unsubstituted Cp ring. [d] Non-planarity of the boryl substituent group defined as 180°-γ(Cipso-B-H-H')

Table 5: Comparison of selected geometry parameters for computed structures of FcBBr$_2$ (**2**) (distances in Å, angles and torsion angles in °).

	BP86				HCTH				B98		B3LYP		Exp[f]		
	SVP/DGA1	SVP	TZVP/DGA1	TZVP	SVP/DGA1	SVP	TZVP/DGA1	TZVP	SVP	TZVP	SVP	TZVP	A	B	Mean
α*[a,g]	12.1	13.5	9.8	11.4	9.5	8.9	7.3	7.5	10.3	8.9	7.9	6.7	17.8	19.0	18.4
β*[b]	4.0	2.8	3.5	2.7	4.2	2.9	3.6	2.7	1.96	1.8	2.0	1.9	4.7	4.1	4.4
Fe-X1	1.667	1.645	1.678	1.658	1.651	1.626	1.659	1.637	1.677	1.692	1.684	1.698	1.644	1.642	1.643
Fe-X2	1.682	1.651	1.692	1.665	1.665	1.631	1.672	1.643	1.679	1.692	1.685	1.698	1.655	1.651	1.653
Fe-Cipso[c]	2.073	2.050	2.076	2.060	2.060	2.039	2.059	2.045	2.067	2.077	2.075	2.083	2.025	2.033	2.029
Fe-C'ipso[c]	2.094	2.068	2.097	2.075	2.076	2.046	2.077	2.052	2.080	2.087	2.082	2.090	2.053	2.054	2.054
B-Cipso	1.540	1.531	1.531	1.523	1.544	1.535	1.535	1.526	1.527	1.519	1.526	1.517	1.484	1.473	1.479
B-Br	2.044	1.943	2.053	1.946	2.033	1.930	2.046	1.936	1.934	1.938	1.936	1.940	1.947	1.921	1.934
B-Br'	2.044	1.943	2.053	1.946	2.033	1.930	2.046	1.936	1.934	1.938	1.936	1.940	1.916	1.946	1.931
γ*[d,g]	-23.7	1.7	-22.7	2.0	-23.4	1.1	-22.8	1.3	0.7	1.0	0.9	1.3	1.8	3.3	2.6
δ[e,g]	4.6	-11.1	5.8	-9.7	6.3	-7.5	7.8	-6.6	-8.1	-7.4	-6.7	-5.9	-18.5	-14.5	-16.5
δ'[e,g]	-4.6	11.1	-5.8	9.7	-6.3	7.5	-7.8	6.6	8.3	7.4	6.7	5.9	9.1	17.3	13.2
Imag. Freq.	–	–	–	–	–	–	–	–	i22	i7	–	–	–	–	–

[a] Bending angle defined as 180°-α(X1-Cipso-B) [b] Bending angle defined as 180° - β(X1-Fe-X2) [c] Cipso is the borylated carbon atom in the substituted Cp ring, C'ipso is the corresponding carbon atom of the unsubstituted Cp ring [d] Non-planarity of the boryl substituent group defined as 180°-γ(Cipso-B-Br'-Br) [e] Torsion angle δ defined as δ(Br-B-Cipso-C2) and δ'(Br'-B-Cipso-C'2) [f] Two independent molecules per unit cell exist in the crystal structure [g] A positive sign indicates that the boron atom / substituents are pyramidalized / bent towards the iron center

50

Table 6: Comparison of selected geometry parameters for computed structures of FcB(Me)Br (**3**) (distances in Å, angles and torsion angles in °).

	BP86				HCTH				B98		B3LYP		Exp[f]
	SVP/DGA1	SVP	TZVP/DGA1	TZVP	SVP/DGA1	SVP	TZVP/DGA1	TZVP	SVP	TZVP	SVP	TZVP	
α*[a]	12.0	14.0	9.5	12.0	9.1	9.9	6.6	8.6	10.1	9.3	8.0	7.3	13.7
β*[b]	3.3	2.8	3.0	2.8	3.4	2.7	3.0	2.8	2.0	2.1	2.1	2.1	1.8
Fe-X1	1.668	1.645	1.679	1.658	1.652	1.628	1.660	1.637	1.681	1.691	1.687	1.697	1.650
Fe-X2	1.683	1.651	1.693	1.664	1.667	1.631	1.673	1.641	1.681	1.692	1.688	1.698	1.661
Fe-C_{ipso}[c]	2.075	2.051	2.081	2.061	2.065	2.038	2.067	2.050	2.072	2.078	2.079	2.084	2.035
Fe-C'_{ipso}[c]	2.095	2.067	2.099	2.074	2.076	2.044	2.078	2.045	2.079	2.087	2.081	2.090	2.052
B-C_{ipso}	1.543	1.539	1.533	1.532	1.546	1.542	1.536	1.534	1.536	1.528	1.534	1.526	1.530
B-Br	2.118	1.971	2.133	1.979	2.103	1.958	2.127	1.968	1.962	1.970	1.965	1.974	(1.739)
B-C(Me)	1.571	1.575	1.564	1.570	1.569	1.573	1.561	1.568	1.572	1.567	1.570	1.565	(1.869)
γ*[d]	5.6	2.9	4.2	2.8	4.4	1.9	3.1	1.3	1.4	1.5	1.2	1.6	(11.0)
δ[e]	-21.5	-13.5	-20.5	-10.6	-20.1	-9.3	-19.1	-6.2	-9.6	-7.8	-6.8	-6.1	(-8.2)
δ'[e]	-8.61	10.5	-9.3	10.3	11.1	7.9	-12.4	8.3	7.2	7.8	6.6	6.8	(21.4)
Imag. Freq.	–	–	–	–	–	–	–	–	i22	i7	–	–	–

[a] Bending angle defined as 180°-α(X1-C_{ipso}-B) [b] Bending angle defined as 180° - β(X1-Fe-X2) [c] C_{ipso} is the borylated carbon atom in the substituted Cp ring, C'_{ipso} is the corresponding carbon atom of the unsubstituted Cp ring [d] Non-planarity of the boryl substituent group defined as 180°-γ(C_{ipso}-B-Br-C(Me)) [e] torsion angle δ defined as δ(C(Me)-B-C_{ipso}-C2) and δ'(Br-B-C_{ipso}-C'2) [f] Experimental data in parentheses indicate a disordered region in the X-ray structure.

51

Table 7: Comparison of selected geometry parameters for computed structures of FcBMe$_2$ (**4**) (distances in Å, angles and torsion angles in °).

	BP86				HCTH				B98		B3LYP		Exp
	SVP/DGA1	SVP	TZVP/DGA1	TZVP	SVP/DGA1	SVP	TZVP/DGA1	TZVP	SVP	TZVP	SVP	TZVP	
α*[a]	11.8	14.8	9.4	12.1	8.7	10.0	7.3	8.0	10.5	8.4	8.8	6.9	13.0
β*[b]	2.4	2.4	2.4	2.2	2.5	2.4	2.4	2.2	1.8	1.7	1.8	1.8	1.8
Fe-X1	1.669	1.645	1.680	1.658	1.652	1.626	1.661	1.637	1.677	1.690	1.683	1.697	1.651
Fe-X2	1.680	1.650	1.690	1.663	1.663	1.629	1.670	1.640	1.678	1.692	1.685	1.699	1.656
Fe-Cipso[c]	2.075	2.052	2.085	2.063	2.062	2.040	2.068	2.048	2.073	2.083	2.079	2.089	2.043
Fe-C'ipso[c]	2.087	2.066	2.091	2.073	2.067	2.043	2.070	2.048	2.078	2.086	2.082	2.090	2.063
B-Cipso	1.560	1.555	1.552	1.550	1.563	1.558	1.556	1.553	1.553	1.547	1.551	1.545	1.545
B-C(Me)	1.592	1.590	1.586	1.586	1.590	1.586	1.584	1.582	1.586	1.583	1.584	1.580	1.578
B-C'(Me)	1.590	1.590	1.587	1.586	1.585	1.585	1.583	1.582	1.586	1.583	1.584	1.580	1.571
γ*[d]	1.9	4.4	1.7	3.7	0.0	2.3	0.5	1.8	1.6	1.6	2.0	1.8	1.9
δ[e]	-11.8	-13.3	-6.2	-10.4	-3.6	-8.0	-4.6	-6.3	-7.0	-5.6	-5.8	-4.4	-9.6
δ'[e]	8.0	13.8	10.0	11.4	10.0	9.5	7.3	7.8	10.5	8.9	9.5	8.0	11.3
Imag. Freq.	–	–	–	–	–	–	–	–	i22	–	–	–	–

[a] Bending angle defined as 180°-α(X1-Cipso-B) [b] Bending angle defined as 180° - β(X1-Fe-X2) [c] Cipso is the borylated carbon atom in the substituted Cp ring, C'ipso is the corresponding carbon atom of the unsubstituted Cp ring [d] Non-planarity of the boryl substituent group defined as 180°-γ(Cipso-B-C'(Me)-C(Me)) [e] torsion angle δ defined as δ(C(Me)-B-Cipso-C2) and δ'(C'(Me)-B-Cipso-C'2)

52

Table 8: Comparison of selected geometry parameters for computed structures of FcBMe(OH) (5) (distances in Å, angles and torsion angles in °).

	BP86				HCTH				B98		B3LYP			Exp[f]	
	SVP/DGA1	SVP	TZVP/DGA1	TZVP	SVP/DGA1	SVP	TZVP/DGA1	TZVP	SVP	TZVP	SVP	TZVP	A	B	Mean
α*[a]	6.3	7.3	5.5	5.2	5.5	6.0	4.7	5.2	5.9	5.1	4.7	3.8	10.9	10.3	10.6
β*[b]	1.4	1.3	1.6	1.4	1.5	1.4	1.6	1.4	0.8	1.1	0.9	1.2	1.9	0.1	1.0
Fe-X1	1.670	1.645	1.680	1.636	1.654	1.624	1.660	1.636	1.678	1.690	1.686	1.697	1.648	1.654	1.651
Fe-X2	1.679	1.648	1.687	1.638	1.663	1.626	1.668	1.638	1.679	1.690	1.686	1.697	1.649	1.654	1.652
Fe-$Cipso$[c]	2.082	2.061	2.088	2.048	2.065	2.042	2.068	2.048	2.079	2.085	2.085	2.090	2.048	2.047	2.048
Fe-C'$ipso$[c]	2.082	2.057	2.088	2.043	2.063	2.036	2.066	2.043	2.075	2.084	2.079	2.088	2.043	2.049	2.046
B-$Cipso$	1.566	1.561	1.556	1.554	1.566	1.562	1.558	1.554	1.559	1.551	1.557	1.548	1.548	1.547	1.548
B-C(Me)	1.378	1.380	1.386	1.382	1.372	1.374	1.381	1.382	1.368	1.375	1.368	1.377	1.370	1.379	1.375
B-O	1.592	1.591	1.587	1.583	1.589	1.588	1.584	1.583	1.588	1.584	1.586	1.581	1.569	1.566	1.568
γ*[d]	0.7	1.8	1.3	1.9	0.2	1.2	0.6	1.9	1.2	2.1	1.2	2.3	-0.6	0.3	-0.2
δ[e]	-4.9	-6.1	-4.5	-4.3	-3.9	-4.3	-3.2	-4.3	-5.2	-4.7	-5.0	-4.3	5.9	-8.8	-1.5
δ'[e]	5.8	6.9	5.5	5.7	5.0	6.1	4.8	5.7	5.0	5.1	3.4	3.9	21.3	6.8	13.8
Imag. Freq.	–	–	–	–	–	–	–	–	–	i29	–	–	–	–	–

[a] Bending angle defined as 180°-α(X1-$Cipso$-B) [b] Bending angle defined as 180° - β(X1-Fe-X2) [c] $Cipso$ is the borylated carbon atom in the substituted Cp ring, C'$ipso$ is the corresponding carbon atom of the unsubstituted Cp ring [d] Non-planarity of the boryl substituent group defined as 180°-γ($Cipso$-B-O-C(Me)) [e] torsion angle δ defined as δ(C(Me)-B-$Cipso$-C2) and δ(O-B-$Cipso$-C'2) [f] Three independent molecules per unit cell exist in the crystal structure; data are given for two conformers, in which the OH group is oriented syn to the methyl group.

53

Table 9: Comparison of selected geometry parameters for computed structures of the FcBMe$_2$•DMAP adduct (**4**•DMAP) (distances in Å, angles and torsion angles in °).

	BP86				HCTH				B98		B3LYP		Exp
	SVP/DGA1	SVP	TZVP/DGA1	TZVP	SVP/DGA1	SVP	TZVP/DGA1	TZVP	SVP	TZVP	SVP	TZVP	
α*[a]	2.0	3.4	2.9	2.0	2.9	4.0	3.9	5.1	2.9	3.4	1.6	-2.3	1.1
β*[b]	1.2	0.6	0.9	0.2	1.4	1.2	1.9	0.8	1.6	0.5	0.5	0.3	1.1
Fe-X1	1.668	1.644	1.680	1.654	1.651	1.628	1.659	1.635	1.677	1.689	1.682	1.693	1.649
Fe-X2	1.676	1.643	1.687	1.657	1.662	1.626	1.668	1.635	1.677	1.691	1.684	1.698	1.648
Fe-Cipso[c]	2.106	2.082	2.112	2.089	2.089	2.075	2.094	2.073	2.108	2.114	2.110	2.114	2.083
Fe-C'ipso[c]	2.083	2.052	2.087	2.059	2.066	2.034	2.067	2.039	2.077	2.085	2.079	2.086	2.036
B-Cipso	1.637	1.631	1.630	1.621	1.640	1.633	1.633	1.628	1.629	1.623	1.623	1.618	1.625
B-C(Me)	1.636	1.634	1.632	1.635	1.634	1.634	1.631	1.629	1.633	1.629	1.632	1.629	1.619
B-C(Me)	1.636	1.634	1.632	1.635	1.634	1.629	1.631	1.629	1.633	1.629	1.632	1.629	1.622
B–N	1.698	1.684	1.700	1.684	1.729	1.708	1.729	1.712	1.685	1.687	1.697	1.699	1.670
γ*[d]	49.6	49.5	49.2	49.8	48.4	49.0	48.1	48.4	49.9	49.7	49.7	49.4	51.1
δ[e]	26.9	27.9	27.5	26.4	27.3	40.7	28.0	29.2	28.1	30.8	19.8	26.4	25.5
δ'[e]	-26.9	-28.0	-27.5	-26.5	-27.3	-15.1	-28.0	-29.0	-28.1	-25.6	-3.2	26.4	-27.5
ε[f]	87.4	87.2	87.4	180.0	87.5	135.8	87.7	87.6	88.6	90.9	177.5	180.0	87.3
ζ[g]	102.4	102.1	102.0	105.8	101.5	103.6	101.4	101.8	102.7	102.9	105.8	105.7	102.7
BDE[h]	14.8	14.3	11.2		9.8	10.2	6.2	5.9	15.3	11.8			
	(15.9)	(15.3)	(12.4)	(12.1)	(10.5)	(10.1)	(7.0)	(6.7)	(16.5)	(13.1)	(13.7)	(9.8)	

[a] Bending angle defined as 180°-α(X1-Cipso-B) [b] Bending angle defined as 180° - β(X1-Fe-X2) [c] Cipso is the borylated carbon atom in the substituted Cp ring, C'ipso is the corresponding carbon atom of the unsubstituted Cp ring [d] Non-planarity of the boryl substituent group defined as 180°-γ(Cipso-B-C'(Me)-C(Me)) [e] torsion angle δ defined as δ(C(Me)-B-C-C2) and δ'(C'(Me)-B-C-C'2) [f] Torsion angle of the pyridyl group in DMAP defined as ε(C(Py)-N(Py)-B-Cipso) [g] Bond angle ζ(N(Py)-B-Cipso). [h] Binding energy D_e (total energy differences in kcal mol^{-1}) of DMAP to **4**. Data given in parentheses relate to the collinear conformer (see text).

54

Table 10: Deviations from experiment (calculated data − experimental data, distances in Å, angles and torsion angles in °)

	BP SVP/DGA1	BP SVP	BP TZVP/DGA1	BP TZVP	HCTH SVP/DGA1	HCTH SVP	HCTH TZVP/DGA1	HCTH TZVP	B98 SVP	B98 TZVP	B3LYP SVP	B3LYP TZVP
Fe-Cipso												
Ferrocene	0.007	-0.016	0.013	-0.007	-0.013	-0.038	-0.009	-0.031	0.014	0.027	0.021	0.034
2	0.042	0.018	0.045	0.026	0.027	0.001	0.027	0.007	0.032	0.041	0.037	0.045
3	0.042	0.016	0.047	0.024	0.027	-0.003	0.029	0.004	0.032	0.039	0.037	0.043
4	0.028	0.006	0.035	0.015	0.011	-0.012	0.016	-0.005	0.022	0.031	0.027	0.036
5	0.035	0.012	0.041	-0.001	0.017	-0.008	0.020	-0.001	0.030	0.038	0.035	0.042
4•DMAP	0.035	0.012	0.040	0.015	0.018	-0.005	0.021	-0.004	0.033	0.040	0.035	0.040
Mean	0.032	0.008	0.037	0.012	0.015	-0.011	0.017	-0.005	0.027	0.036	0.032	0.040
B-Cipso												
2	0.062	0.053	0.053	0.045	0.066	0.057	0.057	0.048	0.049	0.041	0.048	0.039
3	0.013	0.009	0.003	0.002	0.016	0.012	0.006	0.004	0.006	-0.002	0.004	-0.004
4	0.015	0.010	0.007	0.005	0.018	0.013	0.011	0.008	0.008	0.002	0.006	0.000
5	0.019	0.014	0.009	0.007	0.019	0.015	0.011	0.007	0.012	0.004	0.010	0.001
4•DMAP	0.012	0.006	0.005	-0.004	0.015	0.008	0.008	0.003	0.004	-0.002	-0.002	-0.007
Mean [a]	0.024	0.018	0.015	0.011	0.027	0.021	0.019	0.014	0.016	0.009	0.013	0.006
	(0.015)	(0.010)	(0.006)	(0.003)	(0.017)	(0.012)	(0.009)	(0.006)	(0.008)	(0.001)	(0.005)	(0.003)
α*												
2	-6.3	-4.9	-8.6	-7.0	-8.9	-9.5	-11.1	-10.9	-8.1	-9.5	-10.5	-11.7
3	-1.7	0.3	-4.2	-1.7	-4.7	-3.8	-7.1	-5.1	-3.6	-4.5	-5.7	-6.4
4	-1.2	1.9	-3.6	-0.9	-4.3	-2.9	-5.7	-5.0	-2.5	-4.5	-4.2	-6.1
5	-4.2	-3.3	-5.1	-5.3	-5.1	-4.6	-5.9	-5.3	-4.7	-5.5	-5.9	-6.8
Mean	-3.4	-1.5	-5.4	-3.7	-5.8	-5.2	-7.5	-6.6	-4.7	-6.0	-6.6	-7.8

[a] Values in parentheses obtained excluding data for **2**.

55

Table 11: Computed binding energies at various levels of density functional theory for the neutral donor-acceptor complexes $BH_3 \bullet NH_3$, $BH_3 \bullet Pyridine$, $BMe_3 \bullet NH_3$, and $BMe_3 \bullet Pyridine$ (total energy differences given in kcal mol^{-1}).

Method/Basis	$BH_3 \bullet NH_3$	R(B-N)	$BH_3 \bullet py$	R(B-N)	$B(CH_3)_3 \bullet NH_3$	R(B-N)	$B(CH_3)_3 \bullet py$	R(B-N)
BP86/SVP/DGA1	39.2	1.649	39.2	1.610	21.1	1.685	15.2	1.699
BP86/SVP	39.0	1.652	38.9	1.603	19.3	1.691	15.3	1.673
BP86/TZVP/DGA1	34.3	1.659	36.1	1.613	15.7	1.696	12.2	1.690
BP86/TZVP	33.8	1.664	35.8	1.607	14.3	1.702	12.3	1.677
HCTH/SVP/DGA1	35.4	1.650	34.4	1.618	17.4	1.692	9.5	1.724
HCTH/SVP	35.3	1.654	34.2	1.610	15.5	1.692	9.6	1.702
HCTH/TZVP/DGA1	30.4	1.663	31.0	1.623	12.1	1.704	6.5	1.723
HCTH/TZVP	30.0	1.666	30.7	1.615	10.6	1.711	6.5	1.703
B98/SVP	37.6	1.647	36.9	1.612	19.5	1.684	15.2	1.684
B98/TZVP	32.4	1.658	33.7	1.616	14.6	1.695	12.2	1.685
B3LYP/SVP	35.9	1.653	35.1	1.616	17.4	1.696	12.8	1.695
B3LYP/TZVP	30.2	1.665	31.6	1.622	11.9	1.710	9.3	1.700
RIMP2/cc-pVDZ	35.7	1.657	35.9	1.635	23.9	1.680	22.6	1.685
RIMP2/cc-pVTZ	33.9	1.650	37.1	1.620	21.0	1.674	23.3	1.663
RIMP2/cc-pVQZ	32.9	1.646	36.8	1.616	19.9	1.669	22.7	1.659
RIMP2 limit (DTQ)^b	32.3		36.5		19.1		22.2	
CBS-QB3	31.8	1.664^a	35.6	1.621^a	18.5	1.704^a	20.8	1.702^a
CCSD(T)/cc-pVDZ	35.5	1.664						
CCSD(T)/cc-pVTZ	33.7	1.655						
CCSD(T)/cc-pVQZ	32.5	1.650						
CCSD(T) limit (DTQ)^b	31.7							

^{a} B3LYP/6-311G** geometry is used in the CBS-QB3 scheme. ^{b} Extrapolated basis set limit (see text).

56

Table 12: Adiabatic ionization energies (IE) computed from total energy differences obtained at the BP86/TZVP/RI(TZVP)+COSMO (CH$_2$Cl$_2$, ε=8.93) level of density functional theory for substituted ferrocenes Fc-R. All calculations were performed without molecular symmetry (C_1). Experimental redox potentials (see text): **4**: 0.09 V, **4•DMAP**: -0.40 V, **10**: 0.26 V, **10•DMAP**: -0.66 V, **12**: 0.39 V (in CH$_2$Cl$_2$ vs. FcH/FcH⁺)

Species	IE [eV]	ΔIE(Fc/Fc⁺) [eV]	α* (neutral / ion) [°]
FcH	5.14	0.00	25.1 / 5.0
FcBH$_2$ (**1**)	5.48	0.35	13.2 / 3.6
FcBMe$_2$ (**4**)	5.29	0.16	12.1 / 3.3
FcB(Me)Br (**3**)	5.42	0.28	6.1 / 2.2
FcB(Me)(OH) (**5**)	5.19	0.05	10.5 / 2.8
FcBF$_2$	5.45	0.32	11.9 / 3.0
FcBCl$_2$	5.52	0.39	13.2 / 3.6
FcBBr$_2$ (**2**)	5.54	0.41	14.4 / 1.1
FcBI$_2$	5.52	0.38	
fc-(BMe$_2$)$_2$ (**10**)	5.38	0.25	10.7, 10.2 / 2.3, 2.1
1,1',3,3'-fc(BMe$_2$)$_4$ (**12**)	5.53	0.40	(6.3, 3.9)$_U$(6.1,3.5)$_L$ / (1.4, 0.8)$_U$(1.2, 0.9)$_L$ [a]
FcB(NH$_2$)$_2$	5.05	-0.08	1.5 / 0.7
FcBH$_2$•pyridine	4.83	-0.31	0.1 / 2.7
FcBMe$_2$•DMAP (**4•DMAP**)[b]	4.71	-0.43	-3.2 / 0.0
fc-(BMe$_2$•DMAP)$_2$ (**10•DMAP**)	4.54	-0.60	-2.2, -2.3 / -0.4, -0.6

[a] α* values grouped in parentheses refer to upper and lower Cp rings, respectively. [b] Data for the perpendicular conformer (see text), ΔIE for the collinear conformer is -0.38 eV.

57

Table 13: Correlation of the *d*-orbital population at iron in substituted ferrocenes from natural population analyses and the experimentally determined quadrupole splitting (see text).

	a_1' (d_{z^2})	e_1''(d_{xz})	e_1''(d_{yz})	e_2'' $(d_{x^2-y^2})$	e_2'' (d_{xy})	p_1	p_2	Δp^a	Δp_{scaled}^b	QS
FcH	1.960	1.049	1.049	1.765	1.765	2.098	3.530	4.962	2.418	2.418
4	1.951	1.061	1.060	1.714	1.779	2.121	3.493	4.865	2.371	2.309
10	1.950	1.070	1.062	1.725	1.738	2.132	3.463	4.794	2.336	2.082
12	1.946	1.066	1.074	1.692	1.728	2.140	3.420	4.701	2.291	1.891
4•DMAP	1.959	1.048	1.057	1.767	1.756	2.105	3.523	4.942	2.408	2.344
10•DMAP	1.963	1.048	1.054	1.762	1.760	2.102	3.522	4.942	2.408	2.339

[a] Data computed according to eq. (2) [b] Proportionality factor 2.052 obtained as Δp/QS for parent ferrocene.

58

Table 14: Charges derived from NPA analysis of neutral and ionized FcH, **1**, and **1•py**. The analysis has been performed with the NBO routines implemented in Gaussian03 at the BP86/TZVP level on optimized geometries obtained at the BP86/TZVP/RI(TZVP) +COSMO(CH_2Cl_2, ε=8.93) level with the program TURBOMOLE.

	q(Fe)	q(Cp_U) [a]	q(Cp_S) [a]	B	Py
FcH	0.18	-0.09	-0.09	-	-
FcH^+	0.63	0.19	0.19	-	-
Δq	0.45	0.28	0.28	-	-
1	0.21	0.00	-0.31	0.21	-
1$^+$	0.64	0.22	-0.17	0.40	-
Δq	0.43	0.22	0.14	0.19	-
1•pyridine	0.20	-0.10	-0.35	-0.03	0.33
1•pyridine$^+$	0.64	0.13	-0.12	-0.06	0.42
Δq	0.44	0.23	0.23	-0.03	0.09

[a] Group charges (sum over charges of all constituting C and H atoms) for the substituted (Cp_S) and unsubstituted (Cp_U) Cp ring systems.

Table 15: NPA analyses of several points along the angle bending scan of **1** (BP86/TZVP). Charge differences relative to the planar structure are given.

α*	45°	40°	35°	31°	26°	21°	16°	12°	7°	2°	q [b]
Cp [a]	0.10	0.08	0.06	0.05	0.03	0.02	0.01	0.01	0.00	0.00	0.00
Cp-BH$_2$ [a]	-0.04	-0.03	-0.03	-0.02	-0.02	-0.01	-0.01	-0.01	0.00	0.00	-0.21
C$ipso$	0.15	0.12	0.10	0.08	0.06	0.05	0.03	0.02	0.01	0.00	-0.37
BH$_2$ [a]	-0.22	-0.18	-0.15	-0.12	-0.09	-0.07	-0.05	-0.03	-0.01	0.00	0.10
Fe	-0.06	-0.05	-0.03	-0.02	-0.02	-0.01	-0.01	0.00	0.00	0.00	0.21

[a] Charge differences based on group charges given as the sum of charges of all constituting atoms. [b] Total charges obtained for the minimum structure.

Figure 1
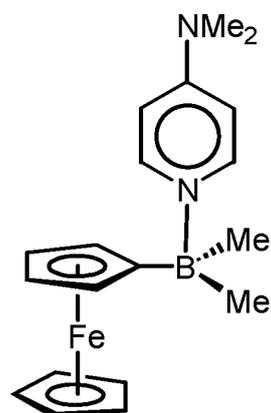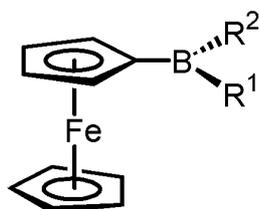
1 : $R^1 = R^2 = H$
2 : $R^1 = R^2 = Br$
3 : $R^1 = Br, R^2 = Me$
4 : $R^1 = R^2 = Me$
5 : $R^1 = OH, R^2 = Me$
6   $R^1 = R^2 = OMe$

4·DMAP
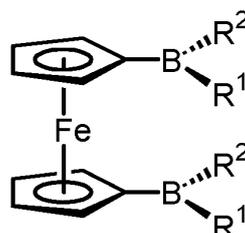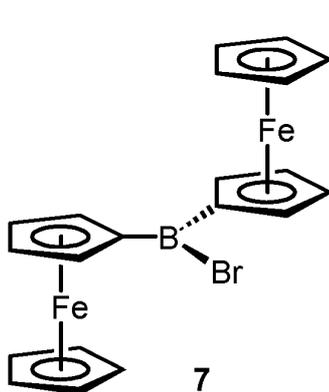
8   : $R^1 = R^2 = Br$
9   : $R^1 = Br, R^2 = Me$
10 : $R^1 = R^2 = Me$
11 : $R^1 = R^2 = OMe$

7
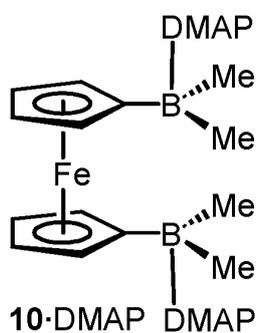
10·DMAP
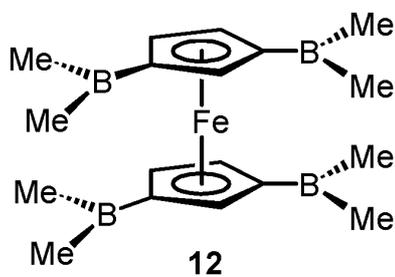
12
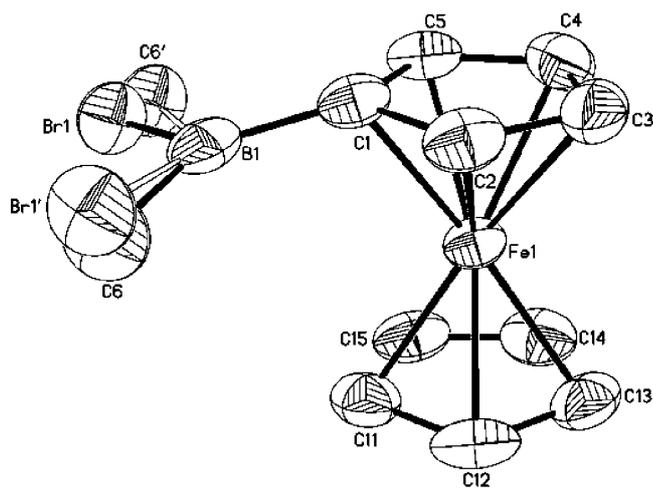
Figure 2

Figure 3
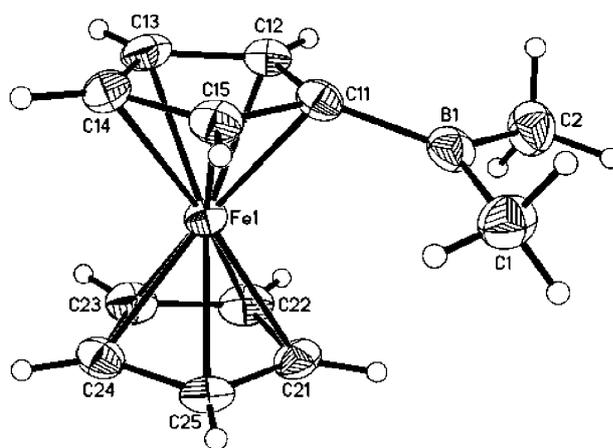
Figure 4
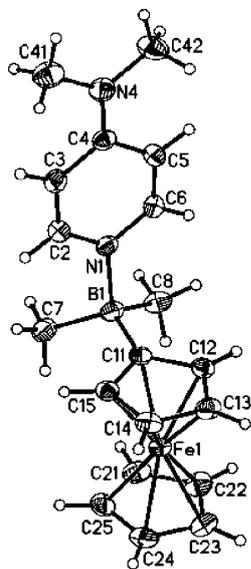
Figure 5
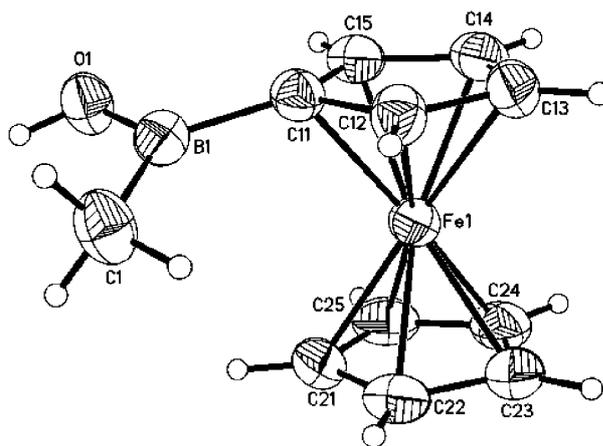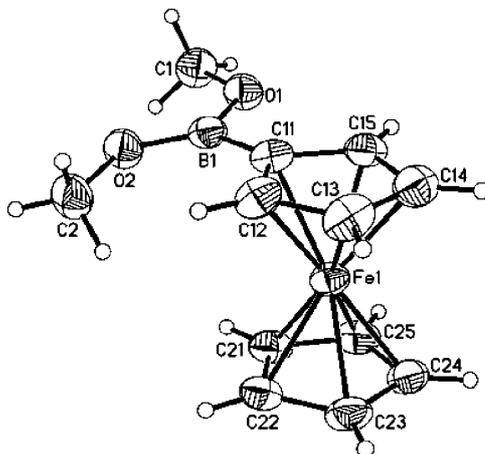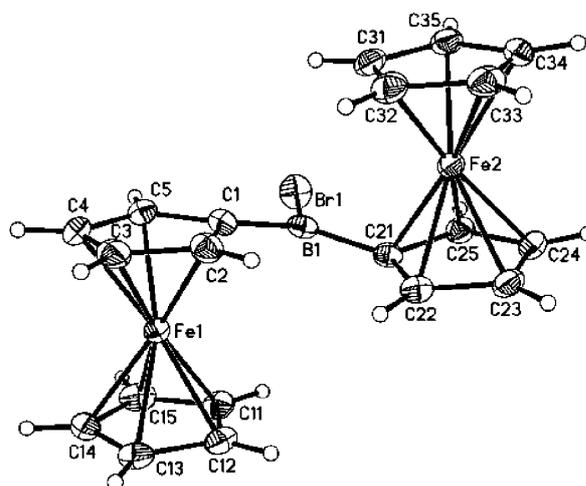
Figure 6
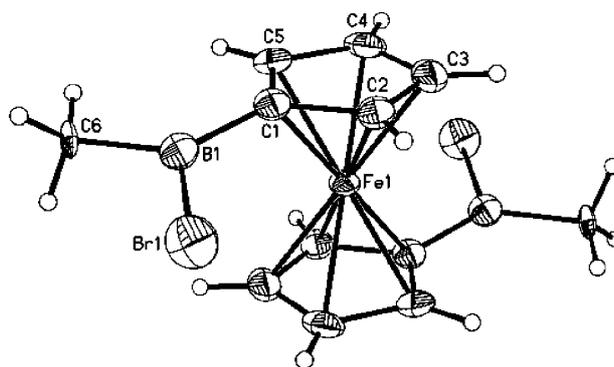
Figure 7
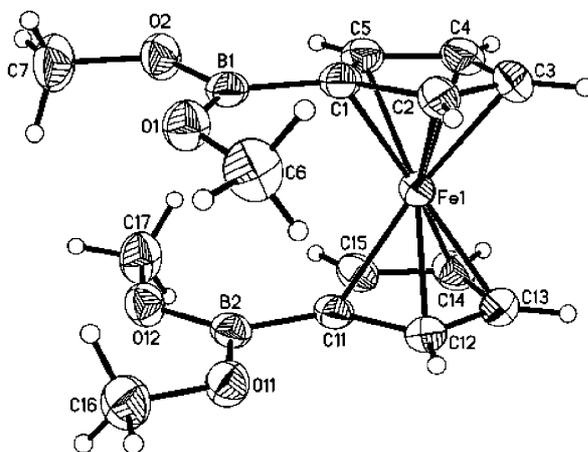
Figure 8

Figure 9

Figure 10
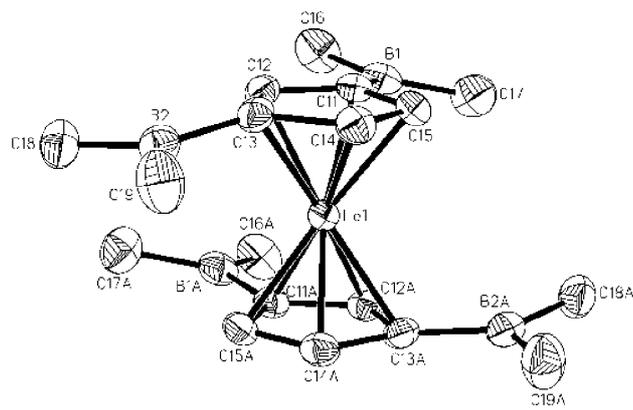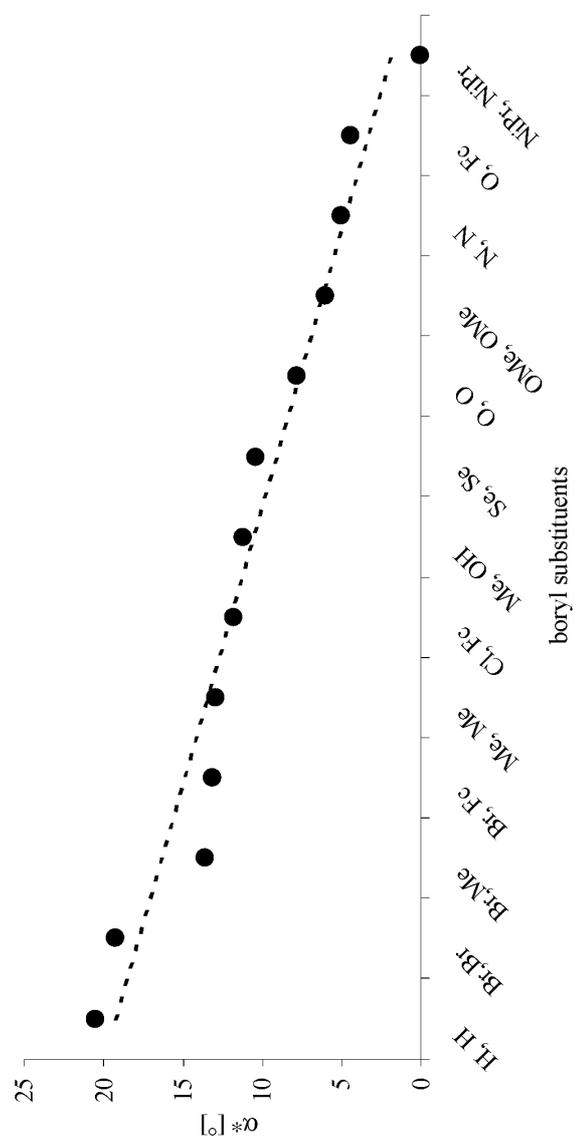
Figure 11

71
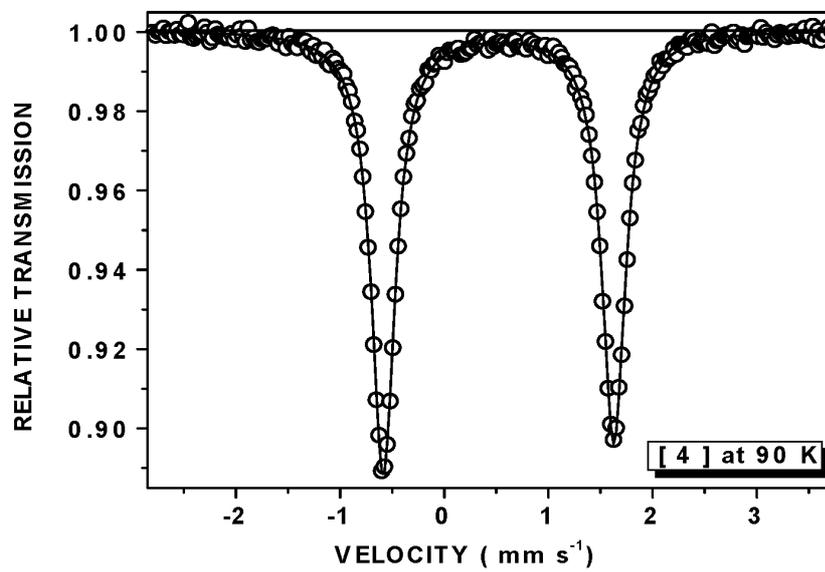
Figure 12

Figure 13
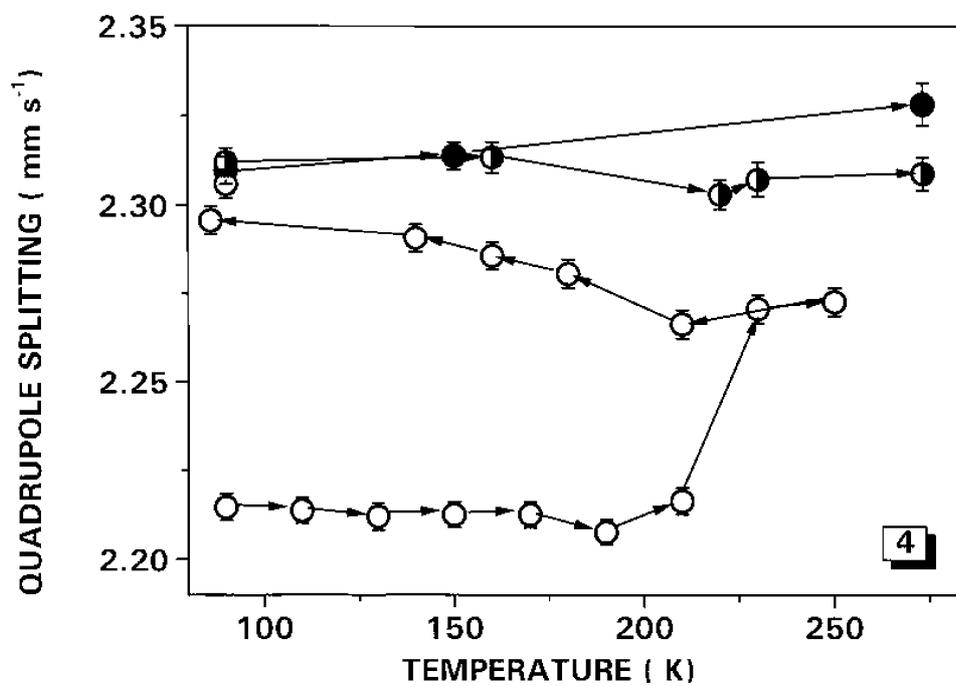
Figure 14
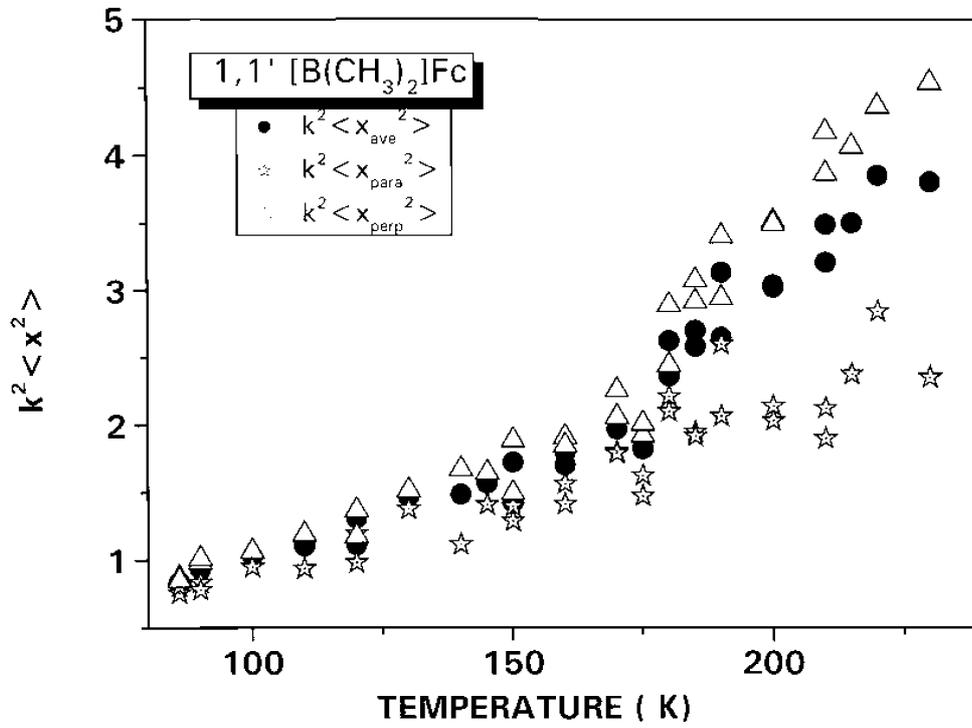
Figure 15
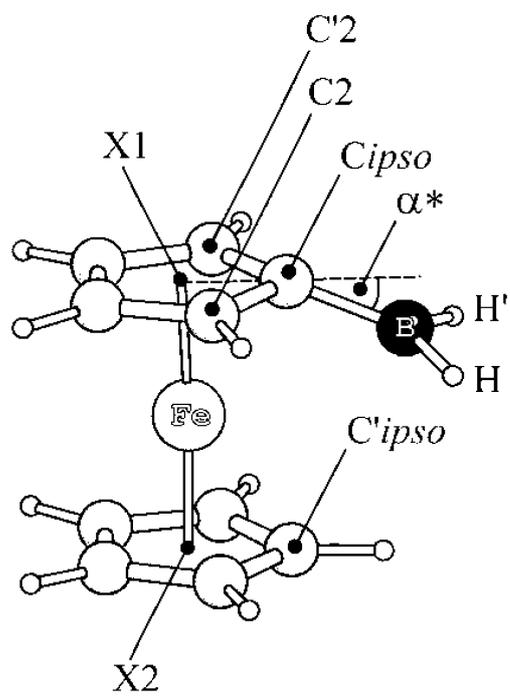
Figure 16
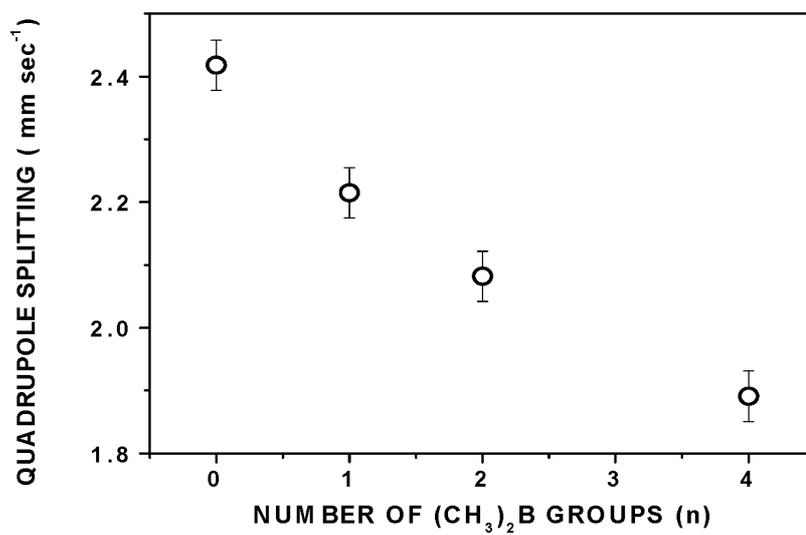
Figure 17
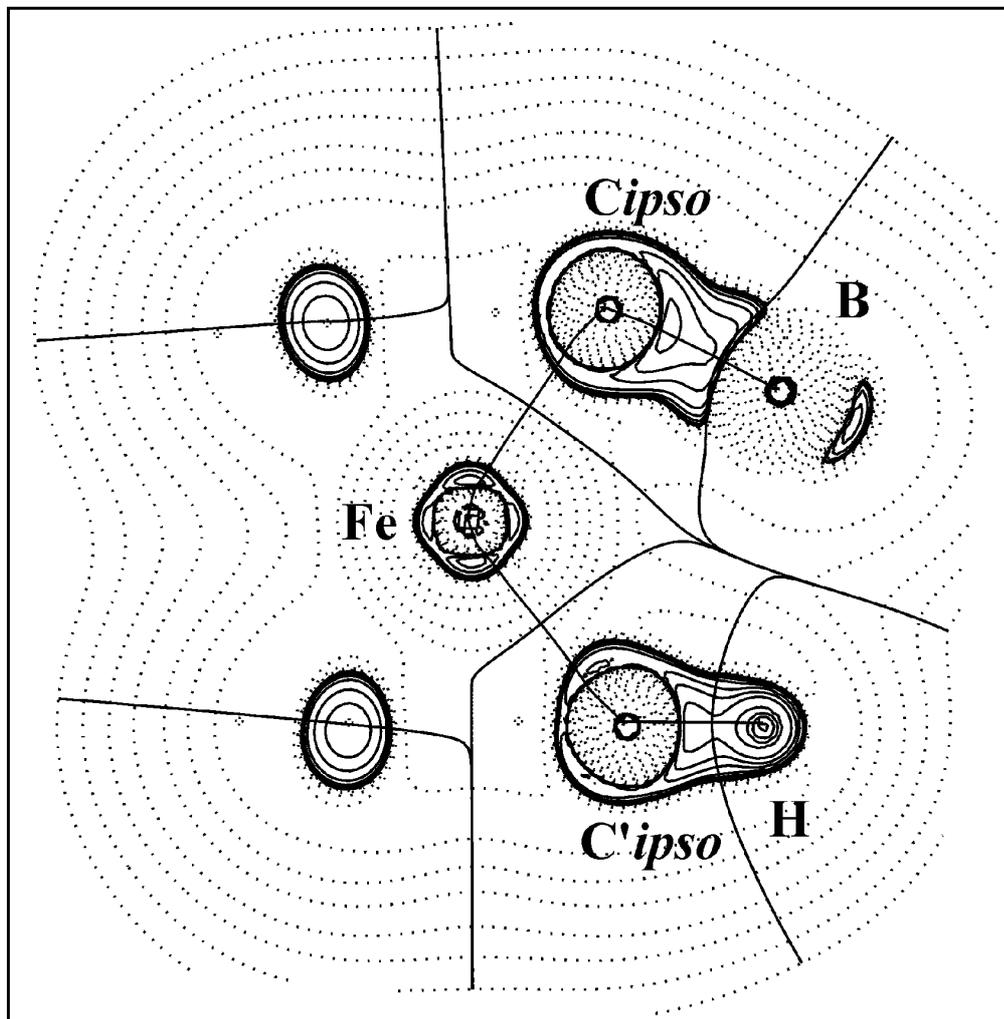
Figure 18
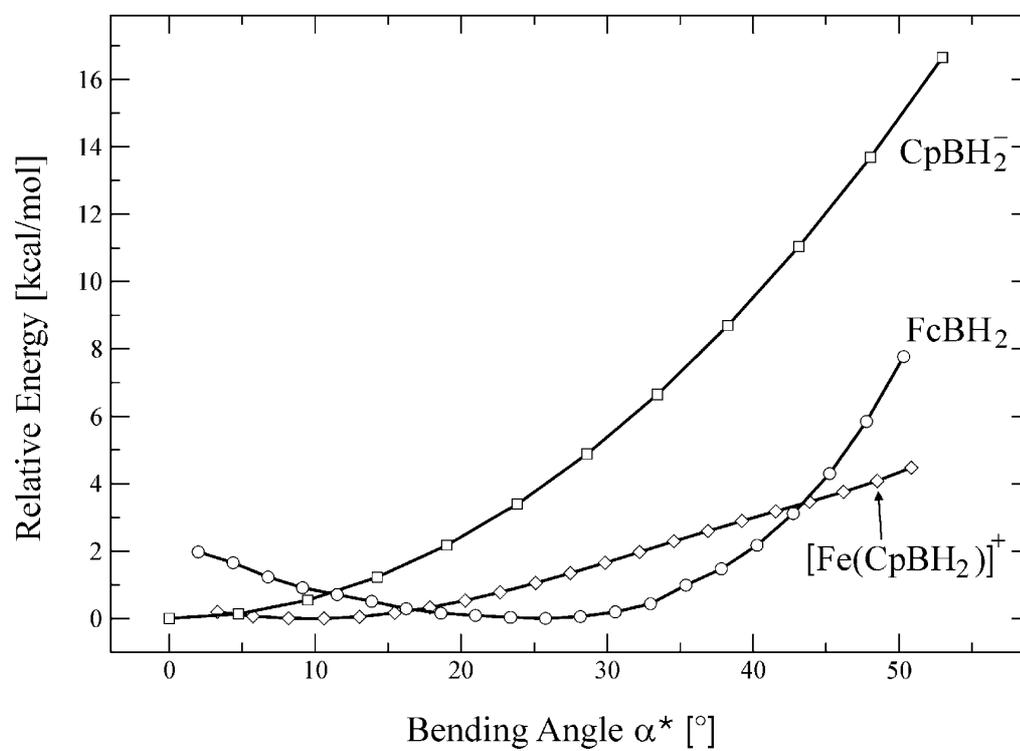
Figure 19:
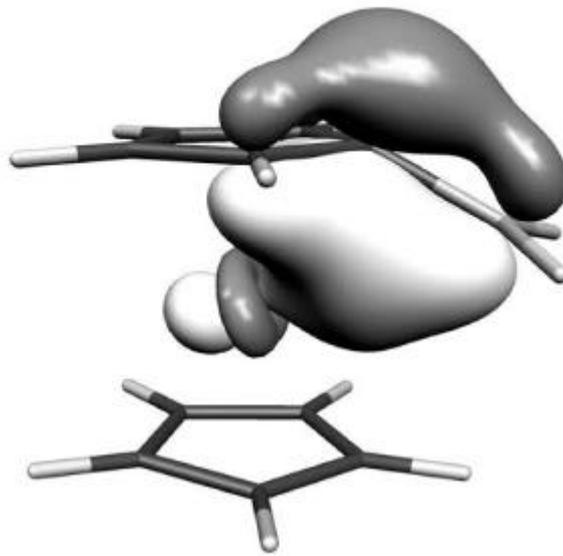
Figure 20
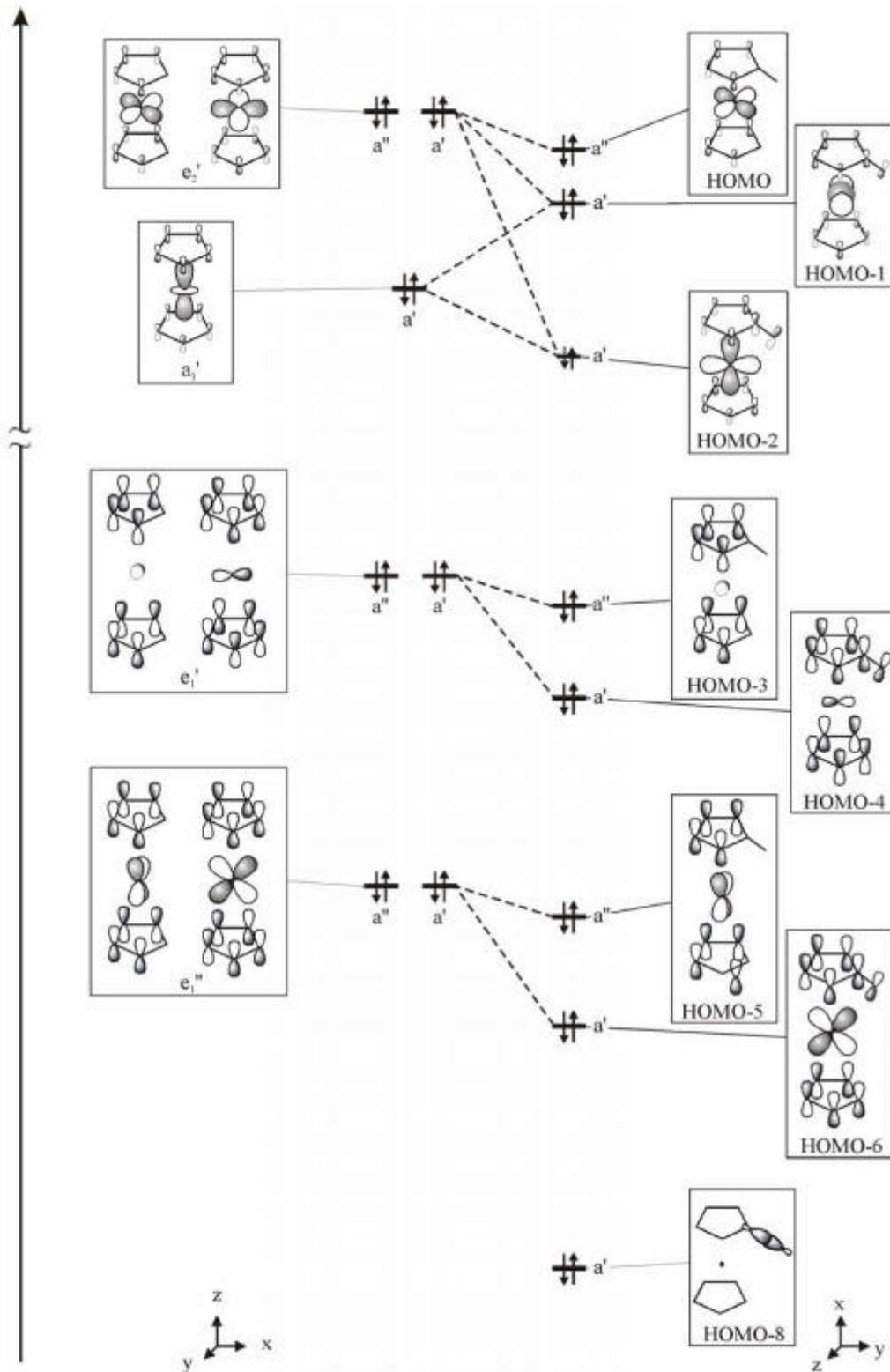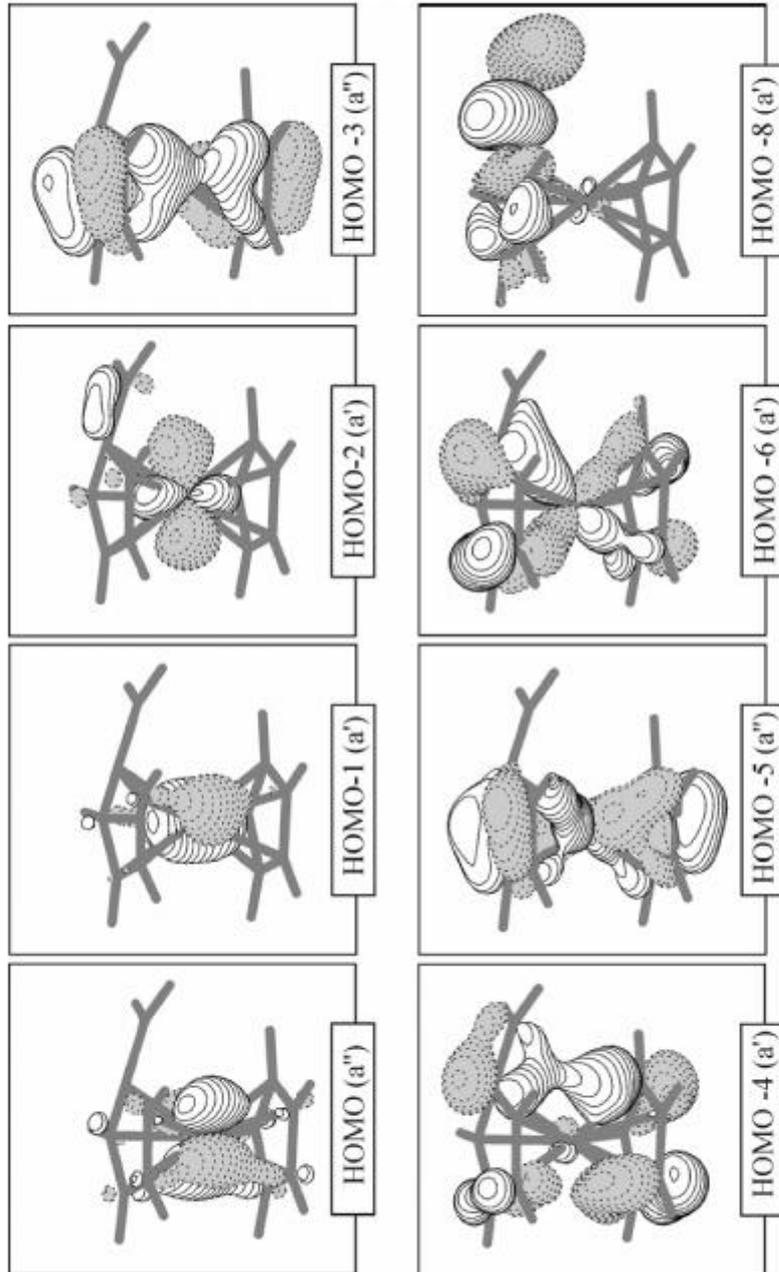
Figure 21

81
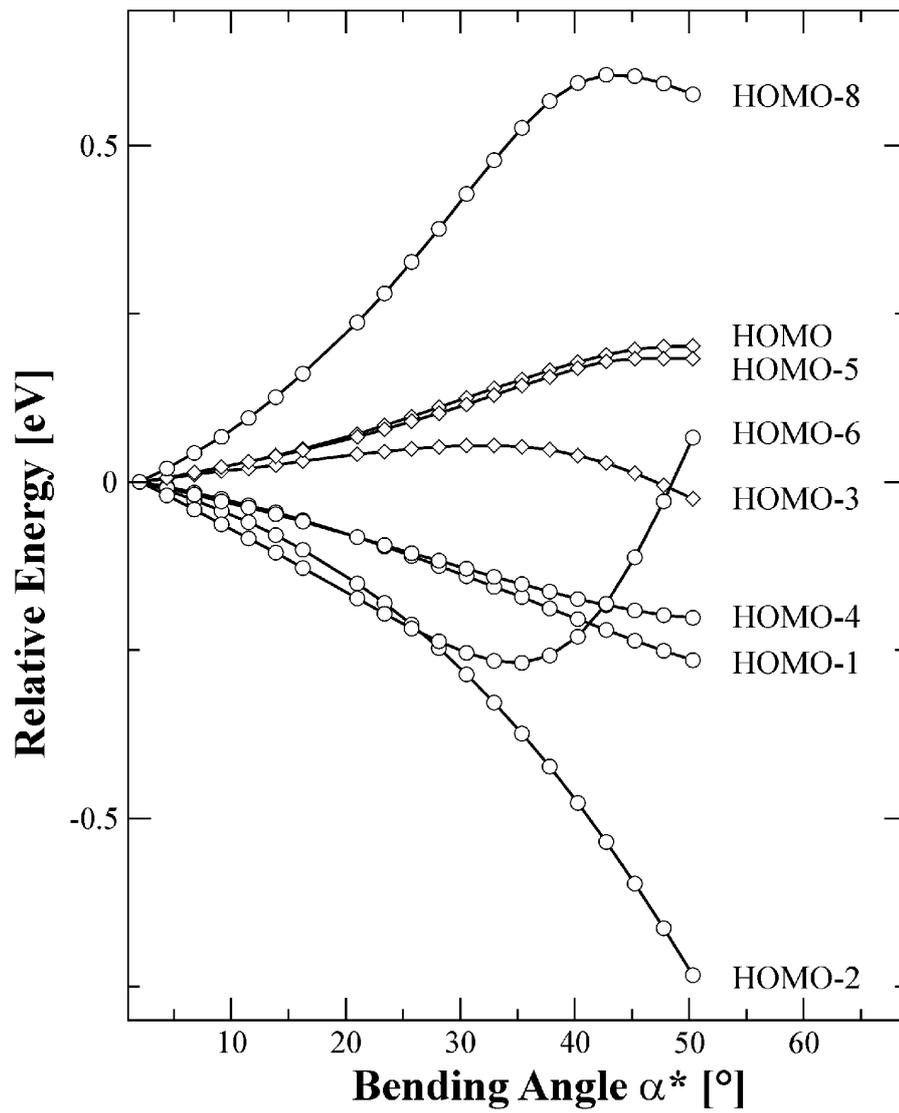
Figure 22

Figure 23a (left)
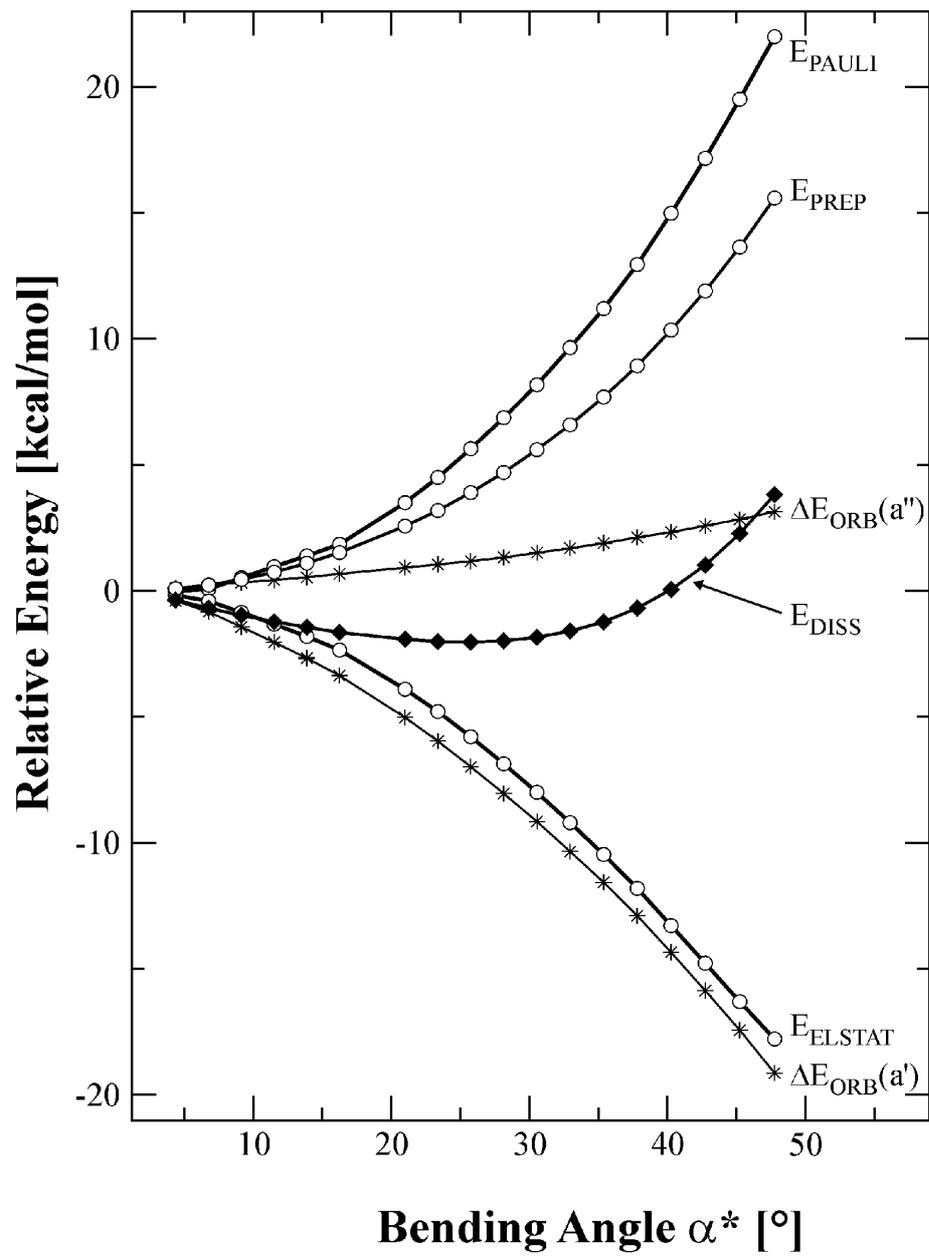
Figure 23b (right)
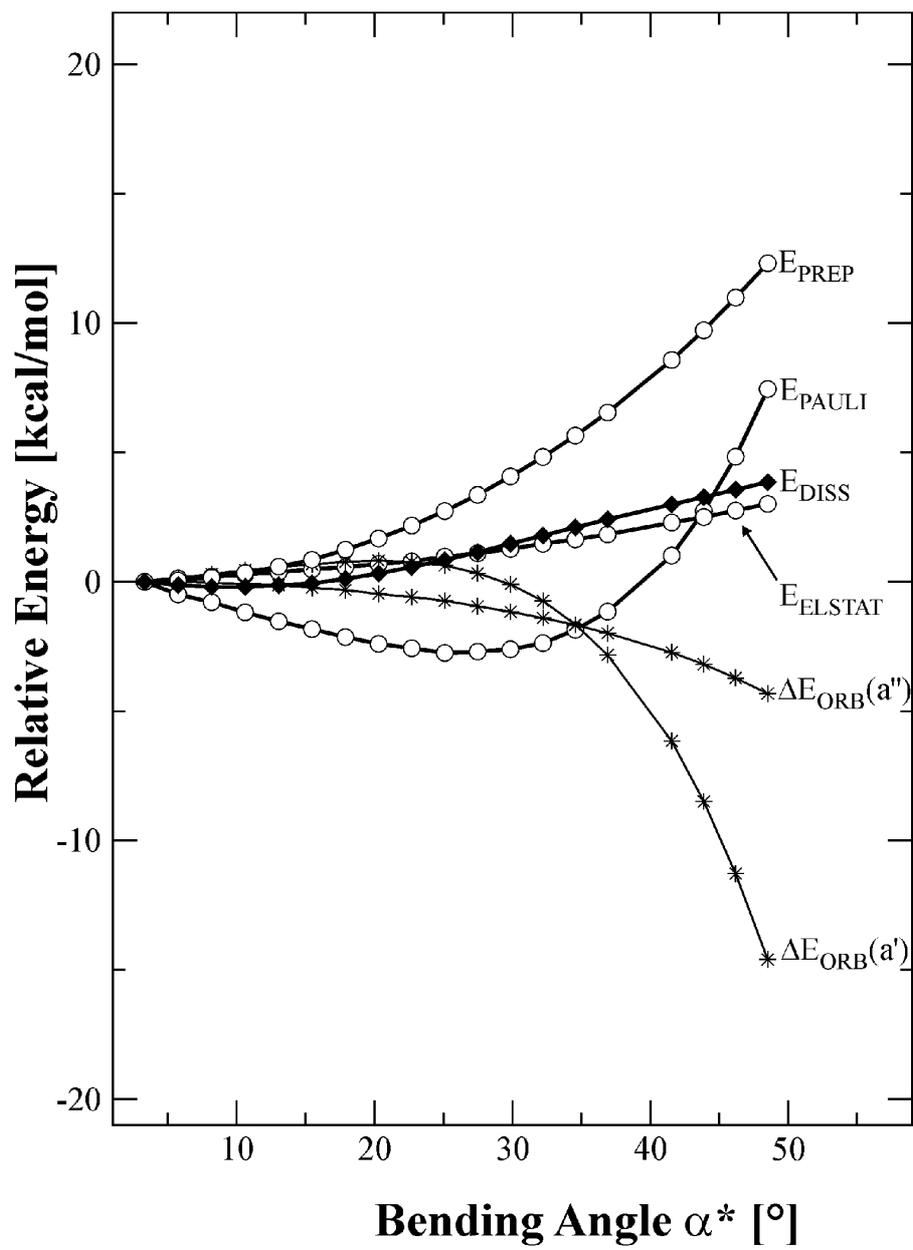
Graphical Abstract
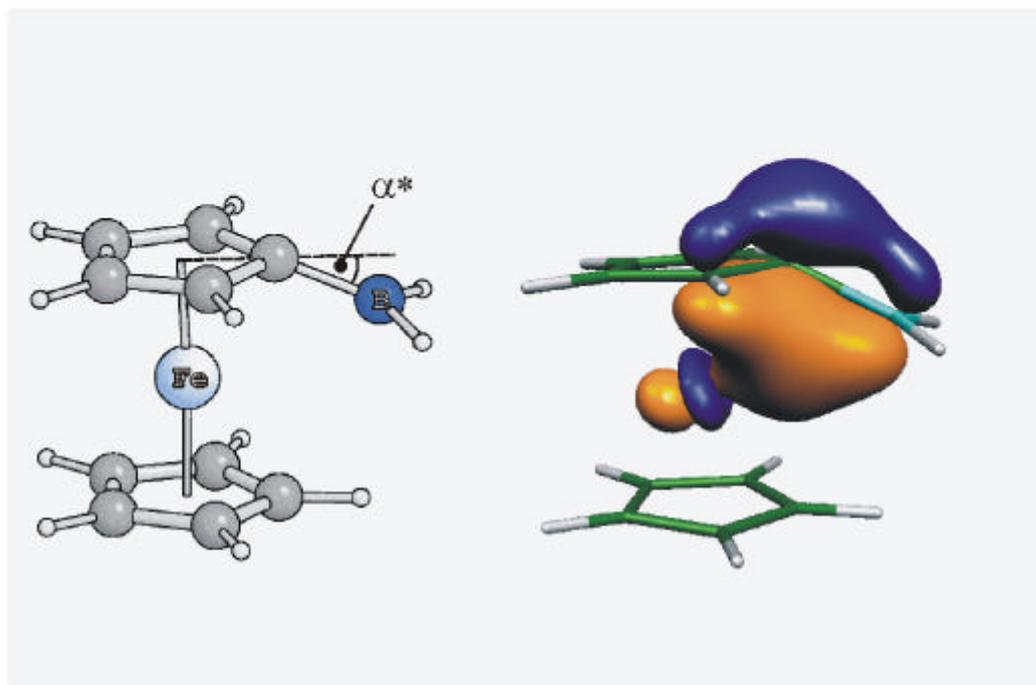
The bending of ligands in selected mono-, di-, and tetraborylated ferrocenes is investigated by means of X-ray crystallography, cyclic voltammetry, and Mössbauer spectroscopy. A detailed quantum chemical analysis of the subtle structural and electronic properties of these species is provided.

3.9 „Electronic interactions in oligoferrocenes with cationic, neutral and anionic tetracoordinated boron bridges"

M. Scheibitz, J. Heilmann, M. Bolte, R. F. Winter, M. Wagner

Dalton Trans. **2004**, *zur Veröffentlichung eingereicht.*

Electronic interactions in oligoferrocenes with cationic, neutral and anionic four-coordinate boron bridges.

Matthias Scheibitz,[a] **Julia B. Heilmann,**[a] **Rainer F. Winter,**[b] **Michael Bolte,**[a] **Jan W. Bats,**[c] **and Matthias Wagner***[a]

[a] *Institut für Anorganische Chemie, J.W. Goethe-Universität Frankfurt, Marie-Curie-Str. 11,*

D-60439 Frankfurt (Main), Germany.

E-mail: Matthias.Wagner@chemie.uni-frankfurt.de

[b] *Institut für Anorganische Chemie, Universität Stuttgart, Pfaffenwaldring 55, D-70569*

Stuttgart, Germany.

[c] *Institut für Organische Chemie, J.W. Goethe-Universität Frankfurt, Marie-Curie-Str. 11,*

D-60439 Frankfurt (Main), Germany.

Summary: Dinuclear and trinuclear ferrocene complexes $\{[Fc_2BMe_2]Li, [Fc\text{-}BMe_2\text{-}fc\text{-}BMe_2\text{-}Fc]Li_2, Fc_2B(pyind), [Fc_2B(bipy)]PF_6, [Fc\text{-}B(bipy)\text{-}fc\text{-}B(bipy)\text{-}Fc](PF_6)_2\}$ bearing anionic, uncharged, and cationic four-coordinate boron bridges have been synthesized (Fc: ferrocenyl; fc: 1,1'-ferrocenylene; pyind: 5-fluoro-2-(2'-pyridyl)indolyl; bipy: 2,2'-bipyridyl). The molecular structures of $[Fc_2BMe_2]Li(12\text{-crown-4})_2$, $[Fc\text{-}BMe_2\text{-}fc\text{-}BMe_2\text{-}Fc](Li(12\text{-crown-}4)_2)_2$, $Fc_2B(pyind)$, and $[Fc_2B(bipy)]PF_6$ were determined by X-ray crystallography. The anionic aggregates $[Fc_2BMe_2]^-$ and $[Fc\text{-}BMe_2\text{-}fc\text{-}BMe_2\text{-}Fc]^{2-}$ are very sensitive to air and moisture whereas bromide salts of their cationic counterparts $[Fc_2B(bipy)]^+$ and $[Fc\text{-}B(bipy)\text{-}fc\text{-}B(bipy)\text{-}Fc]^{2+}$ may be dissolved in water without decomposition. Cyclic voltammograms of the diferrocene species show two well-resolved one-electron transitions separated by 0.21 V $([Fc_2BMe_2]Li; E^{\circ\prime} = -0.43$ V, -0.64 V; *vs.* FcH/FcH^+), 0.18 V $(Fc_2B(pyind); E^{\circ\prime} = -0.03$ V,

-0.21 V), and 0.16 V ([Fc$_2$B(bipy)]PF$_6$; $E^{\circ'}$ = +0.23 V, +0.07 V), which indicates electronic interactions between the two ferrocenyl substituents. Two redox waves with an intensity ratio of 1:2 are observed in the cyclic voltammograms of the trinuclear derivatives [Fc-BMe$_2$-fc-BMe$_2$-Fc]Li$_2$ and [Fc-B(bipy)-fc-B(bipy)-Fc](PF$_6$)$_2$. In the case of the BMe$_2$-bridged species, the electrochemically unique central ferrocenylene unit is oxidized at a much more cathodic potential value ($E^{\circ'}$ = -1.21 V) than the two terminal ferrocenyl substituents ($E^{\circ'}$ = -0.51 V). The opposite is true in the case of the B(bipy)-bridged trimer where oxidation of the terminal ferrocenyl groups ($E^{\circ'}$ = +0.03 V) precedes oxidation of the internal iron atom ($E^{\circ'}$ = +0.26 V). The Fe(II)/Fe(III) redox potentials of the mono- and dianionic species differ to a much larger extent from the redox potential of parent ferrocene ($E^{\circ'}$ • 0 V) than the $E^{\circ'}$ values of the corresponding mono- and dicationic derivatives. Apart from electrostatic interactions, the electrochemical properties of BMe$_2$- and B(bipy)-bridged oligoferrocenes are determined by the pronounced positive inductive effect of triorganoborate substituents together with positive σ/π* hyperconjugation on the one hand and ferrocene-to-B(bipy) charge transfer on the other.

2

Illustrated Contents Entry

Electronic interactions in oligoferrocenes with cationic, neutral and anionic four-coordinate boron bridges.

Matthias Scheibitz, Julia B. Heilmann, Rainer F. Winter, Michael Bolte, and Matthias Wagner*

The dinuclear and trinuclear ferrocene complexes [Fc_2BMe_2]Li, [Fc-BMe_2-fc-BMe_2-Fc]Li_2, Fc_2B(pyind), [Fc_2B(bipy)]PF_6, and [Fc-B(bipy)-fc-B(bipy)-Fc](PF_6)$_2$} have been synthesized and investigated by cyclic voltammetry (pyind: 5-fluoro-2-(2'-pyridyl)indolyl).

Introduction

Research on metal containing polymer precursors and polymers has developed into a fluorishing field of coordination chemistry since the materials created are highly interesting due to their optical, electronic or magnetic properties.[1, 2] Among all the compounds developed so far, organometallic macromolecules are receiving increasing attention since the first high molecular weight poly(ferrocenylenes) **I** (Figure 1) with skeletal iron atoms became available via the ring-opening polymerisation (ROP) of strained ring-tilted [1]ferrocenophanes.[3-5] Our group is particularly interested in boron-bridged oligo(ferrocenylenes) for which the ROP synthesis approach proved to be far less efficient than for the analogous silicon- or germanium-bridged derivatives **I**.[6, 7] In an alternative strategy, the facile formation of boron-nitrogen adduct bonds was exploited for the generation of polymers [-(Me$_2$BC$_5$H$_4$)Fe(C$_5$H$_4$BMe$_2$)-pyrazine-]$_n$ and [-(Me$_2$BC$_5$H$_4$)Fe(C$_5$H$_4$BMe$_2$)-2,2'-bipyridyl-]$_n$.[8-10] A detailed investigation of these and related materials provided strong evidence for charge transfer between the ferrocene donors and the electron-poor organic bridges.[8, 11] The polymers are insoluble in all common solvents; their structure in the solid state was determined by X-ray diffraction. In order to increase the number of iron atoms within the polymer backbone, we then attempted to replace the aromatic amine donors with 3,3',4,4'-tetramethyl-1,1'-diphosphaferrocene. However, no polymeric material was formed upon treatment of this difunctional Lewis base with 1,1'-bis(dimethylboryl)ferrocene or 1,1'-bis(dibromoboryl)ferrocene. While the methyl derivative did not form P-B adducts at all, the bromo derivative just gave an open-chain dinuclear complex featuring only one P-B bond.[12] We therefore came to the conclusion that more strongly Lewis basic ferrocene derivatives were required. One obvious candidate was 1,1'-dilithioferrocene, which is not only easy to prepare but also able to form strong boron-carbon σ bonds. Initial efforts to prepare macromolecules **(Li[II])$_n$** (Figure 1) from 1,1'-bis(dimethylboryl)ferrocene and 1,1'-dilithioferrocene resulted in a mixture of oligomeric products containing substantial amounts

of the cyclic dimer **Li$_2$[III]** (Figure 1), which was isolated by crystallization and turned out to be a highly efficient lithium scavenger.[13] Work is currently in progress to separate the different linear oligomers and to determine their molecular weight by GPC techniques. During these workup and purification steps, it turned out that the compounds **(Li[II])$_n$** are highly sensitive to air. This is in accordance with exploratory electrochemical investigations on our product mixtures which revealed a sizable cathodic shift of the Fe(II)/Fe(III) redox transitions in these materials compared to parent ferrocene.

Since an investigation of well-defined short-chain oligomers is, by itself, already helpful for an understanding of the properties of BMe$_2$-bridged poly(ferrocenylenes), we synthesized the anionic di- and triferrocene complexes **Li[2]** and **Li$_2$[3]** (Scheme 1) in order to study their electrochemical behaviour and to determine their molecular structure in the solid state. For comparison, we also prepared the mono- and dinuclear compounds **6** and **10** (Scheme 2) featuring four-coordinate yet uncharged boron substituents, as well as complexes **[11]PF$_6$** and **[14](PF$_6$)$_2$** (Scheme 3) in which two and three ferrocene moieties are linked via four-coordinate cationic boron bridges.

Results and Discussion

Synthesis and Spectroscopy. The di- and trinuclear ferrocene complexes **Li[2]** and **Li$_2$[3]** were synthesized in THF *via* the reaction of FcBMe$_2$, **1**, with FcLi (1 equiv.) and 1,1'-fc(Li·TMEDA)$_2$ (0.5 equiv.), respectively [Scheme 1; Fc = (C$_5$H$_5$)Fe(C$_5$H$_4$), fc = (C$_5$H$_4$)$_2$Fe]. X-ray quality crystals formed from CH$_2$Cl$_2$ (**Li[2]**) and THF/diethyl ether (**Li$_2$[3]**) after addition of 12-crown-4. Both compounds are highly sensitive to air and moisture. Treatment of the sodium salt **4**, prepared from 5-fluoro-2-(2'-pyridyl)indole and NaH in THF, with FcB(Me)Br, **5**, in toluene gave the monoferrocene derivative **6** in moderate yield (Scheme 2). In order to get access to the analogous diferrocenyl complex **10** (Scheme 2), we first reacted FcBBr$_2$, **7**, with FcSnMe$_3$, **8**, which yielded the dinuclear compound **9** featuring a three-

coordinate boron bridge. Subsequent addition of **4** led to the formation of **10**. Crystals of **6** and **10** suitable for X-ray crystal structure determinations were obtained from $CDCl_3$ and toluene, respectively. In the latter case, the crude material was contaminated with a small amount of ferrocene which could neither be fully removed by column chromatography (dichloromethane/ethyl acetate 10:1) nor by sublimation. Only a few single crystals of **10** were obtained and these contained 0.25 equivs. of ferrocene. Apparently, the ferrocene is necessary to stabilize the crystal packing of compound **10** since numerous attempts to grow single crystals from the ferrocene depleted mother liquor failed. The monocationic diferrocenyl complex **[11]PF₆** is readily available from **9** and 2,2'-bipyridyl (Scheme 3). Using NH_4PF_6 in water, the bromide salt of **[11]⁺** was quantitatively transformed into the corresponding hexafluorophosphate salt which is more suitable for cyclic voltammetric measurements. Similar to the synthesis of **9**, the triferrocene species **13** was prepared from two equivs. of $FcSnMe_3$, **8**, and one equiv. of 1,1'-fc$(BBr_2)_2$, **12**, in toluene. Subsequent addition of 2,2'-bipyridyl followed by salt metathesis gave the target molecule **[14](PF₆)₂** in excellent overall yield (Scheme 3).

The ¹¹B NMR spectra of the compounds under investigation here display characteristic high-field resonances at -21.2 ppm (**Li[2]**), -19.2 ppm (**Li₂[3]**), 4.5 ppm (**6**), 4.1 ppm (**10**), 7.3 ppm (**[11]PF₆**), and 7.2 ppm (**[14](PF₆)₂**) testifying to the presence of four-coordinate boron nuclei.[14, 15] It follows from a comparison of these values that the electron density is indeed highest at the boron atoms of the negatively charged species **Li[2]** and **Li₂[3]**. Removal of the excess electron and replacement of electron releasing methyl groups by electronegative sp² hybridized nitrogen donors leads to a substantial charge depletion at boron as evidenced by a downfield shift of $\Delta(\delta(^{11}B)) = 25.3$ upon going from **Li[2]** to **10**. Introduction of a positive charge, as in the case of **[11]PF₆** and **[14](PF₆)₂**, has only a minor additional effect [cf. $\delta(^{11}B)(\textbf{[11]PF₆}) - \delta(^{11}B)(\textbf{10}) = 3.2$], likely because this charge is not localized at the boron centre but efficiently spread over the entire B(bipy) entity (bipy: 2,2'-bipyridyl). The very

narrow line widths of the ^{11}B NMR signals of **Li[2]** ($h_{1/2}$ = 10 Hz) and **Li$_2$[3]** ($h_{1/2}$ = 20 Hz) are

consistent with a highly symmetric BC$_4$ surrounding as opposed to the less symmetric BC$_2$N$_2$

substitution pattern in, for example, **10** ($h_{1/2}$ = 370 Hz) and **[11]PF$_6$** ($h_{1/2}$ = 250 Hz).

The methyl groups of **Li[2]** and **Li$_2$[3]** resonate at $\delta(^1H)$ = –0.12 and –0.13, respectively. Due

to unresolved $^2J_{BH}$ coupling, both signals appear as broad multiplets. In the ^{13}C NMR spectra,

the methyl substituents give rise to 1:1:1:1 quartets at $\delta(^{13}C)$ = 14.8 ($^1J_{CB}$ = 41.7 Hz; **Li[2]**)

and $\delta(^{13}C)$ = 14.6 ($^1J_{CB}$ = 40.9 Hz; **Li$_2$[3]**). In contrast to **Li[2]**, which exhibits only two ^{1}H-

and two ^{13}C NMR resonances for the substituted cyclopentadienyl rings, four C$_5H_4$ (each

integrating 1H) and four C$_5$H$_4$ signals are found in the case of **6** (C_{ipso} is broadened beyond

detection due to quadrupolar relaxation[14]). This observation agrees well with the molecular

structure suggested for this compound (Scheme 2) since coordination of the unsymmetric 5-

fluoro-2-(2'-pyridyl)indolyl ligand makes the boron atom a chiral centre and renders all C$_5$H$_4$

atoms magnetically inequivalent (similar features are observed in the ^{1}H- and ^{13}C NMR

spectrum of **10**). Consistent with this view, both α and both β protons of a given C$_5$H$_4$ ring in

the 2,2'-bipyridyl derivatives **[11]PF$_6$** and **[14](PF$_6$)$_2$** possess the same chemical shifts. As has

already been discussed in a previous paper on related ferrocene-based 2,2'-

(bipyridyl)boronium salts like **[IV]$^{+16}$** (Figure 2), boron chelation causes characteristic

changes in the ^{1}H- and ^{13}C NMR spectra of the 2,2'-bipyridyl ligand. The resulting shift

values exhibited by **[11]PF$_6$** and **[14](PF$_6$)$_2$** are almost identical to those of compound **[IV]$^+$**

and thus do not merit further discussion.

Crystal structure determinations. Selected crystallographic data of **Li[2]**(12-crown-4)$_2$,

Li$_2$[3](12-crown-4)$_4$, **6**, **10**, and **[11]PF$_6$** are summarized in Table 1. In the lithium

diferrocenyldimethylborate complex **Li[2]**(12-crown-4)$_2$ (monoclinic, $C2/c$), which

crystallizes together with 1 equiv. of CH$_2$Cl$_2$, the [Fc$_2$BMe$_2$]$^-$ anion possesses approximate C_{2v}

symmetry (Figure 3). Intermolecular contacts to the Li(12-crown-4)$_2^+$ counterion correspond

to normal van der Waals interactions. The boron atom maintains an almost perfect tetrahedral

coordination sphere [largest angular distortion from the ideal value of 109°: C(11)-B(1)-C(21) = 105.8(1)°]. B-C bonds to the sp^3-hybridized methyl groups [B(1)-C(1') = 1.634(3) Å, B(1)-C(1'') = 1.642(3) Å] possess the same length as B-C bonds involving the sp^2-hybridized *ipso*-carbon atoms of the cyclopentadienyl rings [B(1)-C(11) = 1.641(3) Å, B(1)-C(21) = 1.638(3) Å], an effect which is also apparent in other ferrocenylborane adducts of the general formula FcB(Me)RR'[13, 16-22]. Significant differences are obvious in the Fe-C distances within the ferrocenyl substituents. While the bond lengths between Fe(1) and the C(31)-cyclopentadienyl ring [Fe(2) and C(1)-cyclopentadienyl] fall in the range between 2.031(2) Å – 2.057(2) Å [2.034(2) Å – 2.052(2) Å] with a mean of 2.045 Å [2.045 Å], the distances between Fe(1) and the C(21)-cyclopentadienyl ring [Fe(2) and C(11)-cyclopentadienyl] are spread over a much broader range between 2.031(2) Å – 2.098(2) Å [2.033(2) Å – 2.102(2) Å] with a mean of 2.053 Å [2.055 Å]. By far the longest Fe-C bonds are established to the ipso-carbon atoms, i.e. Fe(1)-C(21) = 2.098(2) Å and Fe(2)-C(11) = 2.102(2) Å. If this bond stretch was simply due to steric repulsion between the BMe_2 fragment and the C_5H_5 ligands, one would also expect an elongation of the Fe(1)-C(31) and the Fe(2)-C(1) bond. The opposite, however, is true in that they possess the smallest values of all Fe-C bonds. It is important to note in this context that lithium ferrocenylborohydride [FcBH₃]Li(12-crown-4)[22] shows an even larger Fe-C_{ipso} distance (2.110(3) Å) than **Li[2]**(12-crown-4)$_2$ even though any steric strain inflicted by the small BH_3 moiety is certainly negligible. This leads to the conclusion that ferrocene distortion may originate from the electronic rather than the steric properties of the strongly σ-donating borate substituent. The C(11)-B(1) [C(21)-B(1)] vector is directed almost orthogonal to the C(21)-cyclopentadienyl ring [C(11)-cyclopentadienyl ring; cf. C(11)-B(1)-C(21)-C(22) = -88.1(2)°, C(21)-B(1)-C(11)-C(12) = 79.2(2)°; dihedral angle C(11)C(12)C(13)C(14)C(15)//C(21)C(22)C(23)C(24)C(25) = 77.7°].

The trinuclear aggregate **Li₂[3]**(12-crown-4)$_4$ (triclinic, *P*-1; Figure 4) lies on an inversion center and forms separated ion pairs with two Li(12-crown-4)$_2^+$ complexes. All structural

parameters including torsion angles and dihedral angles of the C(11)-ferrocenyl/B(1)Me$_2$/C(21)-ferrocenyl subunit are virtually identical to those of **Li[2]**(12-crown-4)$_2$. The molecular structure of **Li$_2$[3]**(12-crown-4)$_4$ has to be compared with the structure of the isoelectronic carbon-bridged species in its Fe(II)- ([Fc-CMe$_2$-fc-CMe$_2$-Fc]^0)[23] and Fe(III) states ([Fc-CMe$_2$-fc-CMe$_2$-Fc]$^{3+}$)[24]. In contrast to **Li$_2$[3]**(12-crown-4)$_4$, the neutral triferrocene [Fc-CMe$_2$-fc-CMe$_2$-Fc]^0 (monoclinic, $P2_1/a$) adopts an unsymmetrical conformation with inequivalent Fe$\cdots$Fe separations of 5.714 Å and 6.453 Å, both of which are significantly shorter than the Fe(1)$\cdots$Fe(2) distance in **Li$_2$[3]**(12-crown-4)$_4$ (6.731 Å). Similar to **Li$_2$[3]**(12-crown-4)$_4$, the Fe-C$_{ipso}$ bonds in [Fc-CMe$_2$-fc-CMe$_2$-Fc]^0 are longer (2.050(2) Å, 2.056(2) Å, 2.065(2) Å, 2.067(2) Å) than the other iron-carbon bonds. This effect is, however, far less pronounced than in the case of **Li$_2$[3]**(12-crown-4)$_4$ [Fe(1)-C(11) = 2.112(3) Å, Fe(2)-C(21) = 2.115(2) Å] which lends additional support to our hypothesis that Fe-C$_{ipso}$ bond elongation is rooted in the electronic rather than the steric properties of the BMe$_2$ bridge. Only negligible differences are observed in the conformation of [Fc-CMe$_2$-fc-CMe$_2$-Fc](O$_3$SCF$_3$)$_3$ (monoclinic, $C2$) on the one hand and **Li$_2$[3]**(12-crown-4)$_4$ on the other (intramolecular Fe$\cdots$Fe distances in both molecules are 6.536 Å and 6.731 Å, respectively). The triferrocene moieties of both compounds are arranged in the stepped formation that has been predicted by MMX calculations on the related silicon-bridged [Fc-SiMe$_2$-fc-SiMe$_2$-Fc]^{0}[25] to be a minimum energy conformation of such kinds of triferrocene oligomers.

The mononuclear complex **6** (Figure 5) contains a chiral boron centre but crystallizes from CDCl$_3$ as a racemate in the achiral space group $P2_1/c$. The 5-fluoro-2-(2'-pyridyl)indolyl ligand forms both a prototype dative bond [B(1)-N(11) = 1.633(4) Å] and a prototype covalent bond [B(1)-N(21) = 1.565(4) Å] to the boron atom, with the latter being shorter by 0.068(4) Å. Both B-C bonds are again equal within experimental error [B(1)-C(1) = 1.598(5) Å, B(1)-C(31) = 1.609(5) Å]. An inspection of bond angles reveals that the boron atom suffers severe distortions of the ideal tetrahedral configuration with N(11)-B(1)-N(21) =

<center>9</center>

94.3(2)° being the smallest and C(31)-B(1)-C(1) = 118.1(3)° the largest angle. The conformation of **6** is such that the boron-pyridyl bond B(1)-N(11) is directed perpendicular to the ferrocenyl substituent [C(32)-C(31)-B(1)-N(11) = 86.3(3)°] while the second B-N bond lies almost in the plane of the cyclopentadienyl ring [C(32)-C(31)-B(1)-N(21) = -13.8(4)°]. Very similar conformations have been found previously for **[IV]**$^+$ (monoclinic, $P2_1$; Figure 2)[16], the analogous 1,10-phenanthroline derivative (monoclinic, $P2_1/c$)[26], as well as for the two pseudopolymorphs of a related ferrocenylborane adduct[21] featuring a chelating 2,5-bis-(2-pyridyl)pyrazine donor instead of the 2,2'-bipyridyl ligand (both pseudopolymorphs crystallize in the triclinic space group P-1). The experimentally determined conformation of **[IV]**$^+$ was also reproduced by DFT calculations on the monocationic model system **[IV^H]**$^+$ (Figure 2) using B3P86/6-31G(d) for C, B, N, H and the SDD pseudopotential in combination with a DZP valence basis set for Fe.[11] It is important to note in this context, that the two dative boron-nitrogen bonds of **[IV]**$^+$ are significantly different in length. The B-N bond perpendicular to the cyclopentadienyl ring, which relates to B(1)-N(11) in **6**, is 1.613(4) Å long (**[IV^H]**$^+$: 1.596 Å), while the other possesses a length of only 1.580(4) Å (**[IV^H]**$^+$: 1.579 Å). This correspondence between the experimentally determined and the theoretically predicted structures implies that the distortions of the N-B-N fragment are caused by internal molecular forces, as opposed to crystal packing forces. We suggest that a hyperconjugative interaction between the filled p orbital of the *ipso*-carbon atom and the σ* orbital of the parallelly aligned B-N bond may be the reason for the elongation of this bond and provide a pathway for charge-transfer from ferrocene to the B(bipy) acceptor.

Single crystals of **10** (monoclinic, $P2_1/c$) were grown by slow evaporation of its toluene solution at room temperature. The crystal lattice contained two crystallographically independent molecules of **10**, one molecule of toluene and half a molecule of ferrocene in the asymmetric unit. Both molecules **10** possess very similar structural features. Thus, structural parameters of only one of them are given in Figure 6. The position of the C(31)-ferrocenyl

10

group relative to the pyridylindolyl moiety is similar to **6** with torsion angles of C(32)-C(31)-B(1)-N(11) = 86.3(3)° (**6**) and 110.6(7)° (**10**)]. The conformation adopted by the C(51)-ferrocenyl-B(pyridylindolyl) fragment, however, is distinctly different from that of the C(31)-ferrocenyl-B(pyridylindolyl) unit, since the organometallic substituent is rotated by ~180° about its B-C bond [torsion angle C(52)-C(51)-B(1)-N(11) = -117.0(7)°]. Interestingly, the two different conformations correspond to two significantly different B-cyclopentadienyl bond lengths, which amount to 1.629(9) Å in the case of B(1)-C(31) and 1.586(11) Å in the case of B(1)-C(51). Corresponding boron-nitrogen bond lengths possess the same value within the 3σ error margin both in **6** [B(1)-N(11) = 1.633(4) Å, B(1)-N(21) = 1.565(4) Å] and in **10** [B(1)-N(11) = 1.611(9) Å, B(1)-N(21) = 1.573(9) Å].

Attempts to crystallize the B(bipy)-bridged dinuclear ferrocene complex using various different counterions resulted in single crystals of **[11]Br**, **[11]O₃SCF₃**, and **[11]PF₆**. In all three cases, the crystal lattices contained large amounts of solvate molecules. The structures of **[11]Br** and **[11]O₃SCF₃** were thus seriously disordered and could not be refined. A crystal structure determination of **[11]PF₆** (monoclinic, $P2_1/c$) was more successful and confirmed the molecular structure already derived from NMR spectroscopy (Figure 7). The conformation of **[11]PF₆** in the solid state resembles that of its BMe₂-bridged analog **Li[2]**(12-crown-4)₂ (Figure 3) if a 2,2'-bipyridyl ligand is substituted for the two methyl groups [C(11)-B(1)-C(21)-C(22) = 65.7(8), C(21)-B(1)-C(11)-C(12) = -79.9(8)]. Bond lengths and angles of **[11]PF₆** do not depart appreciably from the values observed for other 2,2'-bipyridylboronium substituted ferrocenes.[16, 27-29]

Electrochemical Investigations. Table 2 summarizes the electrochemical parameters of the redox events exhibited by compounds **Li[2]**, **Li₂[3]**, **6**, **10**, **[11]PF₆** and **[14](PF₆)₂**. All electrode potentials discussed in this paragraph are referenced against the

ferrocene/ferricenium couple. For review articles on metal-metal interactions in linked metallocenes see refs.[30, 31].

The electrochemical properties of the dinuclear species **Li[2]**, **10**, and **[11]PF₆**, which have been investigated in CH_2Cl_2 solutions, are considered first (Figure 8). Since the BMe_2 bridged **Li[2]** tends to decompose upon oxidation at room temperature, it was measured at -78 °C. Cyclic voltammograms of **10** and **[11]PF₆** were recorded at 20 °C. Under these conditions, all three compounds display chemically reversible oxidation processes as evidenced by the following criteria: where it is possible to determine them, the current ratios i_{pc}/i_{pa} are constantly equal to 1, the current functions $i_{pa}/v^{1/2}$ remain constant, and the peak-to-peak separations ($\Delta E_{p(i)}$, $\Delta E_{p(t)}$) do not depart appreciably from the value found for the internal ferrocene standard ($\Delta E_{p(FcH)}$, Table 2; theoretically expected value for a chemically and electrochemically reversible one-electron step: 59 mV). It should be noted that deviations from the ideal signal shape in the case of **[11]PF₆** are due to electrode adsorption of the electro-generated trication $[11]^{3+}$. This effect is less pronounced at higher scan rates and absent in CH_3CN solution. All three dinuclear complexes **Li[2]**, **10**, and **[11]PF₆** exhibit two well-resolved Fe(II)/Fe(III) redox waves of relative intensity 1:1 (Table 2). They are assigned to successive one-electron transitions at the two ferrocenyl moieties and point to the presence of an electronic interaction between them. For obvious reasons, the anionic compound **[2]⁻** possesses the most cathodic redox potential ($E°'([2]^-/2)$ = -0.64 V), the neutral species **10** adopts an intermediate position ($E°'(10/[10]^+)$ = -0.21 V), and the cationic molecule **[11]⁺** is oxidized at the most anodic potential ($E°'([11]^+/[11]^{2+})$ = +0.07 V). On the basis of a purely electrostatic model, one would expect the difference in the redox potentials of the two Fe(II)/Fe(III) transitions to be smallest in the case of **Li[2]** and largest in the case of **[11]PF₆**, because the energy required to introduce a third positive charge into $[11]^{2+}$ should be disproportionately larger than the energy required to introduce a first positive charge into the neutral species **2**. The opposite trend, however, is observed in the series **Li[2]** ($E°'([2]^-/2)$ =

-0.64 V, $E^{\circ\prime}(\mathbf{2}/[\mathbf{2}]^+)$ = -0.43 V; $\Delta E^{\circ\prime}$ = 0.21V), $\mathbf{10}$ ($E^{\circ\prime}(\mathbf{10}/[\mathbf{10}]^+)$ = -0.21 V, $E^{\circ\prime}([\mathbf{10}]^+/[\mathbf{10}]^{2+})$

= -0.03 V; $\Delta E^{\circ\prime}$ = 0.18 V), and $[\mathbf{11}]\mathbf{PF_6}$ ($E^{\circ\prime}([\mathbf{11}]^+/[\mathbf{11}]^{2+})$ = +0.07 V, $E^{\circ\prime}([\mathbf{11}]^{2+}/[\mathbf{11}]^{3+})$ =

+0.23 V; $\Delta E^{\circ\prime}$ = 0.16 V). This leads to the conclusion that more subtle mechanisms of

ferrocene-ferrocene interaction have to be taken into account including not only the influence

of counterions but also some degree of charge delocalisation via the four-coordinate boron

bridges. A comparison of the electrochemical properties of $\mathbf{Li[2]}$ and the

ferricenyltris(ferrocenyl)borate zwitterion[32] $\mathbf{V}$ (Figure 2) furnishes further valuable

information. It was anticipated that there would be little or no charge transfer through the

coordinatively saturated boron atom. Cyclic voltammetry, however, revealed four reversible

oxidation potentials at -0.62 V, -0.35 V, -0.15 V, and -0.03 V (cf. $\mathbf{Li[2]}$: $E^{\circ\prime}$ = -0.64 V, -0.43

V). Moreover, a very broad band with a maximum near 2200 nm was detected in the

electronic absorption spectrum of $\mathbf{V}$. Both the presence of an intervalence electronic transition

and the electrochemical data establish $\mathbf{V}$ as a mixed valence system and the authors suggested

that electron transfer may proceed via a through-space mechanism. We note in passing that

the $\Delta E^{\circ\prime}$ values of 0.21 V, 0.18 V, and 0.16 V determined for $\mathbf{Li[2]}$, $\mathbf{10}$, and $[\mathbf{11}]\mathbf{PF_6}$,

respectively, are in the same range as the $\Delta E^{\circ\prime}$ values observed for the $SiMe_2$-bridged

oligo(ferrocenylenes) $Fc\text{-}[\text{-}SiMe_2\text{-}fc\text{-}]_x\text{-}SiMe_2\text{-}Fc$ (x = 0 - 6; $\Delta E^{\circ\prime}$ = ca. 0.2 V).[33] The two

strongly cathodic redox waves of $[\mathbf{11}]\mathbf{PF_6}$ ($E^{\circ\prime}$ = -1.29 V, -2.35 V), each representing a one-

electron transition, are to be assigned to the reduction of the 2,2'-bipyridylboronium bridge,

which is chemically related to the well-known two-electron acceptor diquat[34]. Both electrode

potentials are reasonably close to those previously observed for B(bipy)-centred reductions in

the case of $[\mathbf{IV}]^+$ [$E^{\circ\prime}$ = -1.43 V, -2.23 V (peak potential value); hexafluorophosphate salt in

CH_2Cl_2][16].

At –78 °C, the cyclic voltammogram of $\mathbf{Li_2[3]}$ consists of two redox waves ($E^{\circ\prime}$ = -0.51 V,

-1.21 V), both of them showing features of chemical reversibility (Figure 9). Since the peak

height of the more anodic couple is twice that of the cathodic one, the former is to be attributed to a two-electron transition and the latter to a one-electron transition. Considering the molecular structure of $[3]^{2-}$ which possesses (i) one electronically unique interior ferrocenylene moiety directly attached to two negatively charged –B(Fc)Me$_2$ groups and (ii) two symmetry-related terminal ferrocenyl groups bearing only one anionic substituent, we may safely assume that the central iron atom is oxidized first and the other two subsequently. This assignment is further supported by the electrochemical data of the free macrocycle $[III]^{2-}$ ($E^{\circ\prime}$ = -1.02 V, -1.33 V)[13] and of Li$_2$[1,1'-fc(BMe$_3$)$_2$],[22] which possesses an $E^{\circ\prime}$ value of –1.22 V. Moreover, the formal electrode potential of the terminal ferrocenyl substituents in **Li$_2$[3]** ($E^{\circ\prime}$ = -0.51 V) agrees nicely with the mean redox potential of the diferrocenyl complex **Li[2]** ($E^{\circ\prime}$ = -0.43 V, -0.64 V). The electrochemical behaviour of **Li$_2$[3]** may be compared to that of the isoelectronic complexes Fc-EMe$_2$-fc-EMe$_2$-Fc (E = C, Si). In the cyclic voltammogram of the carbon-bridged derivative, three reversible redox events are resolvable at –0.14 V, 0.00 V, +0.20 V, ratio 1:1:1.[23] Silicon-bridged Fc-SiMe$_2$-fc-SiMe$_2$-Fc in CH$_2$Cl$_2$/CH$_3$CN solution shows only two redox waves with relative intensity of 2:1 ($E^{\circ\prime}$ = -0.03 V, +0.23 V)[33]. In CH$_2$Cl$_2$ solution, however, the -0.03 V wave is resolved into two closely spaced one-electron waves,[25] indicating that the two ferrocenyl end groups are oxidized first, followed by oxidation at the interior site.[23, 33].

The cyclic voltammogram of **[14](PF$_6$)$_2$** is characterized by four redox transitions at $E^{\circ\prime}$ = +0.26 V, +0.03 V, -1.38 V, and -2.16 V with relative peak heights of 1:2:2:2 (Figure 10). Similar to **[11]PF$_6$**, the two anodic processes are due to ferrocene oxidation, while the two cathodic processes are centred at the B(bipy) bridges. At difference with the trinuclear aggregate $[3]^{2-}$ where the interior ferrocenylene moiety is oxidized first, oxidation of the terminal ferrocenyl moieties precedes the electron transfer step at the central iron atom in $[14]^{2+}$. Qualitatively, this can be explained by the fact that the central iron atoms experience twice the electronic charge of the boron substituents and this charge is of opposite sign in both

14

molecules. At first glance we find it, however, counterintuitive that attachment of two negatively charged substituents to ferrocene leads to a huge cathodic shift of its redox potential (cf. the central ferrocenylene moiety in [3]$^{2-}$ gets oxidized at $E°'$ = -1.21 V) whereas the accumulation of four positive charges in [14]$^{4+}$ [two at the B(bipy) bridges and two more at the terminal ferricenyl(III) groups] increases the redox potential of the interior ferrocenylene fragment by as little as +0.26 V with respect to parent ferrocene. Similarly, if we go along the series [FcB(Me)bipy]PF$_6$, [1,1'-fc(B(Me)bipy)$_2$](PF$_6$)$_2$, and [1,1',3,3'-Fe(C$_5$H$_3$(B(Me)bipy)$_2$)$_2$](PF$_6$)$_4$, there is no concomitant increase in the values of the Fe(II)/Fe(III) redox potentials ($E°'$ = -0.02 V, -0.03 V, -0.03 V; in CH$_2$Cl$_2$) with increasing number of positively charged sidegroups.[16] In this context, it is revealing to compare the influence exerted by two different kinds of negatively charged borate substituents on the ferrocene/ferricenium couple. As mentioned above, Li$_2$[1,1'-fc(BMe$_3$)$_2$] possesses a redox potential of $E°'$ = -1.22 V,[22] whereas Tl[FcBpz$_3$] and Tl$_2$[1,1'-fc(Bpz$_3$)$_2$] are oxidized at -0.01 V and -0.02 V, respectively (peak potential values; pz = pyrazol-1-yl)[35]. This leads to the conclusion, that the negative charge of the borate substituent alone is not the determining factor for the $E°'$ value. Apart from the fact that the excess electron is spread over a larger region in the case of Bpz$_3$, which may to some extent reduce its electrostatic effect on the iron atom, the group electronegativity of a Bpz$_3$ moiety is supposed to by considerably higher than that of a BMe$_3$ substituent but comparable to the group electronegativity of the B(Me)bipy fragment. Given that [FcB(Me)bipy]PF$_6$ and Tl[FcBpz$_3$] are oxidized at rather similar electrode potentials, it is tempting to speculate that electrostatic effects are of minor importance for an explanation of the electrochemical properties of Li$_2$[3] and [14](PF$_6$)$_2$ and that a major contribution to the cathodic shift of the Li$_2$[3] redox potential stems from inductive and/or hyperconjugative B(R)Me$_2$-to-ferrocene charge transfer (R = Me, Fc). Charge-transfer between ferrocene and its boron-containing substituent(s) is also apparent in [11]PF$_6$, [14](PF$_6$)$_2$, [FcB(Me)bipy]PF$_6$, [1,1'-fc(B(Me)bipy)$_2$](PF$_6$)$_2$, and [1,1',3,3'-

$Fe(C_5H_3(B(Me)bipy)_2)_2](PF_6)_4$, which give intensely purple-coloured solutions. In these molecules, ferrocene acts as electron donor and the B(Me)bipy substituent as the corresponding acceptor as has been found out by transient absorption measurements using femtosecond pump-probe spectroscopy[11] (see also the paragraph "crystal structure determination" of this paper). However, the amount of charge transferred is obviously too small to cause a significant anodic shift of the Fe(II)/Fe(III) redox potential of ferrocene-based 2,2'-bipyridylboronium salts.

Apart from electron delocalization effects, possible influences of the counterions should also be considered as becomes evident from an inspection of the redox behavior of **Li₂[III]**. The compound crystallizes from THF/diethylether in the presence of 12-crown-4 with one naked Li^+ ion encapsulated in the macrocyclic framework (Figure 1). The other Li^+ ion is complexed by two molecules of crown ether. The contact ion pair {**Li[III]**}⁻, which remains intact in THF solution (^7Li NMR spectroscopical control), is oxidized at -0.58 V (irreversible two-electron process). As a result, the Li^+ ion leaves the cage and a solvent separated species forms. Reduction of the empty macrocycle **III** back to its **[III]²⁻** state occurs in two successive one-electron steps at pronouncedly more cathodic electrode potentials ($E°' = -1.02$ V, -1.33 V).[13] In **[11]PF₆** and **[14](PF₆)₂**, the PF_6^- ion is comparatively small and thus able to approach the cationic fragment rather closely. Moreover, we are using [NBu₄][PF₆] as the supporting electrolyte in our CV measurements, thereby causing a 200fold increase in $[PF_6]^-$ concentration, which can be expected to further promote the formation of contact ion pairs. Thus, the fact, that cationic B(bipy) entities appear to have only a small impact on the Fe(II)/Fe(III) redox potentials may well be due to partial charge compensation. The Li^+ cations of **Li[2]**, **Li₂[3]** and $Li_2[1,1'-fc(BMe_3)_2]$, on the other hand, are deeply embedded in ligand spheres of 12-crown-4 and THF molecules and thus kept at a large distance from the anionic part of the molecule. As a result, any effect of electrostatic forces between the boron

bridges and the iron atoms is expected to be more pronounced within $[2]^-$, $[3]^{2-}$, and $[1,1'\text{-}$ $fc(BMe_3)_2]^{2-}$ as compared to $[11]PF_6$ and $[14](PF_6)_2$.

Conclusion

In order to investigate the potential of four-coordinate boron atoms to mediate electronic communication between two ferrocenyl substituents, we synthesized di- and trinuclear complexes featuring negatively charged BMe_2 bridges on one hand (i.e. **Li[2]**, **Li$_2$[3]**) and positively charged B(bipy) linkers on the other (i.e. **[11]PF$_6$**, **[14](PF$_6$)$_2$**). For comparison, we also prepared the uncharged mono- and diferrocene derivatives **6** and **10** in which the boron atom is chelated by a 2-(2'-pyridyl)indolyl ligand. **Li[2]**(12-crown-4)$_2$ (monoclinic, *C2/c*), **Li$_2$[3]**(12-crown-4)$_4$ (triclinic, *P*-1), **6** (monoclinic, *P2$_1$/c*), **10** (monoclinic, *P2$_1$/c*), and **[11]PF$_6$** (monoclinic, *P2$_1$/c*) were structurally authenticated using X-ray crystallography.

As to be expected, electrostatic forces of attraction or repulsion between the boron bridges and the ferrocene moieties have an influence on the Fe(II)/Fe(III) redox potentials of **Li[2]**, **Li$_2$[3]**, **[11]PF$_6$**, and **[14](PF$_6$)$_2$**). Compared to the FcH/FcH$^+$ standard, a huge cathodic shift is observed in the case of the negatively charged BMe_2-bridged species whereas the 2,2'-bipyridylboronium derivatives are oxidized at more anodic electrode potentials than parent ferrocene. It is also important to note that the cyclic voltammograms of **Li[2]**, **10**, and **[11]PF$_6$** exhibit two well resolved one-electron redox waves rather than one two-electron transition (cf. **Li[2]**: $E^{\circ\prime}$ = -0.43 V / -0.64 V; **10**: -0.03 V / -0.21 V; **[11]PF$_6$**: $E^{\circ\prime}$ = +0.23 V / +0.07 V; in CH_2Cl_2 *vs.* FcH/FcH$^+$). Interestingly, the absolute shift values are significantly larger for anionic $[2]^-$ than for its cationic counterpart $[11]^+$ even though the amount of charge accommodated by both species is the same. Moreover, the $\Delta E^{\circ\prime}$ splitting between the two corresponding Fe(II)/Fe(III) redox waves decreases from 0.21 V in **Li[2]** to 0.18 V in **10** and 0.16 V in **[11]PF$_6$**, which is somewhat surprising because it should be much harder to introduce a third positive charge into $[11]^{2+}$ than to introduce a first positive charge into the

neutral species **2**. This argues against mere electrostatic interactions as the only source of the redox splitting observed in **Li[2]**, **Li₂[3]**, **[11]PF₆**, and **[14](PF₆)₂**. Other factors like the positive inductive effect of $B(R)Me_2$ substituents (R = Fc, fc) and positive hyperconjugation from B-C σ orbitals into π^* orbitals of the C_5H_4 rings are also likely to play an important role. Each of the trinuclear complexes **Li₂[3]** and **[14](PF₆)₂** is characterized by one one-electron wave and one two-electron Fe(II)/Fe(III) transition (**Li₂[3]**: -0.51 V, -1.21 V, ratio 2:1; **[14](PF₆)₂**: +0.03 V, +0.26 V, ratio 1:2). Again, relative potential differences within the same cyclic voltammogram as well as absolute shifts of the redox potentials with respect to the FcH/FcH^+ couple are most pronounced in the BMe_2-bridged aggregate. The electrochemical behaviour of **Li₂[3]** and **[14](PF₆)₂** differs in an important aspect from the redox chemistry of the triferrocenes $Fc\text{-}EMe_2\text{-}fc\text{-}EMe_2\text{-}Fc$ (E = C, Si)[23, 25, 33], which are uncharged isoelectronic analogues of $[3]^{2-}$. In both these molecules, three reversible one-electron redox processes can be resolved under appropriate measurement conditions thereby indicating the degree of electronic interactions to be higher than in **Li₂[3]** and **[14](PF₆)₂**.

The basic idea behind our aim to synthesize poly(ferrocenylenes) with negatively charged borate bridges is to stabilize the Fe(III) state of the constituting ferrocenylene moieties electrostatically and to investigate the electronic and magnetic properties of the macromolecules after (partial) oxidation. Given the background that the zwitterion ferricenyltris(ferrocenyl)borate **V** (Figure 2) is a mixed valence species with electronically communicating iron sites, there appears to be a realistic chance to observe electric conductivity or cooperative magnetic behaviour in related polymeric materials. In the light of our studies on short-chain model systems, however, the initial target polymer **(Li[II])ₙ** (Figure 1) does no longer appear to be the best choice to reach our goal, given the fact that its di- and trinuclear relatives **Li[2]** and **Li₂[3]** (Scheme 1) are not stable upon oxidation at ambient temperature. Moreover, our simple coordination polymerization approach to **(Li[II])ₙ**, which starts from 1,1'-fc(BMe₂)₂ / 1,1'-fcLi₂ and relies on Lewis acid-base pairing, turned out to be

less selective than expected in that it produces considerable amounts of cyclic dimer $Li_2[III]$ (Figure 1).

In contrast to $(Li[II])_n$, the hypothetical B(bipy)-bridged polymer $([VI]PF_6)_n$ (Figure 11) is likely to possess much greater stability as can be deduced from the (electro)chemical properties of its oligomeric congeners $[11]PF_6$ and $[14](PF_6)_2$ (Scheme 3). In addition, macromolecules $([VI]PF_6)_n$ are attractive because they have the potential to act as photoswitchable materials that can be promoted from their diamagnetic ground state $[Fe(II)/R_2B(bipy)^+]$ into a paramagnetic excited state $[Fe(III)/R_2B(bipy)^{0?}]$ upon irradiation with laser light (such a behaviour was observed when the model compound $[1,1'$-$fc(B(Me)bipy)_2](PF_6)_2$ was investigated by transient absorption measurements using femtosecond pump-probe spectroscopy)[11]. Unfortunately, the synthesis protocol for $[11]PF_6$ and $[14](PF_6)_2$ can probably not be developed further to make $([VI]PF_6)_n$ accessible from $1,1'$-$fc(SnMe_3)_2$ / $1,1'$-$fc(BBr_2)_2$ and $2,2'$-bipyridyl. The problem lies in the fact that $1,1'$-$fc(SnMe_3)_2$ undergoes a unique rearrangement reaction when boron halides are added. As the result, 1-stannyl-2-borylferrocenes rather than $1,1'$-diborylferrocenes are obtained as the major product.[36, 37] Thus, a completely different synthesis route is required and we suggest to employ a novel reaction which has only recently been discovered by our group: $FcBBr_2$, **7**, and two equivalents of $HSiEt_3$ produce Fc_2BBr, **9**, in about 90 % yield (Scheme 4; for details see the Experimental Part of this paper). Both in terms of starting material availability and in terms of yield, this procedure is superior to the stannyl route outlined in Scheme 2. The reaction is reminiscent of the chemical behaviour of $[FcBH_3]Li$, which, upon hydride abstraction with $ClSiMe_3$, does not give the free borane but dimerizes to the BH-bridged diferrocene spezies Fc_2BH with concomitant liberation of B_2H_6.[38] We have gathered considerable evidence that $1,1'$-$fc(BBr_2)_2$, **12**, and triethylsilane give oligomers $(VII)_n$ with estimated chain lengths n ranging from 10 to 100 (Scheme 4; n was determined by GPC after $(VII)_n$ had been quenched with $MeOSiMe_3$).[39] Compounds $(VII)_n$ are promising starting

19

materials for the preparation of B(bipy)-bridged polymers **([VI]PF$_6$)$_n$** (Figure 11) Moreover, they may be reacted with organolithium reagents (e.g. PhLi, FcLi) to give more stable derivatives of the initial target compound **(Li[II])$_n$** (Figure 1). These investigations are currently under way in our laboratories together with attempts to optimize the synthesis protocol for **(VII)$_n$** in order to obtain higher molecular weights and a smaller molecular weight distribution.

Experimental

General Considerations

All reactions and manipulations of air-sensitive compounds were carried out in dry, oxygen-free argon using standard Schlenk ware. Solvents were freshly distilled under argon from Na/benzophenone (toluene, benzene, diethyl ether, THF), Na/Pb alloy (hexane, heptane) or from CaH_2 (CH_2Cl_2, $CHCl_3$, CH_3CN) prior to use. NMR: Bruker DPX 250, AMX 250, AMX 400. ^{11}B NMR spectra are reported relative to external $BF_3 \cdot Et_2O$. All NMR spectra were run at room temperature; abbreviations: s = singlet; d = doublet; vtr = virtual triplet; q = quartet; br = broad; m = multiplet; n.r. = multiplet expected in the ^1H NMR spectrum but not resolved; n.o. = signal not observed; bipy = 2,2'-bipyridyl. $FcBBr_2$,[40] $FcB(Me)Br$,[40] $FcBMe_2$,[40] 1,1'-$fc(BBr_2)_2$[41], $FcSnMe_3$,[42] $FcLi$,[43] 1,1'-$fc(Li \cdot TMEDA)_2$,[44] and 5-fluoro-2-(2'-pyridyl)indole[45] were synthesized according to literature procedures.

Synthesis of Li[2]: tBuLi in pentane (1 mL, 1.50 mmol) was added to a solution of ferrocene (0.325 g, 1.75 mmol) in THF (5 mL) at 0 °C. After the resulting mixture had been stirred for 15 min, $FcBMe_2$, **1**, (0.259 g, 1.15 mmol) in THF (3 mL) was added dropwise with stirring at 0 °C. The reaction mixture was stirred for one hour at room temperature, evaporated to dryness *in vacuo* and excess ferrocene was sublimed out overnight at 90 °C/10^{-3} torr. The remaining yellow microcrystalline solid was dissolved in CH_2Cl_2 (5 mL) and 12-crown-4 (0.470 g, 2.67 mmol) was added. After filtration, hexane (0.5 mL) was added to the filtrate. The clear orange solution was kept at −25 °C for 24 h to give orange coloured X-ray quality crystals of **Li[2]**(12-crown-4)$_2 \cdot CH_2Cl_2$. Yield: 0.570 g (58 %). ^{11}B NMR (THF-d_8, 128.4 MHz): δ -21.2 ($h_{1/2}$ = 10 Hz). ^1H NMR (THF-d_8, 400.0 MHz): δ −0.12 (m, 6H, CH_3), 3.64 (s, 32H, CH_2), 3.70, 3.81 (2 × vtr, 2 × 4H, $^3J_{HH}$ ~ $^4J_{HH}$ ~ 1.4 Hz, C_5H_4), 3.84 (s, 10 H, C_5H_5). ^{13}C NMR (THF-d_8, 100.6 MHz): δ 14.8 (q, $^1J_{CB}$ = 41.7 Hz, CH_3), 66.2 (C_5H_4), 67.4 (C_5H_5), 69.6

21

(CH_2), 72.3 (C_5H_4), n.o. (C_{ipso}). ESI-MS: m/z 411 [M-Li]$^-$. The compound is highly sensitive to air and the crystals lose CH_2Cl_2 rapidly when isolated at room temperature; a decent elemental analysis was therefore not obtained.

Synthesis of Li$_2$[3]. FcBMe$_2$, **1**, (0.107 g, 0.47 mmol) and 1,1′-fc(Li·TMEDA)$_2$ (0.074 g, 0.17 mmol) were dissolved in THF (3 mL) at −78 °C. The reaction mixture was allowed to warm to room temperature and stirred for 30 min. Addition of 12-crown-4 (0.326 g, 1.85 mmol) yielded a yellow precipitate. After addition of heptane (3 mL) and stirring for 30 min at room temperature, the solid material was collected on a frit, triturated with heptane (3 × 5 mL) and dried *in vacuo*. A solution of the crude product in THF was layered with diethyl ether by vapour-phase diffusion to yield X-ray quality crystals of **Li$_2$[3]**(12-crown-4)$_4$. Yield: 0.182 g (79 %). NMR spectra of the TMEDA adduct: ^{11}B NMR (128.4 MHz, THF-d_8): δ -19.2 ($h_{1/2}$ = 20 Hz). ^{1}H NMR (400.0 MHz, THF-d_8): δ −0.13 (br, 12H, CH_3), 2.14 (s, NCH_3), 2.29 (s, CH_2), 3.57, 3.63, 3.70, 3.78 (4 × n.r., 4 × 4H, C_5H_4), 3.82 (s, 10H, C_5H_5). ^{13}C NMR (100.6 MHz, THF-d_8): δ 14.6 (q, $^1J_{CB}$ = 40.9 Hz, CH_3), 46.2 (NCH_3), 58.5 (CH_2), 66.0 (C_5H_4), 67.3 (C_5H_5), 67.4, 70.7, 72.1 (C_5H_4), n.o. (C_{ipso}). The compound is highly sensitive to air; a decent elemental analysis was therefore not obtained.

Synthesis of 4: 5-Fluoro-2-(2'-pyridyl)indole was obtained following a literature procedure.[45] Since a complete assignment of its ^{1}H- and ^{13}C NMR resonances has not been published but is helpful for an interpretation of the NMR spectra of the corresponding B-N adducts, the full NMR spectroscopic characterization of 5-fluoro-2-(2'-pyridyl)indole is given here [primed (') signals refer to the pyridyl fragment]: ^{1}H NMR (DMSO-d_6, 250.1 MHz): d 6.93 (ddd, 1H, $^3J_{HF}$ = 9.6 Hz, $^3J_{HH}$ = 8.9 Hz, $^4J_{HH}$ = 2.6 Hz, H-6), 7.09 (dd, 1H, $^4J_{HH}$ = 2.2 Hz, $^4J_{HH}$ = 0.8 Hz, H-3), 7.24 − 7.32 (m, 2H, H-4, H-5'), 7.42 (dd, 1H, $^3J_{HH}$ = 8.9 Hz, $^4J_{HF}$ = 4.7 Hz, H-7), 7.82 (ddd, 1H, $^3J_{HH}$ = 8.0 Hz, $^3J_{HH}$ = 7.4 Hz, $^4J_{HH}$ = 1.8 Hz, H-4'), 7.94 (dvtr, 1H, $^3J_{HH}$ = 8.0 Hz, $^4J_{HH}$ ~ $^5J_{HH}$ ~ 1.2 Hz, H-3'), 8.59 (ddd, 1H, $^3J_{HH}$ = 4.9 Hz, $^4J_{HH}$ = 1.8 Hz, $^5J_{HH}$ = 1.1 Hz, H-6'), 11.71 (n.r., 1H, N-H). ^{13}C NMR (DMSO-d_6, 62.9 MHz): d 100.6 (d, $^4J_{CF}$ = 4.9 Hz, C-3),

104.9 (d, $^2J_{CF}$ = 23.1 Hz, C-4), 110.6 (d, $^2J_{CF}$ = 26.3 Hz, C-6), 113.0 (d, $^3J_{CF}$ = 9.8 Hz, C-7), 120.0 (C-3'), 122.5 (C-5'), 128.5 (d, $^3J_{CF}$ = 10.5 Hz, C-9), 133.9 (C-8), 137.1 (C-4'), 138.9 (C-2), 149.2 (C-6'), 150.0 (C-2'), 157.2 (d, $^1J_{CF}$ = 231.9 Hz, C-5). ^{19}F NMR (DMSO-d$_6$, 235.3 MHz): d -125.0.

For the preparation of the sodium salt **4**, a slurry of sodium hydride (0.030 g, 1.25 mmol) in THF (5 mL) was added to a solution of 5-fluoro-2-(2'-pyridyl)indole (0.200 g, 0.94 mmol) in THF (5 mL) at −78 °C. After H$_2$ evolution had ceased, the mixture was allowed to warm to room temperature, filtered and the filtrate evaporated to dryness *in vacuo*. The off-white residue obtained was used without further purification. Yield: 0.221 g (100 %).

Synthesis of 6: Compound **4** (0.221 g, 0.94 mmol) was suspended in toluene (5 mL), the resulting slurry cooled to −78 °C and a solution of FcB(Me)Br, **5**, (0.255 g, 0.88 mmol) in toluene (10 mL) added slowly with stirring. After warming to room temperature, the reaction mixture was stirred overnight. After filtration, all volatiles were removed from the filtrate under reduced pressure. The resulting solid was further purified by column chromatography (dichloromethane/ethyl acetate 10:1). Yield: 0.190 g (51 %). Orange coloured X-ray quality crystals of **6** were grown by slow evaporation of its CDCl$_3$ solution at room temperature. NMR spectroscopy [primed (') signals refer to the pyridyl fragment]: ^{11}B NMR (CDCl$_3$, 128.4 MHz): d 4.5 ($h_{1/2}$ = 300 Hz). ^{1}H NMR (CDCl$_3$, 250.1 MHz): d 3.78 (s, 5H, C$_5$H$_5$), 3.87, 3.90, 4.09, 4.11 (4 × m, 4 ×1H, C$_5$H$_4$), 6.99 (d, 1H, $^4J_{HH}$ = 0.8 Hz, H-3), 7.00 (vtrd, 1H, $^3J_{HF}$ ~ 9.2 Hz, $^3J_{HH}$ ~ 9.2 Hz, $^4J_{HH}$ = 2.6 Hz, H-6), 7.33 (dd, 1H, $^3J_{HF}$ = 9.4 Hz, $^4J_{HH}$ = 2.6 Hz, H-4), 7.36 (ddd, 1H, $^3J_{HH}$ = 7.3 Hz, $^3J_{HH}$ = 5.7 Hz, $^4J_{HH}$ = 1.4 Hz, H-5'), 7.57 (dd, 1H, $^3J_{HH}$ = 9.1 Hz, $^4J_{HF}$ = 4.7 Hz, H-7), 7.85 (dvtr, 1H, $^3J_{HH}$ = 8.2 Hz, $^4J_{HH}$ ~ $^5J_{HH}$ ~ 1.1 Hz, H-3'), 7.98 (ddd, 1H, $^3J_{HH}$ = 8.2 Hz, $^3J_{HH}$ = 7.3 Hz, $^4J_{HH}$ = 1.3 Hz, H-4'), 8.57 (dvtr, 1H, $^3J_{HH}$ = 5.7, $^4J_{HH}$ ~ $^5J_{HH}$ ~ 1.2 Hz, H-6'). ^{13}C NMR (CDCl$_3$, 100.6 MHz): d 8.3 (CH$_3$), 68.2 (C$_5$H$_5$), 68.8, 69.0, 71.0, 71.3 (C$_5$H$_4$), n.o. (C$_{ipso}$), 97.5 (d, $^4J_{CF}$ = 5.8 Hz, C-3), 105.9 (d, $^2J_{CF}$ = 22.9 Hz, C-4), 111.9 (d, $^2J_{CF}$ = 26.9 Hz, C-6), 114.6 (d, $^3J_{CF}$ = 9.8 Hz, C-7), 118.5 (C-3'), 120.9 (C-5'), 132.3 (d, $^3J_{CF}$

= 10.4 Hz, C-9), 135.8 (C-8), 137.6 (C-2), 140.7 (C-4'), 141.8 (C-6'), 148.8 (C-2'), 157.8 (d,

$^1J_{CF}$ = 234.5 Hz, C-5). ^{19}F NMR (CDCl$_3$, 235.3 MHz): d -125.3. ESI-MS: m/z 422 [M$^+$].

Elemental analysis: Calcd. for C$_{24}$H$_{20}$BFFeN$_2$ (422.08): C, 68.30; H, 4.78; N, 6.64. Found: C,

68.61; H, 4.95; N, 6.33.

Synthesis of 9: *Method A*: A solid mixture of FcBBr$_2$, **7**, (0.710 g, 2.00 mmol) and FcSnMe$_3$,

8, (0.698 g, 2.00 mmol) was dissolved in 20 mL of C$_6$H$_6$ at room temperature and stirred for 8

h, whereupon a colourless precipitate (Me$_3$SnBr) gradually formed. After filtration and

evaporation of solvent under reduced pressure, a red microcrystalline solid was obtained.

Yield: 0.533 g (58 %). *Method B*: To FcBBr$_2$, **7**, (1.836 g, 5.16 mmol) in toluene (20 mL) was

added neat Et$_3$SiH (1.321 g, 11.36 mmol) at −78 °C with stirring. The resulting red solution

was allowed to warm to room temperature and stirred overnight. All volatiles were driven off

in vacuo to yield **9** as red microcrystalline solid. Yield: 1.034 g (87 %). ^{11}B NMR (CDCl$_3$,

128.4 MHz): d 54.9 ($h_{1/2}$ = 540 Hz). ^{1}H NMR (CDCl$_3$, 250.1 MHz): d 4.08 (s, 10H, C$_5$H$_5$),

4.61, 4.64 (2 × vtr, 2 × 4H, $^3J_{HH}$ = $^4J_{HH}$ = 1.8 Hz, C$_5$H$_4$). ^{13}C NMR (CDCl$_3$, 100.6 MHz): d

69.8 (C$_5$H$_5$), 75.0, 76.6 (C$_5$H$_4$), n.o. (C$_{ipso}$).

Synthesis of 10: The compound was synthesized similar to **6** from **4** (0.165 g, 0.71 mmol)

and Fc$_2$BBr, **9**, (0.294 g, 0.64 mmol) in toluene (15 mL). Yield: 0.087 g (23 %). Orange X-ray

quality crystals of **10** were grown by slow evaporation of its toluene solution at room

temperature. NMR spectroscopy [primed (') signals refer to the pyridyl fragment]: ^{11}B NMR

(CDCl$_3$, 128.4 MHz): d 4.1 ($h_{1/2}$ = 370 Hz). ^{1}H NMR (CDCl$_3$, 250.1 MHz): d 3.59 (s, 10 H,

C$_5$H$_5$), 3.99 (m, 2H, C$_5$H$_4$), 4.09 – 4.13 (m, 6H, C$_5$H$_4$), 7.07 (vtrd, 1H, $^3J_{HF}$ ~ 9.2 Hz, $^3J_{HH}$ ~

9.2 Hz, $^4J_{HH}$ = 2.6 Hz, H-6), 7.10 (d, 1H, $^4J_{HH}$ = 0.8 Hz, H-3), 7.39 (dd, 1H, $^3J_{HF}$ = 9.8 Hz,

$^4J_{HH}$ = 2.6 Hz, H-4), 7.45 (ddd, 1H, $^3J_{HH}$ = 7.3 Hz, $^3J_{HH}$ = 5.8 Hz, $^4J_{HH}$ = 1.3 Hz, H-5'), 7.74

(dd, 1H, $^3J_{HH}$ = 9.0 Hz, $^4J_{HF}$ = 4.8 Hz, H-7), 7.91 (dvtr, 1H, $^3J_{HH}$ = 8.1 Hz, $^4J_{HH}$ ~ $^5J_{HH}$ ~ 1.1

Hz, H-3'), 8.03 (ddd, 1H, $^3J_{HH}$ = 8.1 Hz, $^3J_{HH}$ = 7.3 Hz, $^4J_{HH}$ = 1.3 Hz, H-4'), 8.91 (dvtr, 1H,

$^3J_{HH}$ = 5.8 Hz, $^4J_{HH}$ ~ $^5J_{HH}$ ~ 1.2 Hz, H-6'). ^{13}C NMR (CDCl$_3$, 100.6 MHz): d 67.7 (C$_5$H$_5$),

68.4, 68.7, 70.7, 71.5 (C_5H_4), n.o. (C_{ipso}), 98.1 (d, $^4J_{CF}$ = 5.7 Hz, C-3), 106.0 (d, $^2J_{CF}$ = 23.0 Hz, C-4), 112.1 (d, $^2J_{CF}$ = 26.8 Hz, C-6), 115.9 (d, $^3J_{CF}$ = 9.7 Hz, C-7), 118.3 (C-3'), 120.6 (C-5'), 132.4 (d, $^3J_{CF}$ = 10.3 Hz, C-9), 136.4 (C-8), 138.1 (C-2), 140.9 (C-4'), 142.5 (C-6'), 148.6 (C-2'), 157.8 (d, $^1J_{CF}$ = 234.9 Hz, C-5). ^{19}F NMR (CDCl$_3$, 235.3 MHz): d -125.1. ESI-MS: m/z 592 [M$^+$]. Calcd. for $C_{33}H_{26}BFFe_2N_2$ (592.09): C, 66.94; H, 4.43; N, 4.73. Found: C, 66.45; H, 4.62; N, 4.44.

Synthesis of [11]PF$_6$: To a solution of Fc$_2$BBr, **9**, (0.265 g, 0.58 mmol) in toluene (5 mL) was added 2,2'-bipyridyl (0.128 g, 0.82 mmol) in toluene (5 mL) dropwise with stirring at – 78 °C. After stirring for 30 min, the solution was allowed to warm to room temperature whereupon a brown precipitate formed which was collected on a frit and triturated with toluene (10 mL). The crude product was dissolved in water and added dropwise to an aqueous solution of NH$_4$PF$_6$ (0.210 g, 1.29 mmol). The resulting PF$_6$ salt precipitated as brown microcrystalline solid which was collected on a frit and dried in vacuo. Yield: 0.353 g (89 %). Single crystals were obtained by vapour-phase diffusion of diethyl ether into an acetonitrile solution of **[11]PF$_6$**. ^{11}B NMR (CD$_3$CN, 128.4 MHz): d 7.3 ($h_{1/2}$ = 250 Hz). ^{1}H NMR (CD$_3$CN, 250.1 MHz): d 3.86 (s, 10 H, C_5H_5), 4.11, 4.35 (2 × n.r., 2 × 4H, C_5H_4), 8.14 (vtr, 2H, $^3J_{HH}$ ~ 6.3 Hz, bipy-5,5'), 8.64 (vtr, 2H, $^3J_{HH}$ ~ 7.8 Hz, bipy-4,4'), 8.73 (dd, 2H, $^3J_{HH}$ = 8.1 Hz, $^4J_{HH}$ = 1.2 Hz, bipy-3,3'), 9.01 (d, 2H, $^3J_{HH}$ = 5.0 Hz, bipy-6,6'). ^{13}C NMR (CD$_3$CN, 62.9 MHz): d 70.0 (C_5H_5) 71.5, 72.4 (C_5H_4), n.o. (C_{ipso}), 123.9 (bipy-3,3'), 129.4 (bipy-5,5'), 144.7 (bipy-6,6'), 145.7 (bipy-4,4'), 145.8 (bipy-2,2'). ESI-MS: m/z 537 [M-PF$_6$]$^+$. Calcd. for $C_{30}H_{26}BF_6Fe_2N_2P$ (682.02): C, 52.83; H, 3.84; N, 4.11. Found: C, 52.43; H, 3.82; N, 3.85.

Synthesis of [14](PF$_6$)$_2$: A toluene (10 mL) solution of FcSnMe$_3$, **8**, (1.080 g, 3.10 mmol) was added dropwise with stirring at −78 °C to a solution of 1,1'-fc(BBr$_2$)$_2$, **12**, (0.781 g, 1.48 mmol) in 10 mL of toluene. The mixture was allowed to warm to room temperature and stirred for 8 h. The solvent and Me$_3$SnBr were removed overnight at 90 °C/10^{-3} torr. The remaining red oil was dissolved in 20 mL of toluene and 2,2´-bipyridyl (0.462 g, 2.96 mmol)

in toluene (10 mL) was added dropwise at −78 °C whereupon a dark brown precipitate formed. After stirring for one hour at room temperature, the solid material was collected on a frit, triturated with toluene (2 × 10 mL) and hexane (10 mL), and dried *in vacuo*. The crude product was then dissolved in 30 mL of water, filtered and the clear solution added dropwise at room temperature to an aqueous solution of NH_4PF_6 (1.630 g, 10.00 mmol). **[14](PF$_6$)$_2$**, which precipitated quantitatively, was isolated by filtration, triturated with diethyl ether (2 × 10 mL) and dried *in vacuo*. Yield: 1.55 g (89 %). ^{11}B NMR (CD$_3$CN, 128.4 MHz): δ 7.2 ($h_{1/2}$ = 450 Hz). ^{1}H NMR (CD$_3$CN, 400.0 MHz): δ 3.57, 3.62 (2 × n.r., 2 × 4H, C$_5$H$_4$), 3.68 (s, 10H, C$_5$H$_5$), 3.91, 4.26 (2 × n.r., 2 × 4H, C$_5$H$_4$), 8.16 (vtr, 4H, $^3J_{HH}$ ~ 6.4 Hz, bipy-5,5'), 8.68 (vtr, 4H, $^3J_{HH}$ ~ 7.6 Hz, bipy-4,4'), 8.75 (d, 4H, $^3J_{HH}$ = 8.1 Hz, bipy-3,3'), 9.02 (d, 4H, $^3J_{HH}$ = 5.3 Hz, bipy-6,6'). ^{13}C NMR (CD$_3$CN, 100.6 MHz): δ 69.2 (C$_5$H$_5$), 71.0, 71.1, 71.4, 71.6 (C$_5$H$_4$), n.o. (C$_{ipso}$), 124.1 (bipy-3,3'), 129.6 (bipy-5,5'), 144.8 (bipy-6,6'), 145.9 (bipy-2,2'), 146.0 (bipy-4,4'). ESI-MS: *m/z* 444 [M − 2PF$_6$]$^{2+}$. Anal. Calcd for C$_{50}$H$_{42}$B$_2$F$_{12}$Fe$_3$N$_4$P$_2$ (1178.00): C, 50.98; H, 3.59; N, 4.76. Found: C, 50.56; H, 3.45; N, 4.39.

Crystal structure determinations of Li[2](12-crown-4)$_2$, Li$_2$[3](12-crown-4)$_4$, 6, 10, and [11]PF$_6$.

Data collections for **Li[2]**(12-crown-4)$_2$, **Li$_2$[3]**(12-crown-4)$_4$, **6**, and **10** were performed on a STOE IPDS-II two-circle diffractometer with graphite-monochromated MoK$_\alpha$-radiation (λ = 0.71073 Å). The structures were solved with direct methods[46] and refined against F^2 by full-matrix least-squares calculations[47]. Absorption corrections were performed with the MULABS[48] option in PLATON[49]. All non-H atoms have been refined anisotropically, whereas the H atoms have been treated with a riding model, fixing their displacement parameter to 1.2 or 1.5 (for methyl groups) of the value of their parent atom. The asymmetric unit of **Li[2]**(12-crown-4)$_2$·CH$_2$Cl$_2$ contains two anions, two Li cations (each coordinated by two crown ether rings), and two dichloromethane molecules. The anion of **Li$_2$[3]**(12-crown-

4)$_4$ is located on a centre of inversion. As a result of that, there is just half an anion and one Li cation (coordinated by two crown ether rings) in the asymmetric unit. Compound **10** crystallizes with two crystallographically independent but rather similar molecules in the asymmetric unit. Moreover, the crystal lattice contains one molecule of toluene and half a molecule of ferrocene. The Fe atom of the ferrocene molecule is located on a centre of inversion. Consequently, the cp rings are disordered. They simulate a hexagon in which each C atom has an occupation factor of 5/6. Distance restraints were applied to the toluene molecule. A single crystal of **[11]PF$_6$** was measured on a SIEMENS SMART diffractometer at a temperature of about 145(2) K. Repeatedly measured reflections remained stable. An empirical absorption correction with program SADABS[50] gave a correction factor between 0.790 and 1.000. Equivalent reflections were averaged (R(I)$_{internal}$ = 0.073). The structure was determined by direct methods using program SHELXS[46]. All hydrogen atoms were geometrically positioned and were constrained. The unit cell contains two symmetry related solvate regions of 718 Å^3 each. No atoms could be located in the solvate regions. The program PLATON/SQUEEZE[51] was used to model the solvate density. The solvate density was estimated to contain about 405 electrons/cell. The non-hydrogen atoms were refined with anisotropic thermal parameters. The structure was refined on F^2 values using program SHELXL-97[47]. The final difference density was between -2.0 and +3.8 e/ Å^3 near Fe(2). The large displacement parameters of many atoms show the structure to be partly disordered. Especially the PF$_6$ group is severely distorted.

CCDC reference numbers: 246197 (**Li[2](12-crown-4)$_2$**), 246196 (**Li$_2$[3](12-crown-4)$_4$**), 246198 (**6**), 246199 (**10**), and 249276 (**[11]PF$_6$**).

Electrochemical Measurements: Cyclic voltammetry was performed in deaerated acetonitrile and methylene chloride solutions containing [NBu$_4$][PF$_6$] (0.1 mol l^{-1}) as the

supporting electrolyte. All potential values are reported relative to the FcH/FcH^+ redox couple. The cell for voltammetric studies was designed as detailed in ref.[52] Voltammetric scans were referenced by addition of a small amount of ferrocene as internal standard at an appropriate time of the experiment.

References

1   C. U. Pittman, C. E. Carraher, M. Zeldin, J. E. Sheats and B. M. Culbertson, *Metal-Containing Polymeric Materials*, Plenum Press, New York, 1996.

2   R. D. Archer, *Inorganic and Organometallic Polymers*, Wiley-VCH, Weinheim, 2001.

3   D. A. Foucher, B. Z. Tang and I. Manners, *J. Am. Chem. Soc.*, 1992, **114**, 6246.

4   M. T. Nguyen, A. F. Diaz, V. V. Dement'ev and K. H. Pannell, *Chem. Mater.*, 1993, **5**, 1389.

5   P. Nguyen, P. Gómez-Elipe and I. Manners, *Chem. Rev.*, 1999, **99**, 1515.

6   H. Braunschweig, R. Dirk, M. Müller, P. Nguyen, R. Resendes, D. P. Gates and I. Manners, *Angew. Chem., Int. Ed. Engl.*, 1997, **36**, 2338.

7   A. Berenbaum, H. Braunschweig, R. Dirk, U. Englert, J. C. Green, F. Jäkle, A. J. Lough and I. Manners, *J. Am. Chem. Soc.*, 2000, **122**, 5765.

8   M. Fontani, F. Peters, W. Scherer, W. Wachter, M. Wagner and P. Zanello, *Eur. J. Inorg. Chem.*, 1998, 1453; *ibid.* 2087.

9   M. Grosche, E. Herdtweck, F. Peters and M. Wagner, *Organometallics*, 1999, **18**, 4669.

10   R. E. Dinnebier, M. Wagner, F. Peters, K. Shankland and W. I. F. David, *Z. Anorg. Allg. Chem.*, 2000, **626**, 1400.

11   M. D. Thomson, M. Novosel, H. G. Roskos, T. Müller, M. Scheibitz, M. Wagner, F. Fabrizi de Biani and P. Zanello, *J. Phys. Chem. A.*, 2004, **108**, 3281.

12   M. Scheibitz, M. Bolte, H.-W. Lerner and M. Wagner, *Organometallics*, 2004, **23**, 3556.

13   M. Scheibitz, R. F. Winter, M. Bolte, H.-W. Lerner and M. Wagner, *Angew. Chem., Int. Ed. Engl.*, 2003, **42**, 924.

14   H. Nöth and B. Wrackmeyer, *Nuclear Magnetic Resonance Spectroscopy of Boron Compounds*, in *NMR Basic Principles and Progress*, ed. P. Diehl, E. Fluck and R. Kosfeld, Springer, Berlin, 1978.

15   J. Mason, *Multinuclear NMR*, Plenum Press, New York, 1987.

16   F. Fabrizi de Biani, T. Gmeinwieser, E. Herdtweck, F. Jäkle, F. Laschi, M. Wagner and P. Zanello, *Organometallics*, 1997, **16**, 4776.

17   F. Jäkle, T. Priermeier and M. Wagner, *J. Chem. Soc., Chem. Commun.*, 1995, 1765.

18   F. Jäkle, M. Mattner, T. Priermeier and M. Wagner, *J. Organomet. Chem.*, 1995, **502**, 123.

19   F. Jäkle, T. Priermeier and M. Wagner, *Organometallics*, 1996, **15**, 2033.

20   E. Herdtweck, F. Jäkle, G. Opromolla, M. Spiegler, M. Wagner and P. Zanello, *Organometallics*, 1996, **15**, 5524.

21   L. Ding, M. Wagner and M. Bolte, *Acta Crystallogr., Sect C*, 2001, **57**, 162.

22   A. Haghiri Ilkhechi, M. Scheibitz, M. Bolte, H.-W. Lerner and M. Wagner, *Polyhedron*, 2004, in press.

23   S. Barlow, V. J. Murphy, J. S. O. Evans and D. O'Hare, *Organometallics*, 1995, **14**, 3461.

24   R. E. Marsh and A. L. Spek, *Acta Crystallogr., Sect B*, 2001, **57**, 800.

25   K. H. Pannell, V. V. Dementiev, H. Li, F. Cervantes-Lee, M. T. Nguyen and A. F. Diaz, *Organometallics*, 1994, **13**, 3644.

26   T. Gmeinwieser, *Diplomarbeit*, Technische Universität München, 1998.

27   L. Ding, K. Ma, F. Fabrizi de Biani, M. Bolte, P. Zanello and M. Wagner, *Organometallics*, 2001, **20**, 1041.

28   L. Ding, K. Ma, M. Bolte, F. Fabrizi de Biani, P. Zanello and M. Wagner, *J. Organomet. Chem.*, 2001, **637-639**, 390.

29   K. Ma, F. Fabrizi de Biani, M. Bolte, P. Zanello and M. Wagner, *Organometallics*,

        2002, **21**, 3979.

30   S. Barlow and D. O'Hare, *Chem. Rev.*, 1997, **97**, 637.

31   M. C. Böhm, *J. Phys. Chem.*, 1984, **80**, 2704.

32   D. O. Cowan, P. Shu, F. L. Hedberg, M. Rossi and T. J. Kistenmacher,

        J. Am. Chem. Soc., 1979, **101**, 1304.

33   R. Rulkens, A. J. Lough and I. Manners, *J. Am. Chem. Soc.*, 1994, **116**, 797.

34   S. Hünig and I. Wehner, *Heterocycles*, 1989, **28**, 359.

35   F. Fabrizi de Biani, F. Jäkle, M. Spiegler, M. Wagner and P. Zanello, *Inorg. Chem.*,

        1997, **36**, 2103.

36   F. Jäkle, A. J. Lough and I. Manners, *J. Chem. Soc.,Chem. Commun.*, 1999, 453.

37   J. A. Gamboa, A. Sundararaman, L. Kakilis, A. J. Lough and F. Jäkle,

        Organometallics, 2002, **21**, 4169.

38   M. Scheibitz, J. W. Bats, M. Bolte, H.-W. Lerner and M. Wagner, *Organometallics*,

        2004, **23**, 940.

39   M. Scheibitz, *Dissertation*, Universität Frankfurt, 2004.

40   T. Renk, W. Ruf and W. Siebert, *J. Organomet. Chem.*, 1976, **120**, 1.

41   W. Ruf, T. Renk and W. Siebert, *Z. Naturforsch.*, 1976, **31b**, 1028.

42   N. Lenze, B. Neumann, A. Salmon, A. Stammler, H.-G. Stammler and P. Jutzi,

        J. Organomet. Chem., 2001, **619**, 74.

43   F. Rebiere, O. Samuel and H. B. Kagan, *Tetrahedron Lett.*, 1990, **31**, 3121.

44   M. D. Rausch and D. J. Ciappenelli, *J. Organomet. Chem.*, 1967, **10**, 127.

45   Q. Liu, M. S. Mudadu, H. Schmider, R. Thummel, Y. Tao, and S. Wang,

        Organometallics, 2002, **21**, 4743.

46   G. M. Sheldrick, *Acta Crystallogr., Sect. A.*, 1990, **46**, 467.

47   G. M. Sheldrick, *SHELXL-97. A Program for the Refinement of Crystal Structures*, Unversität Göttingen, Germany,1997.

48   R. H. Blessing, *Acta Crystallogr., Sect. A.*, 1995, **51**, 33.

49   A. L. Spek, *Acta Crystallogr., Sect. A.*, 1990, **46**, C34.

50   G. M. Sheldrick, *SADABS*, University of Göttingen, Germany, 2000.

51   P. van der Sluis and A. L. Spek, *Acta Cryst., Sect. A*,1990, **46**, 194.

52   R. F. Winter and F. M. Hornung, *Organometallics*, 1999, **18**, 4005.

Figure Captions

Scheme 1 Synthesis of di- and trinuclear ferrocene complexes **Li[2]** and **Li₂[3]** with anionic four-coordinate boron bridges. (i) + FcLi, THF, 0 °C to r.t.; (ii) + 1,1′-fc(Li·TMEDA)₂, THF, -78 °C to r.t..

Scheme 2 Synthesis of mono- and dinuclear ferrocene complexes **6** and **10** with neutral four-coordinate boron bridges. (i) toluene, -78 °C to r.t.; (ii) benzene, r.t..

Scheme 3 Synthesis of di- and trinuclear ferrocene complexes **[11]PF₆** and **[14](PF₆)₂** with cationic four-coordinate boron bridges. (i) toluene, -78 °C to r.t.; + NH₄PF₆, water, r.t.. (ii) toluene, -78 °C to r.t..

Scheme 4 Alternative synthesis route to **9** and application of this method for the preparation of BBr-bridged oligonuclear complexes **(VII)ₙ**. (i) toluene, -78 °C to r.t..

Figure 1 Poly(ferrocenylenes) **I** generated by ring opening polymerisation of ferroceneophanes, the target polymer **(Li[II])ₙ** and its cyclic congener **Li₂[III]**.

Figure 2 The B(bipy)Me-substituted ferrocene **[IV]⁺**, its model system **[IVᴴ]⁺**, and ferricenyltris(ferrocenyl)borate **V**.

Figure 3 Molecular structure of **Li[2]**(12-crown-4)₂·CH₂Cl₂ (hydrogen atoms and Li(12-crown-4)₂ counterion omitted for clarity; thermal ellipsoids at the 50 % probability level). Selected bond lengths [Å], angles [°], torsion angles [°], and dihedral angles [°]: B(1)-C(11) = 1.641(3), B(1)-C(21) = 1.638(3), B(1)-C(1') = 1.634(3), B(1)-C(1'') = 1.642(3), Fe(1)···Fe(2) = 6.697; C(11)-B(1)-C(21) = 105.8(1), C(11)-B(1)-C(1') = 110.3(2), C(11)-B(1)-C(1'') = 109.2(2), C(1')-B(1)-C(1'') = 111.0(2), C(21)-B(1)-C(1') = 109.7(2), C(21)-B(1)-C(1'') = 110.8(2); C(11)-B(1)-C(21)-C(22) = -88.1(2), C(21)-B(1)-C(11)-C(12) = 79.2(2); C(1)C(2)C(3)C(4)C(5)//C(11)C(12)C(13)C(14)C(15) = 1.2,

C(21)C(22)C(23)C(24)C(25)//C(31)C(32)C(33)C(34)C(35) = 2.3,

C(11)C(12)C(13)C(14)C(15)//C(21)C(22)C(23)C(24)C(25) = 77.7.

Figure 4 Molecular structure of **Li$_2$[3]**(12-crown-4)$_4$ (hydrogen atoms and Li(12-crown-4)$_2$ counterions omitted for clarity; thermal ellipsoids at the 50 % probability level). Selected bond lengths [Å], angles [°], torsion angles [°], and dihedral angles [°]: B(1)-C(11) = 1.641(4), B(1)-C(21) = 1.635(4), B(1)-C(1') = 1.648(5), B(1)-C(1'') = 1.655(4), Fe(1)···Fe(2) = 6.731; C(11)-B(1)-C(21) = 104.9(2), C(11)-B(1)-C(1') = 109.8(2), C(11)-B(1)-C(1'') = 109.8(2), C(1')-B(1)-C(1'') = 111.1(3), C(21)-B(1)-C(1') = 110.4(2), C(21)-B(1)-C(1'') = 110.6(2); C(12)-C(11)-B(1)-C(21) = 88.9(4), C(22)-C(21)-B(1)-C(11) = -78.9(3); C(1)C(2)C(3)C(4)C(5)//C(11)C(12)C(13)C(14)C(15) = 1.1, C(11)C(12)C(13)C(14)C(15)//C(21)C(22)C(23)C(24)C(25) = 99.5. Symmetry transformation used to generate equivalent atoms: -x, -y+1, -z+1.

Figure 5 Molecular structure of **6** (hydrogen atoms omitted for clarity; thermal ellipsoids at the 50 % probability level). Selected bond lengths [Å], angles [°], torsion angles [°], and dihedral angles [°]: B(1)-C(1) = 1.598(5), B(1)-C(31) = 1.609(5), B(1)-N(11) = 1.633(4), B(1)-N(21) = 1.565(4), N(11)-C(12) = 1.357(4), N(21)-C(22) = 1.376(4); C(31)-B(1)-C(1) = 118.1(3), C(31)-B(1)-N(11) = 103.9(2), C(31)-B(1)-N(21) = 110.5(3), N(11)-B(1)-C(1) = 110.0(3), N(11)-B(1)-N(21) = 94.3(2), N(21)-B(1)-C(1) = 116.5(3); C(32)-C(31)-B(1)-N(11) = 86.3(3), C(32)-C(31)-B(1)-N(21) = -13.8(4); C(31)C(32)C(33)C(34)C(35)//C(41)C(42)C(43)C(44)C(45) = 1.2, B(1)N(11)C(12)C(22)N(21)//C(31)C(32)C(33)C(34)C(35) = 86.8.

Figure 6 Molecular structure of **10** (hydrogen atoms omitted for clarity; thermal ellipsoids at the 50 % probability level). Selected bond lengths [Å], angles [°], torsion angles [°], and dihedral angles [°]: B(1)-C(31) = 1.629(9), B(1)-C(51) = 1.586(11), B(1)-N(11) = 1.611(9), B(1)-N(21) = 1.573(9), N(11)-C(12) = 1.349(8), N(21)-C(22) = 1.363(9), Fe(1)···Fe(2) = 5.711; C(31)-B(1)-C(51) = 115.0(6), C(31)-B(1)-N(11) = 109.5(5), C(31)-B(1)-N(21) =

110.0(5), N(11)-B(1)-C(51) = 112.8(5), N(11)-B(1)-N(21) = 94.7(5), N(21)-B(1)-C(51) =

113.1(5); C(32)-C(31)-B(1)-N(11) = 110.6(7), C(32)-C(31)-B(1)-N(21) = 7.8(10), C(32)-

C(31)-B(1)-C(51) = -121.3(8), C(52)-C(51)-B(1)-N(11) = -117.0(7), C(52)-C(51)-B(1)-N(21)

=   -11.0(9),   C(52)-C(51)-B(1)-C(31)   =   116.4(7);

C(31)C(32)C(33)C(34)C(35)//C(41)C(42)C(43)C(44)C(45)   =   2.3,

C(51)C(52)C(53)C(54)C(55)//C(61)C(62)C(63)C(64)C(65)   =   2.7,

C(31)C(32)C(33)C(34)C(35)//C(51)C(52)C(53)C(54)C(55)   =   122.5,

C(31)C(32)C(33)C(34)C(35)//B(1)N(11)C(12)C(22)N(21)   =   68.4,

C(51)C(52)C(53)C(54)C(55)//B(1)N(11)C(12)C(22)N(21) = 54.5.

Figure 7 Molecular structure of **[11]PF$_6$** (hydrogen atoms and PF$_6^-$ counterion omitted for clarity; thermal ellipsoids at the 50 % probability level). Selected bond lengths [Å], angles [°], torsion angles [°], and dihedral angles [°]: B(1)-C(11) = 1.599(9), B(1)-C(21) = 1.616(8), B(1)-N(1) = 1.576(8), B(1)-N(2) = 1.562(9); C(11)-B(1)-N(1) = 111.1(5), C(11)-B(1)-N(2) = 112.0(5), C(21)-B(1)-N(1) = 112.2(5), C(21)-B(1)-N(2) = 112.2(5), C(11)-B(1)-C(21) = 111.6(4), N(1)-B(1)-N(2) = 97.0(4); C(11)-B(1)-C(21)-C(22) = 65.7(8), C(21)-B(1)-C(11)-C(12) = -79.9(8); C(1)C(2)C(3)C(4)C(5)//C(11)C(12)C(13)C(14)C(15) = 5.2, C(21)C(22)C(23)C(24)C(25)//C(31)C(32)C(33)C(34)C(35) = 3.7, C(11)C(12)C(13)C(14)C(15)//C(21)C(22)C(23)C(24)C(25) = 77.3.

Figure 8 Cyclic voltammograms recorded at a platinum electrode on CH$_2$Cl$_2$ solutions containing [NBu$_4$][PF$_6$] (0.1 mol l^{-1}) and a) **Li[2]** (0.6 × 10^{-3} mol/l), b) **10** (0.6 × 10^{-3} mol l^{-1}), **[11]PF$_6$** (0.6 × 10^{-3} mol l^{-1}); only the Fe(II)/Fe(III) redox waves are shown.

Figure 9 Cyclic voltammogram recorded at a platinum electrode on a CH_2Cl_2 solution containing $[NBu_4][PF_6]$ (0.1 mol l^{-1}) and **Li$_2$[3]** (0.5×10^{-3} mol l^{-1}).

Figure 10 Cyclic voltammogram recorded at a platinum electrode on a CH_2Cl_2 solution containing $[NBu_4][PF_6]$ (0.1 mol l^{-1}) and **[14](PF$_6$)$_2$** (0.5×10^{-3} mol l^{-1}).

Figure 11 The B(bipy)-bridged target polymer **([VI]PF$_6$)$_n$**.

Table 1: Crystallographic Data for **Li[2]**(12-crown-4)$_2$·CH$_2$Cl$_2$, **Li$_2$[3]**(12-crown-4)$_4$, **6**, **10**, and **[11]PF$_6$**.

Compound	**Li[2]**(12-cr.-4)$_2$	**Li$_2$[3]**(12-cr.-4)$_4$	**6**
Formula	C$_{38}$H$_{56}$BFe$_2$LiO$_8$ × CH$_2$Cl$_2$	C$_{66}$H$_{102}$B$_2$Fe$_3$Li$_2$O$_{16}$	C$_{24}$H$_{20}$BFFeN$_2$
M	855.20	1354.53	422.08
T/K	100(2)	173(2)	173(2)
Crystal system	monoclinic	triclinic	monoclinic
Space group	$C2/c$	P-1	$P2_1/c$
a/Å	33.7681(17)	9.7070(10)	9.7151(13)
b/Å	25.2931(11)	11.2570(10)	13.5859(14)
c/Å	22.5567(11)	15.763(2)	14.4080(19)
α/°	90	79.386(8)	90
β/°	122.115(3)	80.220(8)	95.585(11)
γ/°	90	86.776(8)	90
V/Å^3	16317.7(13)	1667.8(3)	1892.7(4)
Z	16	1	4
D_c/g cm^{-3}	1.392	1.349	1.481
F(000)	7200	720	872
μ(Mo-Ka)/mm^{-1}	0.891	0.709	0.819
$2\Theta_{max}$/°	55.12	52.74	51.72
Measured reflections	110409	31017	9524
Unique reflections (R_{int})	18539 (0.0826)	6785 (0.0988)	3611 (0.0812)
Observed reflections [I> 2s(I)]	11675	4688	2420
Parameters refined	955	403	262
$R1$ [I>2s(I)]	0.0328	0.0480	0.0433
$wR2$ [I>2s(I)]	0.0536	0.1105	0.0848
GOOF on F^2	0.885	0.934	0.902
Largest diff. peak and hole/eÅ^3	0.758, -0.862	0.683, -0.521	0.548, -0.509

37

Table 1: continued

Compound	**10**	**[11]PF$_6$**
Formula	C$_{33}$H$_{26}$BFFe$_2$.N$_2$ × 0.5 C$_7$H$_8$ × 0.25 C$_{10}$H$_{10}$Fe	C$_{30}$H$_{26}$BF$_6$Fe$_2$N$_2$P
M	684.64	682.01
T/K	173(2)	145(2)
Crystal system	monoclinic	monoclinic
Space group	$P2_1/c$	$P2_1/c$
a/Å	9.1241(12)	12.1586(14)
b/Å	29.760(3)	21.716(4)
c/Å	23.503(3)	15.4748(15)
α/°	90	90
β/°	101.133(10)	108.429(11)
γ/°	90	90
V/Å^3	6261.7(13)	3876.4(9)
Z	8	4
D_c/g cm^{-3}	1.452	1.169
F(000)	2824	1384
μ(Mo-Ka)/mm^{-1}	1.076	0.836
$2\Theta_{max}$/°	51.40	62.06
Measured reflections	54585	62615
Unique reflections (R_{int})	11719 (0.1293)	11213 (0.0664)
Observed reflections [$I > 2s(I)$]	4710	6713
Parameters refined	827	379
$R1$ [$I>2s(I)$]	0.0620	0.1611
$wR2$ [$I>2s(I)$]	0.0959	0.4180
GOOF on F^2	0.740	2.468
Largest diff. peak and hole/eÅ^3	0.409, -0.426	3.788, -2.035

Table 2: Formal Electrode Potentials $E^{\circ\prime}$ (V $vs.$ FcH/FcH$^+$) and Peak-to-Peak Separations ΔE_p (mV, at 0.2 Vs^{-1}) for the F(II)/Fe(III) Redox Changes Exhibited by compounds **Li[2]**, **Li$_2$[3]**, **6**, **10**, **[11]PF$_6$** and **[14](PF$_6$)$_2$**. [a] Formal electrode potentials for the B(bipy)-centered reduction processes in CH$_2$Cl$_2$: $E^{\circ\prime}$ = -1.29 V (ΔE_p = 90 mV), -2.35 V (peak potential value), and in H$_3$CCN : $E^{\circ\prime}$ = -1.39 V (ΔE_p = 80 mV), -2.13 V (ΔE_p = 100 mV). [b]Formal electrode potentials for the B(bipy)-centered reduction processes: $E^{\circ\prime}$ = -1.38 V (ΔE_p = 130 mV), -2.16 V (ΔE_p = 130 mV).

	$E^{\circ\prime}_{terminal}$	$\Delta E_{p(t)}$	$E^{\circ\prime}_{interior}$	$\Delta E_{p(i)}$	T [°C]	solvent	$\Delta E_{p(FcH)}$
Li[2]	-0.43 / -0.64	90 / 100	---	---	-78	CH$_2$Cl$_2$	100
Li$_2$[3]	-0.51	330	-1.21	210	-78	CH$_2$Cl$_2$	250
6	-0.19	140	---	---	20	CH$_2$Cl$_2$	140
10	-0.03 / -0.21	80 / 70	---	---	20	CH$_2$Cl$_2$	70
[11]PF$_6$[a]	+0.23 / +0.07	110 / 100	---	---	20	CH$_2$Cl$_2$	90
	+0.13 / +0.01	90 / 100	---	---	20	H$_3$CCN	70
[14](PF$_6$)$_2$[b]	+0.03	100	+0.26	90	20	H$_3$CCN	80

Scheme 1
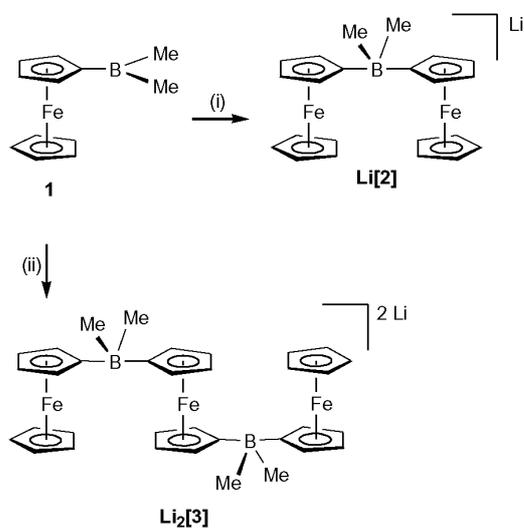
Scheme 2
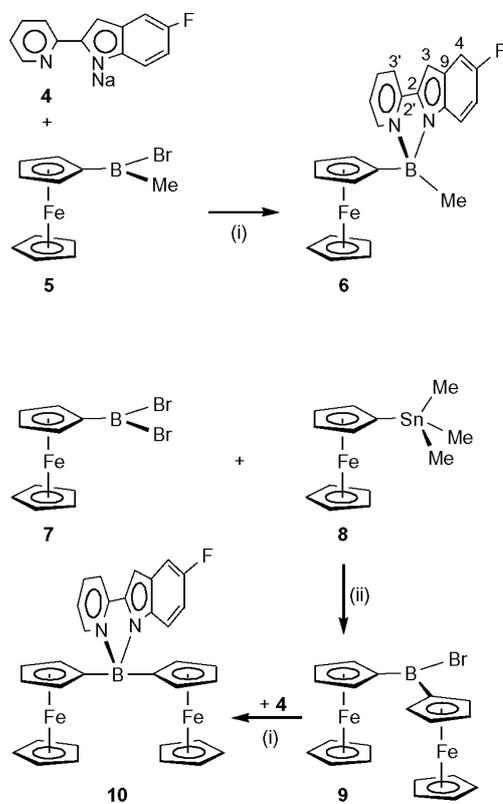
Scheme 3
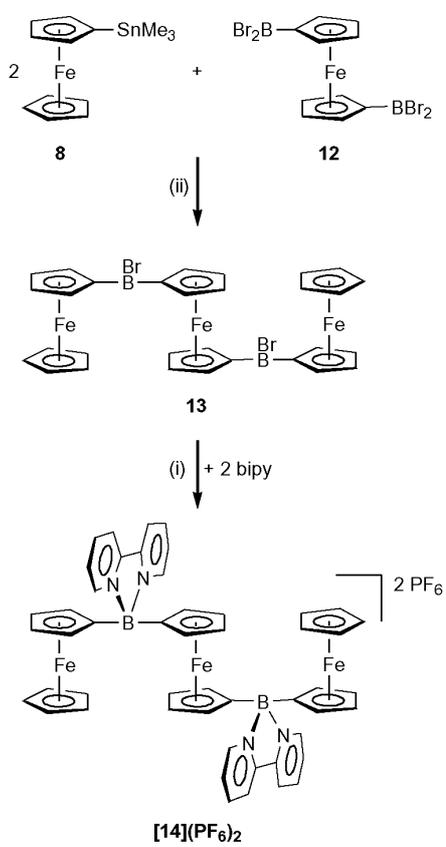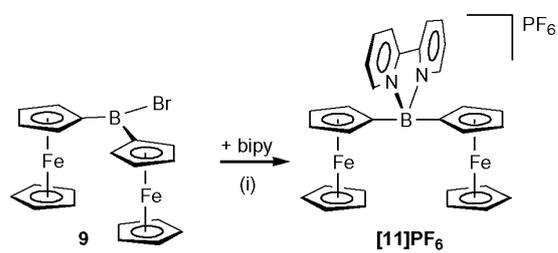
Scheme 4
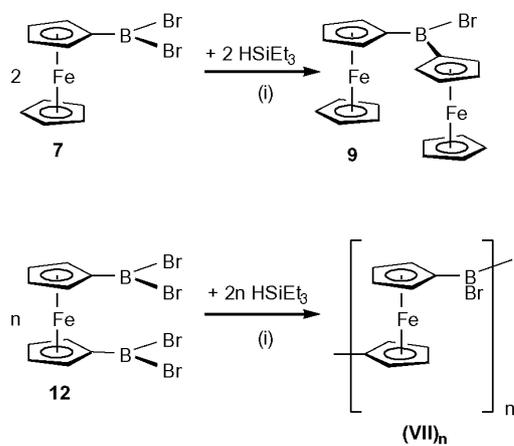
Figure 1
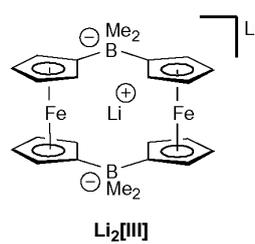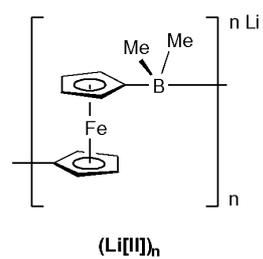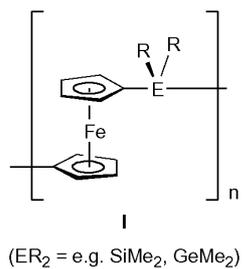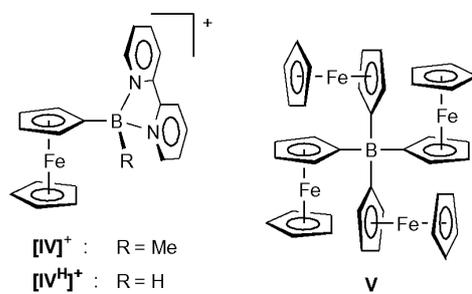
(ER₂ = e.g. SiMe₂, GeMe₂)

(Li[II])ₙ   Li₂[III]

Figure 2

[IV]⁺ : R = Me
[IVᴴ]⁺ : R = H   V

Figure 3

Figure 4

Figure 5

Figure 6

Figure 7

Figure 8

Figure 9

Figure 9

Figure 10

53

Figure 11

([VI]PF$_6$)$_n$
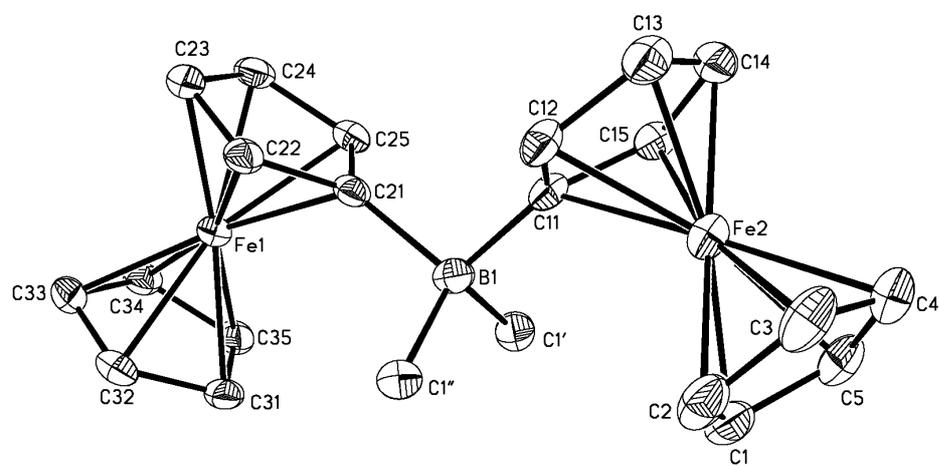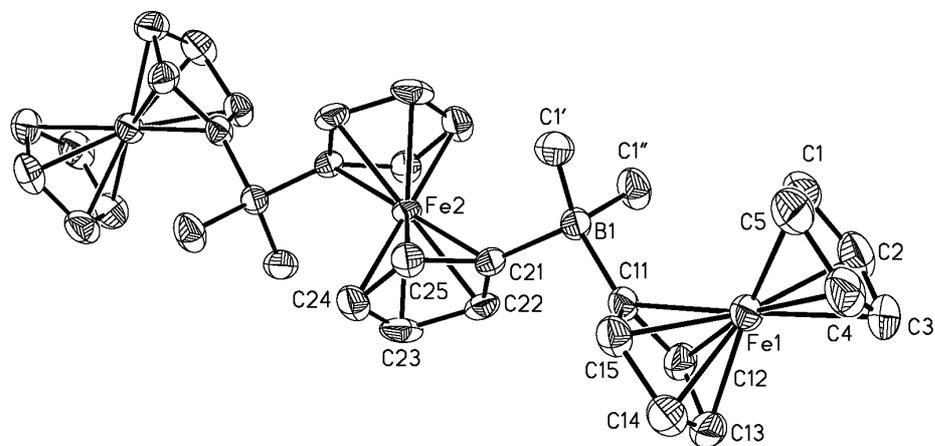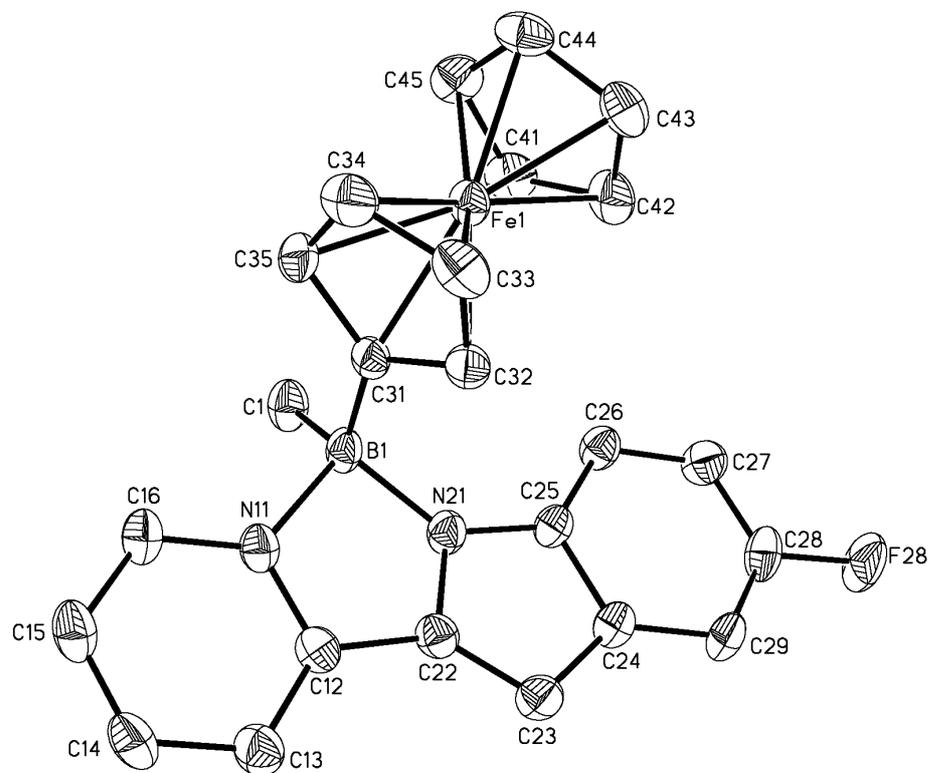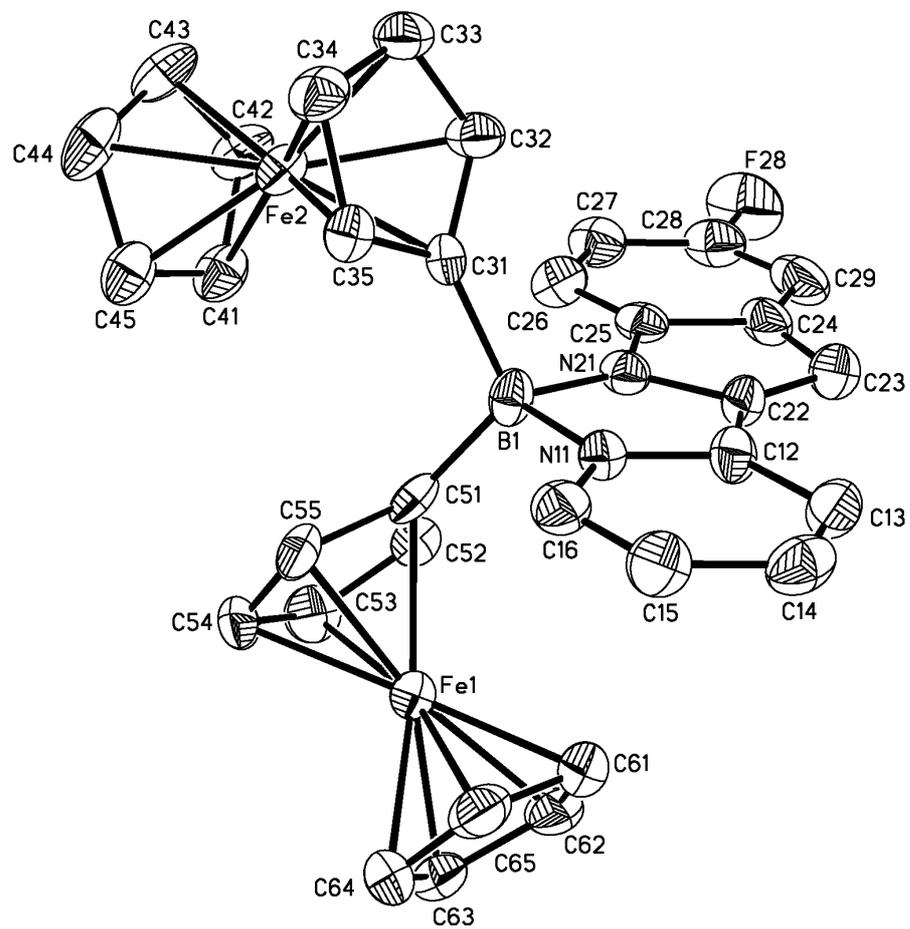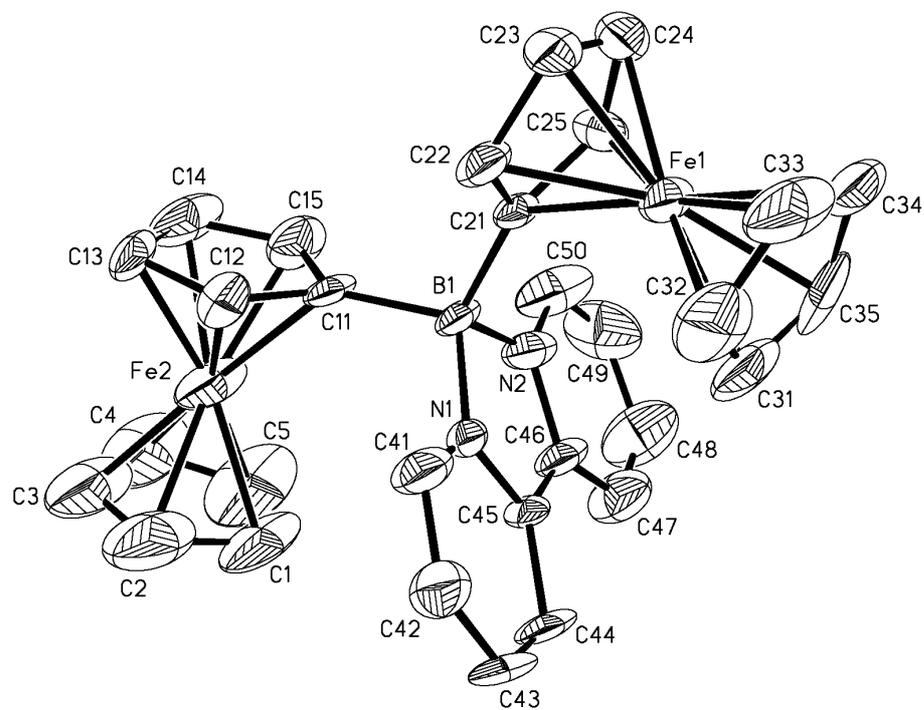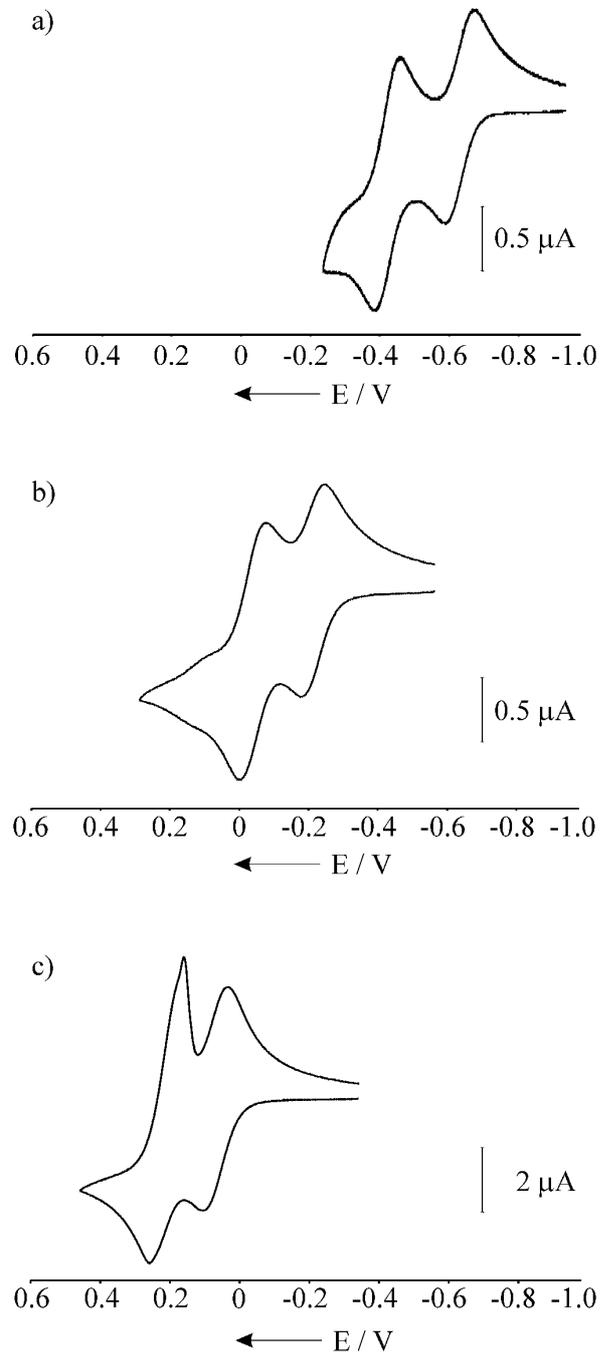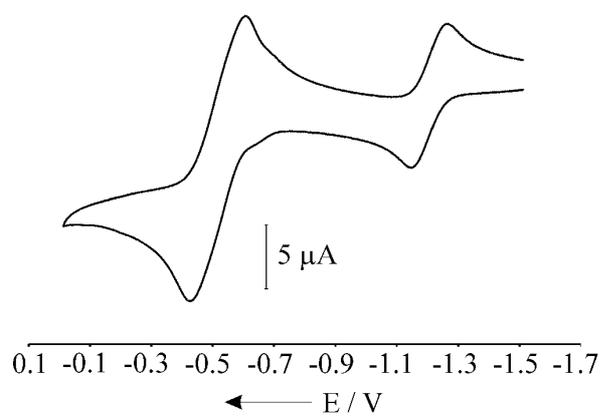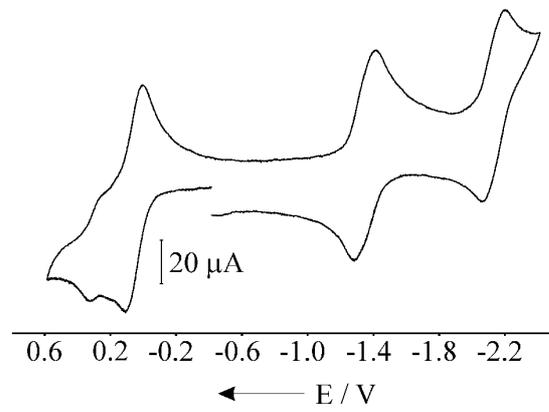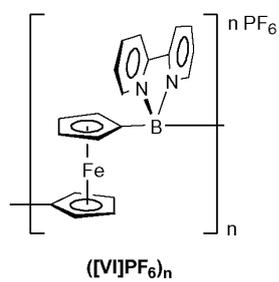
Graphical Abstract
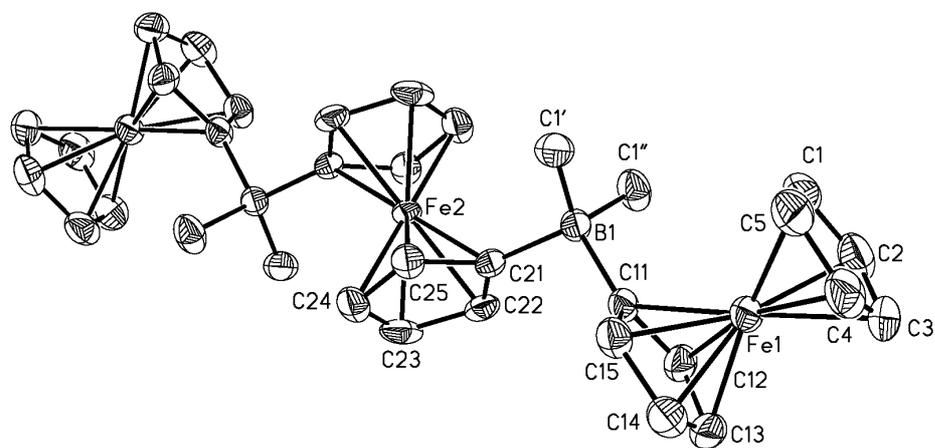
3.10 „Applications of boron-nitrogen- and boron-phosphorus adducts in organometallic chemistry"

K. Ma, M. Scheibitz, S. Scholz, M. Wagner

J. Organomet. Chem. **2002,** *652,* 11 – 19.

ELSEVIER

Applications of boron–nitrogen and boron–phosphorus adducts in organometallic chemistry

Kuangbiao Ma, Matthias Scheibitz, Stefan Scholz, Matthias Wagner *

Institut für Anorganische Chemie, J.W. Goethe-Universität Frankfurt, Marie-Curie-Str. 11, D-60439 Frankfurt (Main), Germany

Dedicated to Professor Karl Wieghardt on the occasion of his 60th birthday

Abstract

Aspects of useful applications of main group Lewis acid–base pairs for the synthesis of sophisticated organometallic architectures are reviewed. Special emphasis is put on the author's own studies of boron–nitrogen and boron–phosphorus adducts and the relevance of the compounds obtained for the development of (i) organometallic materials, (ii) supramolecular entities and (iii) novel homogeneous catalysts. © 2002 Published by Elsevier Science B.V.

Keywords: Ferrocene; Lewis acid–base adducts; tris(1-Pyrazolyl)borate ligands; Coordination polymers; Macrocyclic compounds

1. Introduction

The purpose of this paper is to give a review of a useful synthesis approach to organometallic compounds based on the formation of boron–nitrogen adduct bonds. Our aim is to facilitate the preparation of sophisticated molecular architectures and to generate specific materials which would be much harder to obtain using conventional organic synthesis. To illustrate applications of boron–nitrogen adducts in organometallic chemistry, examples from four different areas have been selected: (1) charge transfer polymers; (2) redox-active macrocycles; (3) switchable ansa-metallocenes and (4) redox-active tris(1-pyrazolyl)borate ligands.

The general concept is summarized in Fig. 1: Two metal complexes, M_1 and M_2, linked by a C–C single bond or a C=C double bond (left), are put face to face to the isoelectronic boron–nitrogen bridged species (right).

Using B–N rather than C–C bonds offers several advantages. First, boron–nitrogen adducts are self-assembling. It can obviously be quite difficult to form C–C bonds in high yield, but it is generally very easy to

add a Lewis basic nitrogen-containing fragment to a Lewis acidic boron-containing fragment and to rely on Lewis acid–base pairing. Second, B–N adduct formation is reversible, and the strength of the respective bond can be influenced by choice of appropriate substituents at boron and nitrogen. It is therefore not just possible to link two fragments together, but one can also separate them again without destroying the individual components.

It is worth mentioning, that self-assembly and reversible bond formation are two key features which make hydrogen bonds so important in nature. In some way, B–N adducts behave similar to hydrogen bridges. However, in most cases they are stronger and therefore easier to control, and they are less destructive to sensitive organometallic compounds than proton donors.

2. Synthesis and physical properties of ferrocenylboranes

Various ways to synthesize borylated organometallic compounds are known to-date. Boryl substituents can be introduced conveniently into the parent complexes by electrophilic substitution with boron halides, which works particularly well in the case of ferrocene, ruthe-

---

* Corresponding author. Fax: +49-69-798-29260.

*E-mail address:* matthias.wagner@chemie.uni-frankfurt.de (M. Wagner).
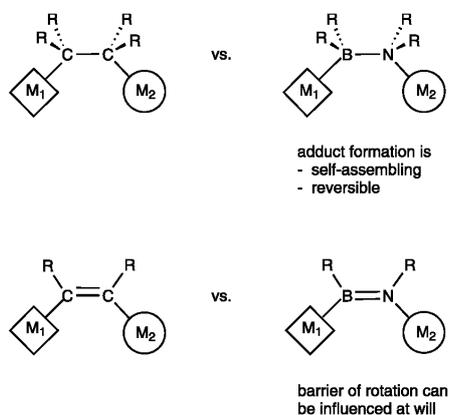
Fig. 1.

nocene and cymantrene (cyclopentadienyl manganese tricarbonyl) [1–3].

Ferrocene reacts with BBr_3 in boiling hexane cleanly and in almost quantitative yield. Depending on the stoichiometry, one or two BBr_2 substituents can be attached to the organometallic backbone to give $FcBBr_2$ (**1**) and 1,1'-fc$(BBr_2)_2$ (**2**), respectively [Fc = $(C_5H_5)Fe(C_5H_4)$; fc = $(C_5H_4)_2Fe$; Fig. 2]. If BBr_3 is employed in large excess, the 1,1',3-triborylated derivative **3** and the 1,1',3,3'-tetraborylated ferrocene **4** are formed in the reaction mixture as well (Fig. 2).

Since the separation and isolation of these species is difficult, **4** is better synthesized by the reaction of ferrocene in neat BBr_3, thereby ensuring exhaustive tetraborylation [4]. Only for the generation of triborylated **3** the selectivity problem has not been solved so far. It can, however, be circumvented by treating monoalkyl ferrocene (rather than ferrocene itself) with boron tribromide under the same reaction conditions as in the case of **4**. As a result, 1-alkyl-1',3,3'-triboryl ferrocene **3a** is obtained in high yield [5].

The molecular structure of $FcBBr_2$ **1** has been investigated by X-ray crystallography (Fig. 2) [6]. The boryl substituent was found to be bent toward the iron atom by a dip angle of almost 20°. A similar structural feature has been observed for the related complexes
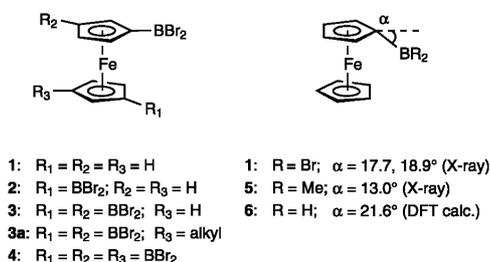
$FcBMe_2$ (**5**) [7] and 1,1'-fc$(BBr_2)_2$ (**2**) [8]. In contrast, the diisopropylamino derivative 1,1'-fc$[B(N^iPr_2)_2]_2$ which bears boryl groups of significantly reduced Lewis acidity, shows no bending of the C_5H_4–$B(N^iPr_2)_2$ moieties [8]. Theoretical calculations based on density functional theory (DFT) have been performed on the model system $FcBH_2$ (**6**) and proved to be in excellent agreement with the experimental findings (Fig. 2) [6]. According to these calculations, an interaction between filled d-type orbitals at iron and the empty p orbital of boron causes bending of the boryl substituent toward the central iron atom. Obviously, the Fe–B interaction becomes stronger with increasing Lewis acidity of the BR_2 side chain. This suggests, that the oxidation state of the iron atom might influence the Lewis acidity of the boryl substituent, and that the redox potential of the Fe(II)/Fe(III) transition should reflect the coordination state of the boron center. This assumption is in accord with cyclic voltammetric measurements: The redox potential (vs. SCE) of the Fe(II)/Fe(III) wave rises from $E^{\circ\prime} = 0.44$ V in parent ferrocene to about 0.65 V in the diborylated derivative 1,1'-fc$(BMe_2)_2$ (**7**) (Fig. 3) [9].

This can easily be explained by the π electron withdrawing nature of the three-coordinate boron atom. When two equiv. of γ-picoline (pic) are added, the Fe(II)/Fe(III) redox potential drops dramatically: The B–N diadduct **8** (Fig. 3) is as easy to oxidize as decamethylferrocene [$E^{\circ\prime}$ (**8**) = −0.12 V vs. SCE; CH_2Cl_2] [9]. This is an important point, because decamethylferrocene is a widely used electron donor in organometallic charge-transfer (CT) complexes—just to mention Miller's molecular ferromagnet $[(C_5Me_5)_2Fe]^+[TCNE]^-$ [10]. The potential of $FcBR_2$ to act as a one-electron donor after a Lewis base has been added is dependent on the nature of the substituents R at boron, which influence the stability of the corresponding base adducts both sterically and electronically. This has been concluded, for example, from reactions of the electron acceptor **9** with various derivatives of ferrocenylboranes.[11] In the case of $FcBMe_2$ **5**, no B–N adduct is formed between the boron atoms and the Lewis-basic pyrazolyl sidearms of **9**. Consequently, no electron transfer from iron to the


1: $R_1 = R_2 = R_3 = H$
2: $R_1 = BBr_2$; $R_2 = R_3 = H$
3: $R_1 = R_2 = BBr_2$; $R_3 = H$
3a: $R_1 = R_2 = BBr_2$; $R_3 = $ alkyl
4: $R_1 = R_2 = R_3 = BBr_2$

1: R = Br; α = 17.7, 18.9° (X-ray)
5: R = Me; α = 13.0° (X-ray)
6: R = H; α = 21.6° (DFT calc.)

Fig. 2.

R = BMe_2
7

R = BMe_2·pic
8
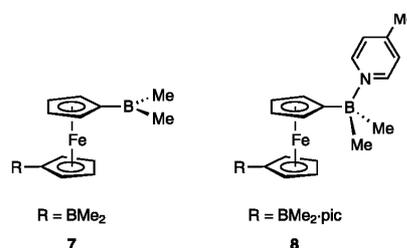
Fig. 3.
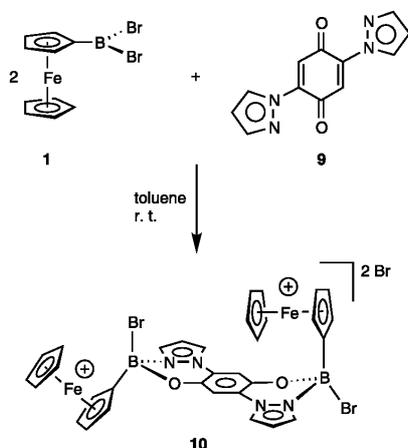
Scheme 1.

quinone ring takes place. In contrast, $FcBBr_2$ **1**, which tends to form strong adducts with aromatic amines, gives an immediate redox reaction with **9**, thereby generating the dinuclear complex **10** in quantitative yield (Scheme 1).

Complex **10** features ferrocene in its Fe(III) state, as well as a hydroquinone core. Given this background, ferrocenylboranes appear to be useful starting materials for the synthesis of (polymeric) CT complexes exploiting the advantages of B–N adduct formation.
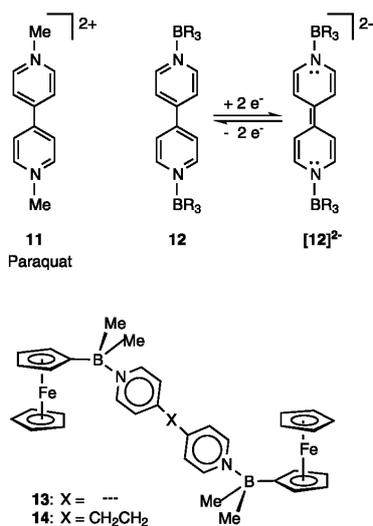

Fig. 4.

3. Ferrocene-based charge-transfer complexes with a boron–nitrogen backbone

Fig. 4 shows the well-known organic electron acceptor paraquat **11**. The molecule is able to reversibly accept two electrons and thus exists in three stable oxidation states [12]. If the $[CH_3]^+$ cations are replaced by the isoelectronic boranes, the B–N diadducts **12** are obtained, which exhibit qualitatively similar electrochemical features as paraquat [13]. Upon addition of electrons, the aromatic system **12** is first transformed into a semiquinone and then into the quinoid dianion $[12]^{2-}$ (Fig. 4).

If one of the substituents R at boron equals ferrocene, the dinuclear aggregate **13** is obtained [9]. In compound **13**, which features two ferrocene donors linked by a paraquat-type electron acceptor, the B–N adducts serve three purposes: (i) they are holding the three components together, (ii) they activate the ferrocene donor, which is oxidized at a significantly lower value than parent ferrocene (**13**: $E^{\circ\prime} = +0.17$ V; FcH: $E^{\circ\prime} = +0.49$ V; DMF vs. SCE), (iii) they activate the acceptor, which can be reduced at less negative potentials than 4,4′-bipyridine itself (**13**: $E^{\circ\prime} = -1.20$, -1.75 V; 4,4′-bipyridine: $E^{\circ\prime} = -1.84$, -2.38 V; DMF vs. SCE) [9].

Complex **13** possesses a highly unusual dark purple color indicative of charge transfer interactions within this molecule. When the extended π-electron system of bipyridine is disrupted by insertion of an ethylene spacer into its central C–C bond, the paraquat-like acceptor is destroyed. Consequently, the color of the respective dinuclear complex **14** changes to yellow (Fig. 4) [9].

Treatment of $1,1'$-$fc(BMe_2)_2$ (**7**) with 4,4′-bipyridine yields a dark purple precipitate, which is insoluble in all common solvents [9]. Its structure in the solid state was determined by high resolution X-ray powder diffraction [14]. The material consists of polymeric chains with
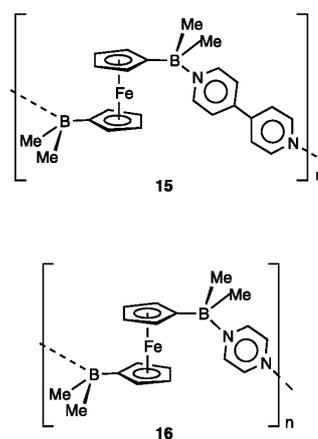

Fig. 5.

alternating ferrocene and bipyridine units (**15**; Fig. 5). Solid **15** can be handled in air without decomposition and is stable up to 240 °C as has been proven by DSC measurements [9].

An analogous green charge transfer polymer **16** (Fig. 5) has been produced from 1,1′-fc(BMe₂)₂ (**7**) and pyrazine and was structurally characterized by single crystal X-ray diffraction [15].

4. Ferrocene-based electron sponges with boron–nitrogen backbone

The two-electron acceptor diquat (**17**, Fig. 6) is chemically related to paraquat **11** (Fig. 4) and thus possesses a very similar redox behavior. As in the case of paraquat, boron analogues [**18**] (2,2′-bipyridylboronium cations) [16] of the diquat molecule exist, which are readily available from the reaction of halogenoboranes with 2,2′-bipyridine. Starting from **1**, **2** and **4**, straight-forward high-yield syntheses of the ferrocenyl 2,2′-bipyridylboronium cations **19**, **20** and **21** have been reported (Fig. 6) [17].

The compounds are highly soluble in polar organic solvents and, except of those derivatives bearing a bromo substituent R at boron, they are stable towards air and moisture. In **19**, **20** and **21**, one, two, and four cationic [B(R)bipy]$^+$ acceptors (R = Br, alkyl, OR*, NR$_2^*$) are covalently attached to a ferrocene donor. All derivatives of these complexes exhibit a dark purple color. The extinction coefficients of the corresponding absorptions in the visible region of the electronic
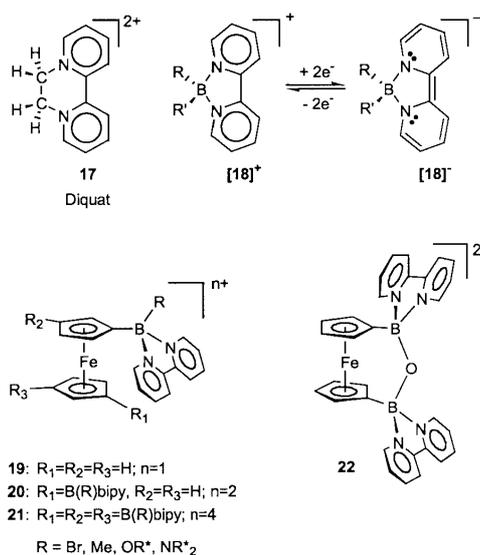
spectrum correlate with the number of pendent [B(R)bipy]$^+$ units. Moreover, ESR spectra of the reduced radical species indicate admixture of Fe-d orbitals to the bipyridine π system. It has therefore been suggested, that the intense color of **19**–**21** is due to a (weak) electronic interaction between the ferrocene center and the bipyridylboronium substituents [17].

In DMF solution and under an inert atmosphere, **19**, **20** and **21** display one chemically reversible oxidation and two consecutive reversible reduction processes. They are thus capable of storing three, five and nine electrons, respectively. There is no significant electronic communication between the individual [B(R)bipy]$^+$ fragments in **20** and **21** [17]. This situation changes when the boron centers of **20** are connected by an oxo bridge. The resulting ansa-ferrocene **22** (Fig. 6) shows four well-resolved one-electron reduction steps rather than the two two-electron reduction waves that had been observed in the case of **20** [18]. It can thus be concluded, that an oxygen bridge significantly promotes the electronic communication between two 2,2′-bipyridylboronium units.

Complexes **20** and **21**, being able to tolerate the loss of one electron, as well as the addition of four and eight electrons, respectively, possess a particularly high redox aptitude. Incorporation of these building blocks into linear or dendritic polymers may therefore lead to the development of efficient novel electron storage media. On principle, the aimed-for macromolecules can be generated either by connecting **20** and **21** via their boron atoms, or by treating the ferrocenylboranes **2** and **4** with ligands possessing at least two chelating Lewis basic sites.

The bromo derivatives (R = Br) of **19**, **20**, and **21** are prone to hydrolysis and alcoholysis. This has been employed for the synthesis of the oxo-bridged species **23** (Fig. 7) [19].

Attempts to apply the controlled hydrolysis of the difunctional complex **20** (R = Br) to the synthesis of linear macromolecules have not been successful so far. Treatment of **20** (R = Br) with one equivalent of water in the presence of triethylamine yields the BOB-bridged


17
Diquat
[**18**]$^+$
[**18**]$^-$

19: R₁=R₂=R₃=H; n=1
20: R₁=B(R)bipy, R₂=R₃=H; n=2
21: R₁=R₂=R₃=B(R)bipy; n=4

R = Br, Me, OR*, NR*₂

22

Fig. 6.

23

**24**: R = H
25: R = CH₂CH₂OH
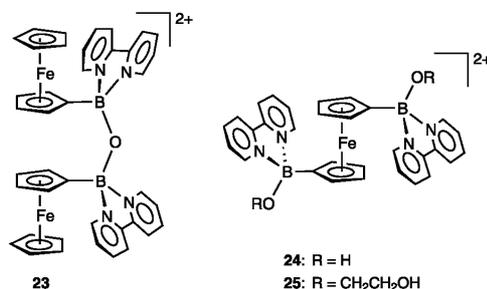
Fig. 7.

ansa-ferrocene **22** (Fig. 6) rather than the corresponding polymer [18]. When excess water is used, the reaction stops at the stage of the open-chain mononuclear hydroxy derivative **24** [19]. Glycol, which is a potential alternative to water as bridging element, has also been tried. However, the reaction rate of an equimolar mixture of **20** (R = Br) and glycol was found to be very low even after addition of excess triethylamine [20]. Only when **20** (R = Br) was dissolved in neat glycol in the presence of triethylamine, a clean and high-yield transformation could be achived. The reaction yielded the air and water stable monomer **25**, which may be polymerized using well-established polyester and poly-urethane chemistry [20].

To generate highly redox-active materials combining the polymeric nature of **15** and **16** with the high solubility and stability of **19–21**, the tetrafunctional

Lewis bases 2,5-bis(2-pyridyl)pyrazine (**26**) [21] and 2,2′:4′,4″:2″,2‴-quaterpyridine (**27**) [22] appeared to be particularly suitable ligands, since they merge 2,2′-bipyridine subunits with pyrazine and 4,4′-bipyridine functionalities, respectively (Fig. 8).

Coordination of one boron atom to **26** turned out to reduce the basicity of the second pyrazine nitrogen atom to such an extent, that a diadduct with a second boron center is not stable anymore. Thus, only mononuclear species like **28** are currently known [23]. In contrast, the 4,4′-bipyridine derivative **27** undergoes formation of stable ferrocenylborane diadducts. However, the reaction of **27** with 1,1′-fc[B(Me)Br]₂ did not lead to polymeric material, but gave the ferrocene-based macrocycle **29** [23]. This is quite a remarkable result, given the fact, that the molecule possesses four chiral boron centers. Ring closure can only occur, if all of them are in the right conformation. Complex **29** was character-ized by NMR spectroscopy, ESI mass spectrometry, cyclic voltammetry and GPC measurements [23]. The structure of a related macrocycle **30**, synthesized from 1,1′-fc[B(Me)(NMe₂)₂]₂ and 2,5-di(pyrazol-1-yl)hydro-quinone (**9**), was elucidated by high resolution X-ray powder diffraction (Fig. 8) [24].

The factors driving the above-mentioned reactions towards macrocycle rather than polymer formation are still under investigation.


26   **27**

28

29

30
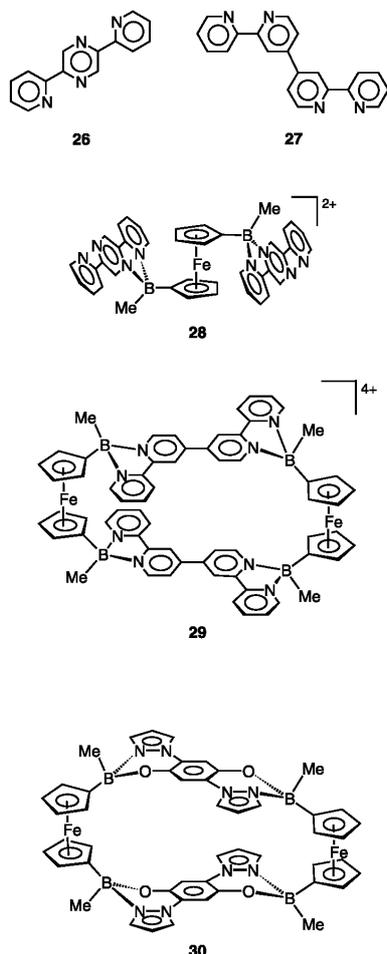
Fig. 8.

5. Ferrocene-based redox-active macrocycles

Boron–nitrogen adduct formation has already been employed successfully for the specific synthesis of large cyclic frameworks.

Ferrocenophanes with bowl-shaped ansa-bridges like **31** [25] (Fig. 9) are promising building blocks for the generation of beltene-like receptor molecules. Various derivatives of **31** are readily accessible from pyrazoles and diborylated ferrocenes, 1,1′-fc[B(R)Br]₂, in multi-gram quantities; most of them (e.g. R = Me, R# = 3,4,5-H) were found to be stable toward air and moisture [26,27].

Cyclic oligomers of **31** possessing a large cavity of well-defined size can be generated by connecting the pyrazolyl rings with rigid spacers. The bridging elements are best attached to the 4-positions of the pyrazoles in order to avoid isomer formation. The reaction of the di(pyrazolyl) ligand **32** with 1,1′-fc[B(Me)Br]₂ results in a mixture of compounds possessing rather similar NMR spectra [19]. From the crude product, the cyclic dimer **33** and the macrocyclic trimer **34** were isolated by GPC separation and characterized by NMR spectroscopy and ESI mass spectrometry (Fig. 9) [19]. Other products possessing even higher molecular masses than **34** were also assembled in the course of the reaction.

31

32

33

34
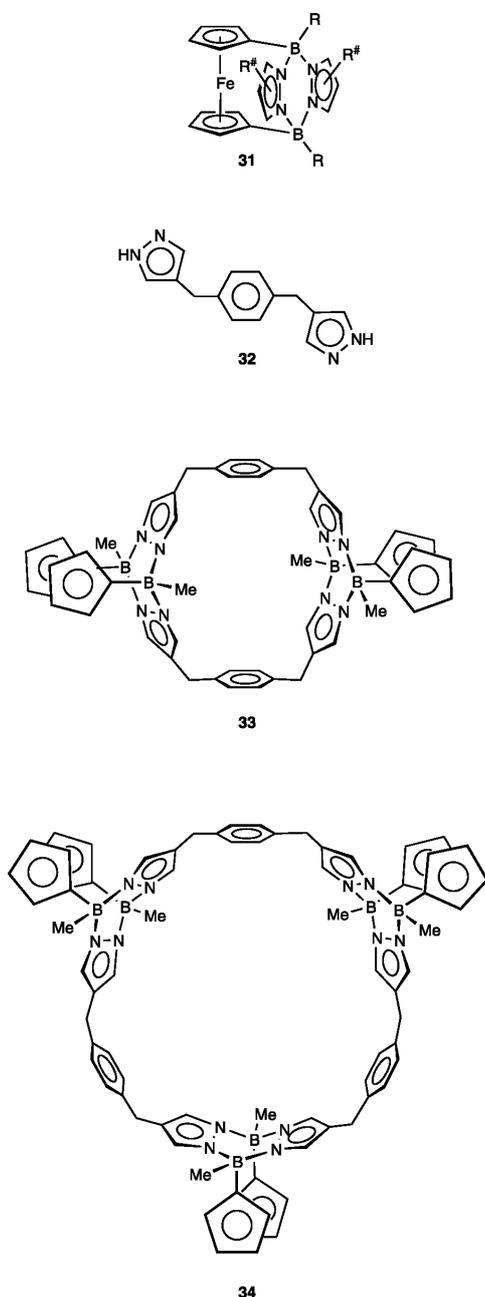
Fig. 9.

All ferrocene units in **33** and **34** have been fixed at the respective macrocyclic framework with both their cyclopentadienyl rings. Any motion of these redox-active groups relative to the main body of the molecule is

prevented. Oxidation of the ferrocene units in **33** and **34**, which is fully reversible, thus generates positive point charges at well-defined positions alongside the cavity. Moreover, derivatives of the bridging ligand **32** bearing substituents, e.g. at the 3,5-positions of the pyrazolyl rings are easily accessible. Following the general synthesis approach for **33** and **34**, it should therefore be possible to design receptor molecules offering a cavity of tailor-made charge, size, hydrophilicity and even chirality. Potential applications in the field of supramolecular chemistry, with the main focus being placed on anion recognition, are currently under investigation.

Recently, an anionic ferrocene-based macrocycle **35** was discovered, which efficiently encapsulates Li^+ cations [7]. The molecule was assembled from 1,1'-fc(BMe$_2$)$_2$ (**7**) and [(C$_5$H$_4$)$_2$Fe]Li$_2$ via B–C adduct formation (Fig. 10).

Work is currently in progress to investigate the stability of the supramolecular complex in solution, the affinity of **35** towards other metal cations and the effect of cation complexation on the ferrocene redox potential.

6. Metallocenes with switchable ansa-bridges

As has already been pointed out, B–N and B–P adducts are not only self-assembling, but can often be cleaved again without destruction of the Lewis acidic or basic components.

It has been suggested that metallocenes bearing a BR$_2$ substituent at one cyclopentadienyl ring and NR$_2$ or PR$_2$ substituents at the other will establish an ansa-bridge as the result of intramolecular acid–base pairing (viz. the ferrocene derivatives **36** and **37**; Fig. 11) [28]. This structural motif would give rise to a ligand sphere, whose conformational rigidity can be influenced at will: while the ansa-bridged form is preferred at low temperature, the adduct equilibrium will be shifted toward an open-chain conformation at elevated temperature.

The stability of the interannular bridge further depends on the choice of substituents at boron, as exemplified in the case of complex **37**. When R = Me, the most efficient way to supply the electron-deficient boron centers with additional electron density lies in the formation of interannular P–B σ-donor bonds. How-


35

Fig. 10.

Fig. 11.

Fig. 12.
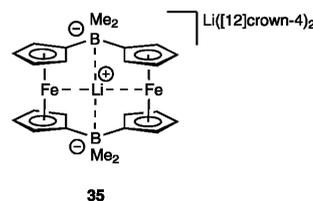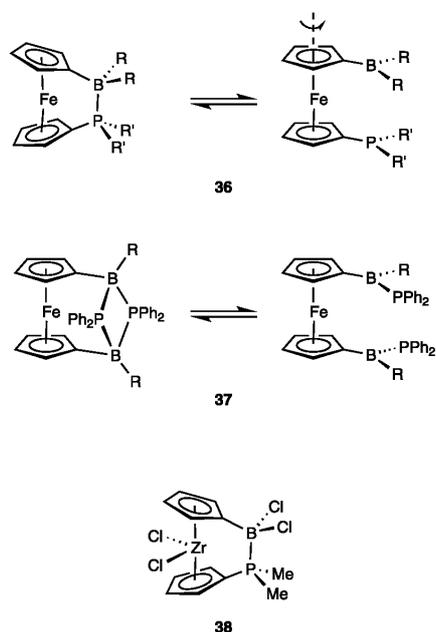
ever, **37** (R = Me) exhibits a remarkable dynamic behavior in its NMR spectra, which indicates a continuous and very fast breaking and re-forming of the B–P ansa-bridge [28]. When R = NR_2^*, N–B π-bonding leads to a significant stabilization of the three-coordinate boron centers. Thus, **37** (R = NR_2^*) adopts an open-chain conformation even at low temperature [28,29].

In the meantime, the concept of 'switchable ansa-bridges' has also been successfully applied to zirconocene chemistry (Fig. 11). Ansa-zirconocenes like **38** appear to be useful catalysts for the homogeneous polymerization of olefins [30]. Depending on the specifically optimized substitution pattern at boron and phosphorus, thermoplastics with tailor-made crystallinity, melting point or glass transition point are obtained. Some of the special properties of these catalysts, which are especially suited for making copolymers and block copolymers, can clearly be attributed to the influence of the donor–acceptor bridge.

7. Ferrocene-based tris(1-pyrazolyl)borate ligands

tris(1-Pyrazolyl)borates ('scorpionates') are today a well-established class of ligands (**39**; Fig. 12, substituents R^1–R^3 at two pyrazolyl rings omitted for clarity) [31,32]. In most complexes, the monoanionic molecule acts as a tripodal six-electron donor. A huge number of derivatives can be generated by varying the group R at boron or the substituents in the 3-, 4- and 5-position of the three pyrazolyl rings.
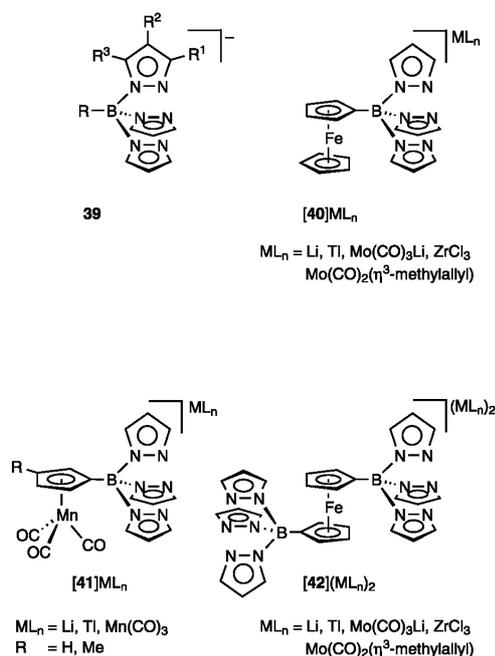
Scorpionate ligands with very specific steric and electronic features are thus easily accessible and have found an extraordinarily wide range of applications (e.g. analytical chemistry, catalysis and metallo-enzyme modelling, materials science) [32,33]. The synthesis of tris(1-pyrazolyl)borates is straightforward and takes advantage from the facile formation of boron nitrogen-bonds; a common procedure starts from $NaBH_4$ and three equivalents of an appropriate pyrazole derivative [31,32].

Recently, ferrocene- and cymantrene-based tris(1-pyrazolyl)borates **[40]**Li–**[42]**Li$_2$ (Fig. 12) have been developed (i) as a contribution to the rapidly growing field of redox-active ligands and (ii) for the synthesis of oligonuclear transition metal complexes [34,35]. Since neither metallocenylboranes, $McBH_2$, nor metallocenylborates, $[McBH_3]^-$, are known to-date (Mc = ferrocenyl, cymantrenyl), alternative starting materials were required. For the synthesis of **[40]**Li and **[41]**Li, metallocenyl dibromoboranes $FcBBr_2$ (**1**) and $CymBBr_2$ have been applied successfully [Cym = $(C_5H_4)Mn(CO)_3$], while the aminoboryl derivative 1,1′-fc[B(NMe$_2$)$_2$]$_2$ had to be used to obtain high yields of **[42]**Li$_2$ and to prevent the formation of ansa-ferrocenes **31** (Fig. 9).

A variety of metal complexes [40]ML_n, [42](ML_n)$_2$ [ML_n = Li, Tl, Mo(CO)$_3$Li, Mo(CO)$_2$(η^3-methylallyl), ZrCl$_3$] and [41]ML_n [ML_n = Li, Tl, Mn(CO)$_3$] have been synthesised and many of them structurally characterised by X-ray crystallography [35,36]. Among those, the Tl(I) complexes showed interesting deviations from the common tridentate binding mode. [40]Tl and [41]Tl (R = H) are polymeric, whereas [41]Tl (R = Me) features cyclic tetramers in the solid state. In all three cases, each scorpionate fragment binds to two different thallium atoms, thereby adopting a bridging position. According to cyclic voltammetric measurements, the Fe(II)/Fe(III) redox potential of [40]ML_n and [42](ML_n)$_2$ is influenced by the chemical nature of the metal complex fragment ML_n coordinated to the scorpionate ligand.

In the (hetero)trinuclear complexes [40]$_2$M [M(II) = Mn, Fe, Co, Ni, Zn; Fig. 13], the two ferrocenyl substituents are electronically non-communicating [37]. However, a striking exception was observed when Cu(II) was employed as the central metal ion. Complex [40]$_2$Cu exhibits two well-resolved one-electron processes, corresponding to the sequential oxidation of the two Fc moieties ($\Delta E^{\circ\prime} = 130$ mV), which indicates some electronic interaction between the two iron atoms in this molecule [37].

It has also been possible to attach two different ferrocenyl scorpionate ligands to the same central metal ion (e.g. **43**, Fig. 13) [38]. When this compound is treated with the difunctional tris(1-pyrazolyl)borate [42]Li$_2$, slow ligand exchange processes take place, leading to the formation of larger oligonuclear aggregates like **44** and **45** (Fig. 13), which have been isolated from the equilibrating mixture by gel permeation chromatography.[38] In the absence of excess ligand, chloroform

solutions of **43**, **44** and **45** are apparently stable for extended periods of time.

8. Further perspectives

Numerous promising applications of B–N and B–P adducts in organometallic chemistry can be envisaged for the future.

The highly directional and self-assembling donor-acceptor bonds are an ideal tool for the crystal engineering of organometallic solids which may lead to novel materials possessing interesting electronic, magnetic or optical properties. Recently, Manners et al. developed novel strategies for the transition metal-catalyzed formation of phosphorus–boron bonds [39]. The resulting rings, chains and macromolecules may find use as precursors to boron phosphide semiconductors.

The reversible breaking and re-forming of main group Lewis acid–base pairs being incorporated into the ligand sphere of a transition metal gives access to organometallic compounds with tailor-made conformational rigidity—e.g. metallocenes with switchable ansa-bridges. As outlined above, this structural motif has already been successfully employed in olefin polymerization. It is likely to find more applications in other areas of homogeneous catalysis. In supramolecular chemistry, switchable B–N adduct bonds as integral part of a receptor framework may help to create molecular cavities whose shape and affinity to certain guest molecules can be influenced at will.

The heavier homologs of boron do not only take part in σ-adduct formation, but π adducts are known as well.

[40]$_2$M
M(II) = Mn, Fe, Co, Ni, Cu, Zn

43

**44**: n = 2
45: n = 3
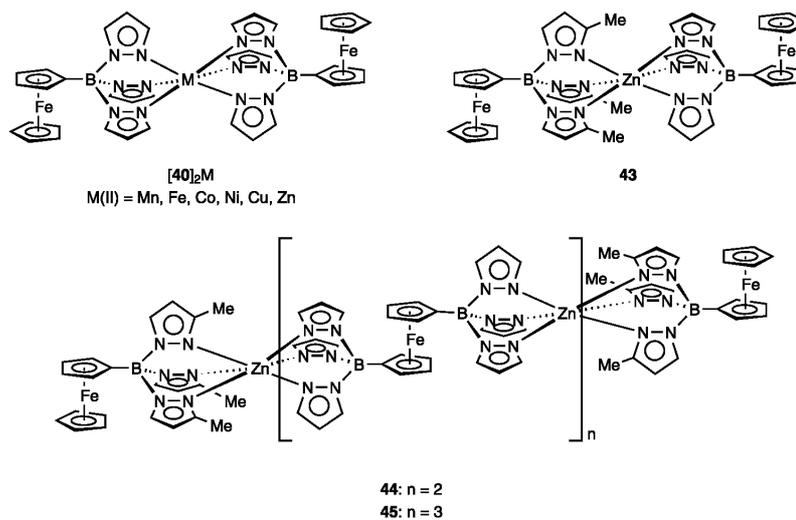
Fig. 13.
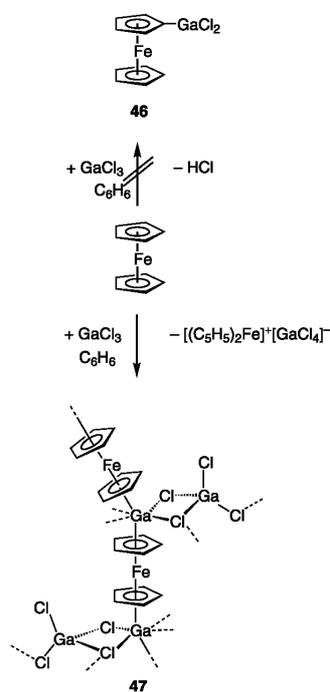
Scheme 2.

Recently, the reaction of ferrocene with gallium trichloride was found to proceed via a completely different pathway as has been observed before in the case of the boron trihalides. No $FcGaCl_2$ (**46**, Scheme 2) is formed, but a redox process yielding $Ga[GaCl_4]$ and ferrocenium tetrachlorogallate takes place instead. From the reaction mixture, crystals of a multidecker sandwich complex **47** featuring an array of alternating Fe(II) and Ga(I) ions were obtained [40].

It is evident, that η^5-coordination of Ga(I) ions to metallocenes may not only influence the chemical behavior of the metal complex, but offers yet another way for the rational assembly of large organometallic aggregates.

References

[1] T. Renk, W. Ruf, W. Siebert, J. Organomet. Chem. 120 (1976) 1.
[2] W. Ruf, M. Fueller, W. Siebert, J. Organomet. Chem. 64 (1976) C45.
[3] W. Ruf, T. Renk, W. Siebert, Z. Naturforsch. Teil B 31 (1976) 1028.
[4] A. Appel, H. Nöth, M. Schmidt, Chem. Ber. 128 (1995) 621.
[5] U. Dörfler, PhD thesis, University of Bayreuth, 1994.
[6] A. Appel, F. Jäkle, T. Priermeier, R. Schmid, M. Wagner, Organometallics 15 (1996) 1188.
[7] M. Scheibitz, M. Wagner, manuscript in preparation.
[8] B. Wrackmeyer, U. Dörfler, W. Milius, M. Herberhold, Polyhedron 14 (1995) 1425.
[9] M. Fontani, F. Peters, W. Scherer, W. Wachter, M. Wagner, P. Zanello, Eur. J. Inorg. Chem. (1998) 1453; ibid. 2087.
[10] J.S. Miller, A.J. Epstein, W.M. Reiff, Science 240 (1988) 40.
[11] L. Ding, F. Fabrizi de Biani, M. Bolte, P. Zanello, M. Wagner, Organometallics 19 (2000) 5763.
[12] S. Hünig, H. Berneth, Top. Curr. Chem. 92 (1980) 1.
[13] S. Hünig, I. Wehner, Liebigs Ann. Chem. (1989) 299.
[14] R.E. Dinnebier, M. Wagner, F. Peters, K. Shankland, W.I.F. David, Z. Anorg. Allg. Chem. 626 (2000) 1400.
[15] M. Grosche, E. Herdtweck, F. Peters, M. Wagner, Organometallics 18 (1999) 4669.
[16] S. Hünig, I. Wehner, Heterocycles 28 (1989) 359.
[17] F. Fabrizi de Biani, T. Gmeinwieser, E. Herdtweck, F. Jäkle, F. Laschi, M. Wagner, P. Zanello, Organometallics 16 (1997) 4776.
[18] L. Ding, K. Ma, F. Fabrizi de Biani, M. Bolte, P. Zanello, M. Wagner, Organometallics 20 (2001) 1041.
[19] K. Ma, M. Wagner, manuscript in preparation.
[20] L. Ding, K. Ma, M. Bolte, F. Fabrizi de Biani, P. Zanello, M. Wagner, J. Organomet. Chem. 637-639 (2001) 390.
[21] A. Neels, H. Stoeckli-Evans, Chimia 47 (1993) 198.
[22] A.J. Downard, G.E. Honey, L.F. Phillips, P.J. Steel, Inorg. Chem. 30 (1991) 2260.
[23] L. Ding, K. Ma, G. Dürner, M. Bolte, F. Fabrizi de Biani, P. Zanello, M. Wagner, J. Chem. Soc. Dalton Trans. (2002) 1566.
[24] R.E. Dinnebier, L. Ding, K. Ma, M.A. Neumann, N. Tanpipat, F.J.J. Leusen, P.W. Stephens, M. Wagner, Organometallics 20 (2001) 5642.
[25] F. Jäkle, T. Priermeier, M. Wagner, J. Chem. Soc. Chem. Commun. (1995) 1765.
[26] F. Jäkle, T. Priermeier, M. Wagner, Organometallics 15 (1996) 2033.
[27] E. Herdtweck, F. Jäkle, G. Opromolla, M. Spiegler, M. Wagner, P. Zanello, Organometallics 15 (1996) 5524.
[28] F. Jäkle, M. Mattner, T. Priermeier, M. Wagner, J. Organomet. Chem. 502 (1995) 123.
[29] E. Herdtweck, F. Jäkle, M. Wagner, Organometallics 16 (1997) 4737.
[30] K.A. Ostoja Starzewski, W.M. Kelly, A. Stumpf, D. Freitag, Angew. Chem. 111 (1999) 2588; Angew. Chem. Int. Ed. Engl. 38 (1999) 2439.
[31] S. Trofimenko, Chem. Rev. 93 (1993) 943.
[32] S. Trofimenko, Scorpionates—The Coordination Chemistry of Polypyrazolylborate Ligands, Imperial College Press, London 1999.
[33] F.T. Edelmann, Angew. Chem. 113 (2001) 1704; Angew. Chem. Int. Ed. Engl. 40 (2001) 1656.
[34] F. Jäkle, K. Polborn, M. Wagner, Chem. Ber. 129 (1996) 603.
[35] S. Guo, J.W. Bats, M. Bolte, M. Wagner, J. Chem. Soc. Dalton Trans. (2001) 3572.
[36] F. Fabrizi de Biani, F. Jäkle, M. Spiegler, M. Wagner, P. Zanello, Inorg. Chem. 36 (1997) 2103.
[37] S. Guo, F. Peters, F. Fabrizi de Biani, J.W. Bats, E. Herdtweck, P. Zanello, M. Wagner, Inorg. Chem. 40 (2001) 4928.
[38] S. Guo, M. Wagner, manuscript in preparation.
[39] H. Dorn, R.A. Singh, J.A. Massey, J.M. Nelson, C.A. Jaska, A.J. Lough, I. Manners, J. Am. Chem. Soc. 122 (2000) 6669.
[40] S. Scholz, J. Green, H.-W. Lerner, M. Bolte, M. Wagner, J. Chem. Soc. Chem. Commun. (2002) 36.

4 Lebenslauf

Name	Matthias Scheibitz
Geburtsdatum	11. Mai 1977
Geburtsort	Köln
Staatsangehörigkeit	deutsch
Familienstand	verheiratet mit Sandra Scheibitz, geborene Eberl
Eltern	Dr. Wolfgang Scheibitz
	Beate Scheibitz, geborene Reinicke

Schulbildung

Grundschule	Nidda-Schule (Frankfurt am Main – Nied)	1983 - 1987
Gymnasium	Helene-Lange-Schule (Frankfurt am Main – Höchst)	1987 - 1993
	Friedrich-Dessauer-Gymnasium (Frankfurt am Main – Höchst)	1993 - 1996
Schulabschluss	Abitur	Juni 1996

Zivildienst	Krankenhaus Höchst	Aug. 1996 - Aug. 1997

Studium

Grundstudium	Johann Wolfgang Goethe-Universität Frankfurt am Main	Okt. 1997 - Sept. 1999
Hauptstudium	Johann Wolfgang Goethe-Universität Frankfurt am Main	Okt. 1999 - Jul. 2001

Diplomarbeit	im Arbeitskreis von Prof. M. Wagner	Aug. 2001 - Feb. 2002
	Johann Wolfgang Goethe-Universität	
	Frankfurt am Main	
	„Ferrocenylborane als Bausteine	
	metallhaltiger Koordinationspolymere"	

Promotion	im Arbeitskreis von Prof. M. Wagner	März 2002 - Aug. 2004
	Johann Wolfgang Goethe-Universität	
	Frankfurt am Main	
	„Neue Wege zu funktionalisierten	
	Ferrocenylboranen und borhaltigen	
	Oligoferrocenen"	

Auslandsaufenthalt

Japan	Organometallic Chemistry Laboratory	Juli 2002 - Sept. 2002
	of "The Institute of Physical and	
	Chemical Research (RIKEN)", Tokyo,	
	in der Arbeitsgruppe von Dr. Zhaomin	
	Hou; selbständige Forschung auf dem	
	Gebiet der Lanthanidchemie	

Eidesstattliche Versicherung

Ich erkläre hiermit an Eides statt, dass ich die vorliegende Dissertation über

Neue Wege zu funktionalisierten Ferrocenylboranen

und borhaltigen Oligoferrocenen

selbständig angefertigt und mich anderer Hilfsmittel als der in ihr angegebenen nicht bedient habe, insbesondere, dass aus schriftlichen Entlehnungen, soweit sie in der Dissertation nicht ausdrücklich als solche mit Angabe der entsprechenden Schrift bezeichnet sind, nicht stattgefunden haben.

Frankfurt am Main, 12. September 2004

Matthias Scheibitz